

University of the Witwatersrand

Faculty of Engineering & the Built Environment

School of Mechanical, Industrial & Aeronautical Engineering



A Dissertation for the Master's Degree in Mechanical Engineering

Project Title:	Parameteric Thermal Process Models of Friction Stir Welding
Candidate:	Mehmet Yildirim Uslu
Supervisor:	Professor Claudia Polese School of Mechanical, Industrial & Aeronautical Engineering

Date: 02/02/2017

Declaration

I, hereby declare that this dissertation is my own, unaided work, except where otherwise acknowledged, which is being submitted for a degree in Masters of Science – Mechanical Engineering, at the University of the Witwatersrand, Johannesburg.

It has not been submitted before for any degree or examination at any other university.

.....

M.Y. Uslu

Date: 02/02/2017

*To my family, who have been ever so patient and bearing with the time I have spent
away. I love you all dearly.*

Acknowledgements

I would like to thank the following people, for whom without this study would not be possible:

- Professor Caludia Polese, my supervisor, for her guidance, assistance, advice and criticism throughout this study, for it would not have been possible without her.
- Mr. Mitchell Leering for his assistance, support and opinions, during the experimental process for this study and obtaining the much needed materials, machinery and equipment.
- The Barloworld Lab staff at The University of the Witwatersrand for their assistance.
- My gratitude to Ms Yuthika Sidhoo for her outstanding dedication, assistance and opinions towards this study.

Abstract

The Friction Stir Welding process is a rotating tool, that consists of a specially designed shoulder and pin, that is plunged into the joining line of the required material and traverses along this line. The friction is induced by the rotating tool causes the workpiece material to rise to an operating temperature of 70% to 90% of the workpiece material's melting temperature and resulting in, no phase change, nor any defects associated with phase change, occurs in the workpiece. The increased temperature of the material causes the shear yield strength to drastically decrease thus allowing the two pieces to plasticise, easily stir around the tool and subsequently join. As the tool traverses along the workpiece, the softened material cools in the wake of the rotating tool and recrystallises, forming a ne grained microstructure.

Attempts to develop an innovative tool to correlate the resulting of thermal models with process parameters are scarce. In this work, 6056-T4 and 6082-T6 Aluminum alloy sheets are friction stir welding at different rotational and translational speeds during the experimental aspect and material 2024-T3 for the analytical calculations. The effects of process parameters on the resulting thermal and mechanical properties are investigated. The results show that the use of coolant during the friction stir weld decrease heat generation substantially, this can also affect the force of the weld. It is also observed that the shear strenght of the processed sheet depends strongly on the rotational and translational speeds as weld as the thermal aspect and varies widely within the processed region, this was shown in this study by evaluating the thermal aspects of different weld types namely the Standard tool, Bobbin tool and the innovative tool. In addition. The proposed approach involves determination of the use of the friction stir welding in different thermal conditions and championing the use of an innovative tool.

Date: 02/02/2017

Table of Contents

Declaration	i
Acknowledgements	iii
Abstract	iv
Table of Figures Images Charts and Graphs	xii
List of tables	xxii
List Of Symbols	xxiii
1. Introduction	1
1.1. The Thermal Process Models of Friction Stir Welding	1
1.2. Problem Statement	1
1.3. Statement Purpose	2
1.4. Definition of Concept	2
2. Literature Survey	4
2.1. Process	6
2.2. Thermal Models	8
2.3. Heat Source Models	9
2.3. Examples of Different Heat Sources	12
2.4. Analytical Models	13
2.5. Experimental Welding Conditions	16
2.6. Contact Conditions	17
2.7. General Heat Generation	20
2.8. Contact Shear Stress	23
2.9. Heat Generation Ratios	25

2.10. Estimation of Contact Conditions	26
2.11. Numerical Models	28
2.12. Example of Different Heat Transfer Coefficients	29
2.13. Experimental Aspect	31
2.14. Process Parameters	31
2.15.1. Welding Parameters	32
2.15.2. Experimental Parameters	33
2.15.3. Test Types	33
2.15.3.1. Standard Test	33
2.15.3.2. Hot Water Applied Test	34
2.15.3.3. The Liquid Nitrogen Applied Test	34
3. The Design of Tools	35
3.1. Tool Shoulders	35
3.2. Shoulder Features	35
3.2.1. Concave Shoulder	35
3.2.2. Scroll Shoulder	36
3.2.3. Convex Shoulder	36
3.3. Pin Designs	37
3.3.1. Round-Bottom Cylindrical Pin	38
3.3.2. Flat-Bottom Cylindrical Pin	38
3.3.3. Truncated Cone Pin	40
3.3.4. Addition of Machined Flats on Pins	41
3.3.5. Whorl Pin	42
3.3.6. MX Triflute Pin	42

3.3.7. Trivex Pin	43
3.3.8. Threadless Pin	44
3.3.9. Retractable Pins	44
4. Theoretical Methodology	45
5. Standard Friction Stir Welding: Design and Experimentation	46
5.1. Analytical Estimation of Heat Generation	46
5.1.1. Heat Generation from the Probe	47
5.1.2. Shear Stress for Sticking Condition	47
5.1.3. Shear Stress for Sliding Condition	48
5.2. Heat Generation Ratios	48
5.3. Heat Generation: Summary of Calculations	61
5.3.1. Heat Generation from the Shoulder	61
5.3.2. Heat Generation from the Probe Side Surface and the Probe Tip	61
5.3.3. Total Heat Generation	62
5.4. Standard tool: SOLIDWORKS Design	65
5.5. Standard Tool: Mode Frontier Simulation	69
5.5.1. Boundaries: Standard Tool Design	75
5.5.2. History Charts, Multi History and Parallel Co-Ordinate Charts: Standard Tool Design	79
6. The Bobbin Tool Friction Stir Welding: Design and Experimentation	86
6.1. Heat Generation: Bobbin Tool	95
6.1.1. Heat Generation from the Top Shoulder	95
6.1.2. Heat Generation from the Probe Side Surface	96
6.1.3. Heat Generation from the Bottom Shoulder	96
6.1.4. Total Heat Generated	96

6.2. Mode Frontier Simulation: Bobbin Tool Design	101
6.2.1. Boundaries: Bobbin Tool Design	106
6.2.2. History Charts and Parallel Co-ordinate Charts: Bobbin Tool Design	110
7. Innovative Friction Stir Welding: Design And Experimentation	115
7.1. Heat Generation: Innovative Tool	125
7.1.1. Heat Generation from the Tool Shoulder	125
7.1.2. Heat Generation from the Probe Side	126
7.1.3. Heat Generation from the Probe Tip	126
7.1.4. Heat Generation from a Modified Copper Bush Side Surface	126
7.1.5. Heat Generation : Modified Copper Bush Tip	126
7.1.6. Total Heat Generation for the Innovative Tool	129
7.2. SolidWorks: Innovative Tool Design	131
7.3. Mode Frontier simulation: Innovative tool Design	136
7.3.1. Boundaries : Innovative tool	139
7.3.2. Multi History Charts and Parallel Co-ordinate Charts: Innovative Tool Design	144
8. Heat Loss Conditions	158
8.1. Standard Tool Heat Loss Conditions	158
8.1.1. Heat Dissipation	158
8.1.2. Heat Loss within the Tool	158
8.1.3. Heat Loss by the Top Surface of the Workpiece	158
8.1.4. Heat Loss by the Bottom Surface of the Workpiece	158
8.2. Mode Frontier Simulation: Standard Tool Heat Loss Conditions	163
8.2.1. Boundaries : Standard Tool Heat Loss Conditions	166
8.2.2. Multi History Charts for Standard Tool Heat Loss Conditions	174

8.3. Bobbin Tool Heat Loss Conditions	182
8.3.1. Mode Frontier Simulation: Bobbin Tool Heat Loss Conditions	184
8.3.2. Boundaries : Bobbin Tool Heat Loss Conditions	187
8.4. Multi History Charts for Bobbin Tool Heat Loss Conditions	193
8.5. Innovative Tool Heat Loss Conditions	200
8.5.1. Mode Frontier Simulation : Innovative tool Heat Loss Conditions	202
8.5.2. Boundaries : Innovative Tool Heat Loss Conditions	204
8.5.3. Multi History Charts : Innovative Tool Heat Loss Conditions	212
9. The Modification of Tools	222
9.1. Comparison of Heat Loss and Heat Generation	222
9.2. Mode Frontier for the Comparison of Heat Generation and Heat Loss	222
9.2.1. Multi History Charts for the Comparison of Heat Generation and Heat Loss	222
9.2.2. Multi History Chart: Innovative tool vs The Application of Water and the Application of Air	233
9.3. The Application of Boiling Water to the Innovative Tool	236
9.3.1. Mode Frontier Simulation :The Application of Boiling Water to the Innovative Tool	240
9.3.2. Boundaries: The Application of Boiling Water to the Innovative Tool	242
9.4. Application of a Hot Liquid and/or Liquid Nitrogen to an Innovative Tool	254
10. Chemical Reactions in Welding	260
10.1. Effect of Nitrogen, Oxygen, and Hydrogen	260
10.2. The Increased Size of the Copper Bar	260
10.3. Boundaries : The Increased Size of the Copper Bush	263
11. Preparation and Plans for Experimentation	267
11.1 Design	269
11.2 Conclusion	270

11.2.1. Analytical Conclusion	270
11.2.2. Analytical Heat Loss	270
11.2.3. Simulation Conclusion	271
11.2.4. Simulated Heat Loss	271
12. Experimentation Aspect of Friction Stir Welding	272
12.1 Machinery	272
12.2. Friction Stir Welding: Experiment	281
12.2.1. Performed Weld Results: Standard Tool Experimentation	281
12.2.2. Performed Weld Results: Innovative Tool	283
12.2.3. Innovative Tool Experimentation: Coolant Applied Tests	289
12.3 Force Data Acquisition	291
12.3.1. Standard Tool: Force Data	291
12.3.2 Innovative Tool: Force Data	292
12.4. Temperature Data	295
12.4.1. Standard Tool Temperature Data	295
12.4.2. Innovative Tool Temperature Data	296
12.5. Comparison Of Temperature: Standard Tool Vs Innovative Tool	297
12.6. Coolant Applied Comparisons	298
12.7. Force Data	299
12.7.1. Standard Tool Force Data	299
12.7.2. Innovative tool Force Data	299
12.7.3. Comparison of Force Data: Standard tool Vs Innovative Tool	300
12.8. Discussion of Experimental Benchmark	301
12.8.1. The Standard Tool Friction Stir Welding	301

12.8.2. The Innovative Tool Friction Stir Welding	302
12.8.3. Standard Tool Vs Innovative Tool: Analytical Results Vs Experimentation	302
12.9. Experimental Conclusion	303
13. Final Conclusion	303
14. Recommendation and Future Work	304
References	305

Table of Figures Images Charts and Graphs

FIG 2.1: Friction Stir Welding Setup	8
FIG 2.2 Surface element used for calculation of total heat input	10
FIG 2.3 Heat source models	14
FIG 2.4 Co-Ordinates and Temperature using 2D Rosenthal Solutions	15
FIG 2.5 Work piece geometry and welding parameters	16
FIG 2.6 Schematic drawing of surface orientation and infinitesimal segment areas	19
FIG 2.7 Heat generation plunge force and torque during a plunge period	26
FIG 2.8 The effect of the work piece backing plates 3D model	30
Image 2.1: a standard tool weld	33
Image 2.2 A depiction of a friction stir weld in water	34
FIG 3.1 Different shoulder features used to improve material flow and shoulder efficiency	35
Image 3.1 A scrolled shoulder tool and truncated cone pin	36
Image 3.2 The convex shoulder curved/ tapered geometries	37
Image 3.3 A concan shoulder with a round bottom pin	38
Image 3.4 The flat bottom pin	39
FIG 3.1: Geometry comparing surface velocities at calibration point for flat-bottom and round-bottom pins	39
Image 3.5: Truncated cone pin and convex shoulder	41
Image 3.6: A stepped spiral pin	41
Image 3.7: Schematics of the Whorl pin variations	42
Image 3.8: Schematic of MX Triflute pin	43
Image 3.9: Photos of Trivex and MX Trivex pins	43
Image 3.10: Example of a threadless pin tool	44
FIG 3.2 The depiction of the retractable pin tool	44
FIG.4.1: Schematic of the weld set up and definition of orientations	45
FIG.4.2: Side view of the FSW tool showing the conical shoulder cap and threaded probe	45
FIG.5.1: Heat generation contributions in analytical estimates	47
Drw. 5.1: The 12 mm tool	51
Drw. 5.2: 5mm Removable Pin with Equidistant Flats	51
Graph. 5.1: Rotational speed per minute vs. heat generation from the shoulder	63
Graph. 5.2: Rotational speed per minute vs. heat generation from the probe side surface	64
Graph. 5.3: Rotational speed per minute vs. heat generation from the probe tip	64
Graph. 5.4: Rotational speed per minute vs. total heat generation	65
Graph. 5.5: Q1, Q2, Q3, QTOTAL vs. Rotational speed	65
Drw. 5.3: Friction Stir Welding Workbench design	66
Drw.5. 4: Friction Stir Welding Workbench design views	67
Drw. 5.5: Friction Stir Welding Tool	68
Image 5.1: Mode Frontier 4.3.1 b20113011	69
Image 5.2: Input Data, Output Data and boundary variables definitions	71

Image 5.3: Workflow Plan created on Mode Frontier	72
Image 5.4: Mode Frontier Input and Output Data connected to Microsoft Excel Workbook	73
Image 5.5: Interactive Selection used between Mode Frontier <i>deneme04.prj</i> and Microsoft Excel Workbook	74
Image 5.6: Al2024-T3 material contact shear stress boundaries (Standard Tool)	76
Image 5.7: Rotational speed boundaries (Standard Tool)	76
Image 5.8: Probe Radius boundaries (Standard Tool)	77
Image 5.9: Shoulder radius boundaries (Standard Tool)	77
Image 5.10: Tool shoulder angle boundaries (Standard Tool)	78
Image 5.11: Probe height boundaries (Standard Tool)	78
Image 5.12: Al2024-T3 material Yield stress boundaries (Standard Tool)	79
Image 5.13 - 5.15: Run simulation	80-81
Chart 5.1: Multi-History Chart: Qshoulder vs. Shoulder radius, Rs	82
Chart 5.2: Parallel Coordinates: Qshoulder vs. Shoulder radius, Rs	82
Chart 5.3: Multi-History Chart: Qprobe, side vs. Tool shoulder cone angle	83
Chart 5.4: Parallel Coordinates: Qprobe side vs. Tool shoulder cone angle	83
Chart 5.5: Multi-History Chart: Qprobe, side vs. tool shoulder radius	84
Chart 5.6: Multi-History Chart: Qshoulder vs. Tool rotational speed	84
Chart 5.7: History Chart: Qshoulder vs. tool shoulder radius	85
FIG. 6.1 Schematic of a bobbin tool consisting of a top shoulder, pin, and bottom shoulder attached to the pin.	86
Image 6.1: The FSW bobbin tool	87
Graph.6.1: Rotational speed per minute vs. heat generation from top shoulder (Bobbin Tool)	97
Graph.6.2: Rotational speed per minute vs. heat generation from the probe side surface	98
Graph. 6.3: Rotational speed per minute vs. heat generation from bottom shoulder	98
Graph. 6.4: Rotational speed per minute vs. total heat generation	99
Graph.6.5: Q1, Q2, Q3, QTOTAL vs. Rotational speed	99
Drw. 6.1: Friction Stir Welding Workbench design & 3D views (Bobbin Tool)	100
Image 6.2: Input Data, Output Data and boundary variables definitions	102
Image 6.3: Workflow Plan created on Mode Frontier (Bobbin Tool)	103
Image 6.4: Mode Frontier Input and Output Data connected to Microsoft Excel Workbook (Bobbin Tool)	104
Image 6.5: Interactive Selection used between Mode Frontier <i>BOBBINTOOL.prj</i> and Microsoft Excel	105
Image 6.6: Al2024-T3 material yield stress boundaries (Bobbin Tool)	106
Image 6.7: Rotational speed boundaries (Bobbin Tool)	106
Image 6.8: Probe Radius boundaries (Bobbin Tool)	107
Image 6.9: Shoulder radius boundaries (Bobbin Tool)	107
Image 6.10: Tool shoulder angle boundaries (Bobbin Tool)	108
Image 6.11: Probe height boundaries (Bobbin Tool)	108
Image 6.12: Al2024-T3 material contact shear stress boundaries (Bobbin Tool)	109

Image 6.13 – 6.15: Run simulation	109-111
Chart 6.1: Multi-History Chart: QTOPshoulder vs. Shoulder radius, Rs	111
Chart 6.2: Parallel Coordinates: Qshoulder vs. Shoulder radius, Rs	112
Chart 6.3: Multi-History Chart: Qprobe, side vs. Tool Probe radius on Bobbin Tool	112
Chart 6.4: Parallel Coordinates: Qprobe side vs. Tool shoulder cone angle	113
Chart 6.5: Multi-History Chart: QBOTTOMshoulder vs. tool shoulder radius	113
Chart 6.6: Multi-History Chart: QBOTTOMshoulder vs. Tool rotational speed	114
Image. 7.1: Optimization of innovative Friction Stir on material Al2024-T3	115
Image 7.2: Copper Sliding Backing bar serves as a conductor due to excessive heat during a Friction Stir Welding process	116
Graph. 7.1: Rotational speed per minute vs. heat generation from the innovative tool shoulder	125
Graph. 7.2 Rotational speed per minute vs. heat generation from the innovative tool probe side surface	127
Graph 7.3: Rotational speed per minute vs. heat generation from copper bush side	127
Graph. 7.4 Rotational speed per minute vs. heat generation from copper bush tip	128
Graph. 7.5 Rotational speed per minute vs. heat generation from the innovative tool probe tip	128
Graph. 7.6 Rotational speed per minute vs. total heat generation from innovative tool	129
Graph. 7.7 Qs, Qpt, Qps, Qcopper-tip, Qcopper-side, QT vs. Rotational speed	130
Drw. 7.1: Modified Copper Bush	131
Drw. 7.2: Modified Sliding Backing Copper Bar (Innovative Tool)	131
Drw 7.3. Friction Stir Welding Workbench 3D design (Innovative Tool)	132
Drw.7.4: Friction Stir Welding Workbench design views (Innovative Tool)	133
Drw 7.5:Friction stir welding workbench design	134
Image 7.3: Input Data, Output Data and boundary variables definitions	135
Image 7.4: Workflow Plan created on Mode Frontier (Innovative Tool)	136
Image 7.5: Mode Frontier Input and Output Data connected to Microsoft Excel Workbook	136
Image 7.6: Interactive Selection used between Mode Frontier deneme04copper.prj	137
Image 7.7: Copper material contact shear stress boundaries (Innovative Tool)	137
Image 7.8: Rotational speed boundaries (Innovative Tool)	138
Image 7.9: Probe Radius boundaries (Innovative Tool)	139
Image 7.10: Shoulder radius boundaries (Innovative Tool)	139
Image 7.11: Tool shoulder angle boundaries (Innovative Tool)	140
Image 7.12: Probe height boundaries (Innovative Tool)	140
Image 7.13: Copper material yield shear stress boundaries (Innovative Tool)	141
Image 7.14: CS-Al2024-T3 material contact shear stress boundaries (Innovative Tool)	141
Image 7.15: Copper yield shear stress boundaries (innovative Tool)	141
Image 7.16 – 7.15: Run simulation	142-143
Chart 7.1: Multi-History Chart: Innovative tool Qshoulder vs Shoulder Radius	144
Chart 7.2: Parallel Coordinates: Qshoulder vs. Shoulder radius, Rs	145
Chart 7.3: Multi-History Chart: innovative tool Qprobe side vs Tool shoulder cone angle	146

Chart 7.4: Parallel Coordinates: Innovative tool Qprobe side vs. Tool shoulder cone angle	147
Chart 7.5: Multi-History Chart: innovative tool Qprobe tip vs Tool tip	148
Chart 7.6: Multi-History: innovative tool shoulder vs Rotational Speed	149
Chart 7.7: Parallel Coordinates: Innovative tool Qshoulder vs. Rotational Speed	150
Chart 7.8: Multi-History Chart: innovative tool probe side vs Rotational Speed	151
Chart 7.9: Parallel Coordinates: Innovative tool Qprobe side vs. Rotational Speed	152
Chart 7.10: Multi-History Chart: innovative tool probe tip vs Rotational Speed	153
Chart 7.11: Parallel Coordinates: Innovative tool Qprobe tip vs. Rotational Speed	154
Chart 7.12 Multi-History Chart: innovative tool QT total heat generation vs RotationalSpeed	155
Chart 7.13: Parallel Coordinates: Innovative tool QT total heat generation vs. Rotational Speed	157
Image 8.1: Employing a backing spar to model the contact condition between work piece and backing plate	158
FIG: 8.1 Heat flow (loss) pathways that is acknowledged	159
Drw 8.1: Thermal Aspect for the Standard Tool Design.	161
Image 8.2: Input Data, Output Data and boundary variables definitions (Heat Loss Conditions)	163
Image 8.3: Workflow Plan created on Mode Frontier (Heat Loss Conditions)	163
Image 8.4: Mode Frontier Input and Output Data connected to Microsoft Excel Workbook (Heat Loss Conditions)	164
Image8.5: Interactive Selection used between Mode Frontier <i>convection mode.prj</i>	164
Image 8.6: The heat transfer coefficient of the upside surface 12.25 W/m ² *K boundaries	166
Image 8.7: The heat transfer coefficient of the downside surface 6.25 W/m ² *K boundaries	167
Image 8.8: Temperature boundaries	167
Image 8.9: The melting temperature boundaries	168
Image 8.10: The Stefan-Boltzmann constant (σ) boundaries	168
Image 8.11: x cross-sectional area 4 mm boundaries	169
Image 8.12: y cross-sectional area 4 mm boundaries	169
Image 8.13: The thermal conductivity boundaries	170
Image 8.14: The length boundaries	170
Image 8.15: The surface emissivity boundaries	171
Image 8.16: a cross-sectional area 500 mm boundaries	171
Image 8.17: b cross-sectional area 115 mm boundaries	172
Image 8.18 – 8.19: Run simulation	172
Chart 8.1: Multi-History Chart: reference temperature and heat conduction to the heat conduction objective	174
Chart 8.2: Multi-History Chart: reference temperature and heat loss by conduction on the upper surface	175

Chart 8.3: Multi-History Chart: reference temperature and the heat loss by conduction on the down surface to $q_{downobj}$ (heat loss on the down surface objective)	176
Chart 8.4: Multi-History Chart: the temperature and the heat loss by conduction on the down surface to the $q_{pobjective}$ (heat loss on the down surface objective)	177
Chart 8.5: Multi-History Chart: temperature and the heat loss by conduction on the upper surface to the $q_{pobjective}$ (heat loss on the upper surface objective)	178
Chart 8.6: Multi-History Chart: representation of the temperature and heat conduction to the heat conduction	179
Chart 8.7: Multi-History Chart: a, the heat loss by conduction on the upper surface to the $q_{pobjective}$	180
Chart 8.8: Multi-History Chart: b, the heat loss by conduction on the down surface to the $q_{downobjective}$	181
FIG 8.2: AMGM material definition (Bobbin Tool)	182
FIG 8.3: AMGM boundary conditions (Bobbin Tool)	183
Drw 8.2: Thermal Aspects for the Bobbin Tool Design	183
Image 8.20: Input Data, Output Data and boundary variables definitions (Bobbin Tool Heat Loss Conditions)	185
Image 8.21: Workflow Plan created by Mode Frontier (Bobbin Tool Heat Loss Conditions)	185
Image 8.23: Interactive Selection used between Mode Frontier <code>bobbintoolconvectionmode.prj</code>	186
Image 8.22: Mode Frontier Input and Output Data connected to Microsoft Excel Workbook (Bobbin Tool Heat Loss Conditions)	186
Image 8.24: x cross-sectional area 4mm boundaries	187
Image 8.25: y cross-sectional area 5mm boundaries	187
Image 8.26: a cross-sectional area 500mm boundaries	188
Image 8.27: b cross-sectional area 115mm boundaries	188
Image 8.28: The heat transfer coefficient of the upside surface boundaries	189
Image 8.29: The reference temperature boundaries	189
Image 8.30: The melting temperature boundaries	190
Image 8.31: The Stefan-Boltzmann constant (σ) boundaries	190
Image 8.32: The thermal conductivity boundaries	191
Image 8.33: The length boundaries	191
Image 8.34: The surface emissivity boundaries	192
Image 8.35 – 8.36: Run simulation	193
Chart 8.9: Normal-Quantile Plot: the a_{plate} , the heat loss by conduction on the upper surface to the $q_{pobjective}$	194
Chart 8.10: Normal-Quantile Plot: x, the heat loss by conduction on the upper surface to the $q_{pobjective}$	195
Chart 8.11: Multi-History Chart: temperature and heat conduction to the heat conduction objective	196

Chart 8.12: Multi-History Chart: temperature and the heat loss by conduction on the upper surface to the q _p objective (heat loss on the upper surface objective)	197
Chart 8.13: Multi-History Chart: reference temperature and heat conduction to the heat conduction objective	198
Chart 8.14: Multi-History Chart: reference temperature and heat loss by conduction on the upper surface	199
Drw 8.3: Thermal Aspect for the Innovative Tool Design	200
Image 8.36: Input Data, Output Data and boundary variables definitions (Innovative Tool Heat Loss Conditions)	202
Image 8.37: Workflow Plan created on Mode Frontier Project as shown in innovative tool convection mode.prj,	203
Image 8.38: Mode Frontier Input and Output Dates connected to Microsoft Excel Workbook (Innovative tool Heat Loss Conditions)	203
8.39: Interactive Selection used between Mode Frontier convection mode.prj	204
Image 8.40: x cross-sectional area 4mm boundaries (Innovative Tool Heat Loss Conditions)	204
Image 8.41: y cross-sectional area 5mm boundaries (Innovative Tool Heat Loss Conditions)	205
Image 8.42: Heat transfer coefficient, upside boundaries (Innovative Tool Heat Loss Conditions)	205
Image 8.43: Reference temperature boundaries (innovative Tool Heat Loss Conditions)	206
Image 8.44: Workpiece melting temperature boundaries (Innovative Tool Heat Loss Conditions)	206
Image 8.45: The Stefan-Boltzmann constant boundaries (Innovative Tool Heat Loss Conditions)	207
Image 8.46: a cross-sectional area 500mm boundaries (Innovative Tool Heat Loss Conditions)	207
Image 8.47: b cross-sectional area 115mm boundaries (Innovative Tool Heat Loss Conditions)	208
Image 8.48: Thermal conductivity boundaries (Innovative Tool Heat Loss Conditions)	208
Image 8.49: The length boundaries (Innovative Tool Heat Loss Conditions)	209
Image 8.50: Surface emissivity boundaries (Innovative Tool Heat Loss Conditions)	209
Image 8.51: K _{copper} boundaries (Innovative Tool Heat Loss Conditions)	210
Image 8.52: h _{down} boundaries (Innovative Tool Heat Loss Conditions)	210
Image 8.53 – 8.54: Run simulation	211
Chart 8.15: Multi-History Chart: The A _{plate} (Aluminium Plate), the heat loss by conduction on the upper surface to the q _p objective	212
Chart 8.16: Multi-History Chart: temperature and heat conduction to the heat conduction objective	213
Chart 8.17: Multi-History Chart: temperature and the heat loss by conduction on the upper surface to the q _p objective (heat loss on the upper surface objective)	214
Chart 8.18: Multi-History Chart: temperature and heat conduction to the heat conduction objective	215

Chart 8.19: Multi-History Chart: temperature and heat loss by conduction on the upper surface	216
Chart 8.20: Normal Quantile Plot: x, length and qcopper to qcopperObj	217
Chart 8.21: Multi-History Chart: temperature and qcopper to the qcopperObj	218
Chart 8.22: Multi-History Chart: temperature and qcopper to the qcopperObj	219
Chart 8.23: Multi-History Chart on Designs Space as created from the Aplate and qcopper to qcopperObj	220
Chart 8.24: Normal Quantile Plot: a, length and qup to qcopperObj	221
Image 9.1: Input Data, Output Data and boundary variables definitions (Heat Generation Vs Heat Loss)	223
Image 9.2: Input Data, Output Data and boundary variables definitions (Heat Generation Vs Heat Loss)	224
Image 9.3: Workflow Plan created by Mode Frontier Project ((Heat Generation Vs Heat Loss)	225
Image 9.4: Mode Frontier Input and Output Data connected to Microsoft Excel Workbook	225
Image 9.5: Interactive Selection used between Mode Frontier <i>comparison.prj</i> and Microsoft Excel Workbook: <i>comparison.xlsm</i>	226
Image 9.6 -9.8: Run simulation	226-227
Chart 9.1: Standard tool Total Heat Generation Vs Bobbin Tool Total Heat Generation	228
Chart 9.2: Bobbin tool total heat generation Vs Innovative Tool total heat generation	229
Chart 9.3: Standard tool total heat generation Vs Innovative Tool total heat generation	230
Chart 9.4: Bobbin tool conduction Vs Standard Tool Conduction	231
Chart 9.5: Bobbin tool conduction Vs Innovative Tool Conduction	232
Image 9.6: Microsoft Excel workbook showing the input and output data of the compareson of conditions	233
Chart 9.6: Applied air Vs Normal Conditions of an innovative tool	234
Chart 9.7: Applied air Vs Applied Water on an innovative tool	235
Chart 9.8: Applied water Vs the Normal Conditions of an innovative tool	236
Chart 9. Multi history chart: innovative tool and standard tools heat generation	237
FIG 9.1: Schematic of mutual dependencies between generated heat and dominant influencing parameters and representing Partial algorithm for generated heat estimation	238
Image 9.10: Workflow Plan created by Mode Frontier Project (The Application of Boiling Water to the Innovative Tool)	241
Image 9.11: Mode Frontier Input and Output Datas connected to Microsoft Excel Workbook linking it to various cells	241
Image 9.13: Contact Shear Stress boundaries (The Application of Boiling Water To The Innovative Tool)	242
Image 9.14: The yield strength of boiling water on the copper bush boundaries	243
Image 9.15: The yield strength applied by the boiling water boundaries	243
Image 9.16: The rotational speed boundaries (The Application of Boiling Water To The Innovative Tool)	244

Image 9.17: The Shoulder radius boundaries (The Application of Boiling Water To The Innovative Tool)	244
Image 9.18: The probe radius boundaries (The Application of Boiling Water To The Innovative Tool)	245
Image 9.19: Tool shoulder angle boundaries (The Application of Boiling Water To The Innovative Tool)	245
Image 9.20: Probe height boundaries (The Application of Boiling Water To The Innovative Tool)	246
Image 9.21: The probe height of the copper bush boundaries (The Application of Boiling Water To The Innovative Tool)	246
Image 9.22: Input Data, Output Data and boundary variables definitions boundaries (The Application of Boiling Water To The Innovative Tool).	247
Chart 9.10: History chart: heat generation for the innovative tool both with boiling water applied (QTWITobj) and the innovative tools normal weld (QTITobj)	248
Plot 9.1: A bubble plot: The heat generation: QTIT vs QTWIT vs CsNORMAL	249
Chart 9.11: History chart: Heat generation of both the standard tool and the innovative tool	250
Plot 9.2: A bubble plot: The heat generation: QTIT vs QTWIT vs CsNORMAL	251
Plot 9.3: A bubble plot: The heat generation between the innovative tool and the innovative tool with added hot liquid	252
Chart 9.12: Multi history chart: The standard tool and the innovative tool with boiling water applied	253
Drw.9.1: 100°C boiling water is applied to the friction stir weld work bench to reduce heat generated from the weld tool	255
Drw.9.2: Ice cold water is applied to the friction stir weld work bench to reduce heat generated from the weld tool	255
Graph 9.1: The Contact Shear Stress Vs the temperature of the weld	257
Plot 9.4: A bubble Graph: Heat generation of the innovative tool Vs the heat generation of the innovative tool with boiling water at 100 °C	258
Plot 9.5: A bubble Graph: Innovative tool Vs the innovative tool when a Hot Liquid or Liquid Nitrogen at -196 °C	259
Plot 9.6: The heat generation comparison: The innovative tool vs the innovative tool with cold liquid	260
Graph 10.1: The heat loss by increasing the outer area of the sliding copper bar	263
Graph 10.2: The heat loss by increasing the radius of the inner area of the sliding backing bar	263
Graph 10.3: The heat loss by increasing the thickness of the sliding backing bar	264
Image 10.1: Radius of the sliding backing bar boundaries	264
Image 10.2: The Inner radius of the sliding backing bar boundaries	265
Image 10.3: The Thickness of the sliding backing bar boundaries	265
Chart 10.1: Multi history chart showing r1 vs r2 vs Q_{loss}	266
Plot 10.1: Bubble plot- The Heat loss of both r1 and r2	267
Drw 11.1: Work bench design	270

Drw 11.2: friction stir welding plates with thermal couple holes	270
Image 12.1: MAHO CNC milling machine used to perform FSW	272
Image 12.2: MAHO CNC milling machine control Panel	273
Image 12.3: Finger gauge used to set alignment and direction of the too	274
Image 12.4: Tool Off-set used to set the straightness of the tool.	274
Image 12.5: The friction stir welding Innovative tool with pin	275
Image 12.6: Feeler gauge used to set space between the tool and the work piece material	275
Image 12.7: Kistler multicomponent force link set used to measure forces	276
Image 12.8: The Kistler multichannel charge amplifier	277
Drw 12.1 Render of standard backing plate to operate with the FSW tool	277
Image 12.9: Placement of the sensors beneath the backing plate	278
Image 12.10: FLIR T640 infrared thermal imaging camera	279
Image 12.11: FLIR thermal camera setup	279
Image 12.12: Infrared thermal capture of weld process using the FLIR T640 thermal camera software “FLIR Tools”	280
Image 12.13: Water being cooled down	280
Image 12.14: A coolant applied weld – Ice cold water at 0.8 °C	281
Image 12.15: The weld for standard tool ice water applied test	
Graph 12.1: Temperature vs Time for the standard tool ice water applied test	281
Image12.16: The weld for the standard tool in normal conditions	282
Graph 12.2: Temperature vs Time for standard tool normal conditions	282
Graph 12.3: Temperature vs Time for the standard tool hot water applied	
Image 12.17: Hot water applied test showing very minor degeneration on the work piece (a) otherwise a successful weld (b).	282
Image 12.18: Subfigures depicting the first run performed	
Image 12.19: Subfigures showing the fifth run	283
Image 12.20: Subfigures of the second run	284
Image 12.21: Subfigures of runs 3 and 4	284
Image 12.22: Subfigures of run 9 and 10	285
Image 12.23: Trails 11(a), 12 (b), 13 (c), 14 (d) and 15 (e)	286
Image 12.24: Copper bushes showing extreme signs of melting	287
Image 12.25: The coolant applied test using ice cold water	288
Image 12.26: Hot Water applied weld	288
Graph 12.4: Force Graph for the Standard tool weld in normal conditions	289
Graph 12.5: Force graph for the standard tool weld ice cold water applied weld	290
Graph 12.6: Force graph for the standard tool hot water applied test	291
Graph 12.7: Innovative tool Normal conditions force graph	292
Graph 12.8: Innovative tool Iced water applied weld force graph for run 18	293
Graph 12.9 Innovative Tool Hot Water applied weld force graph for run 21	293
Graph 12.10: Temperature Vs time: standard tool comparison of Normal conditions and Coolants	295

Graph 12.11: Temperature Vs time: Innovative tool comparison of Normal conditions and Coolants	296
Graph 12.12: Temperature Vs time: Innovative tool comparison of Normal conditions and Coolants	297
Graph 12.13: Ice cold water applied test comparison standard tool vs Innovative tool	299
Graph:12.14: Hot water applied test comparison standard tool vs Innovative tool	299
Graph 12.15: Force data for the Standard tool comparison of a normal weld and coolant applied test	300
Graph 12.16: Force data for the Innovative tool comparison of a normal weld and coolant applied test	300
Graph 12.17 Force comparison for Standard tool and Innovative tool in normal conditions	301
Graph 12.18: Force comparison for Standard tool and Innovative tool ice water applied	301
Graph 12.19: Force comparison for Standard tool and Innovative tool hot water applied	302

List of tables

Table 2.1. Stress-strain data for 2024 T3 [27]	17
Table 2.2. Definition of contact condition, velocity/shear relationship and state variable	18
Table 3.1: Calculated surface velocities of lowest pin location	40
Table 5.1: Analytical estimation of heat generation for the Standard Tool	49
Table 5.2 : Tool Angular Rotational Speed and Rotational Speed for the Standard Tool	49
Table 5.1: Heat Generation from the Shoulder with reference to angular rotation.	52
Table 5.2: Heat Generation for the Probe Tip and Probe Surface.	54
Table 5.3: Total Heat Generation (Standard Tool)	55
Table 5.4 Summary of friction stirring tool dimensions for a given workpiece material	75
Table 6.1: Analytical Estimation of heat generation for the Bobbin Tool	87
Table 6.2: Tool Angular Speed and Rotational Speed for the Bobbin Tool	87
Table 6.3: Heat Generation Calculations for the Top Shoulder (Bobbin Tool)	89
Table 6.5: Heat Generation Calculation for the Tool Shoulder	92
Table 6.6: Total Heat Generation for the Bobbin Tool.	93
Table7.1: Analytical Estimation of Heat Generation for the Innovative Tool.	116
Table7.2: Tool Angular Speed and Rotational Speed for the Innovative Tool.	116
Table 7.3: Heat Generation Calculation for the Innovative Tool Shoulder	118
Table 7.4: The Heat Generation for the Probe side Surface, the Probe Tip, the Copper Bush Side Surface and the Copper Bush Tip.	123
Table 7.5: The Total Heat Generation for the Innovative Tool.	124
Table 8.1 : A reference guideline [20]	167
Table 9.1: References the tensile properties of alloy 2024-T3.	234
Table 9.2: Strength properties determined based on monotonous tensile tests	238
Table 10.1: Effect of Nitrogen, Oxygen, and Hydrogen on Weld Soundness	260
Table 10.2: The heat loss by increasing the outer area of the sliding copper bar	261
Table 10.3: The heat loss by increasing the radius of the inner area of the sliding backing bar	261
Table 10.4: The heat loss by increasing the thickness of the sliding backing bar	261
Table 11.1: Table of experiments	268
Table 12.1: Parameters for the standard tool weld	281
Table 12.2: Parameters used during the innovative tool runs.	285
Table 12.3: Table of maximum and average force values for the standard tool	292
Table 12.4: Table of maximum and average force values for the innovative tool	294

List Of Symbols

Q_1	heat generation from shoulder, W
Q_2	heat generation from probe side, W
Q_3	heat generation from probe pin, W
Q_{total}	total heat generation, W
$R_{shoulder}$	tool shoulder radius, m
R_{probe}	tool probe radius, m
H_{probe}	tool probe height, m
Q	heat generation, W
M	torque, Nm
A	area, m^2
θ	angle, deg
z	dimension along rotation axis, m
α	tool shoulder cone angle, m
τ_{yield}	yield shear stress, Pa
σ_{yield}	yield stress, Pa
$f_{shoulder}$	heat generation ratio from shoulder
$f_{probe\ side}$	heat generation ratio from probe side
$f_{probe\ tip}$	heat generation ratio from probe tip
$\tau_{friction}$	friction shear stress, Pa
$\tau_{contact}$	contact shear stress, Pa
P	contact pressure, Pa
σ	contact pressure, Pa
μ	friction coefficient

ω	tool angular rotation speed, rads^{-1}
δ	contact state variable
r	posotion along tool radius, m
v_{tool}	tool speed of ωr , ms^{-1}
v_{matrix}	matrix speed at interface ωr , ms^{-1}
$\dot{\gamma}$	slip rate interface, ms^{-1}

1. Introduction

1.1. The Thermal Process Models of Friction Stir Welding

Friction Stir Welding (FSW), patented by The Welding Institute [1] in 1991, is a new technique for material joining and processing. Friction Stir Welding is a solid-state welding technology that has been a very comprehensive method for joining non-ferrous materials such as aluminium alloys and copper. It is a solid-state process, occurring below the solidus temperature of the metals being joined. FSW produces welds that are high in quality, strength, and also inexpensive to make. The other main advantage is that it produces no fumes during process and is energy efficient. FSW does not need any filler material as required in conventional welding process and is relatively easy to perform. However, the work piece should be rigidly clamped and welding speeds are low in order to avoid defects like porosity. For aluminium alloys such as the 2000, 5000, 6000, 7000, and 8000 series, the alloys can be easily welded by friction stir welding. During FSW, the work piece is placed on a backup plate and is clamped rigidly to eliminate any degrees of freedom. A cylindrical tool with a pin normally one-third the diameter of the shoulder at the base of the shoulder rotates with a high speed in the range of 300 to 1000 rpm. It is slowly plunged into the work piece until there is contact between the shoulder surface and the work piece which consequently creates heat. The heat is consequently produced due to friction and the plastic deformation of the material. The tool then moves along the designated path on the work piece with a specified travel rate. The pin of the rotating tool hence provides the “*stir*” action in the material of the work piece. This result in a Heat Affected Zone (HAZ) with a better grain refinement required for a good weld joining. One of the main process parameters in FSW is the heat flux. The heat flux should be high enough to keep the maximum temperature in the work piece around 80% to 90% of the melting temperature of the work piece material [2], so that welding defects are avoided. The amount of the heat conducted into the work piece usually generates a good weld in terms of the microstructure of the Heat Affected Zone (HAZ), the residual stress, and the distortion of the work piece. Also the amount of the heat conducted back into the tool dictates the life of the tool. A low amount of heat transfer could lead to breakage of the pin due to its hard material. These factors emphasize the importance of the heat transfer aspect of friction stir welding.

1.2. Problem Statement

The problem in incorporating FSW into manufacturing is that developmental process and testing is expensive from the view point of time, materials, and manpower. Much of the process knowledge is through running experiments for various changes in process parameters and the looking at the resulting metallurgical aspects to analyse the results. This consequently slows down the development of applications for this process. A faster and more cost effective way to examine new aspects regarding friction stir welding is required to reduce actual experimental testing. Finite element modelling is an option which can help determine process parameters that require further experimental testing for validation and analysis. The post-weld microstructure depends largely on how the material is heated, cooled and deformed. Hence a prior knowledge of the temperature evolution within the work piece would help in design of process parameters for a welding application. Research in the field of FSW lap joints has been limited possibly due to proprietary publishing restriction within industry. Hence it would be very beneficial for future development of FSW to understand the process behind FSW of lap joints by the means of Finite Element Analysis (FEA). Two process parameters of interest for FSW lap welds are tool travel rates and

rotational tool velocities. A lot of emphasis has been laid on FEA analysis in previous published papers [3, 4, 5, 6, and 7] hence FEA analysis of these process parameters would broaden the scope of application of FSW lap welds.

1.3. Statement Purpose

The main objectives of this study is to develop and validate three-dimensional thermal models of friction stir welding for butt and lap joints for specific experimental cases and investigate the effect of varying several process parameters on weld temperature history. In order to better understand the process an initial detailed study into butt welds was performed. The developed models would be validated against the published experimental results. The best validated model was used to further perform parametric studies to predict thermal history and temperature distribution necessary for high quality welds. The parametric study was designed to investigate the following:

- Effects of various aluminium alloys such as Al6061-T6, Al5052-H32, AA7050-T451, and Al2024-T3 on work piece temperature evolution.
- Effect of variation of tool travel rates and different work piece materials on work piece temperature evolution.
- Effect of variation of rotational tool velocity for FSW lap weld of Al2024-T3 alloy on work piece temperature evolution.

Such process parameter studies covering parametric conditions not found in the literature would provide insights for further testing and analysis needed for development of process specifications for FSW butt and lap welds. The significance of the research is multi-faceted. The drawbacks abating the adoption of the FSW process for manufacturing commercial aircrafts will be mitigated. This work will also boost the confidence of non-aero manufacturing industries in substituting fusion processes with FSW. Research objectives have been formulated with this intention.

1.4. Definition of Concept

The basic study methodology to be developed a computational thermal model for butt and lap welds based on published experimental data. The correlated model will be extrapolated to perform further parametric studies involving process conditions not seen in the research literature. The unique focus of the study to be investigated thermal modelling of FSW lap welding which has been less researched than butt welding. Mode Frontier is a multi-objective optimization and design environment, written to couple CAD/computer aided engineering (CAE) tools, finite element structural analysis and computational fluid dynamics (CFD) software. It is developed by 'ESTECO SpA' and provides an environment for product engineers and designers. Mode Frontier is a GUI driven software written in Java that wraps around the CAE tool, performing the optimization by modifying the value assigned to the input variables, and analysing the outputs as they can be defined as objectives and/or constraints of the design problem. The logic of the optimization loop can be set up in a graphical way, building up a "workflow" structure by means of interconnected nodes. Serial and parallel connections and conditional switches are available. Mode Frontier builds automatic chains and steers many different external application programs using scripting (DOS script, UNIX shell, Python programming language, Visual Basic, JavaScript, etc) Mode Frontier includes design of experiments (DOE), optimization algorithms and robust design tools, that can be combined and blended to build up the most efficient strategy to solve complex multi-disciplinary problems. Different strategies are available, including random generator sequences, Factorial DoE's, Orthogonal and

Iterative Techniques, as like as D-Optimal or Cross Validation. Monte Carlo and Latin hypercube are available for robustness analysis .When you start the Mode Frontier system, the GUI switches automatically to the Workflow desktop. A mesh independence study will be also performed to identify the effect of mesh density on the temperature evolution through the work piece. The overall temperature evolution through the work piece during welding process will be observed through the generated temperature contour plots and temperature-time history plots.

2. Literature Survey

Friction Stir Welding (FSW) has become a technology of widespread interest because of its numerous advantages, most important of which is its ability to weld otherwise un-weldable alloys. Friction Stir Welding is a solid state joining technique that was invented at The Welding Institute (TWI) in the United Kingdom by Wayne Thomas and colleagues. The first patent submitted by TWI (US Patent No. 5.460.317 in 1991). Although originally perceived as a technology for joining conventionally un-weldable materials, mostly alloys of aluminium, it is currently being investigated for a number of other materials including ferrous alloys like stainless steels.

The research presented in this thesis aims at applying optimization methods to FSW process models. In the literature limited work has been presented on this topic and most work has focused on modelling different aspect of the process, ranging from analytical models describing the temperature field to 3D numerical thermo-mechanical models and residual stress models. The present work focuses on optimization of thermal models of varying complexity and the next section is devoted to different thermal models.

One of the reasons why academic and research interests are being focused on the use of FSW for these materials is its capability of producing high quality solid-state joints. Due to the absence of melting, the temperatures involved are considerably lower than those encountered in fusion welding techniques and the consequent residual thermal stresses are expected to be much lower as well.

However, the motion constraints imposed by the rigid clamping of the weld pieces can lead to significant rise in residual stresses. Residual stresses in welded metals play an important role in understanding the response of a Friction Stir Welded structure subjected to general loading as well as its fatigue crack growth resistance [8]. It is well known that compressive residual stresses tend to retard the growth of fatigue crack while tensile residual stresses have a detrimental accelerating effect. Sutton et al. have reported experimental residual stresses for AA2024-T3 friction stir butt welds.

The use neutron diffraction technique for strain measurements and from there computed the residual stresses using an isotropic, homogeneous form of Hooke's law. They found the longitudinal stress components to be the largest tensile residual stresses and reported a maximum value of 105 MPa with the highest stresses occurring near the crown side of the specimen over the entire FSW region. The highest transverse stress was approximately 75 MPa with the largest stresses occurring at mid-thickness. The through thickness stress component was found to be compressive in the weld zone with a maximum of -40 MPa located near the root side about 12 mm from weld centreline, with a rapid transition to tensile stresses outside the shoulder diameter. [9] Also reported the residual stresses observed in friction stir welded AA-024-T351 sheets using neutron diffraction measurements

Residual stresses are calculated from the measured residual strains with $E=70$ GPa and $\nu = 0.345$, maximum longitudinal stress has been reported to be about 65 MPa on the retreating side and about 55MPa on the advancing side. Inside the weld zone, the maximum of 50 MPa has been reported to be close to the centreline. Additional measurements of 1.5 mm below the top surface and 1.5mm from the bottom surface showed no variation of transverse and normal stresses through the thickness of the sheet while the maximum longitudinal stress was reportedly only 20 MPa at the bottom surface.

Residual stress component in a normal direction was seemingly high. These observations are significantly divergent [8] most likely because of the cooling that was used during welding [10], similar techniques report residual stresses for friction stir welded SS 304 L specimens. The residual longitudinal stresses is to be close to the base metal yield strength with negligible variation in the through thickness direction.

However, reports of significant variation (up to 150 MPa) of the transverse stresses in the through-thickness direction that changed from tensile at the crown-side to compressive at the root side of the weld. The variation is likely due to the faster cooling experienced by the root of the weld relative to the crown because of the intimate contact between the root side and the backing plate. They also noted that the minimum strength region occurs in the HAZ and suggested that the yield strength of the relatively weak HAZ might limit the residual stress levels.

The 300 rpm welds showed finer grain structure as compared with the 500 rpm welds. Both welds had higher strengths than the base metal, but 300 rpm weld had the higher value of the two. 0.2% offset yield strengths for base, 300 rpm weld and 500 rpm welds were reported to be 295, 430 and 360 MPa, respectively. The tensile strengths were 667, 735 and 678 MPa, respectively. The residual stress in the tensile specimens was relieved when the specimens were cut from the welded plate.

It was found that longitudinal stress (σ_{yy}) varied only slightly with depth. The maximum values of σ_{yy} were similar in both welds and close to the base metal yield strength. The region of high tensile, residual and longitudinal stress was found to be wider in the 500 rpm weld (20 mm on either side of centreline) than in the 300 rpm weld (15 mm on either side) due to the higher temperatures. [11] reported residual stress measurements on AA7108T79 alloy and observed that the texture and residual strains produced by thermo-mechanical FSW are not closely coupled as non-uniform plastic deformation could lead to high stress gradients.

The longitudinal maps indicated a through thickness tensile strain field which was not spread perpendicularly to the surface but was tapered with z (depth direction) and outside this region was a steep change of the strain field that levelled out in compression. Transverse orientation peak position patterns showed a smaller but more distinct variation between the face and the root of the weld, [12] implemented an equilibrium-based weighted least square algorithm to reconstruct the residual stress tensors from measured residual stress data. Although it was used stress-free boundary conditions at the edges, the computations indicated the tensile and longitudinal stresses dipped to the compressive side beyond the HAZ. This also came up with fluctuating normal (through-thickness) stress profiles within the HAZ.

In the present study, an attempt has been made to predict the thermal residual stresses developed in metal alloys upon Friction Stir Welding by employing sequentially coupled finite element analyses. In a sequentially coupled analysis, thermal analysis is performed first to generate temperature histories for the welding process which is then utilized as thermal input to the mechanical analysis for the prediction of stresses and strains that are generated owing to the temperature changes within the con-strained metal plates. Aluminium alloys AA2024, AA6061 and stainless steel 304 L, one of the most widely used of stainless steels, has been used as the materials of choice. Experimental temperature and stress measurements are also presented in order to validate the numerically predicted results. A commercially available finite element package, ABAQUS, was used for the computations.

Advantages and Disadvantages

- Little preparation is needed on the workpiece before welding.
- There is no melting of the material, such that there is no need for inert gases to prevent the molten material from reacting with the air. This reduces the complexity of the welding setup and reduces environmental impact.
- Levels are low on residual stress rather than on fusion welding.
- The Friction Stir Welding process can be automated.
- Magnetic forces do not affect the welding process.
- Consumable parts are not used during the weld process, whilst tool life is high.
- There is low distortion.
- Joint strengths can be easily achieved.

As much as the Friction Stir Welding process is efficient and has remarkable advantages it does have a few downsides, the disadvantages are listed as follows:

- Once the weld is completed a hole or keyhole is left behind.
- Extensive testing is needed to determine operating parameters as the process is not accurately modelled.
- A backing plate of high quality is required.
- The need for efficient clamping equipment and a suitable backing plate due to the large forces involved (downward forces up to 50 kN and traversing forces up to 12 kN are shown). This limits the mobility of the process and makes it challenging to do welding on very large parts.

2.1. Process

The Friction Stir Welding (*FSW*) process is presented as they form the basis for the optimization problems considered in this work. FSW is a solid state welding process invented in 1991 by The Welding Institute, [1], saying that the process is solid state means that there is no, or very limited and localised, melting of the material as opposed to conventional methods like arc welding where a central aspect is the melting of the material. The process is affected by many parameters, such as the material properties of the work piece e.g., the thermal conductivity and heat capacity, the environment, for example the temperature of the surroundings, the tool design and other factors. Once the welding setup, such as work piece dimensions and material, has been set, the main process parameters to be chosen, in order to obtain a successful weld, are the tool design and the translational speed u_w and the rotational speed ω . The present work deals primarily with the use of optimization techniques for optimal selection of u_w and ω . In this chapter more details on the FSW process and mathematical modelling of FSW are presented [13]. The basic concept of FSW is remarkably simple. A non-consumable rotating tool with a specially designed pin and shoulder is inserted into the abutting edges of sheets or plates to be joined and traversed along the line of joint. The tool serves two primary functions:

(a) heating of workpiece

(b) movement of material to produce the joint.

The heating is accomplished by friction between the tool and the workpiece and plastic deformation of workpiece. The localized heating softens the material around the pin and combination of tool rotation and translation leads to movement of material from the front of the pin to the back of the pin. As a result of this process a joint is produced in 'solid state'. Because of various geometrical features of the tool, the material movement around the pin can be quite complex.

The process is sketched in FIG. 2.1 which shows the welding setup, including the tool, the work piece and the backing plate, and some terms commonly used in connection to FSW. The tool consists of a cylinder, that is in contact with the top surface of the work pieces, and a probe (sometimes called the pin) of smaller diameter that is forced, by an axial load, into the material between the plates to be welded. The contact area between the cylinder and the work pieces is denoted the shoulder and this contact zone is responsible for a large part of the total heat generation. The probe contributes less to the total heat generation but has the effect of stirring the material from the two plates to create the weld. Many different tool designs exist, with the simplest one being a cylindrical probe attached to a flat shoulder. More complex tools may have conical shoulders and threaded or triangular probe designs, [12] where different tool shapes are compared using experiments and computational fluid dynamics models.

The welding process may be divided into four phases:

- First the plunge action where the rotating, but otherwise stationary, tool is forced into the weld line in the work piece.
- When the shoulder of the tool contacts the work piece surface the tool is kept stationary for a short time known as the dwell period where the work piece gradually heats up and the material surrounding the tool is softened.
- After this, the tool is traversed along the weld line (welding period) to join the two parts before the transverse movement is stopped and the tool is extracted from the material, leaving behind an exit hole, i.e. a hole corresponding to the tool probe [14].
- During the welding period the process may become stationary in the sense that the temperature field and material flow, as seen from the tool, do not change.

Typical values for the welding speed and rotational speed are $u_w \leq 10$ mm/s and $\omega \leq 1500$ rpm. The local velocity of a point on the tool shoulder edge is determined by the rotational speed, the shoulder radius R_{shoulder} and the translational welding velocity. For typical tool dimensions with R_{shoulder} in the order of 10 mm the rotational effect on the local velocity is much greater than the translational velocity effect. The work in this thesis is focused on the welding part of the process. During this phase the work piece material is heated due to the rotation of the tool and then stirred by the probe such that material from the two plates merges and creates the weld.

FSW is well suited for welding aluminium and the majority of work presented in the literature focuses on welding of different aluminium alloys. Yet, also materials like steel and copper, or even dissimilar materials, may be welded with FSW. Industrial use of FSW is found in the marine, aerospace, railroad, and automotive industries where joining of aluminium parts are used, [15] for a list of fields of application.

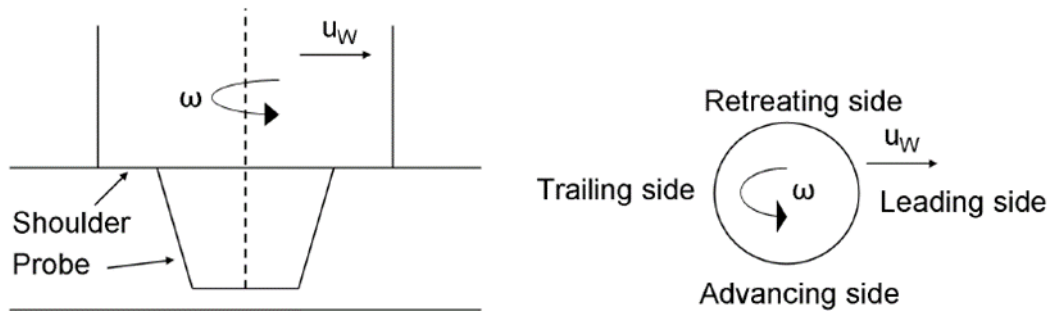
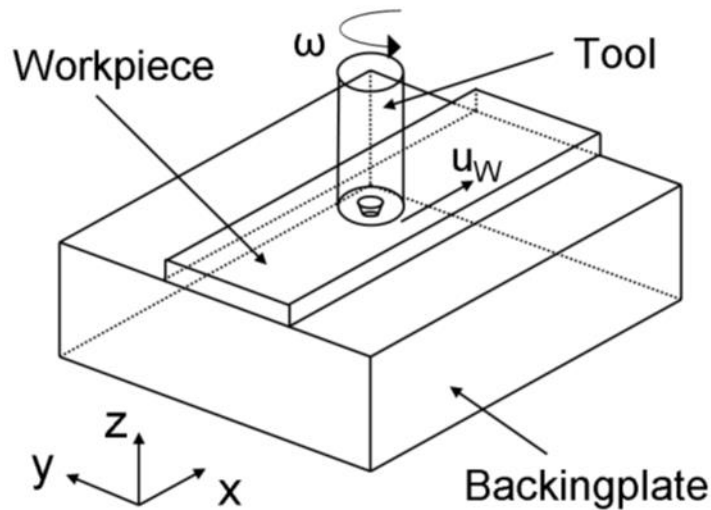


FIG.2.1: Top: Friction Stir Welding setup consisting of- the work piece, the tool and the backing plate. Bottom left: Cross section of the plate with the tool. The figure shows a tool with a flat shoulder and a conical probe, but many other tool designs exist. Bottom right: Terms denoting positions relative to the tool.

2.2. Thermal Models

Thermal aspects play an important role in the modelling and understanding of FSW. While the real process is thermo-mechanical in the sense that the thermal and mechanical aspects of the process are coupled, a purely thermal model may still give important knowledge about FSW and can be used as the first part of, for example, an uncoupled residual stress model or a microstructure model.

Thermal models differ greatly in complexity, from analytical Rosenthal models, Rosenthal (1946), to 3D numerical models, but all are based on the heat conduction equation with suitable boundary and initial conditions. In eqs. 2.1 and 2.2 ρ denotes the material density [kg/m^3], c the heat capacity [J/kgK], T the temperature [K], k the (possibly an isotropic) ρ conductivity [W/mK], q the volume heat input [W/m^3] and u the welding velocity vector [m/s]. The solution procedure and its complexity depends very much on the assumptions made regarding welding setup, geometry, boundary conditions and the type of heat source. Also a distinction between constant or temperature dependent material parameters is important, the latter, e.g., removing the possibility of using analytical Rosenthal solutions.

$$\rho c \frac{\partial T}{\partial t} = \nabla(k\nabla T) + q \quad (2.1)$$

Or in the case of an Eulerian formulation with a convective term

$$\rho c \frac{\partial T}{\partial t} = \nabla(k\nabla T) + q - \rho c u \nabla T \quad (2.2)$$

2.3. Heat Source Models

An important factor when solving the heat conduction equation for a FSW process is the q term, or an equivalent surface flux, that determines the heat input. It is a common approach to model the heat input as a surface flux rather than a volume source and a number of different heat source models are presented below. A distinction can be made between heat generated by Coulomb friction and heat generated by the plastic deformation of material during welding. In Schmidt et al. (2004); Schmidt and Hattel (2004, 2005c) "The contact condition between the tool and the work piece is used to develop expressions for the heat generation. Given the contact pressure ρ , [N/m^2], between the two parts is given by:"

$$\tau = \mu \rho \quad (2.3)$$

Where μ is the friction coefficient, It should be noted that μ and ρ may be non-uniform across the tool-workpiece interface. If the yield shear stress of the workpiece material is larger than the contact shear stress the two surfaces will slide against each other. This is called *sliding* condition. If, on the other hand, the contact shear stress is larger than the yield shear stress of the material it will stick to the tool and rotate with it and the *sticking* condition exists.

Also a combination of the two are possible, if the yield shear stress is smaller than the contact shear stress for small shear rates but not for larger shear rates. In that situation the material will rotate with the tool but at a slower rate. The contact variable δ is defined as

$$\delta = \frac{v_{matrix}}{v_{tool}} \quad (2.4)$$

Based on the contact condition the local heat generation per area can be written as,

$$q(r) = \omega r (\delta \tau_{yield} + (1 - \delta) \tau_{friction}) \quad (2.5)$$

Where, for $\delta = 1$, the total heat generation is due to plastic deformations in the workpiece material and for $\delta = 0$ the heat generation is due only to frictional heat with the friction shear stress $\tau_{friction} = \mu \rho$. ω is the rotational speed and $r = r(x, y)$ is the radial distance from the axis of rotation. For direct use of eq. (1.5) one should have knowledge about the (non-uniform) distribution of δ as well as the shear yield stress τ_{yield} and $\tau_{friction}$. A number of models have been presented in the literature where, instead, the total heat input Q_{total} is prescribed and subsequently used to develop expressions for the local heat input as function of position. Q_{total} , may for example be estimated from experiments.

A decoupled 3D thermo-mechanical model is presented [2] in which the thermal problem is solved before calculating the residual stresses and the distortion of the welded plate. The heat input is generated by the sliding between the tool and the shoulder. In order to account for the heat generation from the probe, the probe diameter $d_{probe} = 0$, thus effectively moving the heat generation from the probe tip to the shoulder. The radially dependent heat input per area $q(r)$, $[W/m^2]$, is given by the expression

$$q(r) = \frac{3Q_{total}r}{2\pi(r_0^3 - r_i^3)} \quad (2.6)$$

Where Q_{total} is the total heat input, $[W]$, r_0 is the outer radius of the shoulder and r_i the inner radius of the shoulder, i.e. in this case $r_i = 0$. Eq. (2.6) is derived and shown in a slightly different form in, among others, Schmidt et al. (2004). For simplicity only heat generation from a flat shoulder with no probe is considered here. The heat generation from a small segment of the shoulder at the distance r from the axis of rotation, see FIG. 2.2

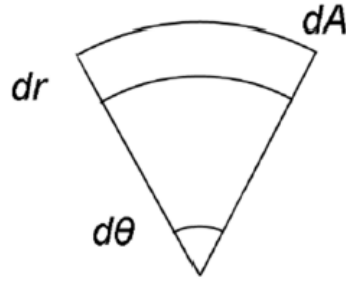


FIG. 2.2: Surface element of size $dA = r d\theta dr$ used for calculation of total heat input.

$$dQ(r) = \omega r \tau dA = \omega \tau r^2 d\theta dr \quad (2.7)$$

Where ω is the rotational speed and τ is the contact shear stress between the tool and the work piece material. The surface segment dA gives a torque contribution of $r\tau dA$. Next, the total heat input can be found by integration over the shoulder area

$$\begin{aligned} Q_{total} &= \int_0^{2\pi} \int_{r_i}^{r_0} \omega \tau r^2 dr d\theta \\ &= \frac{2}{3} \pi \tau \omega (r_0^3 - r_i^3) \end{aligned} \quad (2.8)$$

In the case of sliding, the contact shear stress is given by Coulombs law, $\tau = \tau_{friction} = \mu p$ Assuming that the total downward force P on the tool results in a uniform pressure distribution p , and that the coefficient of friction μ is also uniform, the contact shear stress is [2]:

$$\tau = \mu p = \mu \frac{P}{A_{shoulder}} = \mu \frac{P}{\pi(r_0^2 - r_i^2)} \quad (2.9)$$

For a given point the heat input per area is

$$\frac{Q}{A}(r) = \omega r \tau \quad (2.10)$$

Isolating τ in eq. (2.8) and inserting in eq. (2.10) gives eq. (2.6). Thus the heat generation per area depends linearly on the radial distance to the tool centre, and the total heat input Q_{total} that may be assumed or estimated from experiments, e.g., through torque measurements. An example is given in Dickerson et al. (2003), where it is used that $Q_{total} = \omega T_{measured}$ and $T_{measured}$ is the measured torque. Alternatively, the pressure p and the friction coefficient μ may be assumed or somehow estimated such that substitution of $\tau = \mu p$ into eq. (2.8) gives

$$q = \frac{2}{3} \pi r_0^3 \mu p \quad (2.11)$$

For $r_i = 0$. This may be rewritten as in Frigaard et al. (2001) to

$$q = \frac{4}{3} \pi^2 p N r_0^3 \quad (2.12)$$

Where $N = \frac{w}{2\pi}$ is the number of revolutions per second, In Khandkar and Khan (2001) a 3D transient model of an overlap FSW process is investigated. The heat generation is due to the sliding between the tool shoulder/probe and the work piece material as well as the plastic deformation of the material near the probe. The total heat generation from the probe is set to 3 % of the heat generation from the shoulder. The heat generation is a function of the downward force on the tool, the friction coefficient, rotational speed and is linearly dependent on the distance from the tool centre. Also included in the model is a convective term to take the material transport around the probe into account. In Khandkar et al. (2003) the heat generation per area, q , is modelled as

$$q(r) = \omega r \tau \quad (2.13)$$

Where τ is determined from experimental measurements of the torque during welding. A uniform value of $\tau = 14 \text{ MPa}$ is used for the alloy Al6061-T651 and therefore no assumptions on the value of δ are made. This heat generation was used in a 3D model and applied at the three contact zones between the tool and the workpiece, i.e. at the shoulder, the side of the probe and the tip of the probe. As stated above, the FSW process is coupled in the sense that the heat generation is determined by the mechanical behaviour that in turn depends on the temperature field, thus requiring a thermo-mechanical model. The idea behind the so-called thermal pseudo-mechanical (TPM) model, Schmidt and Hattel (2008), is that the friction shear stress is equal to the yield shear stress. This is the case if sticking is present, i.e. $\delta > 0$. The heat generation in eq. (2.5) is in that case

$$q = \omega r \tau_{yield} \quad (2.14)$$

This result is obtained by integration of the volume heat generation due to the plastic deformation of the material in a shear layer between the tool and stationary matrix material. The material in contact with the tool has the velocity $\delta\omega r$ which together with an assumption of constant strain rate in the shear layer means that the integral of the local plastic heat generation is $q_{pl} = \delta\omega r \tau_y$. This is the first part of eq. (2.5).

Further, if sticking is present, i.e. $\delta > 0$, then $\tau_{friction} = \tau_{yield}$ and eq. (2.5) reduces to eq. (2.14). Generally, τ_{yield} is a decreasing function of the temperature going to zero when $T = T_{solidus}$ where the material changes from solid to liquid phase. This means that when the temperature reaches the solidus temperature for the material the heat generation vanishes, thereby limiting the obtainable maximum temperature. The model thus includes some of the mechanical effects of FSW without solving explicitly for them.

An analysis of different ways of modelling the heat source and its geometry is given in Schmidt and Hattel (2004, 2005) where six cases are considered. The cases are:

- (a) All the heat is generated by the shoulder with no contribution from the probe,
- (b) Heat generation from the shoulder and a volumetric contribution from the probe and
- (c) Heat generation from the shoulder and from the probe surface, with the probe material left out. All three models are solved assuming sliding and sticking, respectively, giving a total of six different cases. In case the sticking condition is assumed the heat is applied as a volume source in a narrow shear layer of thickness 0.5 mm.

One of the conclusions is that the temperature field under the shoulder is greatly affected by the modelling choice whereas the far field temperature fields are almost identical. Thus a detailed heat source model may be needed for studying effects close to the tool while a simpler model may be adequate for studying effects far from the tool.

2.3. Examples of Different Heat Sources

In this example three different heat source models are tested using a 2D Eulerian model
The heat source models that are used:

- TPM model, eq. (2.14),
- A radially dependent model, eq. (2.6) with, $r_i = 0$
- A model with uniform heat input across the tool surface.

No rotational effects are included in the example, meaning that the welding velocity vector is given by $\{u_w 0 0\}^T$. FIG. 2.3 shows the corresponding temperature fields. The total heat input was obtained from the TPM model by integration of eq. (2.14) and this is then applied as the prescribed total heat input in the radially dependent heat source, eq. (2.6), and in the constant heat source model. The TPM model yields a temperature field that is close to constant under the tool and a maximum temperature well below the other two models and just below the solidus temperature set to $T_{solidus} = 805 K$ in this example. The other two models predict much higher maximum temperatures and much less uniform temperatures under the tool as is clear from the temperature plots at the source. The near constant temperature in the TPM model is due to the temperature dependent yield stress used. This effectively turns off the heat source at temperatures close to the solidus temperature, and in that way limits the maximum temperature. The other two models predict almost similar temperature fields and it is noted that the maximum temperature for the radially dependent heat source is located further away from the centre of the source compared to the constant heat source, where the maximum temperature is obtained only slightly behind the tool centre.

The local heat input close to the centre is small for the radially dependent heat source and therefore the maximum temperature is obtained further back. Also note that the temperature fields are symmetric as no rotational effects are included, meaning that the material flows through the heat source parallel to the welding direction.

2.4. Analytical Models

The Rosenthal solutions, Rosenthal (1946), are analytical equations giving the temperature field caused by an area, a line or a point heat source of strength q in one, two and three dimensions, respectively. From a FSW modelling point of view only the 2D and 3D solutions are of interest as they can be used to describe the temperature field around the tool. The solutions are obtained under a number of assumptions. The process is assumed to be steady state meaning that $\frac{\partial T}{\partial t} = 0$, the material properties, k, ρ and c are independent of the temperature and the heat source moves at a constant velocity u_ω . For the 2D solution the heat flow is assumed to be in an infinitely large plane containing the welding direction and the heat source (FIG 2.3) is given by a line perpendicular to the plane, i.e. q has the unit of W/ m. This leads to the equation:

$$T = T_0 + \frac{q}{2\pi k} \exp(-\lambda u_\omega \xi) K_0(\lambda u_\omega r)$$

$$\lambda = \frac{c}{2\pi k}$$

$$r = \sqrt{\xi^2 + y^2}$$
(2.15)

where T_0 is the initial temperature, K_0 is the modified Bessel function of the second kind and zeroth order, ξ and y are the coordinates of the point of interest relative to the heat source, see FIG. 2.4. It is noted that for $r \rightarrow 0$ the temperature $T \rightarrow 0$ and therefore the model does obviously not predict a maximum temperature below the melting temperature as is the case in a real FSW process. The 2D Rosenthal solution.

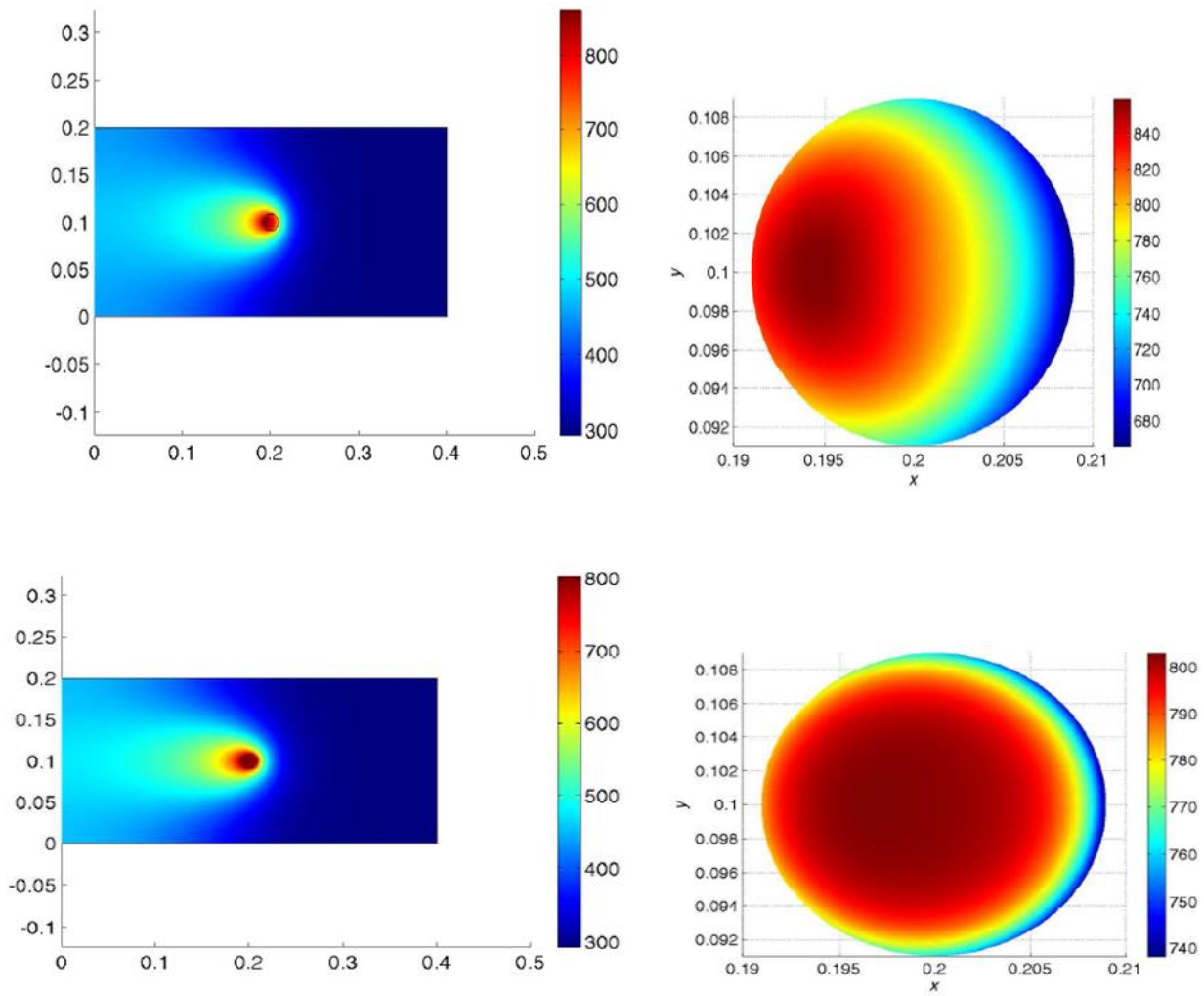


FIG. 2.3: Three different heat source models. The colorbars indicate the temperature [K]. From the top: The TPM model (eq. (1.14), $T_{max} = 803 K$), the radially dependent heat source (eq. (2.6), $T_{max} = 860 K$) and the constant heat source ($T_{max} = 883 K$). The figures to the left show global temperature fields while the right plots show the temperatures at the source. The total heat input is the same in all three examples. Notice the difference in maximum temperature. $T_{solidus}$ in the TPM model was set to 805 K.

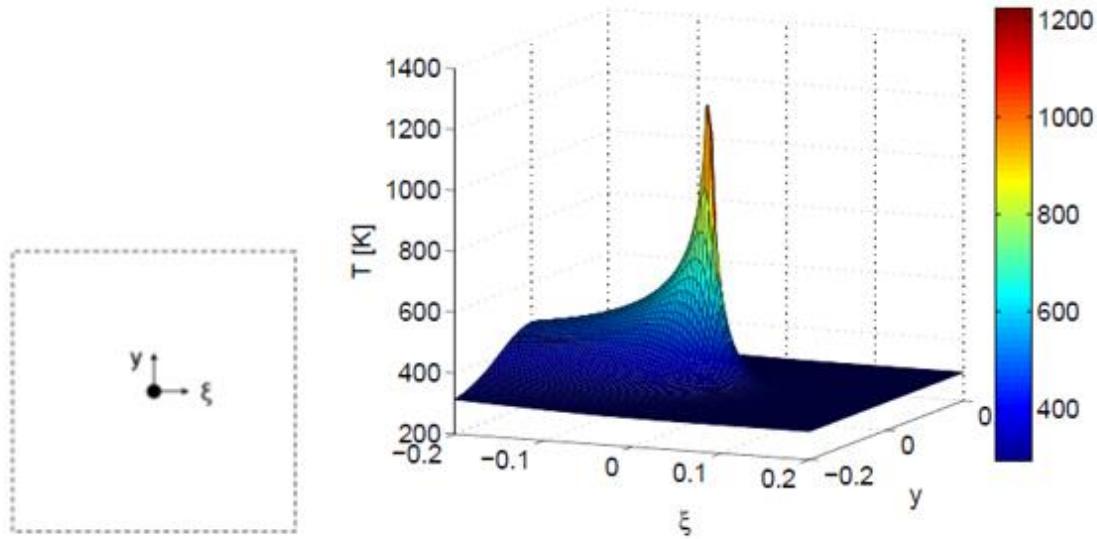


FIG. 2.4: Left: Coordinates in the 2D Rosenthal solution, eq. (2.15). The welding direction is in the positive ξ direction. Dotted lines are used to indicate that the domain is infinitely large. Right: Temperature field obtained from the 2D Rosenthal solution. Note that the temperature approaches infinity at the heat source.

This can be modified to take surface heat loss due to convection into account. Similarly, the solution for the 3D case, in which the heat source is modelled as a point, q has the unit W, in an infinitely large domain is given by

$$T = T_0 + \frac{q}{4\pi k} \exp(-\lambda u_\omega \xi) \frac{\exp(-\lambda u_\omega R)}{R}$$

$$\lambda = \frac{c}{2k}$$

$$R = \sqrt{\xi^2 + y^2 + z^2} \quad (2.16)$$

Again, as $R \rightarrow 0$ the temperature $T \rightarrow 0$.

The two solutions shown here may be extended to take finite width (the 2D case) or finite thickness of the domain into account through the use of the method of images. This method results in the expressions for the temperatures being given by infinite series, in which sources at ever increasing distances are added to the solution.

The Rosenthal solutions described above have been widely used, especially in the early modelling of FSW. In the 3D Rosenthal solution is used to develop a circular heat source resembling the shoulder of the tool by placing sources in a ring around the tool centre and integrating to obtain the full temperature field. The heat is assumed to be generated by Coulomb friction between the tool and the work piece, i.e. $\delta = 0$.

In Fonda and Lambrakos (2002) “The 3D Rosenthal solution taking finite thickness into account was used in an inverse modelling technique to model the temperature field in FSW.” By distributing a number of point sources in the heat affected zone around the tool and scaling the contribution from each one according to the local relative speed an arbitrary temperature field was obtained. Based on experimental welds and hardness measurements the maximum temperature during welding, in a point, was estimated and used to scale the strength of the heat sources in the model. Although the ability of the Rosenthal solutions to model the complex heat source and work piece geometry is limited, they have the advantage of being computationally very fast compared to numerical methods. In the present thesis, the 2D Rosenthal solution is used as a coarse model to assist the optimization of a more expensive finite element model using space and manifold mapping techniques.

2.5. Experimental Welding Conditions

The experiment reported in this work was performed at the DLR facility (German Aerospace Research) using an adapted CNC milling machine. The welding set-up consists of two 3.0 mm thick aluminum panels, 60 mm wide and 150 mm long. The plates are joined through a 105 mm long weld path, starting 15 mm from one edge and finishing 30 mm from the other edge (See FIG. 2.5). The material used in the experimental weld is a heat treatable 2024 T3 alloy, whose thermo-mechanical properties are known in the range from 28 °C to 371 °C [14].

The observed maximum temperature during the experiment is 400°C at the centerline. Therefore, the yield Stress at 400 °C is estimated as 21 MPa at 0 % plastic strain and 25 MPa at 100 % plastic strain (see table 2.1). The welding tool has an interchangeable threaded probe of 6 mm diameter, thread spacing of 0.8 mm and probe length of 3.5 mm. The shoulder has a cone angle of 10° giving an effective probe height of 2.5 mm, leaving a 0.5 mm root layer between the probe tip and the back of the plate.

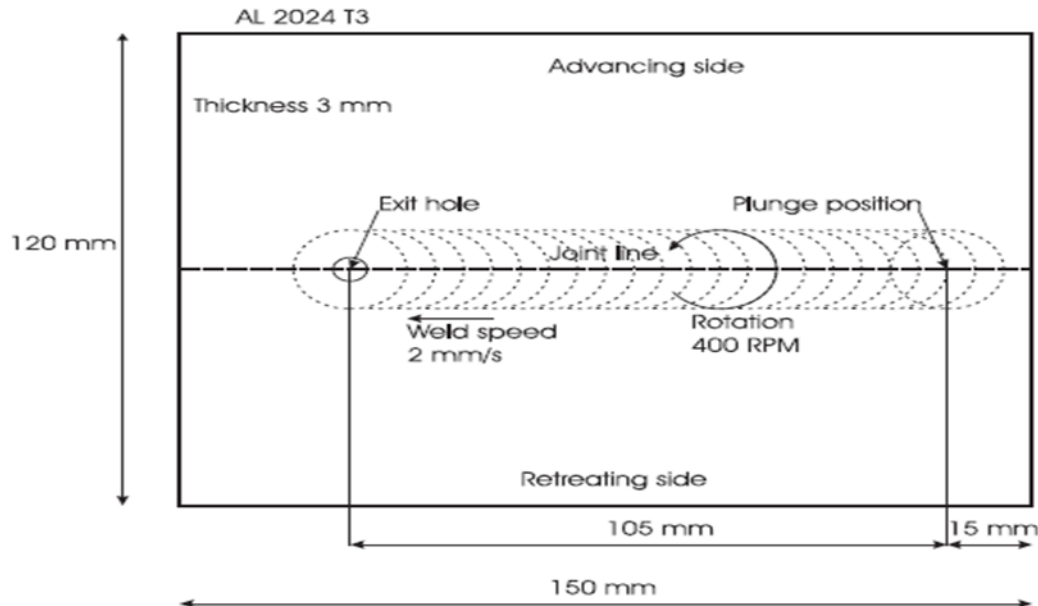


FIG. 2.5: Work piece geometry and welding parameters.

Temperature (°C)	YS at 0% Plastic Strain (MPa)	YS/Plastic Strain (MPa/-)
24	345	483/0.17
100	331	455/0.16
149	310	379/0.11
204	138	186/0.23
260	62	76/0.55
316	41	52/0.55
371	28	34/1.00
400	21	25/1.00

Table 2.1. Stress-strain data for 2024 T3 [27]

Welds were performed at a rotational speed of 400 rpm (41.8 rad s^{-1}), a welding speed of 120 mm min^{-1} (2 mm s^{-1}), a tilt angle of 1° and an effective plunge depth of 0.2 mm. During the welding process, data acquisition enables monitoring of the mechanical load on the milling head, including the torque on the rotating axis and the plunge force.

2.6. Contact Conditions

When modelling the FSW process, the contact condition is the most critical part of the numerical model [15, 16, and 17]. In this case, the Coulomb

Law of friction is applied to describe the shear forces between the tool surface and the matrix. In general, the law estimates the contact shear stress as

$$\tau_{friction} = \mu\rho = \mu\sigma \quad (2.17)$$

Where μ is the friction coefficient, ρ and σ are the contact pressures, Analyzing the contact condition of two infinitesimal surface segments in contact, Coulomb's law predicts the mutual motion between the two segments—whether they stick or slide. The top surface segment originates from the tool and moves with a velocity of ωr , where ω is the rotational speed and r is the distance from the surface segment to the rotation axis.

The lower surface segment originates from the matrix, and the velocity is part of the solution. Let us assume that the matrix is stationary, and contact is about to be initiated. Applying a normal displacement to the tool, produces a mutual bulk response from the matrix and tool, which alters the contact pressure from zero to a state dependent pressure. A complex, dynamic state builds up, which is simplified by assuming the tool response to be rigid, as compared to the softer aluminum matrix. The response from the matrix is described by the behavior of the matrix surface velocity and the reaction shear stress of the interior just below the contact surface. The normal interpretation of Coulomb's law is based on rigid contact pairs, without respect to the internal stress, however, this is not sufficiently representative for this model.

Thus, a more FSW-specific interpretation of the law is described. For this, the three following contact states are defined.

Sticking Condition The matrix surface will stick to the moving tool surface segment, if the friction shear stress exceeds the yield shear stress of the underlying matrix. In this case, the matrix segment will accelerate along the tool surface (finally receiving the tool velocity), until an equilibrium state is established between the contact shear stress and the internal matrix shear stress. At this point, the stationary full sticking condition is fulfilled. In conventional Coulomb's friction law terms, the static friction coefficient relates the reactive stresses between the surfaces.

Sliding Condition If the contact shear stress is smaller than the internal matrix yield shear stress, the matrix segment volume shears slightly to a stationary elastic deformation, where the shear stress equals the 'dynamic' contact shear stress. This state is referred to as the sliding condition.

Partial Sliding/Sticking The last possible state between the sticking and sliding condition is a mixed state of the two. In this case, the matrix segment accelerates to a velocity less than the tool surface velocity, where it stabilizes. The equilibrium establishes when the 'dynamic' contact shear stress equals the internal yield shear stress due to a quasi-stationary plastic deformation rate. This is referred to as the partial sliding/sticking condition. In this model, there is no difference between the dynamic and the static friction coefficients. It is convenient to define a contact state variable, δ , which relates the velocity of the contact points at the matrix surface relative to the tool point in contact. This parameter is a dimensionless slip rate defined as

$$\delta = \frac{v_{matrix}}{v_{tool}} = 1 - \frac{\dot{\gamma}}{v_{tool}} \quad (2.18)$$

$$\dot{\gamma} = v_{tool} - v_{matrix} \quad (2.19)$$

Where $\dot{\gamma}$ is the slip rate and v_{tool} is the position dependent tool velocity of ωr . Table summarizes the relationship between the different contact conditions, As seen, δ acts as a state parameter for the interfacial contact condition. [18,19,20]. Models were established to predict heat generation and material flow using the contact condition as boundary condition in their models, and the results are then compared to experimental observations. Still, it has not yet been revealed which contact condition is the most applicable for FSW.

Condition	Matrix velocity	Tool velocity	Shear stress	State variable
Sticking	$v_{matrix} = v_{tool}$	$v_{tool} = \omega r$	$\tau_{friction} > \tau_{yield}$	$\delta = 1$
Sticking/sliding	$v_{matrix} < v_{tool}$	$v_{tool} = \omega r$	$\tau_{friction} \geq \tau_{yield}$	$0 < \delta < 1$
Sliding	$v_{matrix} = 0$	$v_{tool} = \omega r$	$\tau_{friction} < \tau_{yield}$	$\delta = 1$

Table 2.2. Definition of contact condition, velocity/shear relationship and state variable (dimensionless slip rate).

Three different analytical estimations are suggested, all of which are based on a general assumption of uniform contact shear stress $\tau_{contact}$ and further distinguished by assuming a specific contact condition.

In the first estimation, a sticking interface ($\delta = 1$) is assumed and in the second estimation ($\delta = 0$) interface described by a Coulomb friction condition is assumed. In the case of the sticking condition, the shearing is assumed to occur in a layer very close to the interface and in the sliding condition the shear is assumed to take place at the contact interface. These two types of estimation are distinguished by the assumptions under which the shear stress $\tau_{contact}$ is introduced. The third estimation is used in the case where the partial sliding/sticking condition is assumed. During the FSW process, heat is generated at or close to the contact surfaces, which have complex geometries according to the tool geometry (FIG. 2.6), but for the analytical estimation, a simplified tool design with a conical or horizontal shoulder surface, a vertical cylindrical probe side surface and a horizontal (flat) probe tip surface is assumed.

The conical shoulder surface is characterized by the cone angle α , which in the case of a flat shoulder, is zero. The simplified tool design is presented in figure 4, where Q_1 is the heat generated under the tool shoulder, Q_2 at the tool probe side and Q_3 . At the tool probe tip, hence the total heat generation, $Q_{total} = Q_1 + Q_2 + Q_3$. To derive the different quantities, the surface under examination is characterized by either being conical, vertical or horizontal and the surface orientations relative to the rotation axis are decisive for the expressions.

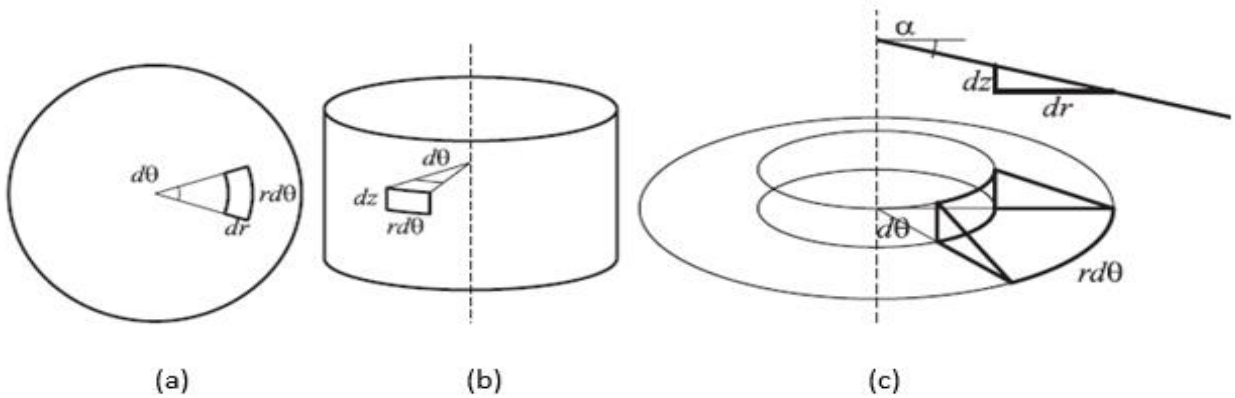


FIG. 2.6: Schematic drawing of surface orientations and infinitesimal segment areas (a) Horizontal (seen from above). (b) Vertical. (c) Conical/tilted. Projection of conical segment area onto horizontal and vertical segments.

Each surface orientation is different, but are based on the same equation for heat generation:

$$dQ = \omega dM = \omega r dF = \omega r \tau_{contact} dF dA \quad (2.20)$$

2.7. General Heat Generation

The following derivations are analytical estimations of heat generated at the contact interface between a rotating FSW tool and a stationary weld piece matrix. The mechanical power due to the traverse movement is not considered, as this quantity is negligible compared to the rotational power.

Surface Orientations

A given surface of the tool in contact with the matrix is characterized by its position and orientation relative to the rotation axis of the tool. If the tool rotation axis is vertical (along the z -axis), then a flat shoulder surface would be horizontal or in the ϑr -plane. A cylindrical surface on the tool would be vertical or in the ϑz -plane. The following subscripts have been used to characterize the orientation of the surface:

–= Horizontal (perpendicular to the rotation axis, circular surface).

|= Vertical (parallel to the rotation axis, cylindrical surface).

\= Conical (tilted with respect to rotation axis, conical surface).

Horizontal. In order to calculate the heat generation from a horizontal circular tool surface rotating around the tool center axis, an infinitesimal segment on that surface is investigated. The infinitesimal segment area $dA_{-} = r d\theta dr$ is exposed to a uniform contact shear stress $\tau_{contact}$. This segment contributes with an infinitesimal force of $dF_{-} = \tau_{contact} dA_{-}$ and torque of $dM_{-} = r dF_{-}$. the heat generation from this segment is:

$$dQ_{-} = \omega r dF_{-} = \omega r^2 \tau_{contact} d\theta dr \quad (2.21)$$

Where r is the distance from the investigated area to the center of rotation, ω is the angular velocity, and $r d\theta$ and dr are the segment dimensions.

Vertical. For a cylindrical surface on the tool, the heat generation from an infinitesimal surface segment with the area of $dA_{|} = d\theta dz$ is

$$dQ_{|} = \omega r dF_{|} = \omega r^2 \tau_{contact} d\theta dz \quad (2.22)$$

Where dz is the segment dimension along the rotation axis, *Conical*, In the case of a conical surface segment, a similar approach is adopted as in the case of the horizontal and vertical. In fact, the force/torque contribution from the tilted segment is split up into the contribution from a horizontal and a vertical segment, as the tilted segment area is projected onto the main planes relative to the tool rotation axis. The tilted orientation is characterized by the cone angle α , which is the angle between the horizontal ($r\vartheta$) plane and the segment orientation in the rz –plane.

$$dF_{\setminus} = dF_{-} + dF_{|} \quad (2.23)$$

The projection of the tilted segment area is given by $dz = \tan \alpha dr$, Inserting this into (2.23) gives

$$\begin{aligned} dA_{|} &= rd\theta dz \\ dz &= \tan \alpha dr = rd\theta \tan \alpha dr \\ dA_{|} &= rd\theta dr \end{aligned} \quad (2.24)$$

$$dF_{\setminus} = \tau_{contact} dA_{+} + \tau_{contact} dA_{|} = \tau_{contact} rd\theta dr (1 + \tan \alpha) \quad (2.25)$$

An interpretation of this is that the segment area is enlarged by the fraction of $\tan \alpha$ compared to a horizontal segment. The modification of the heat generated at the tilted segment is

$$dQ_{\setminus} = \omega r dF_{\setminus} = \omega r^2 \tau_{contact} d\theta dr (1 + \tan \alpha) \quad (2.26)$$

It is possible to characterize a rotation symmetrical FSW tool shoulder and probe surfaces by these three types of surface orientations. The limitation in describing modern FSW tools featuring threads, flutes and facets is recognized.

Heat Generation from the Shoulder

The shoulder surface of a modern FSW tool is in most cases concave or conically shaped. The purpose of this geometric feature is to act as an escape volume as the probe is submerged into the matrix during the plunge operation, secondarily enhancing the extrusion and consolidation of the material during the weld operation.

Previous analytical expressions for heat generation include a flat circular shoulder, in some cases omitting the contribution from the probe [15, 17]. This work extends the previous expressions so that conical shoulder and cylindrical probe surfaces are included. An analytical model for the heat generation, that includes non-uniform pressure distribution or strain rate dependent yield shear stresses, material flow driven by threads or flutes, is not taken into account.

Integration of (2.26) over the shoulder area from R_{probe} to $R_{shoulder}$ gives the shoulder heat generation, Q_1 .

$$\begin{aligned} Q_1 &= \int_0^{2\pi} \int_{R_{probe}}^{R_{shoulder}} \omega \tau_{contact} r^2 (1 + \tan \alpha) dr d\theta \\ &= \frac{2}{3} \pi \tau_{contact} (R_{shoulder}^3 - R_{probe}^3) (1 + \tan \alpha) \end{aligned} \quad (2.27)$$

Heat Generation from the Probe

The probe is simplified to a cylindrical surface with a radius of R_{probe} and a probe height H_{probe} . The heat generated from the probe consists of two contributions; Q_2 from the side surface and Q_3 from the tip surface. Integrating dQ_{\perp} , i.e. (2.22), over the probe side area gives,

$$Q_2 = \int_0^{2\pi} \int_0^{H_{probe}} \omega \tau_{contact} R_{probe}^2 dz d\theta = 2\pi \tau_{contact} \omega R_{probe}^2 H_{probe} \quad (2.28)$$

And integrating the heat flux based on equation (1.21) over the probe tip surface, assuming a flat tip gives

$$Q_3 = \int_0^{2\pi} \int_0^{R_{probe}} \omega \tau_{contact} r^2 dr d\theta = \frac{2}{3} \pi \tau_{contact} \omega R_{probe}^3 \quad (2.29)$$

The three contributions are combined to get the total heat generation estimate Q_{total}

$$Q_{total} = Q_1 + Q_2 + Q_3 \quad (2.30)$$

$$= \frac{2}{3} \pi \tau_{contact} \omega ((R_{shoulder}^3 - R_{probe}^3)(1 + \tan \alpha) + R_{probe}^3 + 3R_{probe}^2 H_{probe}) \quad (2.31)$$

In the case of a flay shoulder, the heat generation expression simplifies to

$$Q_{total} = \frac{2}{3} \pi \tau_{contact} \omega (R_{probe}^3 + 3R_{probe}^2 H_{probe}) \quad (2.32)$$

Which correlates with the results found by Khandkar et al [25]

2.8. Contact Shear Stress

Equation (2.14) is based on the general assumption of a constant contact shear stress as mentioned before, but the mechanisms behind the contact shear stress vary depending on whether the sliding or sticking condition is present.

Shear Stress: Sticking Conditions

If the sticking interface condition is assumed, the matrix closest to the tool surface sticks to it. The layer between the stationary material points and the material moving with the tool has to accommodate the velocity difference by shearing. Using the upper limit formulation to calculate the shear stress for this deformation to take place, it follows that the stress is independent of the width of the deformation layer.

This allows the deformation layer, starting at the tool interface and extending further into the weld matrix, to be treated as a shear line/surface. The position of this shear line/surface is very close to the contact interface, therefore the tool geometry is used to describe it. The yield shear stress τ_{yield} is estimated to be $\frac{\sigma_{yield}}{3}$, where σ_{yield} is the weld material stress

$$\tau_{contact} = \tau_{yield} = \frac{\sigma_{yield}}{\sqrt{3}} \quad (2.32)$$

It is known that the yield stress is independent of pressure, but highly temperature dependent. If the same shear yield stress is applied all over the interface, the assumption of an isothermal interface follows. This gives a modified expression of (2.31), assuming the sticking condition

$$Q_{total, sticking} = \frac{2}{3}\pi \frac{\sigma_{yield}}{\sqrt{3}} \omega ((R_{shoulder}^3 - R_{probe}^3)(1 + \tan \alpha) + R_{probe}^3 + 3R_{probe}^2 H_{probe}) \quad (2.33)$$

Shear Stress : Sliding Conditions

Assuming a friction interface condition where the tool surface and weld material are sliding against each other, the frictional shear stress $\tau_{friction}$ is introduced in the general equation (2.31). The choice of Coulomb's friction law to describe the shear stress estimates the critical friction stress necessary for a sliding condition as

$$\tau_{contact} = \tau_{friction} = \mu \rho = \mu \sigma \quad (2.34)$$

Where μ is the friction coefficient, and ρ and σ are the contact pressures, Thus, for the sliding condition, the total heat generation is given by

$$Q_{total, sliding} = \frac{2}{3}\pi \mu \rho \omega ((R_{shoulder}^3 - R_{probe}^3)(1 + \tan \alpha) + R_{probe}^3 + 3R_{probe}^2 H_{probe}) \quad (2.35)$$

Shear Stress: Partial Sliding/Sticking Conditions

The analytical solution of the heat generation for the partial sliding/sticking condition is simply a combination of the two solutions, respectively, with a kind of weighting function. Note that this is only possible because of the assumption of a uniform distribution of the contact state variable δ over the entire contact surface.

From the partial sliding/sticking condition follows that the slip rate between the surfaces is a fraction of ωr , lowering the heat generation from sliding friction. This is counterbalanced by the additional plastic dissipation due to material deformation. It is convenient to define the weighting function parameter as identical to the contact condition variable or dimensionless slip rate δ , which is described in this paper [18]. This enables a linear combination of the expressions for sliding and sticking

$$\begin{aligned}
 Q_{total} &= \delta Q_{total,sticking} + (1 - \delta) Q_{total,sliding} \\
 &= \frac{2}{3} \pi (\delta \tau_{yield} + (1 - \delta) \mu \rho) x \omega ((R_{shoulder}^3 - R_{probe}^3)(1 + \tan \alpha) + R_{probe}^3 + 3R_{probe}^2 H_{probe})
 \end{aligned} \tag{2.36}$$

where δ is the contact state variable (dimensionless slip rate), τ_{yield} is the material yield shear stress at welding temperature, μ is the friction coefficient, ρ is the uniform pressure at the contact interface, ω is the angular rotation speed, α is the cone angle, $R_{shoulder}$ is the shoulder radius, R_{probe} is the probe radius and H_{probe} is the probe height.

This final expression can estimate the heat generation for $0 \leq \delta \leq 1$, co-responding to sliding when $\delta = 0$, sticking when $\delta = 1$ and partial sliding/sticking when $0 < \delta < 1$. In a special case where the sliding condition and flat shoulder are assumed, equation (1.35) is expressed in terms of the plunge force as:

$$Q_{sliding,plunge\ force} = \frac{2}{3} \omega \mu F (R_{shoulder} + 3 \frac{R_{probe}^2 H_{probe}}{R_{shoulder}}) \tag{2.37}$$

Using the relationship that the pressure equals the force divided by the projected area [17].

2.9. Heat Generation Ratios

Based on the geometry of the tool and independent of the contact condition, the ratio of heat generation, i.e. contributions from the different surfaces compared to the total heat generation, are as follows:

$$f_{shoulder} = \frac{Q_1}{Q_{total}} = \frac{(R_{shoulder}^3 - R_{probe}^3)(1 + \tan \alpha)}{(R_{shoulder}^3 - R_{probe}^3)(1 + \tan \alpha) + R_{probe}^3 + 3R_{probe}^2 H_{probe}} = 0.86$$

$$f_{probe\ side} = \frac{Q_2}{Q_{total}} = \frac{3R_{probe}^2 H_{probe}}{(R_{shoulder}^3 - R_{probe}^3)(1 + \tan \alpha) + R_{probe}^3 + 3R_{probe}^2 H_{probe}} = 0.11$$

$$f_{probe\ tip} = \frac{Q_3}{Q_{total}} = \frac{R_{probe}^3}{(R_{shoulder}^3 - R_{probe}^3)(1 + \tan \alpha) + R_{probe}^3 + 3R_{probe}^2 H_{probe}} = 0.03$$

(2.38)

Where the tool dimensions are $R_{shoulder} = 9\text{ mm}$, $R_{probe} = 3\text{ mm}$, $H_{probe} = 4\text{ mm}$, $\alpha = 10^\circ$. This indicates that, for the specific tool geometry, the shoulder contributes the major fraction of the heat generation and the probe tip heat generation is negligible compared to the total heat generation. This correlates with the results found in [19], noting that the contribution from the probe due to the traverse motion which is not the case in the present estimates.

If the sticking condition is assumed, the analytical estimate (2.33) can be used to deduce the estimated shear stress in the shearing layer when Q is known. This gives an average shear stress of 20.8 MPa, equivalent to a yield stress of $\sqrt{3} \cdot 20.8 = 36.1\text{ MPa}$, for Q equal to the experimental rotational power ($M \times \omega$) of 1752 W at a data point after 15.5 s of welding. The experiment shows a top surface temperature of maximum 400 °C, and 2024-T3 has a yield stress at 371 °C in the range from 28 to 34 MPa [20] where an average value of $\tau = 14\text{ MPa}$ is estimated based on an experimentally measured torque.

Sliding condition. The analytical result for heat generation can be correlated with the plunge force (2.35), if the sliding condition and that $p = F / A_{shoulder}$ are assumed. The plunge force is taken from experimental observations and the estimated analytical heat generation is

$$Q_{sliding,ana} = \frac{2}{3} \mu \omega \frac{F_{exp}}{R_{shoulder}^2} \left((R_{shoulder}^3 - R_{probe}^3)(1 + \tan \alpha) + R_{probe}^3 + 3R_{probe}^2 H_{probe} \right)$$

$$= 1752\text{ W}$$

(2.39)

Based on the experimental plunge force $F = 17.7 \text{ kN}$ observed after 15.5 s of welding. Substituting known values for the parameters, tool dimensions of $R_{\text{shoulder}} = 9 \text{ mm}$, $R_{\text{probe}} = 3 \text{ mm}$, $H_{\text{probe}} = 4 \text{ mm}$, $\alpha = 10^\circ$ and rotation speed of $\omega = 41.8 \text{ rad s}^{-1}$, and solving (2.39) for μ , gives a value of $\mu = 0.3$. The analytical estimate for the heat generation equals the experimental rotational power ($M \times \omega$) of 1752 W only at one data point, i.e. after 15.5s of welding, where the plunge force is 17.7 kN and the torque is 41.9 Nm.

Thus, the heat generation estimated analytically in both cases of sliding and sticking can reproduce the heat generation values obtained experimentally. Thus, there is still a further need for a criterion for determining the contact condition. Since the sliding condition also predicts a proportional relationship for a changing plunge force, the experimental values for the plunge force and torque are examined further, so that the contact condition can be estimated.

2.10. Estimation of Contact Conditions

An interesting analysis is to verify the proportional relationship between the plunge force and the heat generation, which is predicted by (2.39) when the sliding condition is assumed. For this, the relationship between the plunge force and the torque is examined. This analysis is also used to suggest which contact condition is most likely to be present during the experiment. Experimental plunge force and torque. During the experiment, the reaction forces in the three directions are monitored, and of special interest is the plunge force. The plunge force is often used in the estimation of the heat generation, but only a limited number of publications with experimental results of the plunge force are available [17]. Figure 2.7 shows the experimental plunge force and torque using the right y-axes and the corresponding analytical and experimental heat generation using the left y-axis.

As the tool is plunged into the weld panel, the plunge force rises steady during the first part of the plunge action (-13.7 to -8 s) to 21kN and the torque rises to 15Nm. This initial smooth rise in both the torque and the plunge force are caused by the tool probe penetrating the matrix. This is followed by a transient response in both the plunge force and torque (rising to 60Nm), in which a result of the shoulder is getting in contact with the matrix interface.

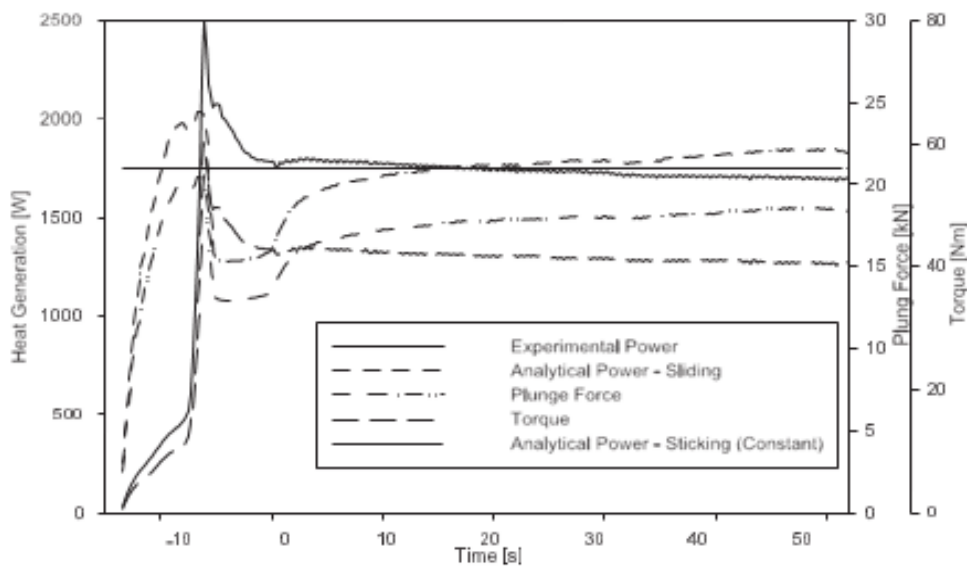


FIG. 2.7: Heat generation (left y-axis), plunge force and torque (right y-axis)

Plunge period –13.7 to –5 s. Dwell period –5 to 0 s. Weld period 0 to 52.5 s. During the dwell period from –5 to 0 s the plunge force drops from 21 to 12 kN where it settles. The torque gradually drops from 60 to 40 Nm. The analytical result for sliding, i.e. $\delta = 0$, predicts a proportional relationship between the plunge force and torque. FIG: 2.7 shows the reaction force and torque, reading the values on the right y-axes.

The proportionality is in theory only fulfilled if the condition is close to sliding, equivalent to a contact variable δ close to 0 and uniform pressure distribution. The proportionality should be applicable during the dwell action where the uniform pressure is most likely to be fulfilled, but this is not supported by the non-proportional relationship between the plunge force and the torque, seen from –5 to 0 s in FIG 2.8.

After the dwell/weld transition at 0 s, the plunge force rises from 13 to 17 kN at the beginning of the weld, finishing at 18.5 kN. The torque starts at 43 Nm, dropping to 41 Nm at the end of the welding period. The traverse motion of the tool in the weld period is initiated by a smooth acceleration up to the welding speed of 2 mm s^{-1} in order to minimize the transient effect. The traverse motion of the tool results in the rise in the plunge force, but a corresponding rise in the torque is not observed. (The measured force to overcome the traverse resistance is less than 0.5 kN, and the traverse power input is therefore less than 1 W.)

The torque seems to stabilize after 5–10 s corresponding to a steady state, which is supported by additional thermal measurements showing virtually identical temperature history profiles at locations traversed at 15 and 35 s after the start of the welding (not reported in this work). The modest change in the plunge force from 10 to 52.5 s could be caused by a machine effect. The tool displacement was set remotely to a fixed value. During welding, the measured machine deflection increases slightly (not shown) and the measured plunge force (shown in FIG. 2.7) increases slightly, also. These effects show that, during welding, a factor acted to displace the tool upwards. This results in an increased deflection of the machine, hence, giving a higher plunge force. A gradual rise in the backing plate and tool temperature (yielding expansion), could be the cause. Thus, the plunge force cannot be used to assess whether or not steady state conditions apply during welding in this case.

The following conclusions are drawn

- After an initial transient period, the torque does not change during welding. This reflects a steady state welding condition.
- The change in the plunge force during steady state welding is most likely caused by the specific machine condition present during the welding process. The modest change in the plunge force does not affect the torque. This indicates that a sticking condition is present.

FIG: 2.7 shows the heat generation as function of time, using the left y-axis. Two power related quantities are shown; the experimental rotational power/heat generation ($M \times \omega$) and combined analytical heat generation (using the experimental plunge force in the analytical expression). During the plunge and dwell period from –13.7 to 0 s the welding panel, backing plate and the tool are preheated with approximately 15 kJ (integration of the rotational power). The maximum heat generation of 2.5 kW occurs when the shoulder first touches the weld panel at –6.1 s and drops to 1.8 kW at the end of the dwell period (0 s). The welding period is initiated by a smooth acceleration of the tool to the welding speed of 2 mm s^{-1} , which gives a rise in plunge force, but a similar effect on the heat generation does not take place, instead the heat generation stabilizes in the range of 1.7–1.8 kW during the 105 mm of welding.

If the sliding is the dominant contact condition, the friction coefficient should attain changing values for positions along the weld path, ranging from 0.27 to 0.35. This is thought not to be likely for the same weld in a steady state condition. As seen in figure 6, heat generation and the torque are nearly constant (even for alternating plunge force) during the dwell and weld period, and this is interpreted as an indication of a sticking or close to sticking contact condition. This is supported by an investigation of the material flow in the welds used in this welding experiment [21, 22].

2.11. Numerical Models

In order to model the thermal aspects of FSW more accurately, numerical methods must be used, for instance finite element or finite difference methods. Numerical methods allow a more detailed geometric representation of the welding setup in which advanced tool shapes as well as the interaction between tool, work piece and backing plate can be modelled. Also temperature dependent material parameters, like the conductivity and yield stress, can be handled by numerical methods in contrast to the analytical Rosenthal equations.

A large number of modelling choices must be made when developing a FSW model, the possibilities include dimension (2D/3D), transient vs. steady state and Eulerian vs. Lagrangian models, i.e. whether the material flows through the mesh or whether the material follows the mesh. Different aspects of the modelling are presented along with some models from the literature. FSW is a non-stationary process as described earlier with the plunge, dwell, welding, and extraction phases [23], and to model the full process a time-dependent model should be used, i.e. by solving eq. (1.1). However, in many cases it is reasonable to assume that the welding phase, when the tool is moving at constant velocity and not too close to the start and end points, is stationary, such that the temperature field around the tool does not change during this phase.

In Schmidt et al. (2004) experimental measurements of torque and plunge force during a welding experiment are shown, and it is found that the values become almost constant during the welding phase which backs the assumption of stationary. The present thesis focuses on thermal models of the stationary phase using a Eulerian framework. The heat equation to be solved is:

$$\begin{aligned} \nabla(-k\nabla T) + \rho c_p u \nabla T &= q \text{ in } \Omega \\ T &= T_0 \text{ on } T_T \\ -k\nabla T \cdot \mathbf{n} &= q_R \text{ on } T_q \end{aligned} \tag{2.40}$$

Where Ω is the computational domain, T_T is a Dirichlet boundary with given temperature T_0 and T_q is a Neumann boundary where the heat flux q_R is given. \mathbf{n} is an outward pointing unit vector normal to the boundary. For an insulating boundary $q_R = 0$ and for boundaries in contact with e.g. air or the backing plate $q_R = h(T - T_A)$ with T_A being the temperature of the neighbouring body or fluid.

This type of model has a number of advantages compared to transient Lagrangian models when only the stationary response is of interest. First of all, it is fast, as just one solution is required and secondly, the heat source is stationary relative to the mesh meaning that a very fine mesh can be used in the vicinity of the heat source while using a coarser mesh further away.

This type of model is however normally not used for modelling more advanced effects, such as residual stresses, where transient Lagrangian models are dominant in the literature, for example in Richards et al and Tutum et al..

An effect that has a large impact on the global temperature fields is the heat loss from the work piece to the backing plate governed by the equation

$$q_R = h(T - T_{bp}) \tag{2.41}$$

Where h is the heat transfer coefficient and T_{bp} the temperature of the backing plate, the heat transfer coefficient is non-uniform across the area of contact and is a function of contact pressure, backing plate material, surface roughness and other factors, thus making it hard to determine appropriate values. Most of the work presented in the literature assumes a uniform h across the contact area.

Examples of values used are: $h = 700 \frac{W}{m^2K}$ in Schmidt and Hattel (2008), $h = 350 \frac{W}{m^2K}$ in Chao et al. (2003) and $h = 5000 \frac{W}{m^2K}$ in Khandkar et al. (2006). In Soundararajan et al. (2005) an attempt is made to relate the heat transfer coefficient to the contact pressure between workpiece and backing plate by calculating the contact pressure for an assumed h value and then assigning a pressure-dependent h –value based on the calculated pressure distribution. They define four zones around the tool in which h varies from $h = 3000 - 4000 \frac{W}{m^2K}$ below the tool to $h = 30 - 300 \frac{W}{m^2K}$ in areas close to the workpiece edges in front of the tool.

Different models with and without backing plates are discussed and different heat transfer coefficients are applied in the model and compared to experimental temperature measurements. Uniform values of $h = 10000 \frac{W}{m^2K}$, $h = 5000 \frac{W}{m^2K}$ and $h = 1000 \frac{W}{m^2K}$ are used.

Also a non-uniform h that take the value $h = 100000 \frac{W}{m^2K}$ under the shoulder, $h = 10000 \frac{W}{m^2K}$ in areas previously covered by the shoulder and $h = 1000 \frac{W}{m^2K}$ in other areas is tested. It is found that the non-uniform heat transfer coefficient was too large under the tool and predicted too low temperatures.[24]

2.12. Example of Different Heat Transfer Coefficients

This example is intended to show the effect of the work piece-backing plate heat transfer coefficient h . A 3D stationary model consisting of the work piece and a steel backing plate, with the heat source given by the TPM model (FIG.2.8), eq. (1.14). Using the TPM model means that the heat input is not the same in the three cases presented and, therefore, the effect of changing h is less readily seen than when using a fixed total heat input. Figure 2.8 shows the work piece temperature field for three different h values. The heat transfer coefficient has a clear influence on the temperature fields by removing heat from the work piece. This is most obvious on the left column of plots where it can be seen how the high temperature regions become more and more localised around the tool as h is increased, where optimization techniques and experimental data are used in order to find optimal values of h that minimize the difference between the calculated and the measured temperatures.

Although most models in the literature deal primarily with the work piece, and in some cases the backing plate, some models also take the tool into account. As well as heat losses to the backing plate, heat is lost to the tool and a welding efficiency can be defined as the ratio of heat that is conducted into the tool to the total mechanical power, [28]. In that paper values of around 10% were determined for two different welding situations. [24] a value of 13 % is mentioned.

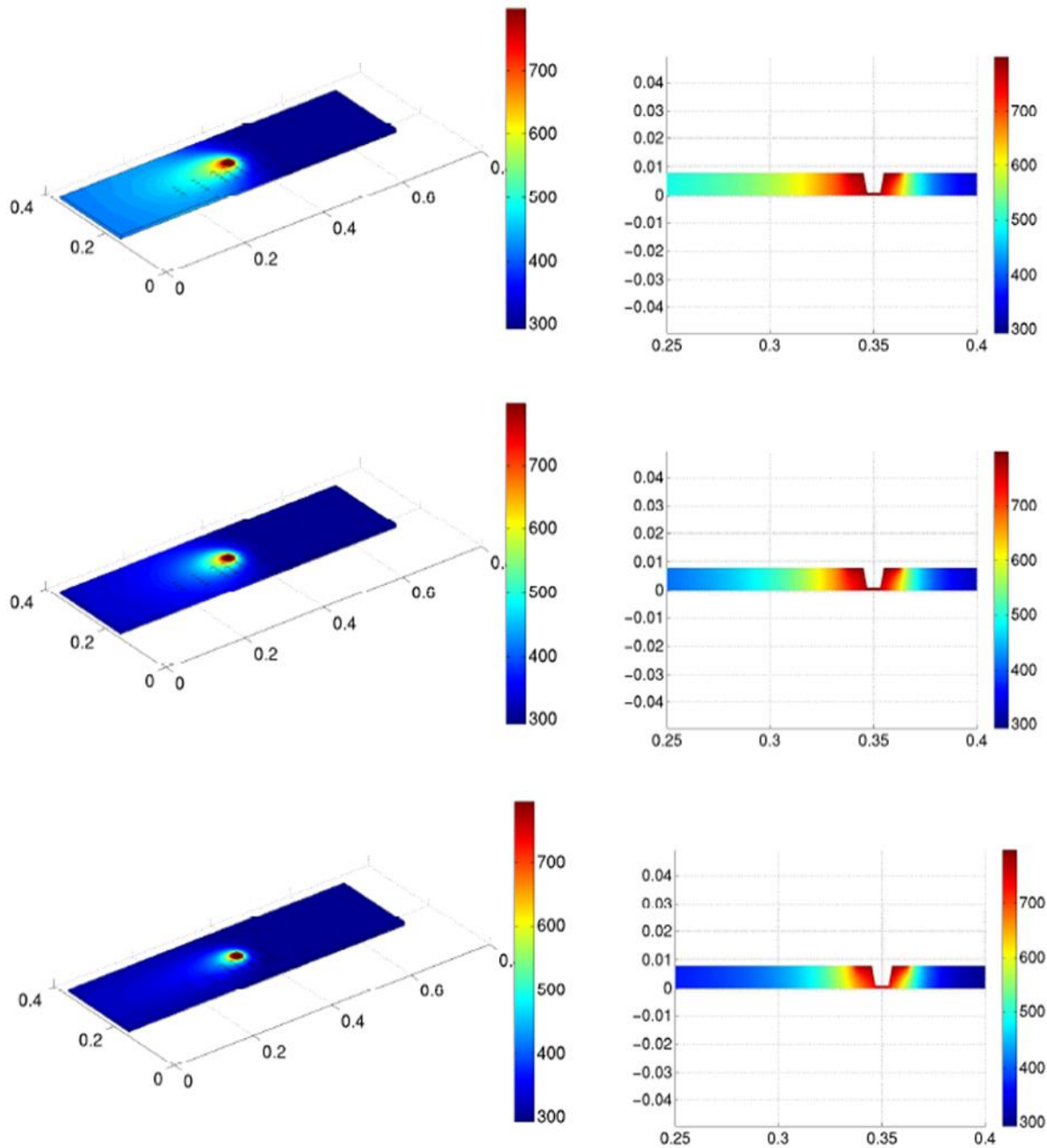


FIG. 2.8: The figure shows the effect of the work piece-backing plate heat transfer coefficient h for a 3D model of the work piece and the backing plate. The left column shows the temperature field in the work piece while the right column shows a cross section of the work piece at the tool. The top row shows results for $h = 50 \frac{W}{m^2K}$, the middle row shows results for $h = 400 \frac{W}{m^2K}$ and the last row shows results for $h = 10000 \frac{W}{m^2K}$. Notice the probe hole and how the temperature decreases when moving away from the tool for increasing h values.

2.13. Experimental Aspect

A general friction stir welding set up consist of a workpiece, which is the material that is to be joined, a tool, consisting of the tool shoulder and the tool pin or probe and lastly a backing plate that is made of a solid reliable material to withstand heat that is generated by the tool.

But a friction stir weld cannot take place unless the correct calculations, simulations and consideration have taken place.

Firstly, is the consideration of the tool shoulder as there are many different types of shoulders and each has their own set of advantages. Certain friction stir welding tool shoulders can also contain features to increase the amount of material deformation produced by the shoulder resulting increased workpiece mixing and higher quality welds. These features can consist of scroll ridges or knurling, grooves and concentric circles which can be machined into any tool profile (Concave, Convex and Flat).

Along with the tool shoulder is pin which is also referred to as a probe, the use of the probe is to provide the corrected heating, by the calculation of speed to joint workpieces.

2.14. Process Parameters

The success of the Friction Stir Welding process depends on a number of parameters, these parameters being both operational parameters due to the nature of the process as well as geometric. In addition to the four primary process parameters some critical parameters to consider are as follows:

- **Tool Geometry:** This includes the diameter of the tools shoulder and pin, pin length, pin taper angel as well as both pin and shoulder features.
- **Clamping System:** A rigid clamping system is required to ensure that no translation motion of the workpiece occurs during welding and that the plasticised material is confined during welding.
- **Tool Rotational Direction:** Either clockwise or anticlockwise.
- **Process Forces:** In particular, the axial force.
- **Tilt Angle:** This is the angle between the tool axis and the normal weld plane.
- **Plunge Depth:** This defines how far the pin is positioned from the backing plate and as a result has a significant effect on the weld quality.
- **Control Methodology:** Typically, either forced or displacement controlled.

Two parameters are very important for the experimental aspect of FSW: tool rotation rate (v , rpm) in clockwise or counterclockwise direction and tool traverse speed (n , mm/min) along the line of joint. The rotation of tool results in stirring and mixing of material around the rotating pin and the translation of tool moves the stirred material from the front to the back of the pin and finishes welding process. Higher tool rotation rates generate higher temperature because of higher friction heating and result in more intense stirring and mixing of material as will be discussed later. However, it should be noted that frictional coupling of tool surface with workpiece is going to govern the heating. So, a monotonic increase in heating with increasing tool rotation rate is not expected as the coefficient of friction at interface will change with increasing tool rotation rate. In addition to the tool rotation rate and traverse speed, another important process parameter is the angle of spindle or tool tilt with respect to the workpiece surface. A suitable tilt of the spindle towards trailing direction ensures that the shoulder of the tool holds the stirred material by threaded pin and move material efficiently from the front to the back of the pin. Further, the insertion depth of pin into the workpieces (also called target depth) is important for producing sound welds with smooth tool shoulders. The insertion depth of pin is associated with the pin height. When the insertion depth is too shallow, the shoulder of tool does not contact

the original workpiece surface. Thus, rotating shoulder cannot move the stirred material efficiently from the front to the back of the pin, resulting in generation of welds with inner channel or surface groove.

The heating is accomplished by friction between the tool and the workpiece and plastic deformation of workpiece. The localized heating softens the material around the pin and combination of tool rotation and translation leads to movement of material from the front of the pin to the back of the pin. As a result of this process a joint is produced in 'solid state'. Because of various geometrical features of the tool, the material movement around the pin can be quite complex. During FSW process, the material undergoes intense plastic deformation at elevated temperature, resulting in generation of fine and equated recrystallized grains. The fine microstructure in friction stir welds produces good mechanical properties.

2.15.1. Welding Parameters

For FSW, two parameters are very important: tool rotation rate (v , rpm) in clockwise or counter clockwise direction and tool traverse speed (n , mm/min) along the line of joint. The rotation of tool results in stirring and mixing of material around the rotating pin and the translation of tool moves the stirred material from the front to the back of the pin and finishes welding process. Higher tool rotation rates generate higher temperature because of higher friction heating and result in more intense stirring and mixing of material as will be discussed later. However, it should be noted that frictional coupling of tool surface with workpiece is going to govern the heating. So, a monotonic increase in heating with increasing tool rotation rate is not expected as the coefficient of friction at interface will change with increasing tool rotation rate. In addition to the tool rotation rate and traverse speed, another important process parameter is the angle of spindle or tool tilt with respect to the workpiece surface. A suitable tilt of the spindle towards trailing direction ensures that the shoulder of the tool holds the stirred material by threaded pin and move material efficiently from the front to the back of the pin. Further, the insertion depth of pin into the workpieces (also called target depth) is important for producing sound welds with smooth tool shoulders. The insertion depth of pin is associated with the pin height. When the insertion depth is too shallow, the shoulder of tool does not contact the original workpiece surface. Thus, rotating shoulder cannot move the stirred material efficiently from the front to the back of the pin, resulting in generation of welds with inner channel or surface groove. When the insertion depth is too deep, the shoulder of tool plunges into the workpiece creating excessive flash. In this case, a significantly concave weld is produced, leading to local thinning of the welded plates. It should be noted that the recent development of 'scrolled' tool shoulder allows FSW with 0° tool tilt. Such tools are particularly preferred for curved joints. Preheating or cooling can also be important for some specific FSW processes. For materials with high melting point such as steel and titanium or high conductivity such as copper, the heat produced by friction and stirring may be not sufficient to soften and plasticize the material around the rotating tool. Thus, it is difficult to produce continuous defect-free weld. In these cases, preheating or additional external heating source can help the material flow and increase the process window. On the other hand, materials with lower melting point such as aluminium, cooling can be used to reduce extensive growth of recrystallized grains and dissolution of strengthening precipitates in and around the stirred zone.

2.15.2. Experimental Parameters

For the experimental aspect of this study the following parameters have been put into consideration as well as parameters for the experiment has been derived from the selection chosen, Materials Al2024-T3 and Al6056 are the said mentioned materials to be used for the weld having rotational speeds of 800,1250,1600,2000 rpm with a feed rate of 300,400 and 500 mm/min in a dwell time of 10-15 seconds.

2.15.3. Test Types

2.15.3.1. Standard Test

The standard test is that of basic friction stir weld, the standard friction stir weld is the most basic of the friction stir welds, consisting of just simply a single shoulder and a single pin to conduct the weld where the tool is held perpendicular to the workpiece. The standard tool has three primary functions.

- A) To heat the workpiece provided the adequacy of thermo-mechanical softening by means of frictional contact with the workpiece.
- B) Stirring of the material to produce a joint, heat transfer from the tool softens the material by means of reducing the yield strength, so that with tool rotation and translation, it will lead to movement of material from the leading edge to the trailing edge of the pin, as a result filling the cavity produced in the tool's wake as the moves forward.
- C) Containment of the hot metal beneath the tool shoulder vertical ow occurs during FSW. It is the role of the FSW tool, in particular the tool's shoulder to contain the material within what will later know as the 'third body region'.

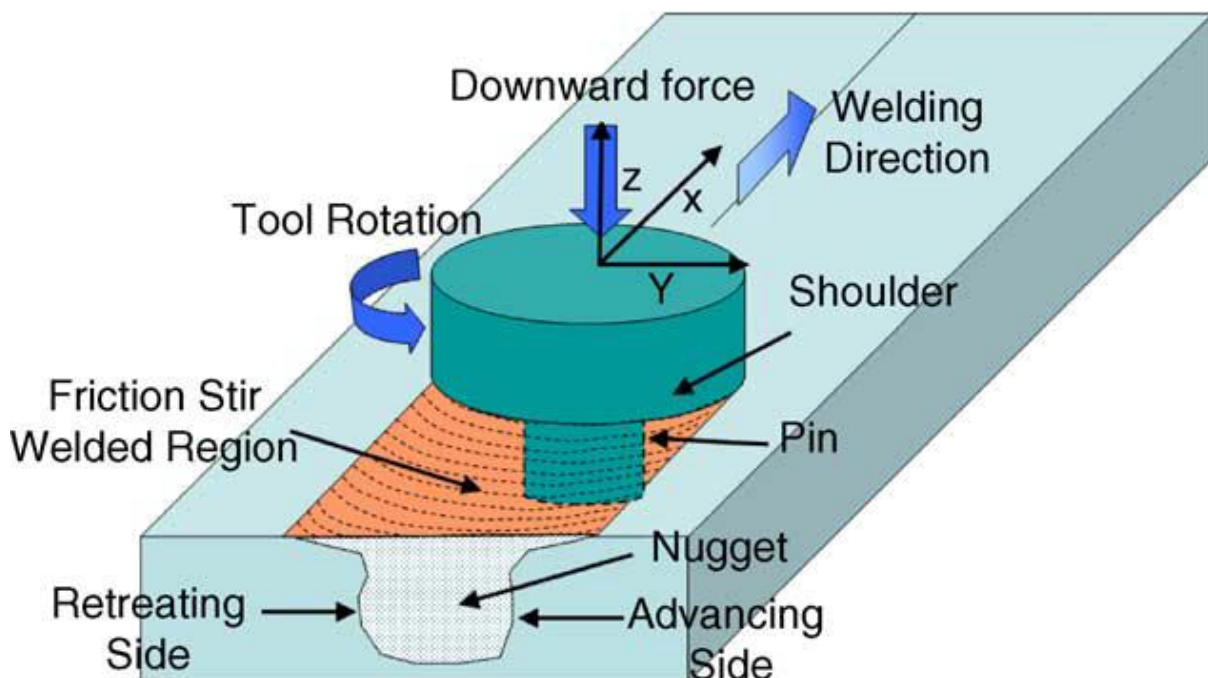


Image 2.1: A Standard tool Weld

2.15.3.2. Hot Water Applied Test

The application of hot water to a friction stir weld is to serve the purpose of reducing heat generation by applying boiling water that is of a 100 °C to lower the heat generation of 184 °C, Boiling is lower than the heat that is emitted from the actual tool hence the cooling properties.

A limited number of works have attempted and simulated the temperature history of a friction stir weld under an external liquid cooling as presented in this present study in which the coolant is modelled as a water flux behind the tool, resulting the cooling effect positive and a reduction of thermal flow adjacent to the tool.

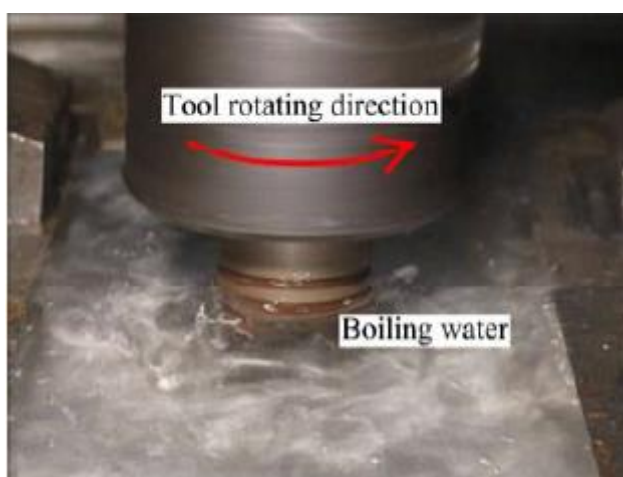


Image 2.2: A depiction of a Friction stir weld process with the application of water.

2.15.3.3. The Liquid Nitrogen Applied Test

liquid nitrogen is demonstrated as an alternative and improved method for creating fine-grained welds in dissimilar metals. Friction-stir welding with liquid nitrogen significantly suppresses the formation of intermetallic compounds because of the lower peak temperature. Furthermore, the temperature profiles plotted during this investigation indicate that the largest amount of ΔT is generated by the weld under liquid nitrogen, which is performed at the lowest temperature. It is shown that in low-temperature FSW, the flow stress is higher, plastic contribution increases, and so adiabatic heating, a result of high strain and high strain-rate deformation, drives the recrystallization process beside frictional heat. The decreasing the starting temperature of workpiece from 30 to -30 °C with liquid nitrogen cooling resulted in a decrease in peak temperature from 330 to 140 °C at a location 10 mm away from the weld centreline, thereby leading to a reduction in the grain size from 10 to 0.8 mm on the material 2024Al and drastically cooling the work piece down.

3. The Design of Tools

3.1. Tool Shoulders

Tool shoulders are designed to produce heat (through friction and material deformation) to the surface and subsurface regions of the work piece. The tool shoulder produces a majority of the deformational and frictional heating in thin sheet, while the pin produces a majority of the heating in thick work pieces. Also, the shoulder produces the downward forging action necessary for weld consolidation.

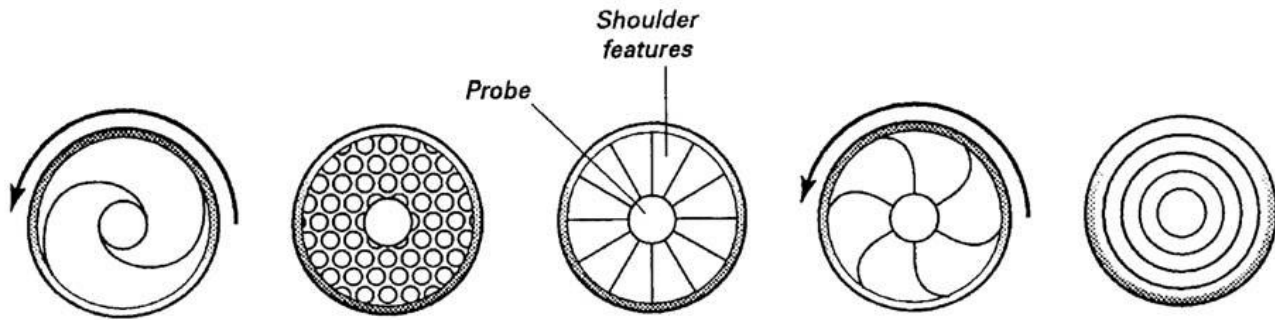


FIG. 3.1: Different shoulder features used to improve material flow and shoulder efficiency. Source: Ref 79

3.2. Shoulder Features

The FSW tool shoulders can also contain features to increase the amount of material deformation produced by the shoulder, resulting in increased work piece mixing and higher-quality friction stir welds [38, 39]. These features can consist of scrolls, ridges or knurling, grooves, and concentric circles (FIG 3.1) and can be machined onto any tool shoulder profile (concave, flat, and convex). Currently, there are published examples of three types of shoulder features: scoops [39], concentric circles, and scrolls [38, 40, 41, 42, 43, 44].

3.2.1. Concave Shoulder

The first shoulder design was the concave shoulder [8], commonly referred to as the standard-type shoulder, and is currently the most common shoulder design in friction stirring. Concave shoulders produce quality friction stir welds, and the simple design is easily machined. The shoulder concavity is produced by a small angle between the edge of the shoulder and the pin, between 6 and 10°. During the tool plunge, material displaced by the pin is fed into the cavity within the tool shoulder. This material serves as the start of a reservoir for the forging action of the shoulder. Forward movement of the tool forces new material into the cavity of the shoulder, pushing the existing material into the flow of the pin. Proper operation of this shoulder design requires tilting the tool 2 to 4° from the normal of the work piece away from the direction of travel; this is necessary to maintain the material reservoir and to enable the trailing edge of the shoulder tool to produce a compressive forging force on the weld. A majority of the friction stir welds produced with a concave shoulder are linear; nonlinear welds are only possible if the machine design can maintain the tool tilt around corners (i.e. multi-axis FSW machine) [24,25,26,27,28,29,30,31,32,33,34,35,36,37].

3.2.2. Scroll Shoulder

Scrolls are the most commonly observed shoulder feature. The typical scrolled shoulder tool consists of a flat surface with a spiral channel cut from the edge of the shoulder toward the centre (Image 3.1). The channels direct deformed material from the edge of the shoulder to the pin, thus eliminating the need to tilt the tool. Removing the tool tilt simplified the friction stirring machine design and allowed for the production of complicated nonlinear weld patterns. Concave shoulder tools also have a tendency to lift away from the work piece surface when the tool travel speed is increased. Replacing the concave shoulder with a scrolled shoulder reduces the tool lift and increases the welding speed. An additional advantage of the scrolled shoulder tool is elimination of the undercut produced by the concave tool and a corresponding reduction in flash. Also, because the tool is normal to the work piece, the normal forces are lower than concave shoulder tools, which must apply load in both the normal and transverse directions to keep the shoulder in sufficient contact. In addition, the material within the channels is continually sheared from the plate surface, thereby increasing the deformation and frictional heating at the surface [39]. Scrolled shoulder tools are operated with only 0.1 to 0.25 mm (0.004 to 0.01 in.) of the tool in contact with the work piece; any additional work piece contact will produce significant amounts of flash. If the tool is too high (insufficient contact), the shoulder will ride on a cushion of material that will smear across the joint line and make a determination of weld quality difficult [39]. Thus, use of the scrolled shoulder requires more positional care than the concave shoulder. The limitations of scrolled shoulder tools include the inability to weld two plates with different thicknesses, an inability to accommodate for work piece thickness variation in the length of the weld, and welding of complex curvatures (especially tight curvatures). Scrolled shoulder tools can weld two plates of different thicknesses, but some amount of material from the thicker plate is expelled in the form of flash.



Image 3.1: Photograph of a scrolled shoulder tool and a truncated cone pin containing three flats

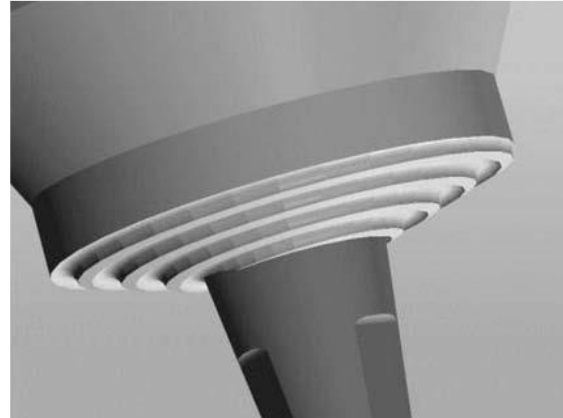
3.2.3. Convex Shoulder

Friction stir tool shoulders can also have a convex profile [39,45,46,47]. Early attempts at TWI to use a tool with a convex shoulder were unsuccessful, because the convex shape pushed material away from the pin. The only reported success with a smooth convex tool was with a 5 mm (0.2 in.) diameter shoulder tool that friction stir welded 0.4 mm (0.015 in.) sheet [45]. Convex shoulder tools for thicker material were only realized with the addition of a scroll to the convex shape [46-48]. Like the scrolls on the flat profile shoulders (see the section “Scroll Shoulder” in this chapter), the scrolls on the convex shoulders move material from the outside of the shoulder in toward the pin. The advantage of the convex shape is that the outer edge of the tool need not be engaged with

the work piece, so the shoulder can be engaged with the work piece at any location along the convex surface. Thus, a sound weld is produced when any part of the scroll is engaged with the work piece, moving material toward the pin. This shoulder design allows for a larger flexibility in the contact area between the shoulder and work piece (amount of shoulder engagement can change without any loss of weld quality), improves the joint mismatch tolerance, increases the ease of joining different-thickness work pieces, and improves the ability to weld complex curvatures. The profile of the convex shoulder can be either tapered [46-49] or curved [38-48] (Image 3.2).



(a)



(b)

Image 3.2: Depictions of the convex shoulder having either (a) curved or (b) tapered geometries

3.3. Pin Designs

Friction stirring pins produce deformational and frictional heating to the joint surfaces. The pin is designed to disrupt the faying, or contacting, surfaces of the work piece, shear material in front of the tool, and move material behind the tool. In addition, the depth of deformation and tool travel speed are governed by the pin design. The focus of this section is to illustrate the different pin designs found in the open literature, including their benefits and drawbacks. In addition to the pins presented in this section, many other viable pin designs are contained within patent or patent application documents that are not contained within the known literature [38]. The reader is encouraged to search the patent literature for additional information about pins not contained within this chapter.

3.3.1. Round-Bottom Cylindrical Pin

The pin cited in the original FSW patent [23] consists of a cylindrical threaded pin with a round bottom (Image 3.3). This pin design was achieved during the TWI group-sponsored project number 5651 and is commonly referred to as the 5651 tool in the friction stir community. Threads are used to transport material from the shoulder down to the bottom of the pin; for example, a clockwise tool rotation requires left-handed threads. A round or domed end to the pin tool reduces the tool wear upon plunging and improves the quality of the weld root directly underneath the bottom of the pin. The best dome radius was specified as 75 % of the pin diameter. It was claimed that as the dome radius decreased (up to a flat-bottom tool), a higher probability of poor-quality weld was encountered, especially directly below the pin. The versatility of the cylindrical pin design is that the pin length and diameter can readily be altered to suit the user's needs [50]. Also, machining a radius at the bottom of the threads will increase tool life by eliminating stress concentrations at the root of the threads.



Image 3.3: Photograph of a concave shoulder with a roundbottom pin

3.3.2. Flat-Bottom Cylindrical Pin

Contrary to the statements made in the previous section about the negative aspects of the flat-bottom cylindrical pin (Image 3.4), the flat-bottom pin design is currently the most commonly used pin design [34,51-52, 53,54,55,56,57,58,59]. Changing from a round-bottom to a flat-bottom pin is attributed to a geometrical argument. The surface velocity of a rotating cylinder increases from zero at the center of the cylinder to a maximum value at the edge of the cylinder. The local surface velocity coupled with the friction coefficient between the pin and the metal dictates the deformation during friction stirring. The lowest point of the flat-bottom pin tilted to a small angle to the normal axis is the edge of the pin, where the surface velocity is the highest (FIG 3.1 a). In contrast, the lowest point of a round-bottom pin is not far from the center of the pin exhibiting a slower surface velocity (FIG 3.1 b). The surface velocities at the lowest points of flat-bottom and round-bottom pins are compared in Table 3.1, assuming a 3° tool tilt, 5 mm (0.2 in.) diameter pin, and a 3.8 mm (0.15 in.) round-bottom pin radius. A larger round-bottom pin radius will reduce the velocity differential, while a smaller pin radius will increase the velocity differential. For this example, the flat-bottom pin has a surface velocity 27.9 times the round-bottom pin. The increased surface velocity at the bottom of the pin would increase the throwing power of the pin, or the ability of the pin to affect metal below the end of the pin. In addition, the flat-bottom pin is easier to machine, and the defects mentioned in the previous section can be eliminated with correct tool parameters and sufficient forging load.

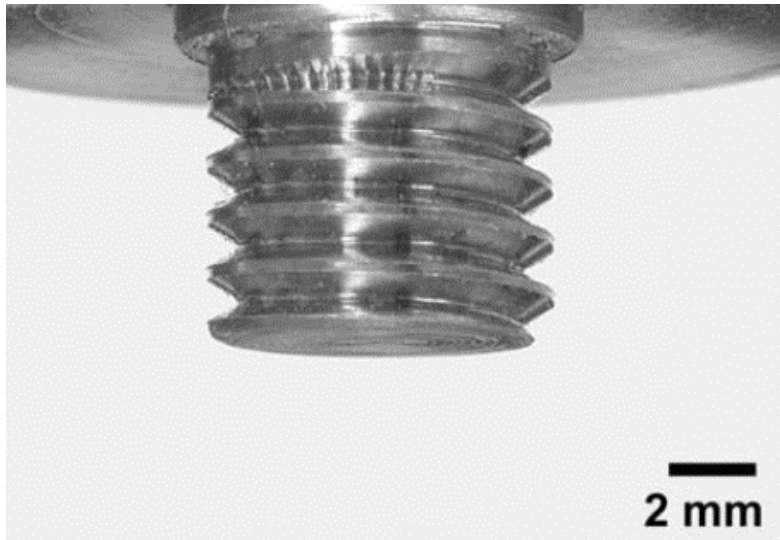


Image 3.4: Photograph of a flat-bottom pin

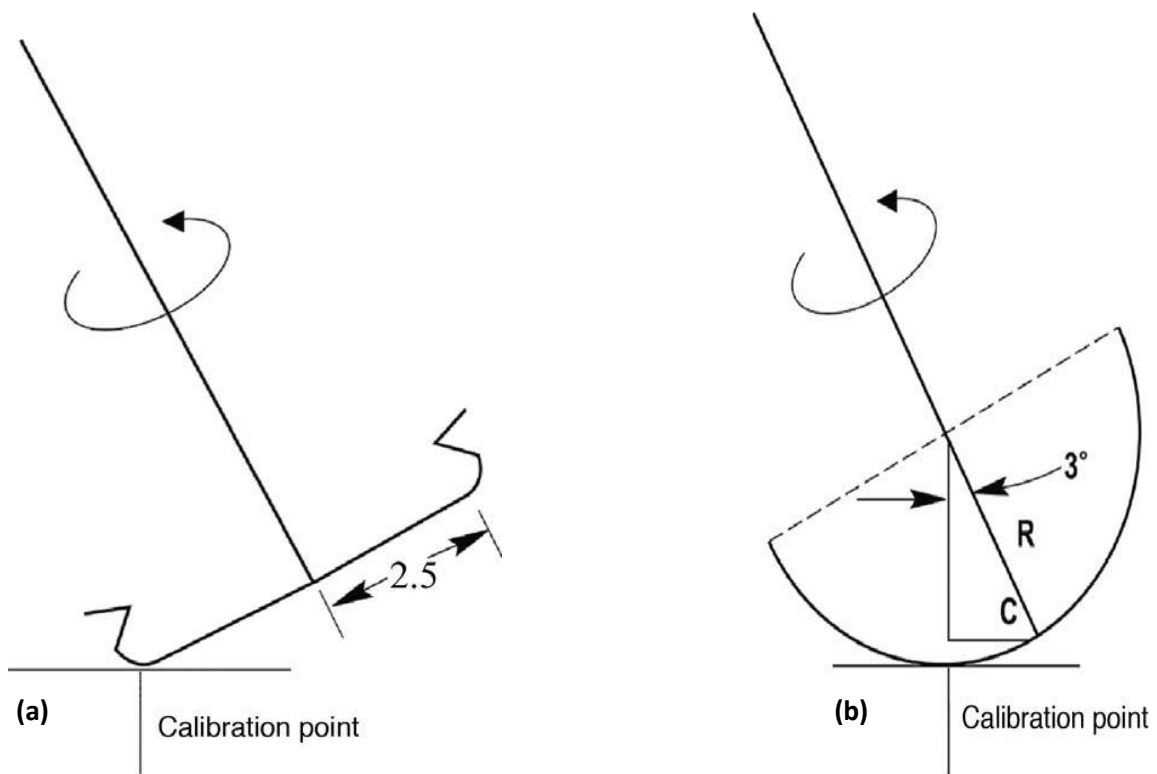


FIG. 3.1: Geometry used to compare surface velocities at calibration point for (a) flat-bottom and (b) round-bottom pins. Source: Ref 86

Tool rpm	Surface velocities, $\text{cm} \cdot \text{min}^{-1}$	
	Flat-bottom pin	Round-bottom pin
200	314	11
400	628	22
600	942	34

Table 3.1: Calculated surface velocities of lowest pin location

3.3.3. Truncated Cone Pin

Cylindrical pins were found to be sufficient for aluminium plate up to 12 mm (0.5 in.) thick, but researchers wanted to friction stir weld thicker plates at faster travel speeds. A simple modification of a cylindrical pin is a truncated cone [41-44-60] (Image 3.5). Truncated cone pins have lower transverse loads (when compared to a cylindrical pin), and the largest moment load on a truncated cone is at the base of the cone, where it is the strongest. A variation of the truncated cone pin is the stepped spiral pin (Image 3.6), a design developed for high-temperature materials [33,61,62,63,64,65]. During the friction stir processing (FSP) of Ni-Al bronze, a threaded profile distorted, and threadless tools did not produce sufficient material flow to obtain 6 mm (0.25 in.) deep deformation regions. Thus, the stepped spiral tool was designed with robust features that survived the 1000 °C (1830 °F) temperatures. The stepped spiral has a square edge and never forms a recess between a step and the following step. Also, the stepped spiral profile can be ground into ceramic tools, where threaded features are not possible. Thus, some PCBN tools contain a stepped spiral pin that increases the volume of material deformed by the pin [48, 64, 66].



Image 3.5: Truncated cone pin and convex shoulder friction stir welding tool.

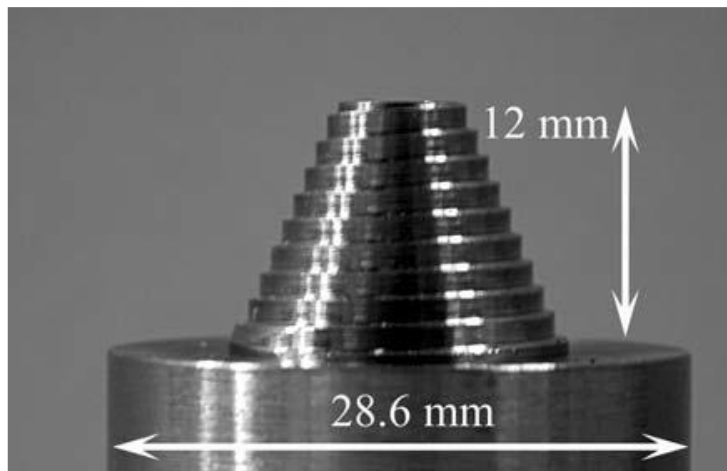


Image 3.6: Photograph of a stepped spiral pin

3.3.4. Addition of Machined Flats on Pins

Thomas et al. [38] found that the addition of flat areas to a pin changes material movement around a pin. The effect of adding flat regions is to locally increase the deformation of the plasticized material by acting as “paddles” and producing local turbulent flow of the plasticized material. Colligan, Xu, and Pickens [41] used 25.4 mm (1 in.) thick 5083-H131 to demonstrate that a reduction in transverse forces and tool torque was directly proportional to the number of flats placed on a truncated cone (up to four flats). Recently, Zettler et al. [43] have examined the FSW of 4 mm (0.16 in.) thick 2024-T351 and 6056-T4 Al alloys as a function of FSW tool parameters for three different pin designs: a non-threaded truncated cone pin, a threaded truncated cone pin, and a threaded truncated cone pin with flats. Welding trials quickly showed that the non-threaded pin produced voids, while the two threaded pins (with and without flats) produced fully consolidated friction stir welds. Adding the flats was shown to increase the weld nugget area and the work piece temperature measured at the plate mid-thickness 12.3 mm (0.5 in.) from the joint centreline when compared to the pin without flats.

3.3.5. Whorl Pin

The next evolution in pin design is the Whorl pin developed by TWI [68,69]. The Whorl pin reduces the displaced volume of a cylindrical pin of the same diameter by 60 %. Reducing the displaced volume also decreases the traverse loads, which enables faster tool travel speeds. The key difference between the truncated cone pin and the Whorl pin is the design of the helical ridge on the pin surface. In the case of the Whorl pin, the helical ridge is more than an external thread, but the helical ridge acts as an auger, producing a clear downward movement. Variations of the Whorl pin include circular, oval, flattened, or re-entrant pin cross sections (Image 3.7) [69]. The significant advantage of the Whorl pin is the ratio of the volume swept by the pin to the pin volume. Cylindrical pins have a ratio of 1.1 to 1, while the Whorl pin has a 1.8 to 1 ratio (when welding 25 mm, or 1 in., thick plate).

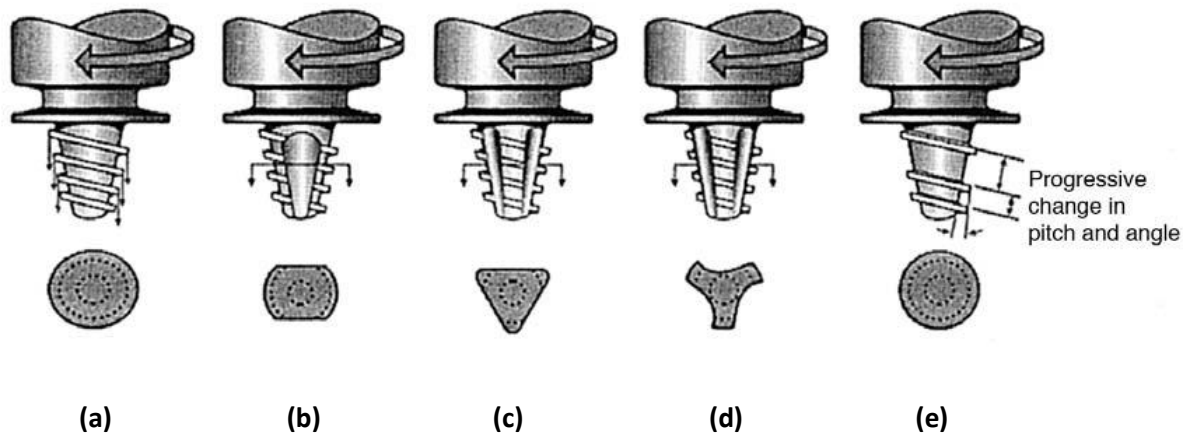


Image 3.7: Schematics of the Whorl pin variations. (a) Oval-shaped probe. (b) Paddle-shaped probe. (c) Three-flat-sided probe. (d) Three-sided re-entrant probe. (e) Changing spiral form and flared probe. [69]

3.3.6. MX Triflute Pin

The MX Triflute pin (TWI) is a further refinement of the Whorl pin (Image 3.8) [68,69]. In addition to the helical ridge, the MX Triflute pin contains three flutes cut into the helical ridge. The flutes reduce the displaced volume of a cylindrical pin by 70 % and supply additional deformation at the weld line. Additionally, the MX Triflute pin has a pin volume swept to pin volume ratio of 2.6 to 1 (when welding 25 mm thick plate). Published examples using Triflute-type pins include FSW 5 mm (0.2 in.) thick 5251 Al [70] and up to 50 mm (2 in.) thick copper. Cederqvist [71] cited that changing to an MX Triflute increased the tool travel speed by 2.5 times over the previous tool design. In addition to welding thick-section copper, the MX Triflute has shown promise for thick-section aluminium alloys. Ma et al. [72] used the FSP of cast A356 Al to demonstrate that a modified Triflute pin (cylindrical pin with three flutes) is more effective in breaking up silicon particles and healing

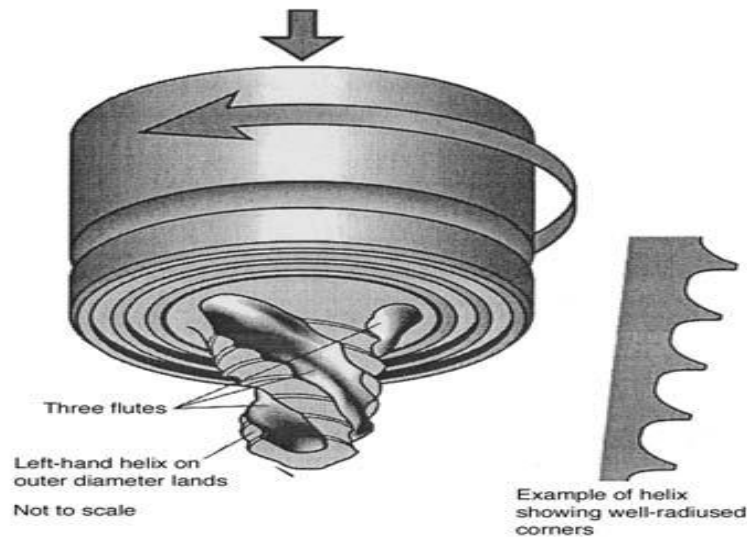


Image 3.8: Schematic of MX Triflute pin. [89]

3.3.7. Trivex Pin

Two-dimensional (2-D) computational fluid dynamics simulations were used to examine material flow around a series of pin designs [72-73]. The simulations used an oval slip model on the 2-D pin profiles to establish the profile that produced the minimum traverse force. The optimal 2-D pin profile was used to produce two versions: the featureless Trivex pin (TWI) and the threaded MX-Trivex pin (TWI) (Image 3.9). Friction stir welding experiments of 6.35 mm (0.25 in.) thick 7075-T7351 Al demonstrated that the Trivex and MX-Trivex pin produced an 18 to 25% reduction of traversing forces and a 12 % reduction in forging (normal) forces in comparison to an MX Triflute pin of comparable dimensions [73-74]. In addition, both the Trivex and Triflute tools produced friction stir welds with comparable tensile strengths.

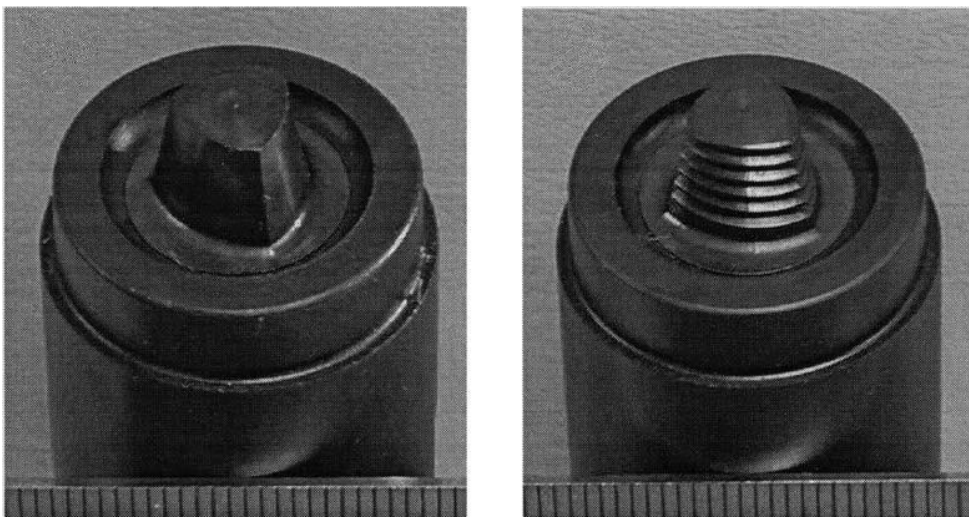


Image 3.9: Photos showing details of Trivex and MX Trivex pins. Scale is in millimetres.

3.3.8. Threadless Pin

Threadless pins are useful in specific FSW applications where thread features would not survive without fracture or severe wear. Tools operating under aggressive environments (high temperature or highly abrasive composite alloys) cannot retain threaded tool features without excessive pin wear; pins for these conditions typically consist of simple designs with robust features. For example, early PCBN pins designed to friction stir weld stainless steels consisted of a truncated cone with three flats at the tip (Image 3.10). Also, Loftus et al. used a featureless cylindrical pin to friction stir weld 1.2 mm (0.05 in.) thick beta 21S Ti. Tools used to friction stir weld thin sheet commonly have fine pins with little surface area for features. The addition of any threads would severely weaken the pin, causing premature pin failure. Thus, thin sheet, for example, 0.4 mm (0.015 in.) thick Mg AZ31 [45] is commonly friction stir welded with threadless tools. Threadless pins have also been used to purposely produce defective welds [40] and to study material flow [43].



Image 3.10: Example of a threadless pin tool. Polycrystalline cubic boron nitride pin tool with three flats at pin tip.

3.3.9. Retractable Pins

The retractable pin tool (RPT) consisted of an actuated pin within a rotating shoulder [75-76] to allow pin length adjustment during FSW (FIG. 3.2). The normal operational mode for these tools was to retract the pin at a prescribed rate as the tool traversed forward. This allowed the closure of exit hole in circumferential friction stir welds. Also, pin lengths could be adjusted to ensure full penetration welds in work pieces with known thickness variations.

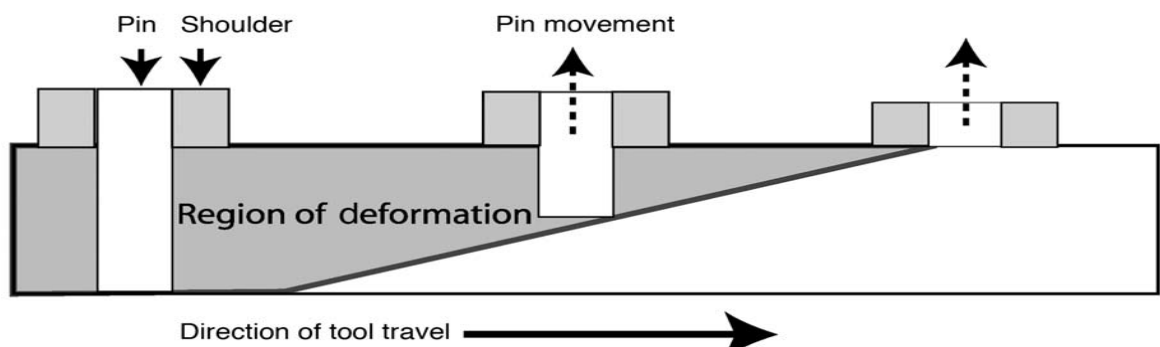


FIG. 3.2: Example of the retractable pin tool technology, where the pin is fully withdrawn into the shoulder (from left to right), thereby eliminating the exit hole (as shown by the region of deformation)

4. Theoretical Methodology

An analytical model for heat generation by friction stir welding, based on different assumptions of the contact conditions between the rotating tool surface and the weld piece is established. The material flow and heat generation are characterized by the contact conditions at the interface, and are described as sliding, sticking or partial sliding/sticking.

A schematic representation of the set-up is illustrated in FIG. 4.1, FIG. 4.2 shows a simplified tool design. In this process, two tool surfaces are needed to perform the heating and joining processes in the friction stir weld. The shoulder surface is the area where the majority of the heat is generated, whereas the probe surface is where the work pieces are joined together and only a fraction of the total heat is generated. Second, the shoulder confines the underlying material so void formation and porosity behind the probe are prevented. The conical tool shoulder helps establish a pressure under the shoulder, but also acts as an escape volume for the material displaced by the probe during the plunge action (FIG. 4.1).

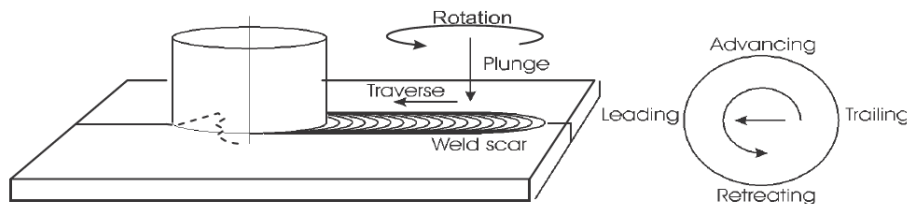


FIG. 4.1: Schematic of the weld set up and definition of orientations

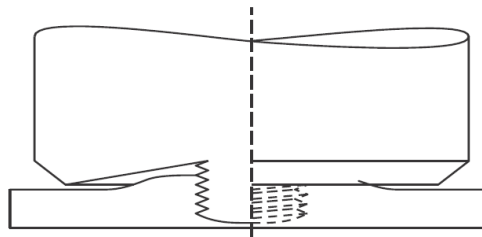


FIG. 4.2: Side view of the FSW tool showing the conical shoulder cap and threaded probe.

5. Standard Friction Stir Welding: Design and Experimentation

5.1. Analytical Estimation of Heat Generation

Three different analytical estimations are made, all of which are based on a general assumption of uniform contact shear stress and further distinguished by assuming contact a specific contact condition. In the first estimation, a sticking interface condition ($\delta = 1$) is assumed and in the second estimation a pure sliding ($\delta = 0$) interface described by a Coulomb friction condition is assumed. In the case of the sticking condition, the shearing is assumed to occur in a layer very close to the interface and in the sliding condition the shear is assumed to take place at the contact interface. The third estimation is used in the case where the partial sliding/sticking condition is assumed.

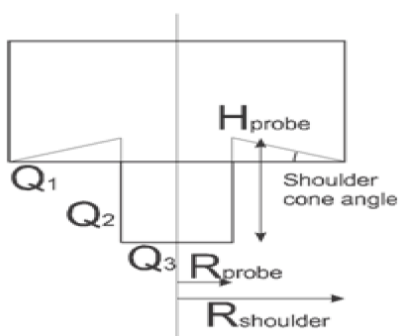


FIG. 5.1: Heat generation contributions in analytical estimates [78]

During the FSW process, heat is generated at or close to the contact surfaces, which have complex geometries according to the tool geometry (FIG. 5.1), but for the analytical estimation, a simplified tool design with a conical shoulder surface, a vertical cylindrical probe side surface and a horizontal (flat) probe tip surface is assumed. The conical shoulder surface is characterized by the cone angle α , which in the case of a flat shoulder, is zero. The simplified tool design is presented in figure 6, where Q_s the heat is generated under the tool shoulder, Q_{ps} at the tool probe side and Q_{pt} at the tool probe tip, hence the total heat generation, $Q = Q_{pt} + Q_{ps} + Q_s$

Following are the equations of the heat generated by all the parts of tool:

Heat generation from the shoulder:

The shoulder surface of a modern FSW tool is in most cases concave or conically shaped. The purpose of this geometric feature is to act as an escape volume as the probe is submerged into the matrix during the plunge operation, secondarily enhancing the extrusion and consolidation of the material during the weld operation.

$$Q_s = \int_0^{2\pi} \int_{R_{probe}}^{R_{shoulder}} \omega \tau_{contact} r^2 (1 + \tan \alpha) dr d\theta$$

$$Q_s = \frac{2}{3} \omega \pi \tau_{cont} \left[\left(\frac{R_{shoulder}}{2} \right)^3 - \left(\frac{d}{2} \right)^3 \right] (1 + \tan \alpha)$$

(5.1)

5.1.1. Heat Generation from the Probe

The probe is simplified to a cylindrical surface with a radius of R_{probe} and a probe height H_{probe} . The heat generated from the probe consists of two contributions; Q_{ps} from the side surface and Q_{pt} from the tip surface.

$$Q_{ps} = \int_0^{2\pi} \int_0^{H_{probe}} \omega \tau_{contact} R_{probe}^2 dz d\theta$$

$$Q_{ps} = 2\omega\pi\tau_{cont} \left(\frac{d}{2}\right)^2 h \quad (5.2)$$

$$Q_{pt} = \int_0^{2\pi} \int_0^{R_{probe}} \omega \tau_{contact} r^2 dr d\theta$$

$$Q_{pt} = \frac{2}{3} \omega\pi\tau_{cont} \left(\frac{d}{2}\right)^3 \quad (5.3)$$

The three contributions are combined to get the total heat generation estimate Q

$$Q = Q_{pt} + Q_{ps} + Q_s$$

$$Q = \frac{2}{3} \omega\pi\tau_{cont} \left[\left(\frac{R_{shoulder}}{2}\right)^2 - \left(\frac{d}{2}\right)^2 \right] (1 + \tan \alpha) + R_{probe}^3 + 3R_{probe}^2 H_{probe} \quad (5.4)$$

5.1.2. Shear Stress for Sticking Condition

If the sticking interface condition is assumed, the matrix closest to the tool surface sticks to it. The layer between the stationary material points and the material moving with the tool has to accommodate the velocity difference by shearing. The yield shear stress τ_{cont} is estimated to be $\frac{\sigma_{plastic}}{\sqrt{3}}$, where σ_{yield} is the weld material yield stress. This result is readily obtained by comparing von Mises yield criterion in uniaxial tension and pure shear. The contact shear stress is then

$$\tau_{cont} = \tau_{plastic} = \frac{\sigma_{yield}}{\sqrt{3}} \quad (5.5)$$

The yield stress is independent of pressure, but highly temperature dependent. If the same shear yield stress is applied all over the interface, the assumption of an isothermal interface follows. This gives a modified expression of (5.6), assuming the sticking condition

$$Q_{sticking\ condition} = \frac{2}{3} \pi \frac{\sigma_{yield}}{\sqrt{3}} \omega \left[\left[\left(\frac{R_{shoulder}}{2} \right)^3 - \left(\frac{d}{2} \right)^3 \right] (1 + \tan \alpha) + \left(\frac{d}{2} \right)^3 + 3 \left(\frac{d}{2} \right)^2 h \right] \quad (5.6)$$

5.1.3. Shear Stress for Sliding Condition

Assuming friction interface conditions where the tool surface and weld material are sliding against each other, the frictional shear stress is $\tau_{friction}$ introduced in the general friction equation (5.7). Coulomb's friction law describes the shear stress the critical friction stress necessary for a sliding condition as

$$\tau_{friction} = \tau_{contat} = \mu \rho = \mu \sigma \quad (5.7)$$

Where μ is the friction coefficient, and ρ and σ are the contact pressures. Thus, for the

Sliding condition, the total heat generation is given by

$$Q_{sticking\ condition} = \frac{2}{3} \pi \mu \rho \omega \left[\left[\left(\frac{R_{shoulder}}{2} \right)^3 - \left(\frac{d}{2} \right)^3 \right] (1 + \tan \alpha) + \left(\frac{d}{2} \right)^3 + 3 \left(\frac{d}{2} \right)^2 h \right] \quad (5.8)$$

5.2. Heat Generation Ratios

Based on the geometry of the tool and independent of the contact condition, the ratio of heat generation, i.e. contributions from the different surfaces compared to the total heat generation, are as follows:

$$f_{shoulder} = \frac{Q_s}{Q_{total}} = \frac{\left[\left(\frac{R_{shoulder}}{2} \right)^3 - \left(\frac{d}{2} \right)^3 \right] (1 + \tan \alpha)}{\left[\left(\frac{R_{shoulder}}{2} \right)^3 - \left(\frac{d}{2} \right)^3 \right] (1 + \tan \alpha) + \left(\frac{d}{2} \right)^3 + 3 \left(\frac{d}{2} \right)^2 h} \quad (5.9)$$

$$f_{probe\ side} = \frac{Q_{ps}}{Q_{total}} = \frac{3 \left(\frac{d}{2} \right)^2 h}{\left[\left(\frac{R_{shoulder}}{2} \right)^3 - \left(\frac{d}{2} \right)^3 \right] (1 + \tan \alpha) + \left(\frac{d}{2} \right)^3 + 3 \left(\frac{d}{2} \right)^2 h} \quad (5.10)$$

$$f_{probe\ tip} = \frac{Q_{pt}}{Q_{total}} = \frac{\left(\frac{d}{2} \right)^3}{\left[\left(\frac{R_{shoulder}}{2} \right)^3 - \left(\frac{d}{2} \right)^3 \right] (1 + \tan \alpha) + \left(\frac{d}{2} \right)^3 + 3 \left(\frac{d}{2} \right)^2 h}$$

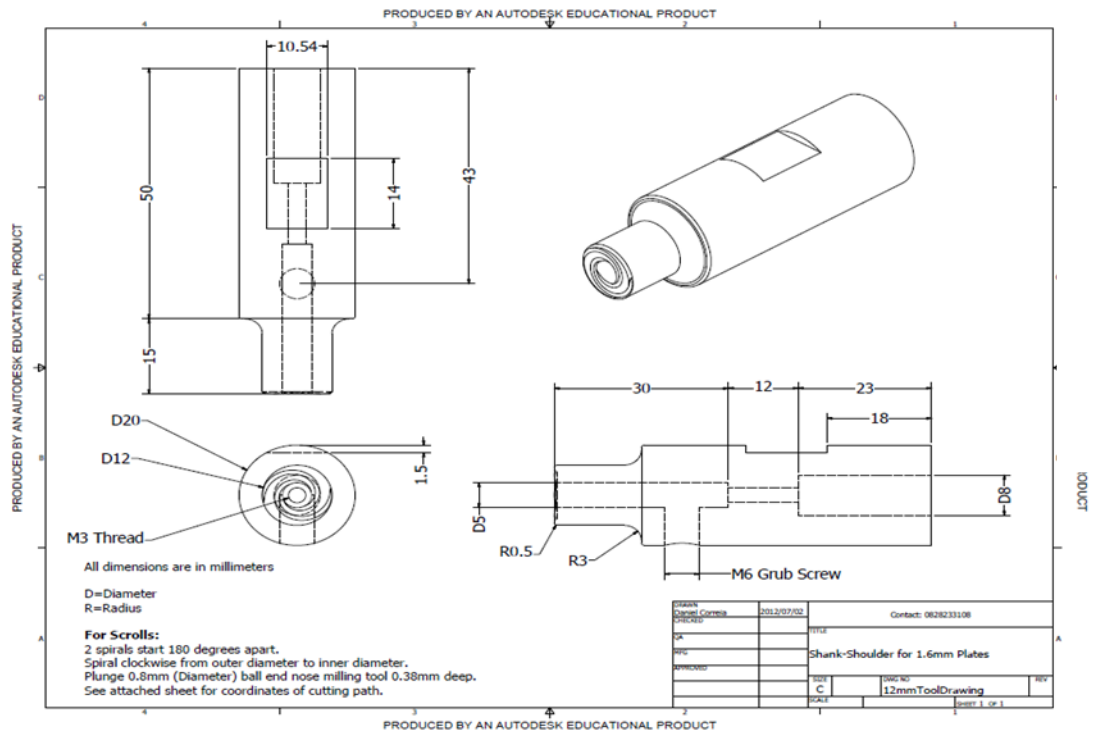
Tool Shoulder ,R	10 mm	0,01 m	Drw. 5.1
Tool Probe radius,R	4 mm	0,004 m	Drw. 5.2
Tool probe height,h	4 mm	0,004 m	
Tool shoulder cone angle	α	0	
Friction Coefficient	μ	0,6	Static Condition
Friction Coefficient	μ	0,4	Sliding Condition
Friction shear stress	μp		
Contact shear stress	τ_{cont}	345 MPa	
Yield stress	σ_{yield}	283 MPa	

Table 5.1: Analytical estimation of heat generation for the Standard Tool

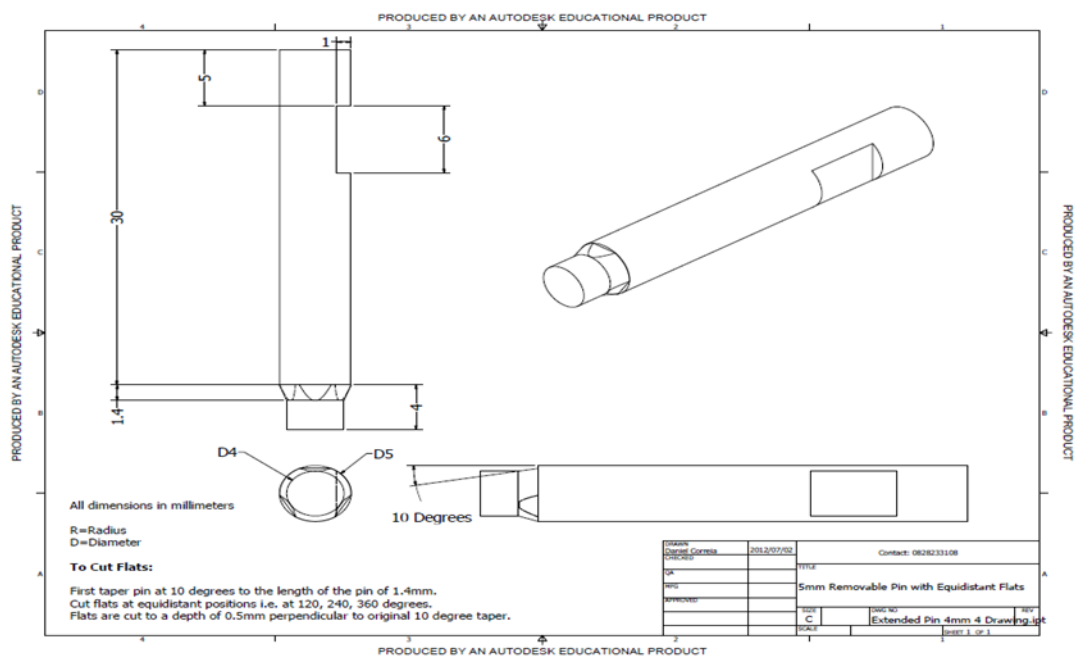
Tool Angular Speed		Rotational Speed
ω	(rad/s)	N (rpm)
ω_1	83.80 rad/s	800 rpm
ω_2	130.89 rad/s	1250 rpm
ω_3	167.55 rad/s	1600 rpm
ω_4	209.44 rad/s	2000 rpm

Table5.2 : Tool Angular Rotational Speed and Rotational Speed for the Standard Tool

The tool shoulder that of which is 12 mm. all of the shoulders are in millimetres. The scroll 2 spirals start at 180 degrees apart, the spiral is clockwise from the outer diameter to the inner diameter with a plunge of 0.8 mm, and the shoulder radius being 0.01 m/10m (Drw.5.1) .The 5 mm removable pin with equidistant position i.e. at 120,240 and 360 degrees. Flats are out to a depth of 0.5 mm perpendicular to the 10 degree taper pin with the tool probe radius being 0.004 m probe.(Drw.5.2)



Drw. 5.1: 12 mm tool drawing [“Correia, D. (2/07/2012), Shank-Shoulder for 1.6mm Plates.University of the Witwatersrand”]



Drw. 5.2: 5mm Removable Pin with Equidistant Flats-[“Correia, D. (2/07/2012), 5mm Removable Pin with Equidistant Flats. University of the Withwatersrand”]

On substituting known values of the parameters, tool dimension, and all other values in derived equations, the heat generation values are as follows:

i) Heat Generation from the Shoulder: from equation 5.1 the values are-

a) For tool angular rotational speed $\omega_1 = 83.80 \text{ rad/s} = 800 \text{ rpm}$

$$Q_{s1} = \frac{2}{3} \omega \pi \tau_{cont} \left[\left(\frac{R_{shoulder}}{2} \right)^3 - \left(\frac{d}{2} \right)^3 \right] (1 + \tan \alpha)$$

$$Q_{s1} = \frac{2}{3} \times \pi \times 345 \times 83.80 \times \left[\left(\frac{0.02}{2} \right)^3 - \left(\frac{0.008}{2} \right)^3 \right] (1 + \tan 0)$$

$$Q_{s1} = \frac{2}{3} \times \pi \times 345 \times 83.80 \times \left[\left(\frac{0.02}{2} \right)^3 - \left(\frac{0.008}{2} \right)^3 \right] (1 + 0)$$

$$Q_{s1} = 56.62 \text{ kW}$$

b) For tool angular rotational speed $\omega_2 = 130.89 \text{ rad/s} = 1250 \text{ rpm}$

$$Q_{s2} = \frac{2}{3} \omega \pi \tau_{cont} \left[\left(\frac{R_{shoulder}}{2} \right)^3 - \left(\frac{d}{2} \right)^3 \right] (1 + \tan \alpha)$$

$$Q_{s2} = \frac{2}{3} \times \pi \times 345 \times 130.89 \times \left[\left(\frac{0.02}{2} \right)^3 - \left(\frac{0.008}{2} \right)^3 \right] (1 + \tan 0)$$

$$Q_{s2} = \frac{2}{3} \times \pi \times 345 \times 130.89 \times \left[\left(\frac{0.02}{2} \right)^3 - \left(\frac{0.008}{2} \right)^3 \right] (1 + 0)$$

$$Q_{s2} = 88.52 \text{ kW}$$

c) For tool angular rotational speed $\omega_3 = 167.55 \text{ rad/s} = 1600 \text{ rpm}$

$$Q_{s3} = \frac{2}{3} \omega \pi \tau_{cont} \left[\left(\frac{R_{shoulder}}{2} \right)^3 - \left(\frac{d}{2} \right)^3 \right] (1 + \tan \alpha)$$

$$Q_{s3} = \frac{2}{3} \times \pi \times 345 \times 167.55 \times \left[\left(\frac{0.02}{2} \right)^3 - \left(\frac{0.008}{2} \right)^3 \right] (1 + \tan 0)$$

$$Q_{s3} = \frac{2}{3} \times \pi \times 345 \times 167.55 \times \left[\left(\frac{0.02}{2} \right)^3 - \left(\frac{0.008}{2} \right)^3 \right] (1 + 0)$$

$$Q_{s3} = 113.31 \text{ kW}$$

d) For tool angular rotational speed $\omega_4 = 209.44 \text{ rad/s} = 2000 \text{ rpm}$

$$Q_{s4} = \frac{2}{3} \omega \pi \tau_{cont} \left[\left(\frac{R_{shoulder}}{2} \right)^3 - \left(\frac{d}{2} \right)^3 \right] (1 + \tan \alpha)$$

$$Q_{s4} = \frac{2}{3} \times \pi \times 345 \times 209.44 \times \left[\left(\frac{0.02}{2} \right)^3 - \left(\frac{0.008}{2} \right)^3 \right] (1 + \tan 0)$$

$$Q_{s4} = \frac{2}{3} \times \pi \times 345 \times 209.44 \times \left[\left(\frac{0.02}{2} \right)^3 - \left(\frac{0.008}{2} \right)^3 \right] (1 + 0)$$

$$Q_{s4} = 141.64 \text{ kW}$$

Q_s (kW)	N (rpm)	ω (rad/s)
56.62	800	83.8
88.52	1250	130.89
113.31	1600	167.55
141.64	2000	209.44

Table 5.1: Heat Generation from the Shoulder with reference to angular rotation.

ii) Heat Generation from the probe side surface and the probe tip: from equation 5.2 and 5.3 the values are-

a) For tool angular rotational speed $\omega_1 = 83.80 \text{ rad/s} = 800 \text{ rpm}$

$$Q_{ps1} = 2 \omega \pi \tau_{cont} \left(\frac{d}{2} \right)^2 h \left(1 + \tan \frac{\beta}{2} \right)$$

$$Q_{ps1} = 2 \times \pi \times 345 \times 83.80 \times \left(\frac{0.008}{2} \right)^2 \times 0.004 \left(1 + \tan \frac{0}{2} \right)$$

$$Q_{ps1} = 2 \times \pi \times 345 \times 83.80 \times \left(\frac{0.008}{2} \right)^2 \times 0.004 (1 + 0)$$

$$Q_{ps1} = 11.63 \text{ kW}$$

$$Q_{pt1} = \frac{2}{3} \omega \pi \tau_{cont} \left(\frac{d}{2} \right)^3$$

$$Q_{pt1} = \frac{2}{3} \times \pi \times 345 \times 83.80 \times \left(\frac{0.008}{2} \right)^3$$

$$Q_{pt1} = 3.87 \text{ kW}$$

b) For tool angular rotational speed $\omega_2 = 130.89 \text{ rad/s} = 1250 \text{ rpm}$

$$Q_{ps2} = 2\omega\pi\tau_{cont} \left(\frac{d}{2}\right)^2 h \left(1 + \tan\frac{\beta}{2}\right)$$

$$Q_{ps2} = 2 \times \pi \times 345 \times 130.89 \left(\frac{0.008}{2}\right)^2 0.004 \left(1 + \tan\frac{0}{2}\right)$$

$$Q_{ps2} = 2 \times \pi \times 345 \times 130.89 \left(\frac{0.008}{2}\right)^2 0.004 (1 + 0)$$

$$Q_{ps2} = 18.16 \text{ kW}$$

$$Q_{pt2} = \frac{2}{3}\omega\pi\tau_{cont} \left(\frac{d}{2}\right)^3$$

$$Q_{pt2} = \frac{2}{3} \times \pi \times 345 \times 130.89 \times \left(\frac{0.008}{2}\right)^3$$

$$Q_{pt2} = 6.07 \text{ kW}$$

c) For tool angular rotational speed $\omega_3 = 167.55 \text{ rad/s} = 1600 \text{ rpm}$

$$Q_{ps3} = 2\omega\pi\tau_{cont} \left(\frac{d}{2}\right)^2 h \left(1 + \tan\frac{\beta}{2}\right)$$

$$Q_{ps3} = 2 \times \pi \times 345 \times 167.55 \left(\frac{0.008}{2}\right)^2 0.004 \left(1 + \tan\frac{0}{2}\right)$$

$$Q_{ps3} = 2 \times \pi \times 345 \times 167.55 \left(\frac{0.008}{2}\right)^2 0.004 (1 + 0)$$

$$Q_{ps3} = 23.24 \text{ kW}$$

$$Q_{pt3} = \frac{2}{3}\omega\pi\tau_{cont} \left(\frac{d}{2}\right)^3$$

$$Q_{pt3} = \frac{2}{3} \times \pi \times 345 \times 167.55 \times \left(\frac{0.008}{2}\right)^3$$

$$Q_{pt3} = 7.75 \text{ kW}$$

d) For tool angular rotational speed $\omega_4 = 209.44 \text{ rad/s} = 2000 \text{ rpm}$

$$Q_{ps4} = 2\omega\pi\tau_{cont} \left(\frac{d}{2}\right)^2 h \left(1 + \tan\frac{\beta}{2}\right)$$

$$Q_{ps4} = 2 \times \pi \times 345 \times 209.44 \left(\frac{0.008}{2}\right)^2 0.004 \left(1 + \tan\frac{0}{2}\right)$$

$$Q_{ps4} = 2 \times \pi \times 345 \times 209.44 \left(\frac{0.008}{2}\right)^2 0.004 (1 + 0)$$

$$Q_{ps4} = 29.05 \text{ kW}$$

$$Q_{pt4} = \frac{2}{3}\omega\pi\tau_{cont} \left(\frac{d}{2}\right)^3$$

$$Q_{pt4} = \frac{2}{3} \times \pi \times 345 \times 209.44 \times \left(\frac{0.008}{2}\right)^3$$

$$Q_{pt4} = 9.67 \text{ kW}$$

Q_{pt} (kW)	N (rpm)	ω (rad/s)
3.87	800	83.8
6.05	1250	130.89
7.75	1600	167.55
9.64	2000	209.44
Q_{ps} (kW)	ω (rpm)	ω (rad/s)
11.63	800	83.8
18.16	1250	130.89
23.24	1600	167.55
29.05	2000	209.44

Table 5.2: Heat Generation for the Probe Tip and Probe Surface.

iii) **Total Heat Generated:** from equation 5.4 the values are-

a) For tool angular rotational speed $\omega_1 = 83.80 \text{ rad/s} = 800 \text{ rpm}$

$$Q = Q_{pt} + Q_{ps} + Q_{st}$$

$$Q = 3.87 + 11.63 + 56.62$$

$$Q = 72.62 \text{ kW}$$

b) For tool angular rotational speed $\omega_2 = 130.89 \text{ rad/s} = 1250 \text{ rpm}$

$$Q = Q_{pt} + Q_{ps} + Q_{st}$$

$$Q = 3.87 + 18.16 + 88.52$$

$$Q = 110.55 \text{ kW}$$

c) For tool angular rotational speed $\omega_3 = 167.55 \text{ rad/s} = 1600 \text{ rpm}$

$$Q = Q_{pt} + Q_{ps} + Q_{st}$$

$$Q = 7.75 + 23.24 + 113.31$$

$$Q = 144.3 \text{ kW}$$

d) For tool angular rotational speed $\omega_4 = 209.44 \text{ rad/s} = 2000 \text{ rpm}$

$$Q = Q_{pt} + Q_{ps} + Q_{st}$$

$$Q = 9.67 + 29.05 + 141.64$$

$$Q = 180.36 \text{ kW}$$

Q (kW)	N (rpm)	ω (rad/s)
72.12	800	83.8
110.55	1250	130.89
144.3	1600	167.55
180.36	2000	209.44

Table 5.3: Total Heat Generation

iv) For Sticking Condition Heat Generated: from equation 5.6 the values are-

a) For tool angular rotational speed $\omega_1 = 83.80 \text{ rad/s} = 800 \text{ rpm}$

$$Q_{sticking\ condition1} = \frac{2}{3} \times \pi \times \frac{\sigma_{yield}}{\sqrt{3}} \times \omega \times \left[\left(\frac{R_{shoulder}}{2} \right)^3 - \left(\frac{d}{2} \right)^3 \right] (1 + \tan \alpha) + \left(\frac{d}{2} \right)^3 + 3 \left(\frac{d}{2} \right)^2 \times h$$

$Q_{sticking\ condition1}$

$$= \frac{2}{3} \times \pi \times \frac{588}{\sqrt{3}} \times 83.80 \times \left[\left(\frac{0.012}{2} \right)^3 - \left(\frac{0.008}{2} \right)^3 \right] (1 + \tan 0) + \left(\frac{0.008}{2} \right)^3 + 3 \left(\frac{0.008}{2} \right)^2 \times 0.004$$

$Q_{sticking\ condition1}$

$$= \frac{2}{3} \times \pi \times \frac{588}{\sqrt{3}} \times 83.80 \times \left[\left(\frac{0.012}{2} \right)^3 - \left(\frac{0.008}{2} \right)^3 \right] (1 + 0) + \left(\frac{0.008}{2} \right)^3 + 3 \left(\frac{0.008}{2} \right)^2 \times 0.004$$

$$Q_{sticking\ condition1} = 120.53 \text{ kW}$$

b) For tool angular rotational speed $\omega_2 = 130.89 \text{ rad/s} = 1250 \text{ rpm}$

$$Q_{sticking\ condition2} = \frac{2}{3} \times \pi \times \frac{\sigma_{yield}}{\sqrt{3}} \times \omega \times \left[\left(\frac{R_{shoulder}}{2} \right)^3 - \left(\frac{d}{2} \right)^3 \right] (1 + \tan \alpha) + \left(\frac{d}{2} \right)^3 + 3 \left(\frac{d}{2} \right)^2 \times h$$

$Q_{sticking\ condition2}$

$$= \frac{2}{3} \times \pi \times \frac{588}{\sqrt{3}} \times 130.89 \times \left[\left(\frac{0.012}{2} \right)^3 - \left(\frac{0.008}{2} \right)^3 \right] (1 + \tan 0) + \left(\frac{0.008}{2} \right)^3 + 3 \left(\frac{0.008}{2} \right)^2 \times 0.004$$

$Q_{sticking\ condition2}$

$$= \frac{2}{3} \times \pi \times \frac{588}{\sqrt{3}} \times 130.89 \times \left[\left(\frac{0.012}{2} \right)^3 - \left(\frac{0.008}{2} \right)^3 \right] (1 + 0) + \left(\frac{0.008}{2} \right)^3 + 3 \left(\frac{0.008}{2} \right)^2 \times 0.004$$

$$Q_{sticking\ condition2} = 188.25 \text{ kW}$$

c) For tool angular rotational speed $\omega_3 = 167.55 \text{ rad/s} = 1600 \text{ rpm}$

$$Q_{sticking\ condition3} = \frac{2}{3} \times \pi \times \frac{\sigma_{yield}}{\sqrt{3}} \times \omega \times \left[\left(\frac{R_{shoulder}}{2} \right)^3 - \left(\frac{d}{2} \right)^3 \right] (1 + \tan \alpha) + \left(\frac{d}{2} \right)^3 + 3 \left(\frac{d}{2} \right)^2 \times h$$

$Q_{sticking\ condition3}$

$$= \frac{2}{3} \times \pi \times \frac{588}{\sqrt{3}} \times 167.55 \times \left[\left(\frac{0.012}{2} \right)^3 - \left(\frac{0.008}{2} \right)^3 \right] (1 + \tan 0) + \left(\frac{0.008}{2} \right)^3 + 3 \left(\frac{0.008}{2} \right)^2 \times 0.004$$

$Q_{sticking\ condition3}$

$$= \frac{2}{3} \times \pi \times \frac{588}{\sqrt{3}} \times 167.55 \times \left[\left(\frac{0.012}{2} \right)^3 - \left(\frac{0.008}{2} \right)^3 \right] (1 + 0) + \left(\frac{0.008}{2} \right)^3 + 3 \left(\frac{0.008}{2} \right)^2 \times 0.004$$

$$Q_{sticking\ condition} = 240.98 \text{ kW}$$

d) For tool angular rotational speed $\omega_4 = 209.44 \text{ rad/s} = 2000 \text{ rpm}$

$$Q_{sticking\ condition4} = \frac{2}{3} \times \pi \times \frac{\sigma_{yield}}{\sqrt{3}} \times \omega \times \left[\left(\frac{R_{shoulder}}{2} \right)^3 - \left(\frac{d}{2} \right)^3 \right] (1 + \tan \alpha) + \left(\frac{d}{2} \right)^3 + 3 \left(\frac{d}{2} \right)^2 \times h$$

$Q_{sticking\ condition4}$

$$= \frac{2}{3} \times \pi \times \frac{588}{\sqrt{3}} \times 209.44 \times \left[\left(\frac{0.012}{2} \right)^3 - \left(\frac{0.008}{2} \right)^3 \right] (1 + \tan 0) + \left(\frac{0.008}{2} \right)^3 + 3 \left(\frac{0.008}{2} \right)^2 \times 0.004$$

$Q_{sticking\ condition4}$

$$= \frac{2}{3} \times \pi \times \frac{588}{\sqrt{3}} \times 209.44 \times \left[\left(\frac{0.012}{2} \right)^3 - \left(\frac{0.008}{2} \right)^3 \right] (1 + 0) + \left(\frac{0.008}{2} \right)^3 + 3 \left(\frac{0.008}{2} \right)^2 \times 0.004$$

$$Q_{sticking\ condition4} = 301.22 \text{ kW}$$

v) For Sliding Condition Heat Generated: from equation 5.7 the values are-

a) For tool angular rotational speed $w_1 = 83.80 \text{ rad/s} = 800 \text{ rpm}$

$$Q_{sticking\ condition1} = \frac{2}{3} \times \pi \times \mu\rho \times \omega \times \left[\left(\frac{R_{shoulder}}{2} \right)^3 - \left(\frac{d}{2} \right)^3 \right] (1 + \tan \alpha) + \left(\frac{d}{2} \right)^3 + 3 \left(\frac{d}{2} \right)^2 \times h$$

$Q_{sticking\ condition1}$

$$= \frac{2}{3} \times \pi \times 345 \times 83.80 \times \left[\left(\frac{0.012}{2} \right)^3 - \left(\frac{0.008}{2} \right)^3 \right] (1 + \tan 0) + \left(\frac{0.008}{2} \right)^3 + 3 \left(\frac{0.008}{2} \right)^2 \times 0.004$$

$Q_{sticking\ condition1}$

$$= \frac{2}{3} \times \pi \times 345 \times 83.80 \times \left[\left(\frac{0.012}{2} \right)^3 - \left(\frac{0.008}{2} \right)^3 \right] (1 + 0) + \left(\frac{0.008}{2} \right)^3 + 3 \left(\frac{0.008}{2} \right)^2 \times 0.004$$

$$Q_{sticking\ condition1} = 122.29 \text{ kW}$$

b) For tool angular rotational speed $w_2 = 130.89 \text{ rad/s} = 1250 \text{ rpm}$

$$Q_{sticking\ condition2} = \frac{2}{3} \times \pi \times \mu\rho \times \omega \times \left[\left(\frac{R_{shoulder}}{2} \right)^3 - \left(\frac{d}{2} \right)^3 \right] (1 + \tan \alpha) + \left(\frac{d}{2} \right)^3 + 3 \left(\frac{d}{2} \right)^2 \times h$$

$Q_{sticking\ condition2}$

$$= \frac{2}{3} \times \pi \times 345 \times 130.89 \times \left[\left(\frac{0.012}{2} \right)^3 - \left(\frac{0.008}{2} \right)^3 \right] (1 + \tan 0) + \left(\frac{0.008}{2} \right)^3 + 3 \left(\frac{0.008}{2} \right)^2 \times 0.004$$

$Q_{sticking\ condition2}$

$$= \frac{2}{3} \times \pi \times 345 \times 130.89 \times \left[\left(\frac{0.012}{2} \right)^3 - \left(\frac{0.008}{2} \right)^3 \right] (1 + 0) + \left(\frac{0.008}{2} \right)^3 + 3 \left(\frac{0.008}{2} \right)^2 \times 0.004$$

$$Q_{sticking\ condition2} = 191.01 \text{ kW}$$

c) For tool angular rotational speed $w_3 = 167.55 \text{ rad/s} = 1600 \text{ rpm}$

$$Q_{sticking\ condition3} = \frac{2}{3} \times \pi \times \mu\rho \times \omega \times \left[\left(\frac{R_{shoulder}}{2} \right)^3 - \left(\frac{d}{2} \right)^3 \right] (1 + \tan \alpha) + \left(\frac{d}{2} \right)^3 + 3 \left(\frac{d}{2} \right)^2 \times h$$

$Q_{sticking\ condition3}$

$$= \frac{2}{3} \times \pi \times 345 \times 167.55 \left[\left(\frac{0.012}{2} \right)^3 - \left(\frac{0.008}{2} \right)^3 \right] (1 + \tan 0) + \left(\frac{0.008}{2} \right)^3 + 3 \left(\frac{0.008}{2} \right)^2 \times 0.004$$

$Q_{sticking\ condition3}$

$$= \frac{2}{3} \times \pi \times 345 \times 167.55 \times \left[\left(\frac{0.012}{2} \right)^3 - \left(\frac{0.008}{2} \right)^3 \right] (1 + 0) + \left(\frac{0.008}{2} \right)^3 + 3 \left(\frac{0.008}{2} \right)^2 \times 0.004$$

$$Q_{sticking\ condition3} = 244.52 \text{ kW}$$

e) For tool angular rotational speed $w_4 = 209.44 \text{ rad/s} = 2000 \text{ rpm}$

$$Q_{sticking\ condition4} = \frac{2}{3} \times \pi \times \mu\rho \times \omega \times \left[\left(\frac{R_{shoulder}}{2} \right)^3 - \left(\frac{d}{2} \right)^3 \right] (1 + \tan \alpha) + \left(\frac{d}{2} \right)^3 + 3 \left(\frac{d}{2} \right)^2 \times h$$

$Q_{sticking\ condition4}$

$$= \frac{2}{3} \times \pi \times 345 \times 209.44 \left[\left(\frac{0.012}{2} \right)^3 - \left(\frac{0.008}{2} \right)^3 \right] (1 + \tan 0) + \left(\frac{0.008}{2} \right)^3 + 3 \left(\frac{0.008}{2} \right)^2 \times 0.004$$

$Q_{sticking\ condition4}$

$$= \frac{2}{3} \times \pi \times 345 \times 209.44 \times \left[\left(\frac{0.012}{2} \right)^3 - \left(\frac{0.008}{2} \right)^3 \right] (1 + 0) + \left(\frac{0.008}{2} \right)^3 + 3 \left(\frac{0.008}{2} \right)^2 \times 0.004$$

$$Q_{sticking\ condition4} = 305 \text{ kW}$$

Based on the heat generated from independent contact conditions, contributions from different surfaces compared to the total heat generated are as follows

$$f_{shoulder} = \frac{Q_s}{Q_{total}}$$

$$= \left[\left(\frac{DR_{shoulder}}{2} \right)^3 - \left(\frac{d}{2} \right)^3 \right] \times (1 + \tan \alpha) / \left[\left(\frac{R_{shoulder}}{2} \right)^3 - \left(\frac{d}{2} \right)^3 \right] \times (1 + \tan \alpha)$$

$$+ \left(\frac{d}{2} \right)^3 + 3 \left(\frac{d}{2} \right)^2 \times h$$

$$f_{shoulder} = \frac{56.62}{72.12}$$

$$= \left[\left(\frac{0.012}{2} \right)^3 - \left(\frac{0.008}{2} \right)^3 \right] \times (1 + \tan 0) / \left[\left(\frac{0.012}{2} \right)^3 - \left(\frac{0.008}{2} \right)^3 \right] \times (1 + \tan 0)$$

$$+ \left(\frac{0.008}{2} \right)^3 + 3 \left(\frac{0.008}{2} \right)^2 \times 0.004$$

$$f_{shoulder} = \frac{56.62}{72.12}$$

$$= \left[\left(\frac{0.012}{2} \right)^3 - \left(\frac{0.008}{2} \right)^3 \right] \times (1 + 0) / \left[\left(\frac{0.012}{2} \right)^3 - \left(\frac{0.008}{2} \right)^3 \right] \times (1 + 0)$$

$$+ \left(\frac{0.008}{2} \right)^3 + 3 \left(\frac{0.008}{2} \right)^2 \times 0.004$$

$$f_{shoulder} = 0.78$$

$$f_{probe\ side} = \frac{Q_{ps}}{Q_{total}} = 3 \times \left(\frac{d}{2} \right)^2 \times h / \left[\left(\frac{R_{shoulder}}{2} \right)^3 - \left(\frac{d}{2} \right)^3 \right] (1 + \tan \alpha) + \left(\frac{d}{2} \right)^3 + 3 \left(\frac{d}{2} \right)^2 \times h$$

$$f_{probe\ side} = \frac{11.63}{72.12}$$

$$= 3 \times \left(\frac{0.008}{2} \right)^2 \times h / \left[\left(\frac{0.012}{2} \right)^3 - \left(\frac{0.008}{2} \right)^3 \right] (1 + \tan 0) + \left(\frac{0.008}{2} \right)^3 + 3 \left(\frac{0.008}{2} \right)^2$$

$$\times 0.004$$

$$f_{probe\ side} = \frac{11.63}{72.12}$$

$$= 3 \times \left(\frac{0.008}{2} \right)^2 \times h / \left[\left(\frac{0.012}{2} \right)^3 - \left(\frac{0.008}{2} \right)^3 \right] (1 + 0) + \left(\frac{0.008}{2} \right)^3 + 3 \left(\frac{0.008}{2} \right)^2$$

$$\times 0.004$$

$$f_{probe\ side} = 0.16$$

$$\begin{aligned}
f_{probe\ tip} &= \frac{Q_{pt}}{Q_{total}} = \left(\frac{d}{2}\right)^3 / \left[\left(\frac{R_{shoulder}}{2}\right)^3 - \left(\frac{d}{2}\right)^3 \right] (1 + \tan \alpha) + \left(\frac{d}{2}\right)^3 + 3\left(\frac{d}{2}\right)^2 \times h \\
f_{probe\ tip} &= \frac{3.87}{72.12} \\
&= (0.008)^3 / \left[\left(\frac{0.012}{2}\right)^3 - \left(\frac{0.008}{2}\right)^3 \right] (1 + \tan 0) + \left(\frac{0.008}{2}\right)^3 + 3\left(\frac{0.008}{2}\right)^2 \\
&\quad \times 0.004 \\
f_{probe\ tip} &= \frac{3.87}{72.12} \\
&= (0.008)^3 / \left[\left(\frac{0.012}{2}\right)^3 - \left(\frac{0.008}{2}\right)^3 \right] (1 + 0) + \left(\frac{0.008}{2}\right)^3 + 3\left(\frac{0.008}{2}\right)^2 \times 0.004 \\
f_{probe\ tip} &= 0.0537
\end{aligned}$$

Percentage of heat with regard the percentage of heat generated by probe tip with regard to total heat generated=16 % and for the rest are show in table, percentage of probe side with respect to total is=5 % and shoulder =78 %

This indicates that, for the specific tool geometry, the tool shoulder contributes major fraction of heat generation whereas the probe tip heat generation is negligible as compared to that of total heat generated.

5.3. Heat Generation: Summary of Calculations

5.3.1. Heat Generation from the Shoulder

The heat generation from a tool shoulder is explained in equation (5.1). As indicated in equation (5.1): Q_s is the heat generation of the tool shoulder which is determined by the angular rotational speed (ω), the contact shear stress of the material [Al2024-T3] ($\tau_{contact}$), the shoulder radius $R_{shoulder}$, the probe radius (R_{probe}) as well as the shoulders cone angle (α). Equation (5.1) is used in this study to determine heat generation from a tool shoulder with four different rotational speeds, formulating to the following values: the speed of 800 rpm resulted to 56.62 kW, 1250 rpm generated 88.52 kW, 1600 rpm went up to 113.31 kW and lastly 2000 rpm generated 141.64 kW. Rotational speed per minute vs. Heat generation from the shoulder represents the analytical analysed increased speed of the tool shoulder which increases the heat generation on the supporting axis: Y: ROTATIONAL SPEED (rpm) and X: HEAT GENERATION FROM THE SHOULDER (kW), N indicating the TOOL ANGULAR ROTATIONAL SPEED (rpm) (Graph 5.1)

5.3.2. Heat Generation from the Probe Side Surface and the Probe Tip

Heat generation from the Probe Side Surface and the Probe Tip is explained in equation (5.2) and equation (5.3). As indicated in both equations, starting with (5.2) Q_{ps} represents the heat generation from the side of the probe, which is determined by the tool probe height (H_{probe}), the tool angular rotational speed (ω), the contact shear stress of the material (Al2024-T3), the tool probe radius (R_{probe}). (5.3) where Q_{pt} represents heat generation from the tip of the probe, the contact shear stress of the material [Al2024-T3] ($\tau_{contact}$) Equation (5.2) and (5.3) is used in this study to determine the heat generation from the probe side surface and the probe tip with four different rotational speeds. This process formulated as follows: At 800 rpm the probe side generated 11.63 kW

and probe tip 3,87 kW. 1250 rpm resulted to probe side surface 18.16 kW and probe pin at 6.05 kW. At 1600 rpm the probe side surface went up to 23.24 kW and the probe pin to 7.75 kW, and lastly the speed of 2000 rpm generated at the probe side surface at 29.05 kW and the probe pin at 9.67 kW. (Graph. 5.2) Rotational speeds per minute vs. from the probe side surface represent the precise speed of the probe side surface against the heat generation on the supporting axis: Y: ROTATIONAL SPEED (rpm) and X: HEAT GENERATION FROM THE PROBE SIDE SURFACE (kW), N representing the TOOL ANGULAR ROTATIONAL SPEED (rpm). (Graph. 3) Rotational speed per minute vs. from the probe pin represents the accurate analysed increased speed of the probe pin which increases the heat generation on the supporting axis: Y: ROTATIONAL SPEED (rpm) and X: HEAT GENERATION FROM THE PROBE PIN (kW), N indicating the TOOL ANGULAR ROTATIONAL SPEED (rpm).

5.3.3. Total Heat Generation

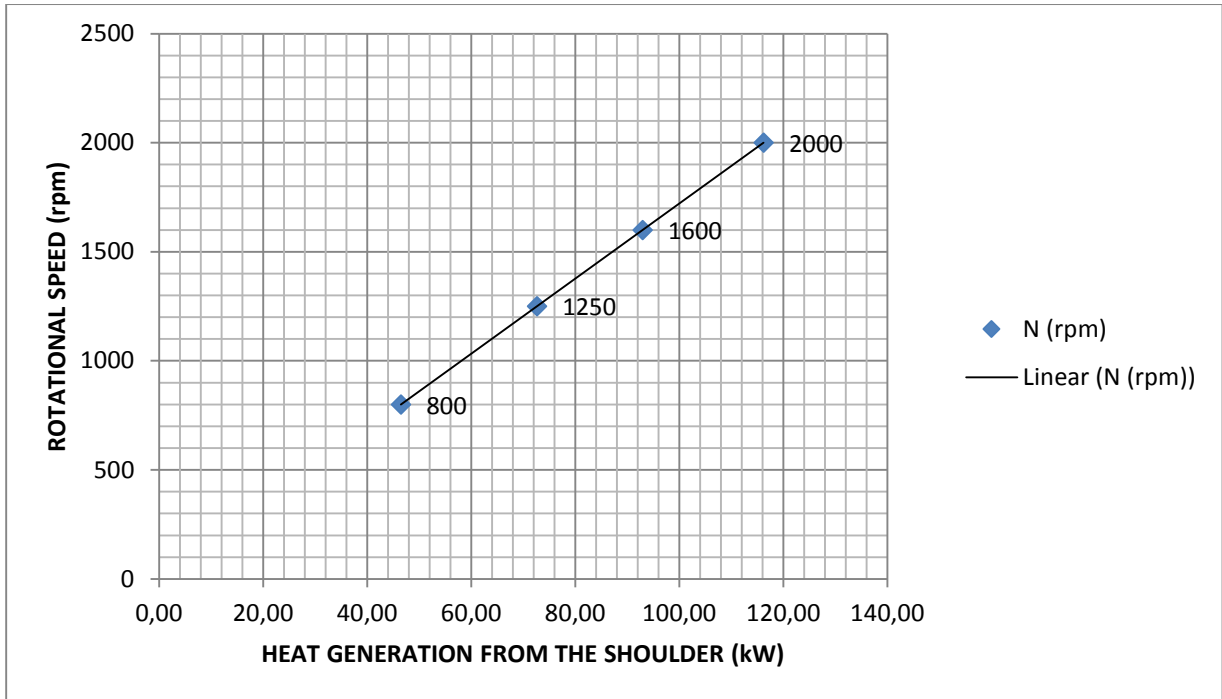
After formulating these three equations (Q1, Q2, Q3) a total will sum up the total heat generation (5.4) [the tool shoulder, the probe side surface and the probe pin] as is indicated in the equation where Q is the heat generation which is determined by the tool angular rotation speed (ω), contact shear stress of the material [Al2024-T3] ($\tau_{contact}$), the shoulders cone angle (α), the tool probe radius (R_{probe}) and the tool probe height (H_{probe}). The totals are as follows: the speed of 800 rpm generated 72.12 kW. 1250 rpm generated 110.55 kW. 1600 rpm resulted to 144.3 kW and 2000 rpm generated 180.36 kW.

Graph. 5.4 Rotational speed per minute vs. from the total heat generation represent the total analysed speed against the heat generation on the supporting axis: Y: ROTATIONAL SPEED (rpm) and X: TOTAL HEAT GENERATION and N indicating the TOOL ANGULAR ROTATIONAL SPEED (rpm).

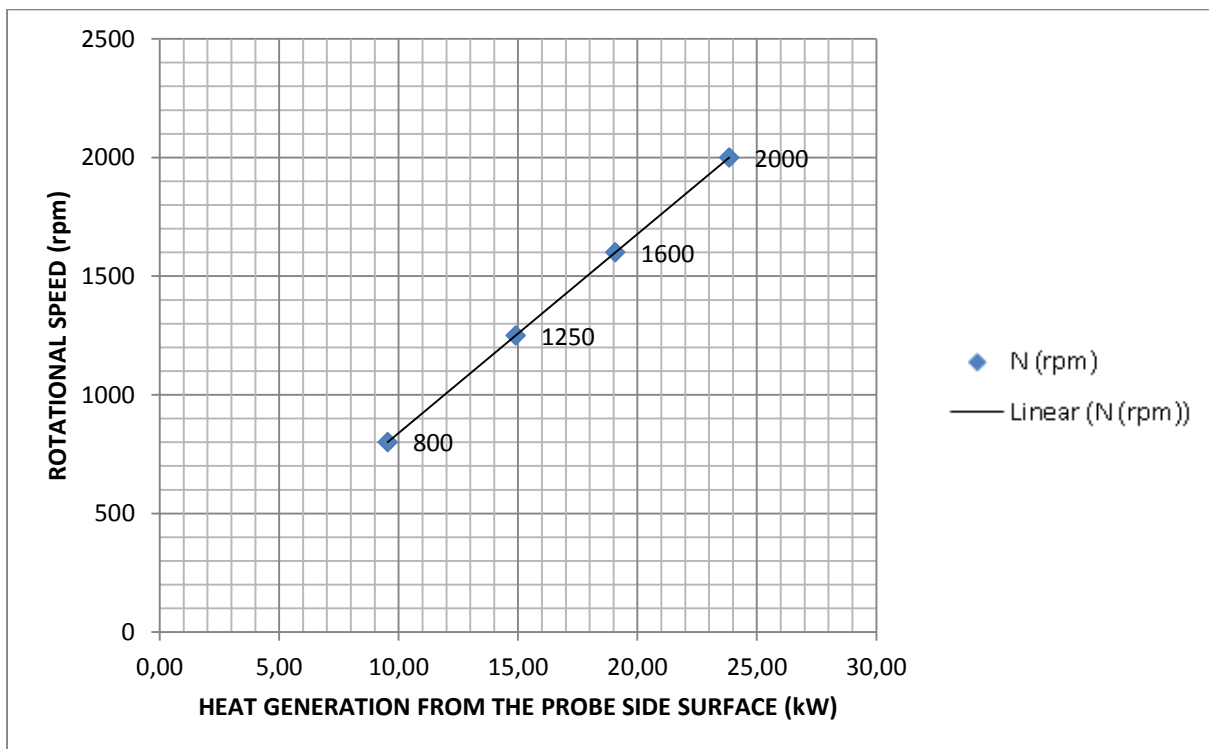
Three cases for this parametric study are considered:

- (1) The tool shoulder
- (2) The probe side surface and
- (3) The probe pin.

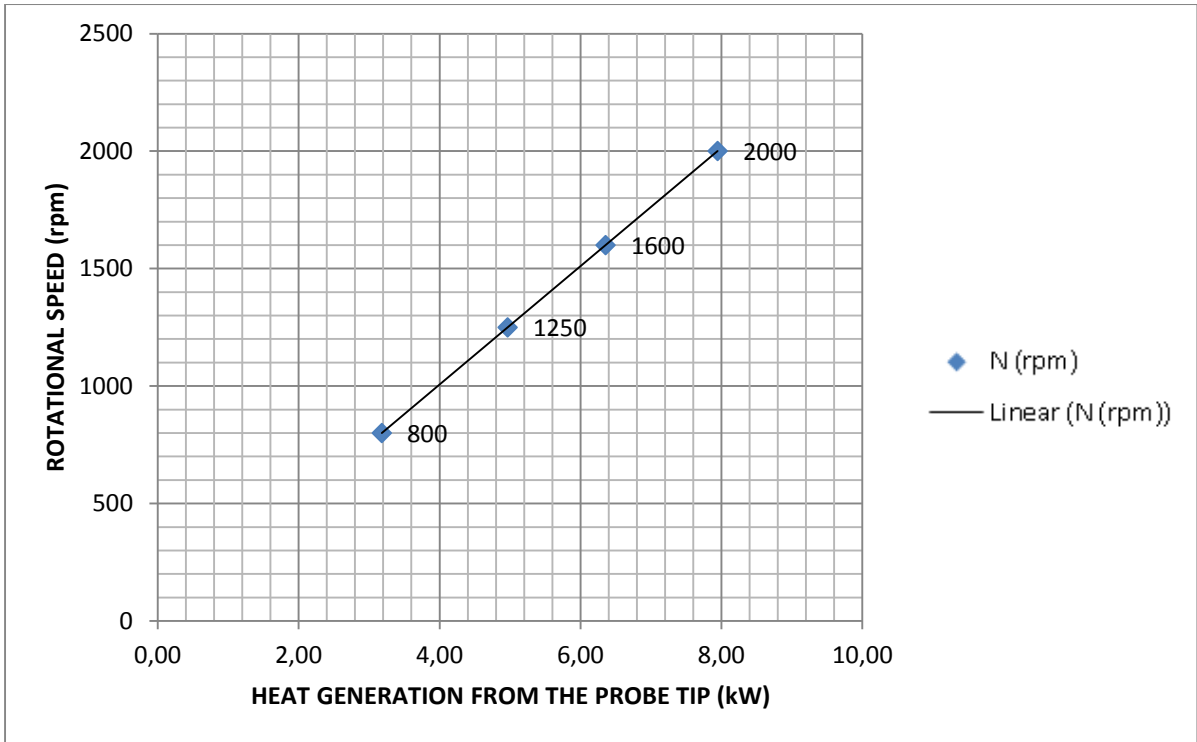
All 3 of these cases for Al2024-T3 had a speed variation between 800 rpm and 2000 rpm. The tools rotational speeds were chosen as such that the obtained work piece heat generation was accurate for a good weld.



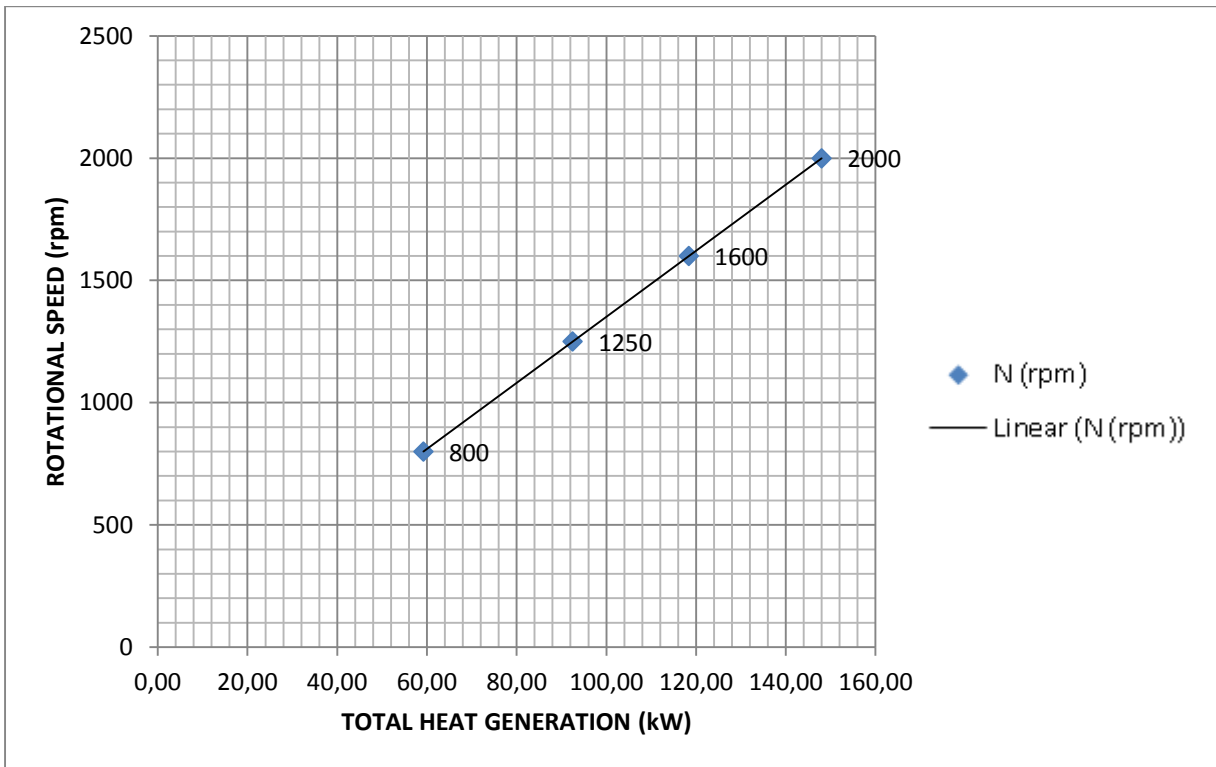
Graph. 5.1 Rotational speed per minute vs. heat generation from the shoulder



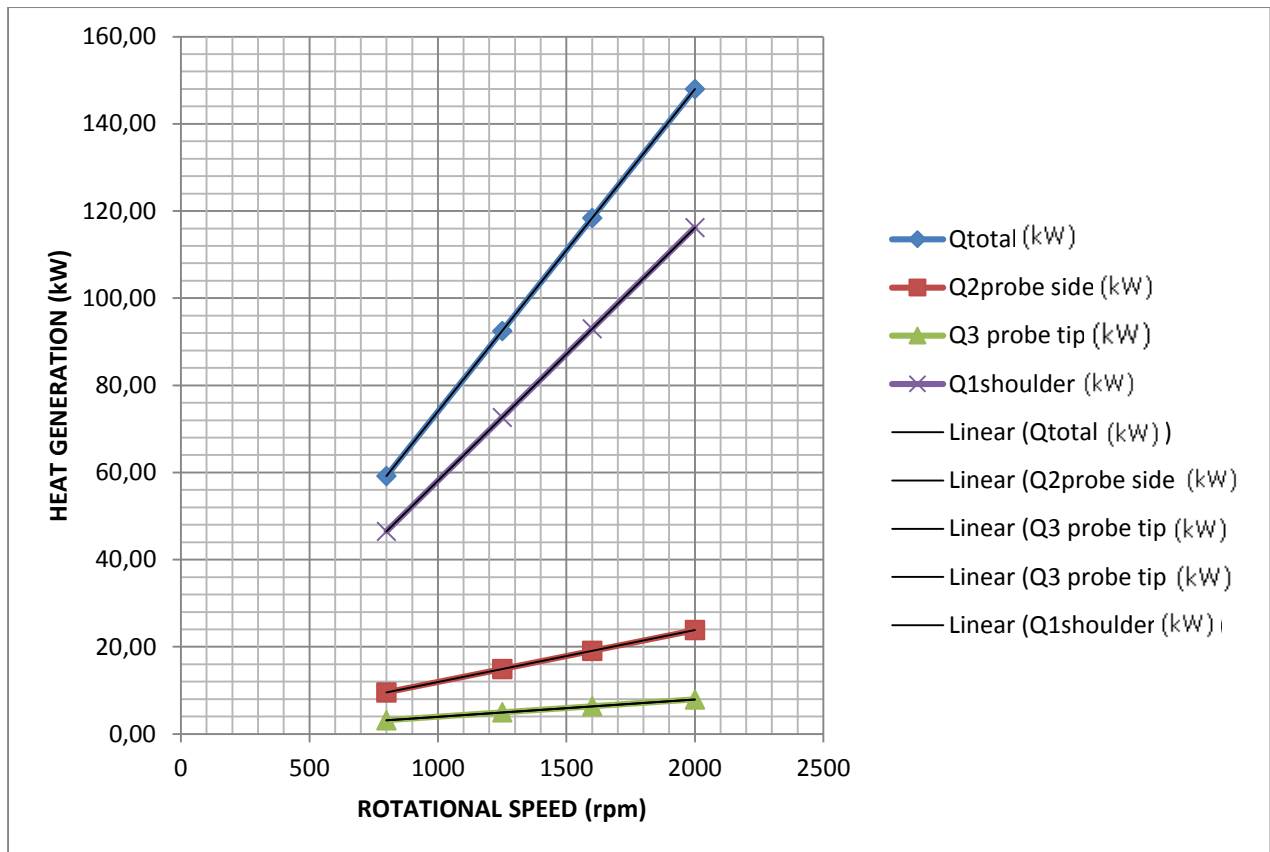
Graph. 5.2 Rotational speed per minute vs. heat generation from the probe side surface



Graph. 5.3 Rotational speed per minute vs. heat generation from the probe tip



Graph. 5.4 Rotational Speed Per Minute Vs. Total Heat Generation

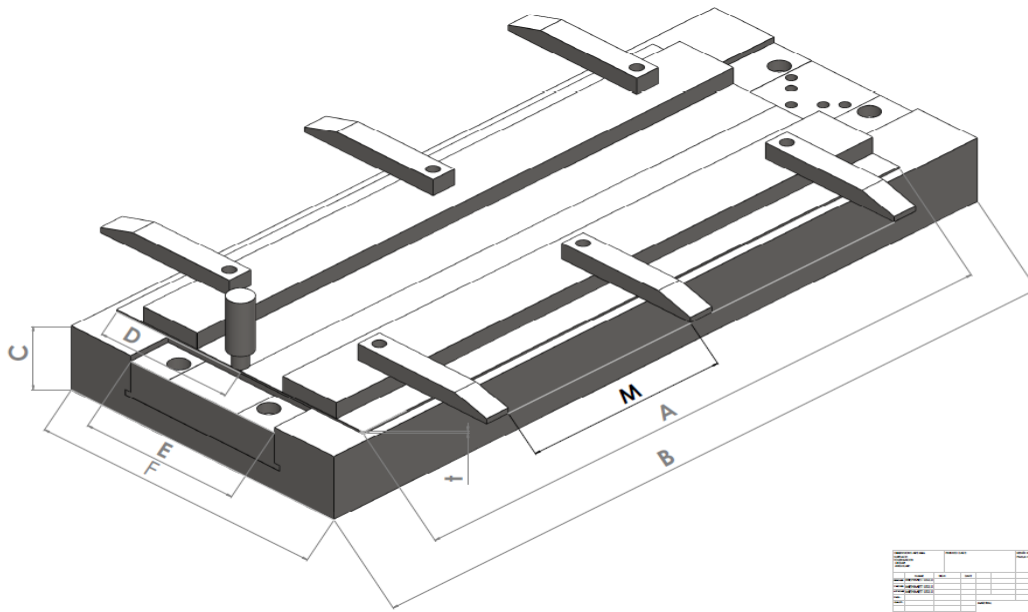


Graph. 5.5 Q1, Q2, Q3, QTOTAL vs. Rotational speed

5.4. Standard tool: SOLIDWORKS Design

SOLIDWORKS is solid modelling CAD (computer-aided design) software that runs on Microsoft Windows and is produced by Dassault Systèmes SOLIDWORKS Corp., a subsidiary of Dassault Systèmes, S. A. (Vélizy, France). SOLIDWORKS is currently used by over 2 million engineers [3] and designers at more than 165,000 companies worldwide. SOLIDWORKS is a Parasolid-based solid modeller, and utilizes a parametric feature-based approach to create models and assemblies. Parameters refer to constraints whose values determine the shape or geometry of the model or assembly. Parameters can be either numeric parameters, such as line lengths or circle diameters, or geometric parameters, such as tangent, parallel, concentric, horizontal or vertical, etc. Numeric parameters can be associated with each other through the use of relations, which allow them to capture design intent. Design intent is how the creator of the part wants it to respond to changes and updates. For example, you would want the hole at the top of a beverage can to stay at the top surface, regardless of the height or size of the can. SOLIDWORKS allows the user to specify that the hole is a feature on the top surface, and will then honour their design intent no matter what height they later assign to the can. Features refer to the building blocks of the part. They are the shapes and operations that construct the part. Shape-based features typically begin with a 2D or 3D sketch of shapes such as bosses, holes, slots, etc. This shape is then extruded or cut to add or remove material from the part. Operation-based features are not sketch-based, and include features such as fillets, chamfers, shells, applying draft to the faces of a part, etc.

A friction stir welding work bench was design to show a 3-d view for a standard tool (Drw.5.3) A friction stir welding work bench is design to show views in both 2-D and 3-D presentations (Drw.5.4).For friction stir welding tool, where D_s is the tool shoulder and D_p is the tool pin is in a 3-D design (Drw.5.5).



Drw. 5.3: Friction Stir Welding Workbench design[*Uslu, M.Y. (2014), Workbench Design, University of the Withwatersrand*]

Aluminium plate length, A (As seen on drw5.3)

Aluminium plate width, D (As seen on drw5.3)

Aluminium plate thickness, t (As seen on drw5.3)

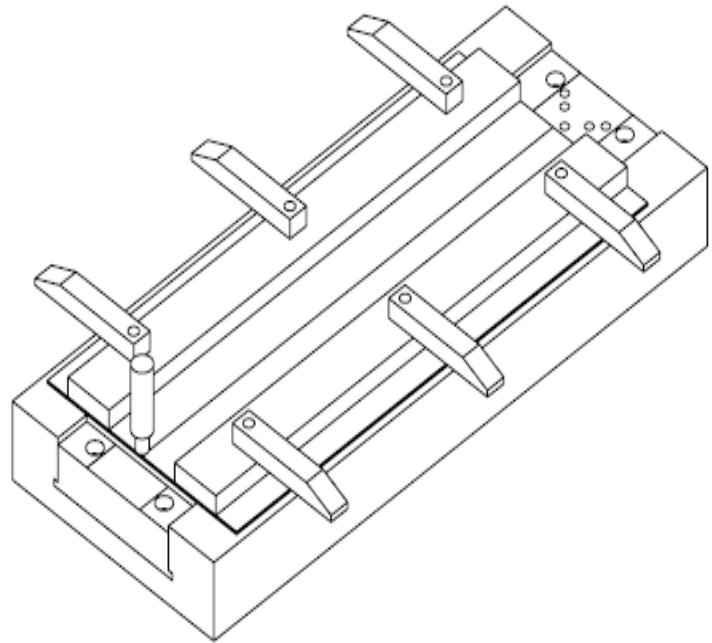
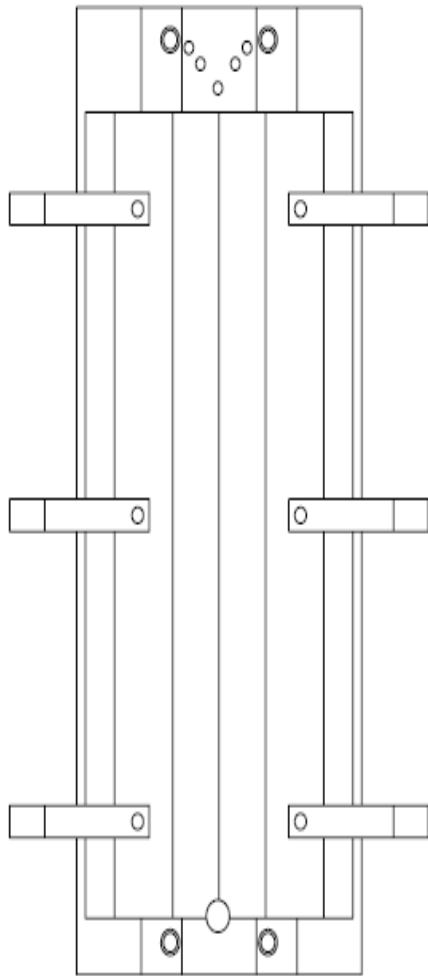
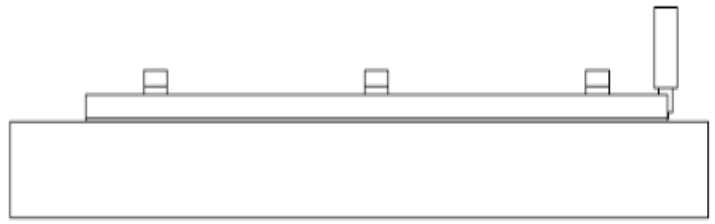
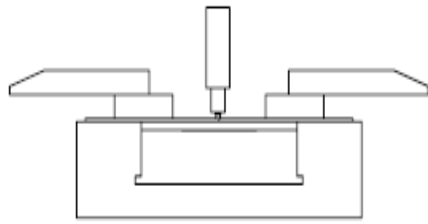
Workbench clamps distance, M (As seen on drw5.3)

Workbench length, B (As seen on drw5.3)

Workbench width, F (As seen on drw5.3)

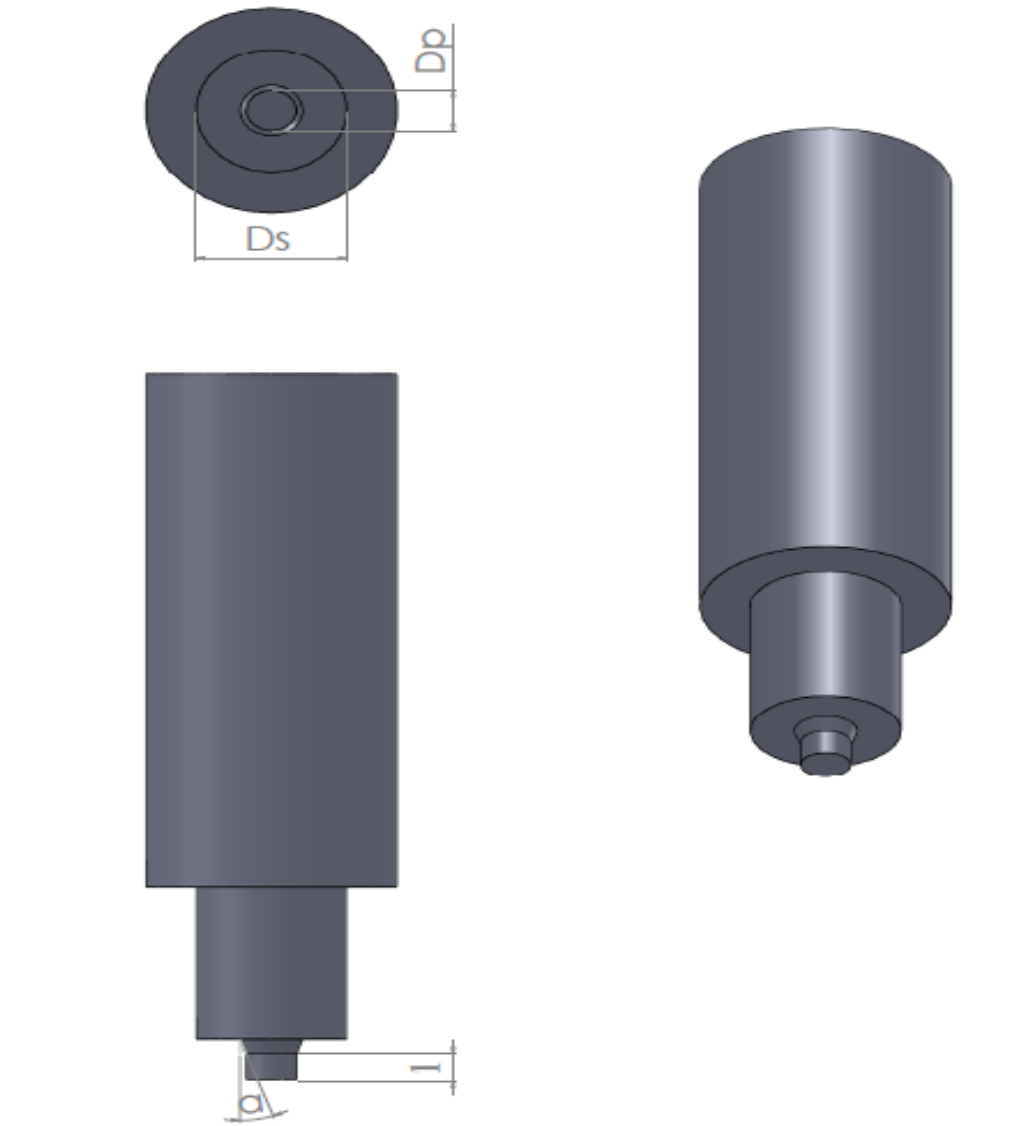
Workbench thickness, C (As seen on drw5.3)

Workbench backing plate width, E (As seen on drw5.3)



Project Information		Date		Scale		Drawing No.	
Author	Uslu, M.Y.	Year	2014	Scale	1:1	Drawing No.	01
Reviewer		Year		Scale		Drawing No.	
Checked		Year		Scale		Drawing No.	
Approved		Year		Scale		Drawing No.	

Drw.5. 4: Friction Stir Welding Workbench design views [Uslu, M.Y. (2014), Friction Stir Welding Workbench design views, University of the Withwatersrand]



Drw. 5.5: Friction Stir Welding Tool [Uslu, M.Y. (2014), Friction Stir Welding Tool, University of the Withwatersrand]

5.5. Standard Tool: Mode Frontier Simulation

Mode Frontier 4.3.1 b20113011 software was used for this design project (Image5.1). ModeFrontier is a multi-objective optimization and design environment, written to couple CAD/computer aided engineering (CAE) tools, finite element structural analysis and computational fluid dynamics (CFD) software. It is developed by 'ESTECO SpA' and provides an environment for product engineers and designers. ModeFrontier is a GUI driven software written in Java that wraps around the CAE tool, performing the optimization by modifying the value assigned to the input variables, and analysing the outputs as they can be defined as objectives and/or constraints of the design problem. The logic of the optimization loop can be set up in a graphical way, building up a "workflow" structure by means of interconnected nodes. Serial and parallel connections and conditional switches are available. ModeFrontier builds automatic chains and steers many different external application programs using scripting (DOS script, UNIX shell, Python programming language, Visual Basic, JavaScript, etc) ModeFrontier includes design of experiments (DOE), optimization algorithms and robust design tools, that can be combined and blended to build up the most efficient strategy to solve complex multi-disciplinary problems. Different strategies are available, including random generator sequences, Factorial DoE's, Orthogonal and Iterative Techniques, as like as D-Optimal or Cross Validation. Monte Carlo and Latin hypercube are available for robustness analysis. When you start the ModeFrontier system, the GUI switches automatically to the Workflow desktop. You can make it active by clicking on the corresponding tab, or selecting Project Work Flow from the main menu. In order to setup the optimization problem, you need to define the entities involved, such as Input Variables, Output Variables, Design Objectives and Design Constraint, as well as the application script to calculate mathematical expressions: in other words, all the entities defining the stream of data from the input to the output end of the system considered, which make up the so-called data flow. In addition to this, you have to define the complete sequence of all the logic events that let the ModeFrontier solve the cone optimization problem, including application scripts as well as the optimization strategy to be applied:

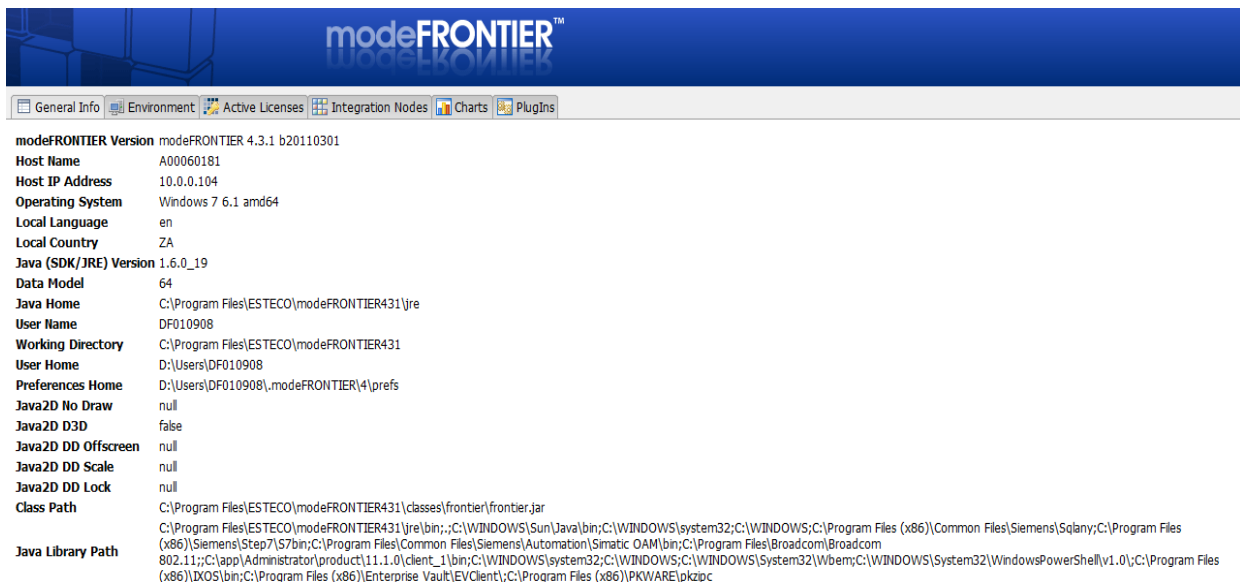


Image 5.1 : Mode Frontier 4.3.1 b20113011 software was used for this design project

Input Data, Output Data and boundary variables definitions as shown on this Microsoft Excel Sheet file name: *mehmet deneme .xism* is used in Mode Frontier for this Design Project: Since each component defining the Workflow is represented by a specific node which can be linked to other nodes, a proper node from the available Node Library toolbar or, alternatively, chosen by using the Workflow Nodes panel. It is shown all the input data output data and boundary variables in a Microsoft Excel workbook. The excel work books is used so that the equation for the rotational speed along with the heat generation is calculated where the results will be used in ModeFrontier to assist in the design (Image 5.2).Once a Workflow Plan created by Mode Frontier Project as shown in *deneme04.prj*, also includes DOE (Design of Experiments) and DOE Sequence, as well as indicating Input Variables, Output Variables, Design Objectives + Gradients, Microsoft Excel Workbook and Logic End(Image5.3).A workflow plan is created using a DoE (Design of Experiments) and a DOE Sequence on a new Overlook. Once this is open workflow nodes can be added on. Variable nodes which are the input nodes and the output nodes are used. Workflow nodes such as the schedulers, the logic switch and logic end is used. An application node is used for excel. A goal node which is the design objective+gradient node. Mode Frontier Input and Output Data is connected to Microsoft Excel Workbook (Image 5.4) .Excel workbook properties are used for basic node configuration where an Excel Workbook is selected (Image 5.3). Once selected the input and out data is connected from the chosen Excel workbook. An Interactive Selection used between Mode Frontier *deneme04.prj* and Microsoft Excel Workbook: *mehmet deneme .xism* to determine Excel Workbook Properties for Mode Frontier (Image 5.5) An interactive selection allows each input and output node to be configured in accordance to the Excel workbook. Where each variable is interactively selected to complete the work plan.

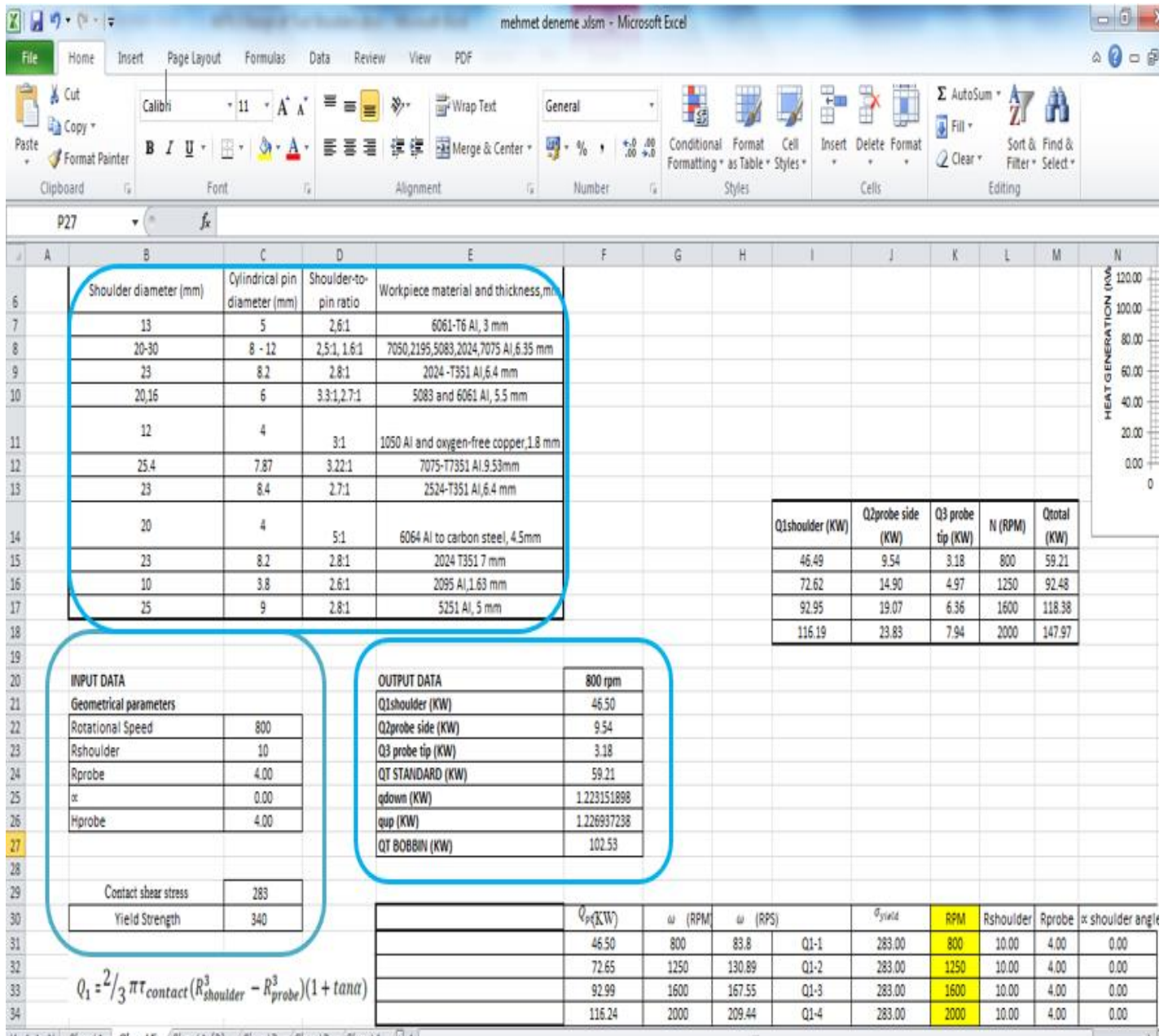


Image 5.2: Input Data, Output Data and boundary variables definitions as shown on this Microsoft Excel Sheet file name: mehmet deneme .xlsm is used in Mode Frontier for this Design Project

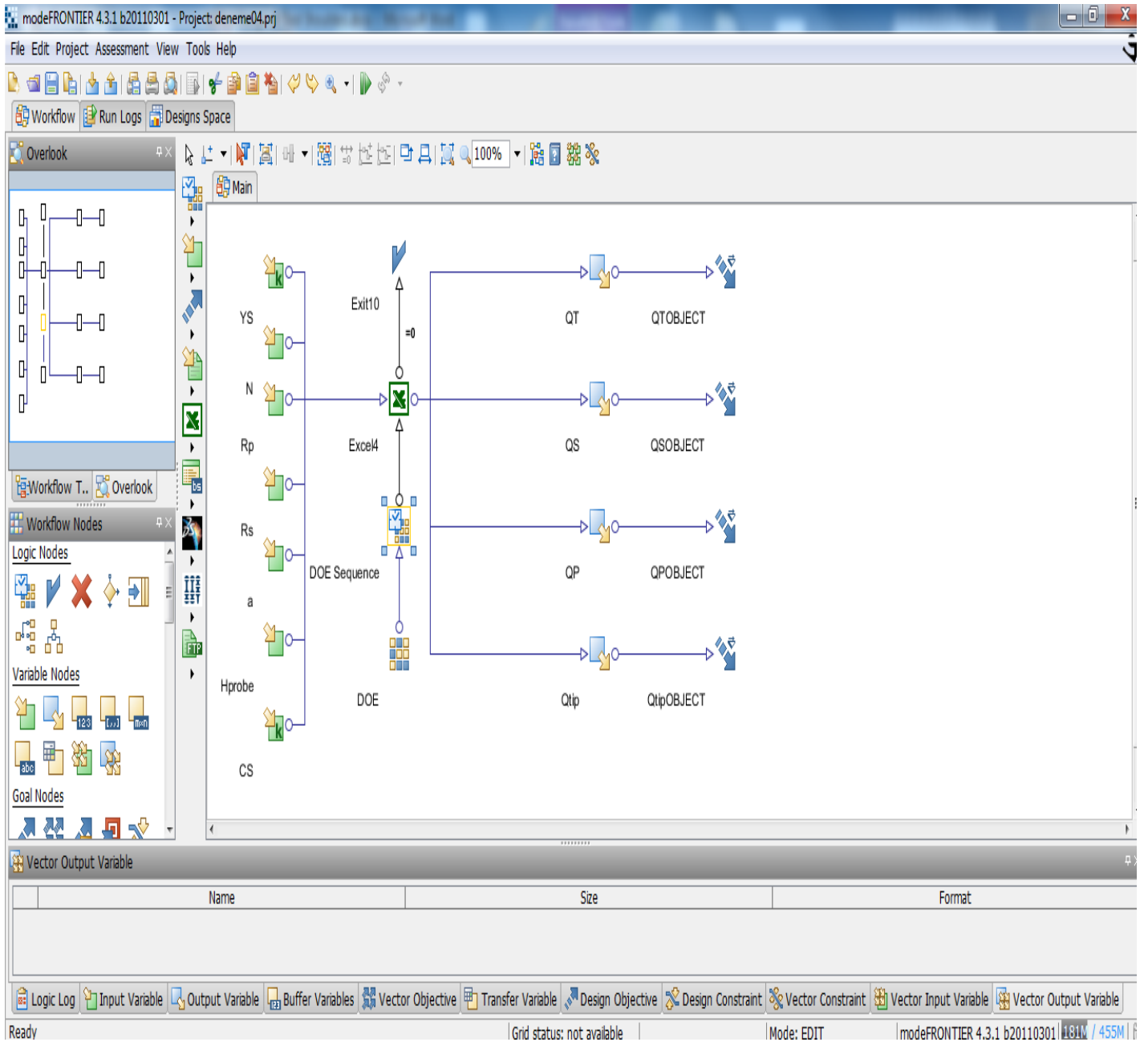


Image 5.3: Workflow Plan created on Mode Frontier Project as shown in *deneme04.prj*, also includes DOE (Design of Experiments) and DOE Sequence, as well as indicating Input Variables, Output Variables , Design Objectives + Gradients, Microsoft Excel Workbook and Logic End

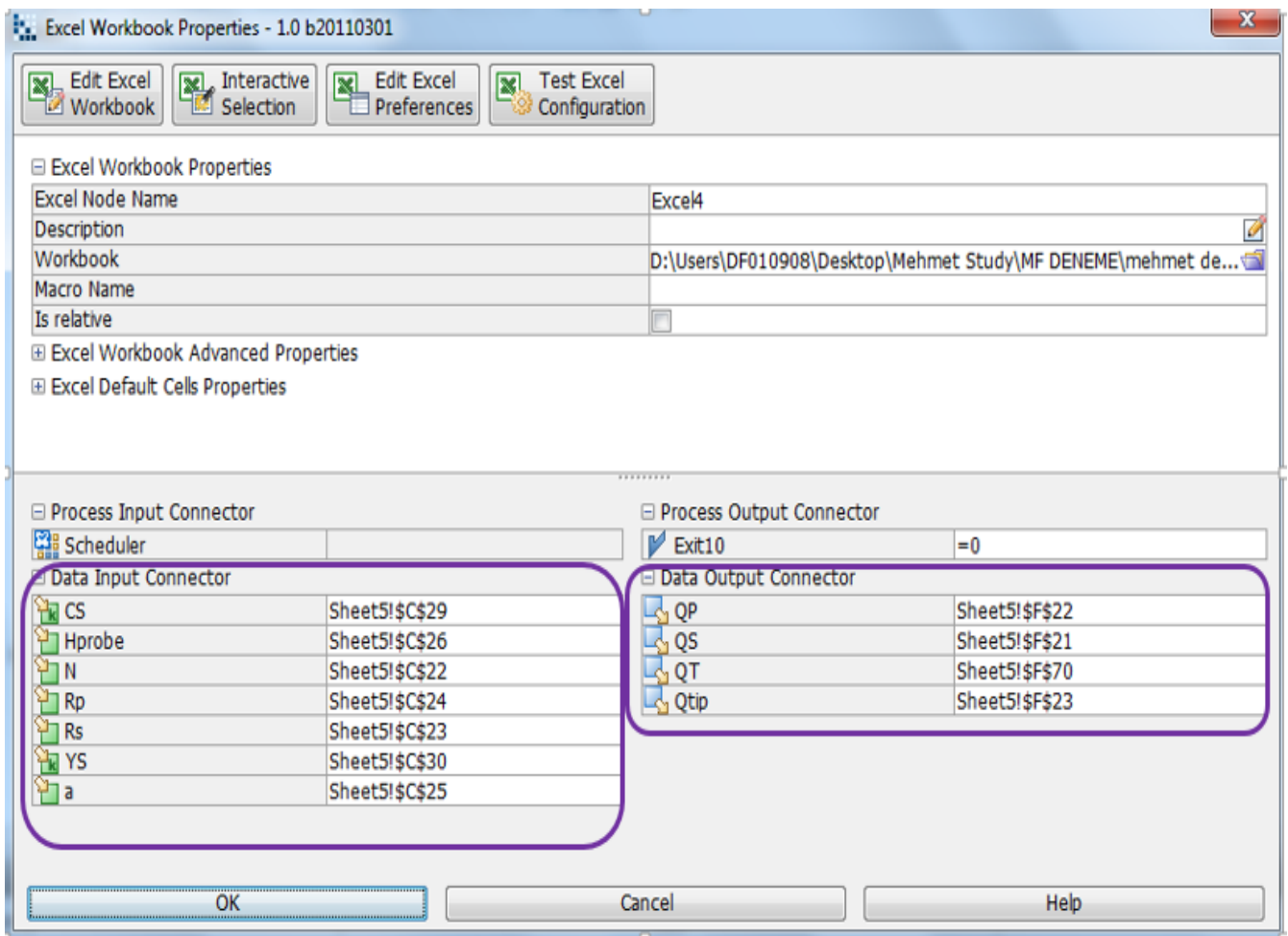


Image 5.4: Mode Frontier Input and Output Datas connected to Microsoft Excel Workbook as shown above

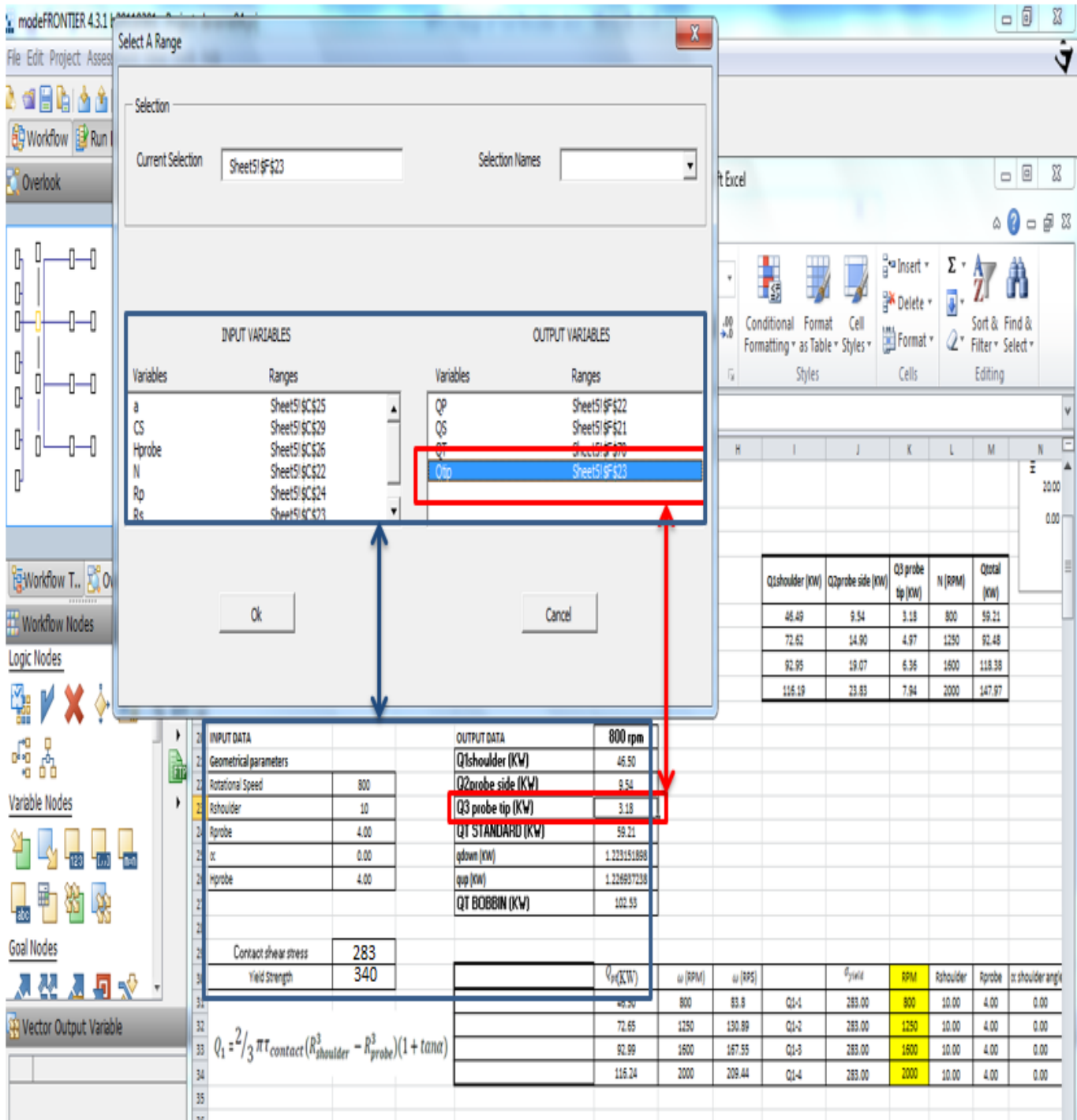


Image 5.5 : Interactive Selection used between Mode Frontier *deneme04.prj* and Microsoft Excel Workbook: *mehmet deneme .xlsx* to determine Excel Workbook Properties for Mode Frontier

5.5.1. Boundaries: Standard Tool Design

A standard tool contact stress as an input variable for Al2024-T3, where the value is 345 MPa and the variable type is constant. (As recorded on the aerospace specification metals/ASM) these variables are chosen by ModeFrontier (Image 5.6). Rotational speed is a variable value between 50 and 3000. 3000 been the maximum speed used in this design (as demonstrated in the lab experiment Telco 17.04.2013) (Image 5.7). An optimal ratio of shoulder diameter to pin diameter is suggested to assist with a tool design, however the ratio (2.5:1 and 1.6:1) is dependent on the aluminium alloy composition and only is applied to 6 mm (0.24 in) thick plate. As the work piece thickness increases, the thermal input from the shoulder decreases, the pin then must supply more thermal energy(In reference with table 5.4) (Image 5.8 &5.9).the tool shoulder cone angle with the variable type being variable with the lower bound is 0.0degrees and upper bound at 90.0 degrees. Height probe(Image 5.10) is used in accordance to the design of the shoulder tool(in reference with Colligan, Xu and Pickens, on the use of practise metal where the demonstration of a reduction in transverse forces, the tool toque is directly proportionated to the numbers of flat place, a pin is the design of the helical ridge of the pin/probe height for both lower and upper bounds) where the variable type being variable and the range properties being upper bound 1.0 and the lower bound being 20.0 (Image 5.11). Yield stress variable is constant and the value 283MPa. The range properties being fixed (as recorded on the aerospace specification metals/ASM) (Image 5.12).

Shoulder diameter		Cylindrical pin diameter		Shoulder-to-pin ratio	Workpiece material and thickness, mm	Ref
mm	in.	mm	in.			
13	0.5	5	0.2	2.6:1	6061-T6 Al, 3 mm	9
20–30	0.8–1.2	8–12	0.3–0.5	2.5:1, 1.6:1	7050, 2195, 5083, 2024, 7075 Al, 6.35 mm	11
23	0.9	8.2	0.32	2.8:1	2024-T351 Al, 6.4 mm	20
20,16	0.8, 0.6	6	0.24	3.3:1, 2.7:1	5083 and 6061 Al, 5.5 mm	21
12	0.5	4	0.16	3:1	1050 Al and oxygen-free copper, 1.8 mm	23
25.4	1.0	7.87	0.31	3.22:1	7075-T7351 Al, 9.53 mm	24
23	0.9	8.4	0.33	2.7:1	2524-T351 Al, 6.4 mm	26
20	0.79	4	0.16	5:1	6064 Al to carbon steel, 4.5 mm	54
23	0.9	8.2	0.32	2.8:1	2024-T351, 7 mm	72
10	0.4	3.8	0.15	2.6:1	2095 Al, 1.63 mm	74
25	1.0	9	0.35	2.8:1	5251 Al, 5 mm	101

Table 5.4 Summary of friction stirring tool dimensions for a given workpiece material

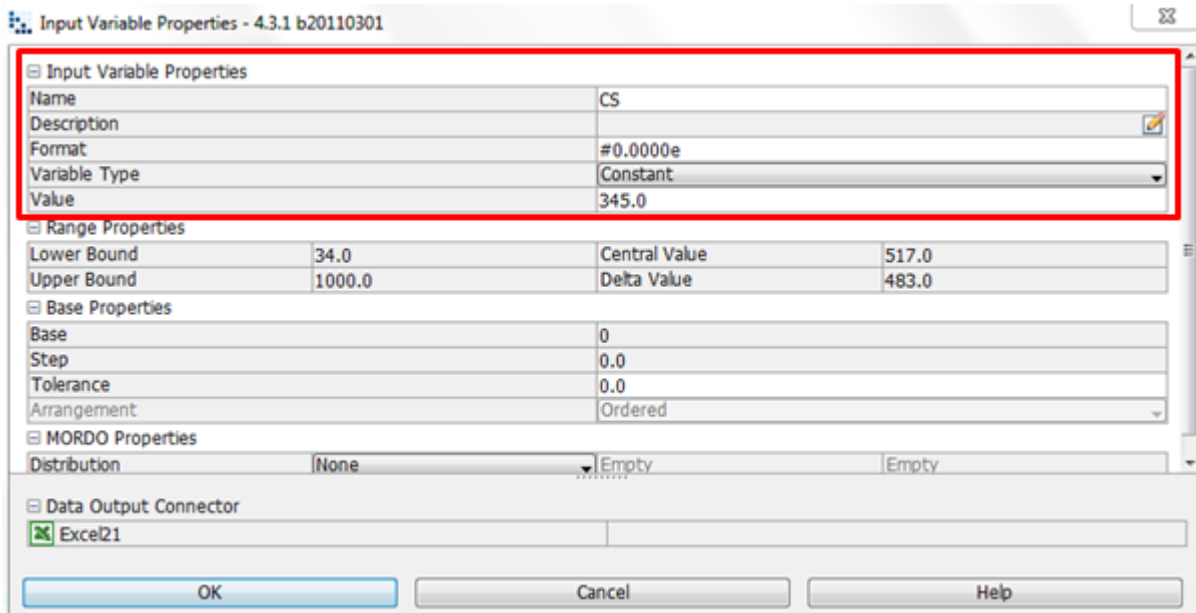


Image 5.6 : Al2024-T3 material contact shear stress 345 MPa is chosen, where the variable type constant hence the lower and upper bound is fixed

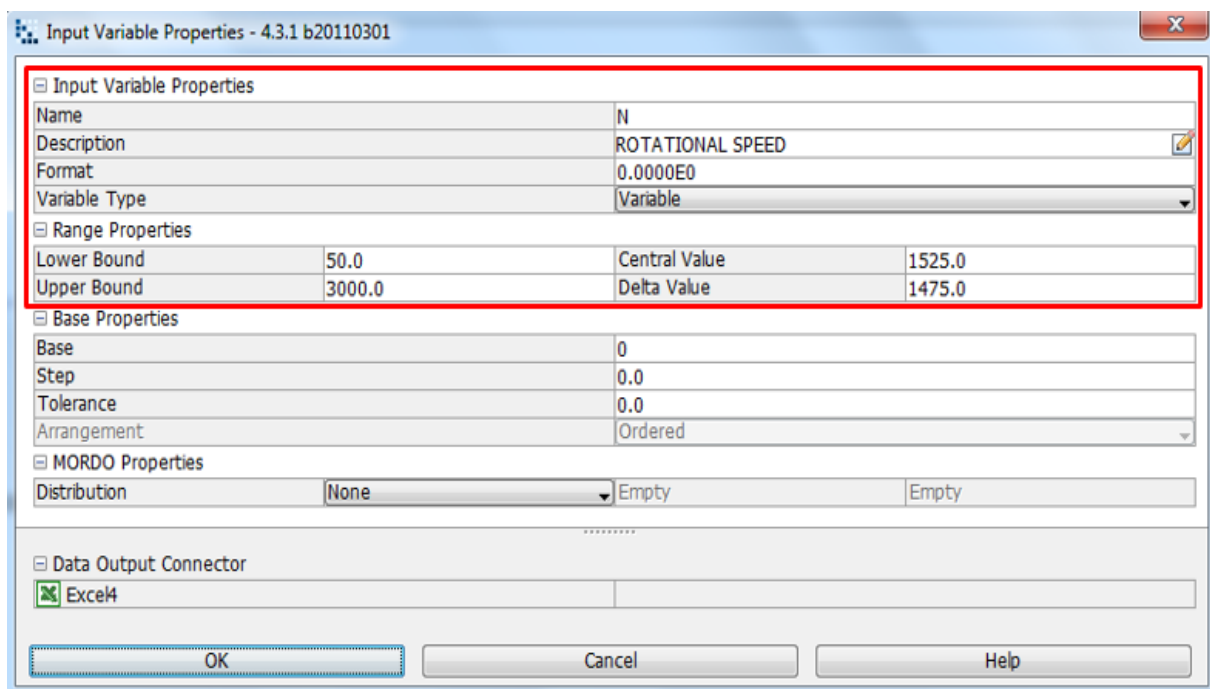


Image 5.7: Rotational speed is determined by lower and upper bound range properties, as shown in the input variable node properties dialog.

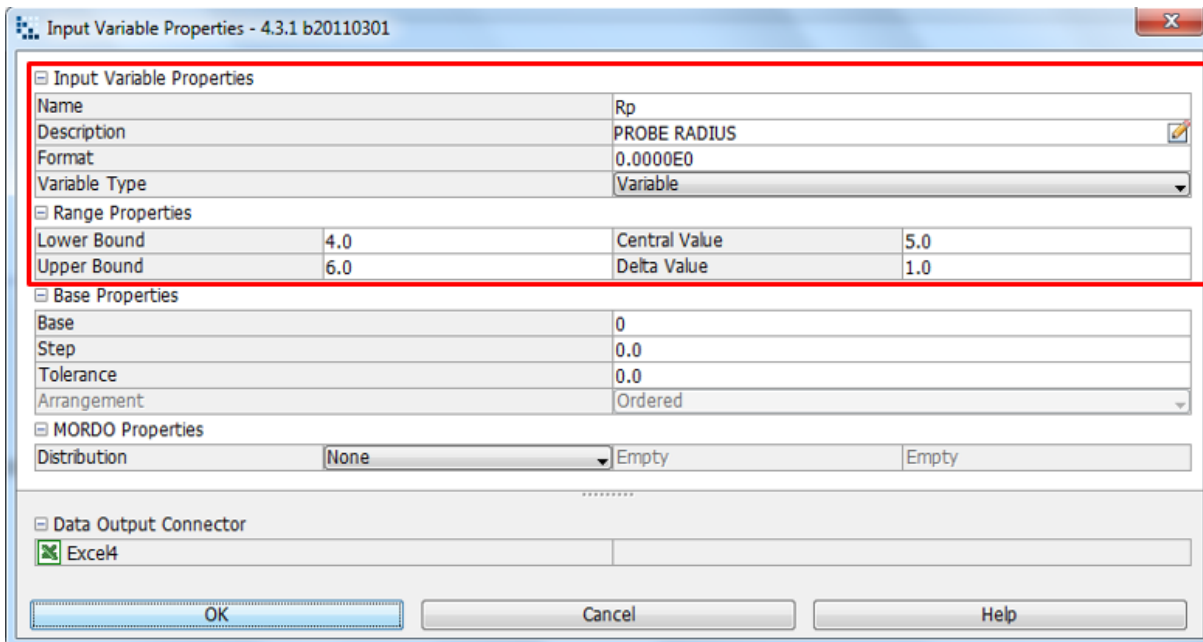


Image 5.8: Probe Radius is determined by lower and upper bound range properties, as shown in the input variable node properties dialog

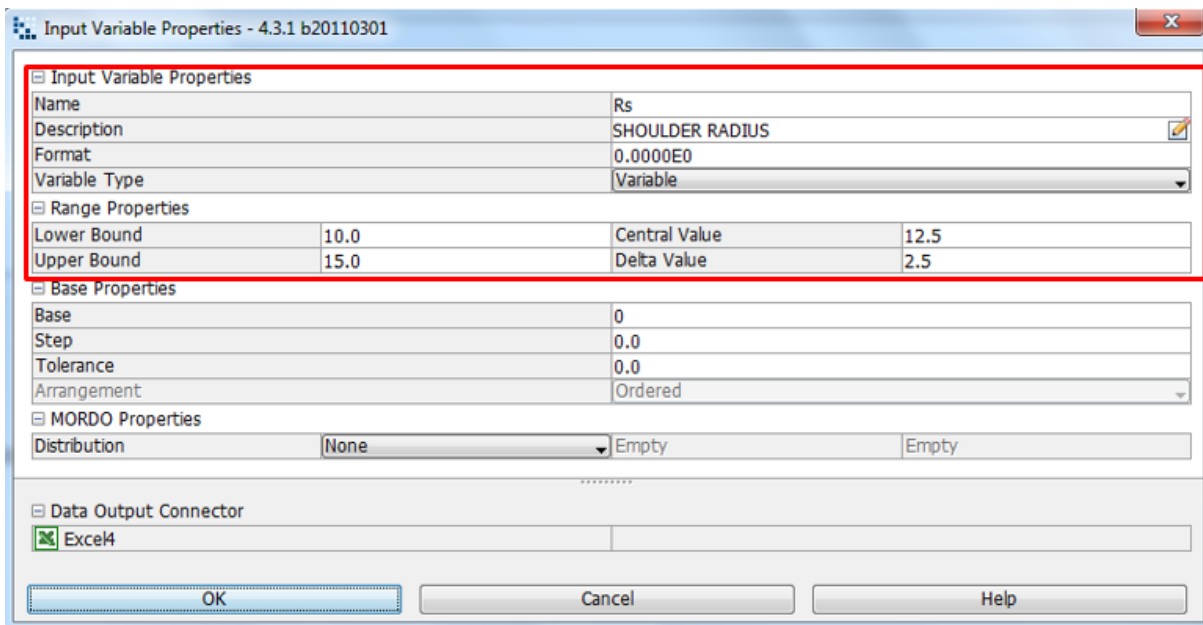


Image 5.9: Shoulder radius is determined by lower and upper bound range properties, as shown in the input variable node properties dialog

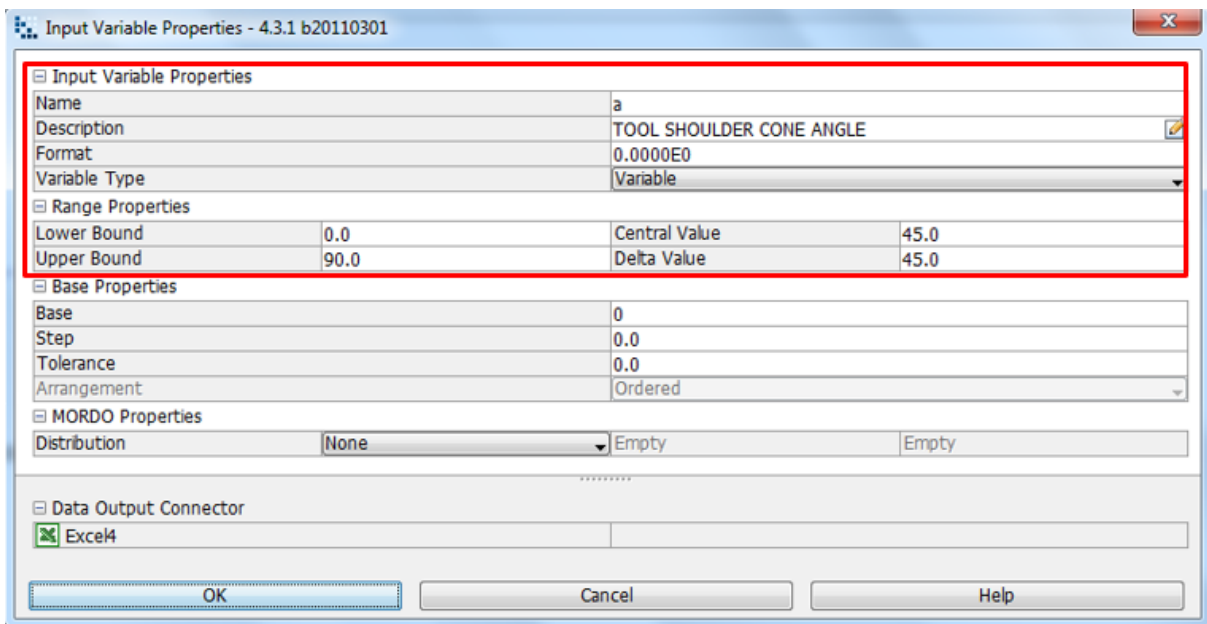


Image 5.10: Tool shoulder angle is determined by lower and upper bound range properties, as shown in the input variable node properties dialog

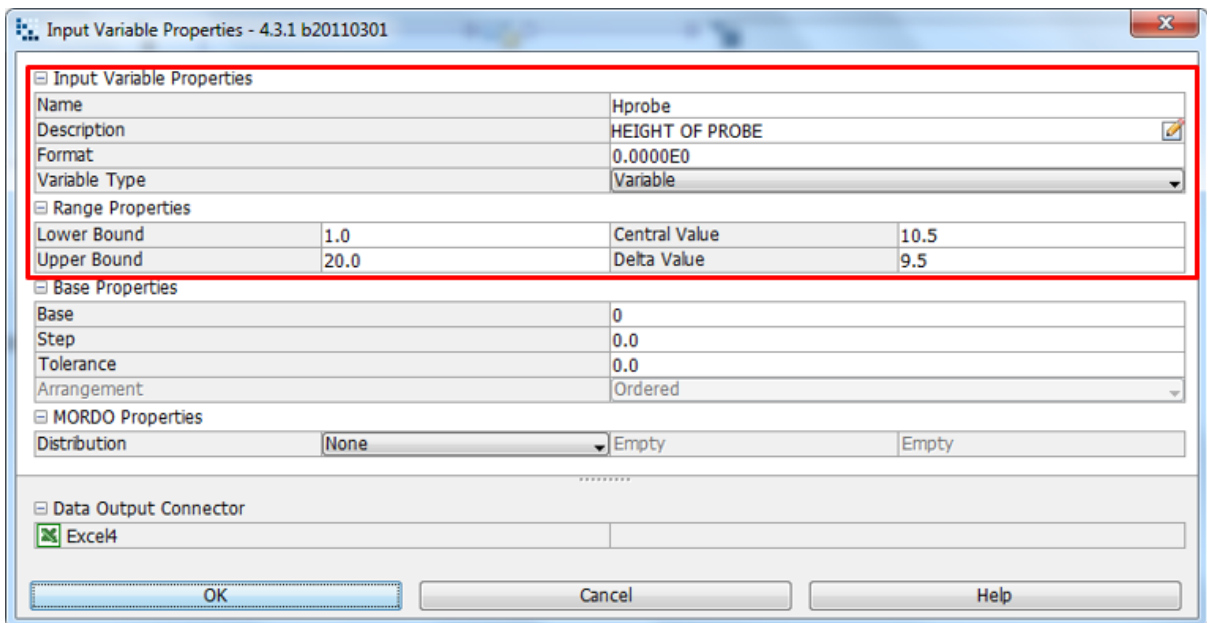


Image 5.11: Probe height is determined by lower and upper bound range properties, as shown in the input variable node properties dialog

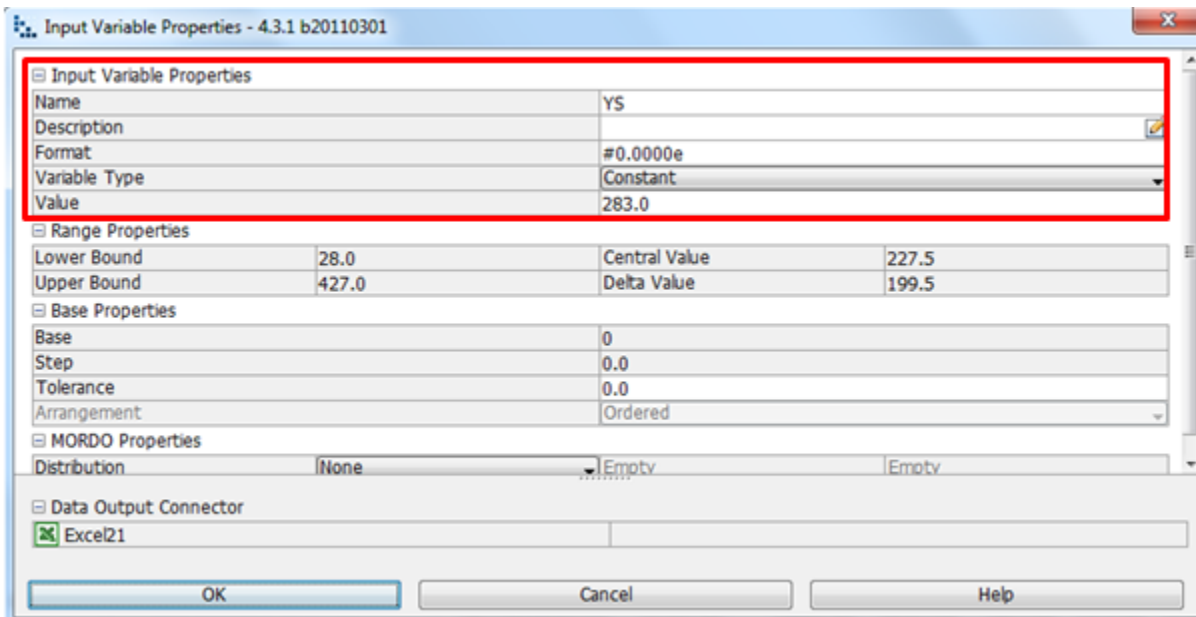


Image 5.12 : Al2024-T3 material Yield stress 283 MPa is chosen, where the variable type constant hence the lower and upper bound is fixed

5.5.2. History Charts, Multi History and Parallel Co-Ordinate Charts: Standard Tool Design

The history chart is a two dimensional plot that can be used as a time series chart. In this chart, quantities can be plotted as a function of the design ID which identifies the sequence of the design generated. In a single object optimization problem, the history charts shows how the optimization algorithm evolves, designs that are violating constrain are orange whereas feasible solutions are plotted in white. A history chart displays the moving average: a technical analyst tool. A simple moving average (SMA) smoothen a data series and makes it easier to spot trends. A simple moving average is formed by computing the average design value over a specific number of periods (MA samples). In addition the history a display of an analyst tool that measures the relative highness or lowness of design value, it consists of a middle band (represented by the SMA: the underweight average of the previous design with valid values. i.e. not NaN) an upper band (the SMA plus the standard deviations) and a lower band (the SMA minus the standard deviations). The project starts once a run project has started (Image 5.13). An index (Image5.14) before the initial project design commences. To create this chart firstly input variables, out variables and objectives need to selected (Image 5.15).The history chart shows the variations for Probe Side Heat Generation and Rotational Speed. A history chart highlights in an easy way, the minimum and the maximum feasible design values: the bottom chart area displays the minimum feasible design value while the top of the chart area display feasible design value. A multi history chart is a two dimensional plot that can be used as a time series chart for two or more variables. In this chart, quantities are plotted as a function of the design ID which identifies the sequence of design generated. It is equal to a history chart except that it is possible to plot more than one variable at the same time. One particular of this chart is that it is possible to associated variables to a second axis with its boundaries, grid and format. A multi history can display each design with customizable symbol representing the type (real & feasible, real & unfeasible, virtual & feasible, virtual & unfeasible, real & error and virtual & error) or the variable series it is belonging to. In a chart it is possible to highlight the marked designs type

visualization and category visualization. A representation of the heat generation from a standard tool shoulder (Chart 5.1) when the indicated rotational speed increases the heat generation also increases. A clear representation of the accurately increased rotational speed of the tool shoulder and the increased heat generation exerted. This chart also verifies that the design is feasible (Chart 5.2). Representation of heat generation of a tool shoulder that has been generated by the increased rotation of a tool probe radius (Chart 5.3). In a representation for a parallel co-ordinated chart to show feasibility the increased heat generation from the tool probe side form a tool shoulder cone angle (Chart 5.4). (Chart 5.5) is a representation of the heat generation from a standard tool shoulder. As shown when the indicated rotational speed of the tool shoulder increases the heat generation of the probe side also increase. The heat generation from a tool shoulder which is determined by the speed of the tool rotation is represented by (Chart 5.6). A history chart based on the heat generation of the shoulder determined by the tool shoulder radius is accurately represented by (Chart 5.7).

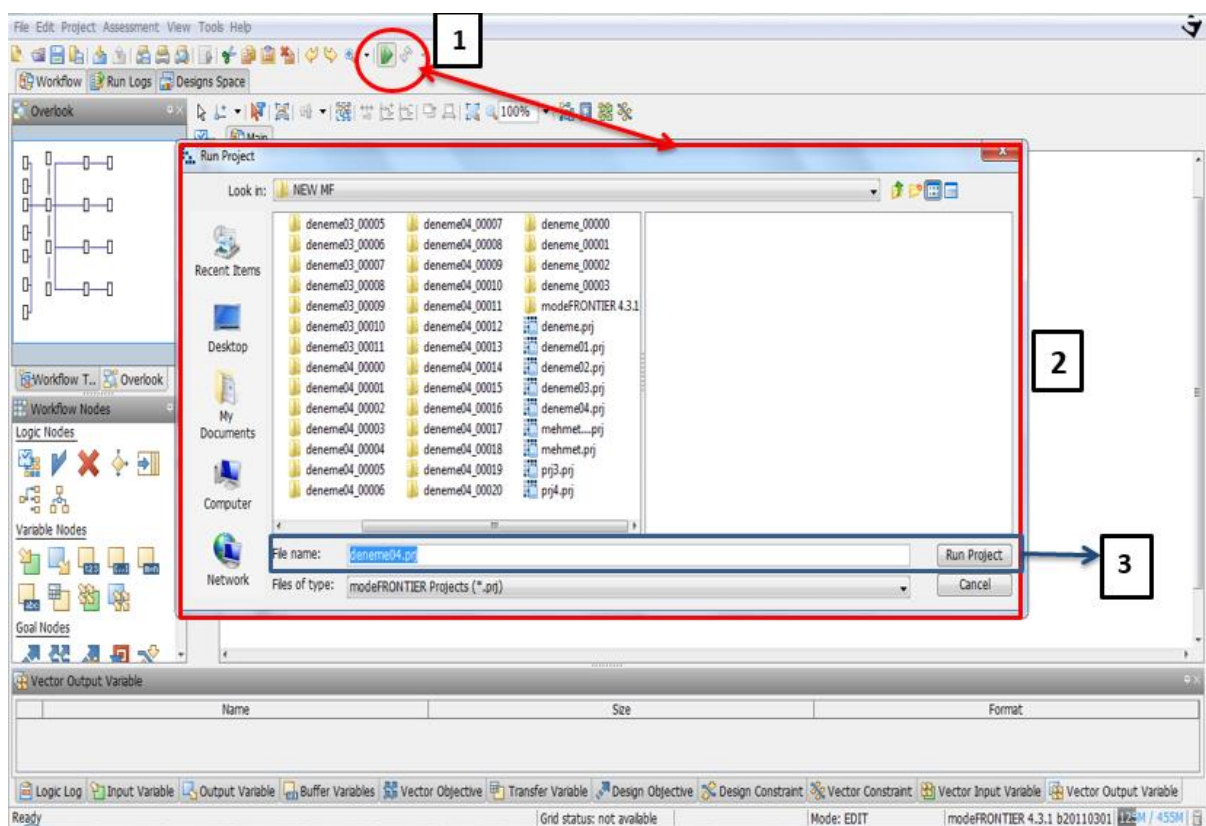


Image 5.13 : Click on run/stop icon(1). Run project box will pop up(2). Click on run project(3) to start design project.

Image 5.14 : Before project runs, a project info index will be shown. As seen in the above image.

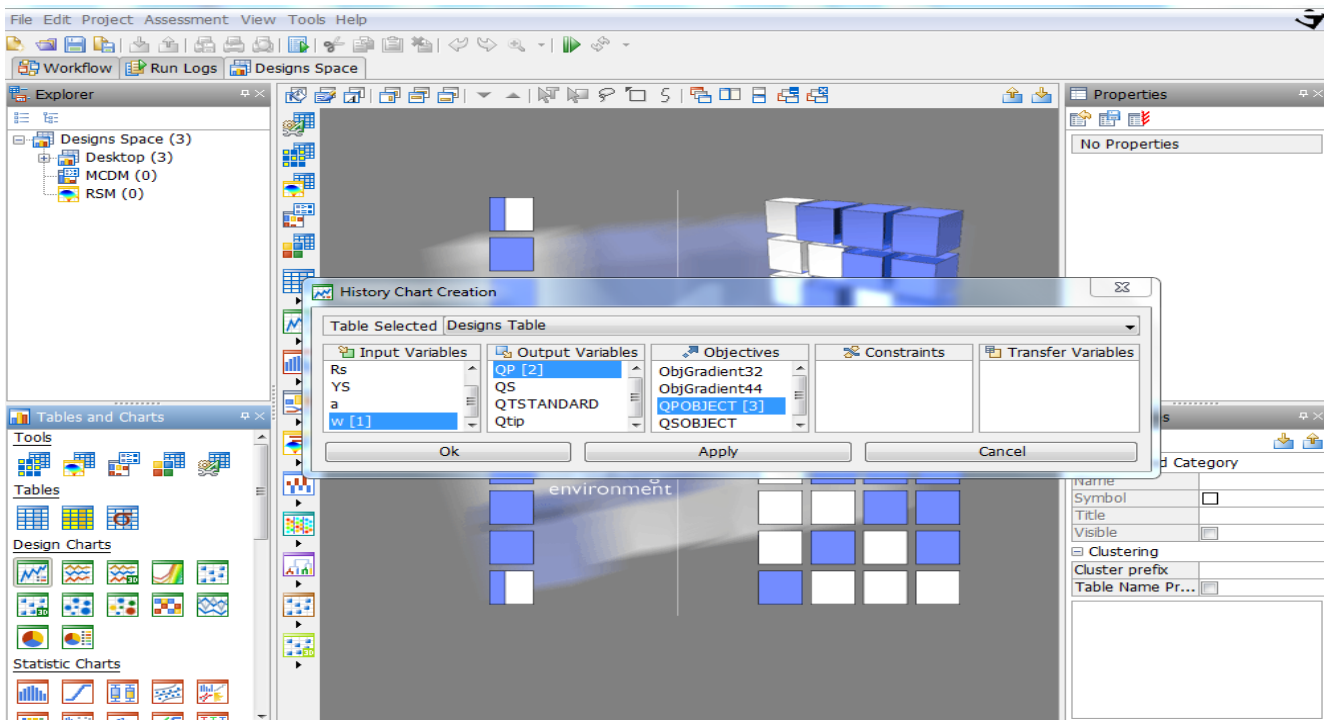
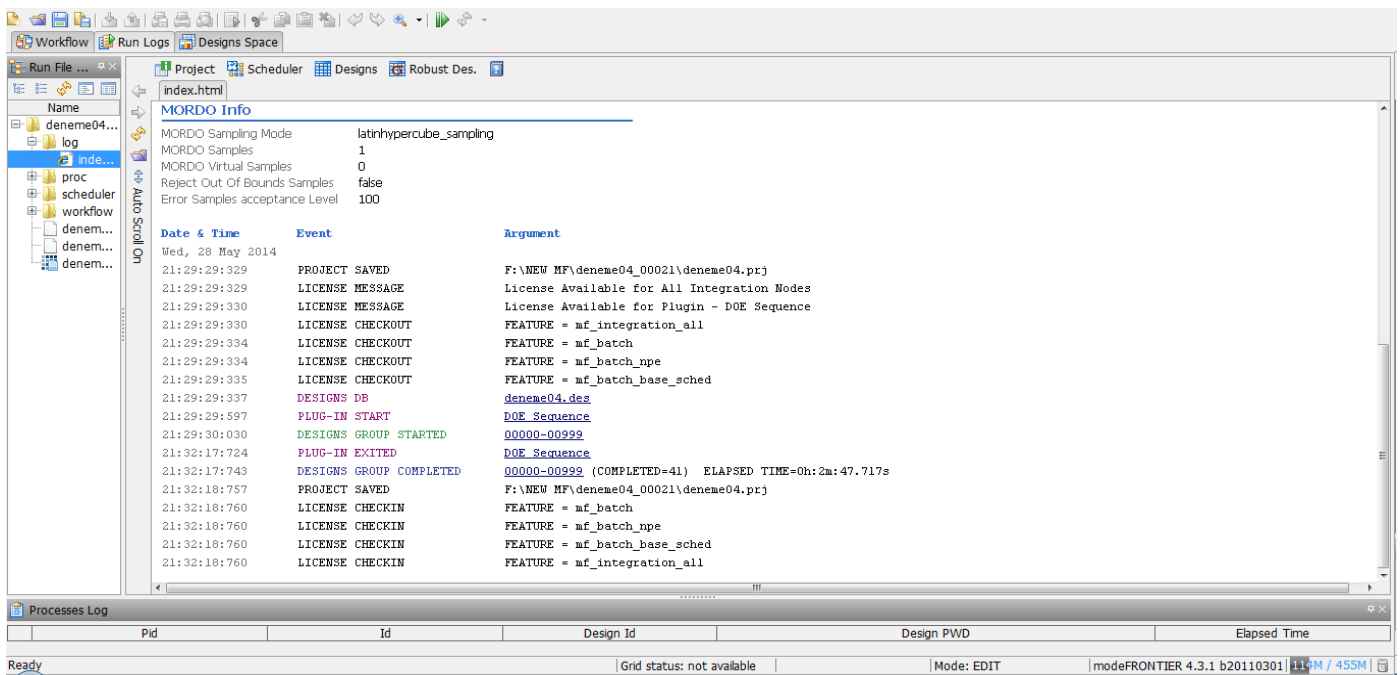


Image 5.15 : History Chart created on Mode Frontier Designs Space as shown above for Probe Side Heat Generation and Rotational Speed

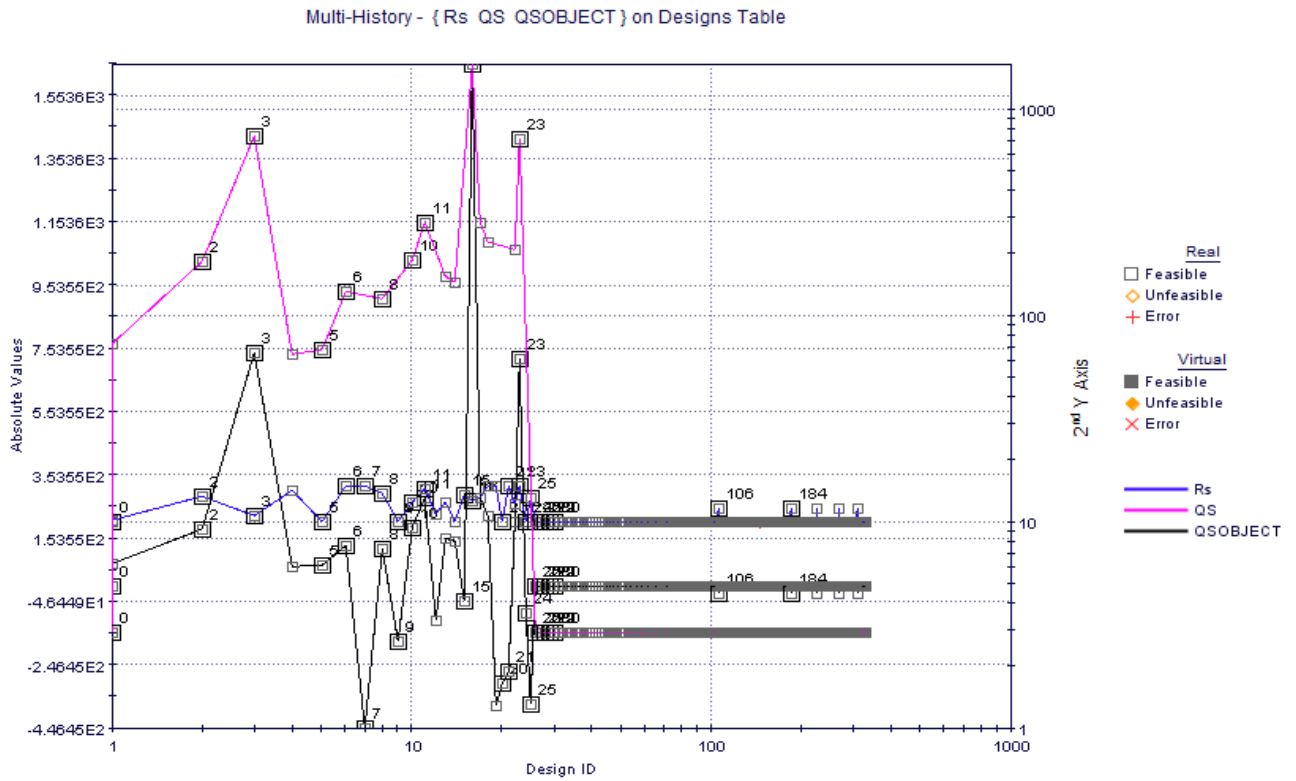


Chart 5.1: Multi-History Chart on Designs Space as created from Qshoulder vs. Shoulder radius, Rs

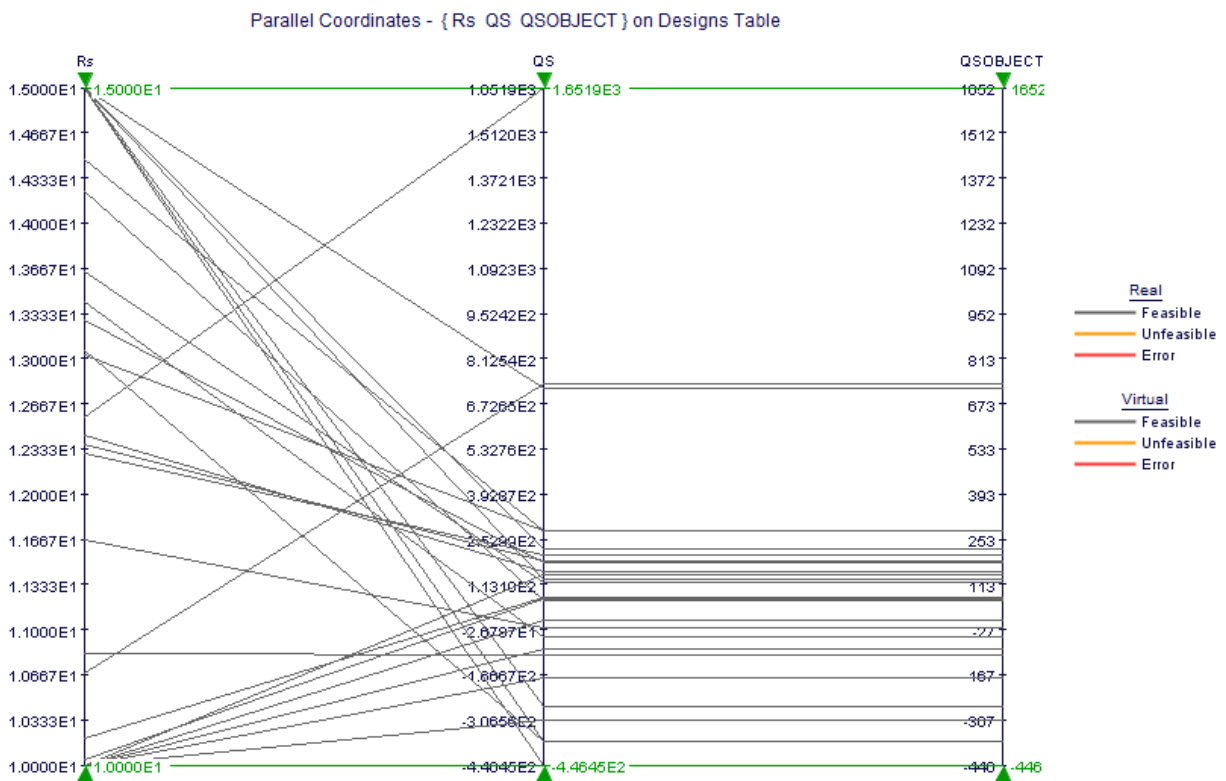


Chart 5.2: Parallel Coordinates as created from Qshoulder vs. Shoulder radius, Rs

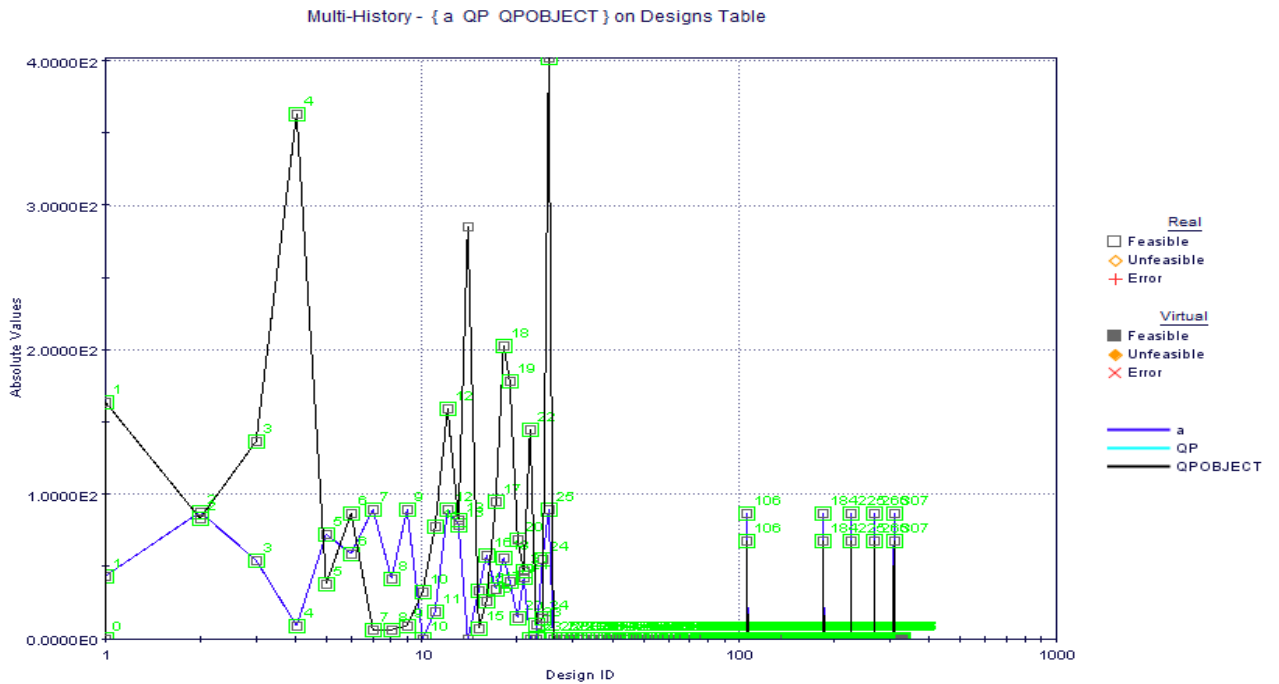


Chart 5.3: Multi-History Chart on Designs Space as created from Qprobe, side vs. Tool shoulder cone angle

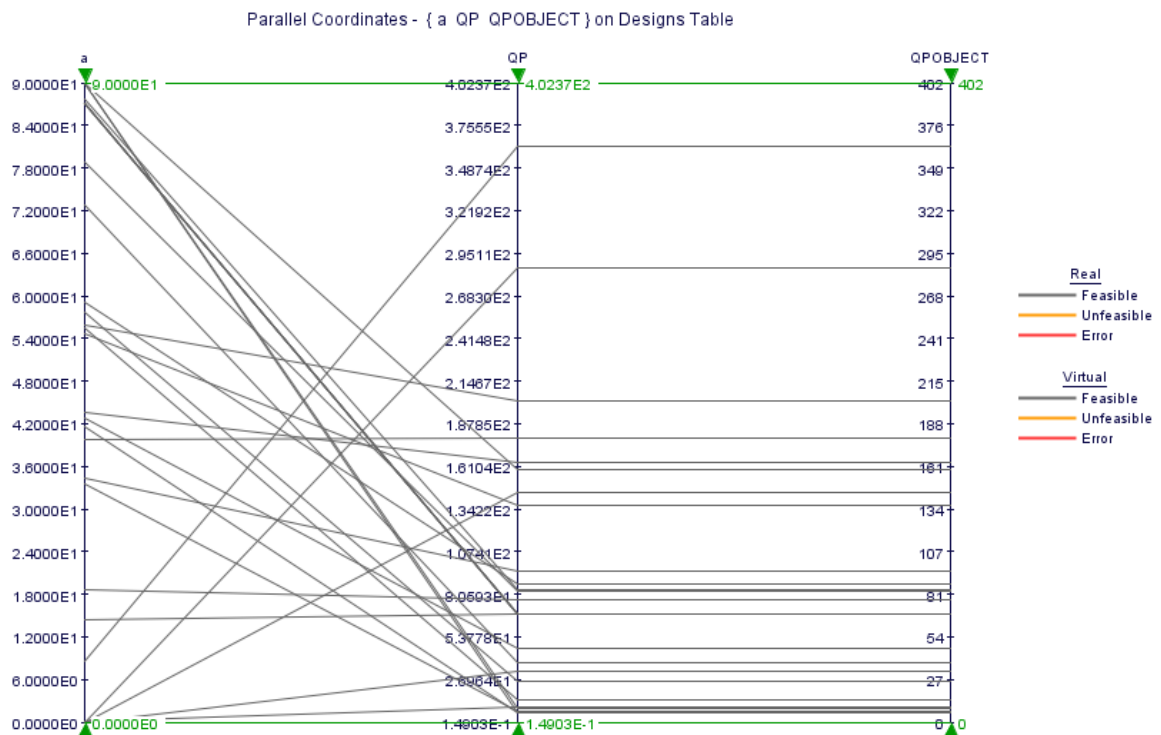


Chart 5.4: Parallel Coordinates as created from Qprobe side vs. Tool shoulder cone angle

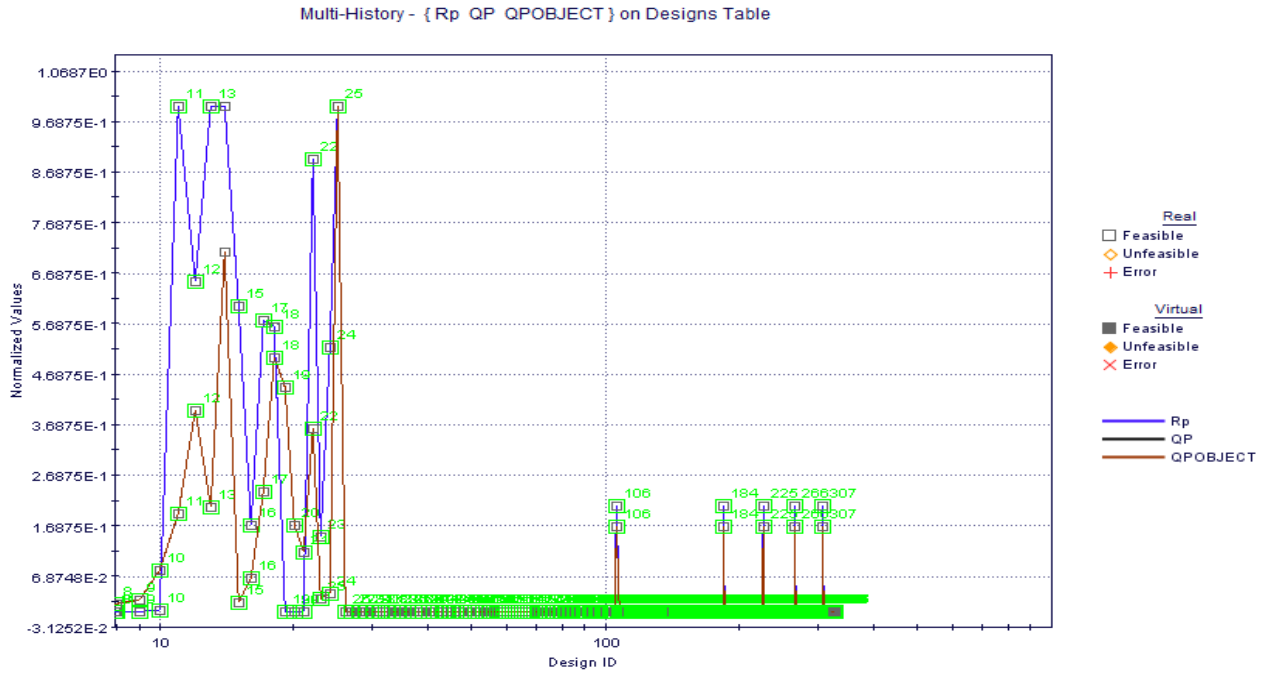


Chart 5.5 : Multi-History Chart on Designs Space as created from Qprobe, side vs. tool shoulder radius

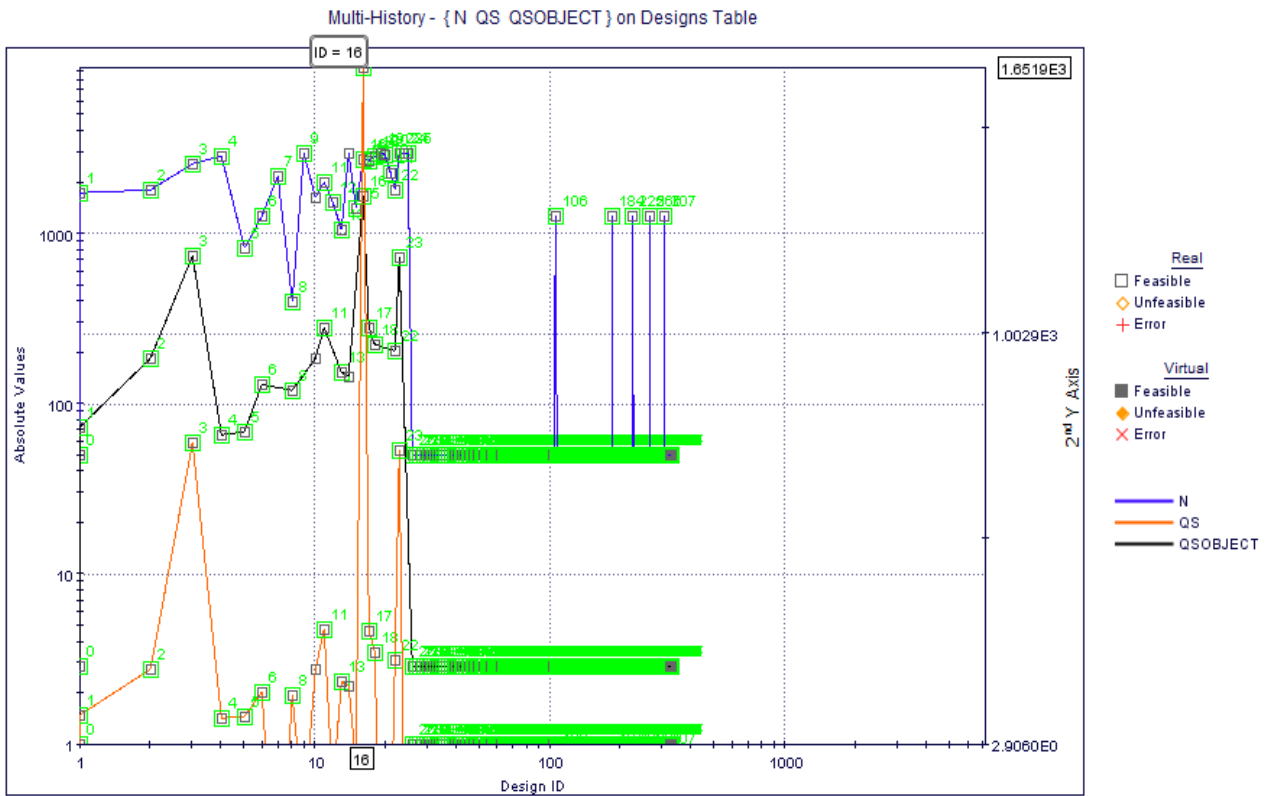


Chart 5.6: Multi-History Chart on Designs Space as created from Qshoulder vs. Tool rotational speed

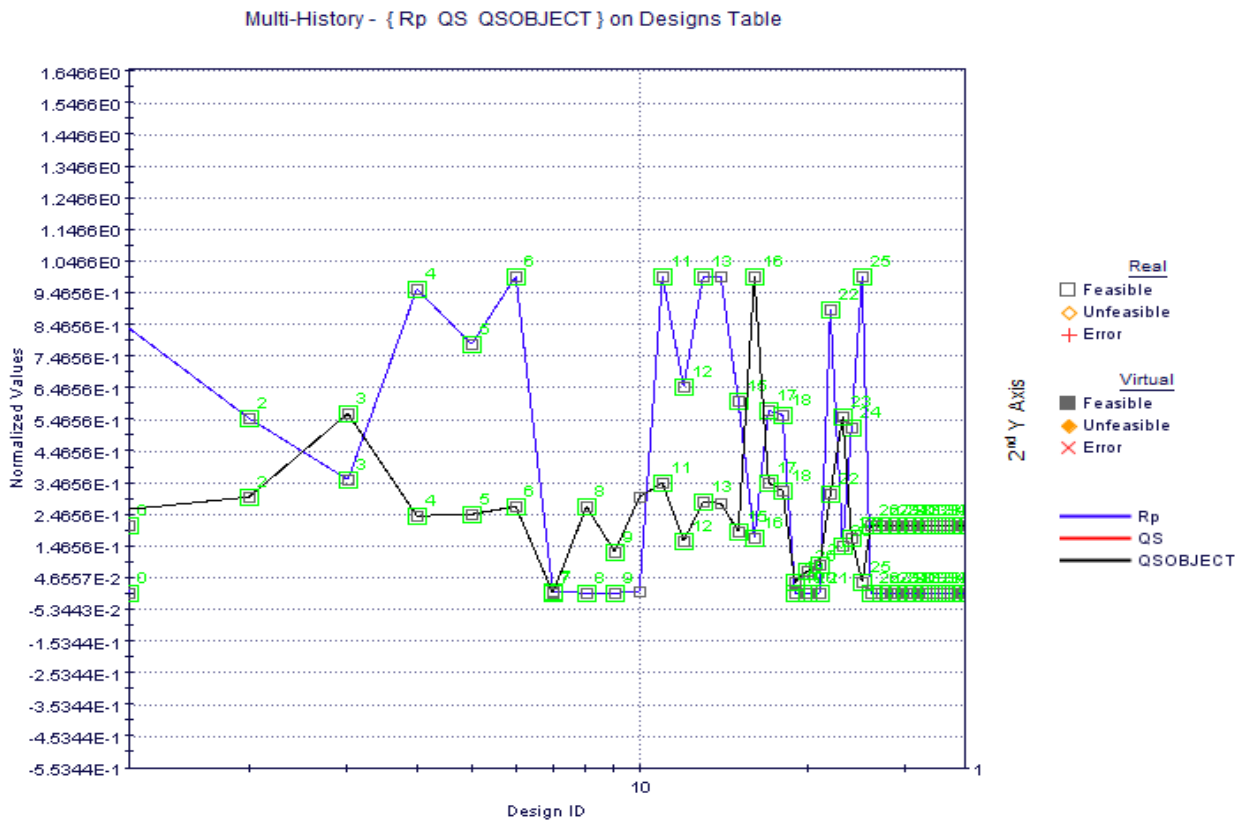


Chart 5.7: History Chart on Designs Space as created from Qshoulder vs. tool shoulder radius

6. The Bobbin Tool Friction Stir Welding: Design and Experimentation

Bobbin tools consist of two shoulders, one on the top surface and one on the bottom surface of the work piece, connected by a pin fully contained within the work piece (FIG. 6.1). The bobbin tool concept was included in the first FSW patent by TWI [23], but initial trials had problems with weld nugget containment due to improper shoulder design. The next iteration of bobbin tools used a fixed shoulder-to-shoulder distance and the scrolled shoulder tool [68], which eliminated the need to tilt the tool. However, subsequent FSW trials showed that the fixed shoulder distance bobbin tools had issues with pin fractures that were attributed to thermal expansion stresses between the tool and work piece. The final bobbin tool iteration included the RPT [75], which allowed the relative movement between the shoulders to maintain a constant force between the shoulders. The bobbin tool works by placing the bottom or reacting scrolled shoulder onto the end of a retractable pin. This is typically done by first drilling a hole through the work piece, inserting the threaded pin, and securing the second shoulder to the pin. During FSW, the bottom shoulder is drawn toward the top shoulder (using the RPT technology) until the desired force is reached. Because the two shoulders are reacting together to form the friction stir weld, the bobbin tool is also known as the self-reacting tool. The primary advantages of bobbin tools include ease of fixturing (no anvil is needed), the elimination of incomplete root penetration, and increased tool travel speeds due to heating from both shoulders [79]. Fixed shoulder-to-shoulder distance bobbin tools are now possible with the convex scrolled shoulder [46-49]. This bobbin tool configuration does not require the bottom shoulder actuation (RPT) to produce a sound weld and simplifies the design of FSW machines. Bobbin tools have successfully joined thick aluminium plates from 8 to 25.4 mm (0.3 to 1 in.) [79] and thin aluminium plate from 1.8 to 3 mm (0.07 to 0.12 in.). However, several considerations must be made when dealing with the bobbin tools [79]. Careful cleaning of the tools after each weld is necessary to maintain the needed load by actuating the pin and bottom shoulder. During welding, material can extrude between the pin and shoulder, making removal of the bottom shoulder difficult. Thermal comparisons between the bobbin and conventional tools show that the maximum temperature for the bobbin tools is 50 °C (90 °F) higher than the conventional tool [81]. This behaviour is attributed to the backing anvil in conventional FSW acting as a heat sink. As would be expected with higher temperatures, the forging forces were 4 to 8 times less for the bobbin tool than conventional FSW.

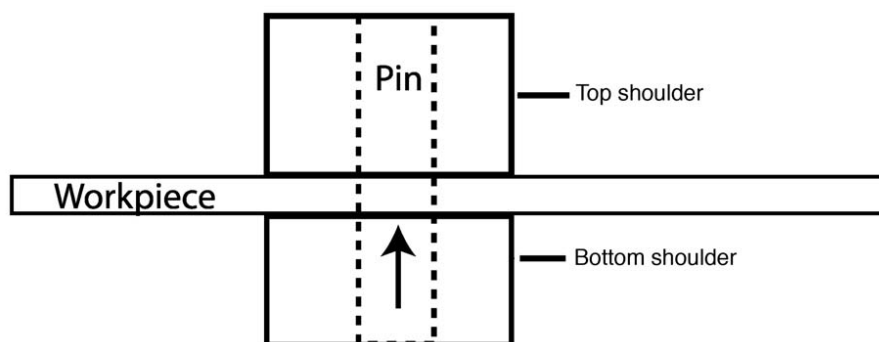


FIG. 6.1 Schematic of a bobbin tool consisting of a top shoulder, pin, and bottom shoulder attached to the pin. The friction stir weld is produced when the pin is moved upward, forcing the bottom shoulder to react against the top shoulder.



(a) Baseline bobbin tool in this study



(b) Schematic of a tool in action

Image 6.1: The FSW bobbin tool

Tool Shoulder ,R	10 mm	0,01 m	Drw. 5.1
Tool Probe radius,R	4 mm	0,004 m	Drw. 5.2
Tool probe height,h	2 mm	0,002 m	
Tool shoulder cone angle	α	0	
Friction Coefficient	μ	0,6	Static Condition
Friction Coefficient	μ	0,4	Sliding Condition
Friction shear stress	μp		
Contact shear stress	τ_{cont}	345 MPa	
Yield stress	σ_{yield}	283 MPa	

Table 6.1: Analytical Estimation of heat generation for the Bobbin Tool

Tool Angular Speed		Rotational Speed
ω	(rad/s)	N (rpm)
ω_1	83.80 rad/s	800 rpm
ω_2	130.89 rad/s	1250 rpm
ω_3	167.55 rad/s	1600 rpm
ω_4	209.44 rad/s	2000 rpm

Table 6.2: Tool Angular Speed and Rotational Speed for the Bobbin Tool

On substituting known values of the parameters, tool dimension, and all other values in derived equations, the heat generation values are as follows:

i) Heat Generation from the Top Shoulder: from equation 5.1 the values are-

a) For tool angular rotational speed $\omega_1 = 83.80 \text{ rad/s} = 800 \text{ rpm}$

$$Q_{ts1} = \frac{2}{3} \omega \pi \tau_{cont} \left[\left(\frac{R_{shoulder}}{2} \right)^3 - \left(\frac{d}{2} \right)^3 \right] (1 + \tan \alpha)$$

$$Q_{ts1} = \frac{2}{3} \times \pi \times 345 \times 83.80 \times \left[\left(\frac{0.02}{2} \right)^3 - \left(\frac{0.008}{2} \right)^3 \right] (1 + \tan 0)$$

$$Q_{s1} = \frac{2}{3} \times \pi \times 345 \times 83.80 \times \left[\left(\frac{0.02}{2} \right)^3 - \left(\frac{0.008}{2} \right)^3 \right] (1 + 0)$$

$$Q_{ts1} = 56.62 \text{ kW}$$

b) For tool angular rotational speed $\omega_2 = 130.89 \text{ rad/s} = 1250 \text{ rpm}$

$$Q_{ts2} = \frac{2}{3} \omega \pi \tau_{cont} \left[\left(\frac{R_{shoulder}}{2} \right)^3 - \left(\frac{d}{2} \right)^3 \right] (1 + \tan \alpha)$$

$$Q_{ts2} = \frac{2}{3} \times \pi \times 345 \times 130.89 \times \left[\left(\frac{0.02}{2} \right)^3 - \left(\frac{0.008}{2} \right)^3 \right] (1 + \tan 0)$$

$$Q_{ts2} = \frac{2}{3} \times \pi \times 345 \times 130.89 \times \left[\left(\frac{0.02}{2} \right)^3 - \left(\frac{0.008}{2} \right)^3 \right] (1 + 0)$$

$$Q_{s2} = 88.52 \text{ kW}$$

c) For tool angular rotational speed $\omega_3 = 167.55 \text{ rad/s} = 1600 \text{ rpm}$

$$Q_{ts3} = \frac{2}{3} \omega \pi \tau_{cont} \left[\left(\frac{R_{shoulder}}{2} \right)^3 - \left(\frac{d}{2} \right)^3 \right] (1 + \tan \alpha)$$

$$Q_{ts3} = \frac{2}{3} \times \pi \times 345 \times 167.55 \times \left[\left(\frac{0.02}{2} \right)^3 - \left(\frac{0.008}{2} \right)^3 \right] (1 + \tan 0)$$

$$Q_{ts3} = \frac{2}{3} \times \pi \times 345 \times 167.55 \times \left[\left(\frac{0.02}{2} \right)^3 - \left(\frac{0.008}{2} \right)^3 \right] (1 + 0)$$

$$Q_{ts3} = 113.31 \text{ kW}$$

d) For tool angular rotational speed $\omega_4 = 209.44 \text{ rad/s} = 2000 \text{ rpm}$

$$Q_{ts4} = \frac{2}{3} \omega \pi \tau_{cont} \left[\left(\frac{R_{shoulder}}{2} \right)^3 - \left(\frac{d}{2} \right)^3 \right] (1 + \tan \alpha)$$

$$Q_{ts4} = \frac{2}{3} \times \pi \times 345 \times 209.44 \times \left[\left(\frac{0.02}{2} \right)^3 - \left(\frac{0.008}{2} \right)^3 \right] (1 + \tan 0)$$

$$Q_{ts4} = \frac{2}{3} \times \pi \times 345 \times 209.44 \times \left[\left(\frac{0.02}{2} \right)^3 - \left(\frac{0.008}{2} \right)^3 \right] (1 + 0)$$

$$Q_{ts4} = 141.64 \text{ kW}$$

Q_{ts} (kW)	N (rpm)	ω (rad/s)
56.62	800	83.8
88.52	1250	130.89
113.31	1600	167.55
141.64	2000	209.44

Table 6.3: Heat Generation Calculations for the Top Shoulder.

ii) Heat Generation from the Probe Side Surface: from equation 1.2 the values are-

a) For tool angular rotational speed $\omega_1 = 83.80 \text{ rad/s} = 800 \text{ rpm}$

$$Q_{ps1} = 2 \omega \pi \tau_{cont} \left(\frac{d}{2} \right)^2 h \left(1 + \tan \frac{\beta}{2} \right)$$

$$Q_{ps1} = 2 \times \pi \times 345 \times 83.80 \times \left(\frac{0.008}{2} \right)^2 \times 0.002 \left(1 + \tan \frac{0}{2} \right)$$

$$Q_{ps1} = 2 \times \pi \times 345 \times 83.80 \times \left(\frac{0.008}{2} \right)^2 \times 0.002 (1 + 0)$$

$$Q_{ps1} = 5.81 \text{ kW}$$

b) For tool angular rotational speed $\omega_2 = 130.89 \text{ rad/s} = 1250 \text{ rpm}$

$$Q_{ps2} = 2\omega\pi\tau_{cont} \left(\frac{d}{2}\right)^2 h \left(1 + \tan\frac{\beta}{2}\right)$$

$$Q_{ps2} = 2 \times \pi \times 345 \times 130.89 \left(\frac{0.008}{2}\right)^2 0.002 \left(1 + \tan\frac{0}{2}\right)$$

$$Q_{ps2} = 2 \times \pi \times 345 \times 130.89 \left(\frac{0.008}{2}\right)^2 0.002 (1 + 0)$$

$$Q_{ps2} = 9.08 \text{ kW}$$

c) For tool angular rotational speed $\omega_3 = 167.55 \text{ rad/s} = 1600 \text{ rpm}$

$$Q_{ps3} = 2\omega\pi\tau_{cont} \left(\frac{d}{2}\right)^2 h \left(1 + \tan\frac{\beta}{2}\right)$$

$$Q_{ps3} = 2 \times \pi \times 345 \times 167.55 \left(\frac{0.008}{2}\right)^2 0.002 \left(1 + \tan\frac{0}{2}\right)$$

$$Q_{ps3} = 2 \times \pi \times 345 \times 167.55 \left(\frac{0.008}{2}\right)^2 0.002 (1 + 0)$$

$$Q_{ps3} = 11.63 \text{ kW}$$

d) For tool angular rotational speed $\omega_4 = 209.44 \text{ rad/s} = 2000 \text{ rpm}$

$$Q_{ps4} = 2\omega\pi\tau_{cont} \left(\frac{d}{2}\right)^2 h \left(1 + \tan\frac{\beta}{2}\right)$$

$$Q_{ps4} = 2 \times \pi \times 345 \times 209.44 \left(\frac{0.008}{2}\right)^2 0.002 \left(1 + \tan\frac{0}{2}\right)$$

$$Q_{ps4} = 2 \times \pi \times 345 \times 209.44 \left(\frac{0.008}{2}\right)^2 0.002 (1 + 0)$$

$$Q_{ps4} = 14.53 \text{ kW}$$

Q_{ps} (kW)	N (rpm)	ω (rad/s)
5.81	800	83.8
9.08	1250	130.89
11.63	1600	167.55
14.52	2000	209.44

Table 6.4: Heat Generation Calculations for the Probe Side Surface

iii) **Heat Generation from the Bottom Shoulder:** from equation 5.1 the values are-

a) For tool angular rotational speed $\omega_1 = 83.80 \text{ rad/s} = 800 \text{ rpm}$

$$Q_{bs1} = \frac{2}{3} \omega \pi \tau_{cont} \left[\left(\frac{R_{shoulder}}{2} \right)^3 - \left(\frac{d}{2} \right)^3 \right] (1 + \tan \alpha)$$

$$Q_{bs1} = \frac{2}{3} \times \pi \times 345 \times 83.80 \times \left[\left(\frac{0.02}{2} \right)^3 - \left(\frac{0.008}{2} \right)^3 \right] (1 + \tan 0)$$

$$Q_{bs1} = \frac{2}{3} \times \pi \times 345 \times 83.80 \times \left[\left(\frac{0.02}{2} \right)^3 - \left(\frac{0.008}{2} \right)^3 \right] (1 + 0)$$

$$Q_{bs1} = 56.62 \text{ kW}$$

b) For tool angular rotational speed $\omega_2 = 130.89 \text{ rad/s} = 1250 \text{ rpm}$

$$Q_{bs2} = \frac{2}{3} \omega \pi \tau_{cont} \left[\left(\frac{R_{shoulder}}{2} \right)^3 - \left(\frac{d}{2} \right)^3 \right] (1 + \tan \alpha)$$

$$Q_{bs2} = \frac{2}{3} \times \pi \times 345 \times 130.89 \times \left[\left(\frac{0.02}{2} \right)^3 - \left(\frac{0.008}{2} \right)^3 \right] (1 + \tan 0)$$

$$Q_{bs2} = \frac{2}{3} \times \pi \times 345 \times 130.89 \times \left[\left(\frac{0.02}{2} \right)^3 - \left(\frac{0.008}{2} \right)^3 \right] (1 + 0)$$

$$Q_{bs2} = 88.52 \text{ kW}$$

c) For tool angular rotational speed $\omega_3 = 167.55 \text{ rad/s} = 1600 \text{ rpm}$

$$Q_{bs3} = \frac{2}{3} \omega \pi \tau_{cont} \left[\left(\frac{R_{shoulder}}{2} \right)^3 - \left(\frac{d}{2} \right)^3 \right] (1 + \tan \alpha)$$

$$Q_{bs3} = \frac{2}{3} \times \pi \times 345 \times 167.55 \times \left[\left(\frac{0.02}{2} \right)^3 - \left(\frac{0.008}{2} \right)^3 \right] (1 + \tan 0)$$

$$Q_{bs3} = \frac{2}{3} \times \pi \times 345 \times 167.55 \times \left[\left(\frac{0.02}{2} \right)^3 - \left(\frac{0.008}{2} \right)^3 \right] (1 + 0)$$

$$Q_{bs3} = 113.31 \text{ kW}$$

d) For tool angular rotational speed $\omega_4 = 209.44 \text{ rad/s} = 2000 \text{ rpm}$

$$Q_{bs4} = \frac{2}{3} \omega \pi \tau_{cont} \left[\left(\frac{R_{shoulder}}{2} \right)^3 - \left(\frac{d}{2} \right)^3 \right] (1 + \tan \alpha)$$

$$Q_{bs4} = \frac{2}{3} \times \pi \times 345 \times 209.44 \times \left[\left(\frac{0.02}{2} \right)^3 - \left(\frac{0.008}{2} \right)^3 \right] (1 + \tan 0)$$

$$Q_{bs4} = \frac{2}{3} \times \pi \times 345 \times 209.44 \times \left[\left(\frac{0.02}{2} \right)^3 - \left(\frac{0.008}{2} \right)^3 \right] (1 + 0)$$

$$Q_{bs4} = 141.64 \text{ kW}$$

Q_s (kW)	N (rpm)	ω (rad/s)
56.62	800	83.8
88.52	1250	130.89
113.31	1600	167.55
141.64	2000	209.44

Table 6.5: Heat Generation Calculation for the Tool Shoulder

iii) **Total Heat Generated:** from equation 1.4 the values are-

f) For tool angular rotational speed $\omega_1 = 83.80 \text{ rad/s} = 800 \text{ rpm}$

$$Q_{T1} = Q_{ts1} + Q_{ps1} + Q_{bs1}$$

$$Q_{T1} = 56.62 + 5.81 + 56.62$$

$$Q_{T1} = 119.05 \text{ kW}$$

g) For tool angular rotational speed $\omega_2 = 130.89 \text{ rad/s} = 1250 \text{ rpm}$

$$Q_{T2} = Q_{ts2} + Q_{ps2} + Q_{bs2}$$

$$Q_{T2} = 88.52 + 9.08 + 88.52$$

$$Q_{T2} = 186.12 \text{ kW}$$

h) For tool angular rotational speed $\omega_3 = 167.55 \text{ rad/s} = 1600 \text{ rpm}$

$$Q_{T3} = Q_{ts3} + Q_{ps3} + Q_{bs3}$$

$$Q_{T3} = 113.31 + 11.63 + 113.31$$

$$Q_{T3} = 238.25 \text{ kW}$$

i) For tool angular rotational speed $\omega_4 = 209.44 \text{ rad/s} = 2000 \text{ rpm}$

$$Q_{T4} = Q_{ts4} + Q_{ps4} + Q_{bs4}$$

$$Q_{T4} = 141.64 + 14.53 + 141.64$$

$$Q_{T4} = 297.81 \text{ kW}$$

Q_T (kW)	N (rpm)	ω (rad/s)
119.05	800	83.8
186.12	1250	130.89
238.25	1600	167.55
297.81	2000	209.44

Table 6.6: Total Heat Generation for the Bobbin Tool.

Based on the heat generated from independent contact conditions, contributions from different surfaces compared to the total heat generated are as follows

$$f_{\text{shoulder}} = \frac{Q_{ts1}}{Q_{\text{total1}}}$$

$$= \left[\left(\frac{R_{\text{shoulder}}}{2} \right)^3 - \left(\frac{d}{2} \right)^3 \right] \times (1 + \tan \alpha) / \left[\left(\frac{R_{\text{shoulder}}}{2} \right)^3 - \left(\frac{d}{2} \right)^3 \right] \times (1 + \tan \alpha)$$

$$+ \left(\frac{d}{2} \right)^3 + 3 \left(\frac{d}{2} \right)^2 \times h$$

$$f_{\text{top-shoulder}} = \frac{56.62}{119.05}$$

$$= \left[\left(\frac{0.012}{2} \right)^3 - \left(\frac{0.008}{2} \right)^3 \right] \times (1 + \tan 0) / \left[\left(\frac{0.012}{2} \right)^3 - \left(\frac{0.008}{2} \right)^3 \right] \times (1 + \tan 0)$$

$$+ \left(\frac{0.008}{2} \right)^3 + 3 \left(\frac{0.008}{2} \right)^2 \times 0.002$$

$$f_{\text{top-shoulder}} = \frac{56.62}{119.05}$$

$$= \left[\left(\frac{0.012}{2} \right)^3 - \left(\frac{0.008}{2} \right)^3 \right] \times (1 + 0) / \left[\left(\frac{0.012}{2} \right)^3 - \left(\frac{0.008}{2} \right)^3 \right] \times (1 + 0)$$

$$+ \left(\frac{0.008}{2} \right)^3 + 3 \left(\frac{0.008}{2} \right)^2 \times 0.002$$

$$f_{\text{top-shoulder}} = 0.47$$

$$f_{\text{probe side}} = \frac{Q_{ps1}}{Q_{\text{total1}}} = 3 \times \left(\frac{d}{2} \right)^2 \times h / \left[\left(\frac{R_{\text{shoulder}}}{2} \right)^3 - \left(\frac{d}{2} \right)^3 \right] (1 + \tan \alpha) + \left(\frac{d}{2} \right)^3 + 3 \left(\frac{d}{2} \right)^2 \times h$$

$$f_{\text{probe side}} = \frac{5.81}{119.05}$$

$$= 3 \times \left(\frac{0.008}{2} \right)^2 \times h / \left[\left(\frac{0.012}{2} \right)^3 - \left(\frac{0.008}{2} \right)^3 \right] (1 + \tan 0) + \left(\frac{0.008}{2} \right)^3 + 3 \left(\frac{0.008}{2} \right)^2$$

$$\times 0.002$$

$$f_{\text{probe side}} = \frac{5.81}{119.05}$$

$$= 3 \times \left(\frac{0.008}{2} \right)^2 \times h / \left[\left(\frac{0.012}{2} \right)^3 - \left(\frac{0.008}{2} \right)^3 \right] (1 + 0) + \left(\frac{0.008}{2} \right)^3 + 3 \left(\frac{0.008}{2} \right)^2$$

$$\times 0.002$$

$$f_{\text{probe side}} = 0.048$$

$$\begin{aligned}
f_{bottom-shoulder} &= \frac{Q_{bs1}}{Q_{total1}} = \left(\frac{d}{2}\right)^3 / \left[\left(\frac{D}{2}\right)^3 - \left(\frac{d}{2}\right)^3\right] (1 + \tan \alpha) + \left(\frac{d}{2}\right)^3 + 3\left(\frac{d}{2}\right)^2 \times h \\
f_{bottom-shoulder} &= \frac{56.62}{119.05} \\
&= (0.008)^3 / \left[\left(\frac{0.012}{2}\right)^3 - \left(\frac{0.008}{2}\right)^3\right] (1 + \tan 0) + \left(\frac{0.008}{2}\right)^3 + 3\left(\frac{0.008}{2}\right)^2 \\
&\quad \times 0.002 \\
f_{bottom-shoulder} &= \frac{56.62}{119.05} \\
&= (0.008)^3 / \left[\left(\frac{0.012}{2}\right)^3 - \left(\frac{0.008}{2}\right)^3\right] (1 + 0) + \left(\frac{0.008}{2}\right)^3 + 3\left(\frac{0.008}{2}\right)^2 \times 0.002 \\
f_{bottom-shoulder} &= 0.47
\end{aligned}$$

Percentage of heat with regard the percentage of heat generated by bottom shoulder with regard to total heat generated = 47 % and for the rest are show in table, percentage of probe side with respect to total is=4.8 % and shoulder =47 %

6.1. Heat Generation: Bobbin Tool

6.1.1. Heat Generation from the Top Shoulder

With the use of equation (5.1) it is explainable the heat generation of a bobbin tool top shoulder. The heat generation (Q_{ts1}) is determine by the angular rotational speed (ω), the shoulders cone angle (α), the contact shear stress of the material [Al2024-T3] ($\tau_{contact}$) and both the shoulder radius (D) and probe radius (d).

During this specific study equation (5.1) is recorded by increasing rotational speeds to determine the outcome of the heat generation from the top shoulder of the bobbin tool. where the Initial weld with four different rotational speeds is performed as follows: The speed of 800 rpm resulted to 56.62 kW, 1250 rpm generated 88.52 kW, 1600 rpm went up to 113.31 kW and lastly the increased speed 2000 rpm generated 141.64 kW.

Rotational speed per minute vs. heat generation from top shoulder shows accurate analysed details of the increased heat generation of the bobbin tools top shoulder with an increased rotational speed, with N indicating the rotational speed, the Y axis representing ROTATIONAL SPEED and X axis representing THE HEAT GENERATION OF THE TOP SHOULDER, Q (kW). (Graph. 6.1)

6.1.2. Heat Generation from the Probe Side Surface

The heat generation from the probe side surface (Q_{ps}) of the bobbin tool which is formulated by the angular rotational speed (ω), the contact shear stress of the material [Al2024-T3] ($\tau_{contact}$), the probe radius (d) and the tool probe height (h) (Equation 5.2)

The evaluation of the heat generation from the probe side surface formulated to the following values: 800 rpm generated 5.81 kW. 1250 rpm increased to 9.08 kW. 1600 rpm went up to 11.63 kW and 2000 rpm had a generation of 14.53 kW.

Rotational speed per minute vs. heat generation from the probe side surface represent the precise increased speed of the tool and shows accurate analysed details of all increased heat generated exerted from the bobbin tools probe side surface. As shown on the graph the Y axis represents ROTATIONAL SPEED while the X represents THE HEAT GENERATION PROBE SIDE, Qps (kW) and N acts as an indicator for the exact TOOL ANGULAR ROTATIONAL SPEED (Graph. 6.2)

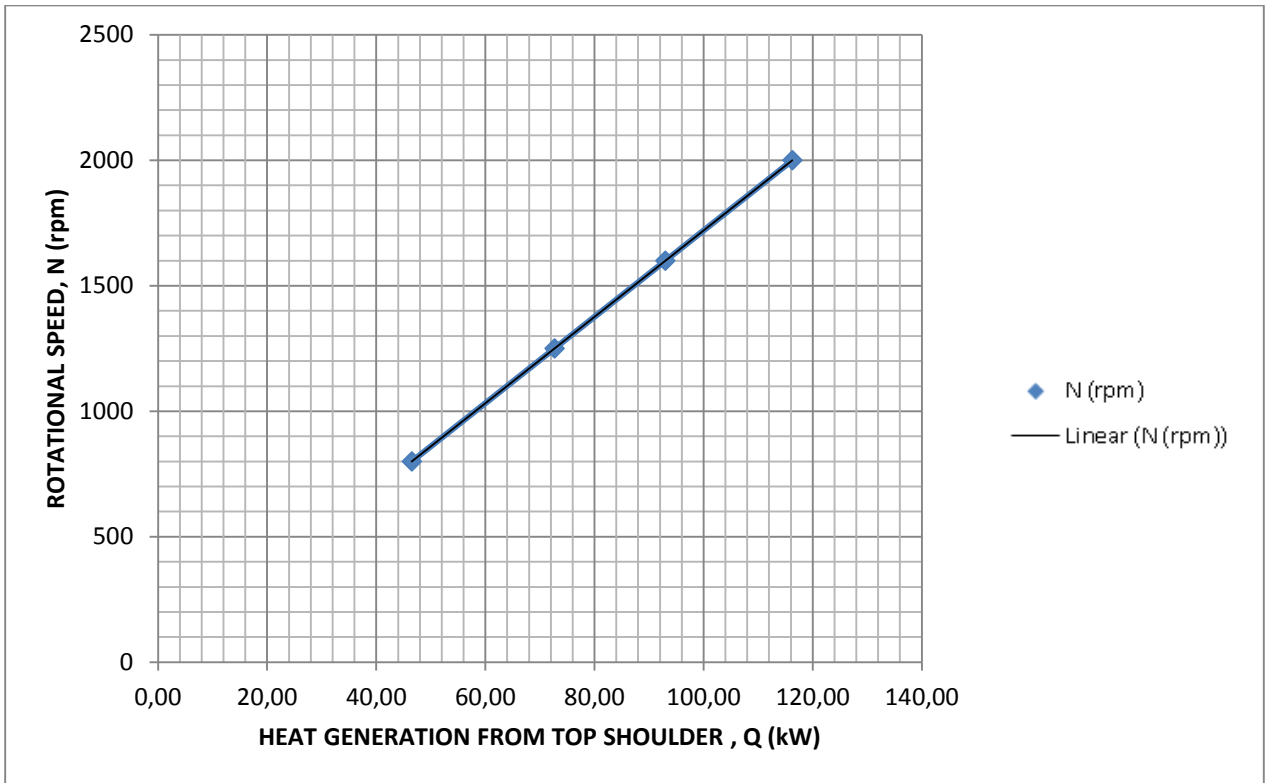
6.1.3. Heat Generation from the Bottom Shoulder

Equation (5.1) is also used to formulate the heat generation of the bottom shoulder. Hence explanation is similar: The heat generation (Q_{bs1}) is determining by the angular rotational speed (ω), the shoulders cone angle (α), the contact shear stress of the material [Al2024-T3] ($\tau_{contact}$) and both the shoulder radius (D) and probe radius (d). Equation (5.1) is used in this study to determine the heat generation from the bottom shoulder with four different rotational speeds(Graph 6.3). This process formulated as follows: 800 rpm went up to 56.62 kW. 1250 rpm generated 88.52 kW. 1600 rpm resulted 113.31 kW. And lastly 2000 rpm exerted a heat generation of 141.64 kW. Rotational speed per minute vs. heat generation from bottom shoulder is a representation of the total analysed speed increased to the increased heat generation on the supporting axis: Y: ROTATIONAL SPEED (rpm) X: HEAT GENERATION FROM THE BOTTOM SHOULDER and N as an indication for TOOL ANGULAR ROTATIONAL SPEED (rpm).

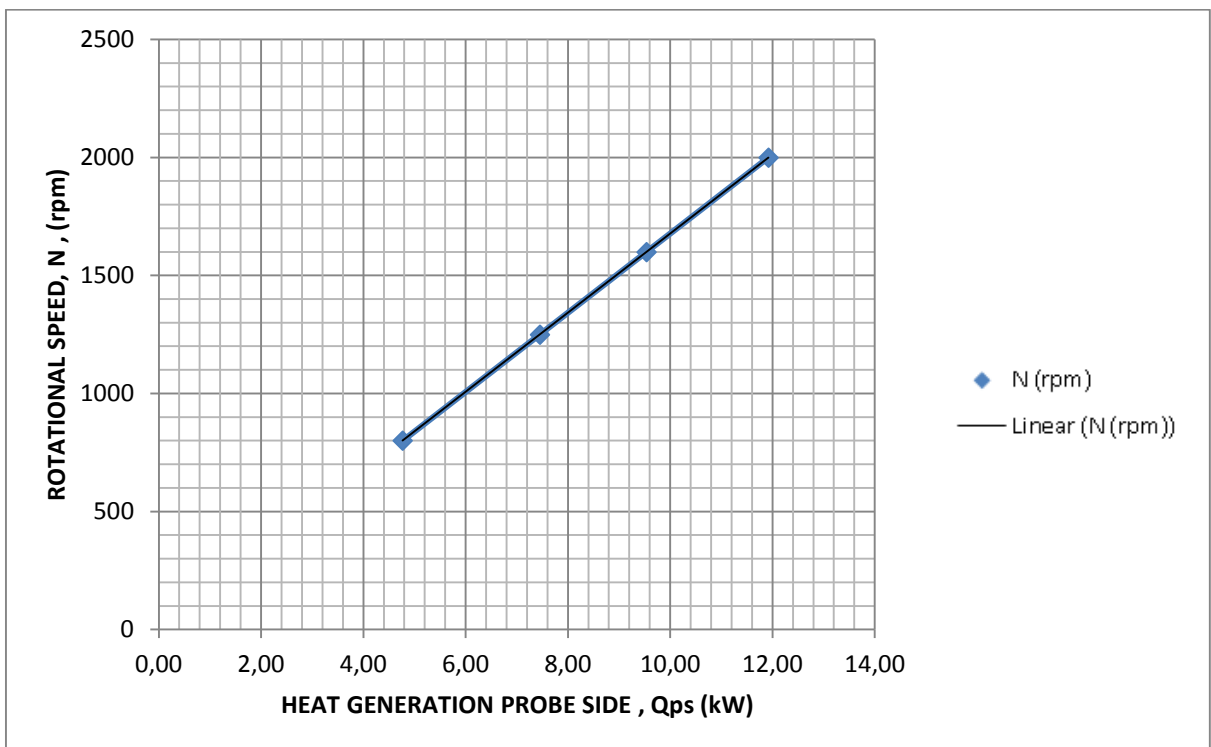
6.1.4. Total Heat Generated

The following equations(Q_1, Q_2, Q_3) is used to formulate the total heat generation from a bobbin tool (the top shoulder, the probe side surface and the bottom shoulder), as is indicated in the equation where Q is the heat generation which is determined by the angular rotational speed (ω), the shoulders cone angle (α), the contact shear stress of the material [Al2024-T3] ($\tau_{contact}$), both the shoulder radius (D) and probe radius (d) and the tool probe height (h). The total values are as follows: 800 rpm generated 56.62. 1250 rpm went up to 88.52. 1600 rpm resulted to 113.31 kW and the increased speed of 2000 rpm generated 141.64. Graph 6.4. Rotational speeds per minute vs. total heat generation represent the total analysed speed against the heat generation on the supporting axis: Y: ROTATIONAL SPEED (rpm) and X: TOTAL HEAT GENERATION and N indicating the TOOL ANGULAR ROTATIONAL SPEED (rpm).

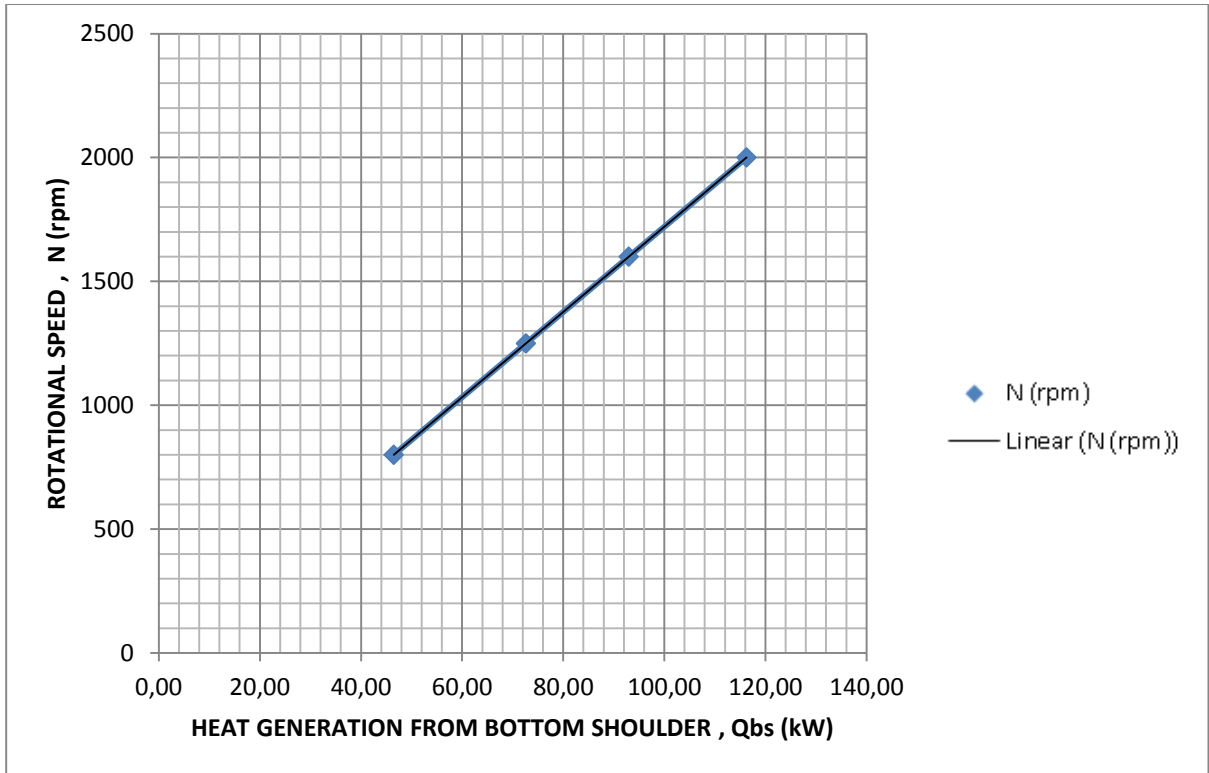
The variations of rotational speed for this specific tool are of the same nature as the standard tool. The same material has been used Al2024-T3. The heat generation varied according to the constant tools rpm; similar to the standard tool the faster the rotational speed the higher the heat generation is, as there is more time for localized work piece heating. For all speeds is a constant difference in heat generation between the top shoulder, the probe side surface and the bottom shoulder.



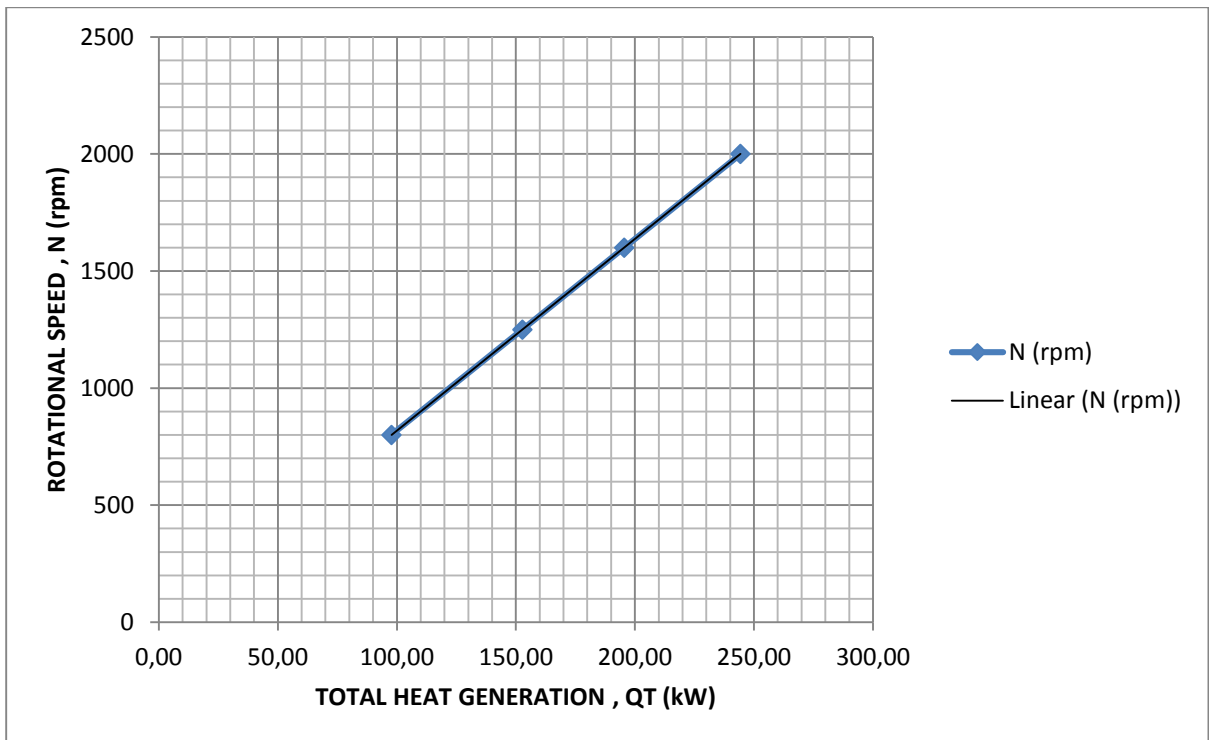
Graph.6.1: Rotational speed per minute vs. heat generation from top shoulder



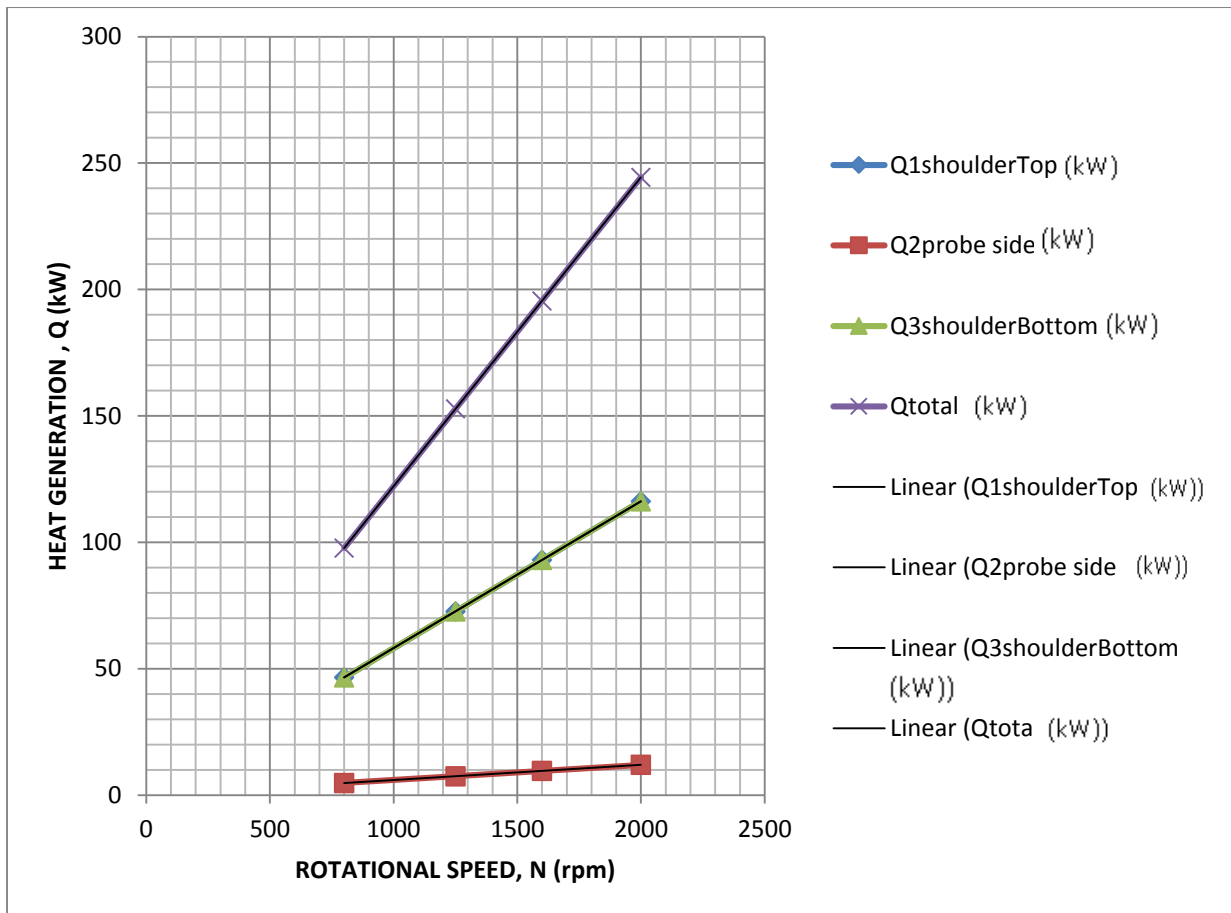
Graph.6.2: Rotational speed per minute vs. heat generation from the probe side surface



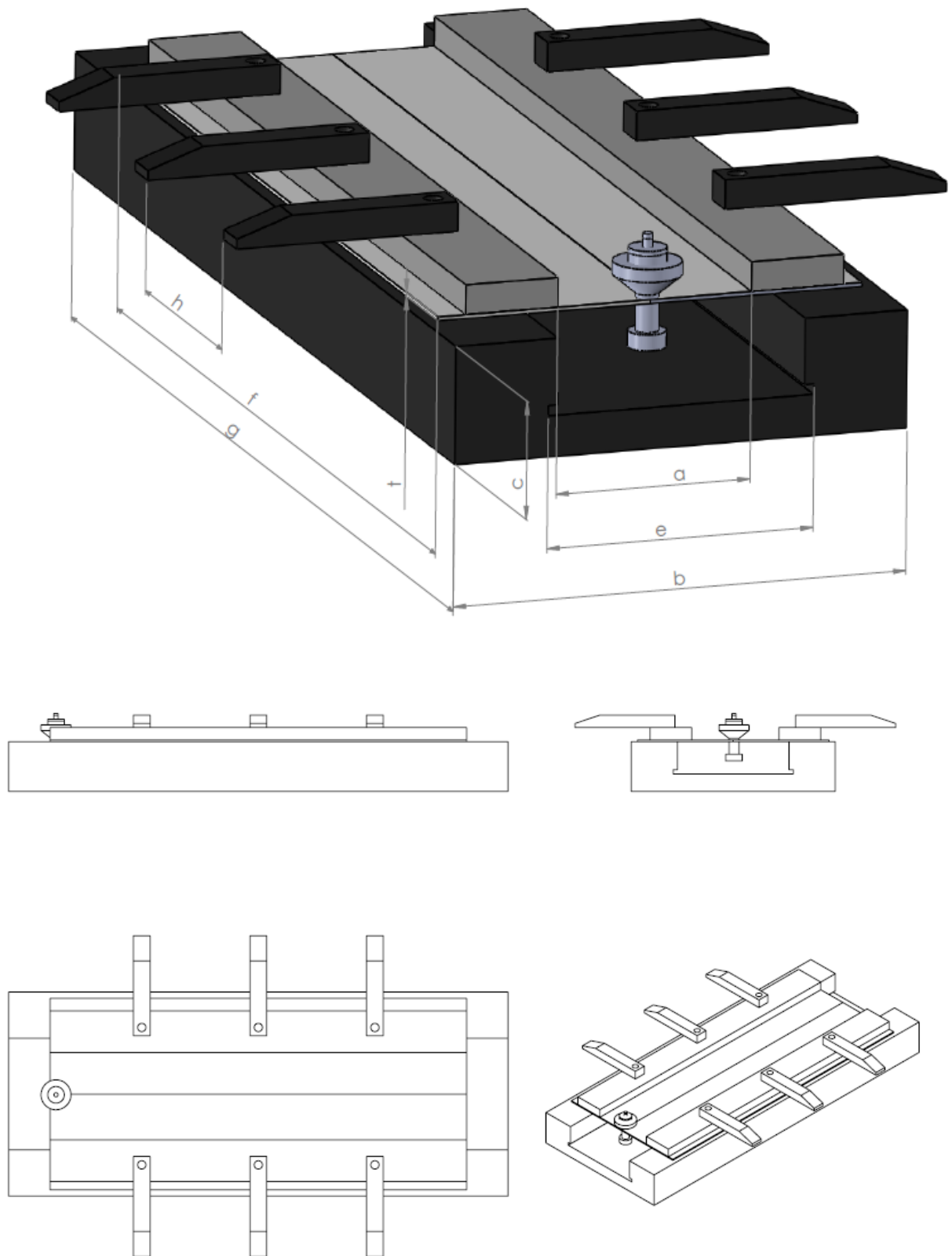
Graph. 6.3: Rotational speed per minute vs. heat generation from bottom shoulder



Graph. 6.4: Rotational speed per minute vs. total heat generation



Graph.6.5: Q1, Q2, Q3, QTOTAL vs. Rotational speed



Drw. 6.1: Friction Stir Welding Workbench design & 3D views-Bobbin Tool [Uslu, M.Y, 2013, FSW Work Bench Design, University of the Witwatersrand]

Aluminium plate length, f (As seen on drw.6)

Aluminium plate width, d (As seen on drw.6)

Aluminium plate thickness, t (As seen on drw.6)

Workbench clamps distance, h (As seen on drw.6)

Workbench length, g (As seen on drw.6)

Workbench width, b (As seen on drw.6)

Workbench thickness, c (As seen on drw.6)

Workbench backing plate width, e (As seen on drw.6)

6.2. Mode Frontier Simulation: Bobbin Tool Design

Input Data, Output Data and boundary variables definitions as shown on this Microsoft Excel Sheet file name: *bobbin tool .xlsm* is used in Mode Frontier for this Design Project (Image 6.2) In (image 6.3) it is shown all the input data output data and boundary variables in a Microsoft Excel workbook. The excel work books is used so that the equation for the rotational speed along with the heat generation is calculated where the results will be used in ModeFrontier to assist in the design. The Workflow Plan created by Mode Frontier Project as shown in *BOBBINTOOL.prj*, also includes DOE (Design of Experiments) and DOE Sequence, as well as indicating Input Variables, Output Variables, Design Objectives + Gradients, Microsoft Excel Workbook and Logic End (Image 6.4). A workflow plan is created using a DoE (Design of Experiments) and a DOE Sequence on a new Overlook. Once this is open workflow nodes can be added on. Variable nodes which are the input nodes and the output nodes are used. Workflow nodes such as the schedulers, the logic switch and logic end is used. An application node is used for excel. And a goal node which is the design objective+gradient node. Excel workbook properties are used for basic node configuration (Image 6.5) where an Excel Workbook is selected (Image 6.3). Once selected the input and out data is connected from the chosen Excel workbook. An Interactive Selection used between Mode Frontier *BOBBINTOOL.prj* and Microsoft Excel Workbook: *bobbin tool .xlsm* to determine Excel Workbook Properties for Mode Frontier. An interactive selection allows each input and output node to be configured in accordance to the Excel workbook. Where each variable is interactively selected to complete the work plan.

bobbin tool.xlsm - Microsoft Excel

File Home Insert Page Layout Formulas Data Review View PDF

Cut Copy Paste Format Painter Clipboard

Calibri 11 A A

B I U

Wrap Text Merge & Center

General

Conditional Formatting Format Cell Insert Delete

O26 fx

BOBBIN TOOL

INPUT DATA				
Geometrical parameters				
Rotational Speed	800	1250	1600	2000
R _{shoulder}	10	10	10	10
R _{probe}	4.00	4.00	4.00	4.00
α	0.00	0.00	0.00	0.00
H _{probe}	2.00	2.00	2.00	2.00
t, Al. plate thickness	2	2	2	2
Contact shear stress	340	340	340	340
Yield Strength	283	283	283	283

OUTPUT DATA	800 rpm	1250 rpm	1600 rpm	2000 rpm
Q1 top-shoulder (KW)	46.48	72.62	92.95	116.19
Q2 probe side (KW)	4.77	7.45	9.53	11.92
Q3 bottom shoulder (KW)	46.48	72.62	92.95	116.19
QT BOBBIN (KW)	97.72	152.69	195.44	244.30

$$Q_1 = \frac{2}{3}\pi\tau_{contact}\omega(R_{shoulder}^3 - R_{probe}^3)(1 + \tan\alpha)$$

$$Q_2 = 2\pi\tau_{contact}\omega R_{probe}^2 H_{probe}$$

$$Q_3 = \frac{2}{3}\pi\tau_{contact}\omega(R_{shoulder}^3 - R_{probe}^3)(1 + \tan\alpha)$$

Image 6.2: Input Data, Output Data and boundary variables definitions as shown on this Microsoft Excel Sheet file name: *bobbin tool .xlsm* is used in Mode Frontier for this Design Project

modeFRONTIER 4.3.1 b20110301 - Project: BOBBINTOOL.prj

File Edit Project Assessment View Tools Help

Workflow Run Logs Designs Space

Overlook

Main

Exit10
=0

Excel4

DOE Sequence

DOE

QTBABBIN QTBABBINObject

QSHOULDERTOP QSHOULDERTOPObject

QPROBE QPROBEObject

QSHOULDERBOTTOM QSHOULDERBOTTOMObject

YS
N
Rp
Rs
a
Hprobe
CS

Output Variable

	Name	
0	QSHOULDERTOP	0.0000E0
1	QPROBE	0.0000E0
2	QSHOULDERBOTTOM	0.0000E0

Logic Log Input Variable Output Variable Buffer Variables Vector Objective Transfer Variable Design Objective Design Constraint Vector Cons

Ready Grid status: not available Mode: EDIT

Image 6.3: Workflow Plan created on Mode Frontier Project as shown in *BOBBINTOOL.prj*, also includes DOE (Design of Experiments) and DOE Sequence, as well as indicating Input Variables, Output Variables , Design Objectives + Gradients, Microsoft Excel Workbook and Logic End

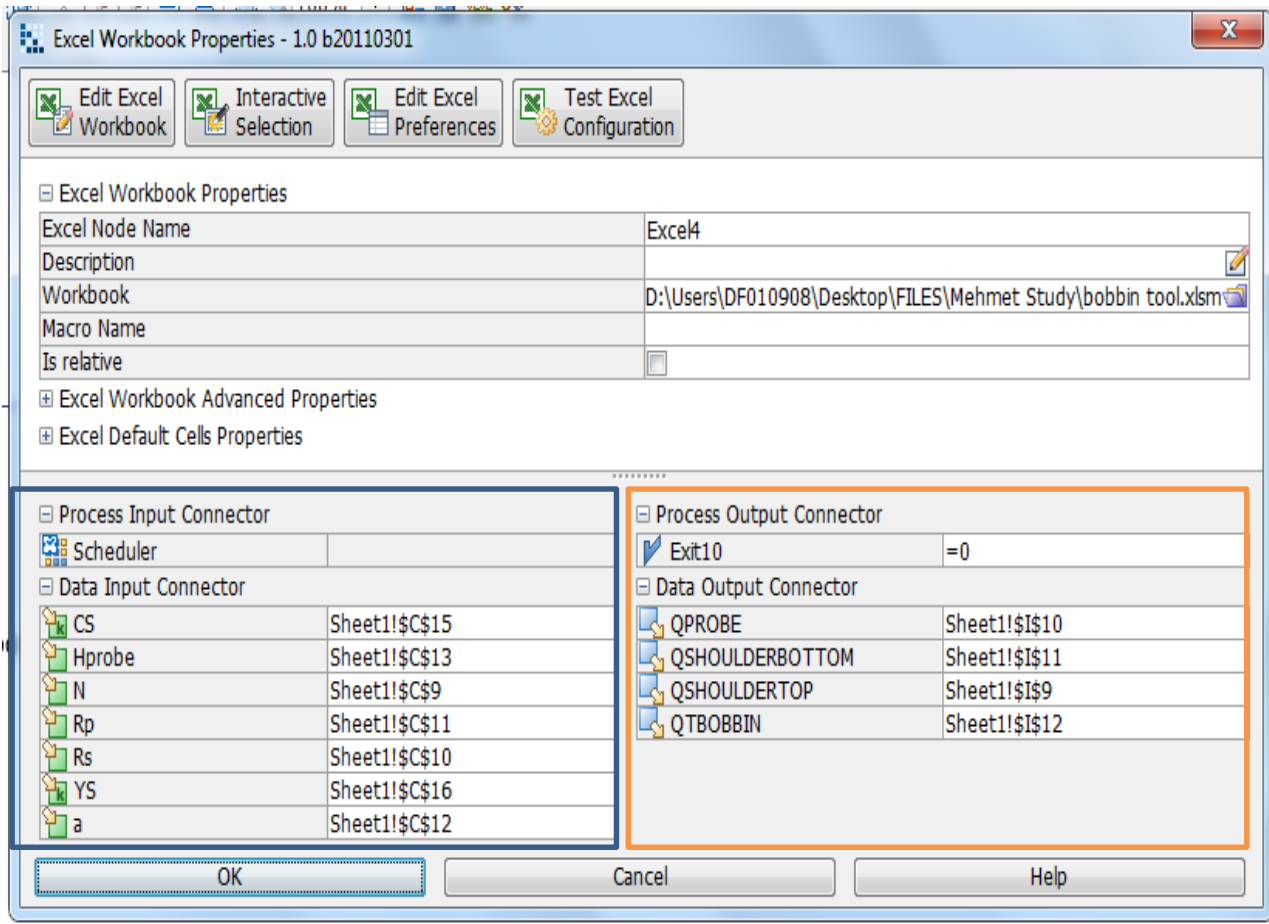


Image 6.4: Mode Frontier Input and Output Datas connected to Microsoft Excel Workbook as shown above

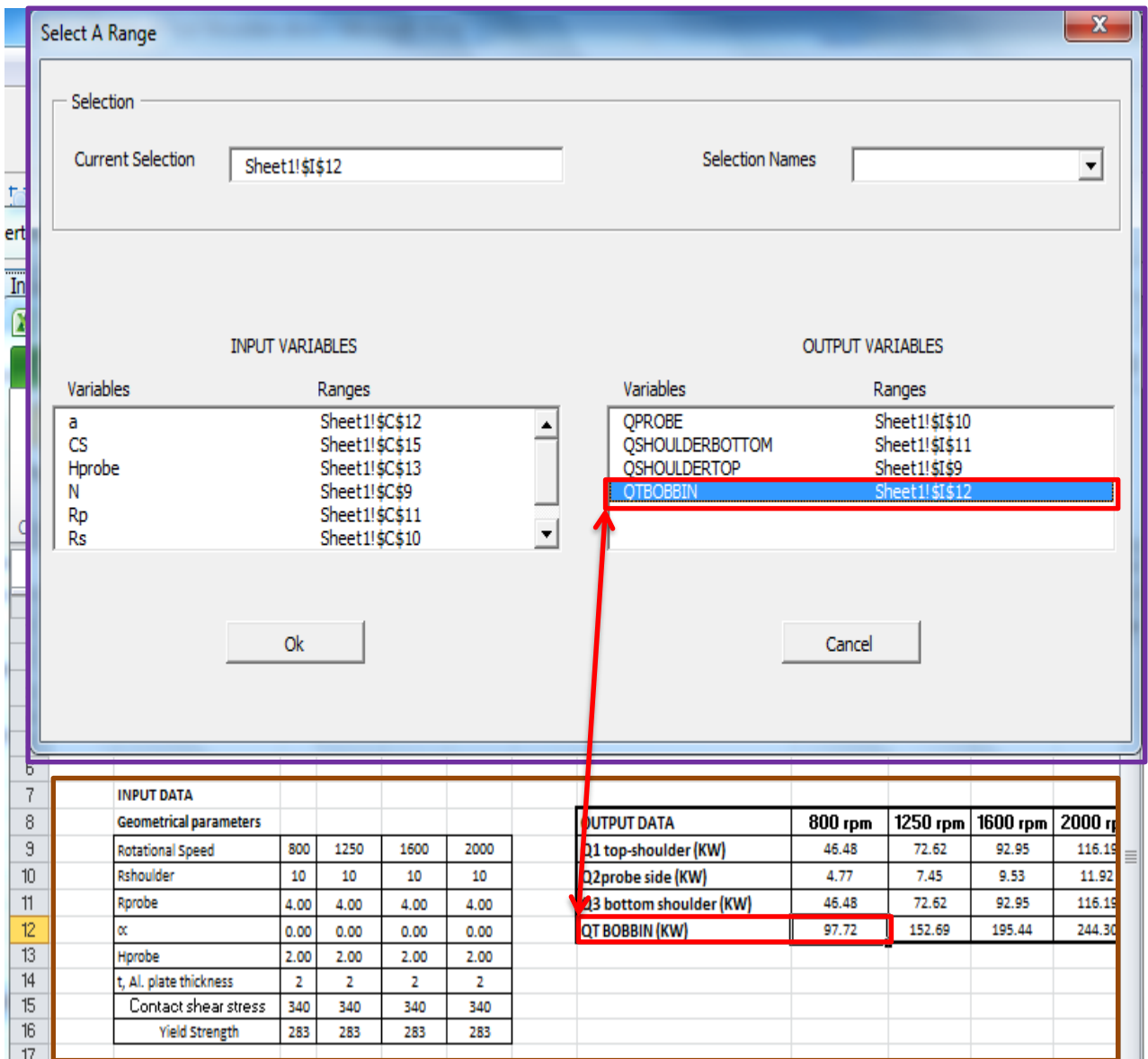


Image 6.5: Interactive Selection used between Mode Frontier *BOBBINTOOL.prj* and Microsoft Excel Workbook: *bobbin tool .xism* to determine Excel Workbook Properties for Mode Frontier

6.2.1. Boundaries: Bobbin Tool Design

The boundaries for the bobbin tool are in similar reference to the standard tool, the boundaries are as follows: yield stress, rotational speed, probe radius, shoulder radius, tool cone shoulder angle, probe height and the contact stress. (Images 6.6-6.12)

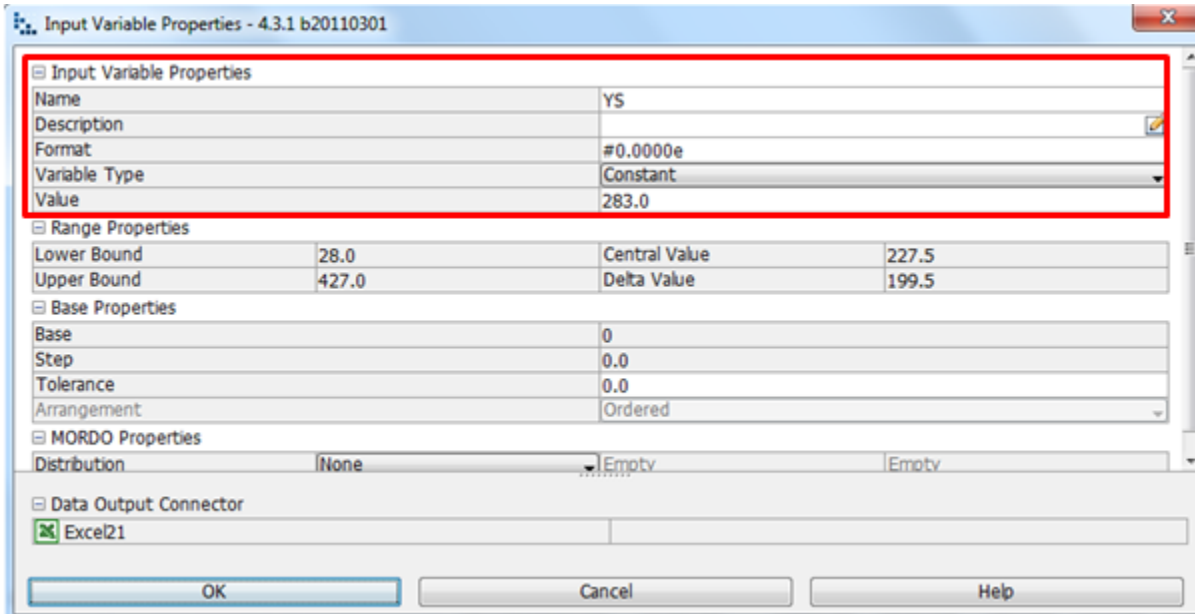


Image 6.6: Al2024-T3 material yield stress 283MPa is chosen, where the variable type constant hence the lower and upper bound is fixed

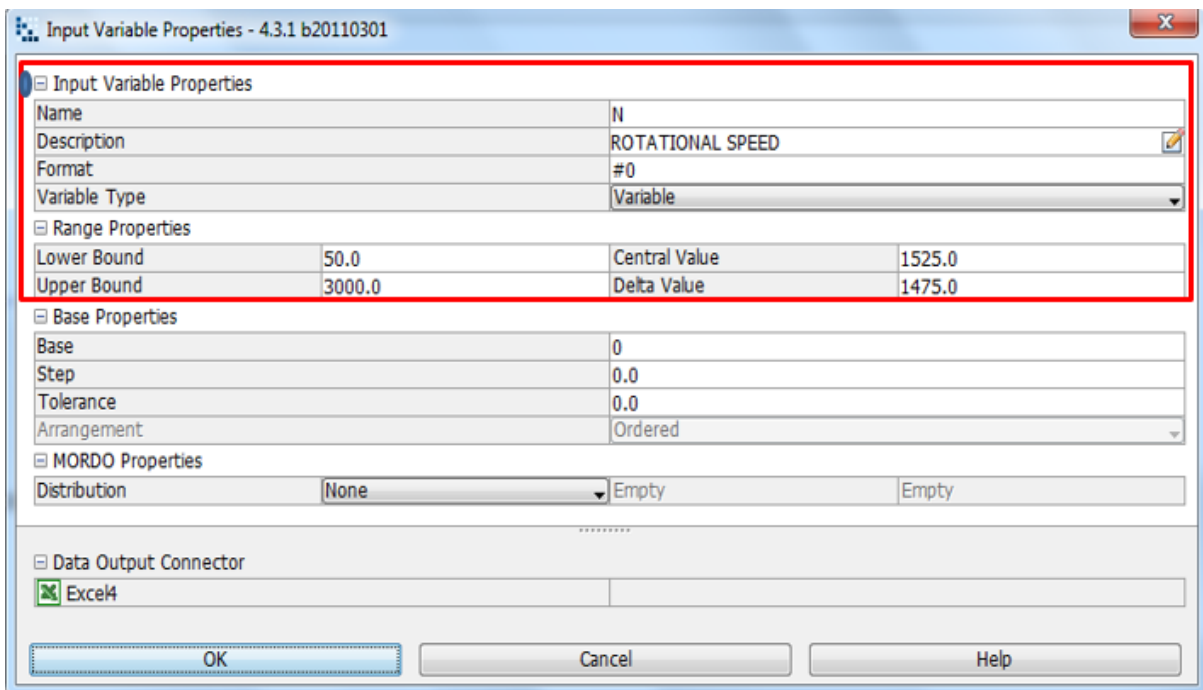


Image6.7: Rotational speed is determined by lower and upper bound range properties, as shown in the input variable node properties dialog.

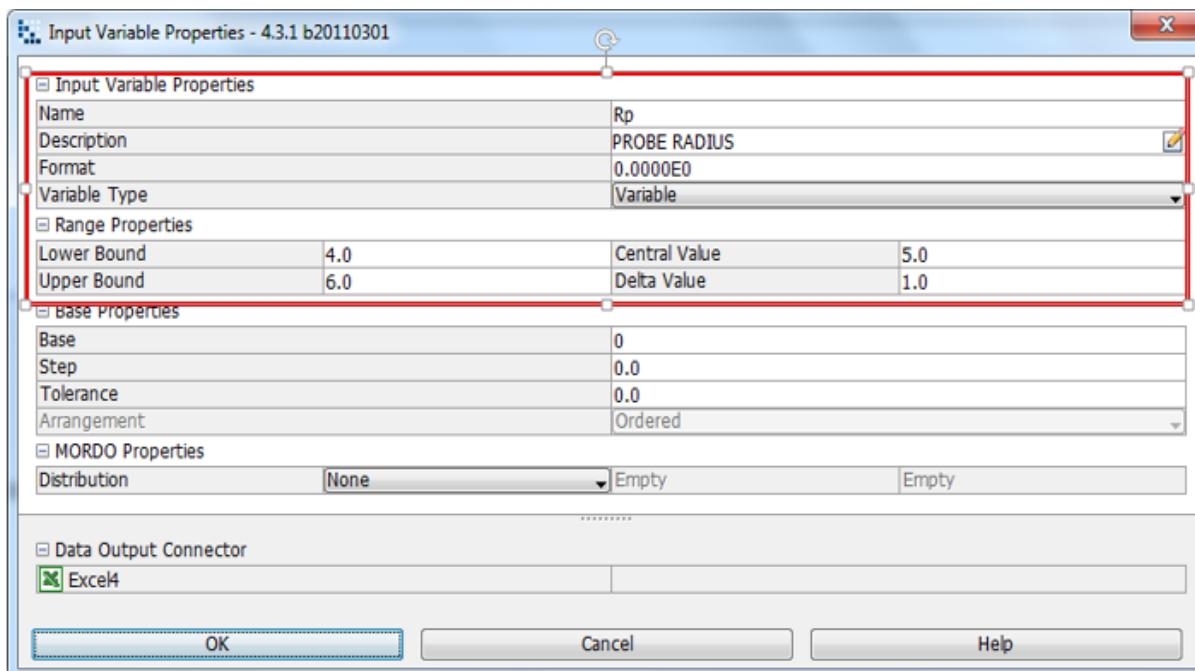


Image 6.8: Probe Radius is determined by lower and upper bound range properties, as shown in the input variable node properties dialog

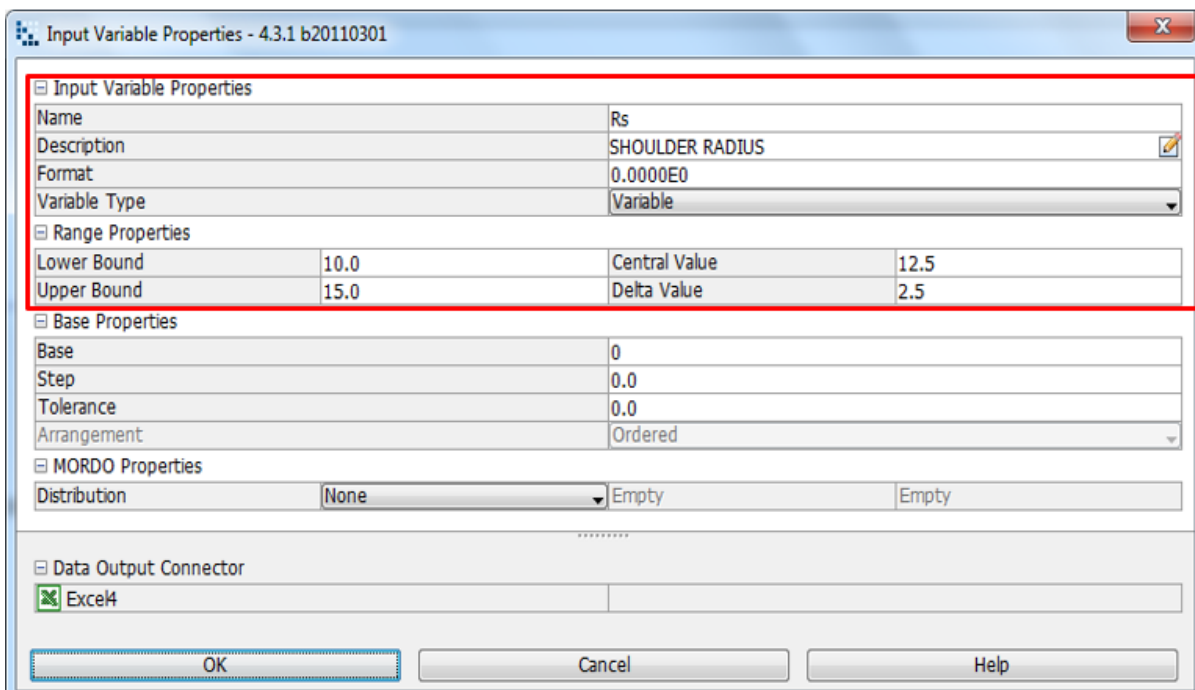


Image 6.9: Shoulder radius is determined by lower and upper bound range properties, as shown in the input variable node properties dialog

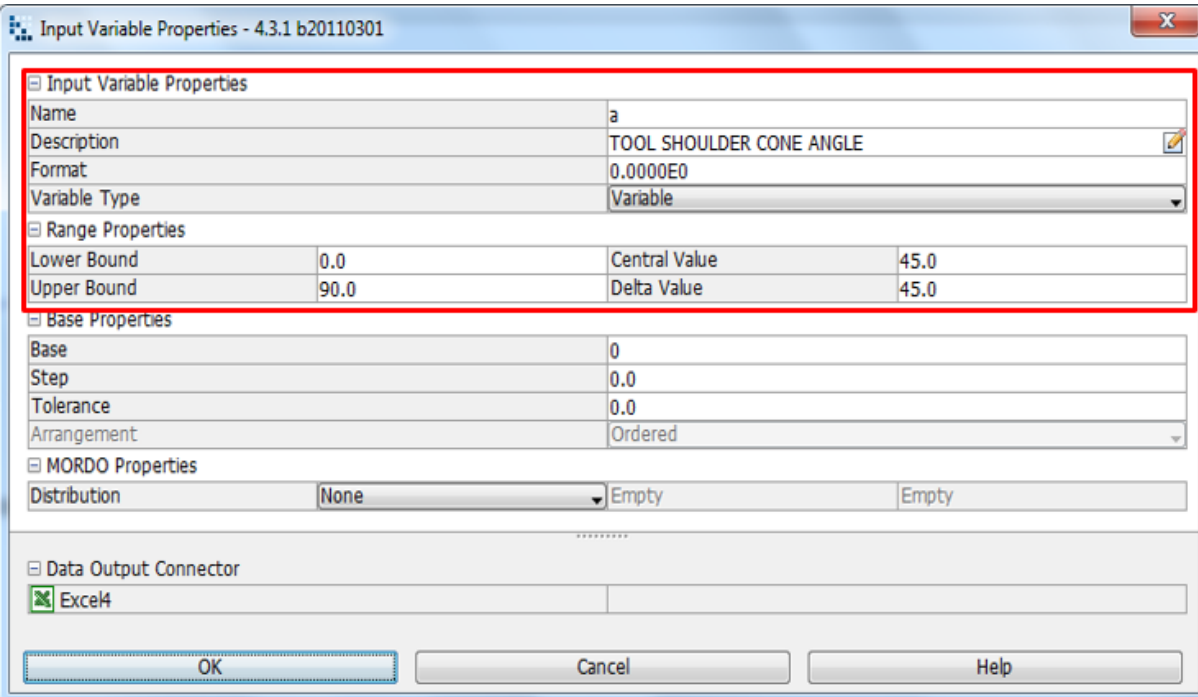


Image 6.10: Tool shoulder angle is determined by lower and upper bound range properties, as shown in the input variable node properties dialog

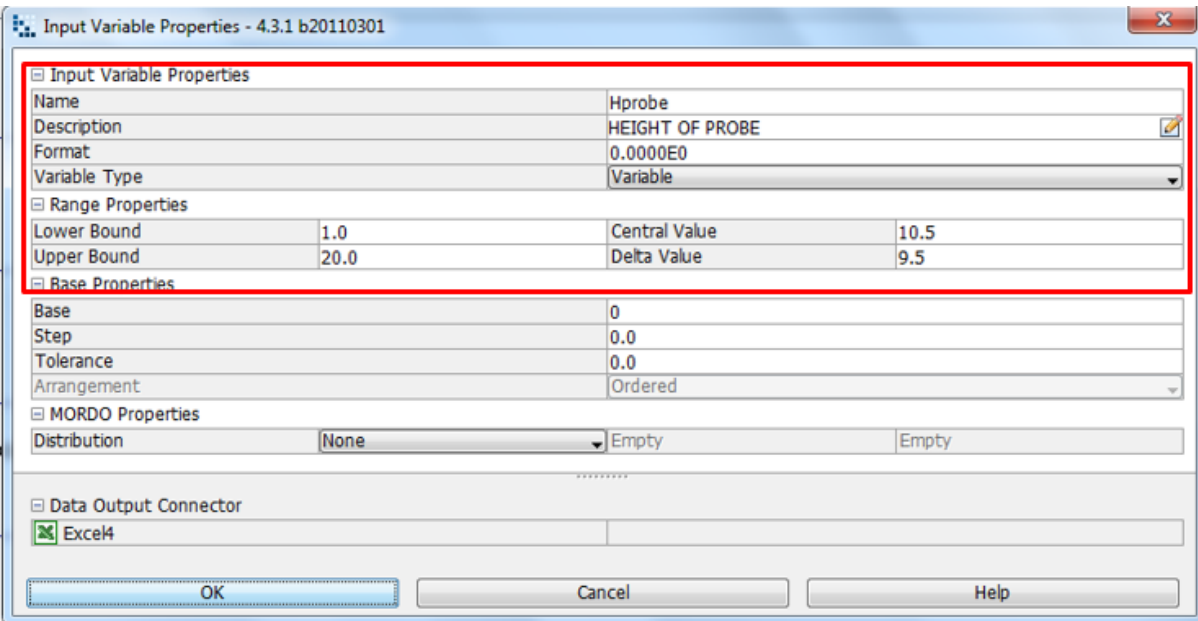


Image 6.11: Probe height is determined by lower and upper bound range properties, as shown in the input variable node properties dialog

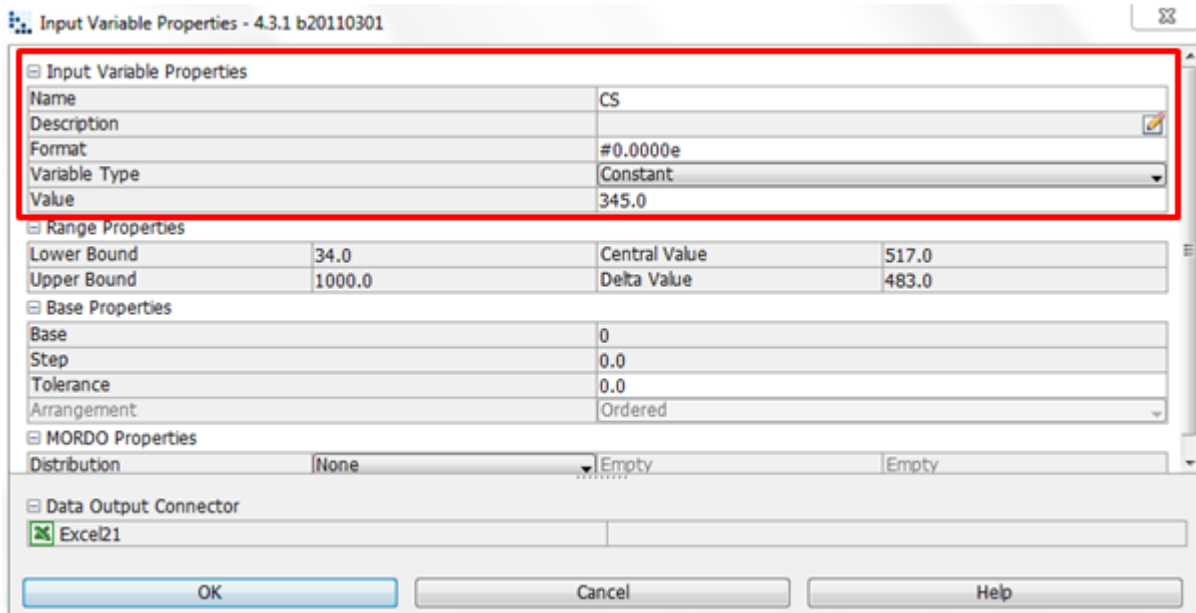


Image 6.12: Al2024-T3 material contact shear stress 345 MPa is chosen, where the variable type constant hence the lower and upper bound is fixed

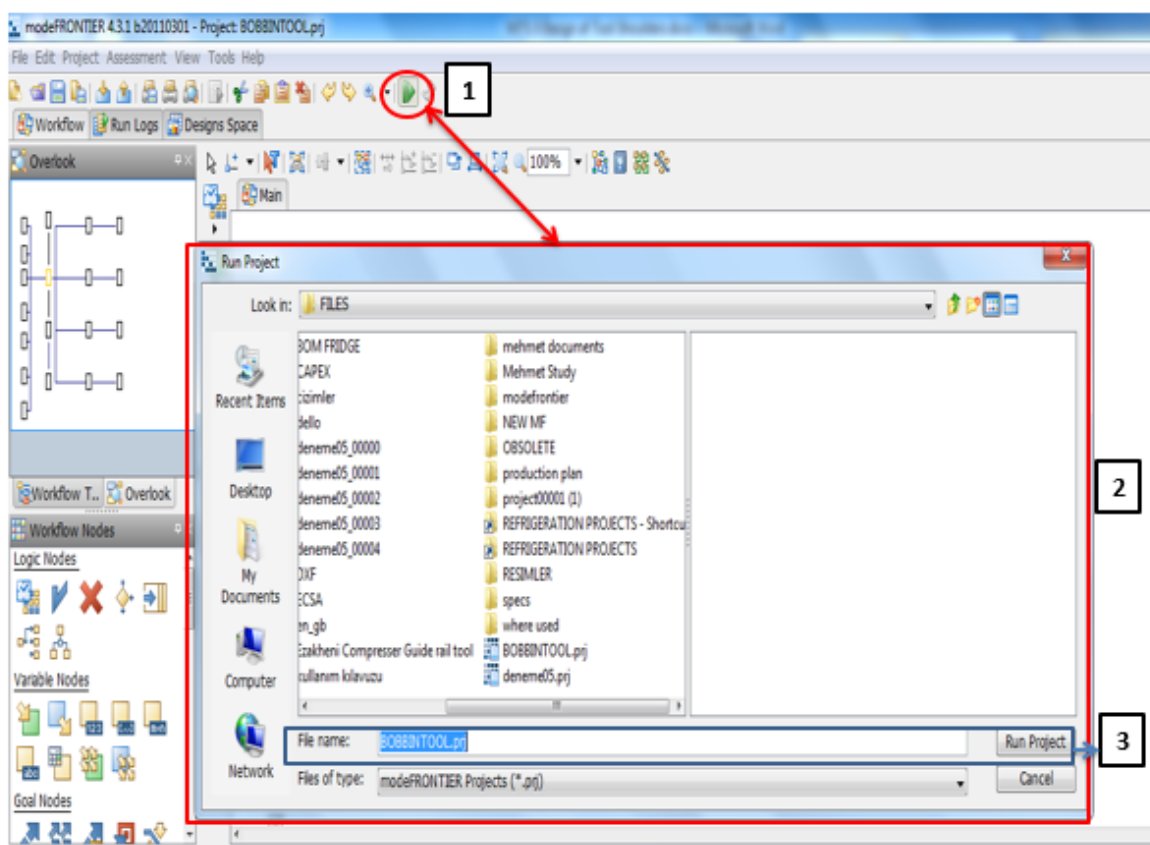


Image 6.13: Click on run/stop icon (1). Run project box will pop up (2). Click on run project (3) to start design project.

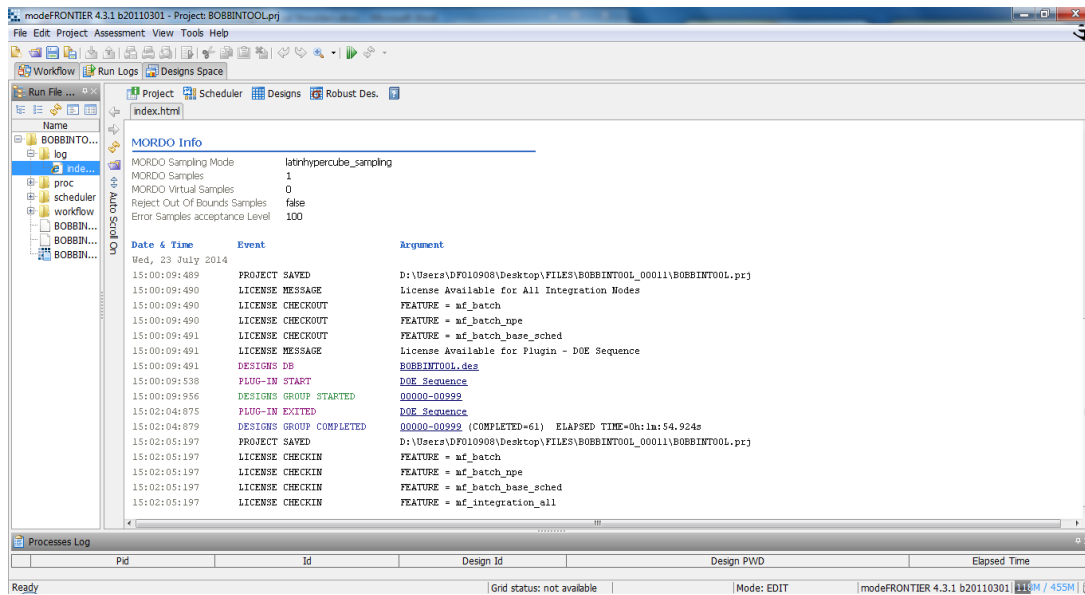


Image 6.14: Before project runs, a project info index will be shown. As seen in the above image.

6.2.2. History Charts and Parallel Co-ordinate Charts: Bobbin Tool Design

Multi-History Chart on Designs Space as created from QTOPshoulder vs. Shoulder radius, R_s shows that when the rotational speed increases the heat generation of the top shoulder increases as well (Image 6.15). The graph also demonstrates that the design is feasible on a virtual scale (Chart 6.1). Multi-History Chart on Designs Space as created from Q Probe, side vs. Tool shoulder cone angle on Bobbin Tool shows the increase on the heat generation of the probe side surface on the effect of the rotational speed of the tool shoulder cone angle. The charts also indicates that the design is feasible on a virtual scale (Chart 6.3), Multi-History Chart on Designs Space as created from QBOTTOMshoulder vs. tool shoulder radius is a representation of the heat generation of the bottom shoulder as the effect of the rotational speed of the tool shoulder radius. (Chart 6.5). QBOTTOMshoulder vs. Tool rotational speed represents that when the rotational speed increases the heat generation of the top shoulder increases as well. The graph also demonstrates that the design is feasible on a virtual scale (Chart 6.6). A parallel co-ordinate chart is used for the purpose to display multivariate data. It proves useful for visualizing designs in a particular range. This type of chart allows the creation of a filter for the selection of the most interesting solution in the data base; the filter is created by dragging the filter arrows up and down. This way the variables lower and upper limits can be set. And if a variables value goes out the define range, its design will not be shown. Parallel Coordinates as created from Qshoulder vs. Shoulder radius, R_s indicates accurately the increased rotational speed of the top shoulder and the increased heat generation exerted. Showing that it is a feasible design both on a real and virtual scale (Chart 6.2). Parallel Coordinates as created from Qprobe side vs. Tool shoulder cone angle is an accurate analysis of the heat generation due to the increase in rotational speed, making the design feasible on a real and virtual scale (Chart 6.4).

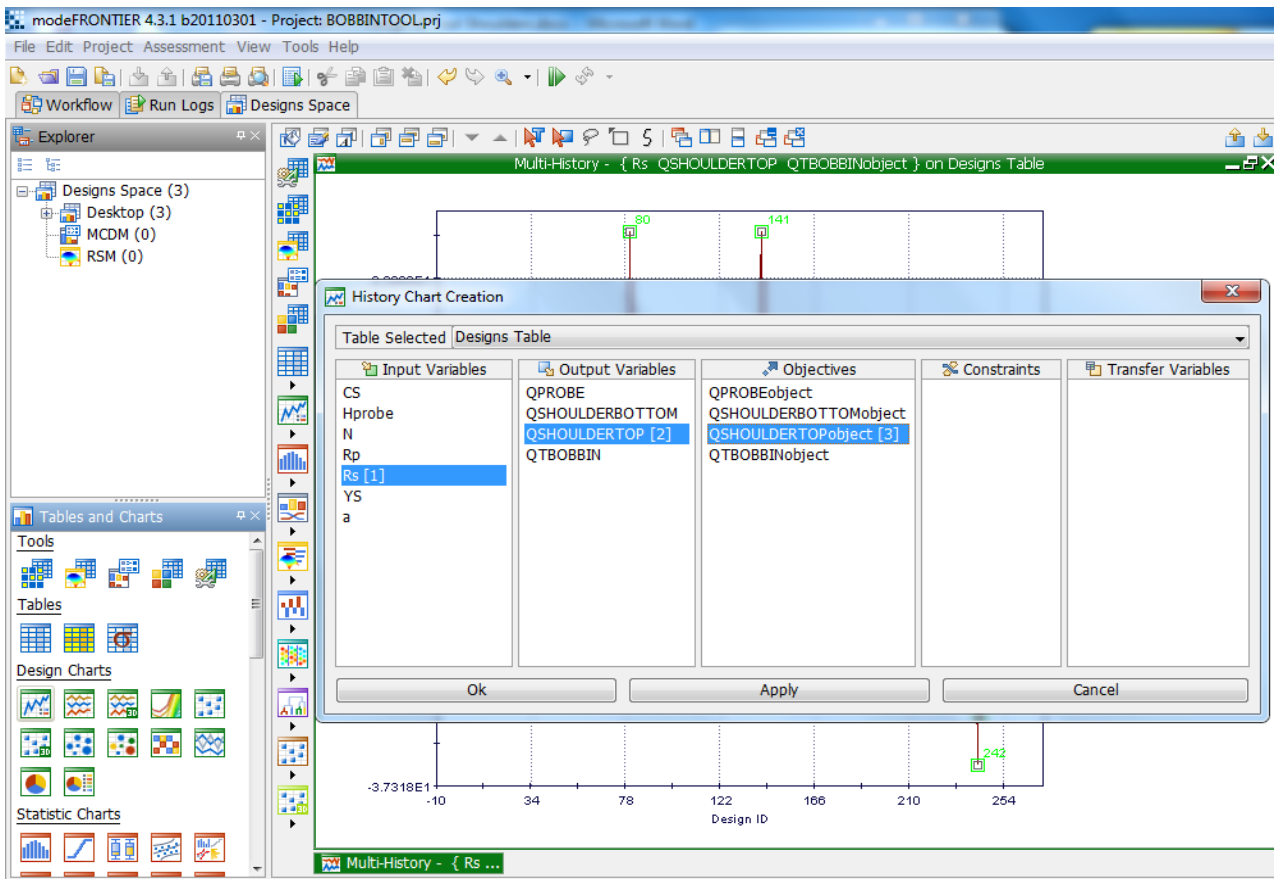


Image 6.15: History Chart created on Mode Frontier Designs Space as shown above for Probe Side Heat Generation and Rotational Speed

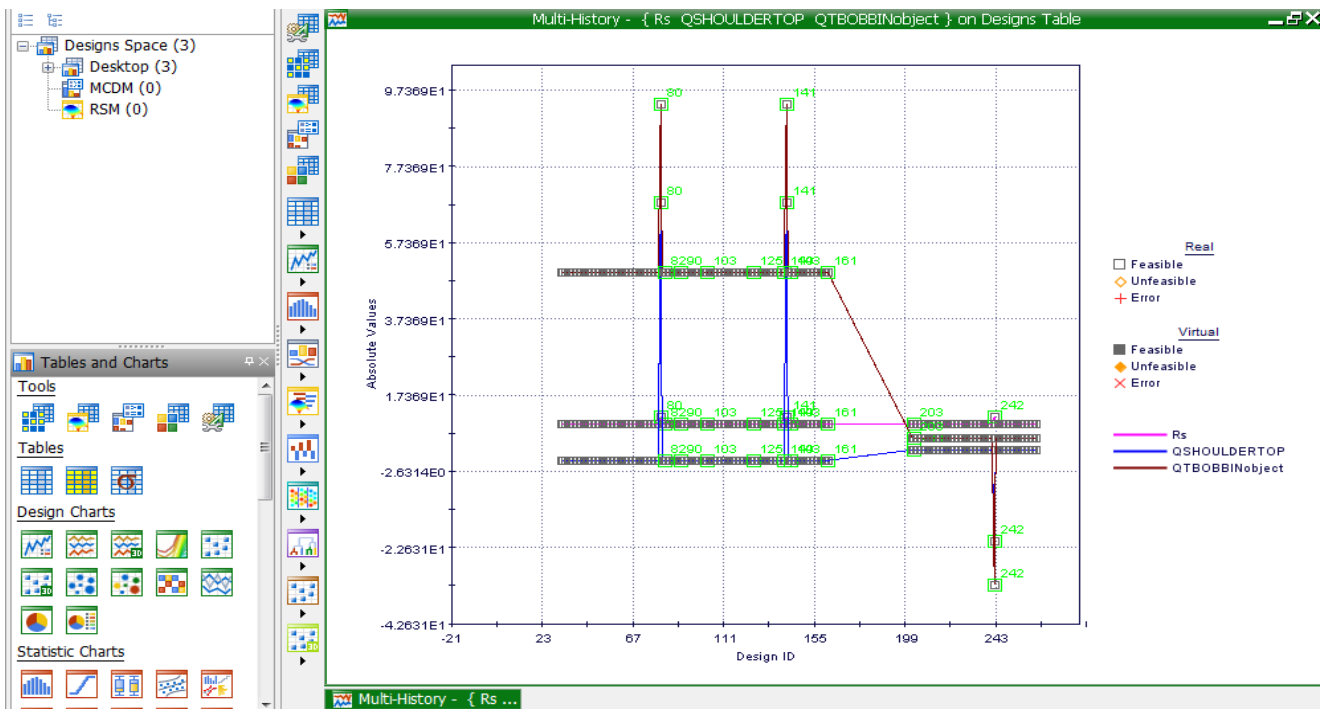


Chart 6.1: Multi-History Chart on Designs Space as created from QTOPshoulder vs. Shoulder radius, Rs

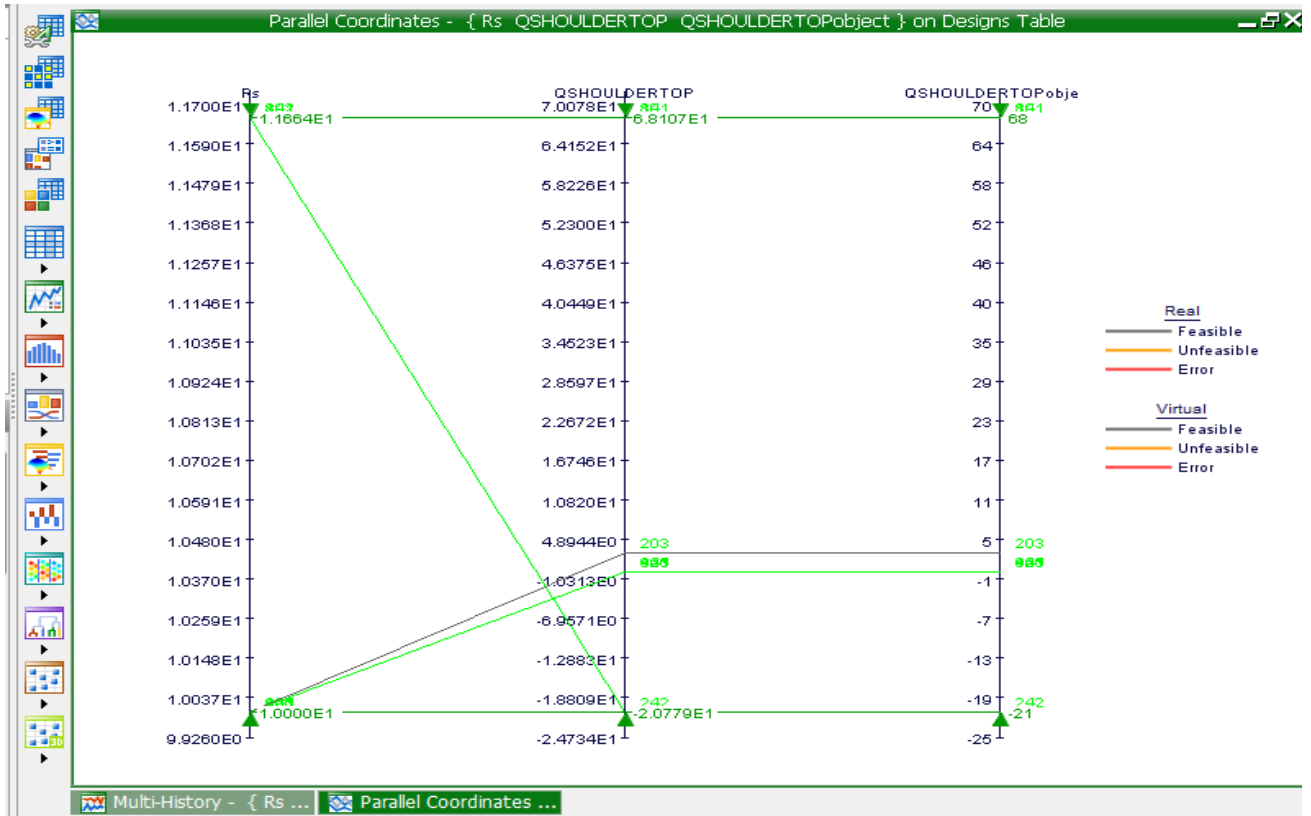


Chart 6.2 : Parallel Coordinates as created from Qshoulder vs. Shoulder radius, Rs

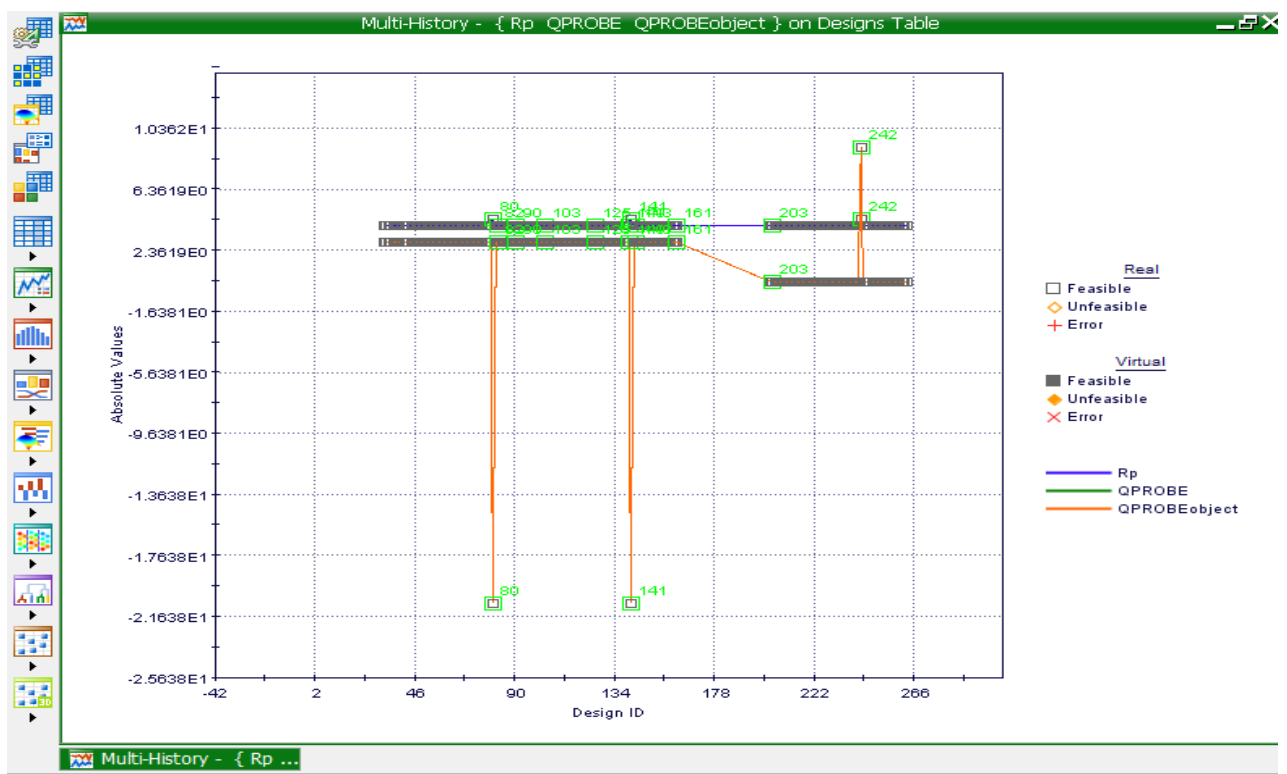


Chart 6.3 : Multi-History Chart on Designs Space as created from QProbe, side vs. Tool Probe radius on Bobbin Tool

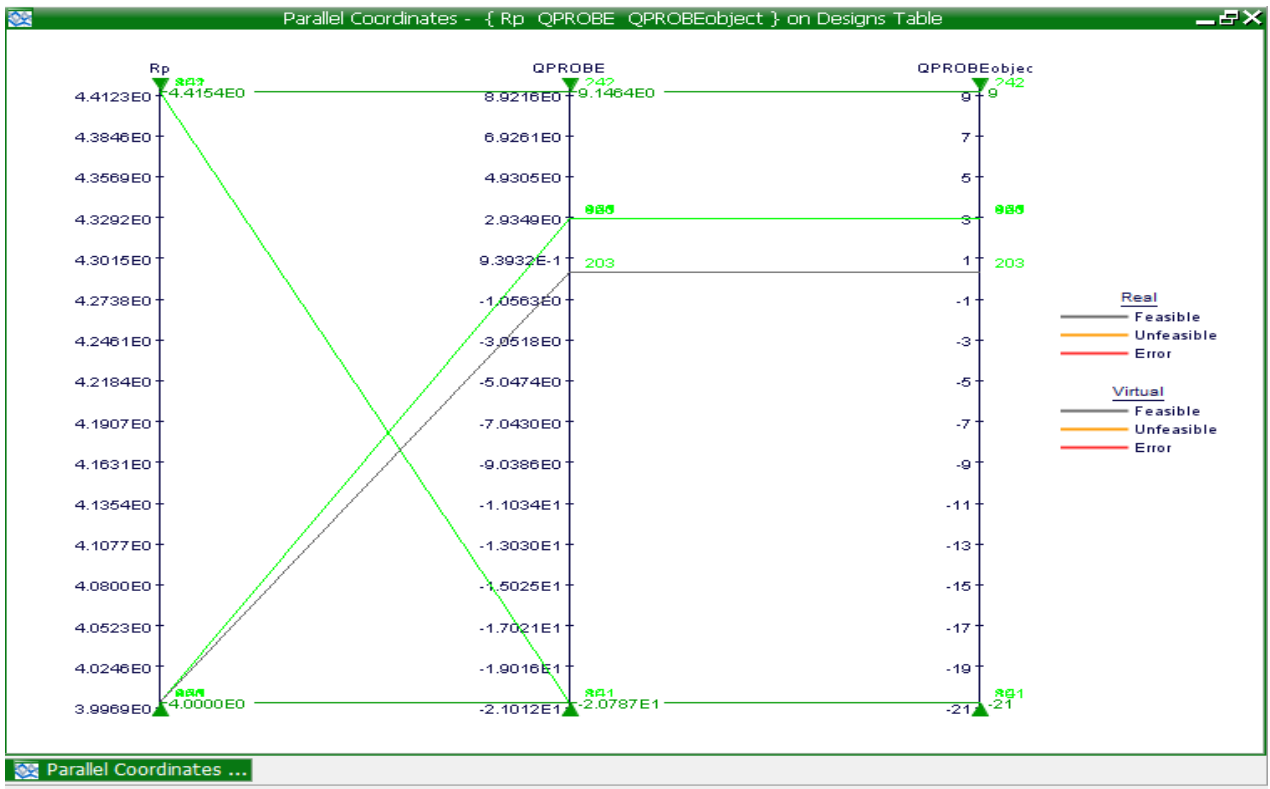


Chart 6.4: Parallel Coordinates as created from Qprobe side vs. Tool shoulder cone angle

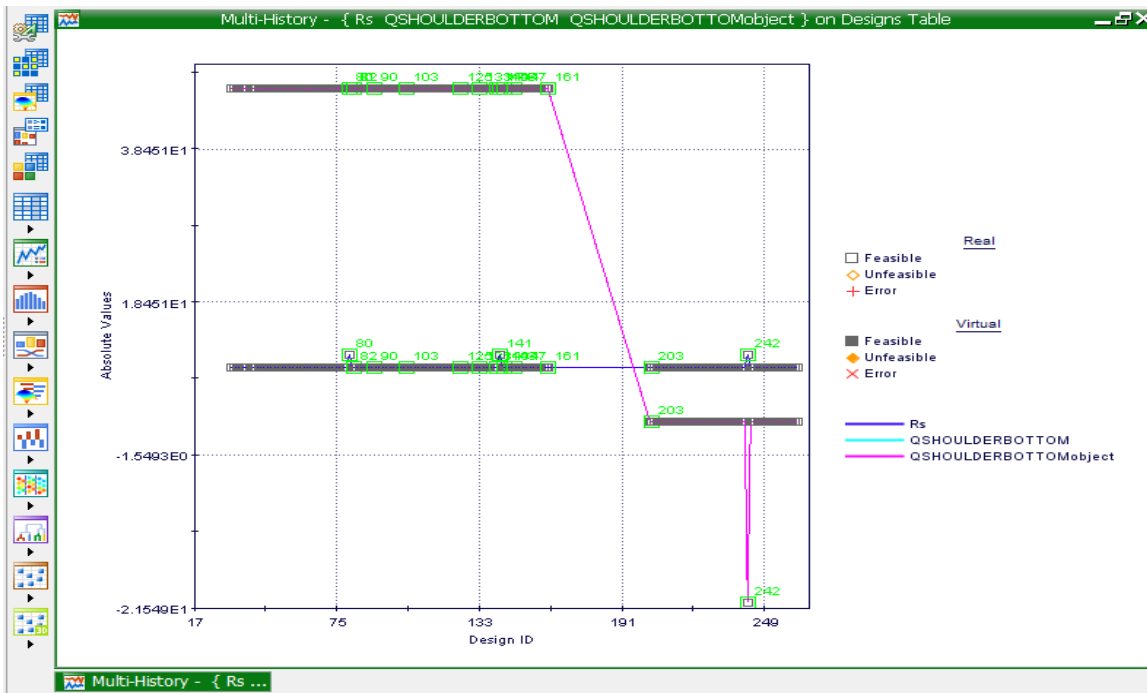


Chart 6.5: Multi-History Chart on Designs Space as created from QBOTTOMshoulder vs. tool shoulder radius

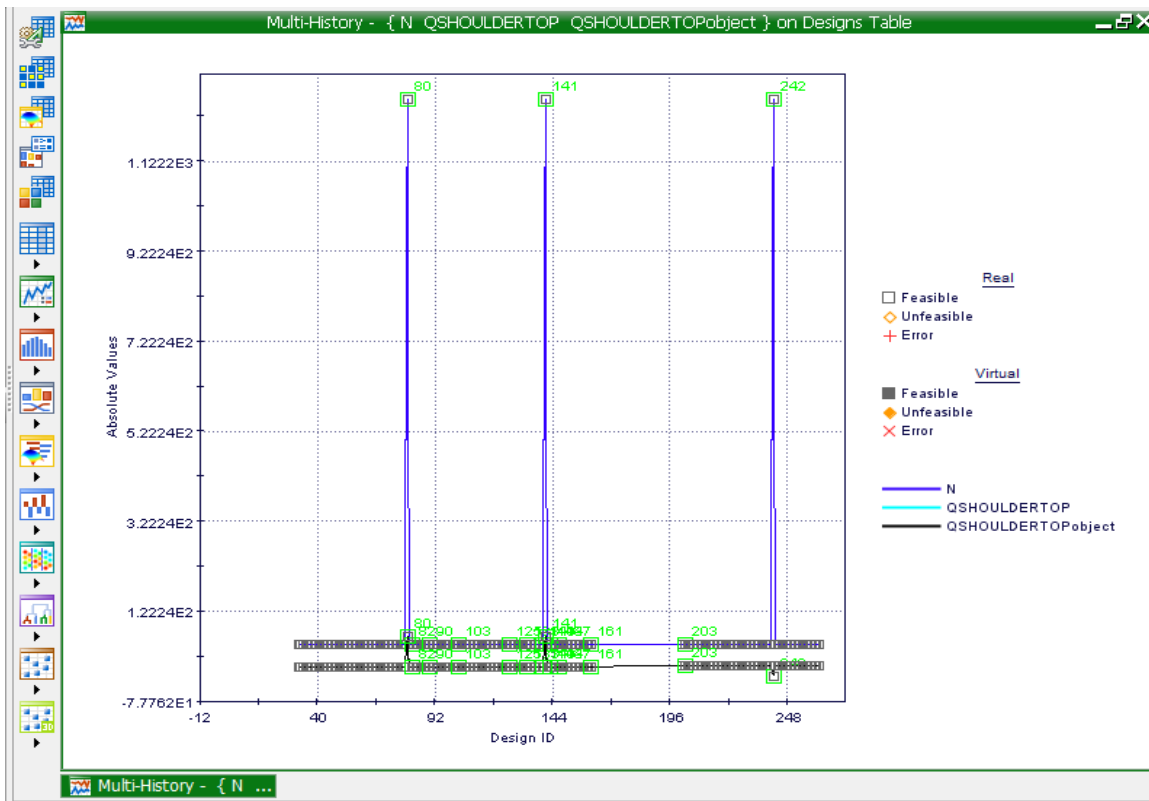


Chart 6.6: Multi-History Chart on Designs Space as created from QBOTTOMshoulder vs. Tool rotational speed

7. Innovative Friction Stir Welding: Design And Experimentation

Friction stir welding is performed on the material Al2024-T3 (Image 7.1). A sliding bar is used as a sliding backing bar. With ball transfer units with ball transfer units that would be of a similar dimension. It is also through that a sliding backing bar would aid in clamping support. The sliding backing bar is made out of copper (Image 7.2) for the purpose of conduction due to the fact that when a weld is performed there is an extra exertion of heat generation. Putting a copper bush into a sliding copper bar are similar in many ways but the use off a sliding copper bar allows us to change a copper bush after each weld. For the use of cost saving alternative, excluding the sliding copper bar is more cost effective as both sliding copper bar and copper bush share the same mechanical properties and thermal behaviour.

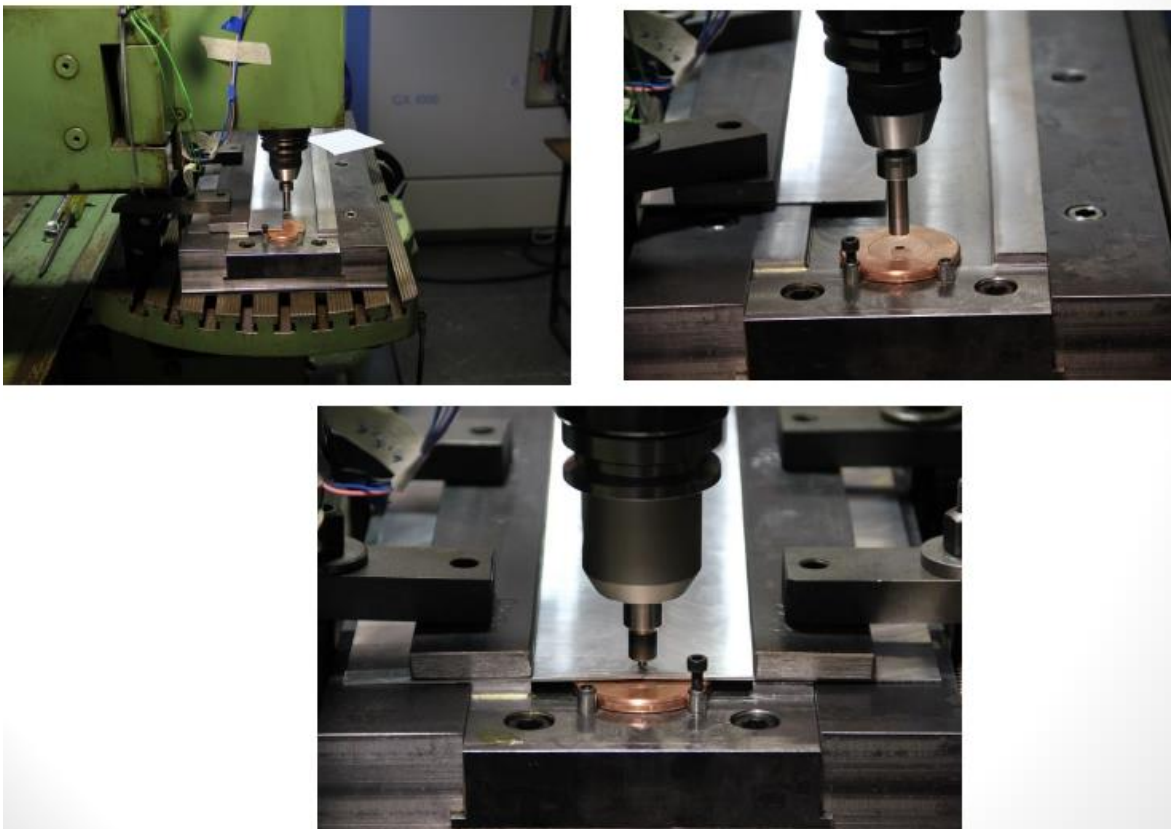


Image. 7.1: Optimization of innovative Friction Stir on material Al2024-T3 [82].

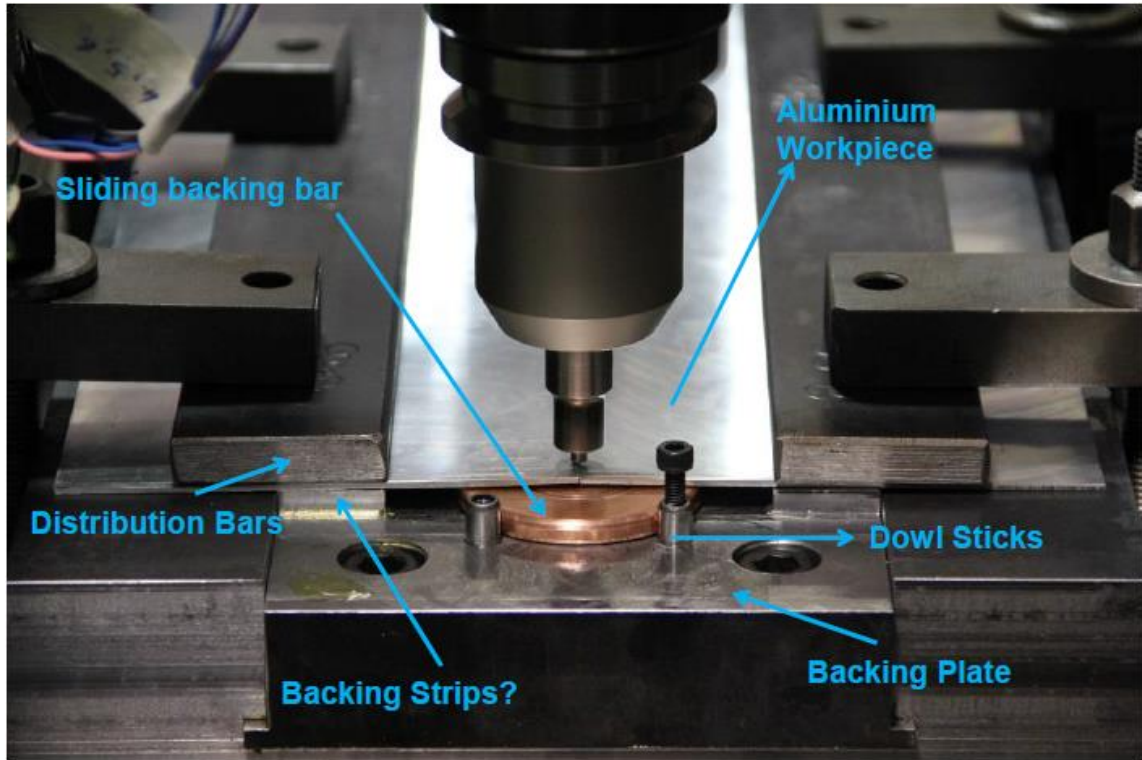


Image 7.2: Copper Sliding Backing bar serves as a conductor due to excessive heat during a Friction Stir Welding process [82].

Tool shoulder radius	10 mm	0.01 m	Drw 5.1
Tool probe height	4 mm	0.004 m	
Tool shoulder cone angle	α	0	
Friction Coefficient	μ	0.6	static condition
Friction Coefficient	μ	0.4	sliding condition
Yield stress	σ_{yield}	283 MPa	
Contact shear stress	τ_{cont}	345 MPa	
Copper Yield stress	σ_{yield}	117 MPa	

Table7.1: Analytical Estimation of Heat Generation for the Innovative Tool.

Tool Angular Speed		Rotational Speed
ω	(rad/s)	N (rpm)
ω_1	83.80 rad/s	800 rpm
ω_2	130.89 rad/s	1250 rpm
ω_3	167.55 rad/s	1600 rpm
ω_4	209.44 rad/s	2000 rpm

Table7.2: Tool Angular Speed and Rotational Speed for the Innovative Tool.

On substituting known values of the parameters, tool dimension, and all other values in derived equations, the heat generation values are as follows:

i) Heat Generation from the Shoulder: from equation 1.1 the values are-

a) For tool angular rotational speed $\omega_1 = 83.80 \text{ rad/s} = 800 \text{ rpm}$

$$Q_{s1} = \frac{2}{3} \omega \pi \tau_{cont} \left[\left(\frac{R_{shoulder}}{2} \right)^3 - \left(\frac{d}{2} \right)^3 \right] (1 + \tan \alpha)$$

$$Q_{s1} = \frac{2}{3} \times \pi \times 345 \times 83.80 \times \left[\left(\frac{0.02}{2} \right)^3 - \left(\frac{0.008}{2} \right)^3 \right] (1 + \tan 0)$$

$$Q_{s1} = \frac{2}{3} \times \pi \times 345 \times 83.80 \times \left[\left(\frac{0.02}{2} \right)^3 - \left(\frac{0.008}{2} \right)^3 \right] (1 + 0)$$

$$Q_{s1} = 56.62 \text{ kW}$$

b) For tool angular rotational speed $\omega_2 = 130.89 \text{ rad/s} = 1250 \text{ rpm}$

$$Q_{s2} = \frac{2}{3} \omega \pi \tau_{cont} \left[\left(\frac{R_{shoulder}}{2} \right)^3 - \left(\frac{d}{2} \right)^3 \right] (1 + \tan \alpha)$$

$$Q_{s2} = \frac{2}{3} \times \pi \times 345 \times 130.89 \times \left[\left(\frac{0.02}{2} \right)^3 - \left(\frac{0.008}{2} \right)^3 \right] (1 + \tan 0)$$

$$Q_2 = \frac{2}{3} \times \pi \times 345 \times 130.89 \times \left[\left(\frac{0.02}{2} \right)^3 - \left(\frac{0.008}{2} \right)^3 \right] (1 + 0)$$

$$Q_{s2} = 88.52 \text{ kW}$$

c) For tool angular rotational speed $\omega_3 = 167.55 \text{ rad/s} = 1600 \text{ rpm}$

$$Q_{s3} = \frac{2}{3} \omega \pi \tau_{cont} \left[\left(\frac{R_{shoulder}}{2} \right)^3 - \left(\frac{d}{2} \right)^3 \right] (1 + \tan \alpha)$$

$$Q_{s3} = \frac{2}{3} \times \pi \times 345 \times 167.55 \times \left[\left(\frac{0.02}{2} \right)^3 - \left(\frac{0.008}{2} \right)^3 \right] (1 + \tan 0)$$

$$Q_{s3} = \frac{2}{3} \times \pi \times 345 \times 167.55 \times \left[\left(\frac{0.02}{2} \right)^3 - \left(\frac{0.008}{2} \right)^3 \right] (1 + 0)$$

$$Q_{s3} = 113.31 \text{ kW}$$

d) For tool angular rotational speed $\omega_4 = 209.44 \text{ rad/s} = 2000 \text{ rpm}$

$$Q_{s4} = \frac{2}{3} \omega \pi \tau_{cont} \left[\left(\frac{R_{shoulder}}{2} \right)^3 - \left(\frac{d}{2} \right)^3 \right] (1 + \tan \alpha)$$

$$Q_{s4} = \frac{2}{3} \times \pi \times 345 \times 209.44 \times \left[\left(\frac{0.02}{2} \right)^3 - \left(\frac{0.008}{2} \right)^3 \right] (1 + \tan 0)$$

$$Q_{s4} = \frac{2}{3} \times \pi \times 345 \times 209.44 \times \left[\left(\frac{0.02}{2} \right)^3 - \left(\frac{0.008}{2} \right)^3 \right] (1 + 0)$$

$$Q_{s4} = 141.64 \text{ kW}$$

Q_s (kW)	N (rpm)	ω (rad/s)
56.62	800	83.8
88.52	1250	130.89
113.31	1600	167.55
141.64	2000	209.44

Table 7.3: Heat Generation Calculation for the Innovative Tool Shoulder

ii) **Heat Generation from the Probe Side Surface and the Probe Tip:** from equation 1.2 and 1.3 the values are-

a) For tool angular rotational speed $\omega_1 = 83.80 \text{ rad/s} = 800 \text{ rpm}$

$$Q_{ps1} = 2\omega\pi\tau_{cont} \left(\frac{d}{2}\right)^2 h \left(1 + \tan\frac{\beta}{2}\right)$$

$$Q_{ps1} = 2 \times \pi \times 345 \times 83.80 \times \left(\frac{0.008}{2}\right)^2 0.004 \left(1 + \tan\frac{0}{2}\right)$$

$$Q_{ps1} = 2 \times \pi \times 345 \times 83.80 \times \left(\frac{0.008}{2}\right)^2 0.004 (1 + 0)$$

$$Q_{ps1} = 11.63 \text{ kW}$$

$$Q_{pt1} = \frac{2}{3}\omega\pi\tau_{cont} \left(\frac{d}{2}\right)^3$$

$$Q_{pt1} = \frac{2}{3} \times \pi \times 345 \times 83.80 \times \left(\frac{0.008}{2}\right)^3$$

$$Q_{pt1} = 3.87 \text{ kW}$$

b) For tool angular rotational speed $\omega_2 = 130.89 \text{ rad/s} = 1250 \text{ rpm}$

$$Q_{ps2} = 2\omega\pi\tau_{cont} \left(\frac{d}{2}\right)^2 h \left(1 + \tan\frac{\beta}{2}\right)$$

$$Q_{ps2} = 2 \times \pi \times 345 \times 130.89 \times \left(\frac{0.008}{2}\right)^2 0.004 \left(1 + \tan\frac{0}{2}\right)$$

$$Q_{ps2} = 2 \times \pi \times 345 \times 130.89 \times \left(\frac{0.008}{2}\right)^2 0.004 (1 + 0)$$

$$Q_{ps2} = 18.16 \text{ kW}$$

$$Q_{pt2} = \frac{2}{3}\omega\pi\tau_{cont} \left(\frac{d}{2}\right)^3$$

$$Q_{pt2} = \frac{2}{3} \times \pi \times 345 \times 130.89 \times \left(\frac{0.008}{2}\right)^3$$

$$Q_{t2} = 6.05 \text{ kW}$$

c) For tool angular rotational speed $\omega_3 = 167.55 \text{ rad/s} = 1600 \text{ rpm}$

$$Q_{ps3} = 2\omega\pi\tau_{cont} \left(\frac{d}{2}\right)^2 h \left(1 + \tan\frac{\beta}{2}\right)$$

$$Q_{ps3} = 2 \times \pi \times 345 \times 167.55 \left(\frac{0.008}{2}\right)^2 0.004 \left(1 + \tan\frac{0}{2}\right)$$

$$Q_{ps3} = 2 \times \pi \times 345 \times 167.55 \left(\frac{0.008}{2}\right)^2 0.004 (1 + 0)$$

$$Q_{ps3} = 23.24 \text{ kW}$$

$$Q_{pt3} = \frac{2}{3}\omega\pi\tau_{cont} \left(\frac{d}{2}\right)^3$$

$$Q_{pt3} = \frac{2}{3} \times \pi \times 345 \times 167.55 \times \left(\frac{0.008}{2}\right)^3$$

$$Q_{pt3} = 7.75 \text{ kW}$$

d) For tool angular rotational speed $\omega_4 = 209.44 \text{ rad/s} = 2000 \text{ rpm}$

$$Q_{ps4} = 2\omega\pi\tau_{cont} \left(\frac{d}{2}\right)^2 h \left(1 + \tan\frac{\beta}{2}\right)$$

$$Q_{ps4} = 2 \times \pi \times 345 \times 209.44 \left(\frac{0.008}{2}\right)^2 0.004 \left(1 + \tan\frac{0}{2}\right)$$

$$Q_{ps4} = 2 \times \pi \times 345 \times 209.44 \left(\frac{0.008}{2}\right)^2 0.004 (1 + 0)$$

$$Q_{ps4} = 29.05 \text{ kW}$$

$$Q_{pt4} = \frac{2}{3}\omega\pi\tau_{cont} \left(\frac{d}{2}\right)^3$$

$$Q_{pt4} = \frac{2}{3} \times \pi \times 345 \times 209.44 \times \left(\frac{0.008}{2}\right)^3$$

$$Q_{pt4} = 9.67 \text{ kW}$$

iii) **Heat Generation from the Modified Copper Bush Side:** from equation 1.2 and the values are-

a) For tool angular rotational speed $\omega_1 = 83.80 \text{ rad/s} = 800 \text{ rpm}$

$$Q_{pcopperside1} = 2\omega\pi\tau_{cont} \left(\frac{d}{2}\right)^2 h \left(1 + \tan\frac{\beta}{2}\right)$$

$$Q_{pcopperside1} = 2 \times \pi \times 67.55 \times 83.80 \times \left(\frac{0.008}{2}\right)^2 0.006 \left(1 + \tan\frac{0}{2}\right)$$

$$Q_{pcopperside1} = 2 \times \pi \times 67.55 \times 83.80 \times \left(\frac{0.008}{2}\right)^2 0.006 (1 + 0)$$

$$Q_{pcopperside1} = 3.41 \text{ kW}$$

b) For tool angular rotational speed $\omega_2 = 130.89 \text{ rad/s} = 1250 \text{ rpm}$

$$Q_{pcopperside2} = 2\omega\pi\tau_{cont} \left(\frac{d}{2}\right)^2 h \left(1 + \tan\frac{\beta}{2}\right)$$

$$Q_{pcopperside2} = 2 \times \pi \times 67.55 \times 130.89 \times \left(\frac{0.008}{2}\right)^2 0.006 \left(1 + \tan\frac{0}{2}\right)$$

$$Q_{pcopperside2} = 2 \times \pi \times 67.55 \times 130.89 \times \left(\frac{0.008}{2}\right)^2 0.006 (1 + 0)$$

$$Q_{pcopperside2} = 5.34 \text{ kW}$$

c) For tool angular rotational speed $\omega_3 = 167.55 \text{ rad/s} = 1600 \text{ rpm}$

$$Q_{pcopperside3} = 2\omega\pi\tau_{cont} \left(\frac{d}{2}\right)^2 h \left(1 + \tan\frac{\beta}{2}\right)$$

$$Q_{pcopperside3} = 2 \times \pi \times 67.55 \times 167.55 \times \left(\frac{0.008}{2}\right)^2 0.006 \left(1 + \tan\frac{0}{2}\right)$$

$$Q_{pcopperside3} = 2 \times \pi \times 67.55 \times 167.55 \times \left(\frac{0.008}{2}\right)^2 0.006 (1 + 0)$$

$$Q_{pcopperside3} = 6.83 \text{ kW}$$

d) For tool angular rotational speed $\omega_4 = 209.44 \text{ rad/s} = 2000 \text{ rpm}$

$$Q_{\text{copperside4}} = 2\omega\pi\tau_{\text{cont}} \left(\frac{d}{2}\right)^2 h \left(1 + \tan\frac{\beta}{2}\right)$$

$$Q_{\text{pcopperside4}} = 2 \times \pi \times 67.55 \times 209.44 \left(\frac{0.008}{2}\right)^2 0.006 \left(1 + \tan\frac{0}{2}\right)$$

$$Q_{\text{pcopperside4}} = 2 \times \pi \times 67.55 \times 209.44 \left(\frac{0.008}{2}\right)^2 0.006 (1 + 0)$$

$$Q_{\text{pcopperside4}} = 8.54 \text{ kW}$$

iv) Heat Generation from the Modified Copper Bush Tip: from equation 1.3 the values are-

a) For tool angular rotational speed $\omega_1 = 83.80 \text{ rad/s} = 800 \text{ rpm}$

$$Q_{\text{coppertip1}} = \frac{2}{3}\omega\pi\tau_{\text{cont}} \left(\frac{d}{2}\right)^3$$

$$Q_{\text{coppertip1}} = \frac{2}{3} \times \pi \times 67.55 \times 83.80 \times \left(\frac{0.008}{2}\right)^3$$

$$Q_{\text{pt1}} = 0.76 \text{ kW}$$

b) For tool angular rotational speed $\omega_2 = 130.89 \text{ rad/s} = 1250 \text{ rpm}$

$$Q_{\text{coppertip2}} = \frac{2}{3}\omega\pi\tau_{\text{cont}} \left(\frac{d}{2}\right)^3$$

$$Q_{\text{coppertip2}} = \frac{2}{3} \times \pi \times 67.55 \times 130.89 \times \left(\frac{0.008}{2}\right)^3$$

$$Q_{\text{coppertip2}} = 1.19 \text{ kW}$$

c) For tool angular rotational speed $\omega_3 = 167.55 \text{ rad/s} = 1600 \text{ rpm}$

$$Q_{\text{coppertip3}} = \frac{2}{3}\omega\pi\tau_{\text{cont}} \left(\frac{d}{2}\right)^3$$

$$Q_{\text{coppertip3}} = \frac{2}{3} \times \pi \times 67.55 \times 167.55 \times \left(\frac{0.008}{2}\right)^3$$

$$Q_{\text{coppertip3}} = 1.52 \text{ kW}$$

d) For tool angular rotational speed $\omega_4 = 209.44 \text{ rad/s} = 2000 \text{ rpm}$

$$Q_{coppertip4} = \frac{2}{3} \omega \pi \tau_{cont} \left(\frac{d}{2}\right)^3$$

$$Q_{coppertip4} = \frac{2}{3} \times \pi \times 67.55 \times 209.44 \times \left(\frac{0.008}{2}\right)^3$$

$$Q_{coppertip4} = 1.90 \text{ kW}$$

Q_{ps} (kW)	N (rpm)	ω (rad/s)
11.63	800	83.8
16.16	1250	130.89
23.24	1600	167.55
29.05	2000	209.44
Q_{pt} (kW)	N (rpm)	ω (rad/s)
3.87	800	83.8
6.05	1250	130.89
7.75	1600	167.55
9.67	2000	209.44
$Q_{pcopperside}$ (kW)	ω (rpm)	ω (rad/s)
3.41	800	83.8
5.34	1250	130.89
6.83	1600	167.55
8.54	2000	209.44
$Q_{pcoppertip}$ (kW)	ω (rpm)	ω (rad/s)
0.76	800	83.80
1.19	1250	130.89
1.52	1600	167.55
1.90	2000	209.44

Table 7.4: The Heat Generation for the Probe side Surface, the Probe Tip, the Copper Bush Side Surface and the Copper Bush Tip.

iii) **Total Heat Generated:** from equation 1.4 the values are-

e) For tool angular rotational speed $\omega_1 = 83.80 \text{ rad/s} = 800 \text{ rpm}$

$$QT_1 = Q_{ps1} + Q_{pcopper1} + Q_{st1} + Q_{coppertip1} + Q_{pt1}$$

$$QT_1 = 11.63 + 3.41 + 56.62 + 0.76 + 3.87$$

$$QT_1 = 76.29 \text{ kW}$$

f) For tool angular rotational speed $\omega_2 = 130.89 \text{ rad/s} = 1250 \text{ rpm}$

$$QT_2 = Q_{ps2} + Q_{pcopper2} + Q_{st2} + Q_{coppertip2} + Q_{pt2}$$

$$QT_2 = 18.16 + 5.34 + 88.52 + 1.19 + 6.05$$

$$QT_2 = 119.26 \text{ kW}$$

g) For tool angular rotational speed $\omega_3 = 167.55 \text{ rad/s} = 1600 \text{ rpm}$

$$QT_3 = Q_{ps3} + Q_{pcopper3} + Q_{st3} + Q_{coppertip3} + Q_{pt3}$$

$$QT_3 = 23.24 + 6.83 + 113.31 + 1.52 + 7.75$$

$$QT_3 = 152.65 \text{ kW}$$

h) For tool angular rotational speed $\omega_4 = 209.44 \text{ rad/s} = 2000 \text{ rpm}$

$$QT_4 = Q_{ps4} + Q_{pcopper4} + Q_{st4} + Q_{coppertip4} + Q_{pt4}$$

$$QT_4 = 29.05 + 8.54 + 141.64 + 1.90 + 9.67$$

$$QT_4 = 190.8 \text{ kW}$$

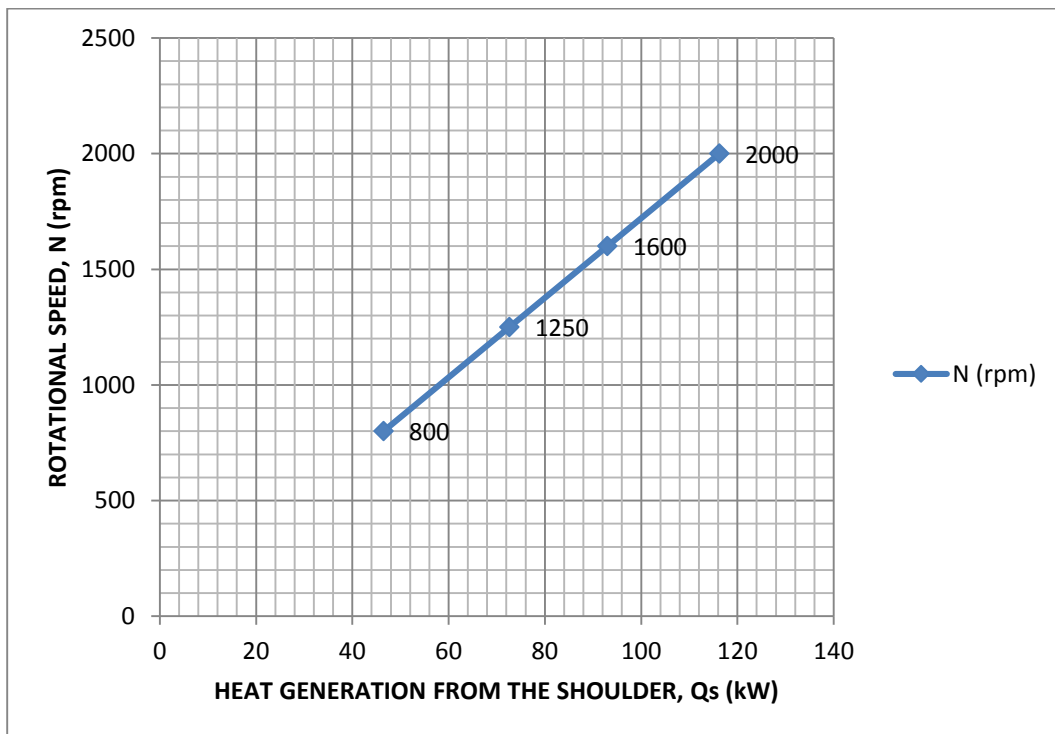
QT (kW)	N (rpm)	ω (rad/s)
76.29	800	83.8
119.26	1250	130.89
152.65	1600	167.55
190.8	2000	209.44

Table 7.5: The Total Heat Generation for the Innovative Tool.

7.1. Heat Generation: Innovative Tool

7.1.1. Heat Generation from the Tool Shoulder

The heat generation of the innovative tool shoulder (Q_s) is explained by the calculations of equations (5.1), which is determined by the angular rotational speed (ω), the contact shear stress of the material Al2024-T3 (τ_{cont}), the shoulder's cone angle (α), the probe radius (d) and the shoulder radius (D). Equation (5.1) is used in this study to determine the heat generation from the innovative tool shoulder at 4 different rotational speeds. Each of these rotational speeds exerted the following kW of heat generation when the rotational speed has been increased. 800 rpm generated heat of 56.62 kW. 1250 rpm had equated to a heat generation of 88.52 kW. 1600 rpm exerted an increasing heat generation of 113.31 kW and lastly the rotational speed of 2000 rpm accumulated a heat generation of 141.64 kW. The calculation total of the innovative tool shoulder is accurately analysed (Graph 7.1) with representing axis, Y representing Rotational Speed (rpm), X representing the Heat Generation From The Tool Shoulder (Q_s) kW and N being the Angular Rotational Speed (rpm).



Graph. 7.1: Rotational speed per minute vs. heat generation from the innovative tool shoulder

7.1.2. Heat Generation from the Probe Side

The heat generation from the probe side surface for the innovative tool is represented by equation (5.2) represents the exertion of heat that has been generated from the following increased rotational speeds 800 rpm, 1250 rpm, 1600 rpm and 2000 rpm. The heat generation from the probe side surface (Q_{ps}) is determined by the probe height (h), the probe radius (d), the tool angular rotational speed (ω) and the contact shear stress of the material Al2024-T3 (τ_{cont}). The process formulated as follows, 800 rpm generated 11.63 kW. 1240 rpm resulted in an increase of 18.16 kW. 1600 rpm the probe side surface had an increased heat generation of 23.24 KW and lastly 2000 rpm exerted an accumulated heat generation of 29.05 kW. The formulation totals of the probe side surface was represented precisely to show the heat generation due to an increased rotational speed (Graph 7.2) with axis Y representing Rotational Speed (rpm), the X axis representing the Heat Generation Of The Probe Side Surface (Q_{ps}) and N indicating the Angular Rotational Speed (rpm).

7.1.3. Heat Generation from the Probe Tip

Heat generation from the Probe Tip of the innovative tool is explained in (5.3). As indicated in both equations, where Q_{pt} represents heat generation from the tip of the probe, the contact shear stress of the material [Al2024-T3] ($\tau_{contact}$) Equation (5.3) is used in this study to determine the heat generation from the probe tip with four different rotational speeds. This process formulated as follows: At 800 rpm generated 3,87 kW. 1250 rpm at 6.05 kW. At 1600 rpm the probe pin to 7.75 kW, and lastly the speed of 2000 rpm the probe pin generated a heat of 9.67 kW (Graph 7.3) Rotational speed per minute vs. from the probe pin represents the accurate analysed increased speed of the probe pin which increases the heat generation on the supporting axis: Y: ROTATIONAL SPEED (rpm) and X: HEAT GENERATION FROM THE PROBE PIN (kW), N indicating the TOOL ANGULAR ROTATIONAL SPEED (rpm).

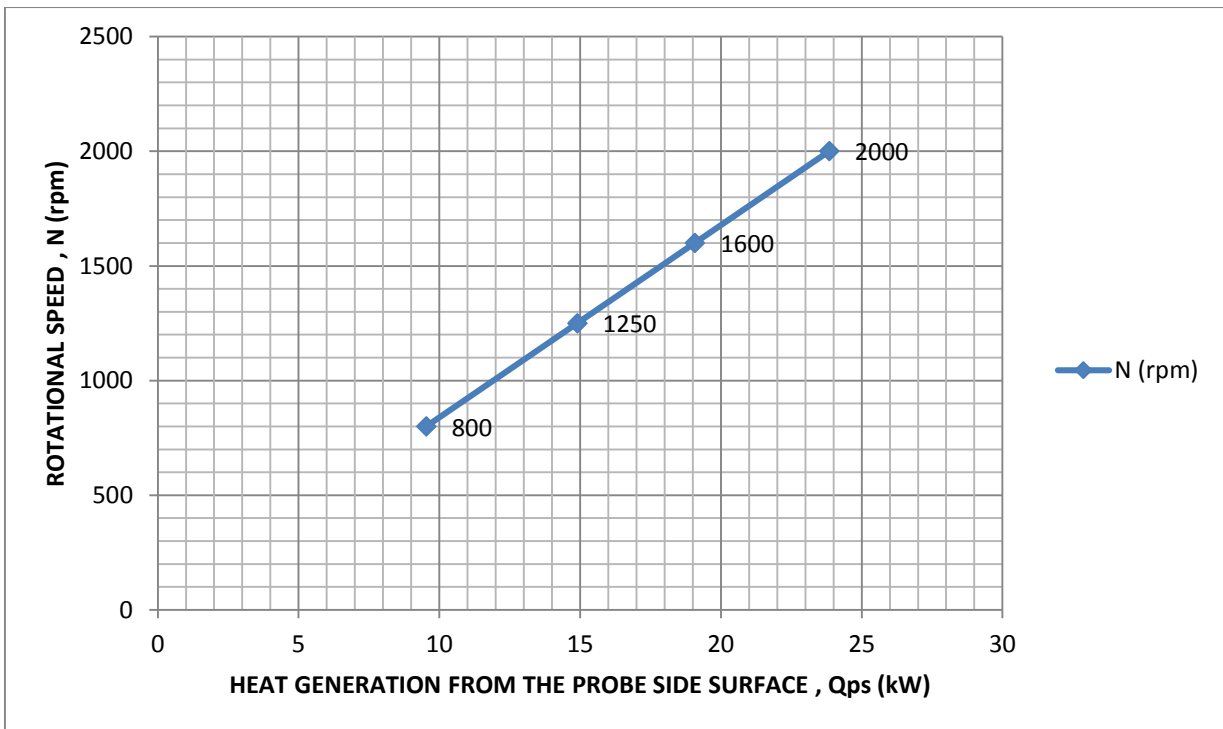
7.1.4. Heat Generation from a Modified Copper Bush Side Surface

The heat generation for the modified copper bush side surface of an innovative tool is calculated with equation (5.2), where ($Q_{pcopper}$) is the heat generated by the modified copper bush which is determined by the probe height (h), the probe radius (d), the tool angular rotational speed (ω) and the Copper Contact shear stress 67.55MPa (τ_{cont}). The process formulated as follows, 800 rpm generated heat up to 3.41 KW. 1250 rpm resulted to an increase of 5.34 kW. 1600 rpm exerted a generation of 6.83 KW and finally 2000 rpm at a generation of 8.54 kW. Making the Modified Copper Bush the best material for a sliding backing bar to maintain heat generation during a weld. An analytical analysis (Graph 7.4) is shown with the axis Y Representing Rotational Speed (rpm), the axis X representing the Heat Generation from a Modified Copper Bush and N indicating the Angular Rotational Speed.

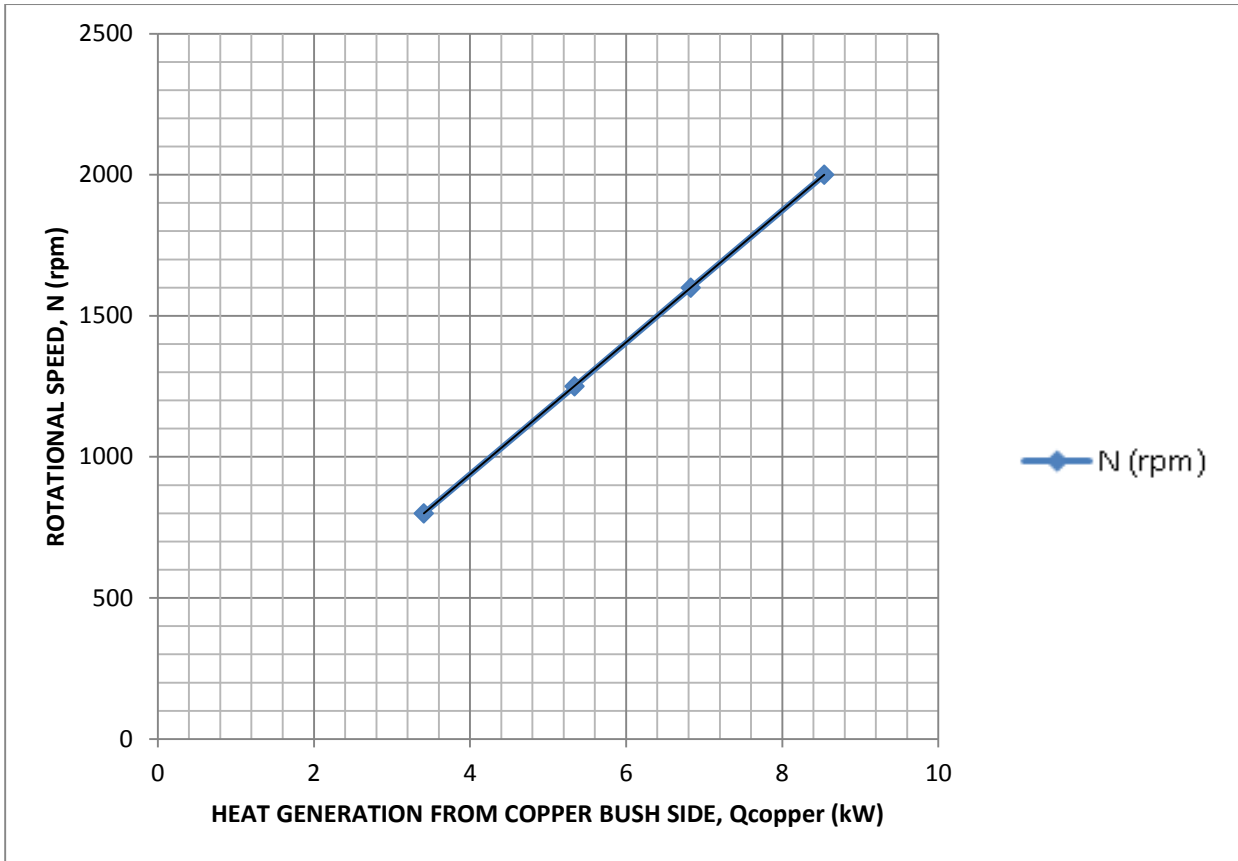
7.1.5. Heat Generation : Modified Copper Bush Tip

The heat generation between the modified copper bush and the tool tip of an innovative tool is calculated with equation (7.2), where ($Q_{pcopper}$) is the heat generated by the modified copper bush which is determined by the probe height (h), the probe radius (d), the tool angular rotational speed (ω) and the Copper Contact shear stress 67.55 MPa (τ_{cont}). The process formulated as follows, 800 rpm generated heat up to 0.76 KW. 1250 rpm resulted to an increase of 1.19 kW. 1600 rpm exerted a generation of 1.52 kW and lastly the rotational speed of 2000 rpm generating 1.90 kW. An accurate analysis (Graph 7.5) is shown respectively with the axis Y Representing Rotational

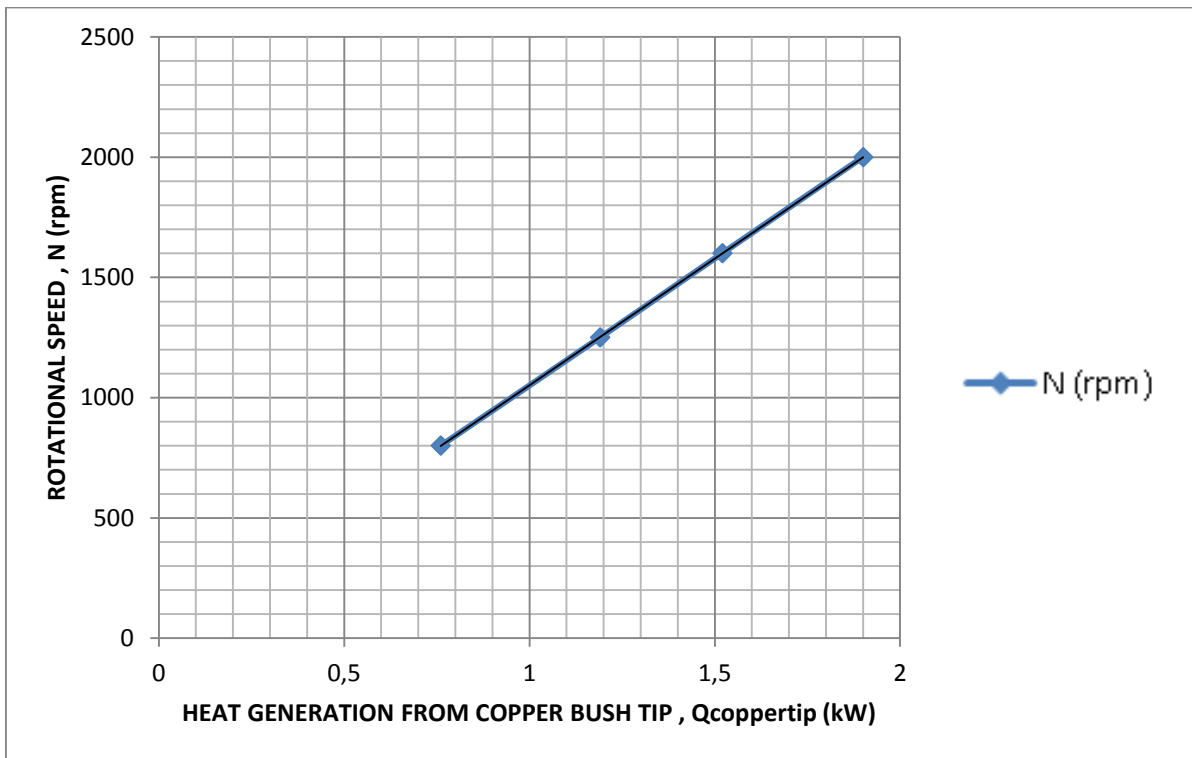
Speed (rpm), the axis X representing the Heat Generation from a Modified Copper Bush and N indicating the Angular Rotational Speed.



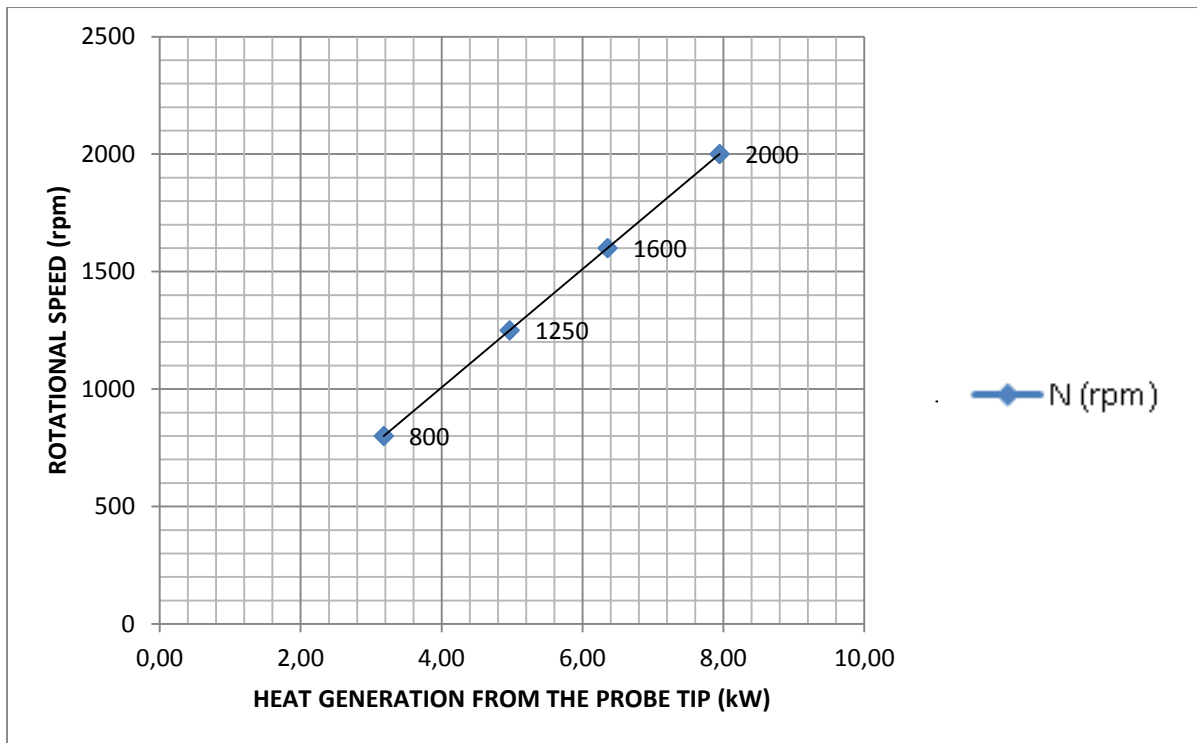
Graph. 7.2 Rotational speed per minute vs. heat generation from the innovative tool probe side surface



Graph 7.3: Rotational speed per minute vs. heat generation from copper bush side



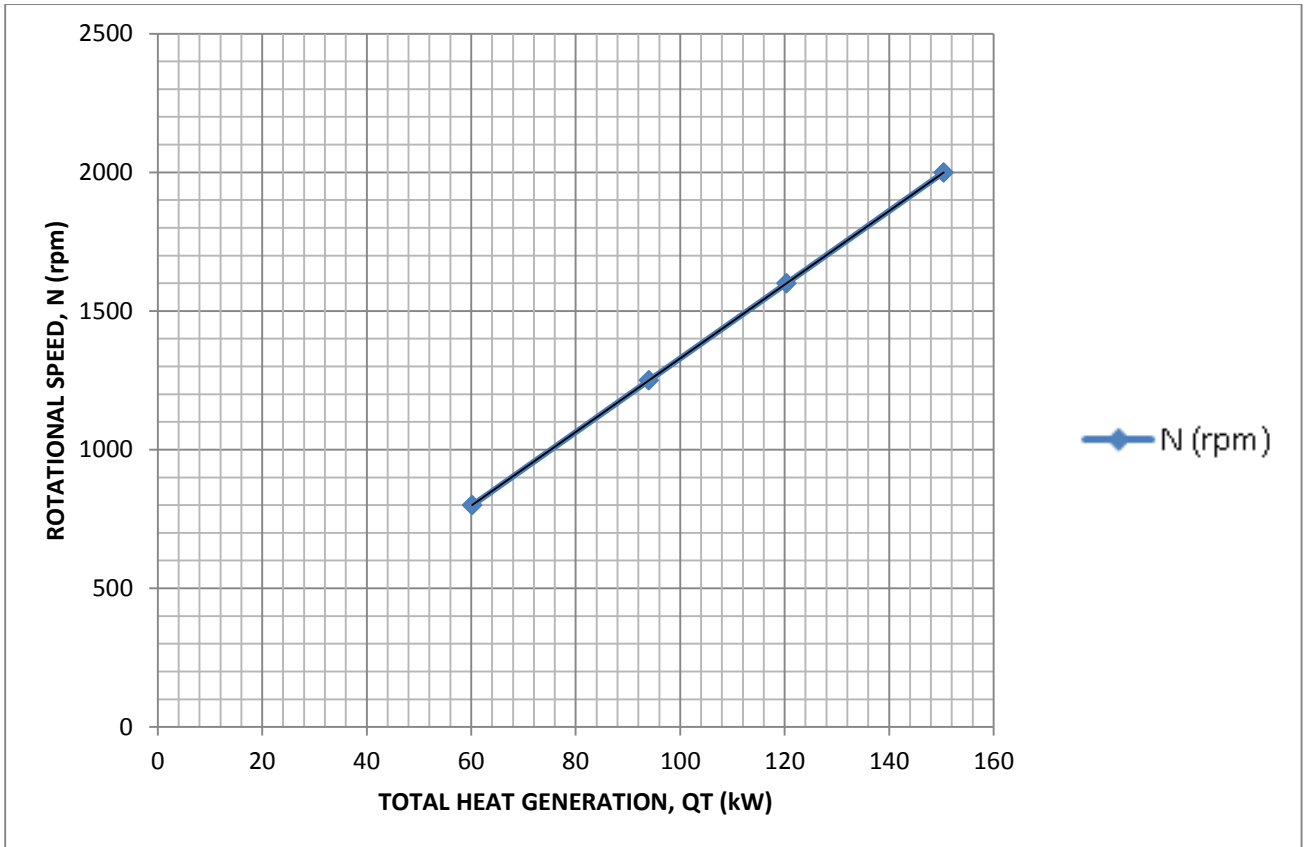
Graph 7.4 Rotational speed per minute vs. heat generation from copper bush tip



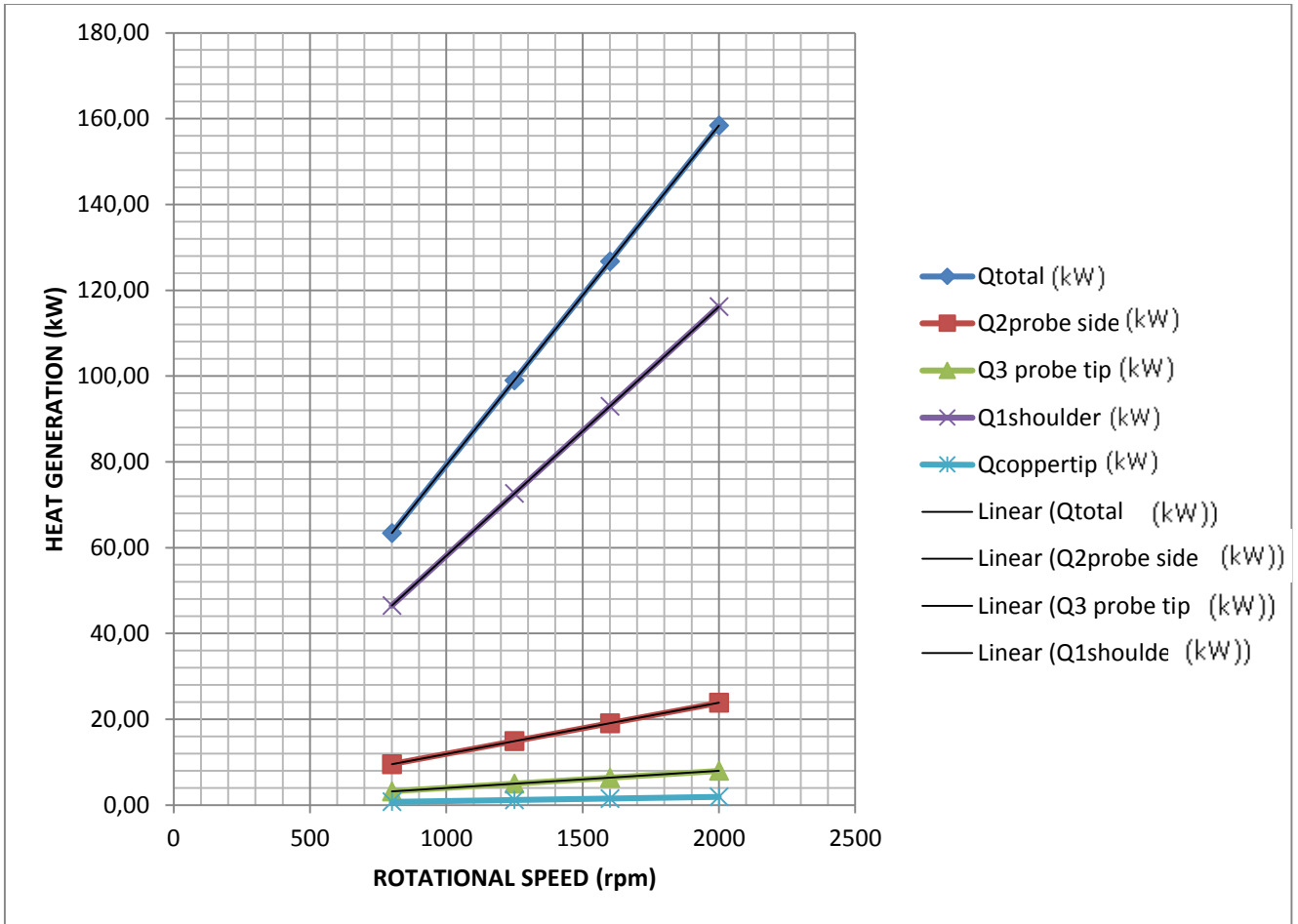
Graph. 7.5 Rotational speed per minute vs. heat generation from the innovative tool probe tip

7.1.6. Total Heat Generation for the Innovative Tool

After formulating these three equations (Q_s , Q_{ps} , $Q_{copperside}$, $Q_{coppertip}$) a final total will sum for the total heat generation where Q is the heat generation which is determined by the tool angular rotation speed (ω), contact shear stress of the material [Al2024-T3] ($\tau_{contact}$), the shoulders cone angle (α), the tool probe radius (d) and the tool probe height (H_{probe}). The total calculation is as follows with 800 rpm generated a heat of 76.29 kW. 1250 rpm exerted 119.26 kW. 1600 rpm had an exponential heat generation of 152.35 kW and lastly 2000 rpm accumulated a heat generation of 190.8 kW. The Rotational speed per minute vs. from the total heat generation from an innovative tool (Graph 7.6) represent the total analysed speed against the heat generation on the supporting axis: Y: Rotational Speed (rpm) and X: Total Heat Generation and N indicating the Tool Angular Rotational Speed (rpm).



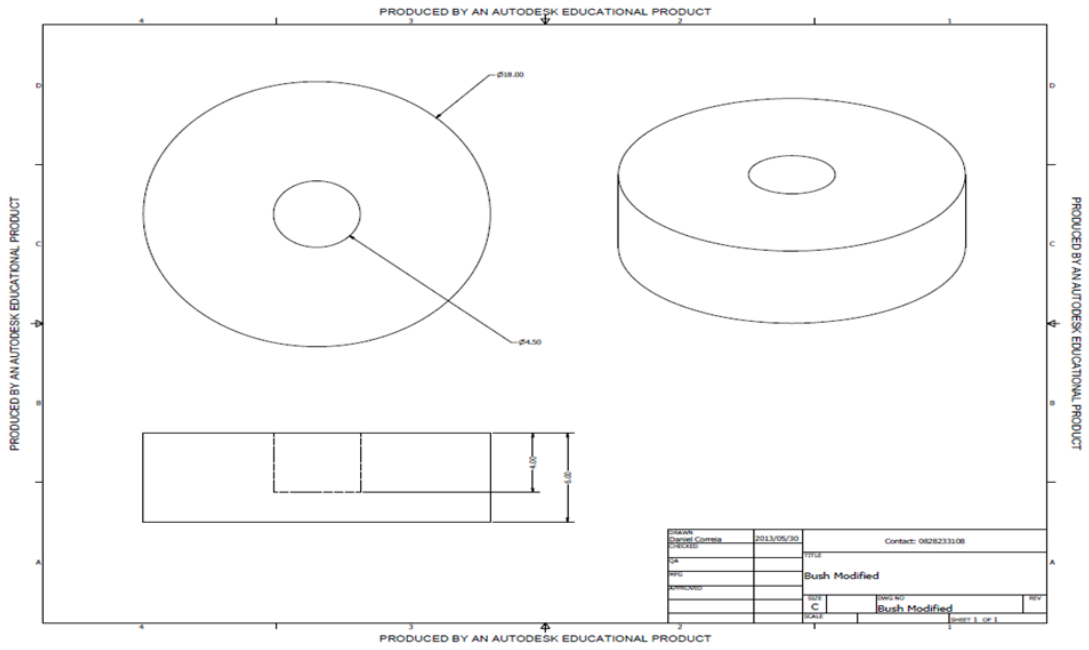
Graph. 7.6 Rotational speed per minute vs. total heat generation from innovative tool



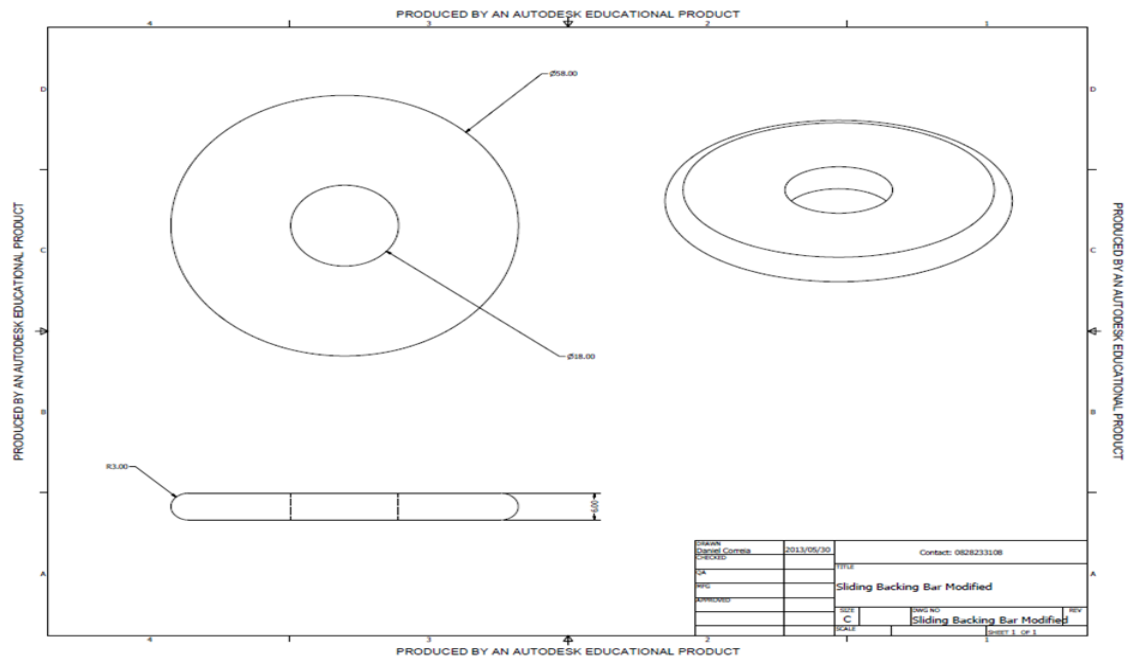
Graph. 7.7 Qs, Qpt, Qps, Qcopper-tip, Qcopper-side, QT vs. Rotational speed

7.2. SolidWorks: Innovative Tool Design

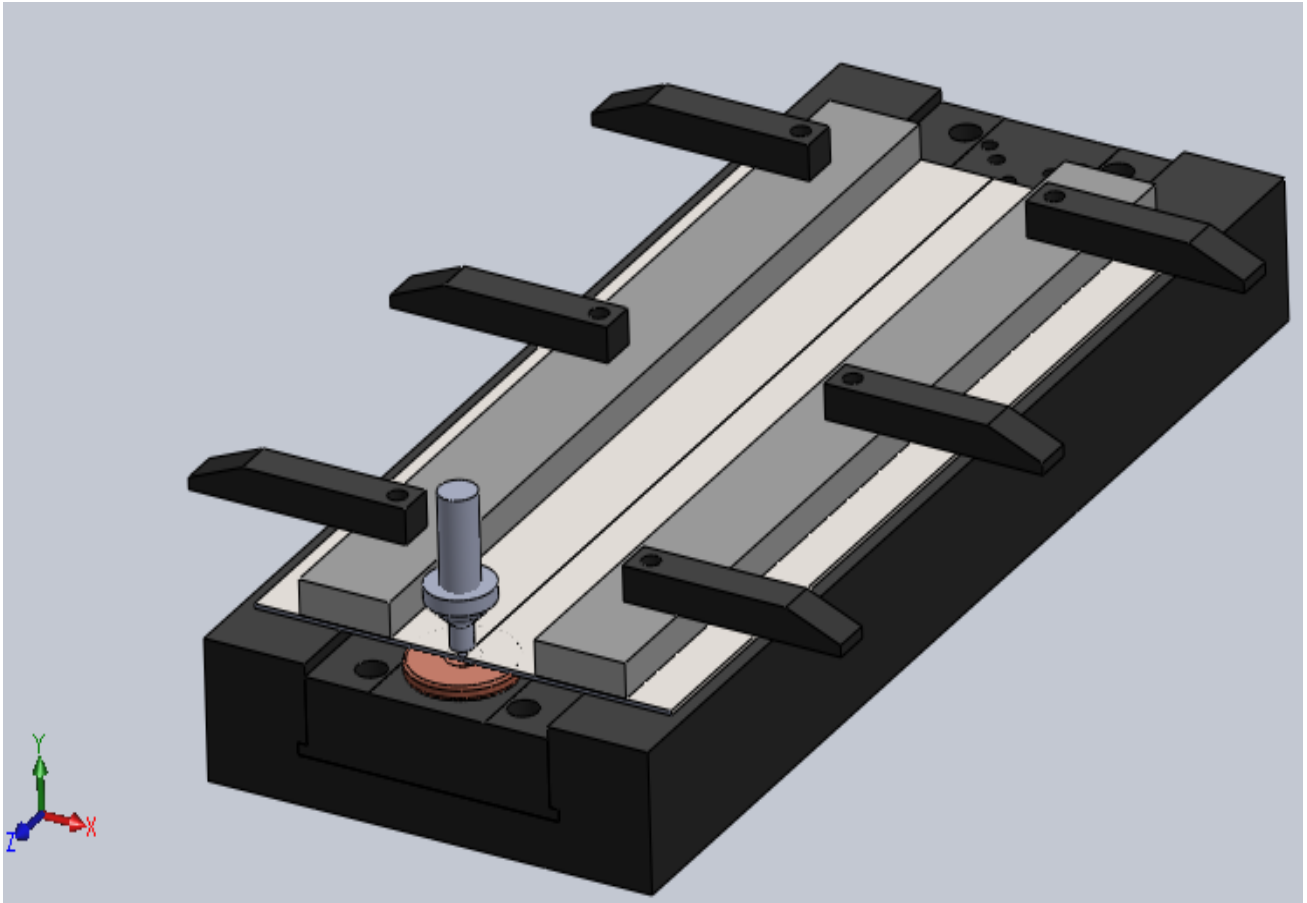
The Modified Copper Bush with a Tool shoulder radius, $R = 10$ mm where the outer side of the bush been 18 mm and the inner 4,50 mm (Drw 7.1) and the Modified Sliding Backing Copper Bar with the outer side been 58 mm and the inner copper bar been 18 mm (Drw 7.2) is shown in both a 2-D and 3-D representation .The innovate tool workbench has been created in 3-D with copper sliding backing copper bar (Drw 7.3), the innovative tool friction stir weld dimensional views (Drw 7.4) and an innovative work bench design (Drw 7.5) with the aid of the SolidWorks software programme. The use of copper to design the sliding backing bar is in its unique ability to conduct heat, hence the reason for the usage to avoid the overheating and/or melting of participating metals



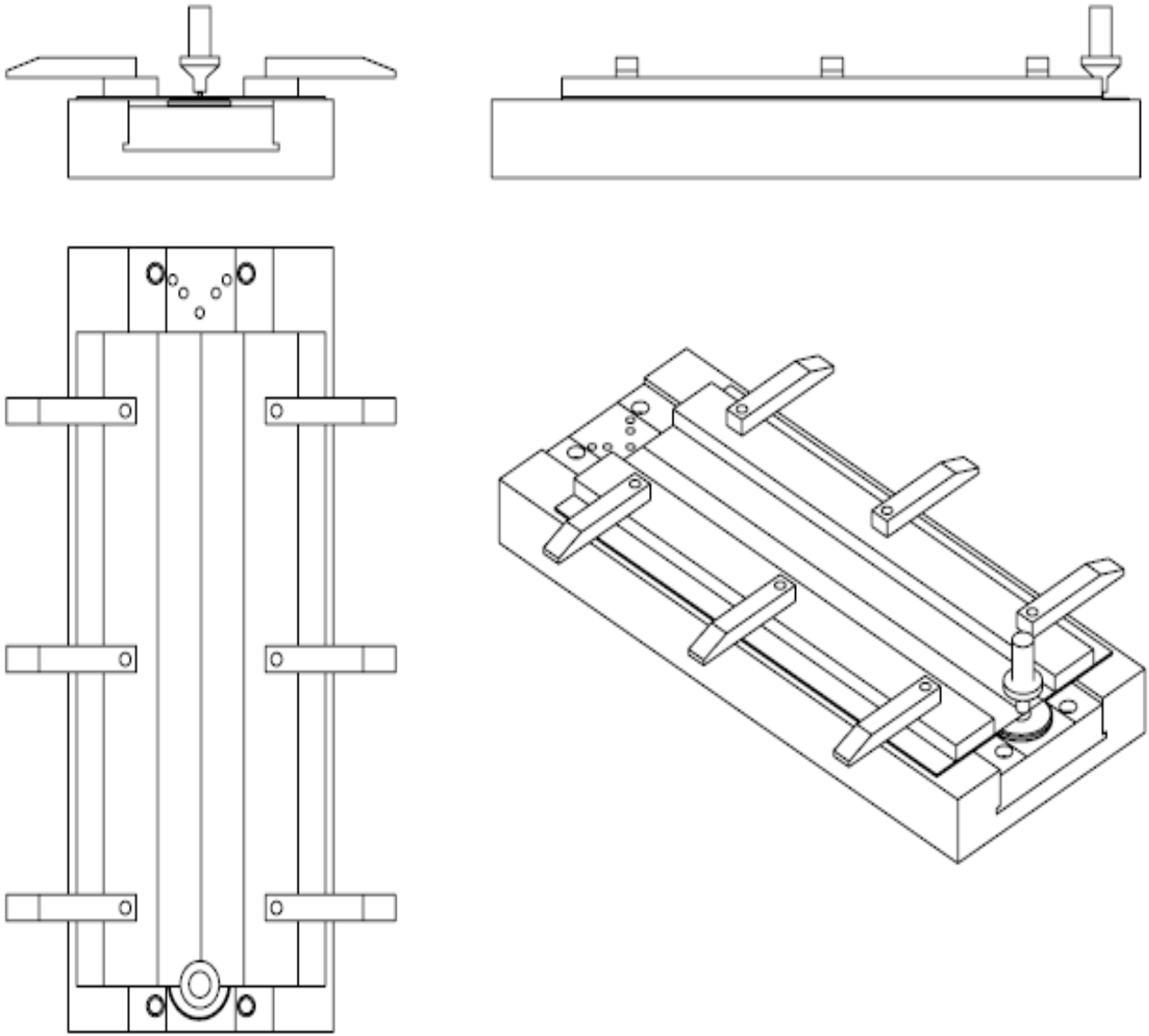
Drw. 7.1: Modified Copper Bush [*D, Correia, (30/05/2015), Bush Modified. University of the Witwatersrand*]



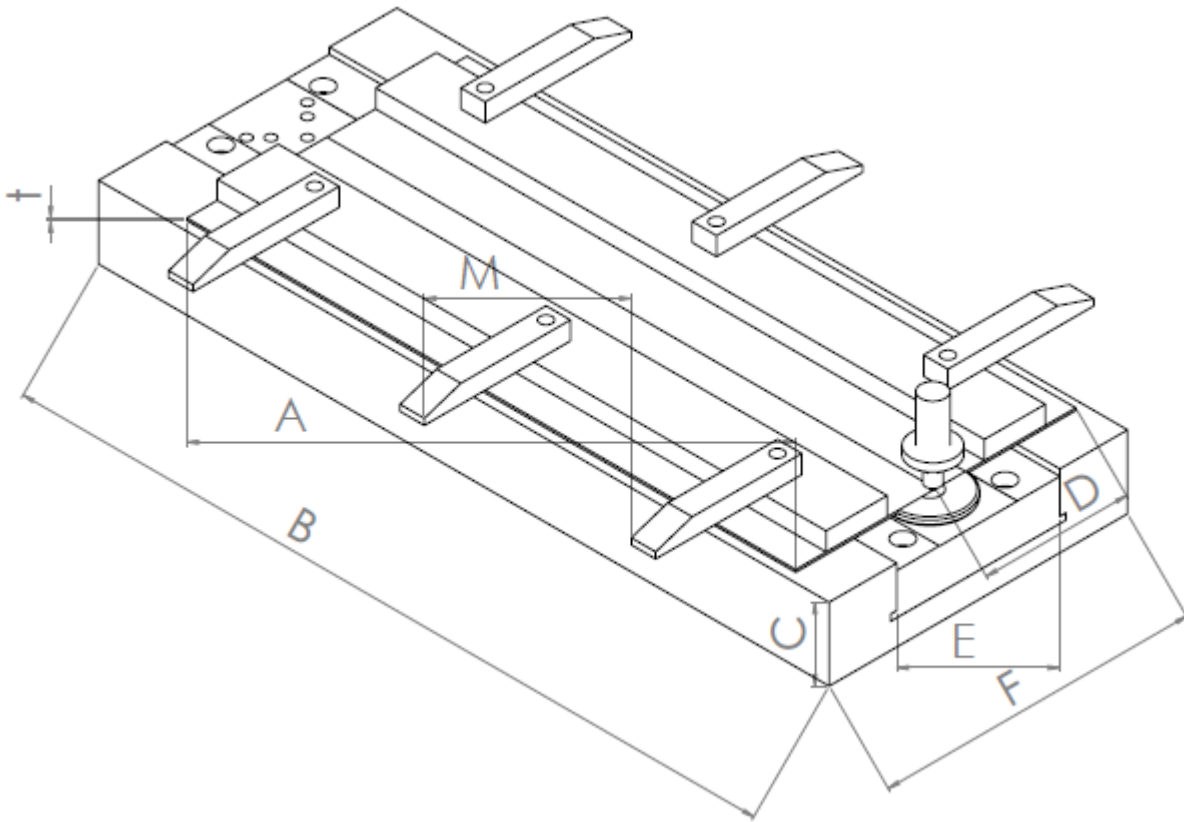
Drw. 7.2: Modified Sliding Backing Copper Bar- [*Correia, D, (30/05/2015), Sliding Backing Bar Modified. University of the Witwatersrand*]



Drw 7.3. Friction Stir Welding Workbench 3D design



Drw.7.4: Friction Stir Welding Workbench design views



Drw.7.5: Friction Stir Welding Workbench design

Aluminium plate length, A (As seen on drw.7.5)

Aluminium plate width, D (As seen on drw.7.5)

Aluminium plate thickness, t (As seen on drw.7.5)

Workbench clamps distance, M (As seen on drw.7.5)

Workbench length, B (As seen on drw.7.5)

Workbench width, F (As seen on drw.7.5)

Workbench thickness, C (As seen on drw.7.5)

Workbench backing plate width, E (As seen on drw.7.5)

7.3. Mode Frontier simulation: Innovative tool Design

Input Data, Output Data and boundary variables definitions as shown on this Microsoft Excel Sheet file name mehmet deneme-copper.xlsm is used in Mode Frontier for this Design Project: Since each component defining the Workflow is represented by a specific node which can be linked to other nodes, a proper node from the available Node Library toolbar or, alternatively, chosen by using the Workflow Nodes panel. It is shown all the input data output data and boundary variables in a Microsoft Excel workbook. The excel work books is used so that the equation for the rotational speed along with the heat generation is calculated where the results will be used in ModeFrontier to assist in the design (Image 7.3).Once a Workflow Plan created by Mode Frontier Project as shown in deneme04.prj, also includes DOE (Design of Experiments) and DOE Sequence, as well as indicating Input Variables, Output Variables, Design Objectives + Gradients, Microsoft Excel Workbook and Logic End(Image 7.4).A workflow plan is created using a DoE (Design of Experiments) and a DOE Sequence on a new Overlook. Once this is open workflow nodes can be added on. Variable nodes which are the input nodes and the output nodes are used. Workflow nodes such as the schedulers, the logic switch and logic end is used. An application node is used for excel. A goal node which is the design objective+gradient node. Mode Frontier Input and Output Data is connected to Microsoft Excel Workbook .Excel workbook properties are used for basic node configuration where an Excel Workbook is selected (Image 7.5). Once selected the input and out data is connected from the chosen Excel workbook. An Interactive Selection used between Mode Frontier deneme04copper.prj and Microsoft Excel Workbook: mehmet deneme-copper.xlsm to determine Excel Workbook Properties for Mode Frontier (Image 7.6) An interactive selection allows each input and output node to be configured in accordance to the Excel workbook. Where each variable is interactively selected to complete a work plan.

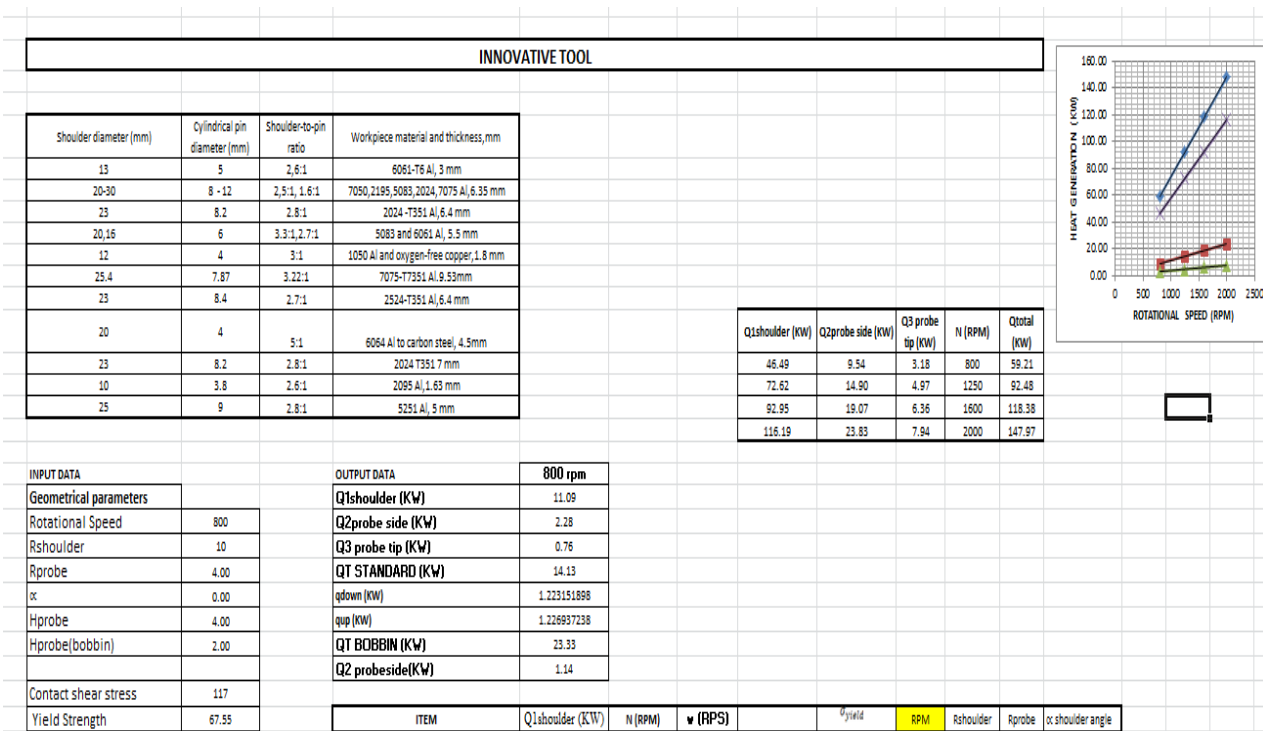


Image 7.3: Input Data, Output Data and boundary variables definitions as shown on this Microsoft Excel Sheet file name: mehmet deneme-copper.xlsm is used in Mode Frontier for Design Project

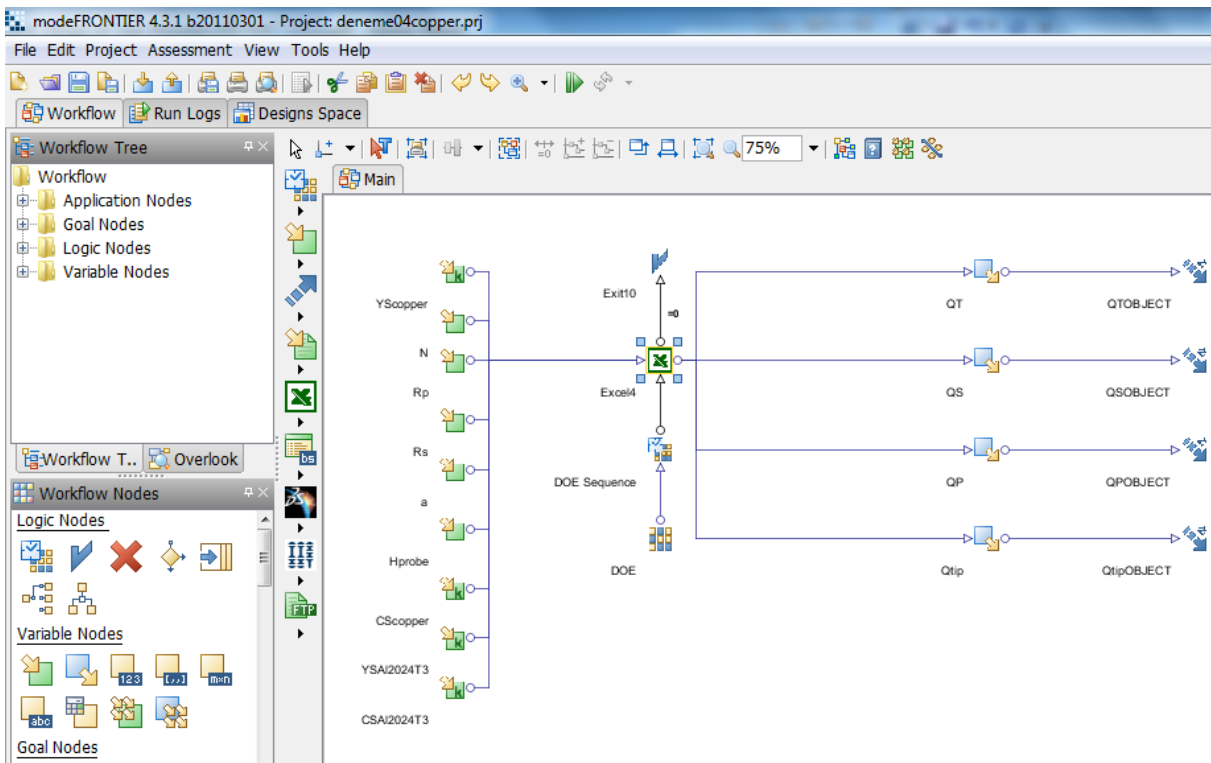


Image 7.4 : Workflow Plan created on Mode Frontier Project as shown in *deneme04copper.prj*, also includes DOE (Design of Experiments) and DOE Sequence, as well as indicating Input Variables, Output Variables<Design Objectives + Gradients, Microsoft Workbook and Logic End

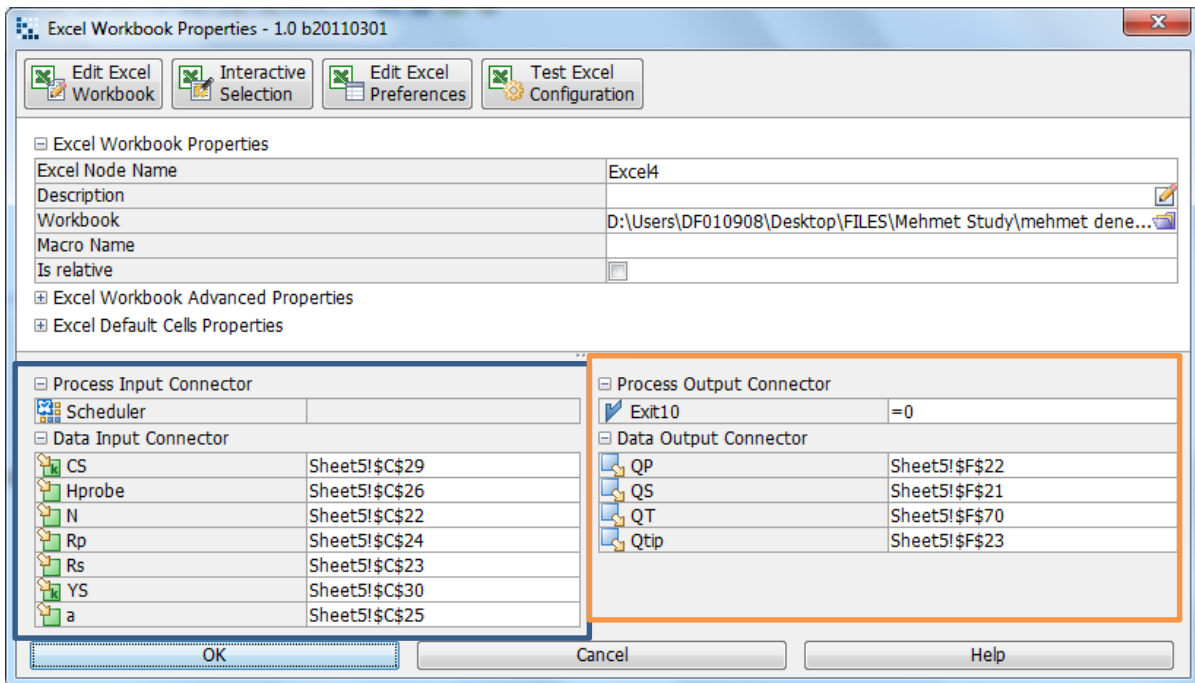


Image 7.5: Mode Frontier Input and Output Data connected to Microsoft Excel Workbook as shown above for innovative tool

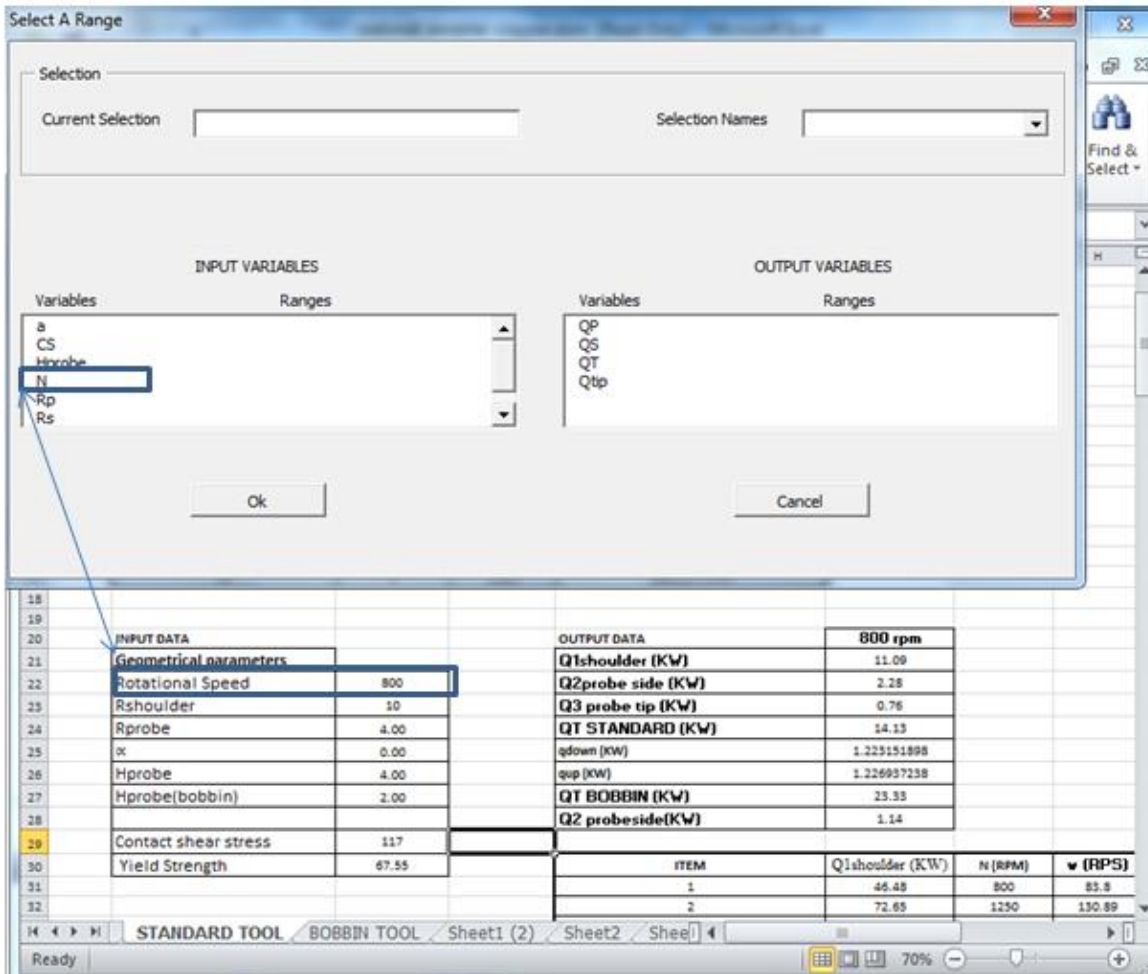


Image 7.6: Interactive Selection used between Mode Frontier [deneme04copper.prj](#)

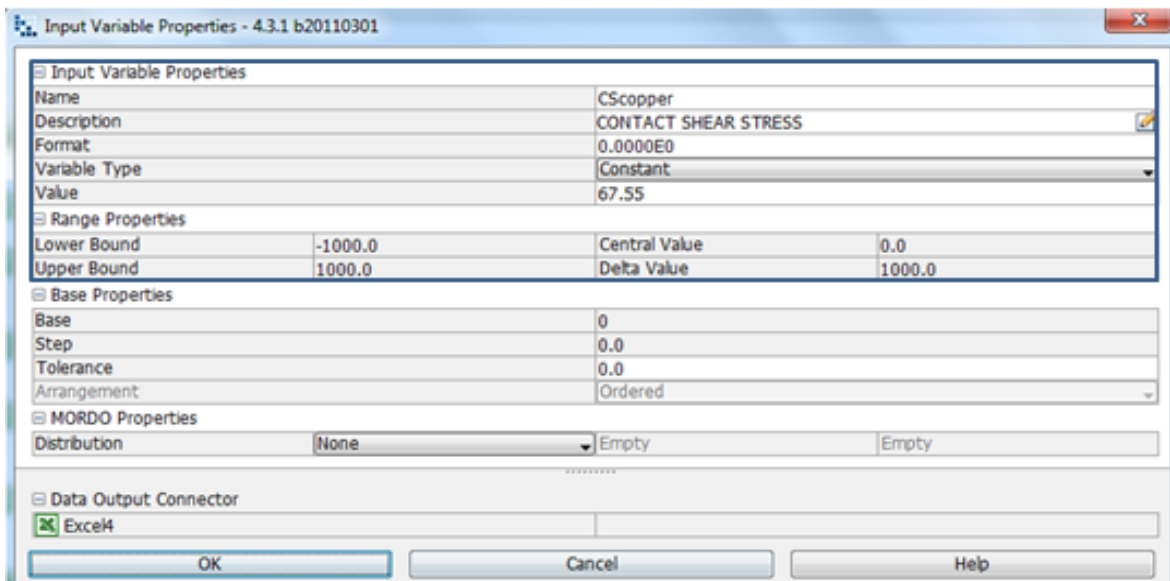


Image 7.7: Copper material contact shear stress 67.55 MPa is chosen, where the variable type is constant hence the lower and upper bound is fixed

7.3.1. Boundaries : Innovative tool

An innovative tools contact shear stress as an input variable for copper, where the value is 67,55 MPa (as per ref <http://asm.metmab.com>) and the variable type is constant. The range properties being fixed (Image 7.7). Rotational speed is a variable that is in accordance with both the standard tool and bobbin tool) (Image 7.8). An optimal ratio of shoulder diameter to pin diameter is suggested to assist with a tool design, however the ratio (2.5:1 and 1.6:1) (table 7.4) is dependent on the aluminium alloy composition and only is applied to 6 mm (0.24 in) thick plate. As the work piece thickness increases, the thermal input from the shoulder decreases, the pin then must supply more thermal energy (Image 7.9&7.10).The tool shoulder cone angle with the variable type being variable with the upper bound at 90.0 degrees. Height probe (Image 7.11) is used in accordance to the design of Modified Sliding Backing Copper Bar which is for the conduction of extra heat given of during a weld (in referencing to Drw.8 taken from Telco where the dimensions used in accordance to the work bench and backing bars for support) where the variable type being variable and the range properties being upper bound 1.0 and the lower bound being 20.0 (Image 7.12). Copper yield shear stress variable type is constant and the value 117,0 MPa. (Image7.13). The material yield stress/ YS copper has fixed bounds, (as per ref <http://asm.metmab.com>) with a variable that is constant and a value of 117,0 MPa. The Copper contact shear stress has fixed bounds, the range properties been, (as per ref <http://asm.metmab.com>) with a variable that remains constant and a value 283.0 MPa (Image 7.14). The projects start once a run project has started (Image 7.15). An index (Image 7.16) before the initial project design commences. The history chart highlights in an easy way, the minimum and the maximum feasible design values: the bottom chart area displays the minimum feasible design value while the top of the chart area display feasible design value (Image 7.17).

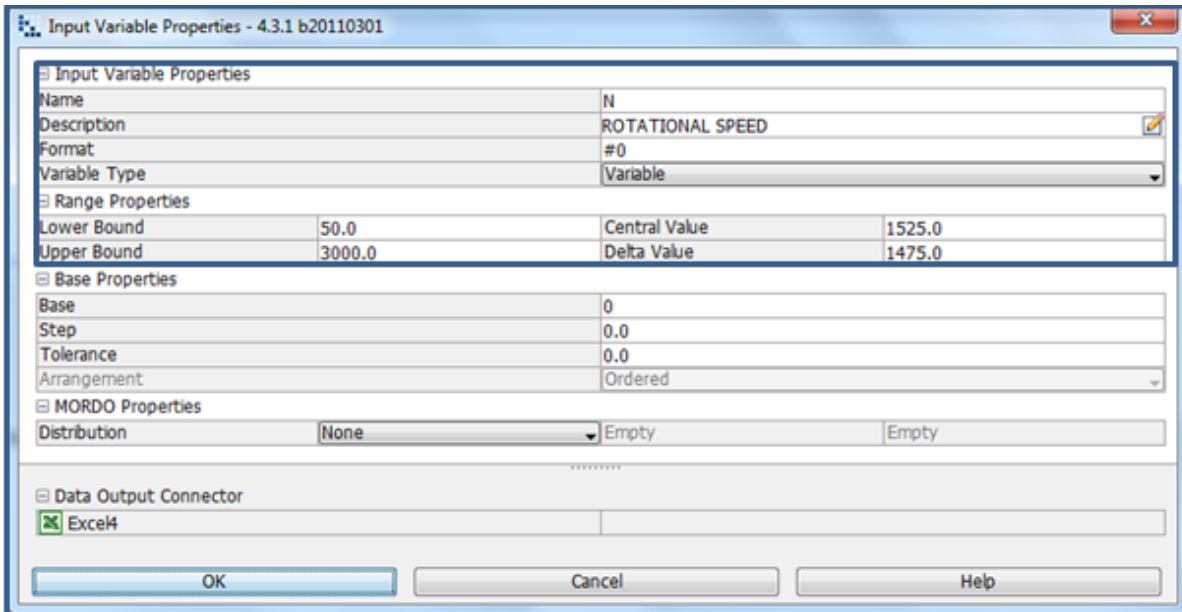


Image 7.8: Rotational speed is determined by lower and upper bound range properties, as shown in the input variable node properties dialog

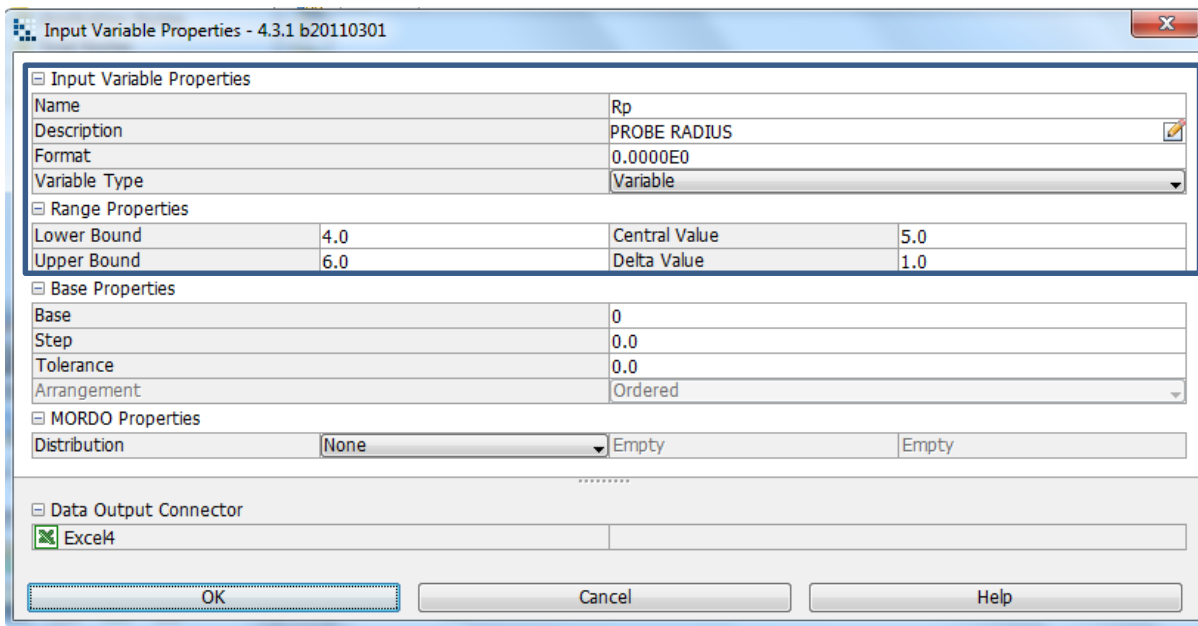


Image 7.9: Probe Radius is determined by lower and upper bound range properties, as shown in the input variable node properties dialog

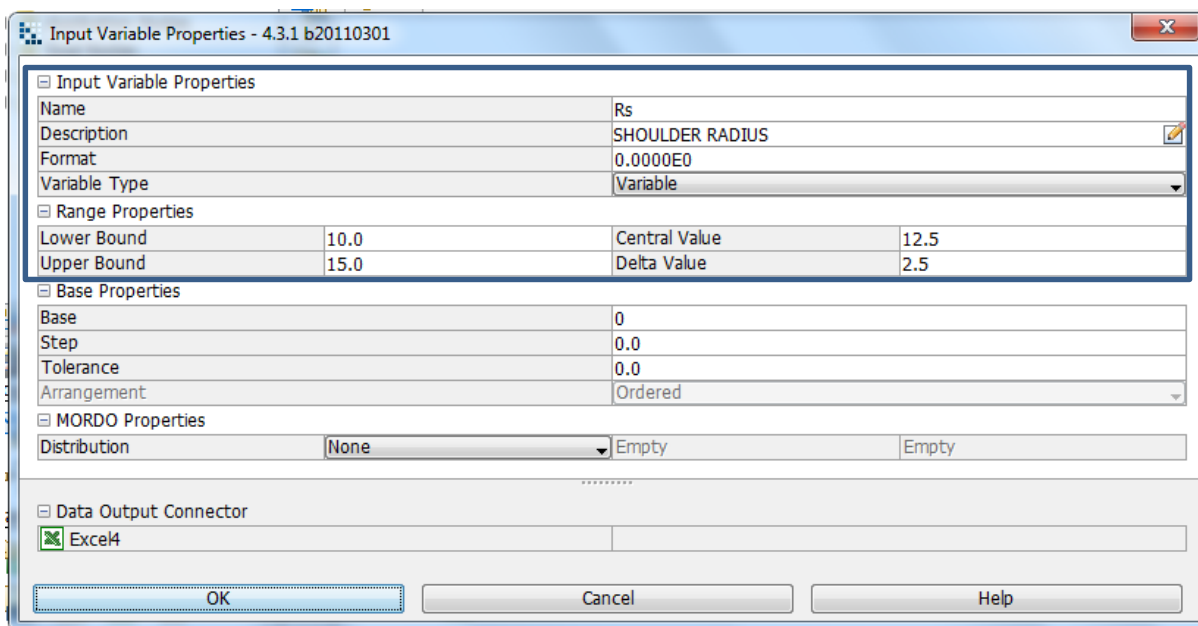


Image 7.10: Shoulder radius is determined by lower and upper bound range properties, as shown in the input

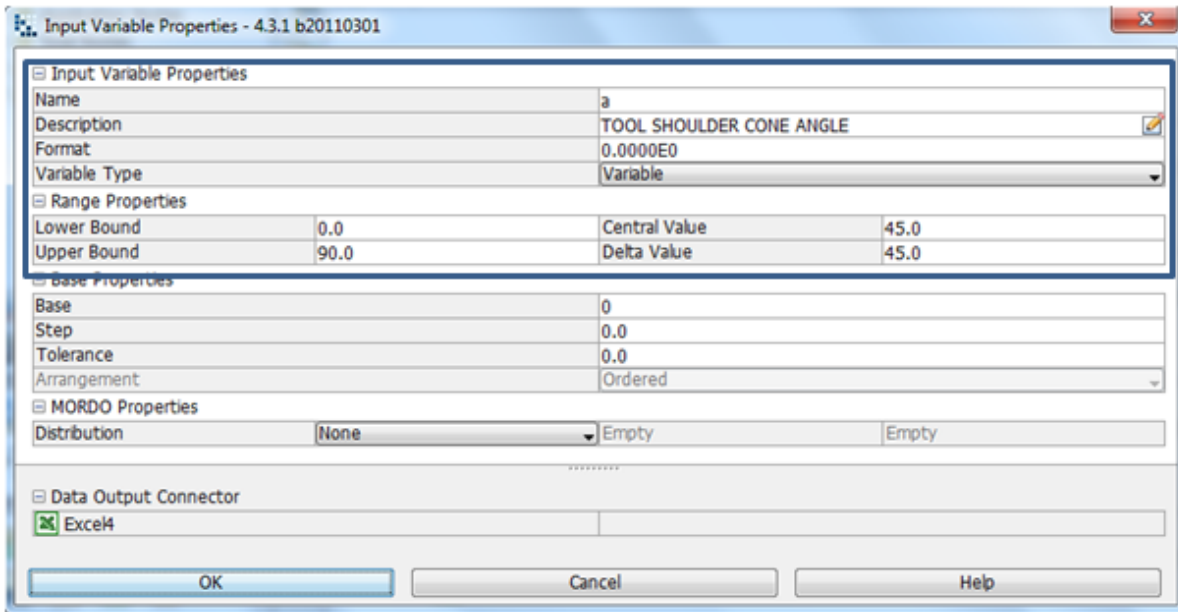


Image 7.11: Tool shoulder angle is determined by lower and upper bound range properties, as shown in the input variable node properties dialog

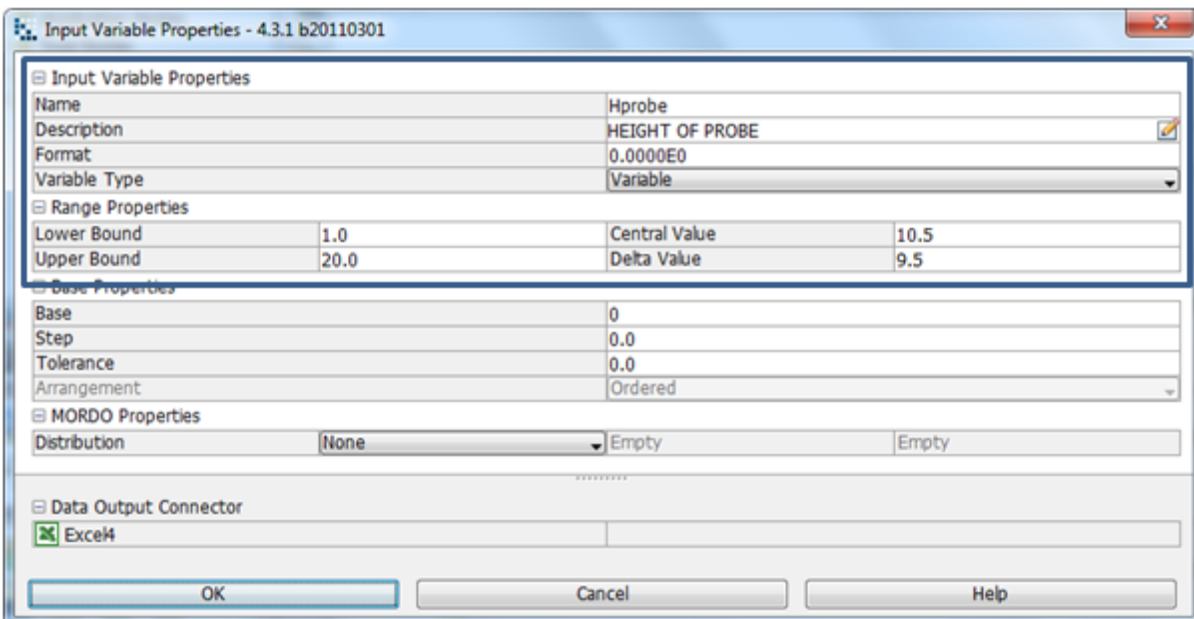


Image 7.12: Probe height is determined by lower and upper bound range properties, as shown in the input variable node properties dialog

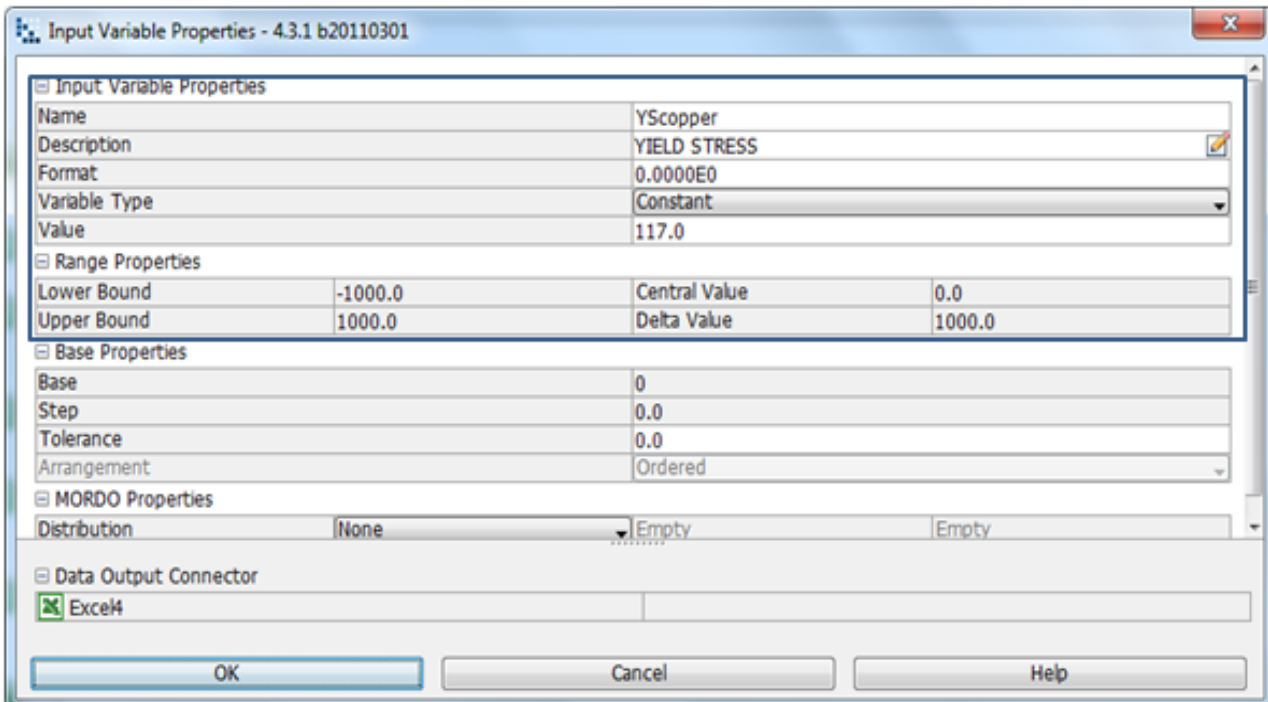


Image 7.13: Copper material yield shear stress 117 MPa is chosen, where the variable type constant hence the lower and upper bound is fixed

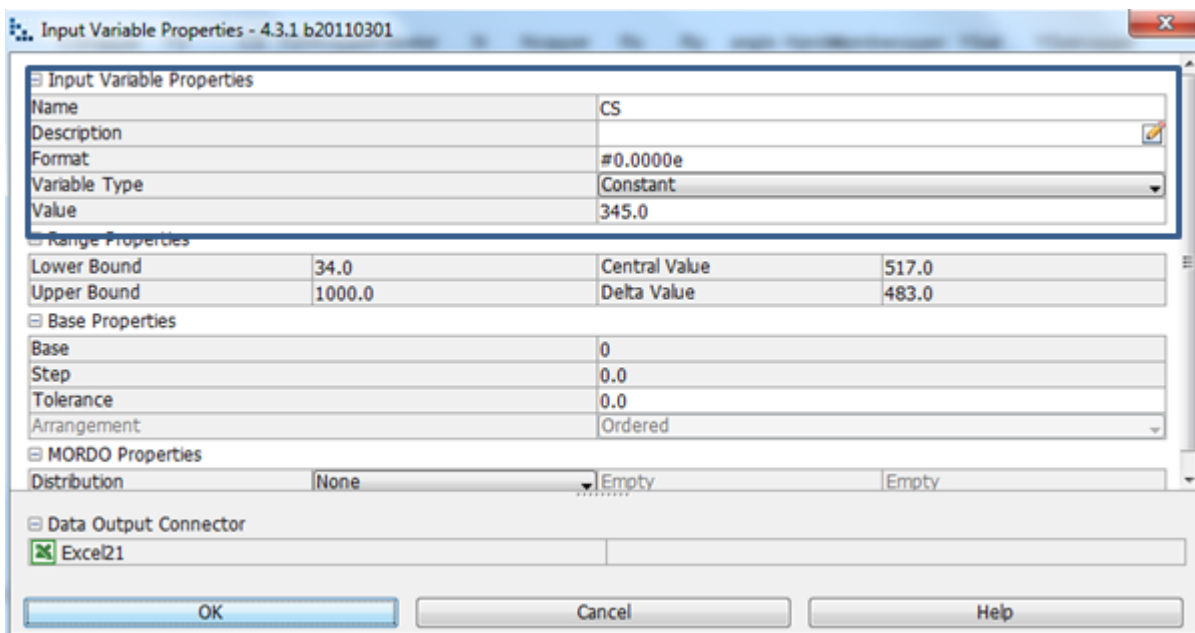


Image 7.14: CS-Al2024-T3 material contact shear stress 345 MPa is chosen, where the variable type constant hence the lower and upper bound is fixed

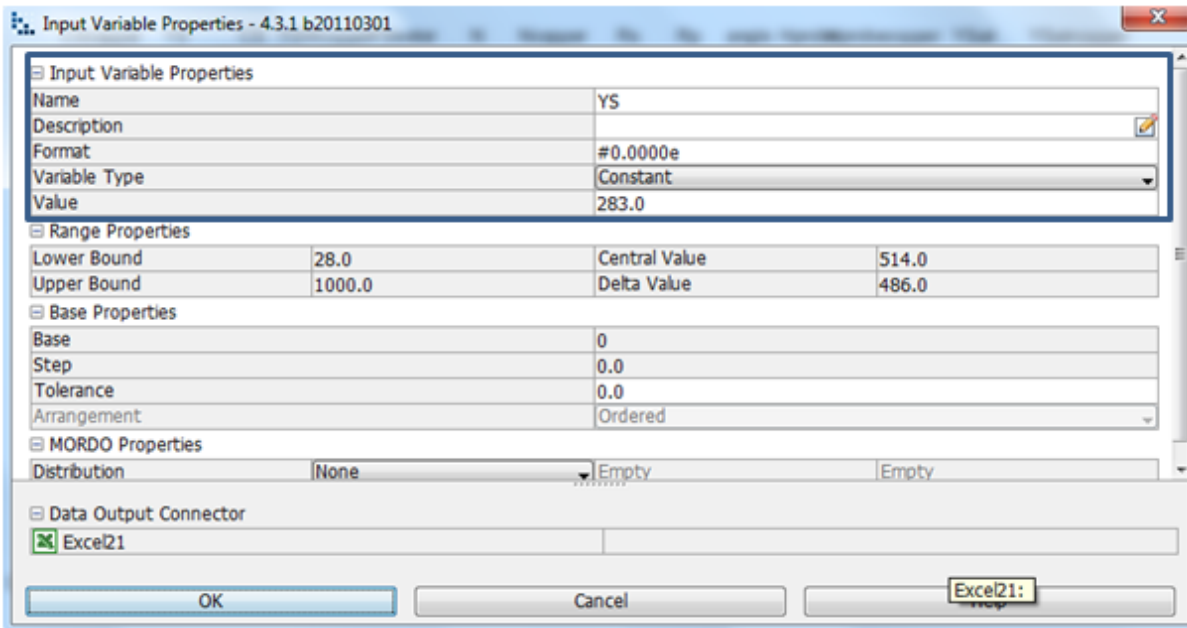


Image 7.15: Copper yield shear stress is chosen where value is 283 MPa and the variable type constant hence the lower and upper bound is fixed

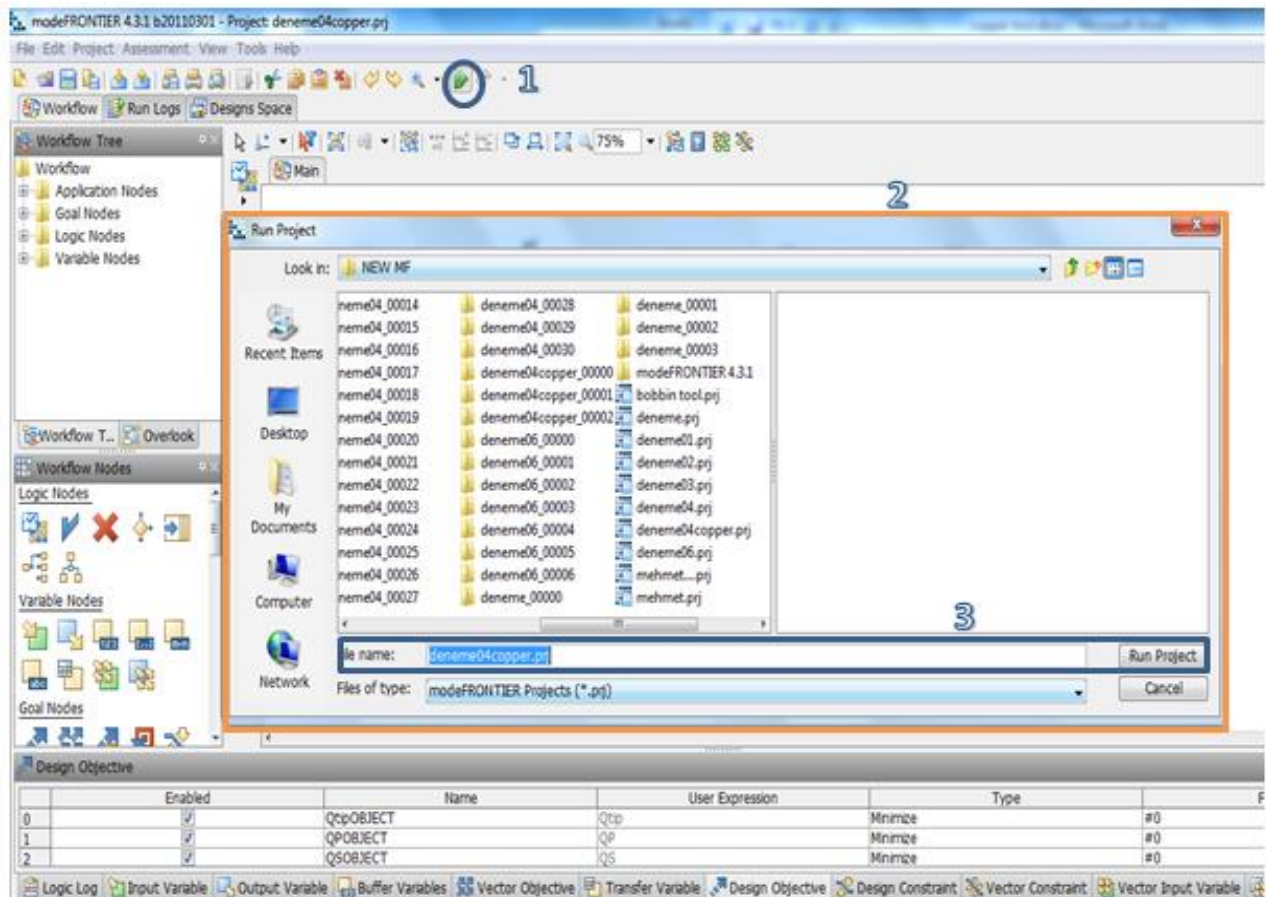


Image 7.16: Click on run/stop icon (1). Run project box will pop up (2). Click on run project (3) to start design project

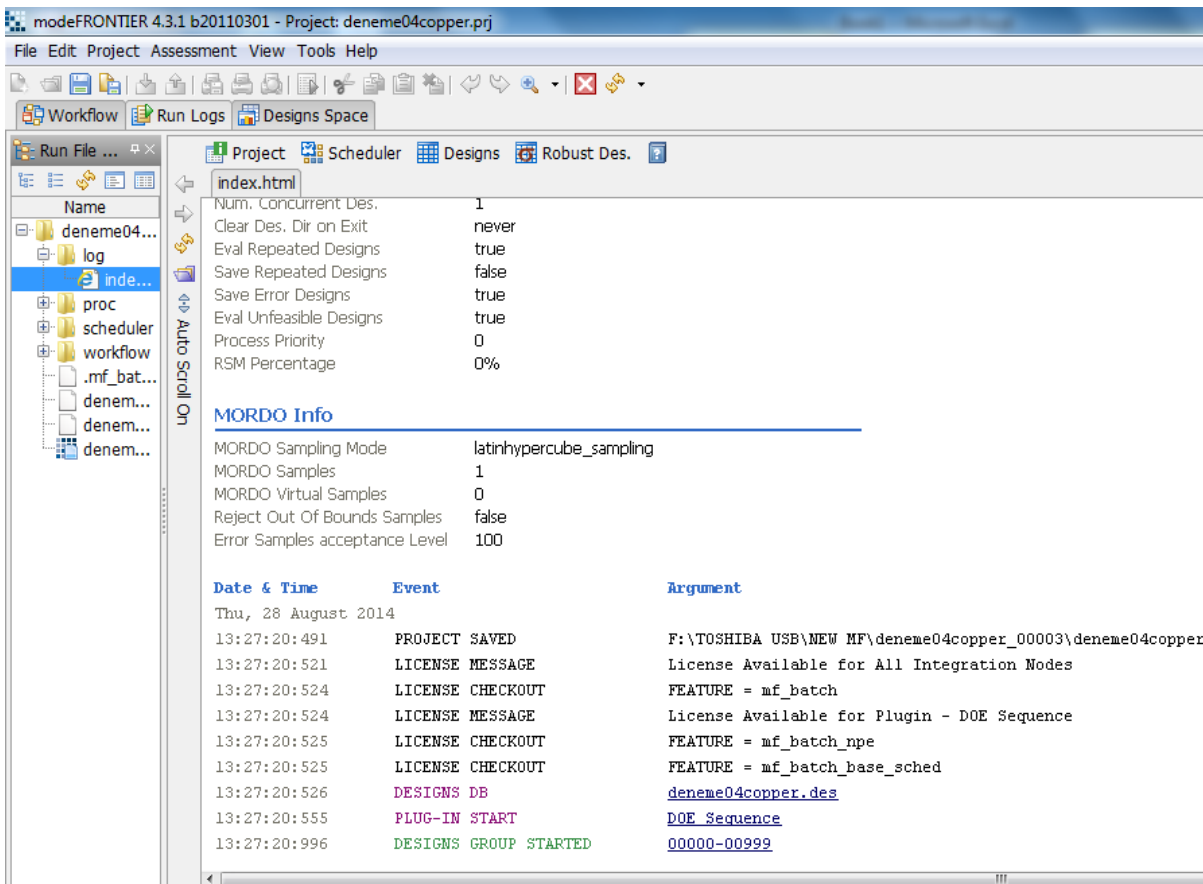


Image 7.17: Before project runs, a project info index will be shown. As seen in the above image.

7.3.2. Multi History Charts and Parallel Co-ordinate Charts: Innovative Tool Design

The history chart for an innovative tool, heat generation of the shoulder versus the shoulder radius is a representation of the feasibility of the design both on a real and virtual (Chart 7.1), the same for the parallel co-ordinates, demonstrating the increased feasibility that has been created by the design (Chart 7.2). The multi history chart (Image 7.3) shows a clear representation of the Qpobject increased heat generation from the tools probe side surface and the tool shoulders cone angle, parallel coordinates have been created from the innovative tool Qprobe vs. the tool shoulder cone angle (Chart 7.4). Heat generation from the probe tip (Qprobe) vs. tool tip is represented on a Multi history chart (Chart 7.5) which demonstrates the feasibility both real and virtual and the increased heat generation from the Qtipobject. The multi history chart (Chart 7.6) are a creation from the tool Qshoulder vs rotational speed. (Image 7.7) shows a representation of the heat generations that is increased by rotational speed on a parallel co-ordinate chart. Multi history as created from Innovative tool Qprobe tip vs. Rotational Speed (Chart 7.8) Once all is formulated, Parallel Co-ordinates (Chart 7.9) has been accurately created to represent the total heat generation (QT) versus the rotational speed, it then demonstrates the increased heat generation and feasibility, multi history is created from the innovative tool QT vs. rotational speed (Chart 7.10). Parallel co-ordinates as created from the design QT vs. Rotational speed (Chart 7.11). Multi-History Chart is from the innovative tools QT total heat generation vs. Rotational Speed to indicate feasibility, (Chart 7.12) thereafter a Parallel co-ordinate chart demonstrates the increased feasibility of the tool (Chart 7. 13).

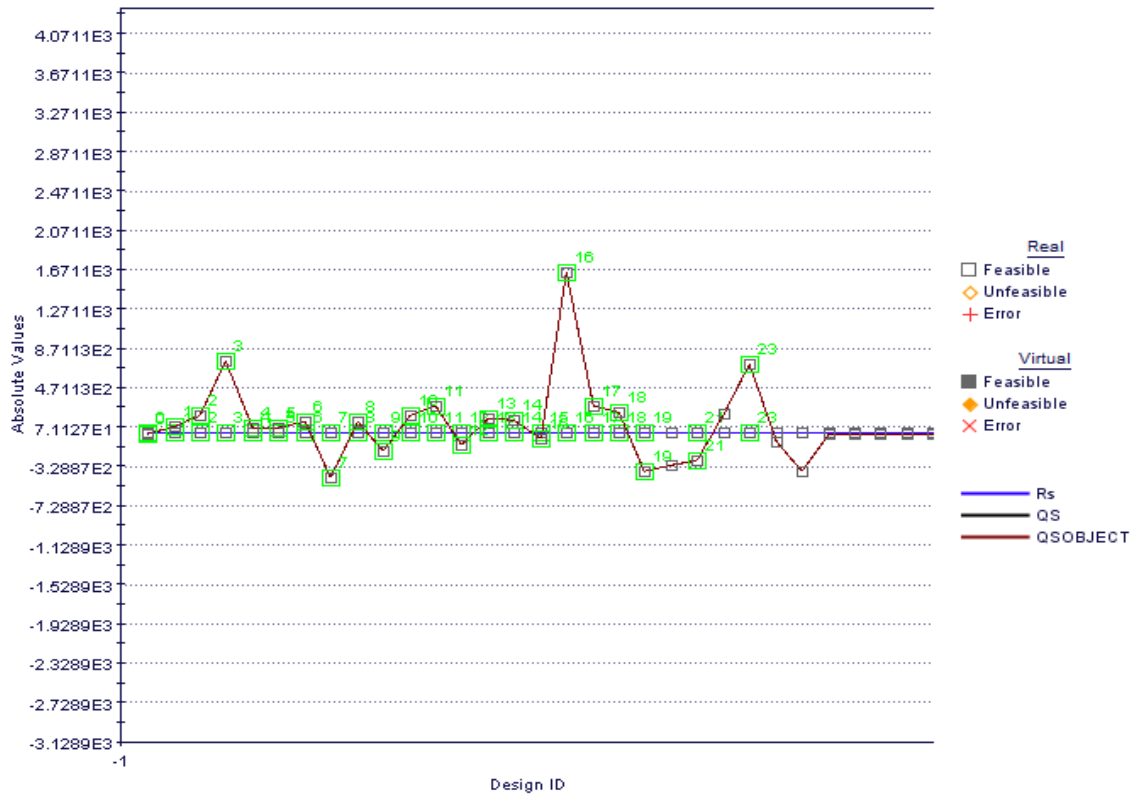


Chart 7.1: Multi-History Chart on Designs Space as created from Innovative tool Qshoulder vs Shoulder Radius

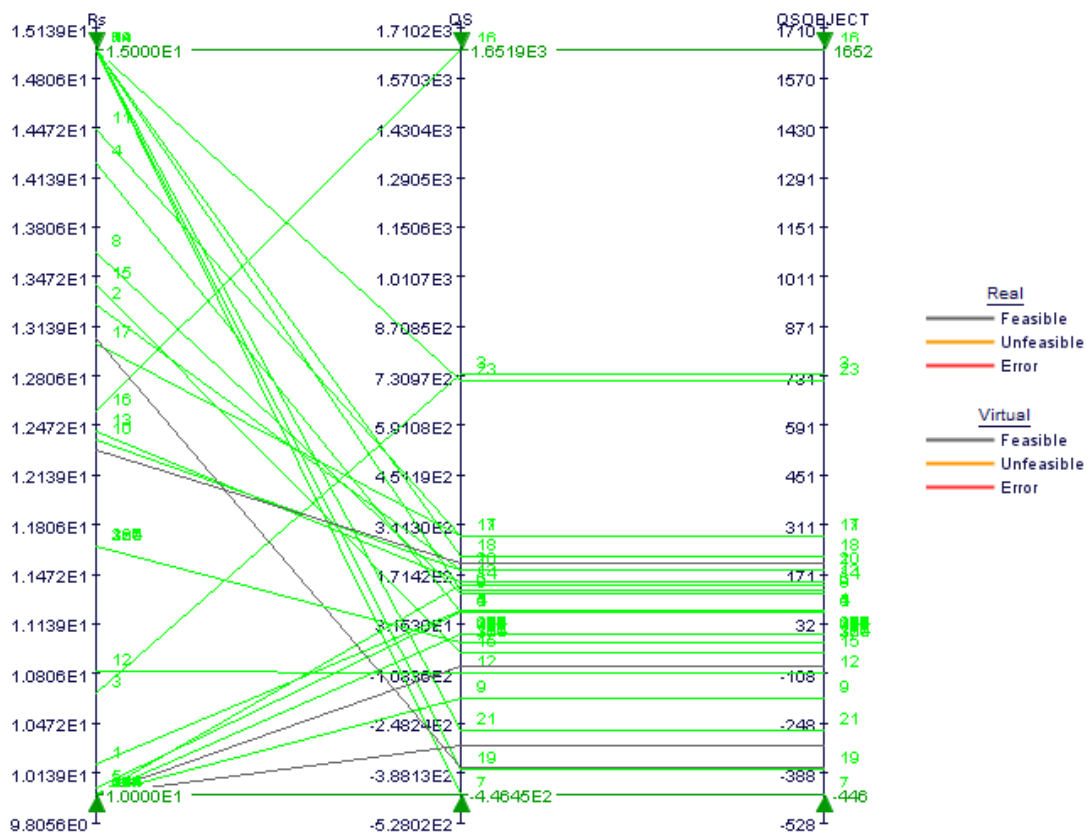


Chart 7.2: Parallel Coordinates as created from Qshoulder vs. Shoulder radius, Rs

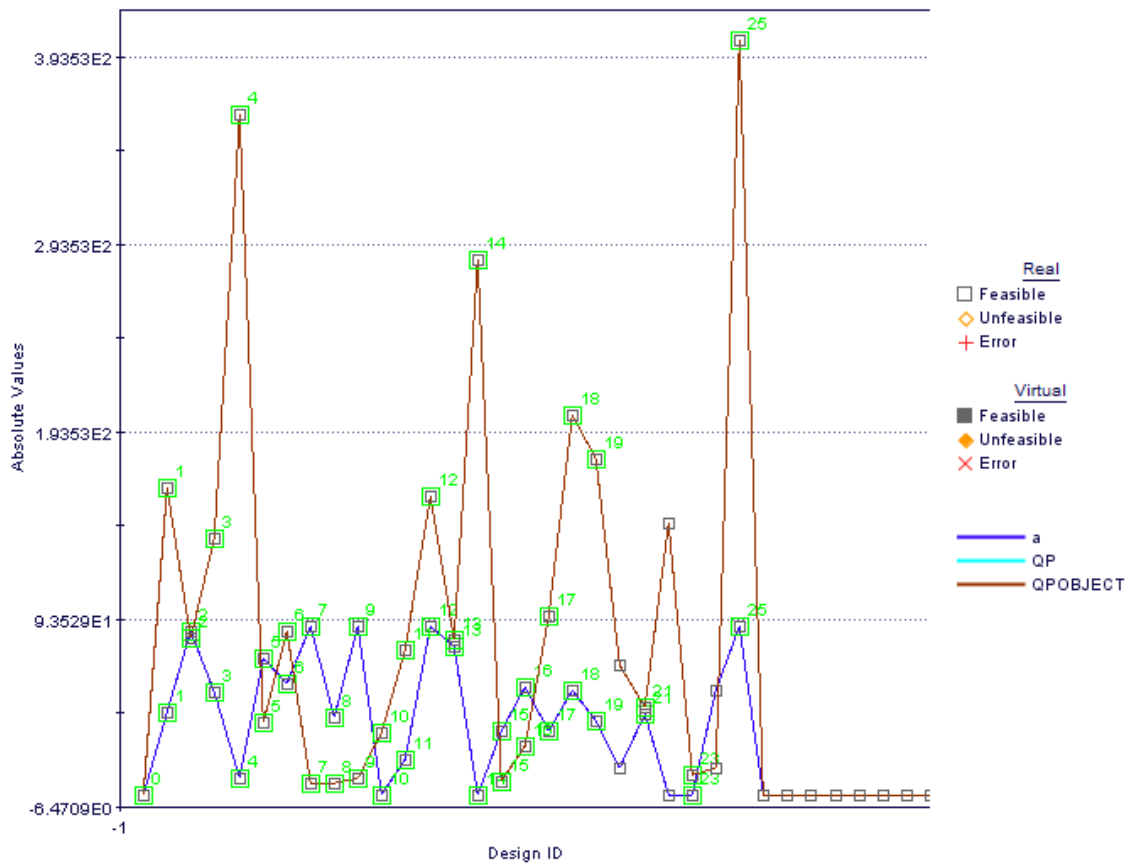


Chart 7.3: Multi-History Chart on Designs Space as created from innovative tool Qprobe side vs Tool shoulder cone angle

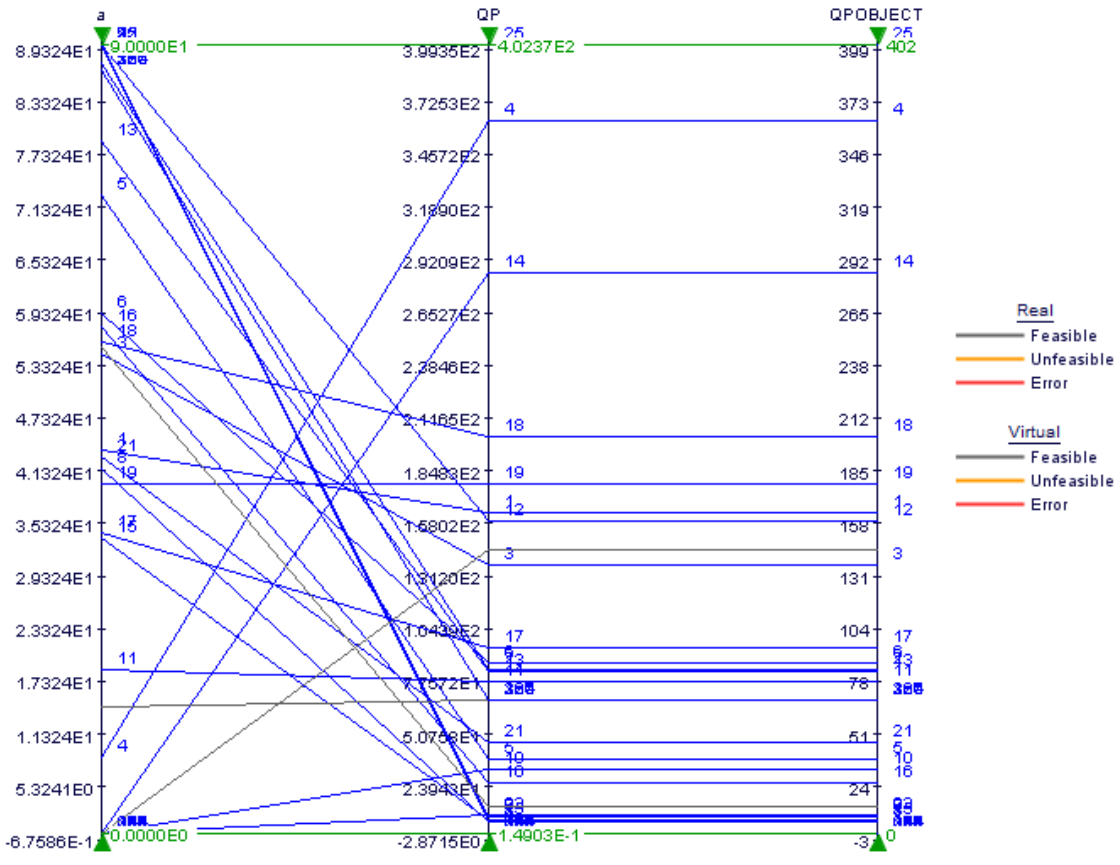


Chart 7.4: Parallel Coordinates as created from Innovative tool Qprobe side vs. Tool shoulder cone angle

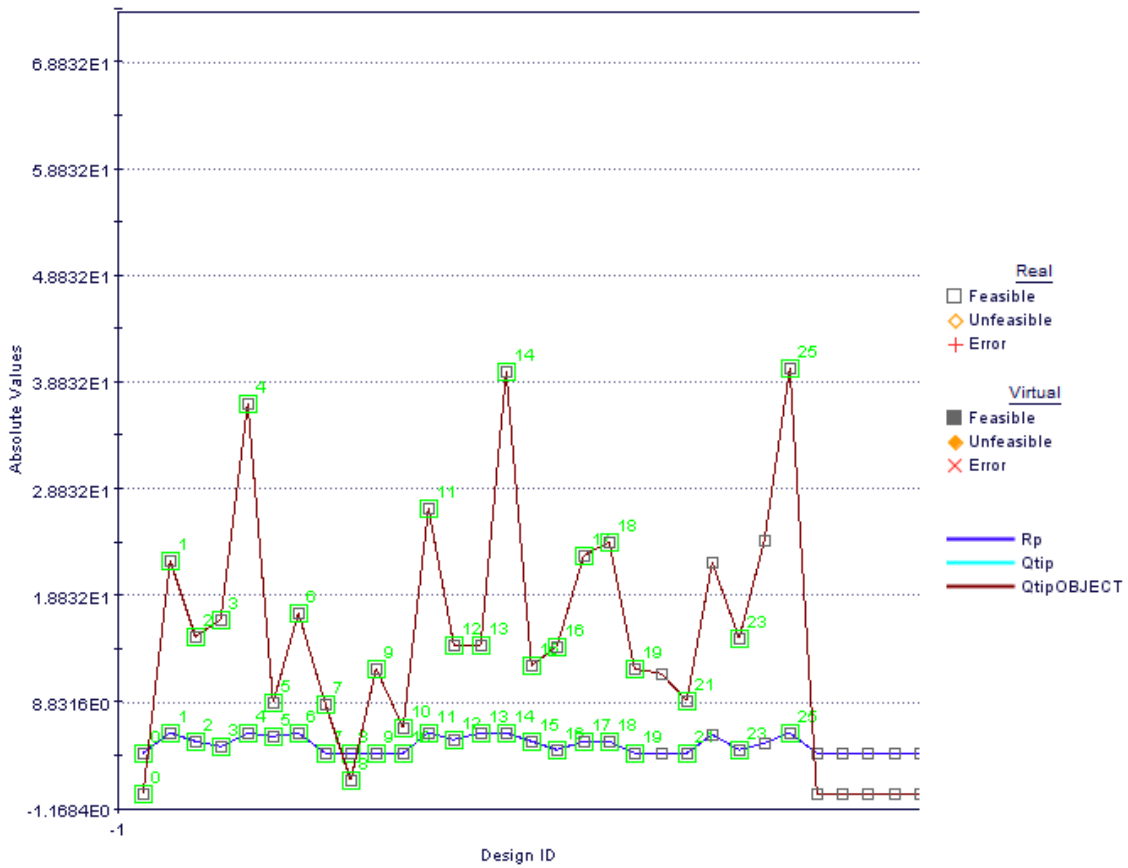


Chart 7.5: Multi-History Chart on Designs Space as created from innovative tool Qprobe tip vs Tool tip

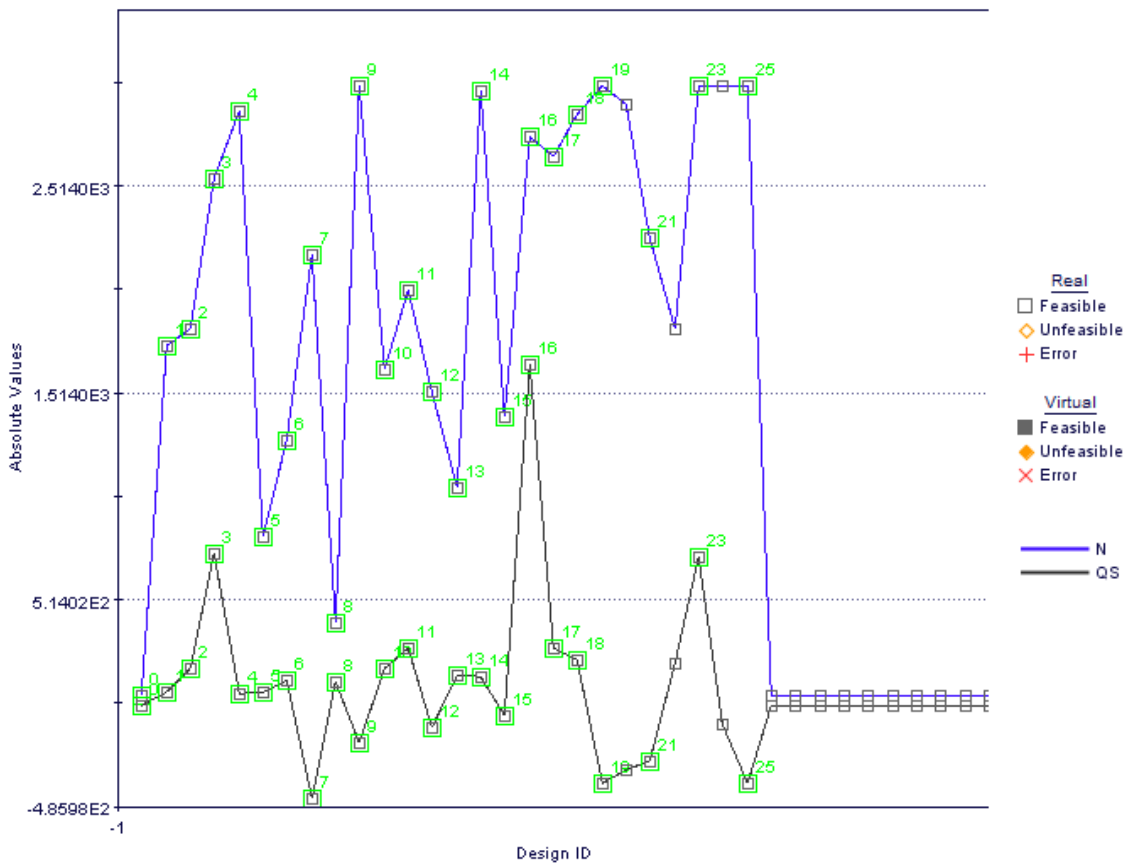


Chart 7.6: Multi-History Chart on Designs Space as created from innovative tool shoulder vs Rotational Speed

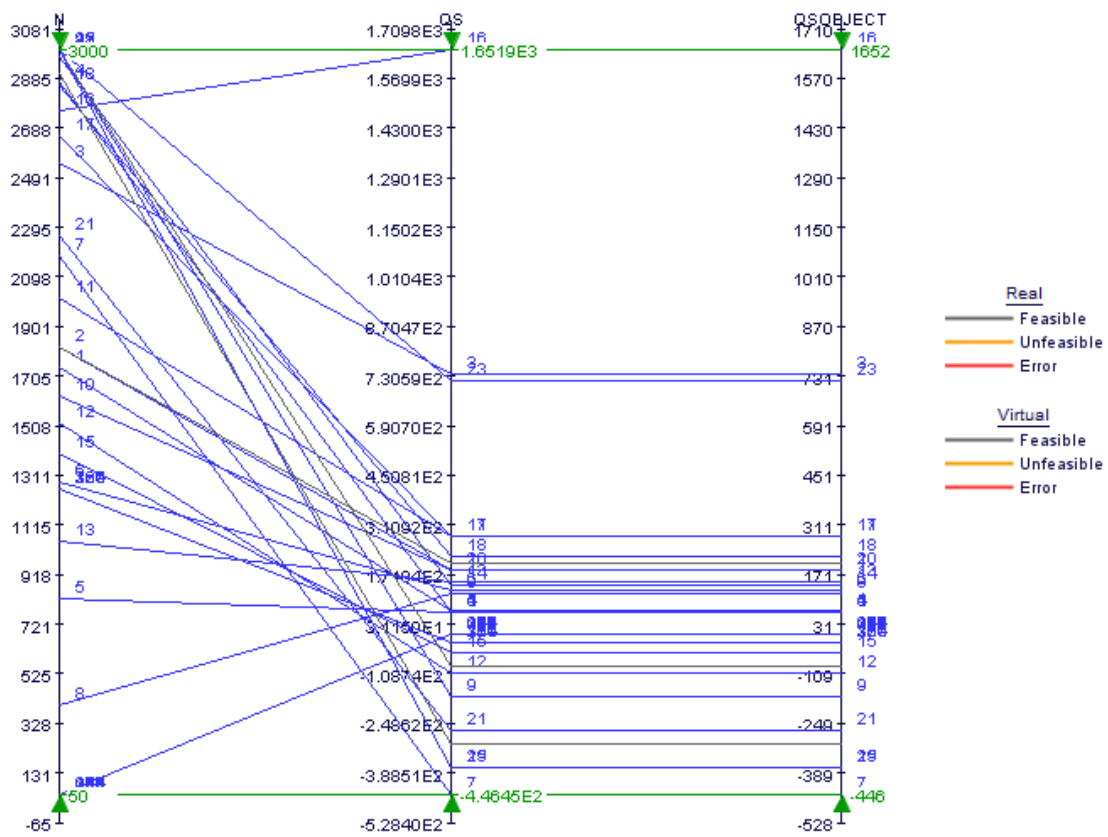


Chart 7.7: Parallel Coordinates as created from Innovative tool Qshoulder vs. Rotational Speed

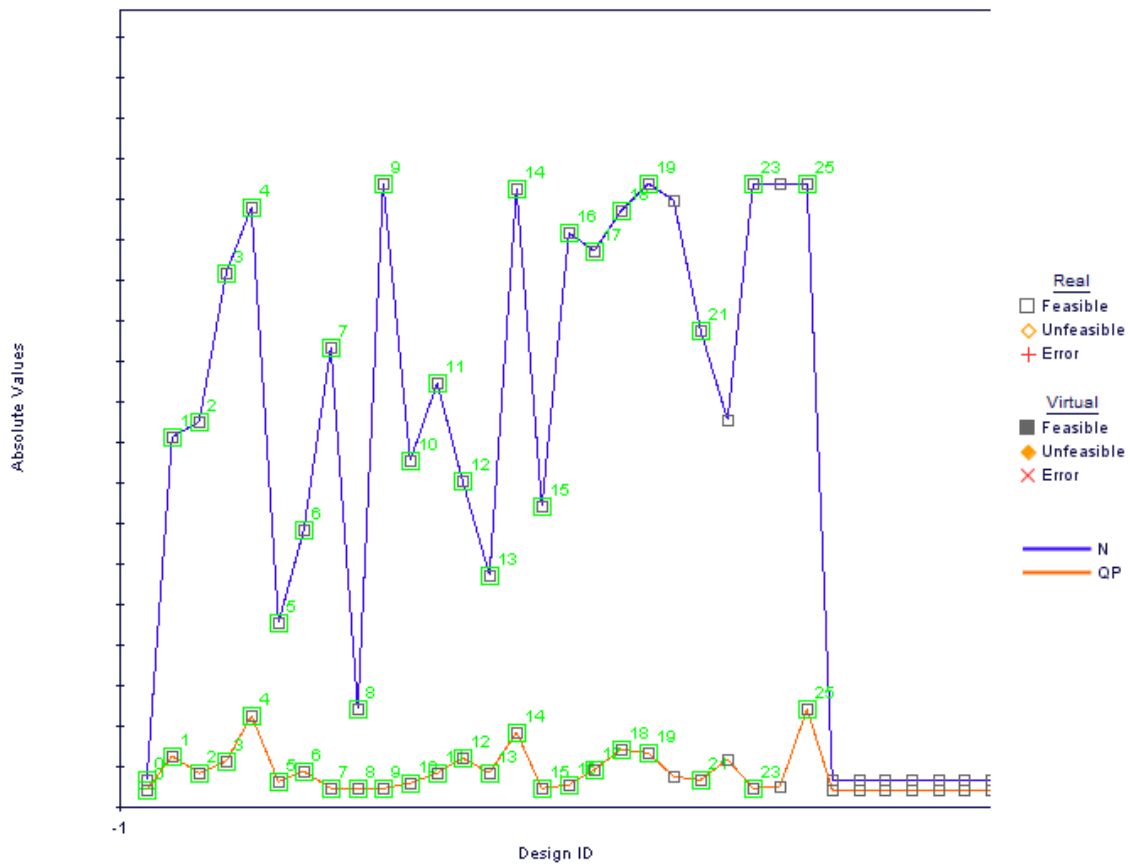


Chart 7.8: Multi-History Chart on Designs Space as created from innovative tool probe side vs Rotational Speed

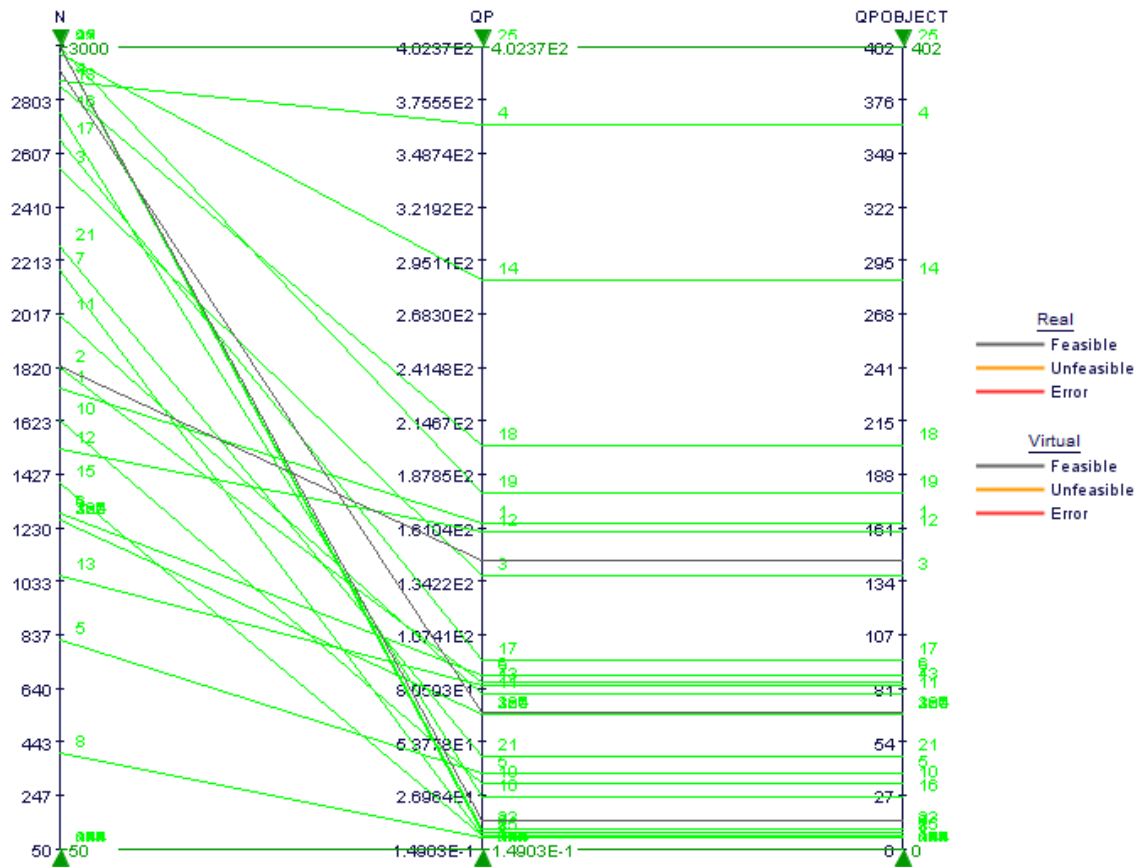


Chart 7.9: Parallel Coordinates as created from Innovative tool Qprobe side vs. Rotational Speed

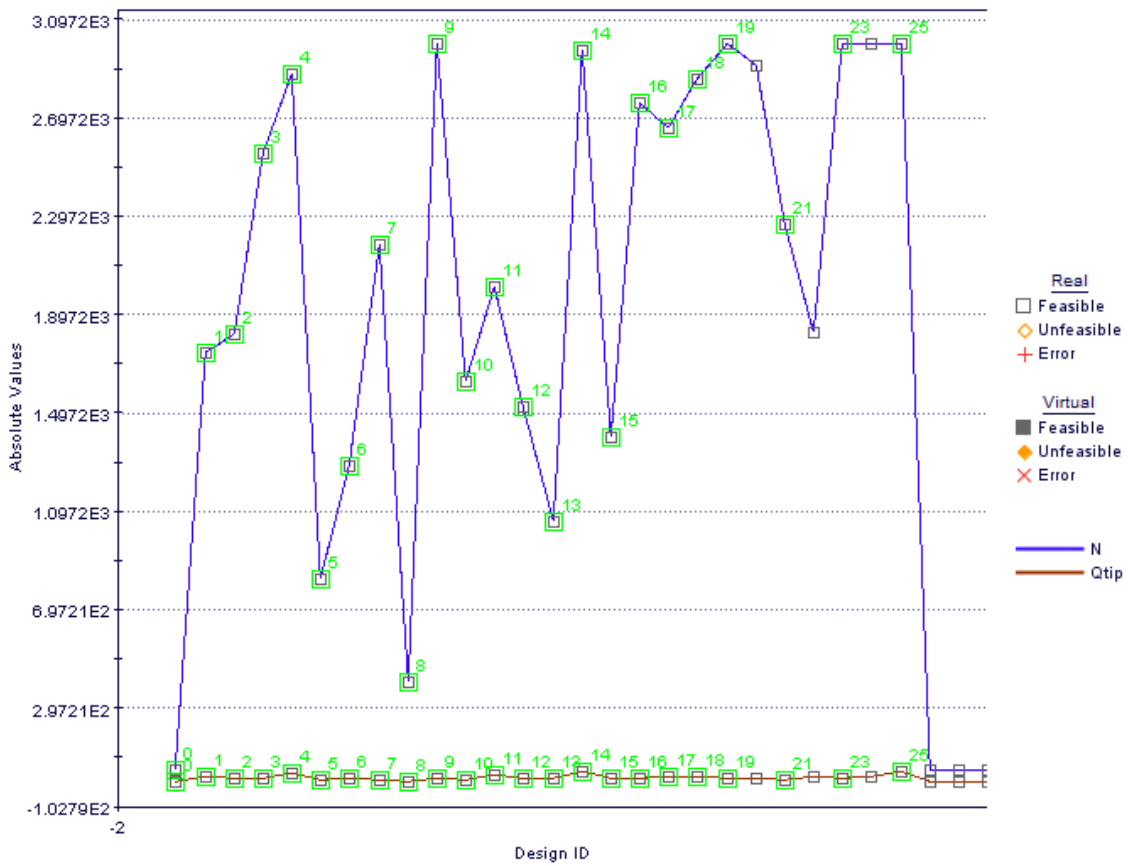


Chart 7.10: Multi-History Chart on Designs Space as created from innovative tool probe tip vs Rotational Speed

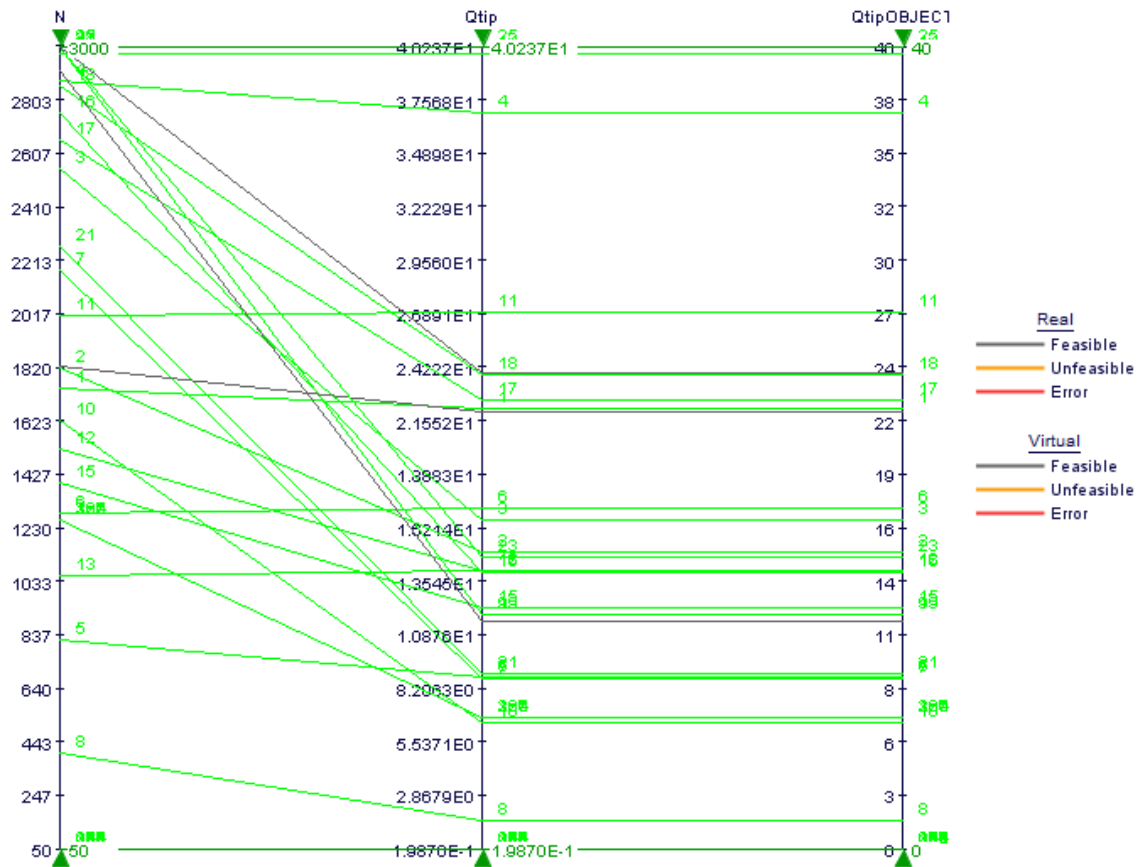


Chart 7.11: Parallel Coordinates as created from Innovative tool Qprobe tip vs. Rotational Speed

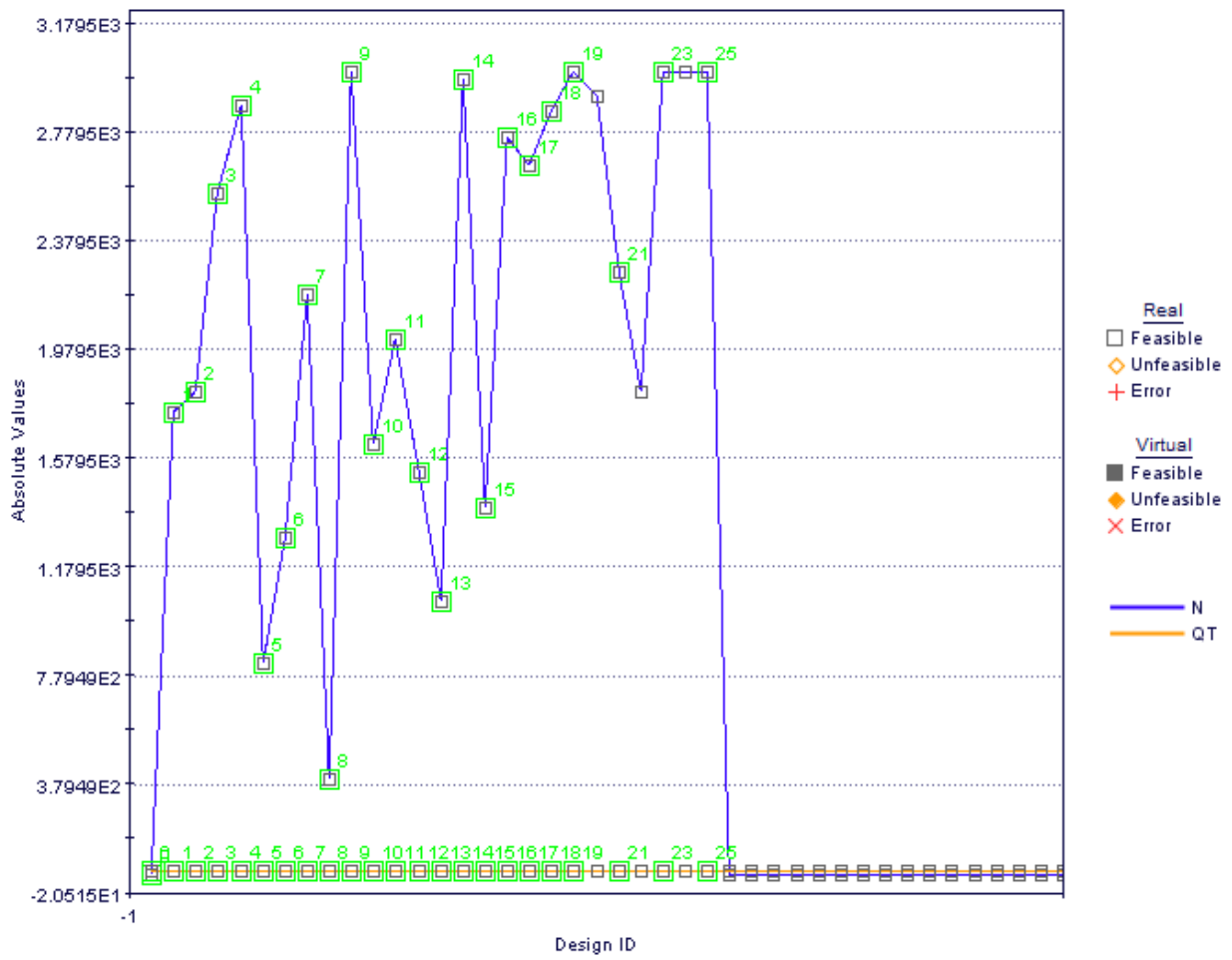


Chart 7.12 Multi-History Chart on Designs Space as created from innovative tool QT total heat generation vs Rotationa Speed

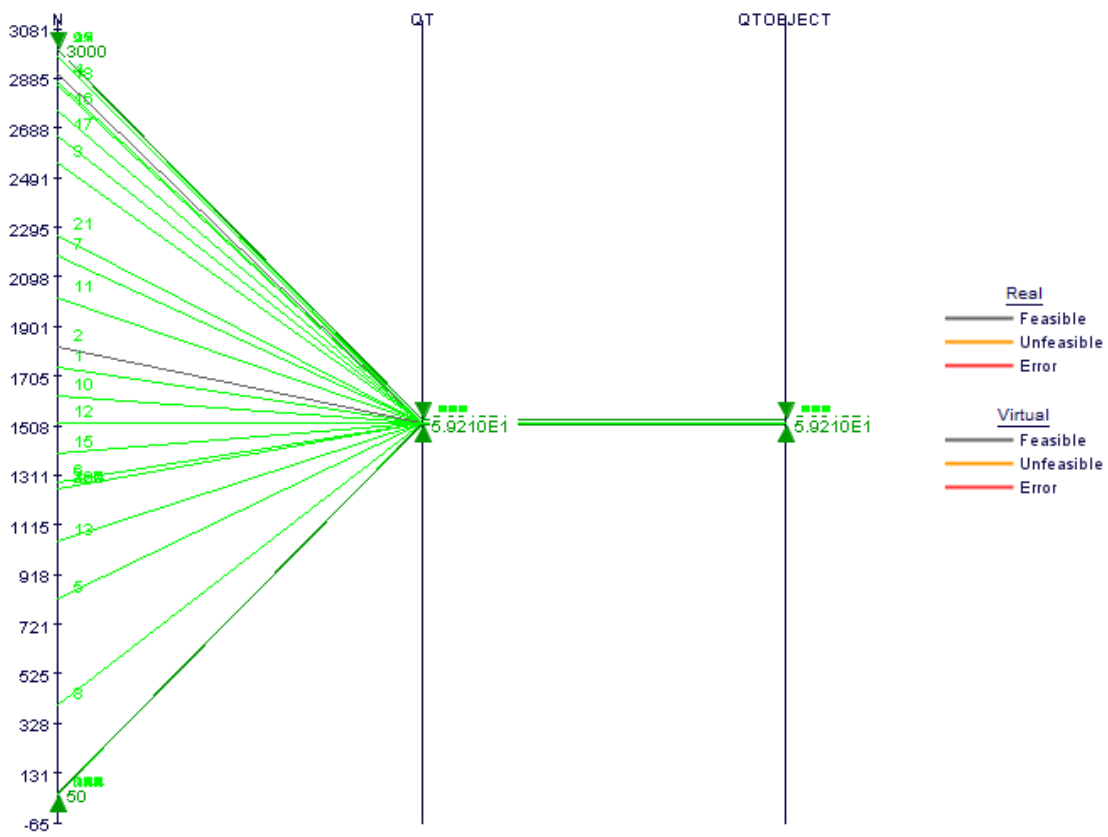


Chart 7.13: Parallel Coordinates as created from Innovative tool QT total heat generation vs. Rotational Speed

8. Heat Loss Conditions

8.1. Standard Tool Heat Loss Conditions

8.1.1. Heat Dissipation

Heat generation and heat dissipation must be adjusted and balanced to obtain an agreement with experimental temperature values [82]. As mentioned before, the heat in FSW is generated by the frictional effect and by plastic deformation associated with material stirring. The heat is dissipated into the work piece leading to the TMAZ and the HAZ, depending on the thermal conductivity coefficient of the base material. The heat loss occurs by means of conduction to the tool and the backing plate, and also by means of convective heat loss to the surrounding atmosphere. The heat lost through convection/radiative is considered negligible [83].

8.1.2. Heat Loss within the Tool

Only a small fraction of the heat is lost within the tool itself. This value may be estimated from a simple heat flow model for the tool. Measuring the temperature at two locations along the tool axis, allows a simple evaluation of the heat losses into the tool. The value of the heat loss into the tool has been studied using this approach, leading to similar conclusions. After modelling the temperature distributions in the tool and comparing it with experimental results, various authors conclude that the heat loss is about 5% [84, 85].

8.1.3. Heat Loss by the Top Surface of the Workpiece

The boundary condition for heat exchange between the top surface of the work piece and the surroundings, beyond the shoulder, involves considering both the convective and the radiative heat transfer, which can be estimated using the following differential equation [83]:

$$-k \frac{\partial T}{\partial z} \Big|_{top} = \sigma \varepsilon (T^4 - T_a^4) + h(T - T_a) \quad (8.1)$$

Where σ is the Stefan–Boltzmann constant, ε is the emissivity, a T is the ambient temperature and h is the heat transfer coefficient at the top surface.

8.1.4. Heat Loss by the Bottom Surface of the Workpiece

Most of the FSW process heat is dissipated through the backing plate due to the contact with the clamps. The heat loss through the contact interface between the bottom of the work piece and the backing plate has been introduced in numerical models using different approaches [5]. In fact, the contact conditions between the work piece and the backing plate must be carefully described at the moment of the modelling process. Thus various options can be considered:

- No backing plate. The lower surface of the work piece is assumed to be adiabatic;
- Perfect contact between work piece and backing plate;
- Perfect contact under the tool region only. This option is suggested by experimental observations: the high pressures under the tool lead to a visible indentation of the upper surface of the blanking plate along a width approximately equal to the diameter of the tool shoulder (Fig. 8).
- Introduction of a value for the convection coefficient between the work piece and the backing plate.

Ulysse did not include the backing plate in the model, using the assumption of simply adiabatic conditions at the work piece/backing interface [86]. A reasonable agreement between predicted and measured temperatures was attained, although measured temperatures tended to be consistently over-predicted by the model. Other authors consider the presence of a backing plate in the model and simulate the contact condition between the work piece and the backing plate. Colegrove et al. proposed a contact conductance of $1000 \text{ Wm}^{-2}\text{K}^{-1}$ between the work piece and the backing plate, except under the tool region where a perfect contact is modelled [74].

The majority of dissipated heat flows from the work piece to the backing plate at the interface under the tool. Owing to the applied pressure, the conductance gap in this location is smaller than the conductance gap to the surrounding areas, and by this way locally maximizing the heat flow. The use of a backing spar, in opposition to a fully backing plate, reduces the number of equations to be solved and shortens the computer processing time, while still capturing the essential nature of heat flow between the work piece and backing plate [2] (Image 8.1). The width of the backing spar is usually equal to the tool diameter, and the height varies within the thicknesses range of the backing plate. Khandkar et al. use a 12 mm backing plate [17], Hamilton et al. assume 25.4 mm [87], while Colegrove et al. adopt a 60 mm backing plate [13]. It can be concluded that the larger the thickness of the backing plate, the greater the heat dissipation.

Zahedul et al. propose a value for the convection coefficient between the work piece and the backing plate by comparing the results of their 3D finite element models with the experimental results [88]. They compare four different bottom convection coefficients and conclude that a value too high for this coefficient leads to an underestimating of the maximum temperature.

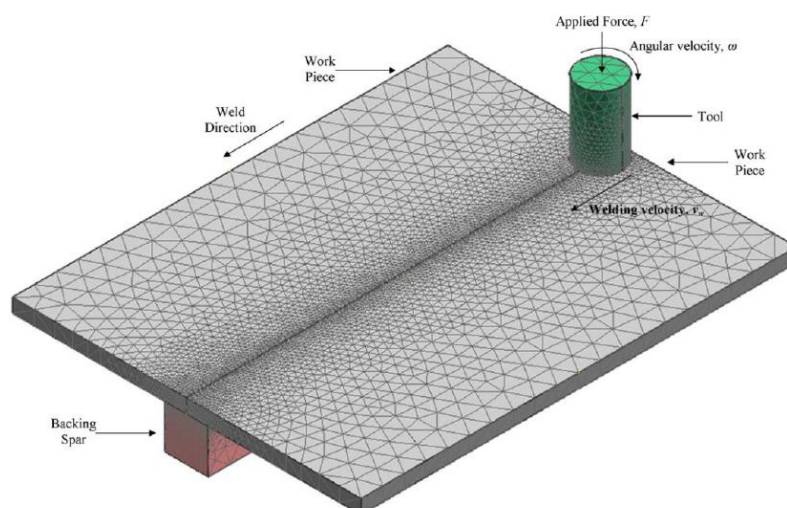


Image 8.1: Employing a backing spar to model the contact condition between work piece and backing plate [2]

In the case of FSW the tool is just not part of the heat source but is itself a not insignificant avenue for heat loss. This avenue along with all other avenues for heat loss is presented schematically in (FIG 8.1) and incorporated within the flow (loss) of heat equation (denoted by Q = thermal energy),

$$Q_{total} = Q_{stir\ zone} + Q_{tool} + Q_{workpieces} + Q_{atmosphere} + Q_{backing\ bar} + Q_{clamps} \quad (8.2)$$

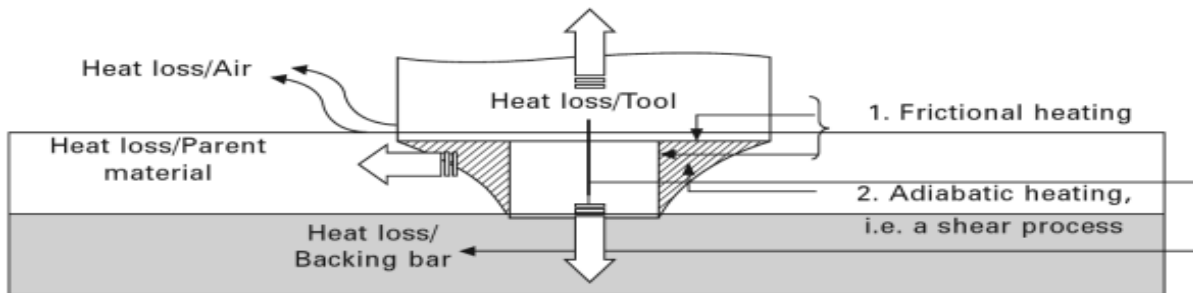


FIG: 8.1 Heat flow (loss) pathways that are acknowledged in the literature to occur during classical, i.e. single-sided, friction stir welds [50]

Obviously the thermal diffusivity, i.e. the ratio of thermal conductivity to the volumetric heat capacity of the materials, and the subsequent masses involved in each of the heat loss pathways, represented in fig 15 will and do have and do have an impact on weld formation. If the diffusivity is high, for example, the material cooling rate is high and the HAZ of the joint will be small. Conversely, a lower diffusivity leads to slower cooling and a larger HAZ. Furthermore, the rate of heat transfer will depend on the ability during FSW to maintain constant temperature gradients between the heat source and heat sink/s, i.e. this corresponds to the temperature difference potential or concentration potential energy that heat energy will flow from one region to another.

Evidence as to the importance heat loss avenues have in terms of stir zone formation is no better portrayed than through changes to backing bar material when used in FSW. Traditionally the backing bar or anvil material used for classical or single-sided friction stir welds has consisted of a structural steel that not only supports but also limits the potential for diffusion bonding of the aluminium to the anvil during processing. These steels normally have a thermal conductivity of between 10 and 20% that of the aluminium alloy being friction stir welded. Hence the anvil material acts not just to support the work piece but also as a barrier controlling heat transfer during processing.

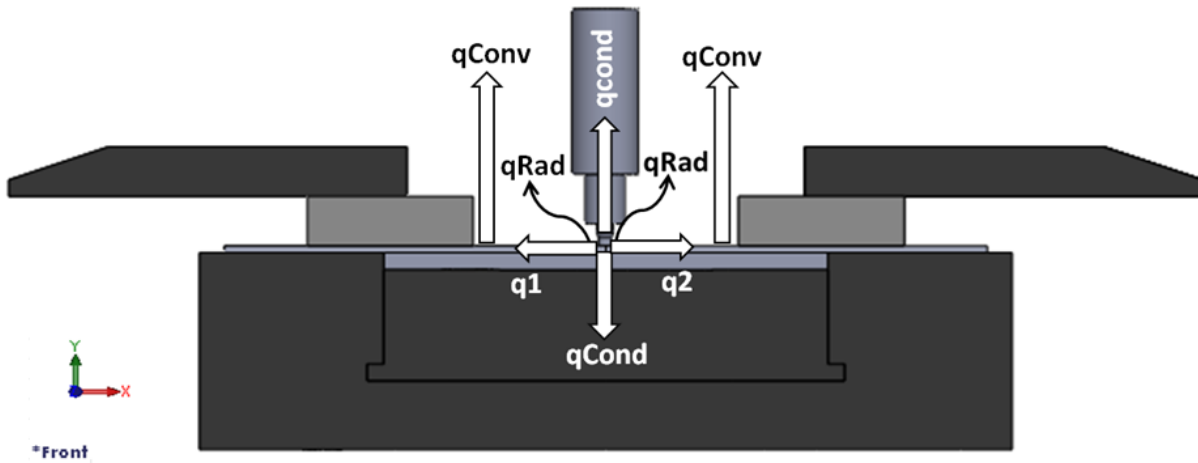
The temperature and the rate at which heat is lost is an important consideration when it comes to all hot working fabrications practices. For the case of precipitation hardening, i.e. heat treatable aluminium alloys, it is generally desirable, when producing these alloys to maintain as high a working temperature as possible, one which approaches but also inhibits undue melting. This is because higher temperatures are seen to help minimise recrystallization after solution heat treatment which further benefits strengths and stress corrosion resistance. Additionally it is desirable to achieve adequate homogenisation, though this is not always necessary since to eliminate soluble second phase particles it is the ability to return the soluble elements to solution during solution heat treatment that is important. A good solution is more readily achieved if the soluble elements have been in a solution at some point during processing. For thinner products this may not be necessary since coarse particles may be broken up during fabrication and so can be more readily returned to solution during an intermediate anneal or during a solution heat treatment. A homogenisation or intermediate anneal is necessary in order to

precipitate Cr, Zr or Mn from solid solution. This is an important processing step since the size and distribution of these particles determine the final degree of recrystallization. Here either increased time or temperature can be used to increase the solution of the soluble elements.

Since both temperature and time play a significant role in determining the microstructure and subsequent properties of precipitation hardening alloys it should come to no surprise that processing conditions including the backing bar and tool material type used to produce a friction stir weld through their capacity to transfer heat can and do have considerable influence when it comes to weld formation.

Zetter 2008 notes that the relative amounts of heat which can be lost through each of the major heat loss avenues, negating air have the potential to vary with increasing weld length over and above 2m of friction stir weld length. Additionally Zettler demonstrates that the relative amounts of heat and the direction loss are in fact influenced by the temperature of the tool and the ability of the tool support structure(spindle) to maintain a constant temperature gradient between the heat source (tool/ work piece interaction) and this avenue of heat transfer. The fact that there exists no standard set of FSW parameters which can be actively transferred to give optimized mechanical properties for the FSW for any commercial grade aluminium alloy and that process parameters are themselves not readily transferable across different welding machines has for a long time indicated that the construction of the FSW machine plays a much more significant role in processing parameter selection than it has been previously accredited for. The variability which exists in the literature for FSW parameters are not as many we would like to believe, a consequence of process robustness. It is true to say that FSW is a forgiving process in that for any welding machine there exist a window of parameters which will produce flaw free welds with good mechanical properties, unlike parameters established for other industrial deformation processes cannot be directly transfer across machines, however, makes it real just how dependent the process is on the thermal influence provided by the result of machine and clamping construction.

Naturally, FSW parameters such as tool rotation speed contribute to how rapidly the tool heats up. Higher the tools rotational speed will result in a greater friction heat at the work piece. A slip at the interface between the tool and the work piece further increases the potential for more heat to be lost vertically through the tool away from the stir zone and not radially into the work piece. As a consequence, process efficiency diminishes since the thermal energy is developed is not completely utilised in the development of the stir zone formation. At the same time an increasing tool temperature causes the tool support structure to heat up, the capacity to maintain heat uptake through the toll will therefore be subject to the ability of the tool support (The spindle construction) to provide for constant temperature gradients between the heat source and this avenue of heat loss. The effect of a diminishing temperature gradient between the heat source and heat sinks is not a new phenomenon to the FSW process.



Drw 8.1: Thermal Aspect for the Standard Tool Design. [Uslu, M.Y, (2014), *Thermal aspect standard tool design*, University of the Witwatersrand]

$$h_{up} = 12.25 \text{ W/m}^2\text{K}$$

$$h_{down} = 6.25 \text{ W/m}^2\text{K}$$

$$q_b = 100 \text{ W/m}^2\text{K}$$

$$T_0 = 25 \text{ }^\circ\text{C} = 299 \text{ K}$$

$$T = 662 \text{ }^\circ\text{C} = 935 \text{ K}$$

$$\sigma = 5.67 \times 10^{-8} \text{ Wm}^{-2}\text{K}^{-4}$$

$$\varepsilon = 0.3$$

$$x = 4 \text{ mm}$$

$$y = 5 \text{ mm}$$

$$a = 500 \text{ mm}$$

$$b = 115 \text{ mm}$$

$$L_1 = 2 \times 10^{-3} \text{ m}$$

$$L_2 = 2 \times 10^{-3} \text{ m}$$

$$K = 120 \text{ W/mK}$$

$$q_p = A_{plate} h_{up}(T_0 - T) + \varepsilon\sigma(T_{amb}^4 - T^4)$$

$$q_{up} = 0.115 \times 10^{-6} \times 12.25 \times (299 - 935) + 0.3 \times 5.67 \times 10^{-8} (299^4 - 935^4)$$

$$q_{up} = 2375.355885 \text{ W}$$

$$q_{down} = h_{down}(T_0 - T) + \varepsilon\sigma(T_{amb}^4 - T^4)$$

$$q_{down} = 6.25 \times (299 - 935) + 0.3 \times 5.67 \times 10^{-8} (299^4 - 935^4)$$

$$q_{down} = 1936.515885 \text{ W}$$

$$q_{cond} = AK(T - T_{amb})/L$$

$$q_{cond} = 20 \times 10^{-6} \times 120 \times (935 - 299) / 4 \times 10^{-3}$$

$$q_{cond} = 381.6 \text{ W}$$

(8.3)

8.2. Mode Frontier Simulation: Standard Tool Heat Loss Conditions

Input Data, Output Data and boundary variables definitions as shown on this Microsoft Excel Sheet file name [convection calculation modefrontier.xlsx](#) is used in Mode Frontier for this Design Project (Image 8.2): Since each component defining the Workflow is represented by a specific node which can be linked to other nodes, a proper node from the available Node Library toolbar or, alternatively, chosen by using the Workflow Nodes panel. It is shown all the input data output data and boundary variables in a Microsoft Excel workbook. The excel work books is used so that the equation for the rotational speed along with the heat generation is calculated where the results will be used in ModeFrontier to assist in the design .Once a Workflow Plan created by Mode Frontier Project as shown in deneme04.prj, also includes DOE (Design of Experiments) and DOE Sequence, as well as indicating Input Variables, Output Variables, Design Objectives + Gradients, Microsoft Excel Workbook and Logic End (Image 8.3). A workflow plan is created using a DoE (Design of Experiments) and a DOE Sequence on a new Overlook. Once this is open workflow nodes can be added on. Variable nodes which are the input nodes and the output nodes are used. Workflow nodes such as the schedulers, the logic switch and logic end is used. An application node is used for excel. A goal node which is the design objective+gradient node. Mode Frontier Input and Output Data is connected to Microsoft Excel Workbook .Excel workbook properties are used for basic node configuration where an Excel Workbook is selected. Once selected the input and out data is connected from the chosen Excel workbook (Image 8.4). An Interactive Selection used between Mode Frontier [convection mode.prj](#) and Microsoft Excel Workbook: [convection calculation modefrontier.xlsx](#) to determine Excel Workbook Properties for Mode Frontier. An interactive selection (Image 8.5) allows each input and output node to be configured in accordance to the Excel workbook. Where each variable is interactively selected to complete a work plan.

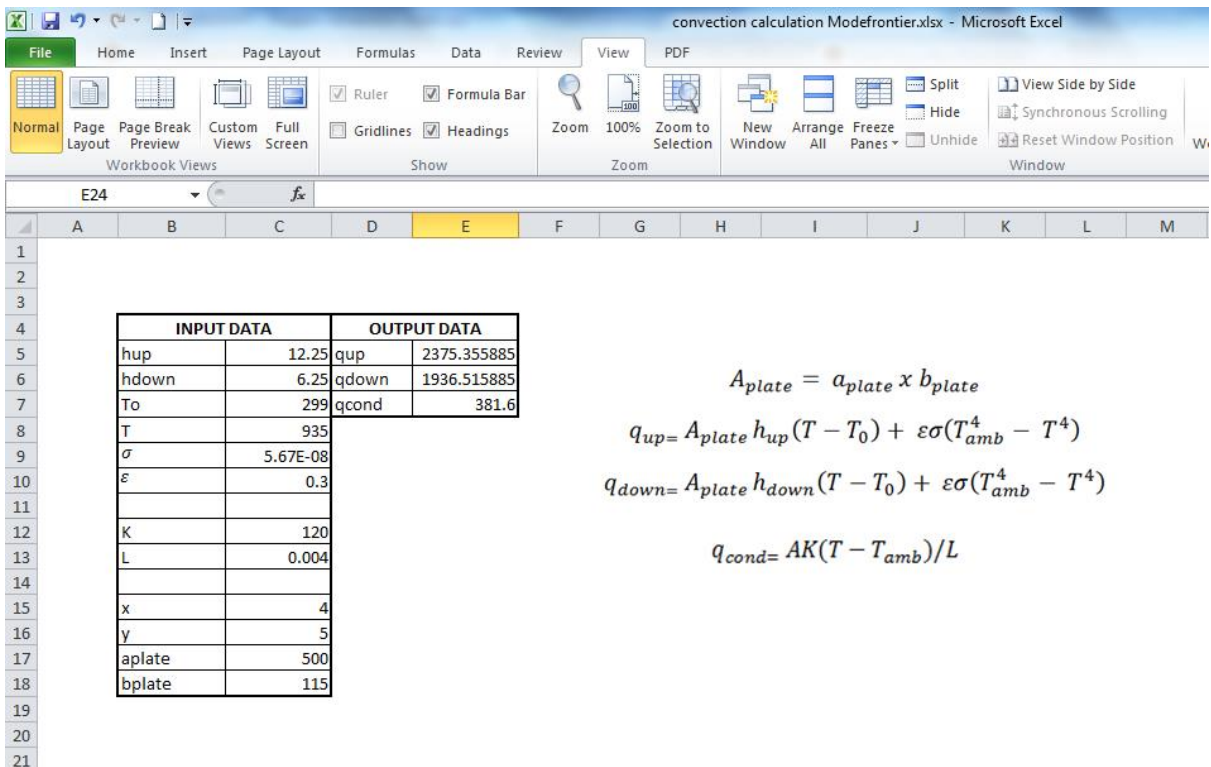


Image 8.2: Input Data, Output Data and boundary variables definitions as shown on this Microsoft Excel Sheet file name: convection calculation modefrontier.xlsx is used in Mode Frontier for Design Project

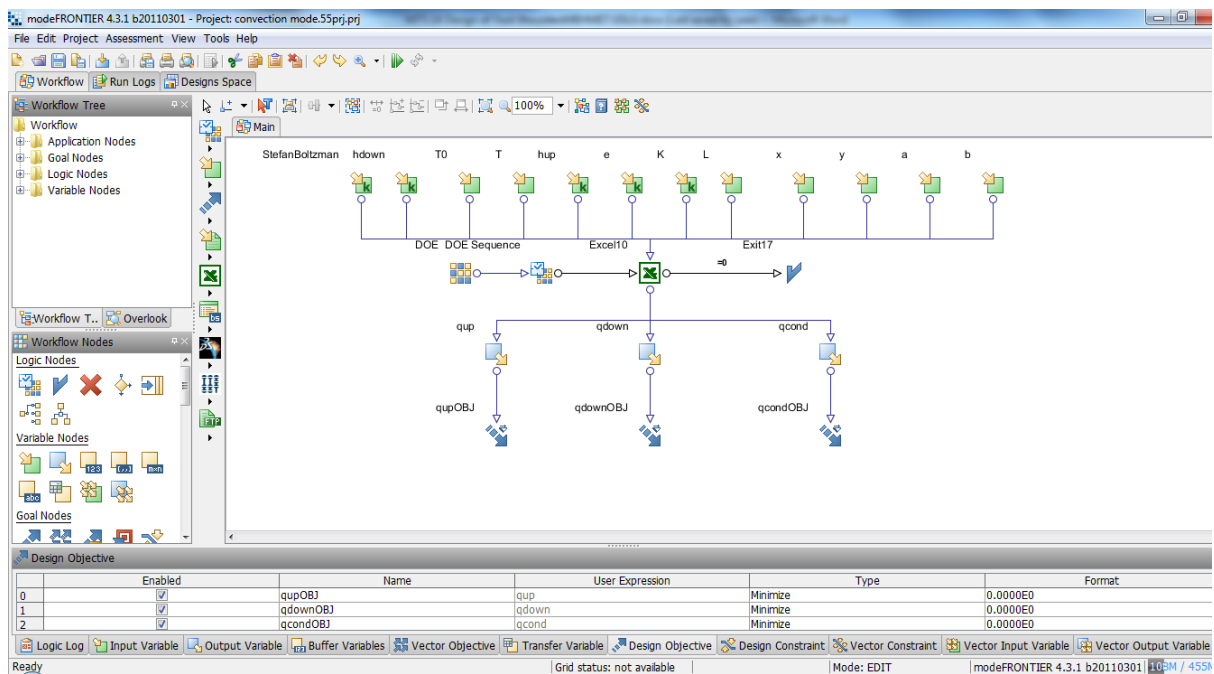


Image 8.3: Workflow Plan created on Mode Frontier Project as shown in convection mode.prj, also includes DOE (Design of Experiments) and DOE Sequence, as well as indicating Input Variables, Output Variables, Design Objectives + Gradients, Microsoft Workbook and Logic End

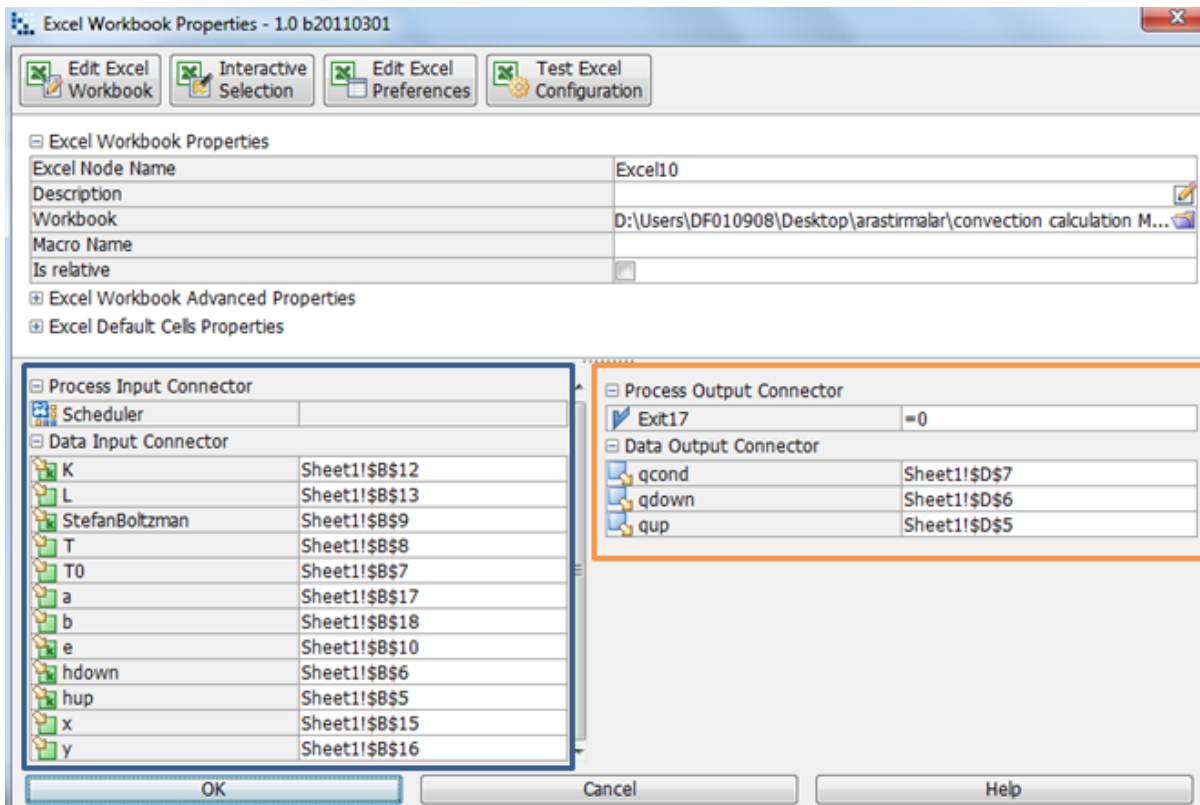


Image 8.4: Mode Frontier Input and Output Data connected to Microsoft Excel Workbook as shown above for standard tool

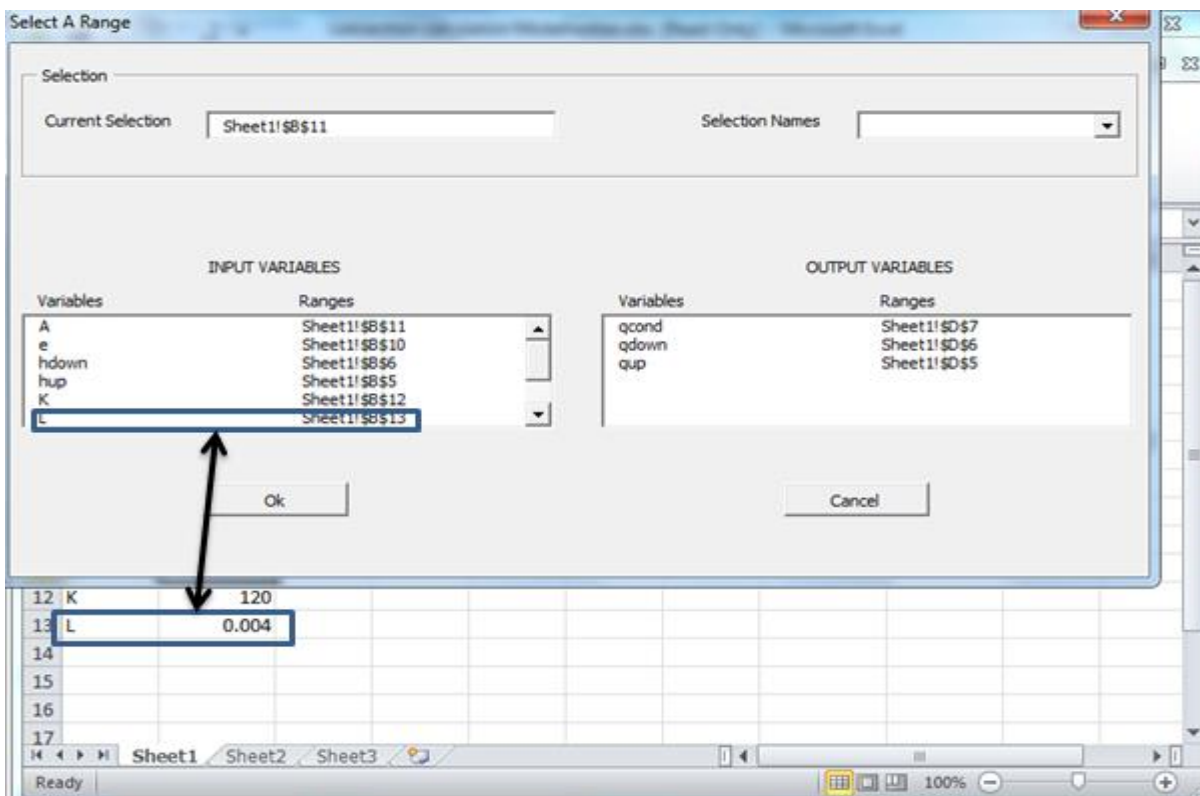


Image8.5: Interactive Selection used between Mode Frontier *convection mode.pri*

8.2.1. Boundaries : Standard Tool Heat Loss Conditions

A standard tools heat transfer co-efficient has an input variable for hup (heat loss by conduction on the upper surface). The heat transfer co-efficient in mechanics is the proportionality co-efficient between the heat flux and the thermodynamic driving force for the flow of heat where the value is 12, 25 W/m²*K[73] hence the range properties are fixed (Image 8.6), The heat transfer for the variable co-efficient for hdown (heat loss by conduction on the lower surface) where the value is 6,25 [20] with the variable type remaining constant and range properties that remain fixed (Image 8.7), The ambient temperature (To) of 300K is determined by the range properties where the upper bound been 353.0 and the lower bound been 273.0 [20] (Image 8.8), The melting temperature a work piece is at 935 K which is determine by the range properties where the lower bound is 573.0 and the upper bound is 1100.0 and the variable type been variable(Image 8.9), The variable properties Stefan-Boltzmann, which is the total intensity radiated over the work piece as the temperature increases or simply a statement that the total radiant heat energy emitted from the work piece surface is proportional to the fourth power of the peaking temperature(in reference with The Engineering Tool Box), has a variable type that is constant which has fixed range properties with a value 5.67E-8 (Image 8.10), The cross sectional area x, has the area of 4 mm, where the variable type that varies with range properties where the lower bound is 2.0 and the upper bound been 6.0 (Image 8.11). The cross sectional area y , has the area of 4 mm, where the variable type that varies with range properties where the lower bound is 2.0 and the upper bound been 6.0 [20] (Image 8.12). The thermal conductivity of the material Al2024-T3 describes the transportation of heat through the material. Thermal conductivity is thus a material specific property used for characterizing steady transportation of heat (Image: 8.13). The input variable property has a value of 120W/mK[20] with a variable property that is constant making the range property fixed, The length input variable properties has an indication of the given length (4 mm) with a variable type been variable and the range properties been lower bound 1.0 and upper bound 10.0 (Image 8.14), the surface emissivity has a variable type that is constant with a value of 0.3 with a variable type that is constant and range properties that are fixed(in reference with Colligan,Xu and Pickens, on the use of practise metal where the demonstration of a reduction in transverse forces Ref14). Certain ranges of properties are also obtained by varying the thickness of the surface finished [20] (Image 8.15), The cross section area a is 500 mm with variable properties that varies, range properties been lower bound 360.0 and the upper bound 600.0 and lastly the cross sectional area b is 115 mm has a variable type that varies and have of the following lower bound at 67.0 and the upper bound which is 122.5 (Image 8.16). b is cross-sectional area 115 mm is chosen, where the variable type is variable hence the lower and upper bound varies (Image 8.17). The projects starts once a run project has started and then an index will appear before the initial project design commences (Images 8.18 & 8.19).

NAME	EXPRESSION	DESCRIPTION
T0	300[K]	Reference temperature
T_melt	933[K]	Workpiece melting temperature
rho_pin	7800[kg/m ³]	Pin density
k_pin	42[W/(m*K)]	Thermal conductivity
Cp_pin	500[J/(kg*K)]	Specific heat capacity
h_upside	12.25[W/(m ² *K)]	Heat transfer coefficient, upside
h_downside	6.25[W/(m ² *K)]	Heat transfer coefficient, downside
epsilon	0.3	Surface emissivity
u_weld	1.59[mm/s]	Welding speed
mu	0.4	Friction coefficient
n	637[1/min]	Rotation speed (RPM)
omega	2*pi[rad]*n	Angular velocity (rad/s)
F_n	25[kN]	Normal force
r_pin	6[mm]	Pin radius
r_shoulder	25[mm]	Shoulder radius
A_s	pi*(r_shoulder ² -r_pin ²)	Shoulder surface area

Table 8.1 : A reference guideline [20]

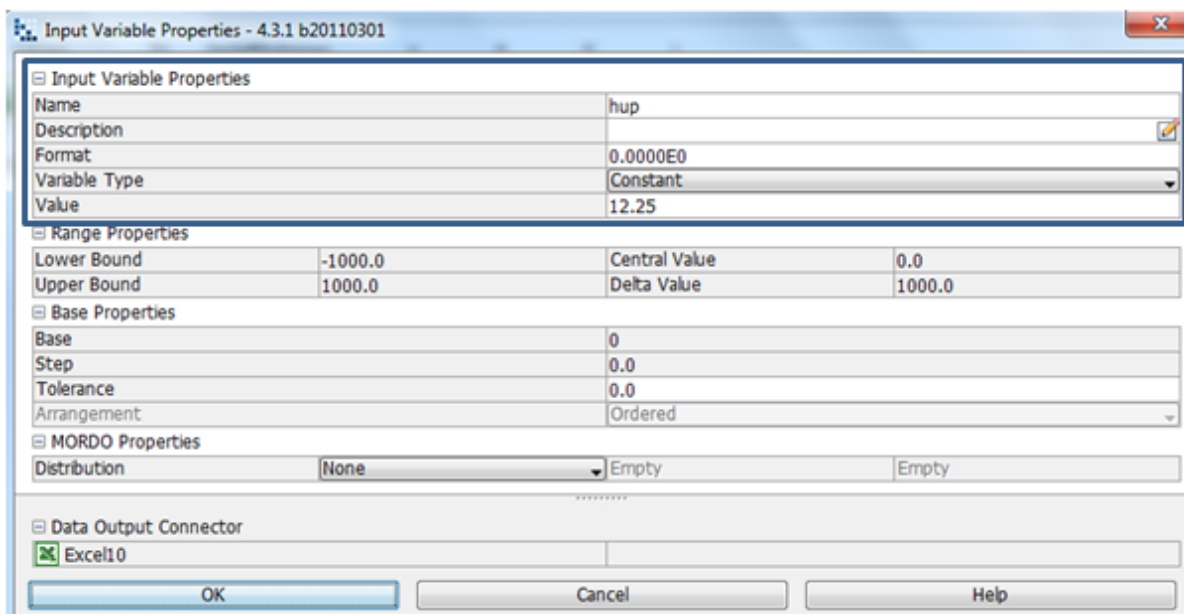


Image 8.6: The heat transfer coefficient of the upside surface 12.25 W/m²*K is chosen, where the variable type is constant hence the lower and upper bound is fixed

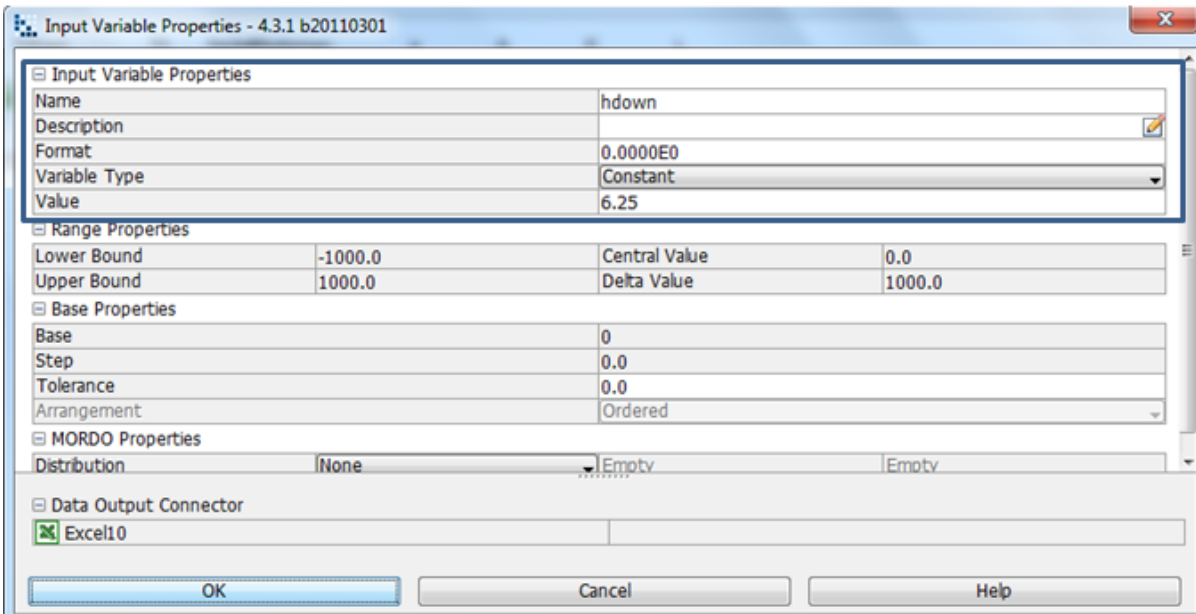


Image 8.7: The heat transfer coefficient of the downside surface $6.25 \text{ W/m}^2\cdot\text{K}$ is chosen, where the variable type is constant hence the lower and upper bound is fixed.

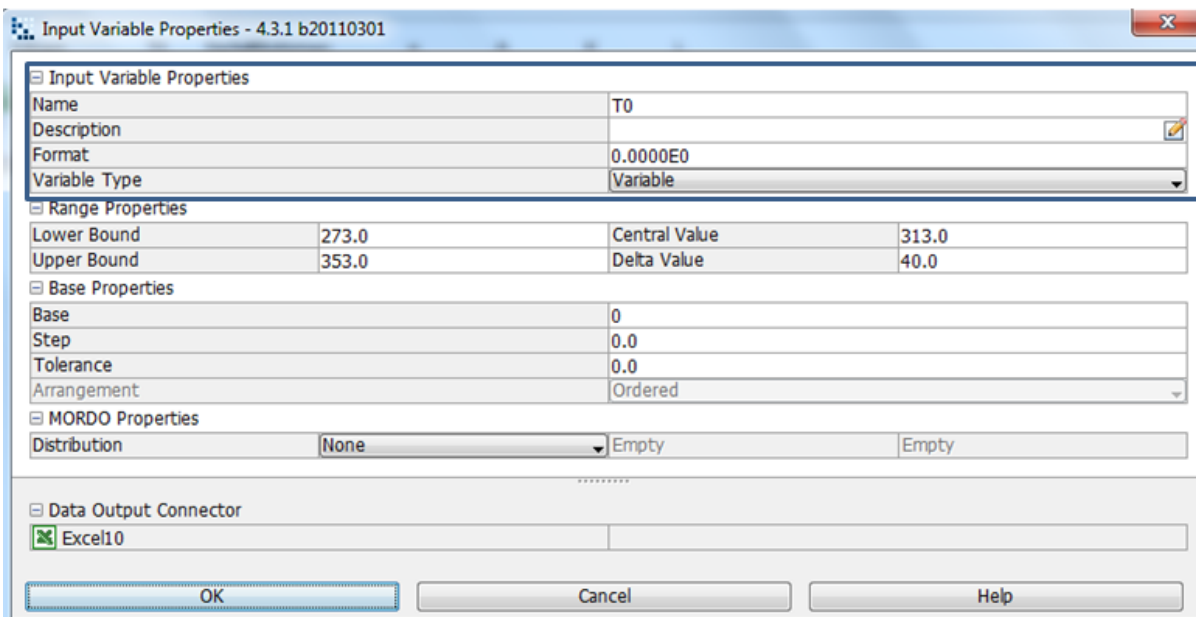


Image 8.8: The reference temperature 300 K is determined by lower and upper bound range properties, as shown in the input variable node properties dialog.

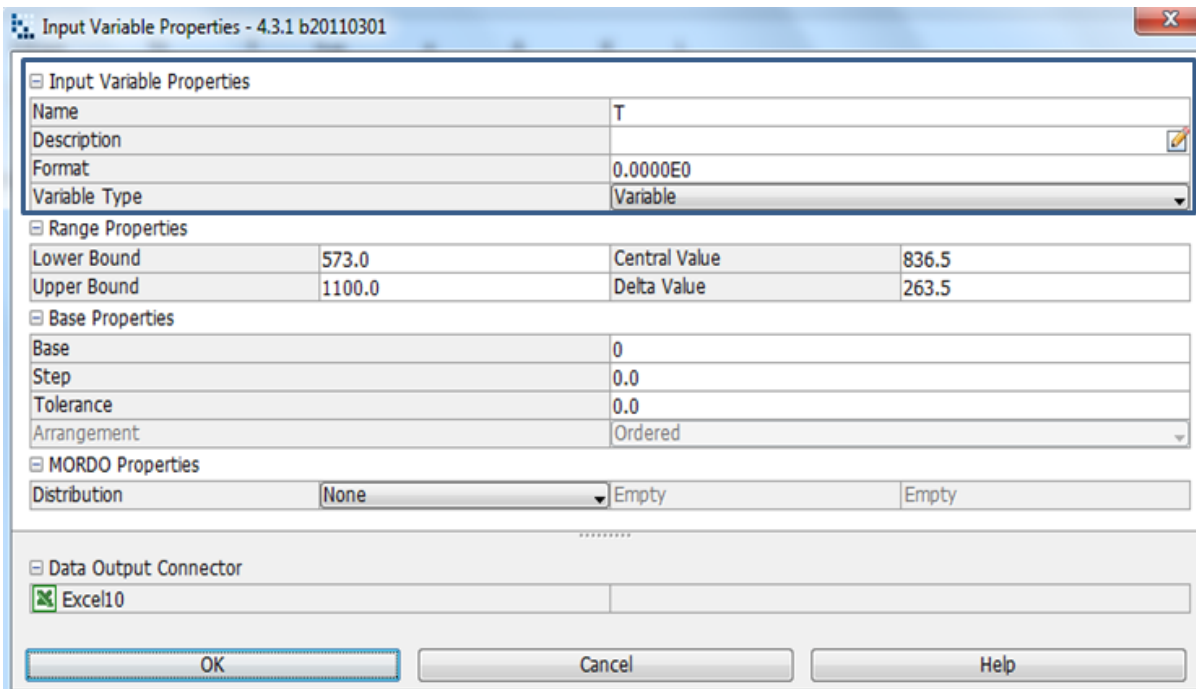


Image 8.9: The melting temperature of 2935 K for the work piece is determined by lower and upper bound range properties, as shown in the input variable node properties dialog.

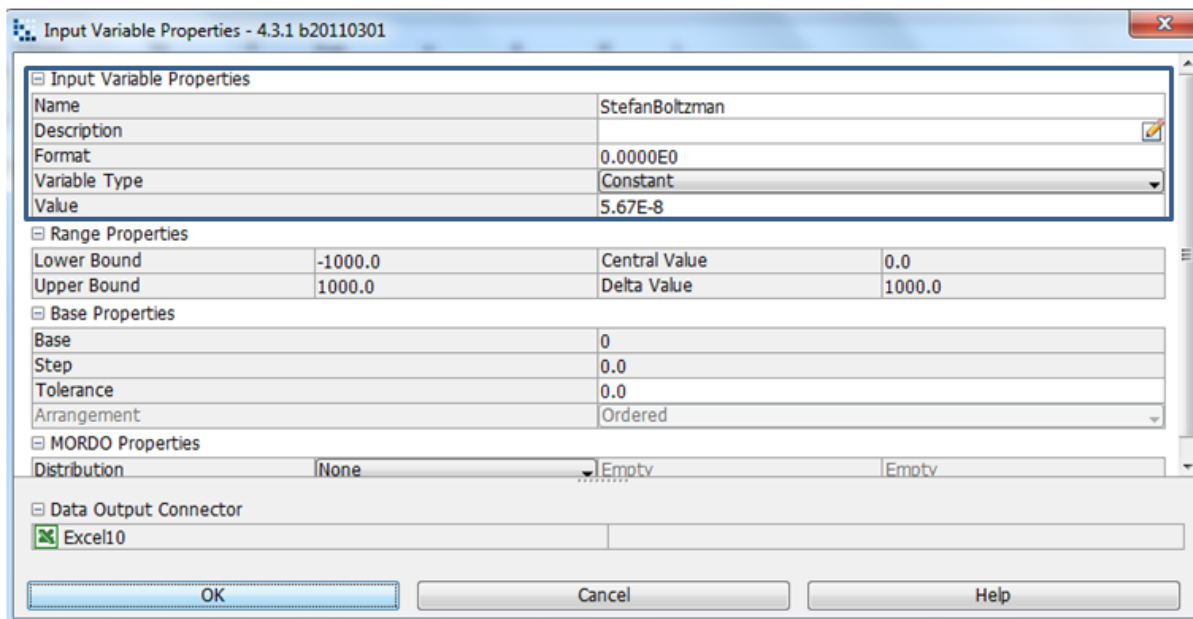


Image 8.10: The Stefan-Boltzmann constant (σ) $5.67 \times 10^{-8} \text{ Wm}^{-2} \text{ K}^{-4}$ is chosen, where the variable type is constant hence the lower and upper bound is fixed.

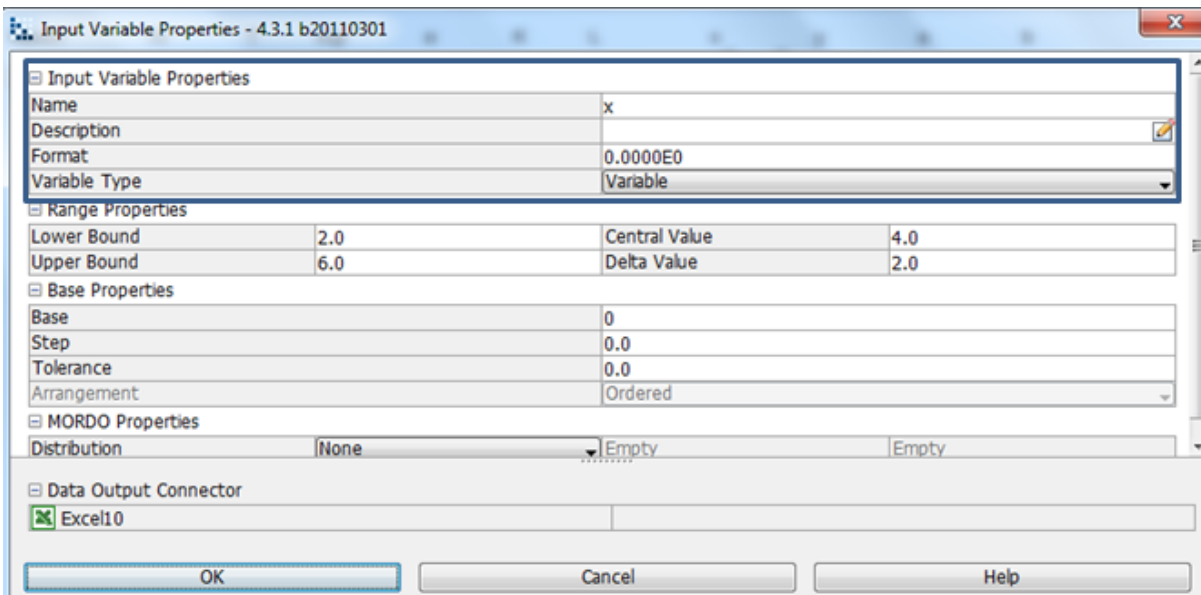


Image 8.11: x is cross-sectional area 4 mm is chosen, where the variable type is variable hence the lower and upper bound varies.

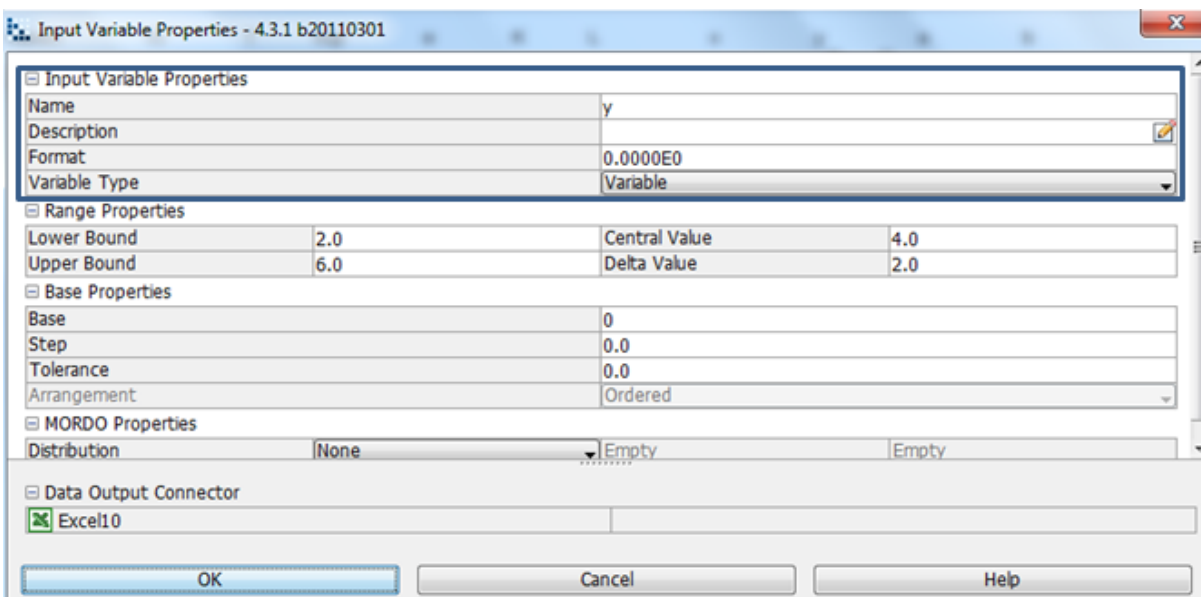


Image 8.12: y is cross-sectional area 4mm is chosen, where the variable type is variable hence the lower and upper bound varies.

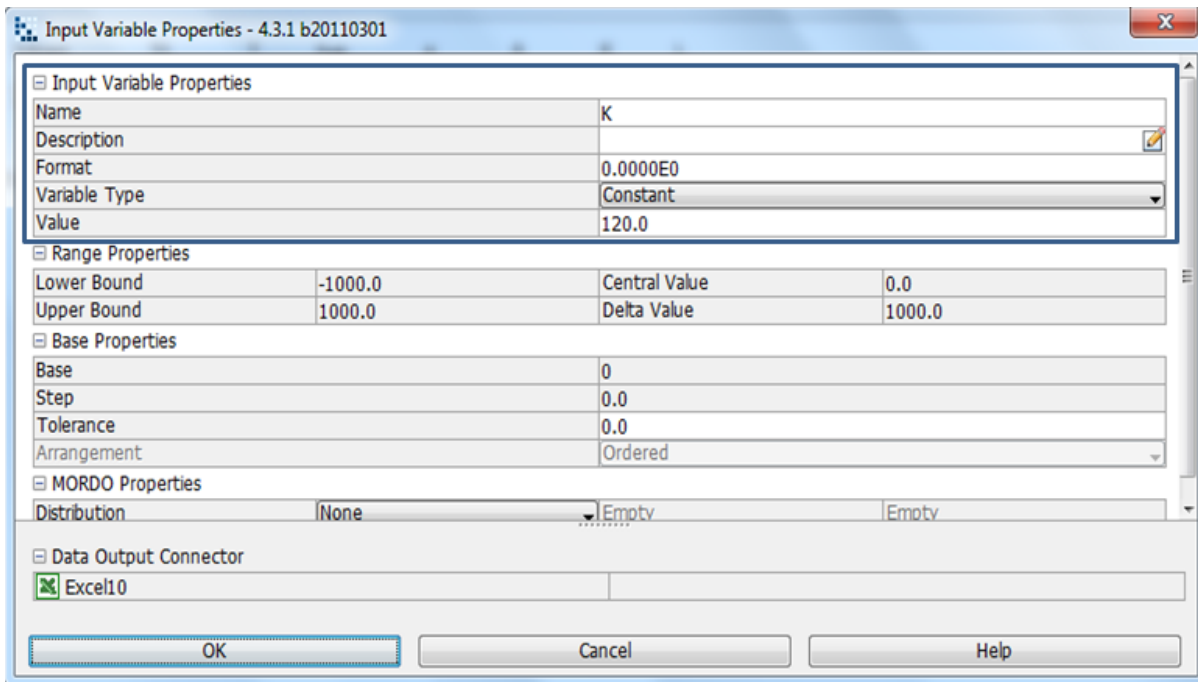


Image 8.13: The thermal conductivity of 120 W/mK is chosen, where the variable type is constant hence the lower and upper bound is fixed.

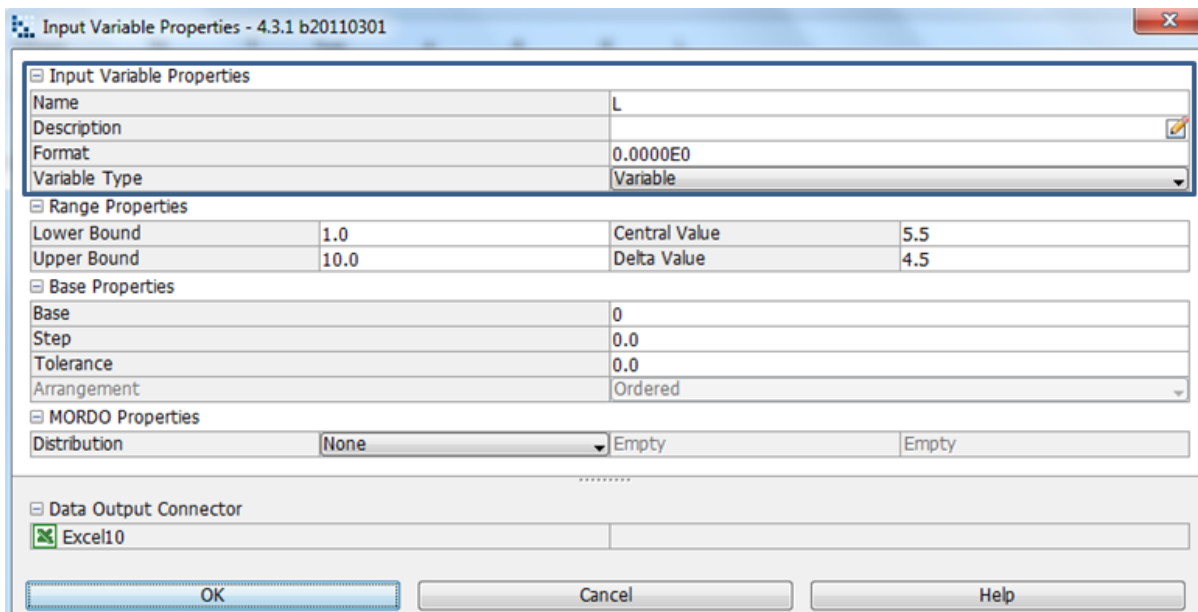


Image 8.14: The length of 4 mm is chosen, where the variable type is variable hence the lower and upper bound varies.

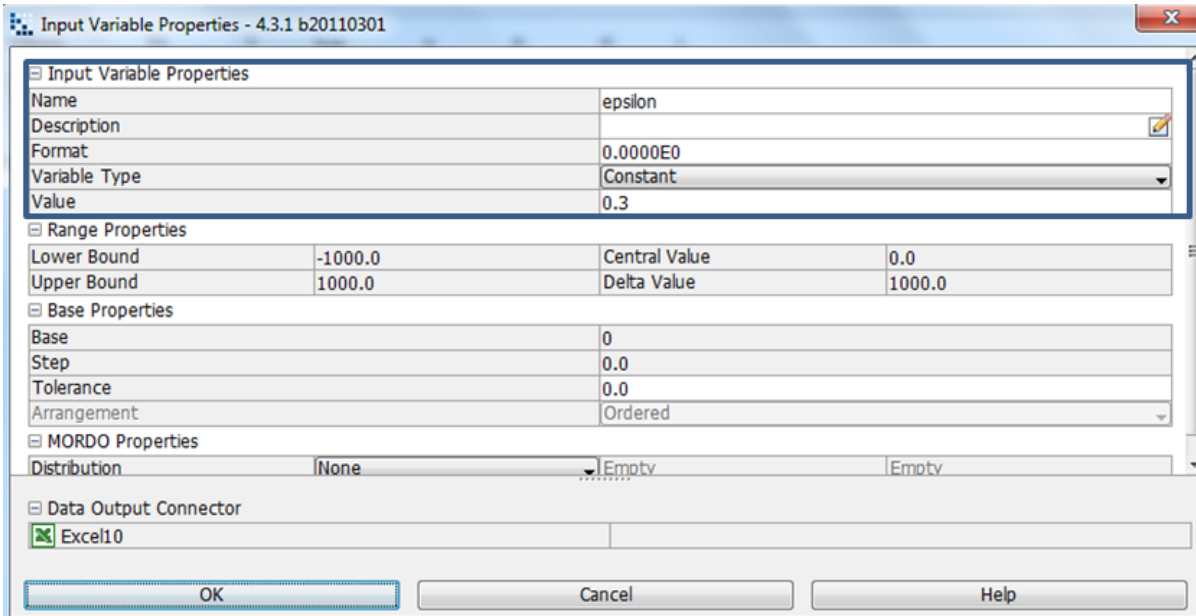


Image 8.15: The surface emissivity of 0.3 is chosen, where the variable type is constant hence the lower and upper bound is fixed.

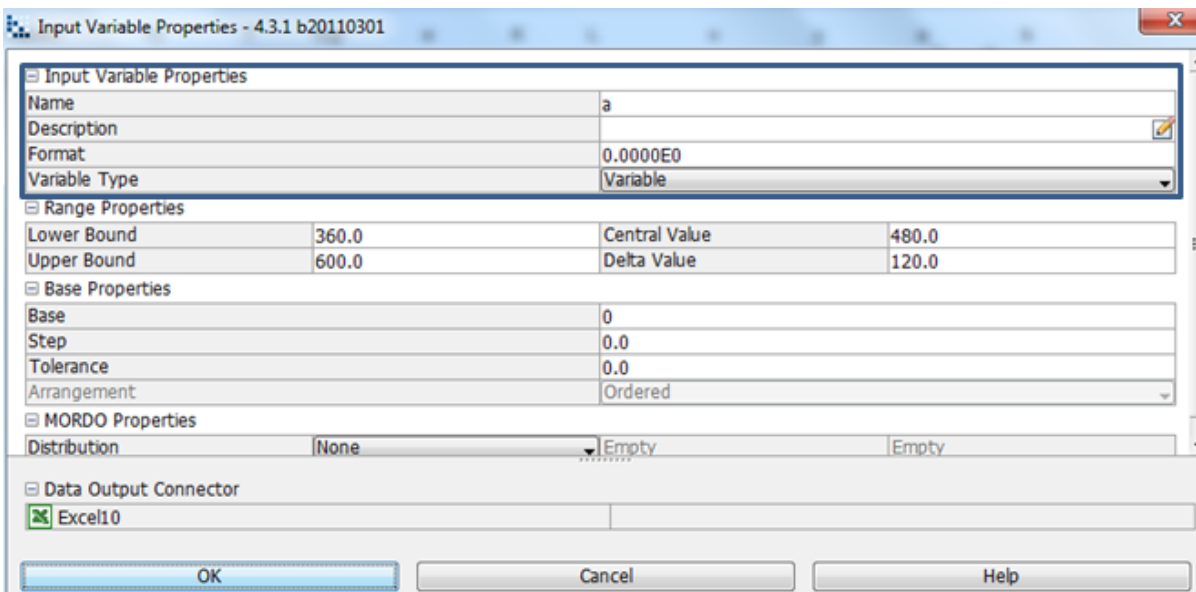


Image 8.16: a is cross-sectional area 500 mm is chosen, where the variable type is variable hence the lower and upper bound varies.

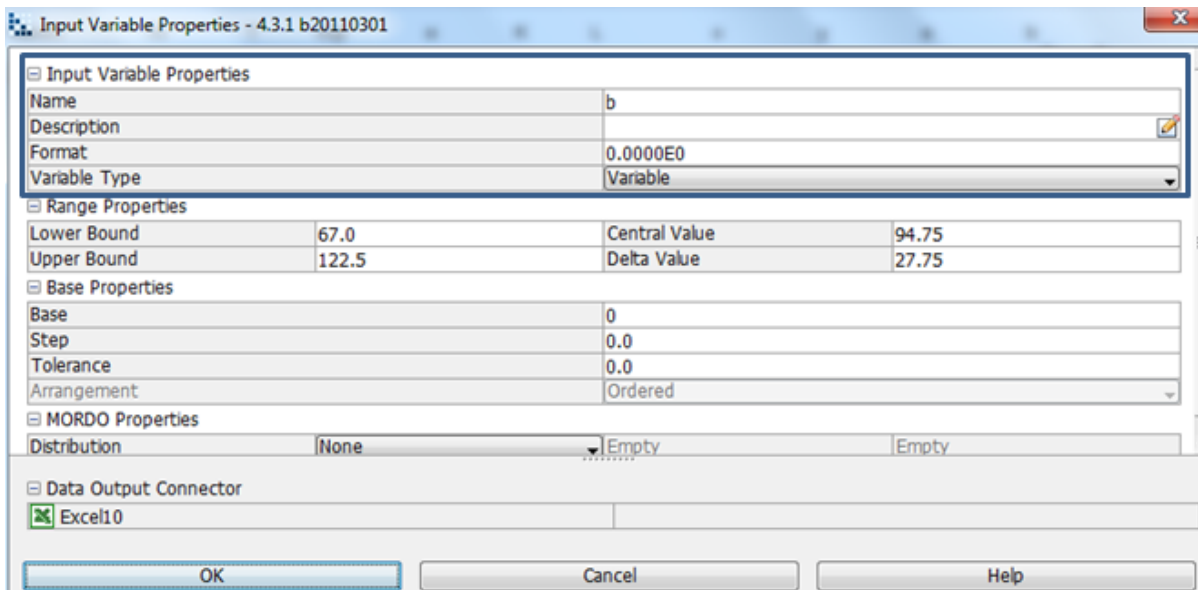


Image 8.17: b is cross-sectional area 115 mm is chosen, where the variable type is variable hence the lower and upper bound varies.

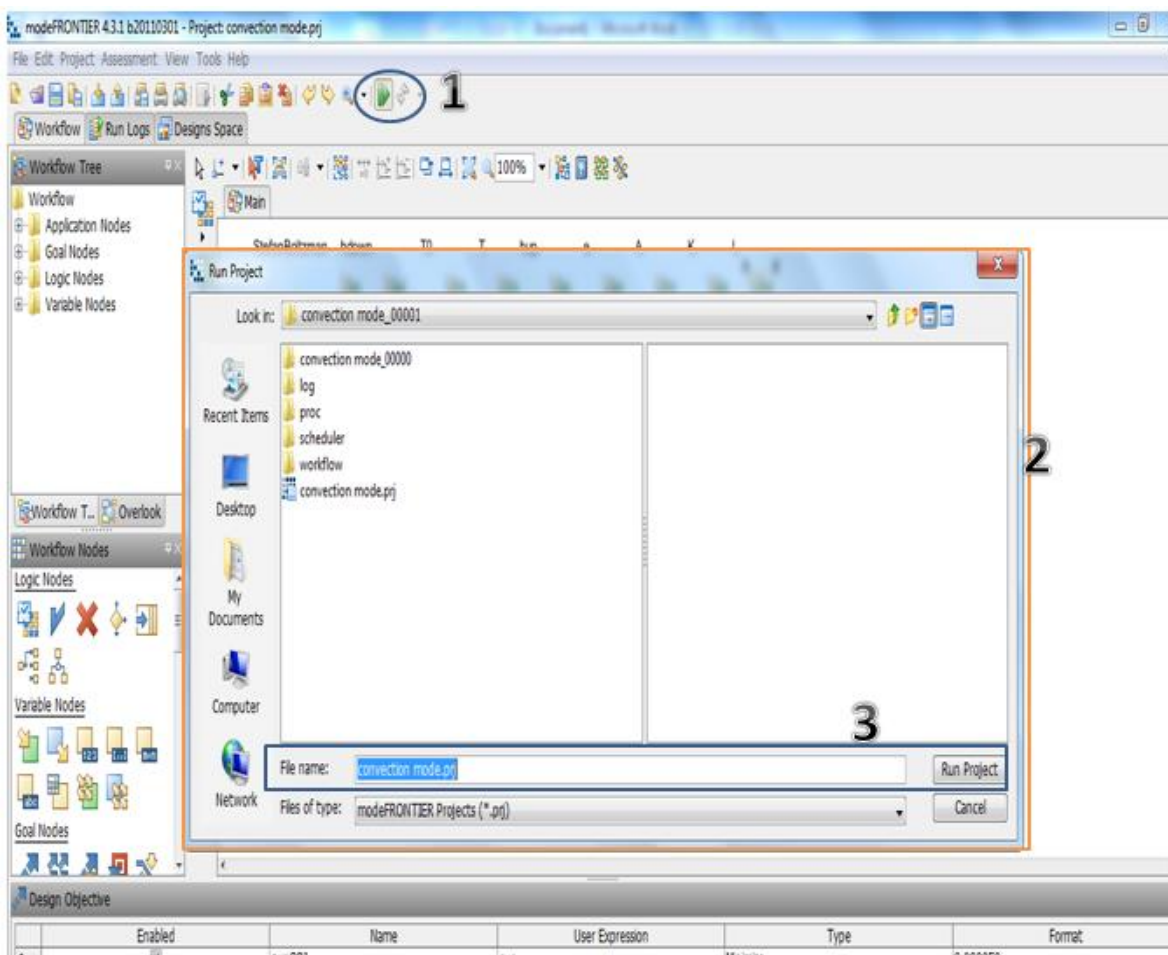


Image 8.18: Click on run/stop icon (1). Run project box will pop up (2). Click on run project (3) to start design project.

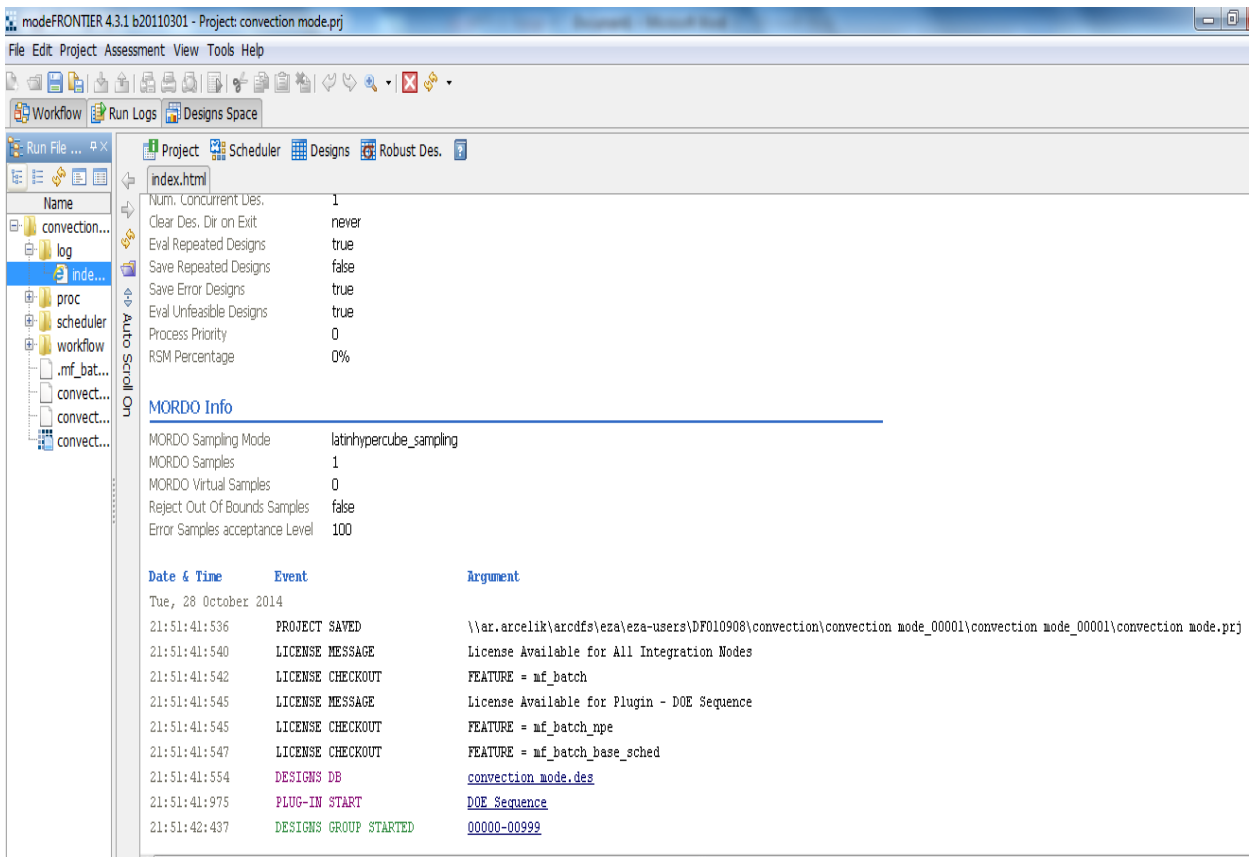


Image8.19: Before project runs, a project info index will be shown. As seen in the above image.

8.2.2. Multi History Charts for Standard Tool Heat Loss Conditions

The multi history chart that represents the reference temperature and heat conduction to the heat conduction objective shows the design is feasible in reality(Chart 8.1), the multi history chart for the reference temperature and heat loss by conduction on the upper surface shows and represents that the design is feasible on a real scale(Chart 8.2), the reference temperature and the heat loss by conduction on the down surface to qdownobj (heat loss on the down surface objective) is represented on a multi history chart showing that design is feasible on a real scale (Chart 8.3), The temperature and the heat loss by conduction on the down surface to qdownobj (heat loss on the down surface objective) is represented on a multi history chart showing that design is feasible on a real scale (Chart 8.4), the multi history chart that represents the temperature and the heat loss by conduction on the upper surface to the qpobjective(heat loss on8 the upper surface objective) shows feasibility on a real scale(Chart 8.5), the representation of the temperature and heat conduction to the heat conduction objective is clearly indicated on the multi history chart showing the designs feasibility in reality(Chart 8.6), the a multi history chart shows that the Aluminium Plate, the heat loss by conduction on the upper surface to the qpobjective has a feasible design on a real scale(Chart 8.7) and lastly the feasibility of b and heat loss by conduction on the surface can be achieved on a real scale (Chart 8.8)

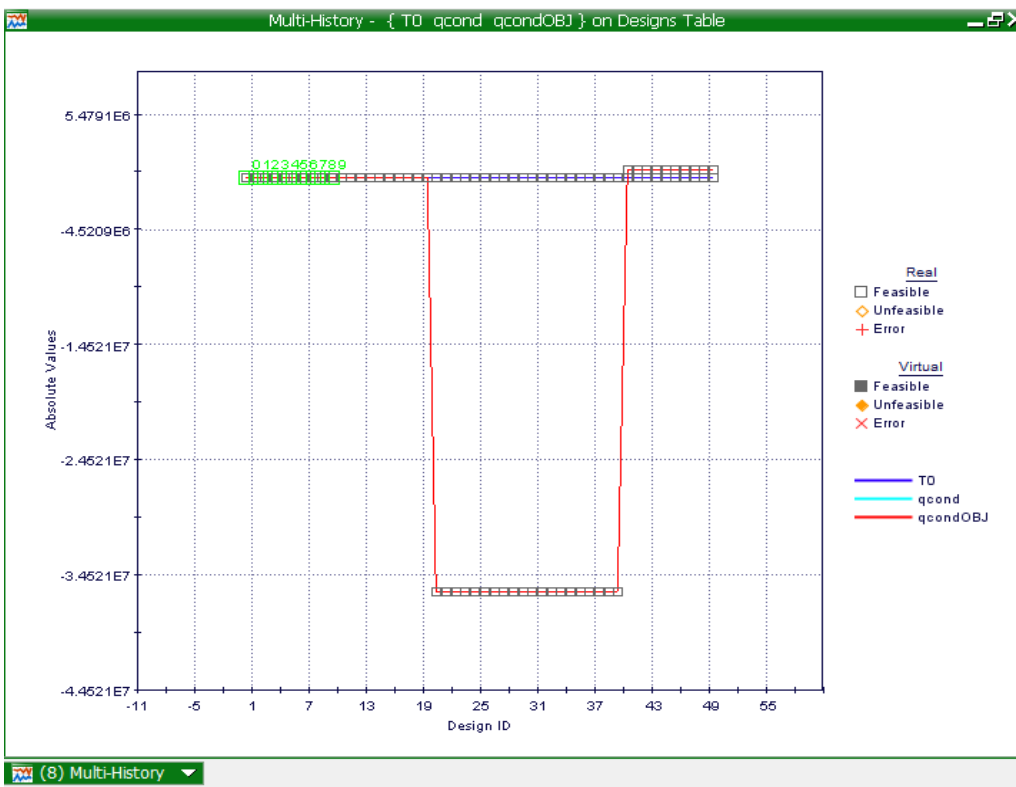


Chart 8.1: Multi-History Chart on Designs Space as created from reference temperature and heat conduction to the heat conduction objective.

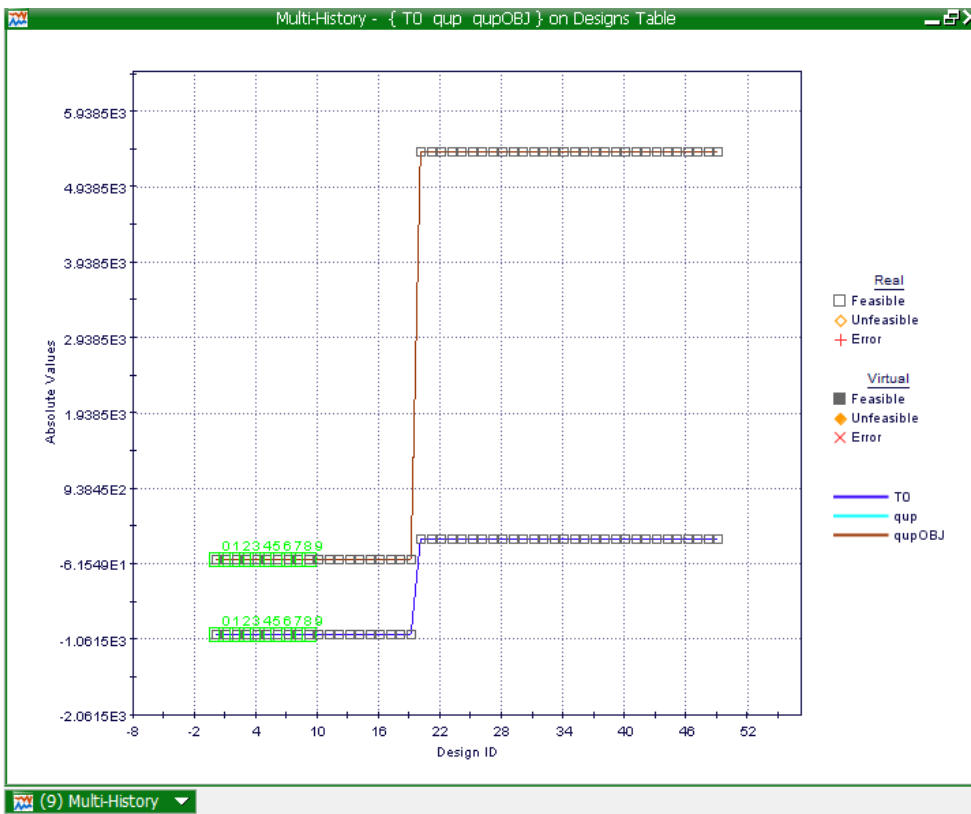


Chart 8.2: Multi-History Chart on Designs Space as created from reference temperature and heat loss by conduction on the upper surface.

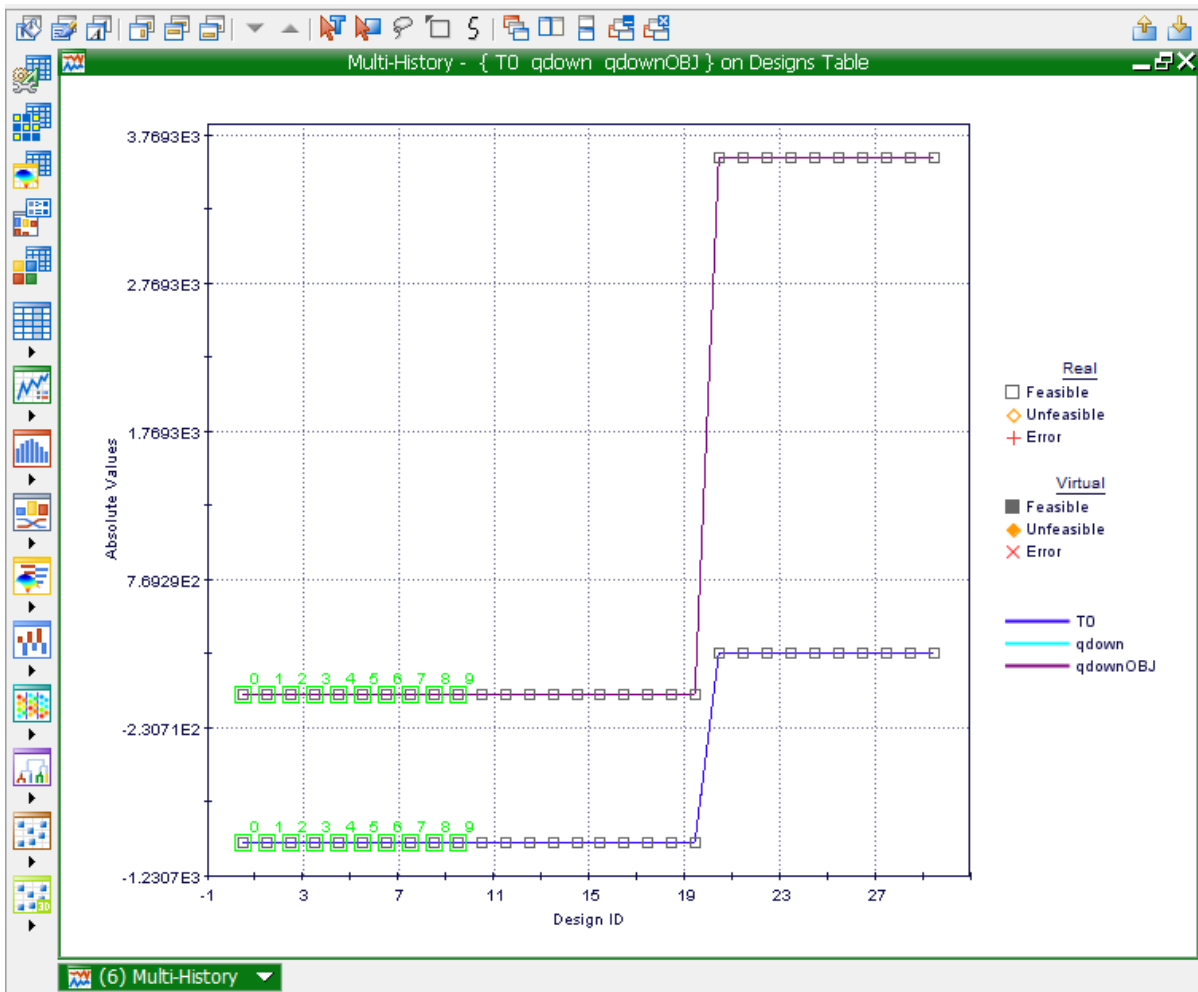


Chart 8.3: Multi-History Chart on Designs Space as created from the reference temperature and the heat loss by conduction on the down surface to qdownobj (heat loss on the down surface objective).

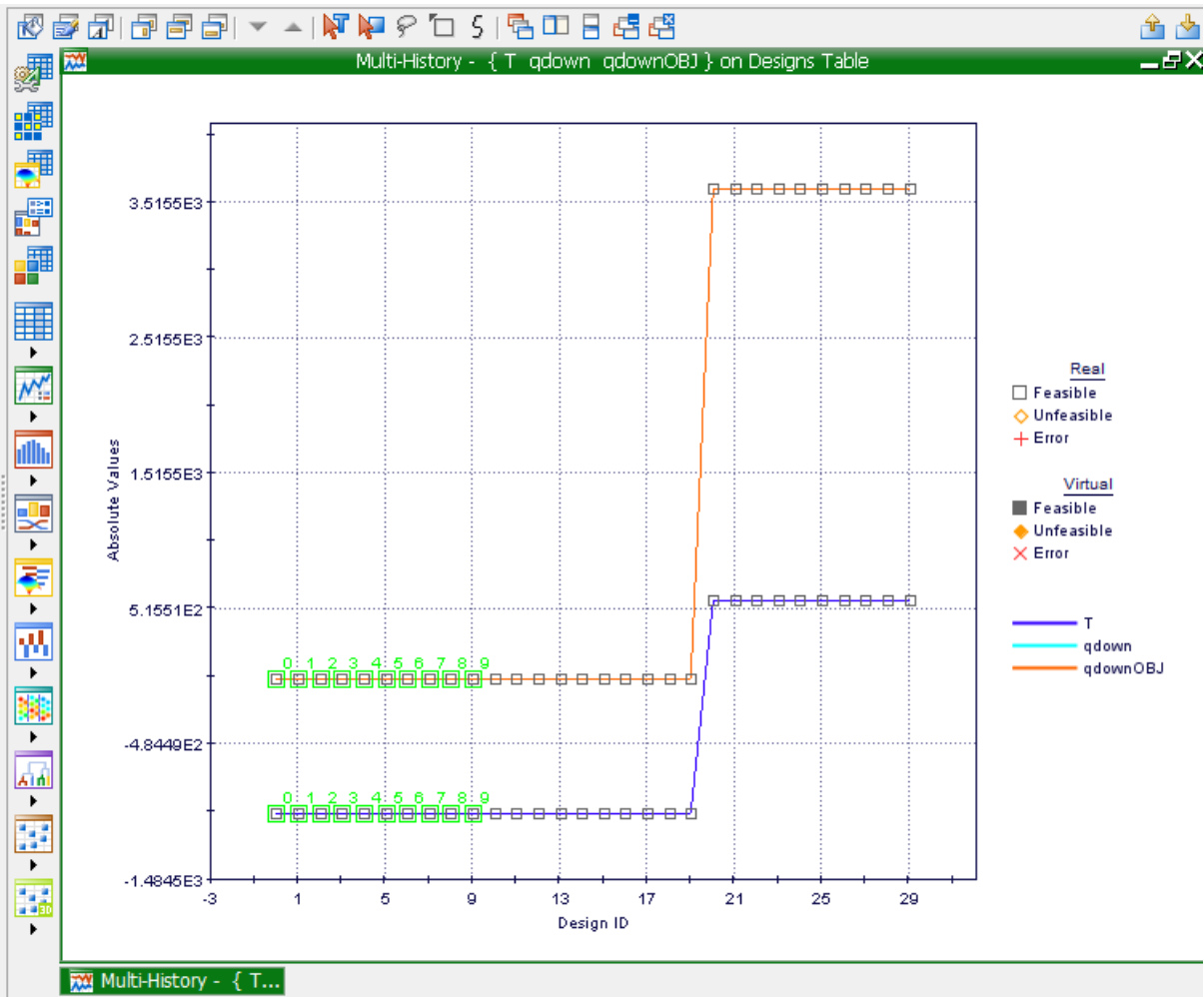


Chart 8.4: Multi-History Chart on Designs Space as created from the temperature and the heat loss by conduction on the down surface to the qdown objective (heat loss on the down surface objective).

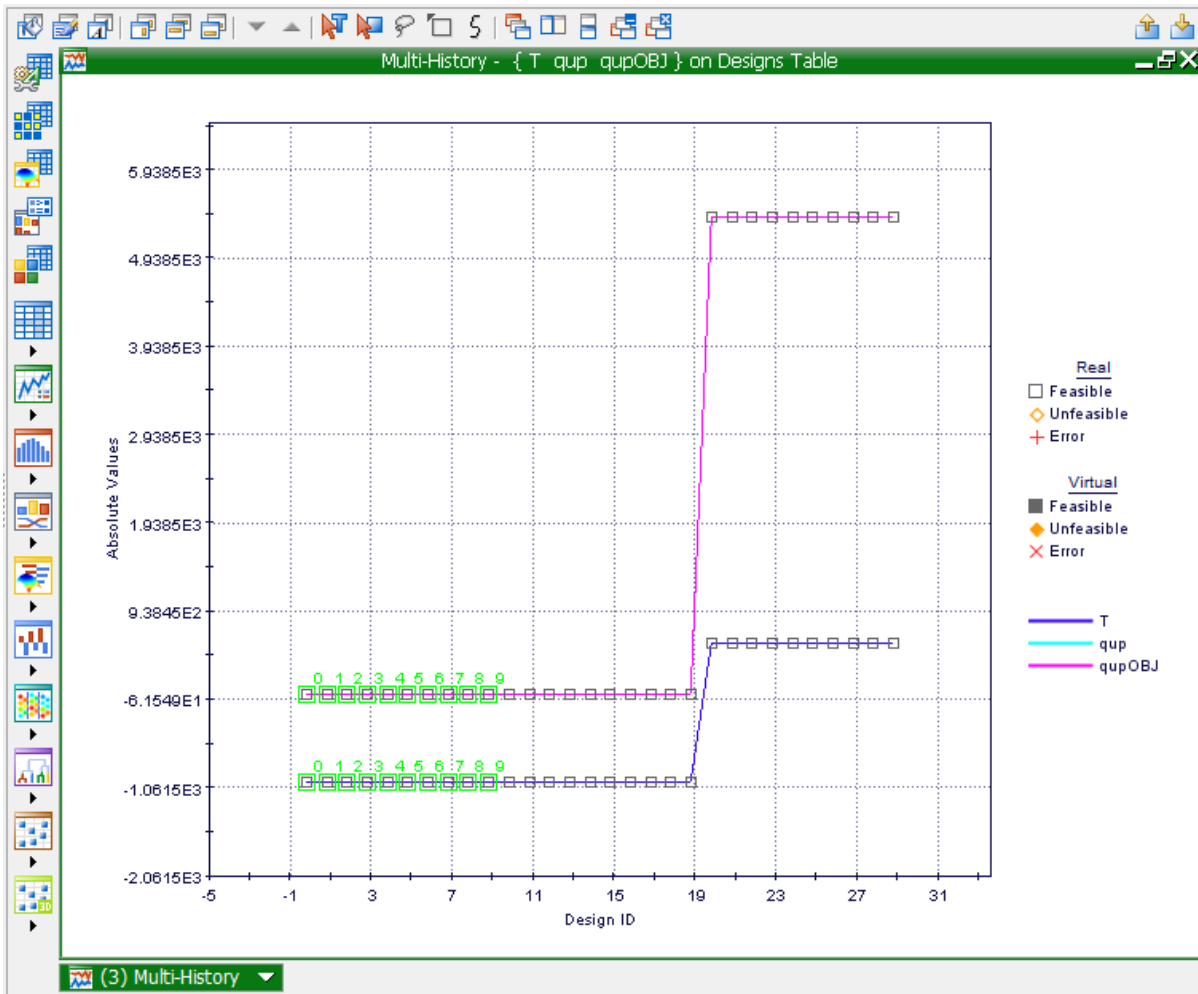


Chart 8.5: Multi-History Chart on Designs Space as created from temperature and the heat loss by conduction on the upper surface to the qpobjective (heat loss on the upper surface objective).

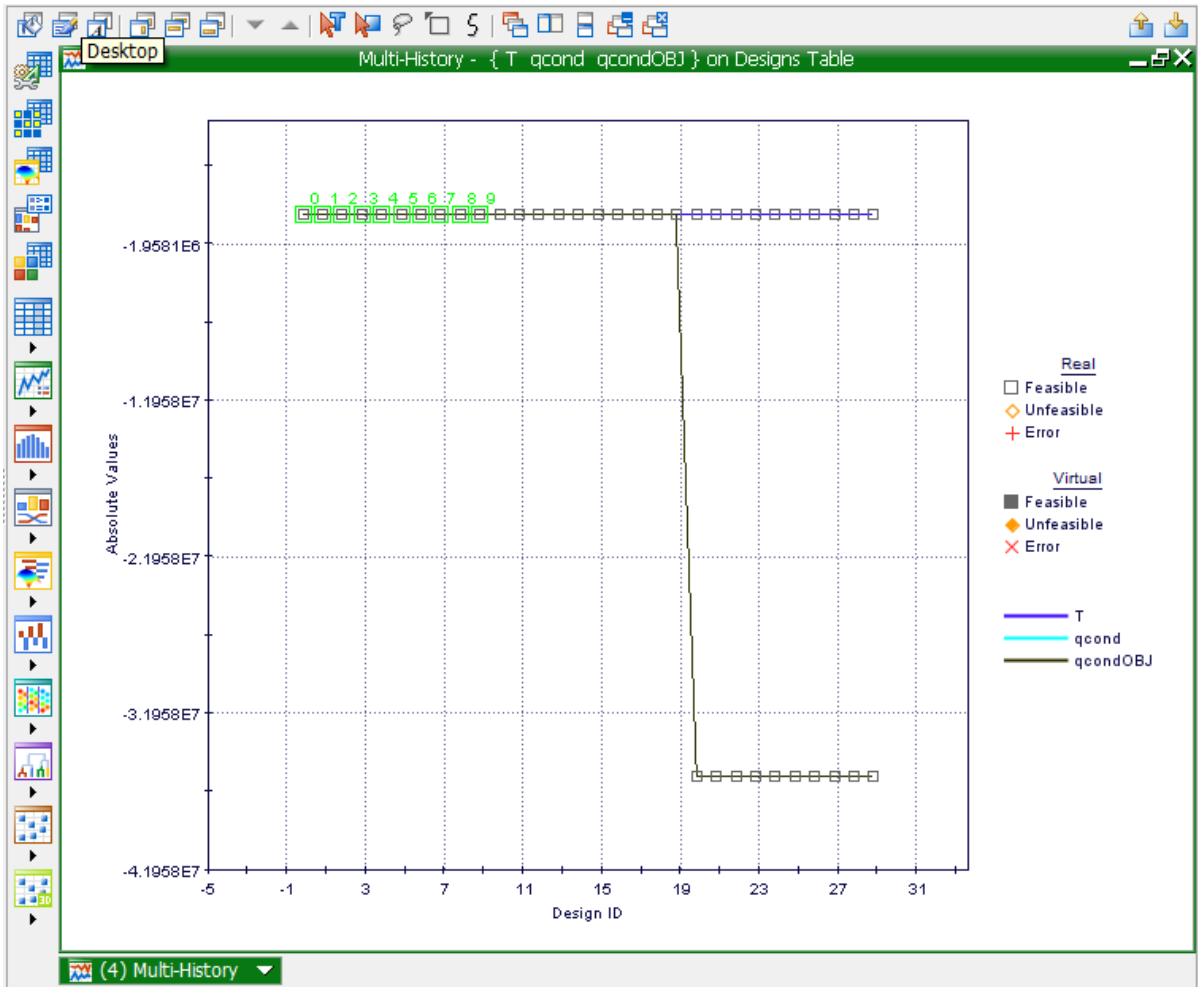


Chart 8.6: Multi-History Chart on Designs Space as created from the representation of the temperature and heat conduction to the heat conduction objective.

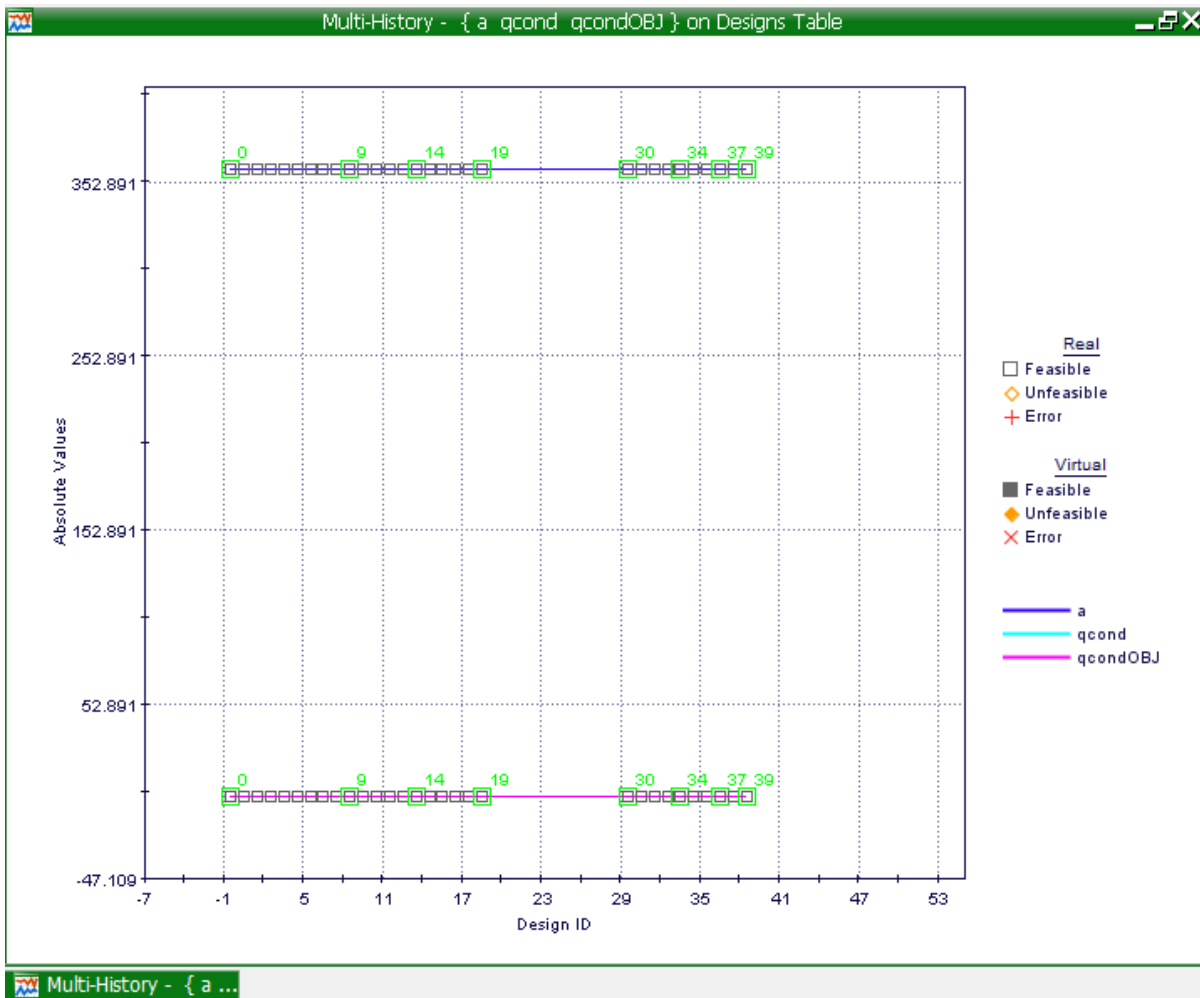


Chart 8.7: Multi-History Chart on Designs Space as created from a, the heat loss by conduction on the upper surface to the qobjective.

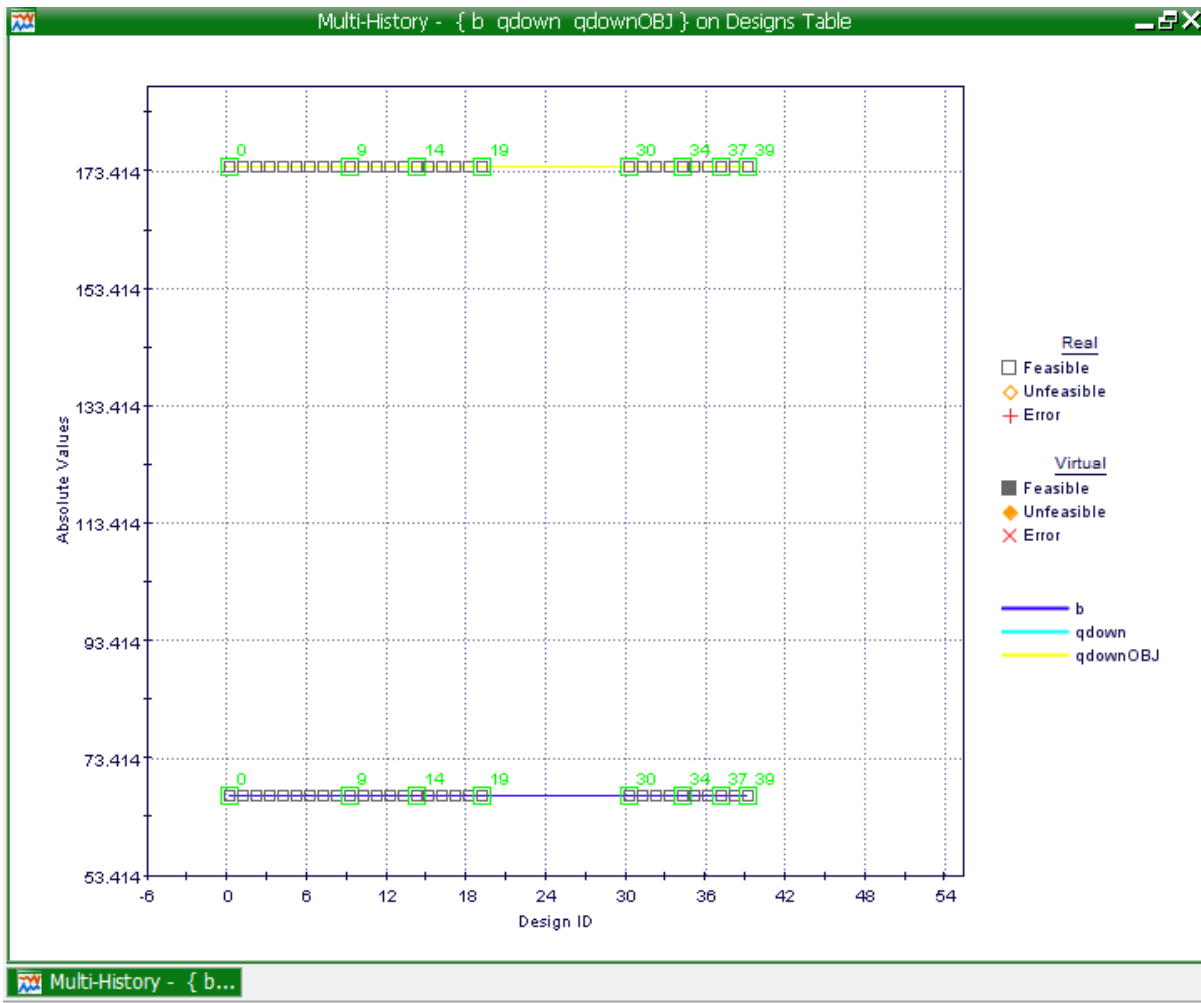
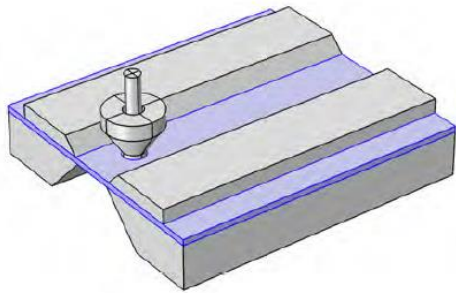


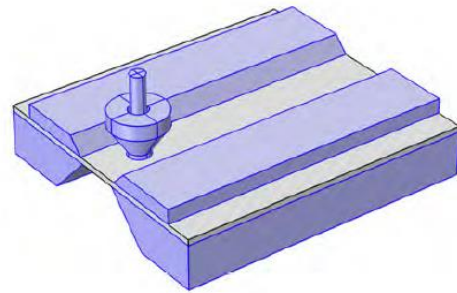
Chart 8.8: Multi-History Chart on Designs Space as created from b, the heat loss by conduction on the down surface to the qdownobjective.

8.3. Bobbin Tool Heat Loss Conditions

In the bobbin tool, the heat convection (q_{Conv}) is seen to be exerted through the material (Al2024-T3), the radial heat transfer moves outwards towards the opposite direction of the tool (q_{Rad}) and conduction happens from within the tool (q_{Cond}) providing equal conduction throughout the tool and work piece. The bobbin tool weld will obviously show softening which is considerably more developed in the lower half of the weld- the reason for this can be attributed to the fact that heat loss from other than that of the work piece is into the air, where heat loss is considered to be marginal [96]

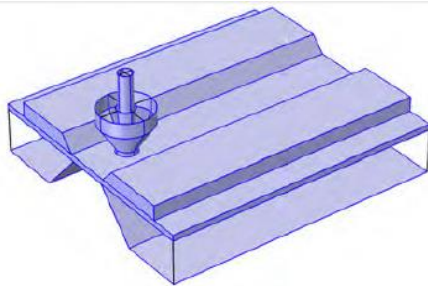


(a) Work piece made of AA2024

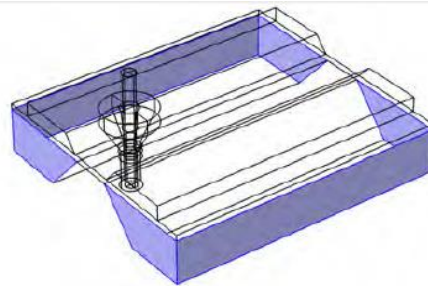


(b) Tool, clamps and table made of high-strength steel

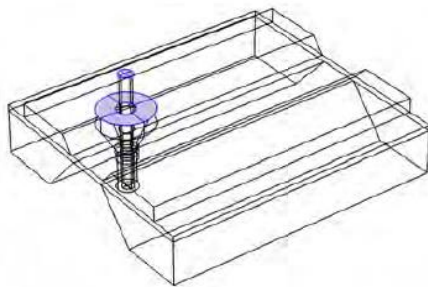
FIG 8.2: AMGM material definition



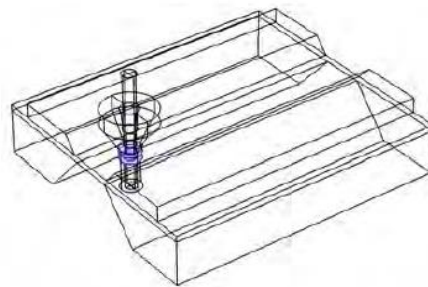
(a) Convection to air



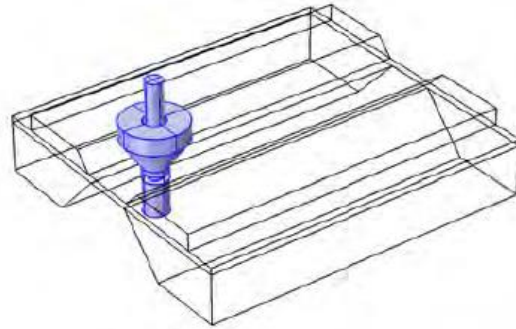
(b) Convection to table



(c) Convection to machine spindle

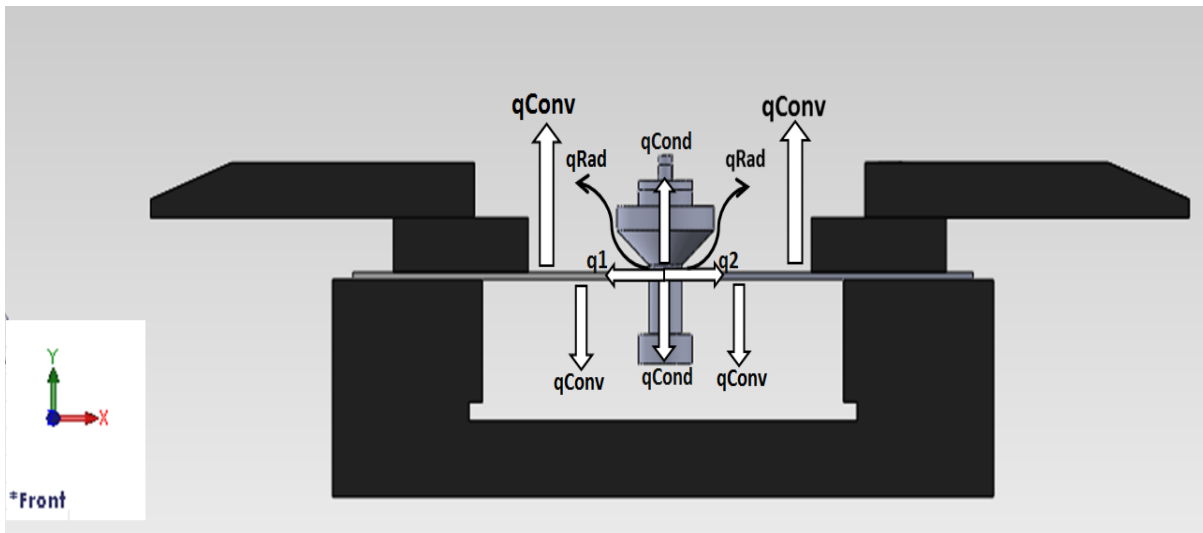


(d) Prescribed TPM heat source



(e) Convective tool rotation

FIG 8.3: AMGM boundary conditions



Drw 8.2: Thermal Aspects for the Bobbin Tool Design. [Uslu, M.Y, (2014), Thermal aspect- Bobbin Tool design, University of the Witwatersrand]

$$h_{up} = 12.25 \text{ W/m}^2\text{K}$$

$$h_{down} = 6.25 \text{ W/m}^2\text{K}$$

$$q_b = 100 \text{ W/m}^2\text{K}$$

$$T_0 = 25 \text{ }^\circ\text{C} = 299 \text{ K}$$

$$T = 662 \text{ }^\circ\text{C} = 935 \text{ K}$$

$$\sigma = 5.67 \times 10^{-8} \text{ Wm}^{-2}\text{K}^{-4}$$

$$\varepsilon = 0.3$$

$$x = 4 \text{ mm}$$

$$y = 5 \text{ mm}$$

$$a = 500 \text{ mm}$$

$$b = 115 \text{ mm}$$

$$L_1 = 2 \times 10^{-3} \text{ m}$$

$$L_2 = 2 \times 10^{-3} \text{ m}$$

$$K = 120 \text{ W/mK}$$

$$q_{up} = 2A_{plate} (h_{up}(T_0 - T) + \varepsilon\sigma(T_{amb}^4 - T^4))$$

$$q_{up} = 2 \times 0.115 \times 10^{-6} \times (12.25 \times (299 - 935) + 0.3 \times 5.6710^{-8} (299^4 - 935^4))$$

$$q_{up} = 4750.711771 \text{ W}$$

$$q_{cond} = 2AK(T - T_{amb})/L$$

$$q_{cond} = 2 \times 20 \times 10^{-6} \times 120 \times (935 - 299) / 4 \times 10^{-3}$$

$$q_{cond} = 2550.36 \text{ W}$$

8.3.1. Mode Frontier Simulation: Bobbin Tool Heat Loss Conditions

Input Data, Output Data and boundary variables definitions as shown on this Microsoft Excel Sheet file name [convection calculation modefrontier.xlsx](#) is used in Mode Frontier for this Design Project (Image 8.20): Since each component defining the Workflow is represented by a specific node which can be linked to other nodes, a proper node from the available Node Library toolbar or, alternatively, chosen by using the Workflow Nodes panel. It is shown all the input data output data and boundary variables in a Microsoft Excel workbook. The excel work books is used so that the equation for the rotational speed along with the heat generation is calculated where the results will be used in ModeFrontier to assist in the design .Once a Workflow Plan created by Mode Frontier Project as shown in deneme04.prj, also includes DOE (Design of Experiments) and DOE Sequence, as well as indicating Input Variables, Output Variables, Design Objectives + Gradients, Microsoft Excel Workbook and Logic End (Image 8.21). A workflow plan is created using a DoE (Design of Experiments) and a DOE Sequence on a new Overlook. Once this is open workflow nodes can be added on. Variable nodes which are the input nodes and the output nodes are used. Workflow nodes such as the schedulers, the logic switch and logic end is used. An application node is used for excel. A goal node which is the design objective+gradient node. Mode Frontier Input and Output Data is connected to Microsoft Excel Workbook .Excel workbook properties are used for basic node configuration where an Excel Workbook is selected. Once selected the input and out data is connected from the chosen Excel workbook (Image 8.22). An Interactive Selection used between Mode Frontier [convection mode.prj](#) and Microsoft Excel Workbook: [convection calculation modefrontier.xlsx](#) to determine Excel Workbook Properties for Mode Frontier. An interactive selection (Image 8.23) allows each input and output node to be configured in accordance to the Excel workbook. Where each variable is interactively selected to complete a work plan.

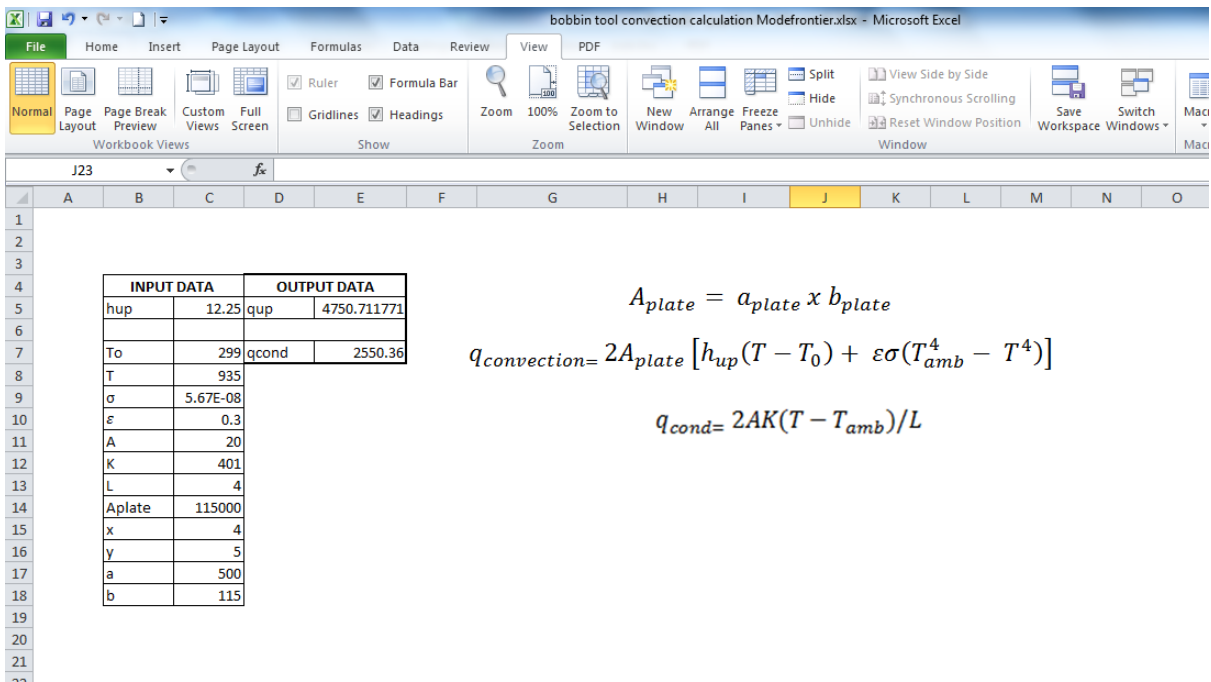


Image 8.20: Input Data, Output Data and boundary variables definitions as shown on this Microsoft Excel Sheet file name: *bobbin tool convection calculation Modefrontier.xlsx* is used in Mode Frontier for Design Project

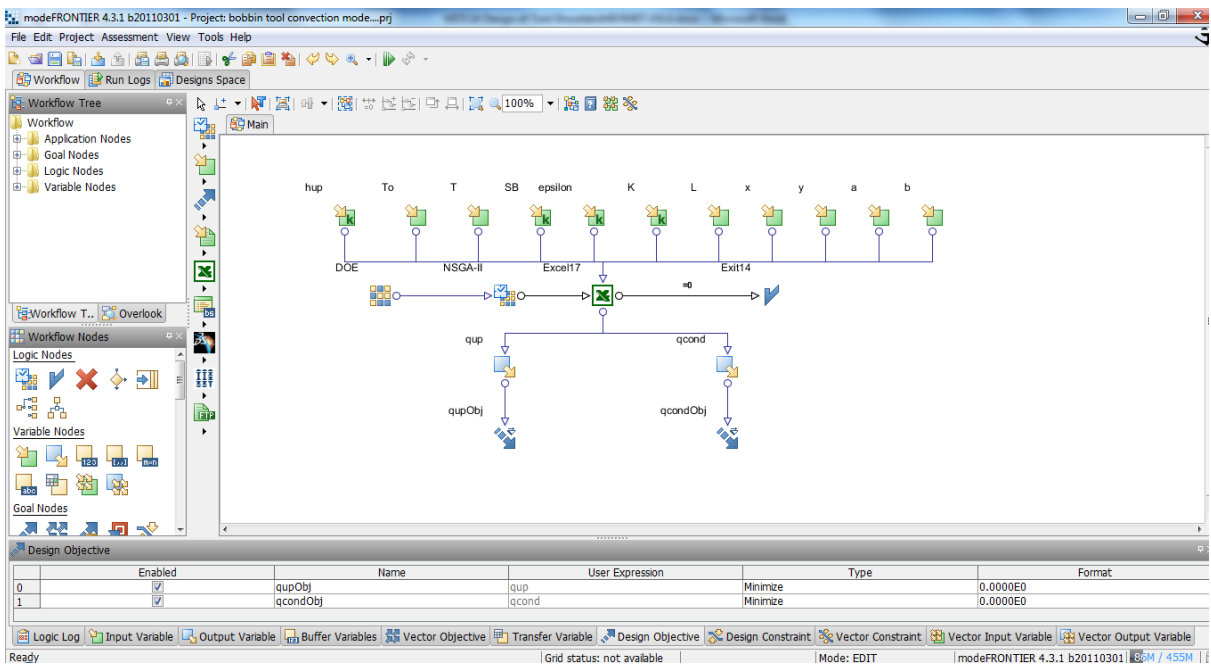


Image 8.21: Workflow Plan created on Mode Frontier Project as shown in *bobbin tool convection mode.prj*, also includes DOE (Design of Experiments) and DOE Sequence, as well as indicating Input Variables, Output Variables<Design Objectives + Gradients, Microsoft Workbook and Lojic End

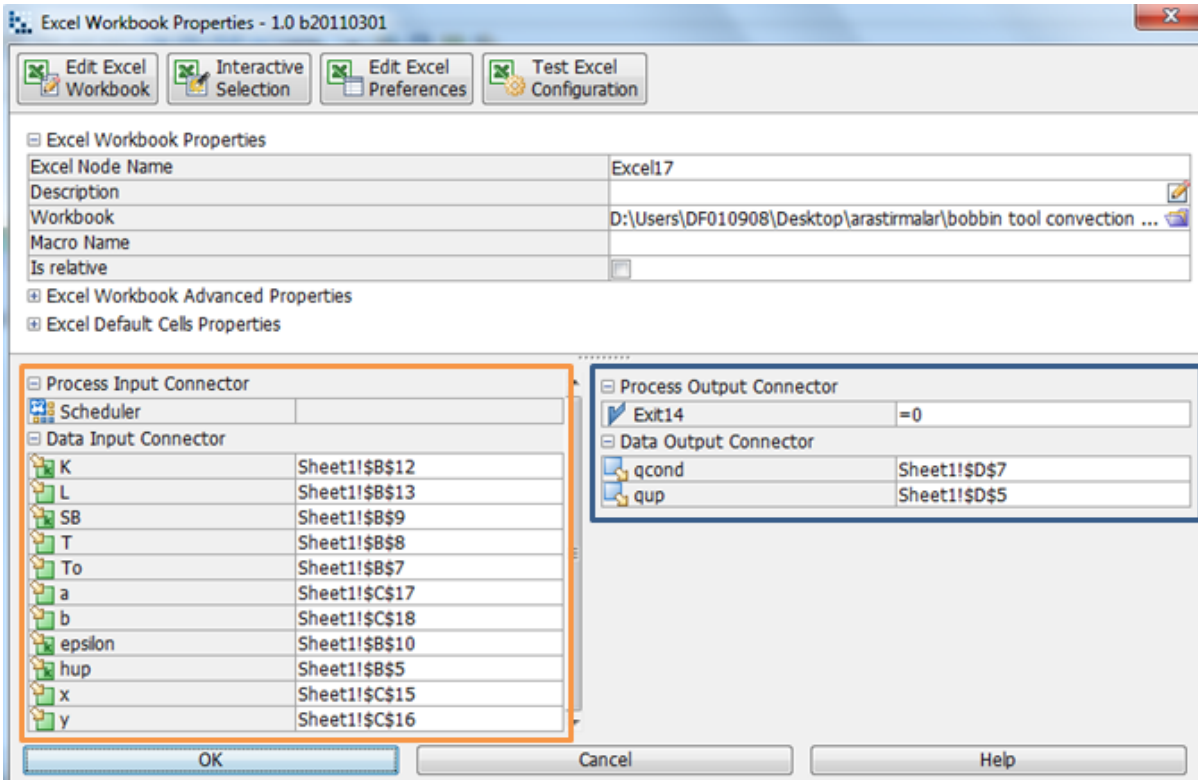


Image 8.22: Mode Frontier Input and Output Data connected to Microsoft Excel Workbook as shown above for the bobbin tool

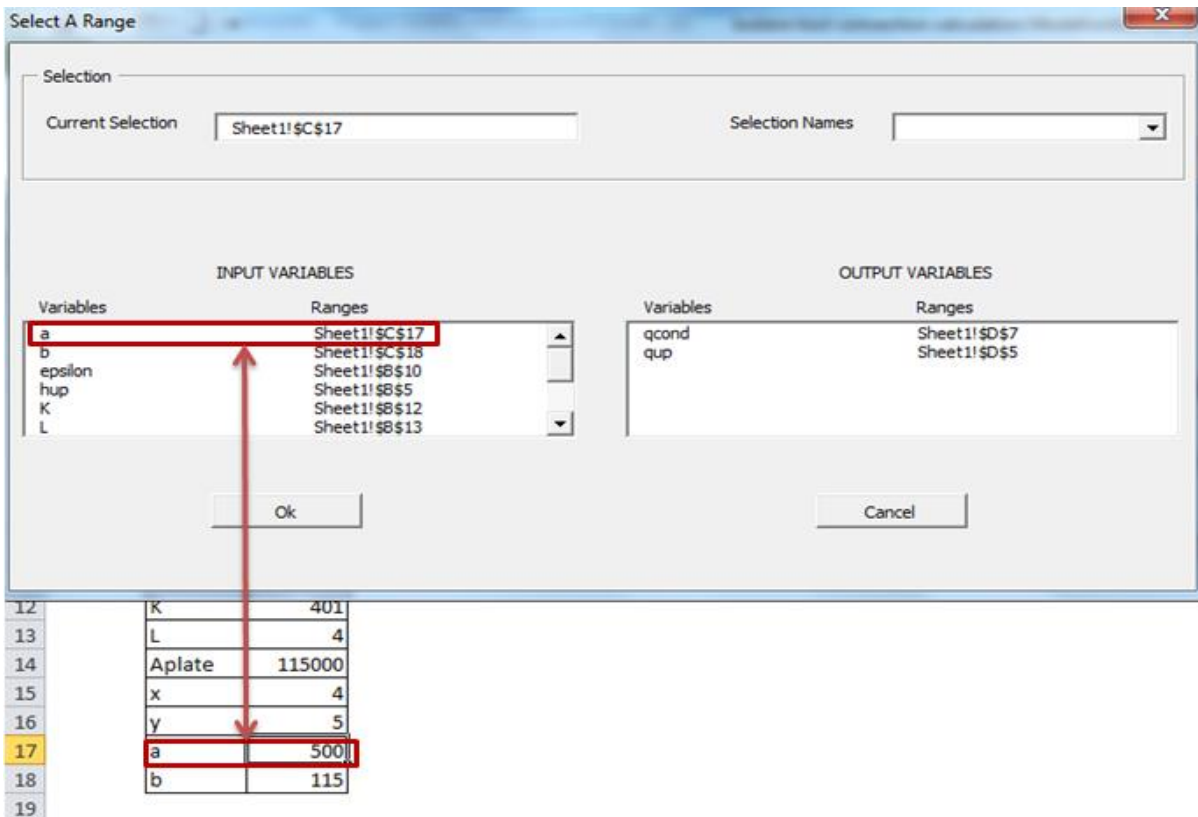


Image 8.23: Interactive Selection used between Mode Frontier *bobbin tool convection mode.prj*

8.3.2. Boundaries : Bobbin Tool Heat Loss Conditions

The boundaries for the bobbin tool are in similar reference to the standard tool, the boundaries are as follows: x,y,a,b,hup,TO,T,Stefan-Boltzmann,K,L,epsilon

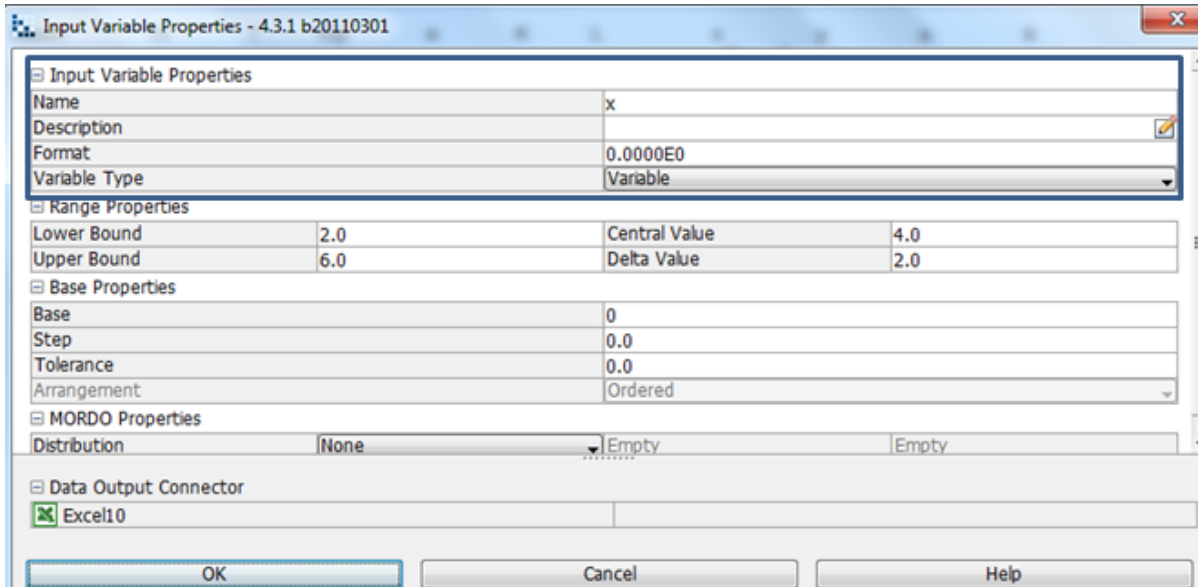


Image 8.24: x is cross-sectional area 4 mm is chosen, where the variable type is variable hence the lower and upper bound varies.

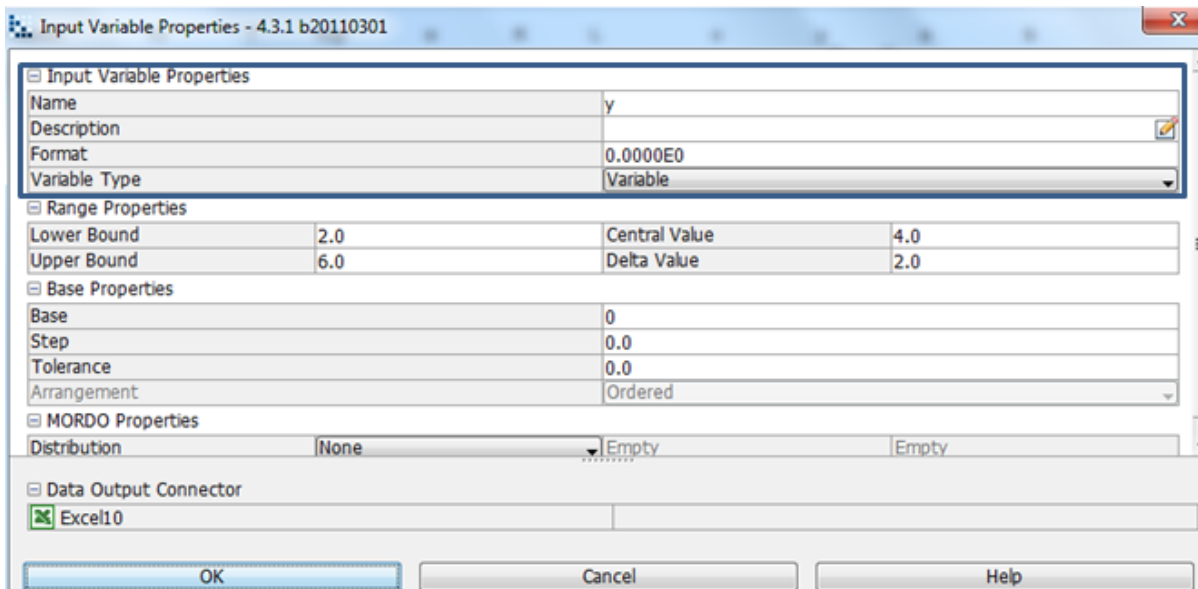


Image 8.25: y is cross-sectional area 5mm is chosen, where the variable type is variable hence the lower and upper bound varies.

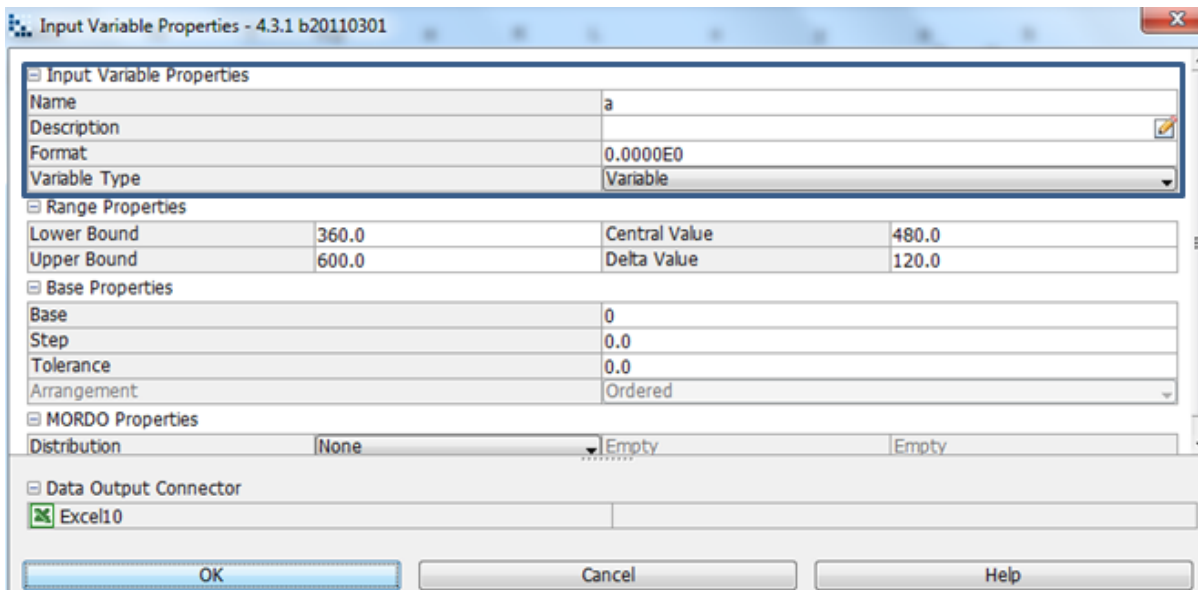


Image 8.26: a is cross-sectional area 500 mm is chosen, where the variable type is variable hence the lower and upper bound varies.

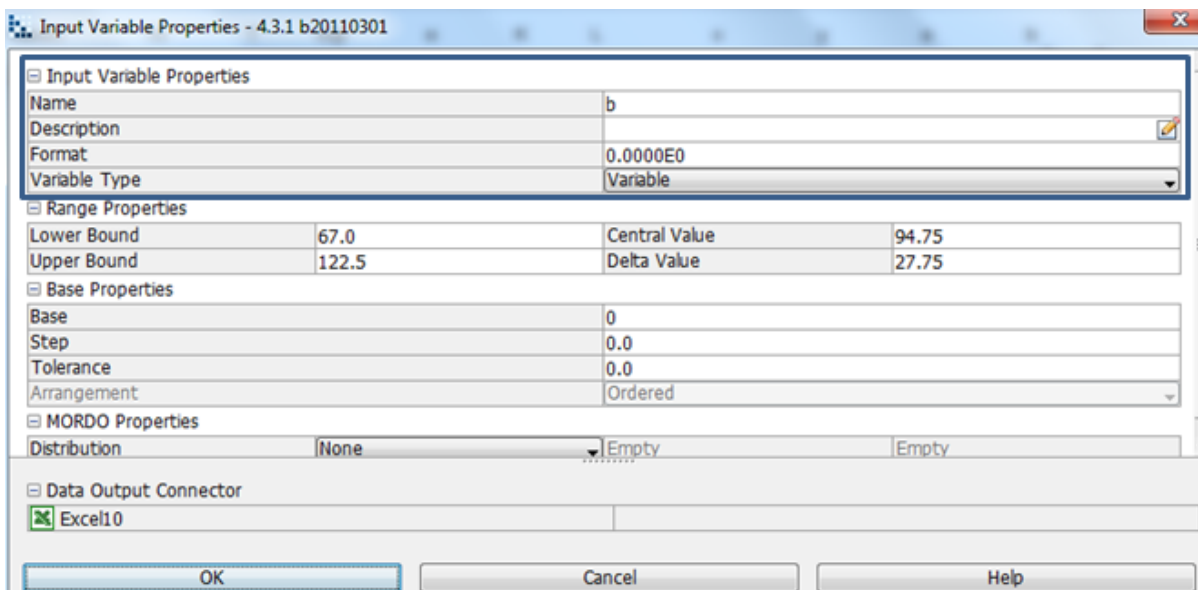


Image 8.27 : b is cross-sectional area 115 mm is chosen, where the variable type is variable hence the lower and upper bound varies.

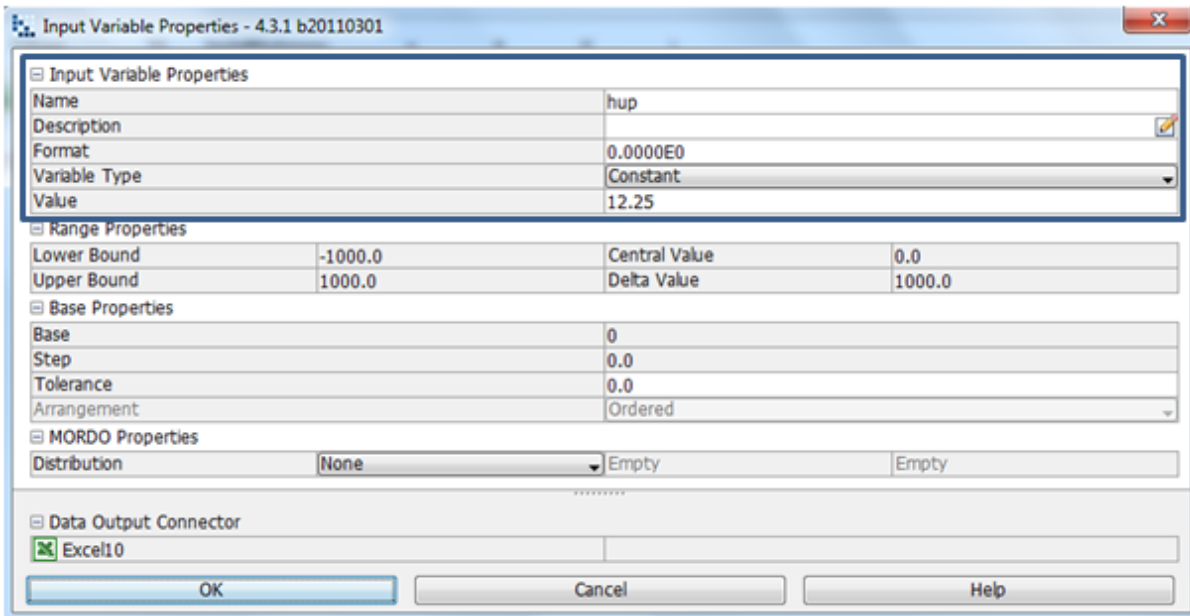


Image 8.28: The heat transfer coefficient of the upside surface $12.25 \text{ W/m}^2\cdot\text{K}$ is chosen, where the variable type is constant hence the lower and upper bound is fixed

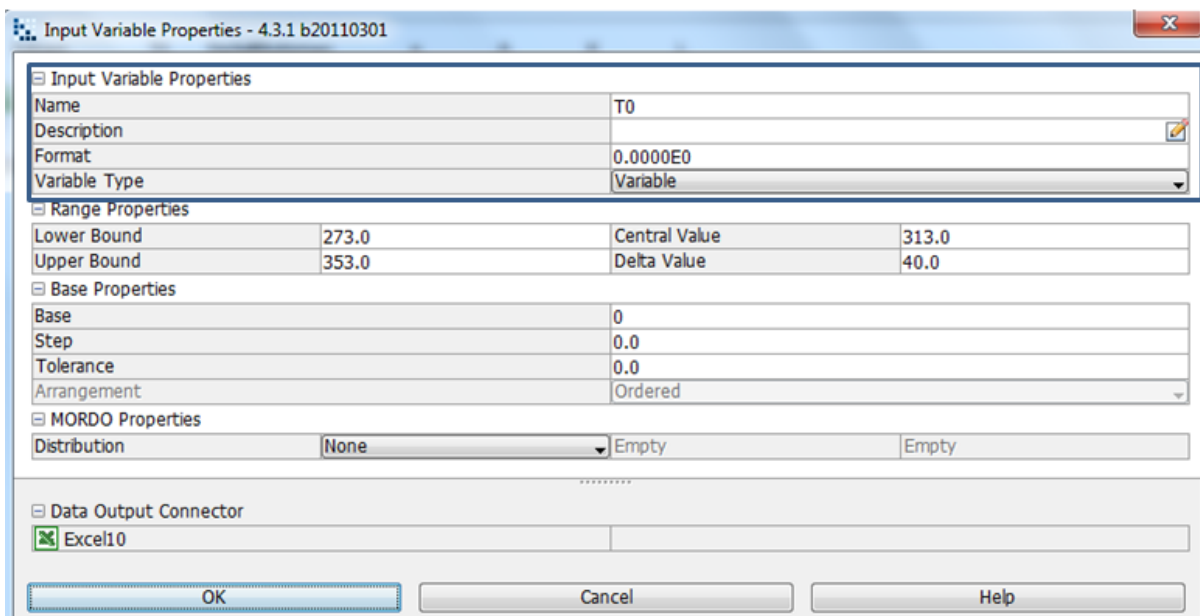


Image 8.29: The reference temperature 300 K is determined by lower and upper bound range properties, as shown in the input variable node properties dialog.

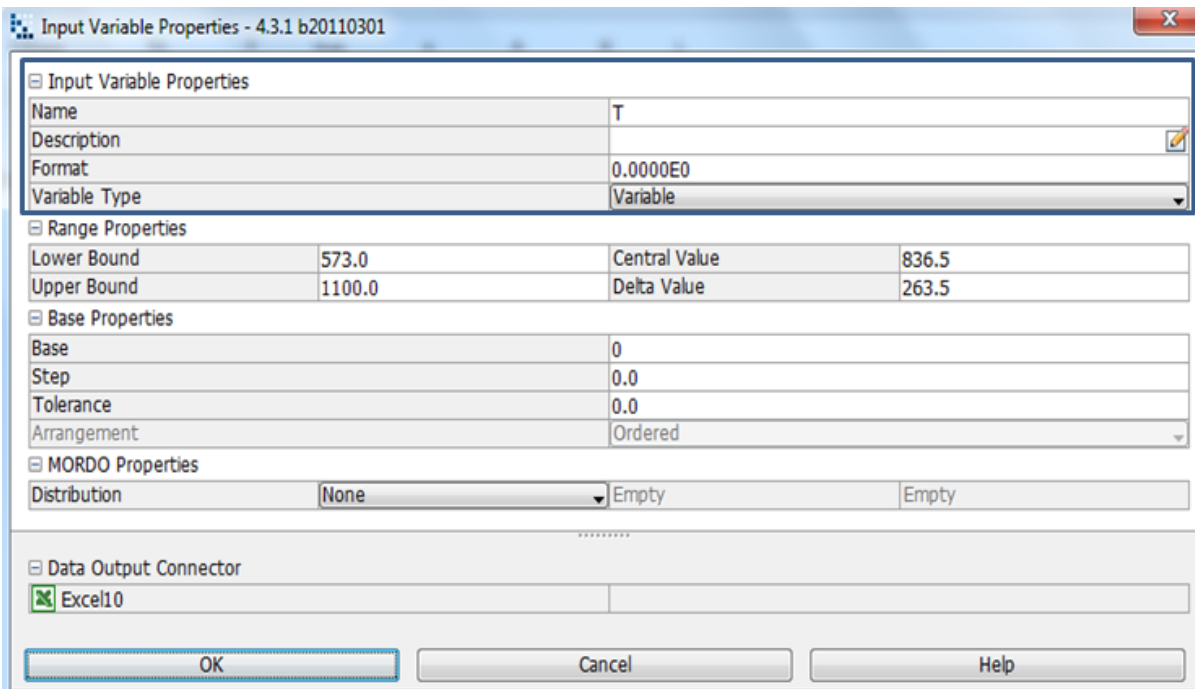


Image 8.30: The melting temperature of 935 K for the work piece is determined by lower and upper bound range properties, as shown in the input variable node properties dialog

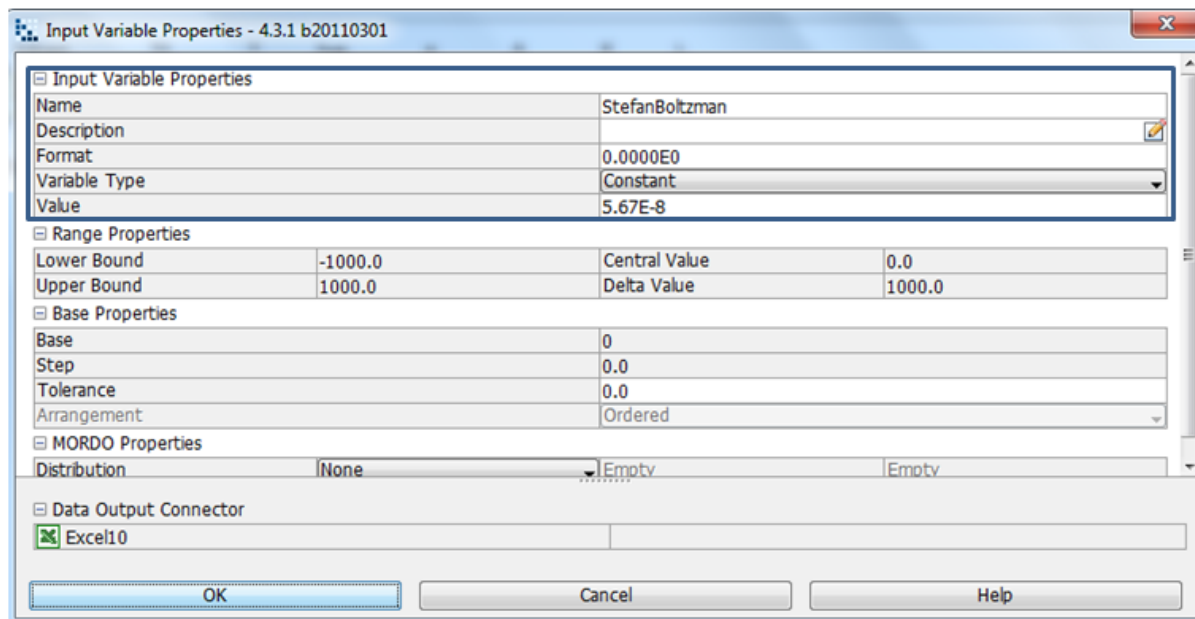


Image 8.31: The Stefan-Boltzmann constant (σ) $5.67 \times 10^{-8} \text{ Wm}^{-2}\text{K}^{-4}$ is chosen, where the variable type is constant hence the lower and upper bound is fixed

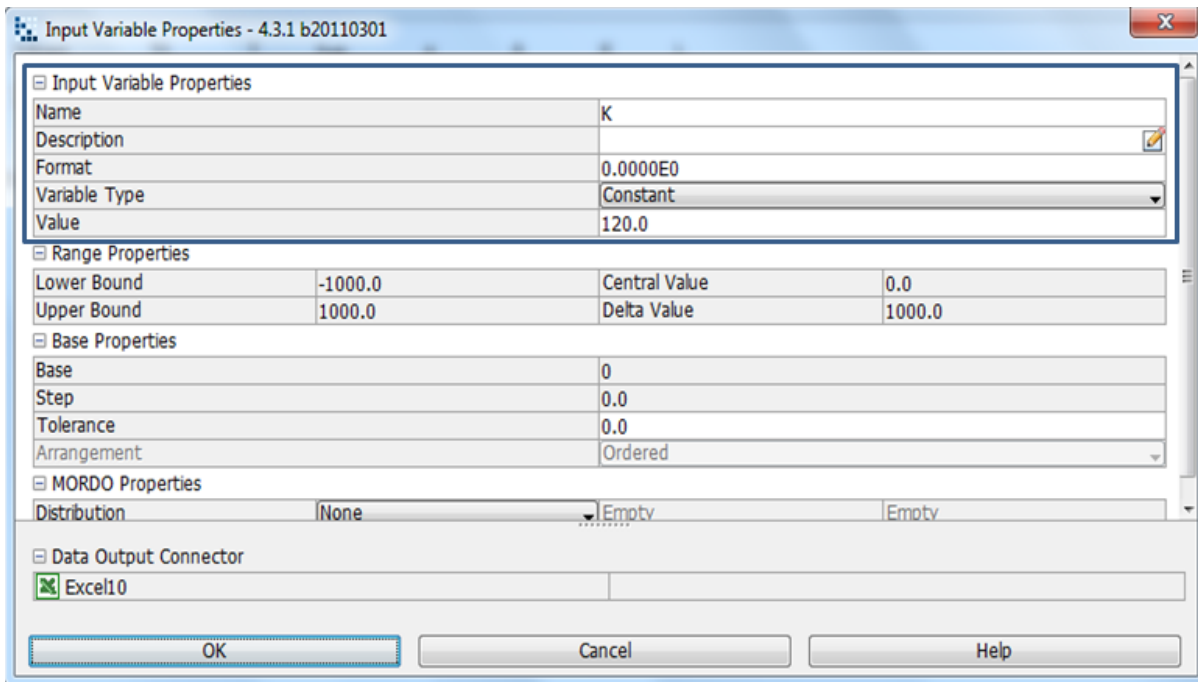


Image 8.32: The thermal conductivity of 120 W/mK is chosen, where the variable type is constant hence the lower and upper bound is fixed

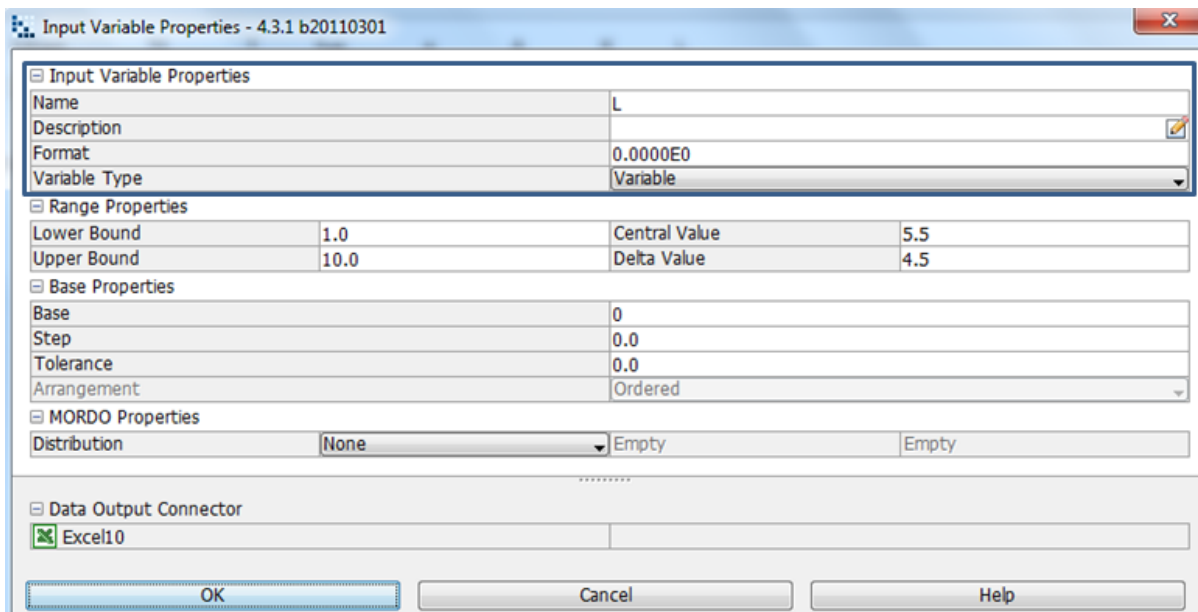


Image 8.33: The length of 4 mm is chosen, where the variable type is variable hence the lower and upper bound varies.

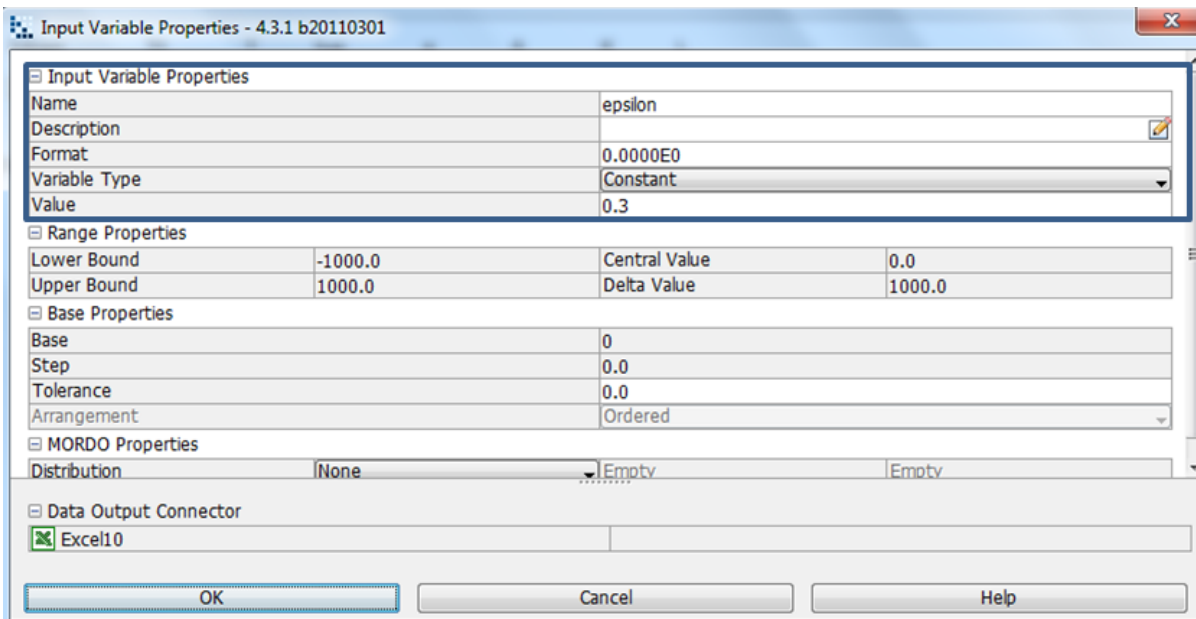


Image 8.34: The surface emissivity of 0.3 is chosen, where the variable type is constant hence the lower and upper bound is fixed.

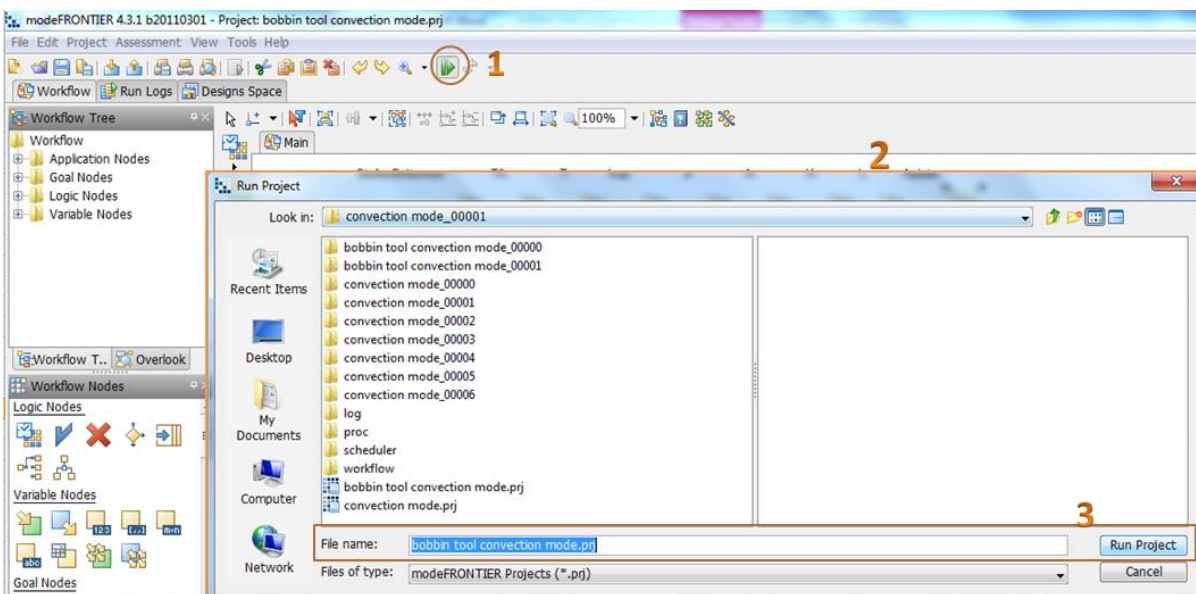


Image 8.35: Click on run/stop icon (1). Run project box will pop up (2). Click on run project (3) to start design project

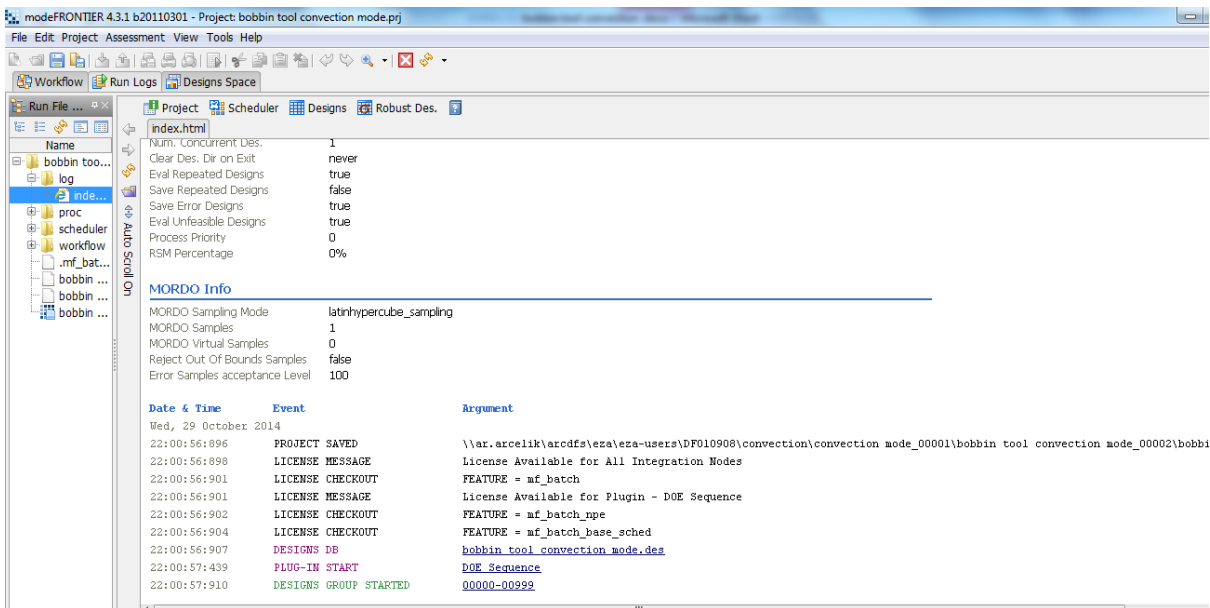


Image 8.36: Before project runs, a project info index will be shown. As seen in the above image.

8.4. Multi History Charts for Bobbin Tool Heat Loss Conditions

The Normal Quantile Plot is a representation of a probability plot, a representation of the heat loss by conduction on the upper surface (hup) against the qupobjective is shown as created from y (Chart 8.9). The heat loss by conduction on the upper surface (hup) against the qupobjective as created from x is shown to be represented on a normal quantile plot (Chart 8.10), the representation of the temperature and heat conduction to the heat conduction objective is clearly indicated on the multi history chart showing the designs feasibility in reality (Chart 8.11), the multi history chart that represents the temperature and the heat loss by conduction on the upper surface to the qupobjective(heat loss on the upper surface objective) shows feasibility on a real scale (Chart 8.12), The multi history chart that represents the reference temperature and heat conduction to the heat conduction objective shows the design is feasible in reality(Chart 8.13), the multi history chart for the reference temperature and heat loss by conduction on the upper surface shows and represents that the design is feasible on a real scale (Chart 8.14).

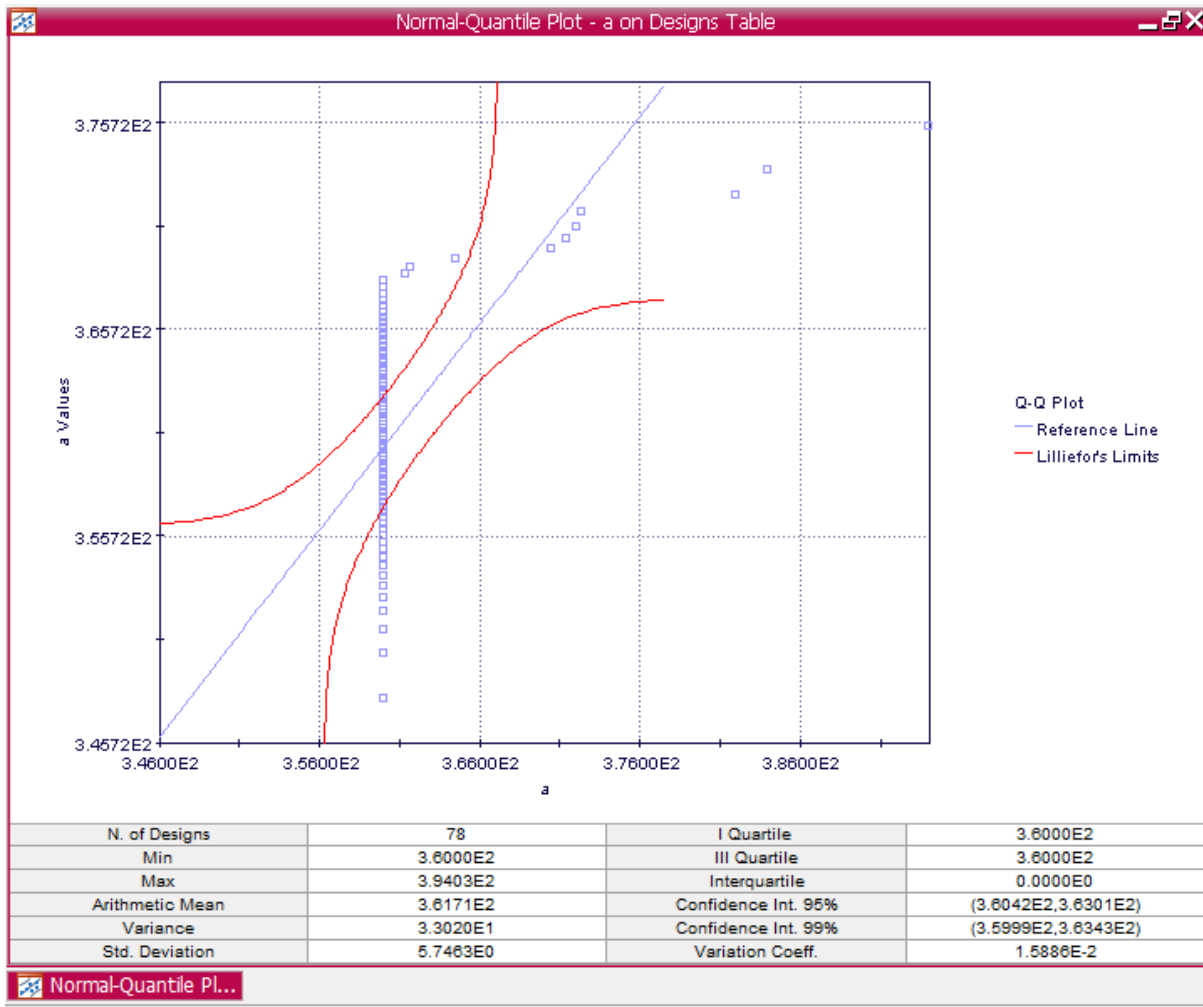


Chart 8.9: Normal-Quantile Plot on Designs Space as created from the aplate, the heat loss by conduction on the upper surface to the qupobjective

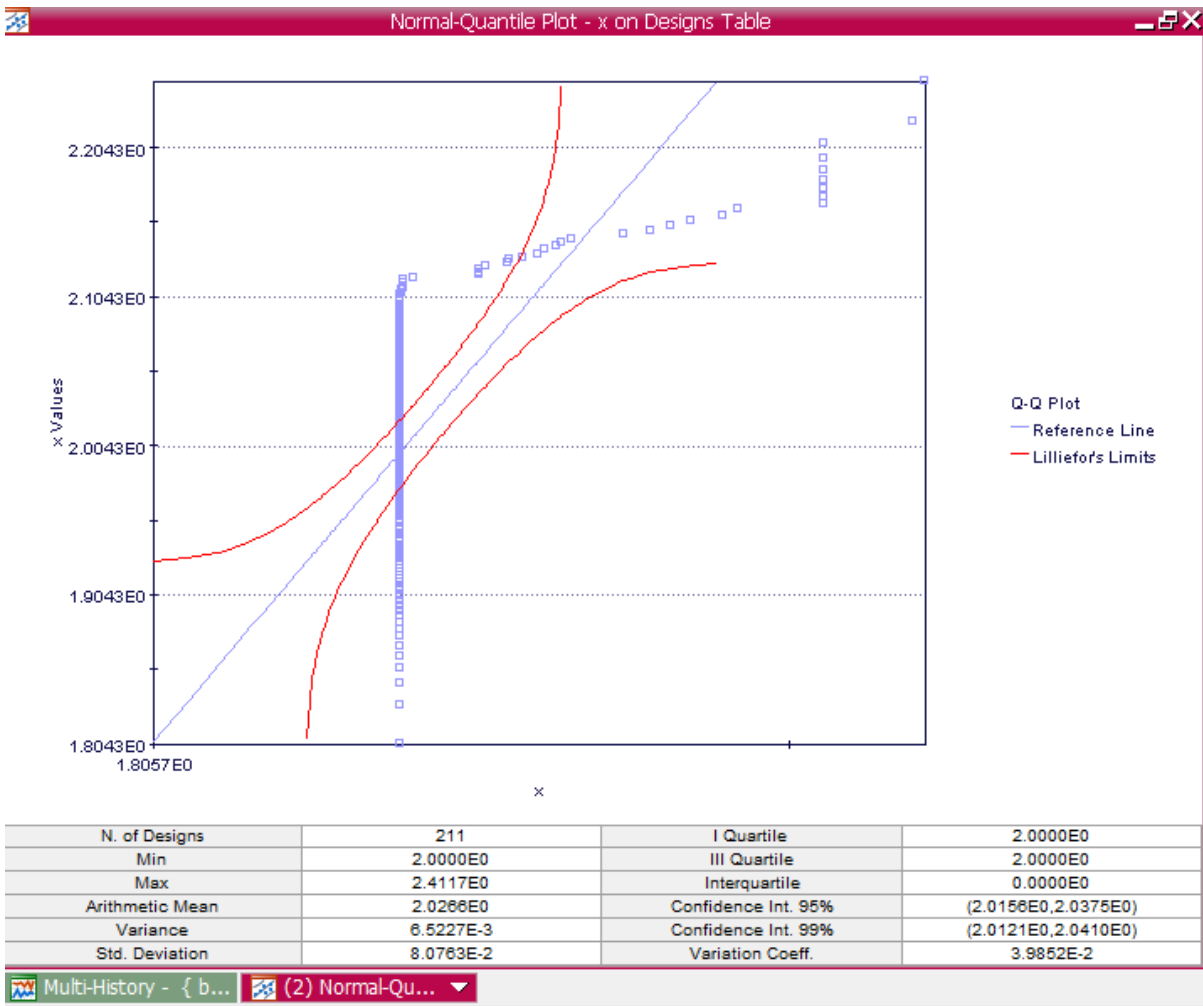


Chart 8.10: Normal-Quantile Plot on Designs Space as created from the x, the heat loss by conduction on the upper surface to the qobjective

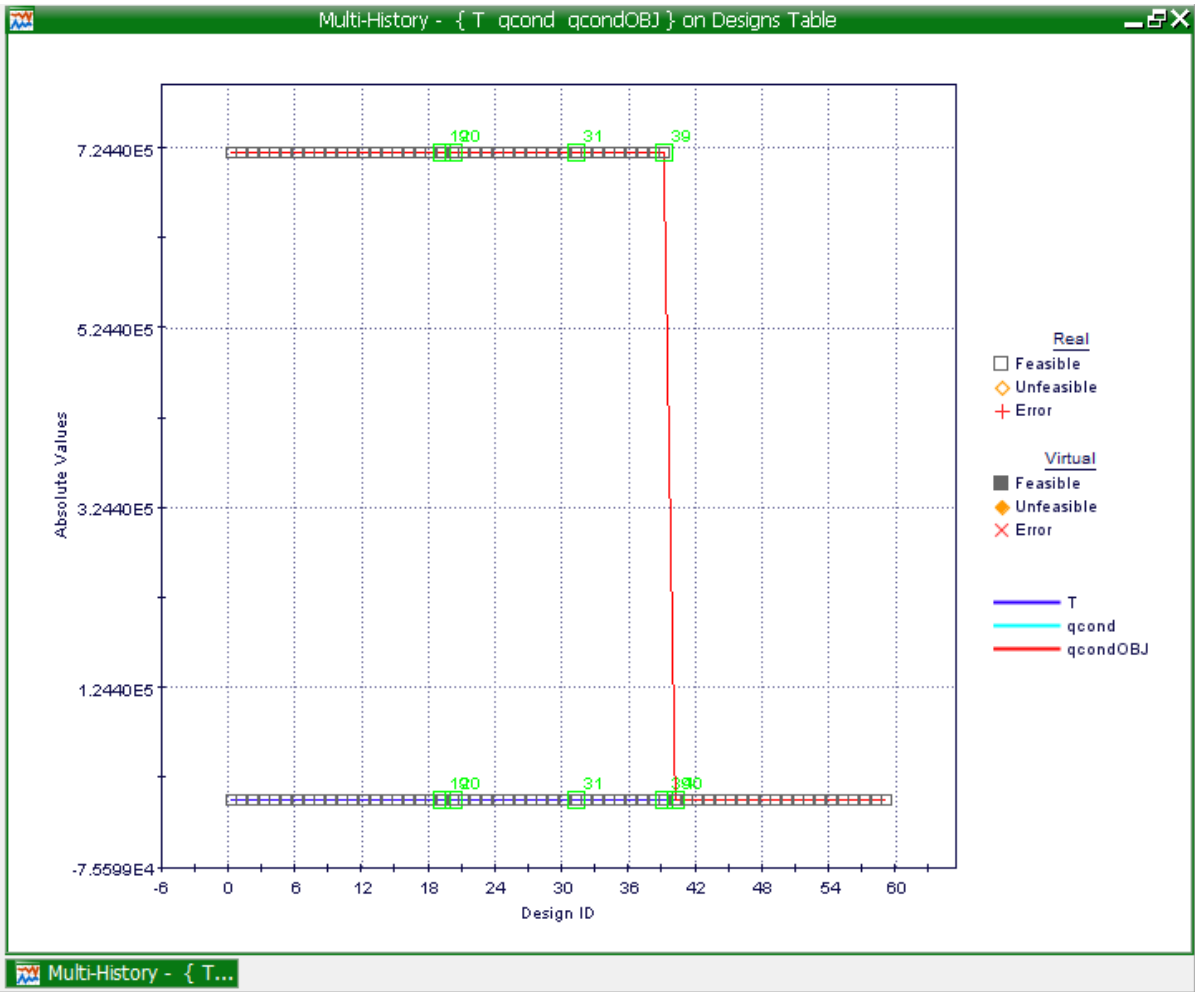


Chart 8.11: Multi-History Chart on Designs Space as created from the representation of the temperature and heat conduction to the heat conduction objective.

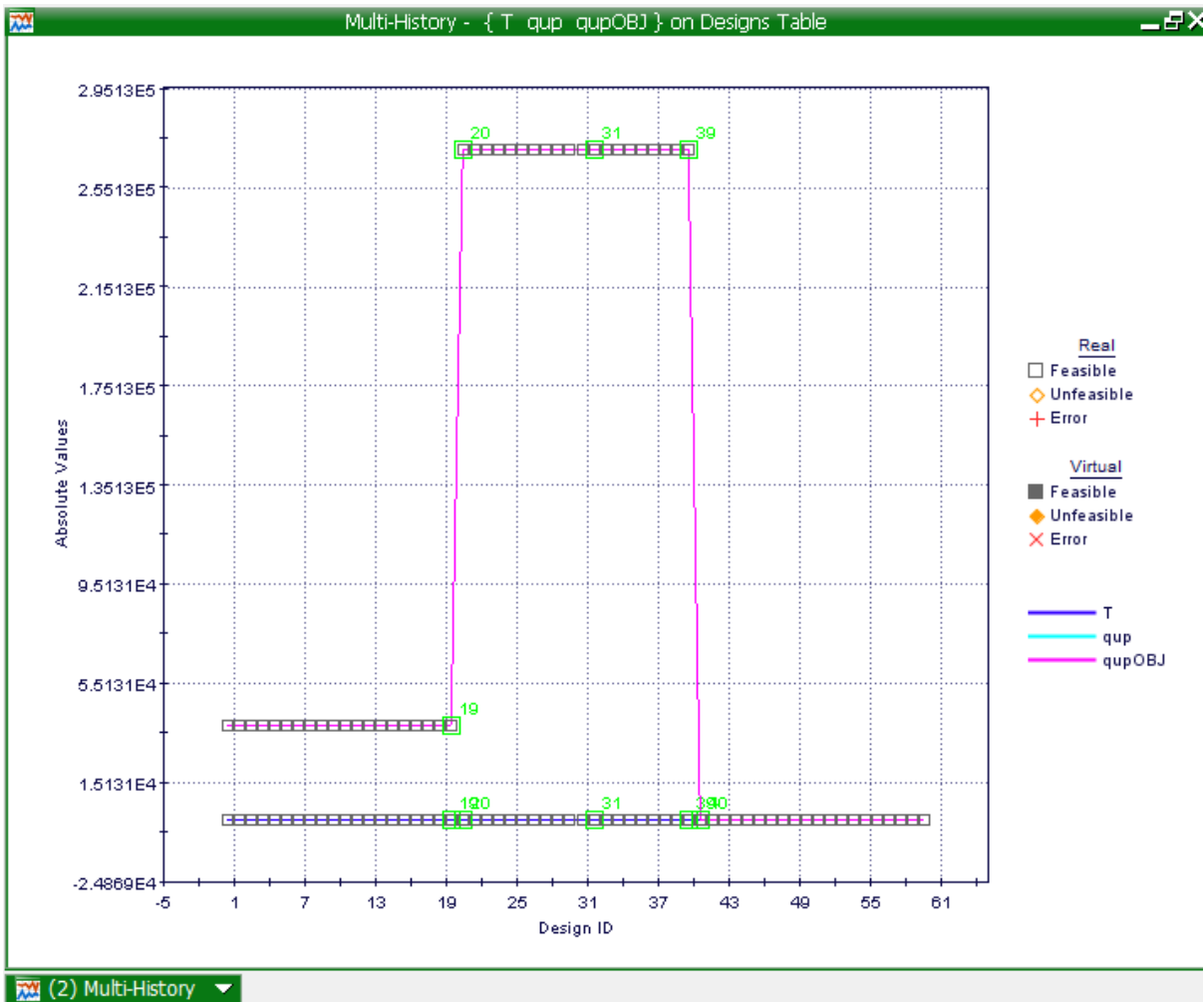


Chart 8.12: Multi-History Chart on Designs Space as created from temperature and the heat loss by conduction on the upper surface to the qcpobjective (heat loss on the upper surface objective).

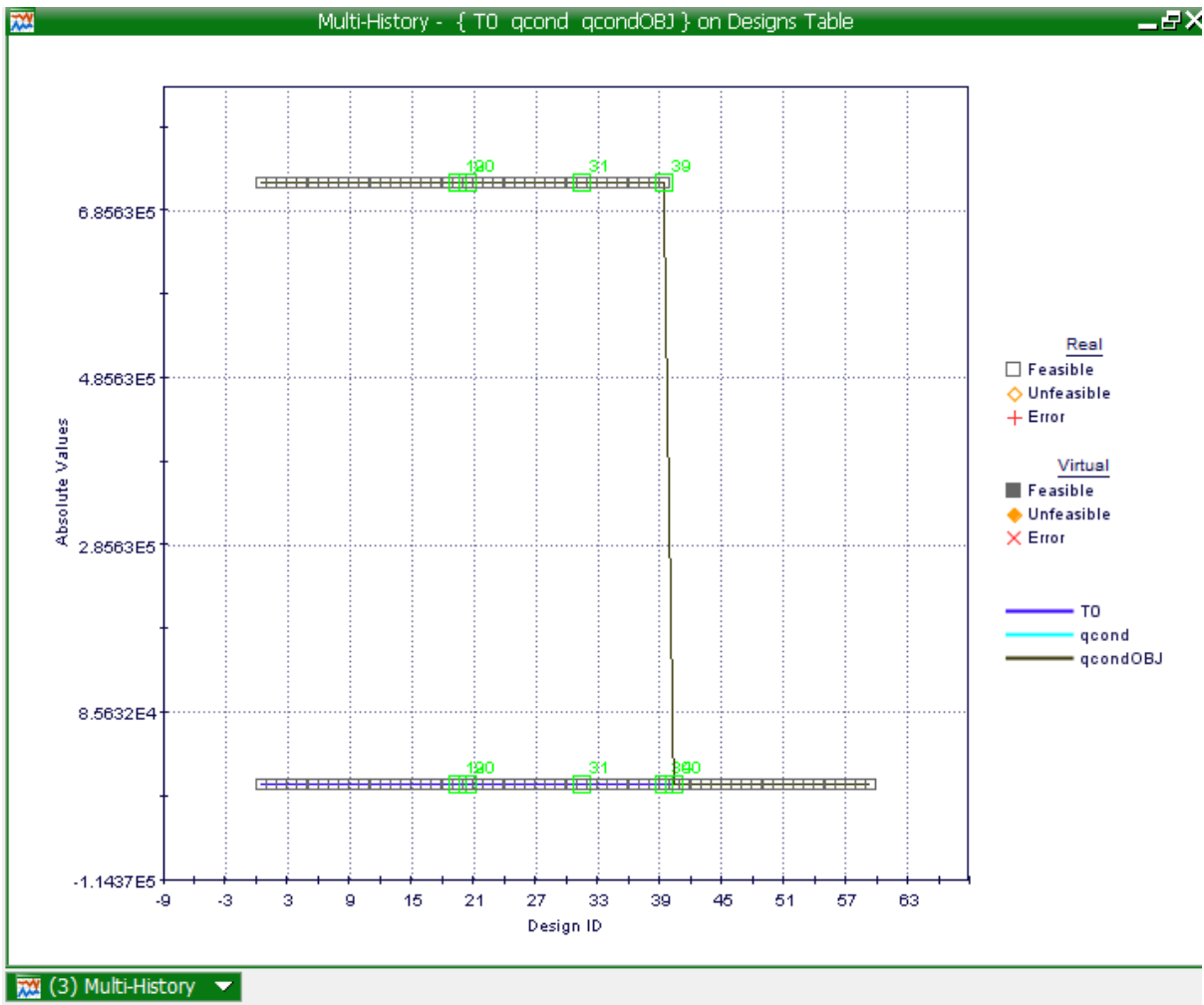


Chart 8.13: Multi-History Chart on Designs Space as created from reference temperature and heat conduction to the heat conduction objective

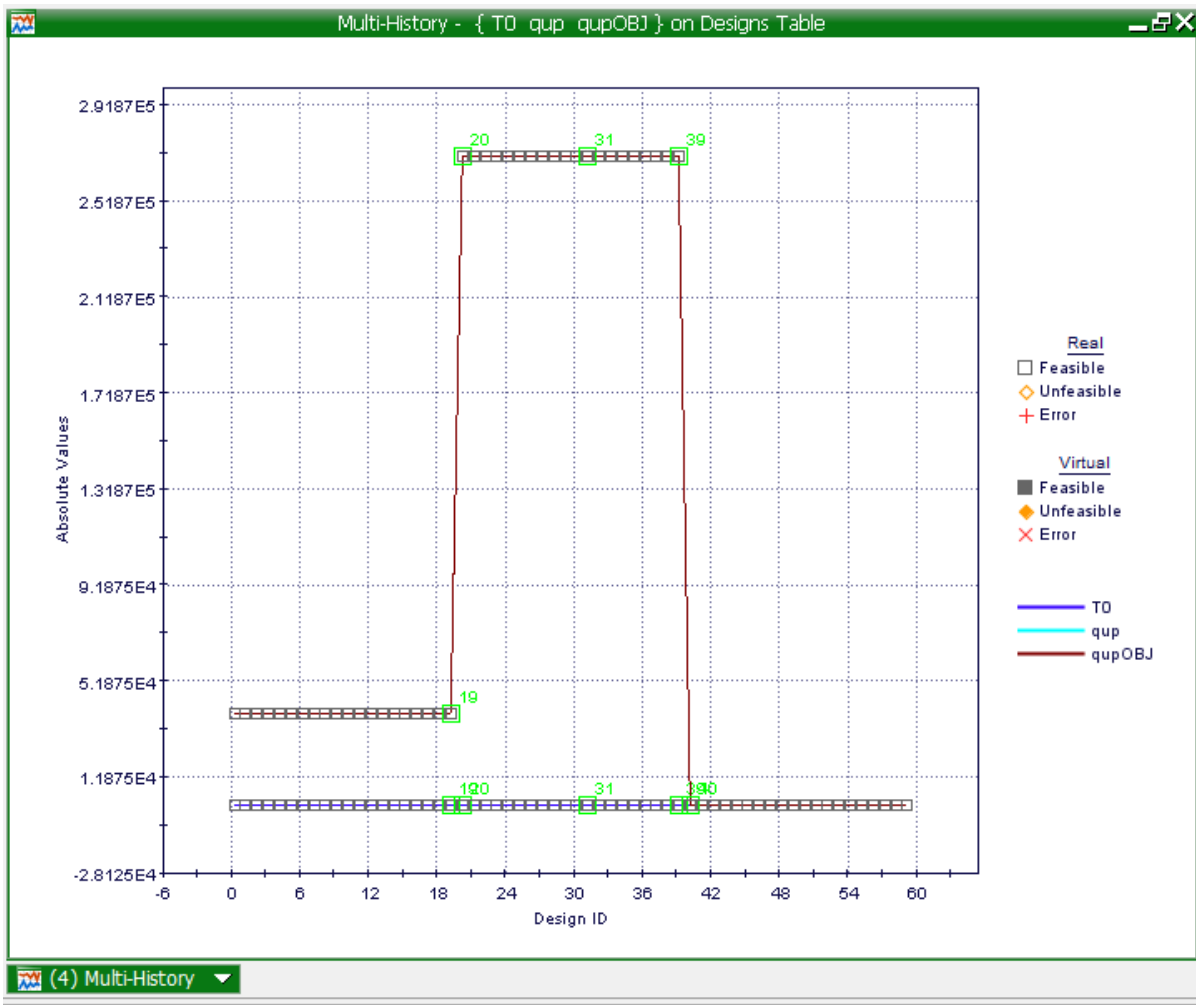
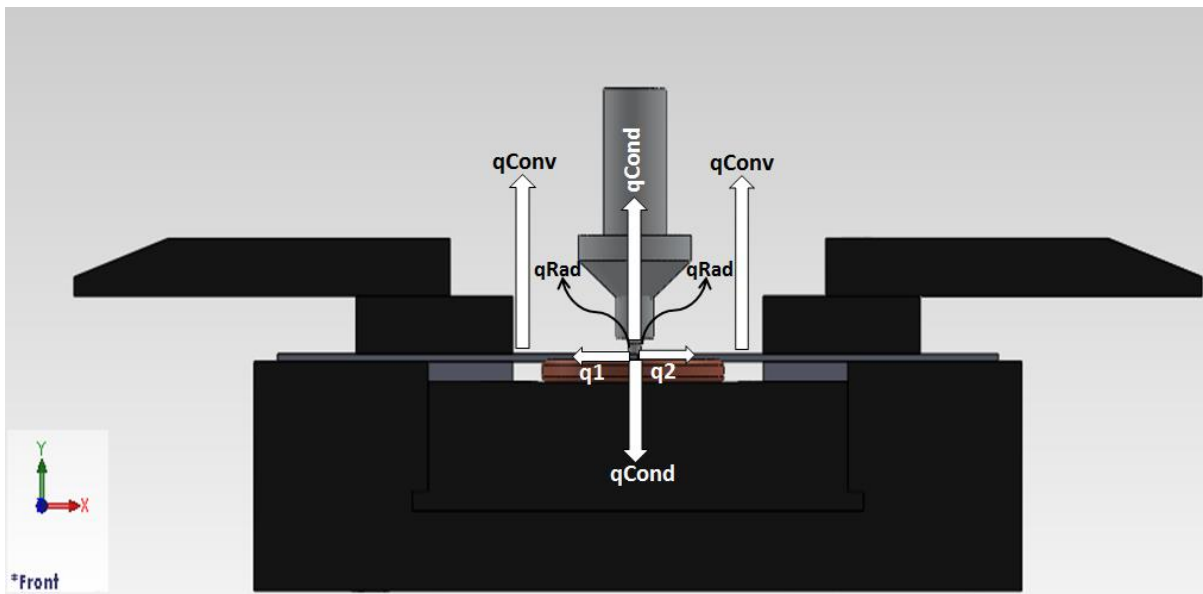


Chart 8.14: Multi-History Chart on Designs Space as created from reference temperature and heat loss by conduction on the upper surface.

8.5. Innovative Tool Heat Loss Conditions

During a friction stir weld the heat loss or heat convection (q_{Conv}) from the place area of the innovative tool is exerted upwards whilst the radial (q_{Rad}) heat transfer from the tool probe is shown to flow around the tool, the copper bush in the innovative tool shows true purpose when the weld commences when the copper bush conducts (q_{Cond}) heat flow for both the tool and the workbench, preventing the melting. Obviously the thermal diffusivity for example the ratio of thermal conductivity to the volumetric heat capacity of the materials, and the subsequent masses involved in each of the heat loss pathways. In the case of FSW the tool is just not part of the heat source but is itself a not insignificant avenue for heat loss. This avenue along with all other avenues for heat loss is presented schematically and incorporated within the flow loss of heat equation.



Drw 8.3: Thermal Aspect for the Innovative Tool Design [Uslu, M.Y, (2014), *Thermal aspect of the innovative tool design, University of the Witwatersrand*]

$$h_{up} = 12.25 \text{ W/m}^2\text{K}$$

$$h_{down} = 6.25 \text{ W/m}^2\text{K}$$

$$q_b = 100 \text{ W/m}^2\text{K}$$

$$T_0 = 25 \text{ }^\circ\text{C} = 299 \text{ K}$$

$$T = 662 \text{ }^\circ\text{C} = 935 \text{ K}$$

$$\sigma = 5.67 \times 10^{-8} \text{ Wm}^{-2}\text{K}^{-4}$$

$$\varepsilon = 0.3$$

$$x = 4 \text{ mm}$$

$$y = 5 \text{ mm}$$

$$a = 500 \text{ mm}$$

$$b = 115 \text{ mm}$$

$$L_1 = 2 \times 10^{-3} \text{ m}$$

$$L_2 = 2 \times 10^{-3} \text{ m}$$

$$K = 120 \text{ W/mK}$$

$$q_{up} = A_{plate} (h_{up}(T_0 - T) + \varepsilon\sigma(T_{amb}^4 - T^4))$$

$$q_{up} = 0.115 \times 10^{-6} \times (12.25 \times (299 - 935) + 0.3 \times 5.6710^{-8} (299^4 - 935^4))$$

$$q_{up} = 2375.355885 \text{ W}$$

$$q_{down} = A_{plate} (h_{down}(T_0 - T) + \varepsilon\sigma(T_{amb}^4 - T^4))$$

$$q_{up} = 0.115 \times 10^{-6} \times (6.25 \times (299 - 935) + 0.3 \times 5.6710^{-8} (299^4 - 935^4))$$

$$q_{down} = 1936.515885 \text{ W}$$

$$q_{cond} = AK(T - T_{amb})/L$$

$$q_{cond} = 20 \times 10^{-6} \times 120 \times (935 - 299) / 4 \times 10^{-3}$$

$$q_{cond} = 381.6 \text{ W}$$

$$q_{copper} = AK(T - T_{amb})/L$$

$$q_{cond} = 20 \times 10^{-6} \times 401 \times (935 - 299) / 4 \times 10^{-3}$$

$$q_{cond} = 1275.18 \text{ W}$$

8.5.1. Mode Frontier Simulation : Innovative tool Heat Loss Conditions

Input Data, Output Data and boundary variables definitions as shown on this Microsoft Excel Sheet file name convection calculation modefrontier.xlsx is used in Mode Frontier for this Design Project: Since each component defining the Workflow is represented by a specific node which can be linked to other nodes, a proper node from the available Node Library toolbar or, alternatively, chosen by using the Workflow Nodes panel. It is shown all the input data output data and boundary variables in a Microsoft Excel workbook. The excel work books is used so that the equation for the rotational speed along with the heat generation is calculated where the results will be used in ModeFrontier to assist in the design (Image 8.38).Once a Workflow Plan created by Mode Frontier Project as shown in deneme04.prj, also includes DOE (Design of Experiments) and DOE Sequence, as well as indicating Input Variables, Output Variables, Design Objectives + Gradients, Microsoft Excel Workbook and Logic End(Image 8.39).A workflow plan is created using a DoE (Design of Experiments) and a DOE Sequence on a new Overlook. Once this is open workflow nodes can be added on. Variable nodes which are the input nodes and the output nodes are used. Workflow nodes such as the schedulers, the logic switch and logic end is used. An application node is used for excel. A goal node which is the design objective+gradient node. Mode Frontier Input and Output Data is connected to Microsoft Excel Workbook .Excel workbook properties are used for basic node configuration where an Excel Workbook is selected (Image 8.40). Once selected the input and out data is connected from the chosen Excel workbook. An Interactive Selection used between Mode Frontier convection mode.prj, and Microsoft Excel Workbook: convection calculation modefrontier.xlsx to determine Excel Workbook Properties for Mode Frontier (Image 8.41) An interactive selection allows each input and output node to be configured in accordance to the Excel workbook. Where each variable is interactively selected to complete a work plan.

INPUT DATA		OUTPUT DATA	
hup	12.25	qup	2375.35589
hdown	6.25	qdown	1936.51589
To	299	qcond	381.6
T	935	qcopper	1275.18
σ	5.67E-08		
ε	0.3		
A	0.00002		
K	120		
L	4		
Aplate	0.115		
Kcopper	401		
x	4		
y	5		
a	500		
b	115		

$$A_{plate} = a_{plate} \times b_{plate}$$

$$q_{up} = A_{plate} h_{up} (T - T_0) + \epsilon \sigma (T_{amb}^4 - T^4)$$

$$q_{down} = A_{plate} h_{down} (T - T_0) + \epsilon \sigma (T_{amb}^4 - T^4)$$

$$q_{cond} = AK(T - T_{amb})/L$$

Image 8.36: Input Data, Output Data and boundary variables definitions as shown on this Microsoft Excel Sheet file name: innovative tool convection calculation Modefrontier.xlsx is used in Mode Frontier for Design Project

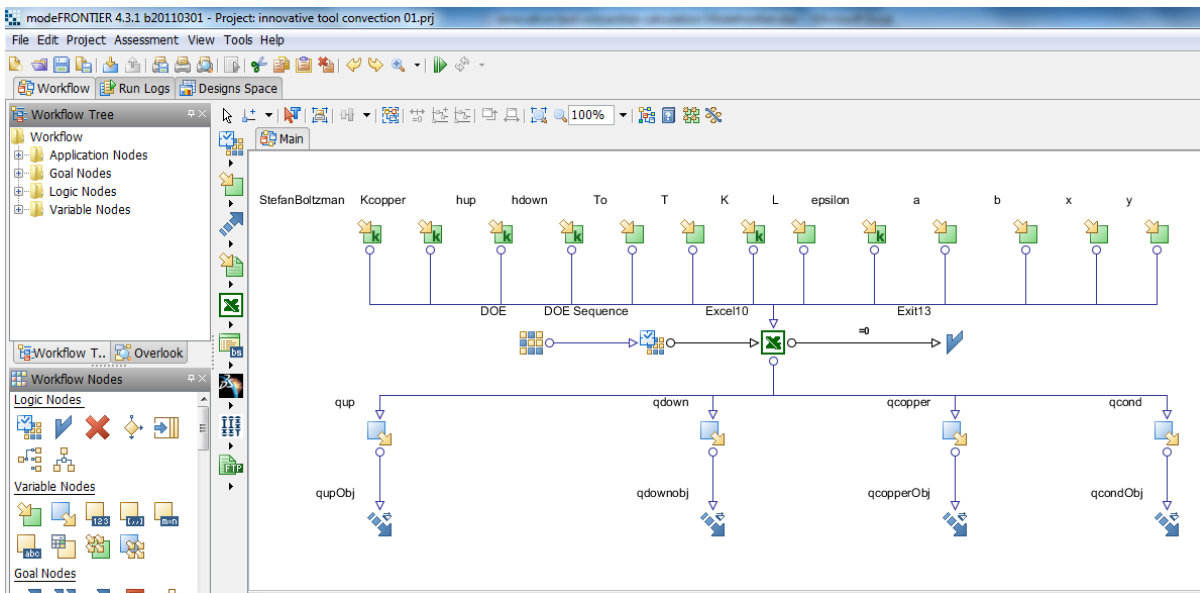


Image 8.37: Workflow Plan created on Mode Frontier Project as shown in *innovative tool convection mode.prj*, also includes DOE (Design of Experiments) and DOE Sequence, as well as indicating Input Variables, Output Variables<Design Objectives + Gradients, Microsoft Workbook and Logic End

Process Input Connector		Process Output Connector	
Scheduler		Exit13	=0
Data Input Connector		Data Output Connector	
A	Sheet1!\$B\$11	qcond	Sheet1!\$D\$7
Aplate	Sheet1!\$B\$14	qcopper	Sheet1!\$D\$8
K	Sheet1!\$B\$12	qdown	Sheet1!\$D\$6
Kcopper	Sheet1!\$B\$15	qup	Sheet1!\$D\$5
L	Sheet1!\$B\$13		
StefanBoltzman	Sheet1!\$B\$9		
T	Sheet1!\$B\$8		
To	Sheet1!\$B\$7		
epsilon	Sheet1!\$B\$10		
hdown	Sheet1!\$B\$6		
hup	Sheet1!\$B\$5		

Image 8.38: Mode Frontier Input and Output Dates connected to Microsoft Excel Workbook as shown above for innovative tool

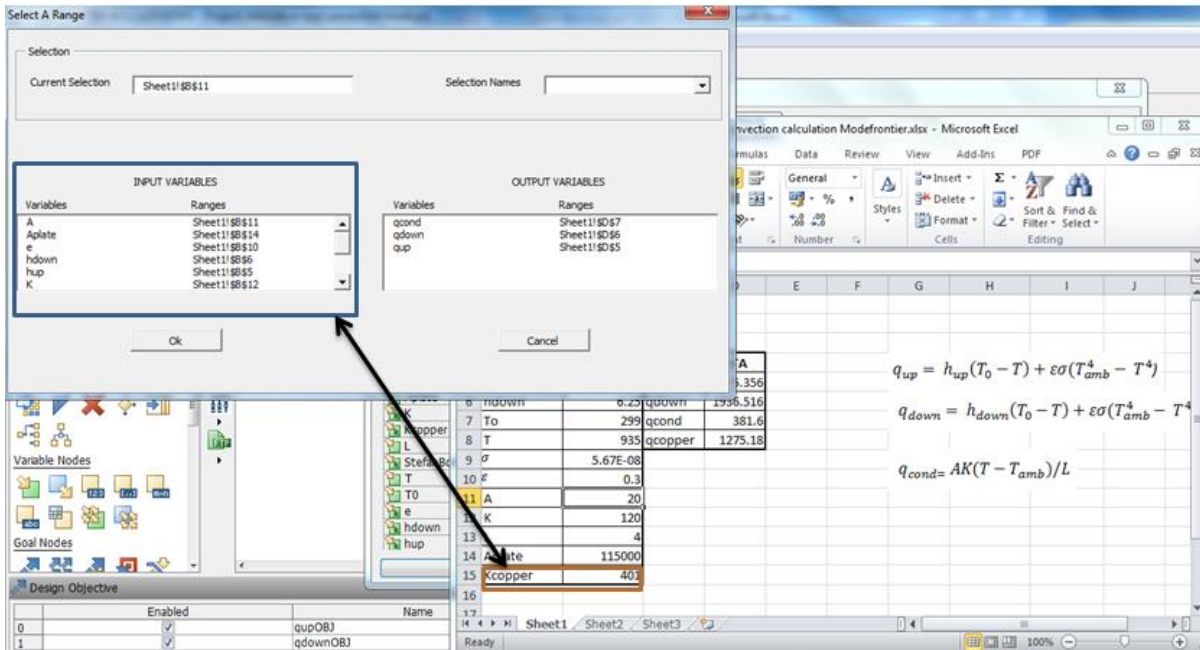


Image 8.39: Interactive Selection used between Mode Frontier *convection mode.prj*

8.5.2. Boundaries : Innovative Tool Heat Loss Conditions

The boundaries for the innovative tool loss boundaries are in similar reference to the standard tool heat loss, the boundaries are as follows: as follows: x, y, a, b, hup, TO, T, Stefan-Boltzmann, K, L, epsilon. Kcopper, Copper is a major conductor, as discussed earlier in this study, the copper bush in the innovative tool served the purpose as a conductor to conduct extra heat generation given off by the innovative tool and prevent melting of any materials(in reference with telco), this makes the copper bush a constant variable and range properties that are fixed and a value of 401.0 and lastly hdown has a variable type that is constant with a value of 6.25 and range properties that is fixed. The projects starts once a run project has started and then an index will appear before the initial project design commences.

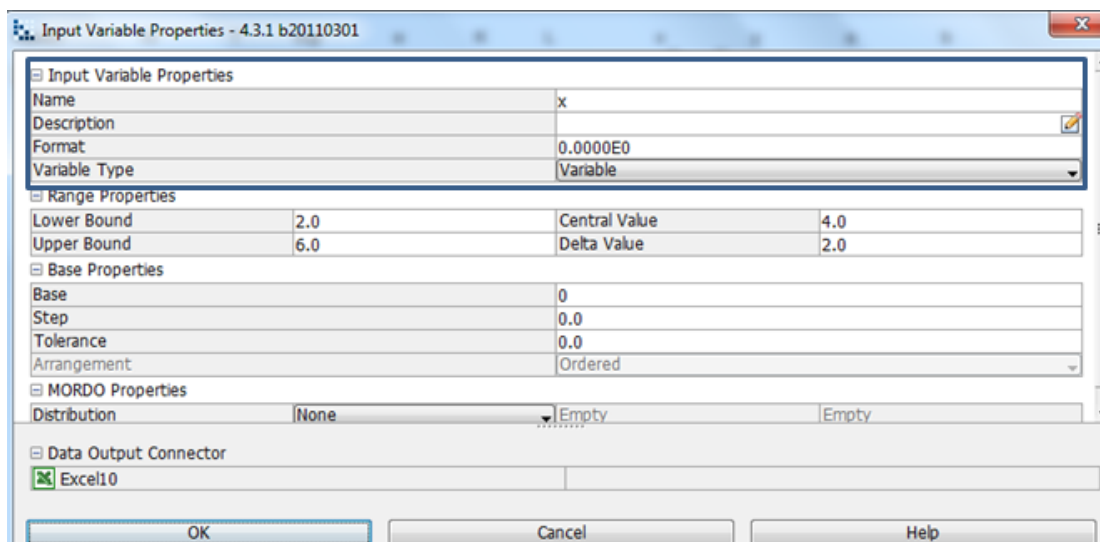


Image 8.40: x is cross-sectional area 4 mm is chosen, where the variable type is variable hence the lower and upper bound varies.

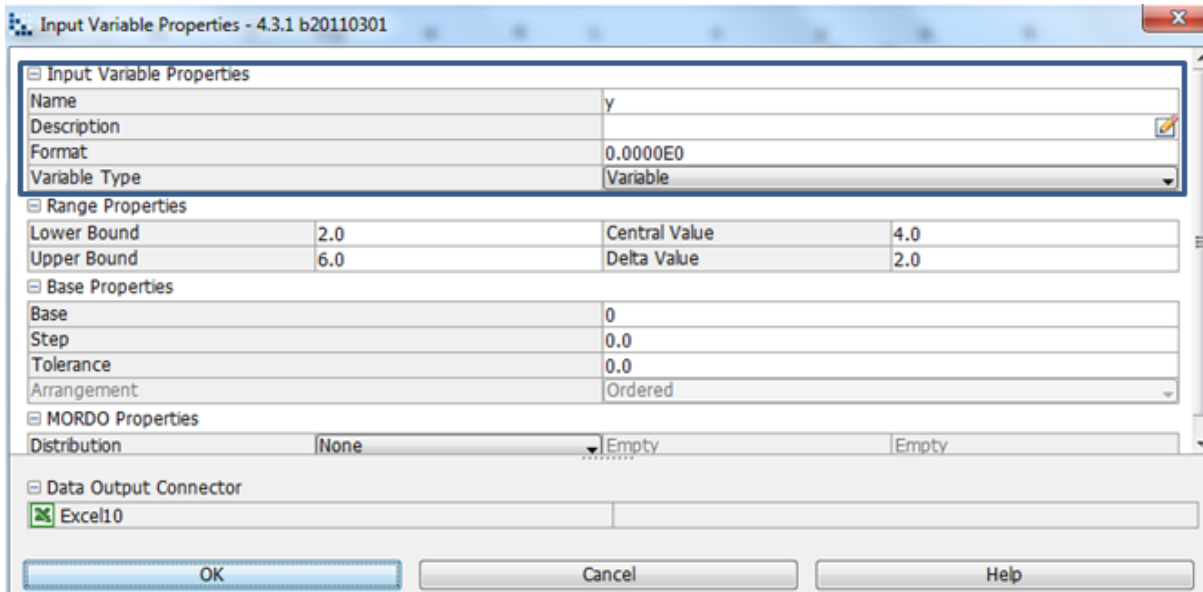


Image 8.41: y is cross-sectional area 5 mm is chosen, where the variable type is variable hence the lower and upper bound varies.

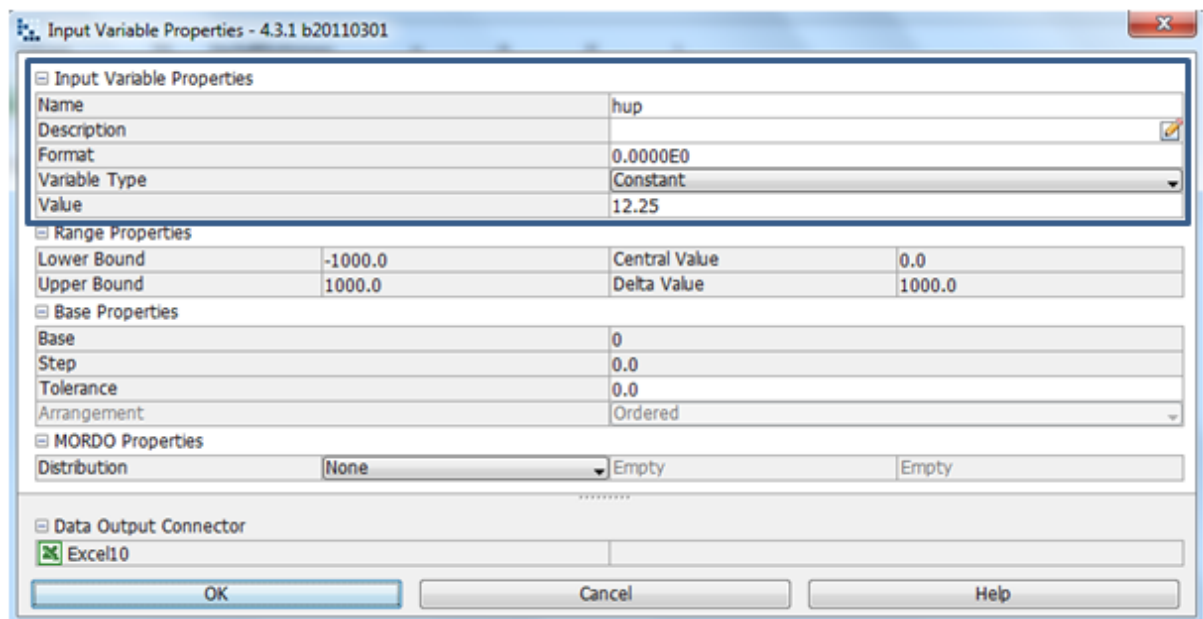


Image 8.42: Heat transfer coefficient, upside 12.25 W/m²*K is chosen, where the variable type is constant hence the lower and upper bound is fixed

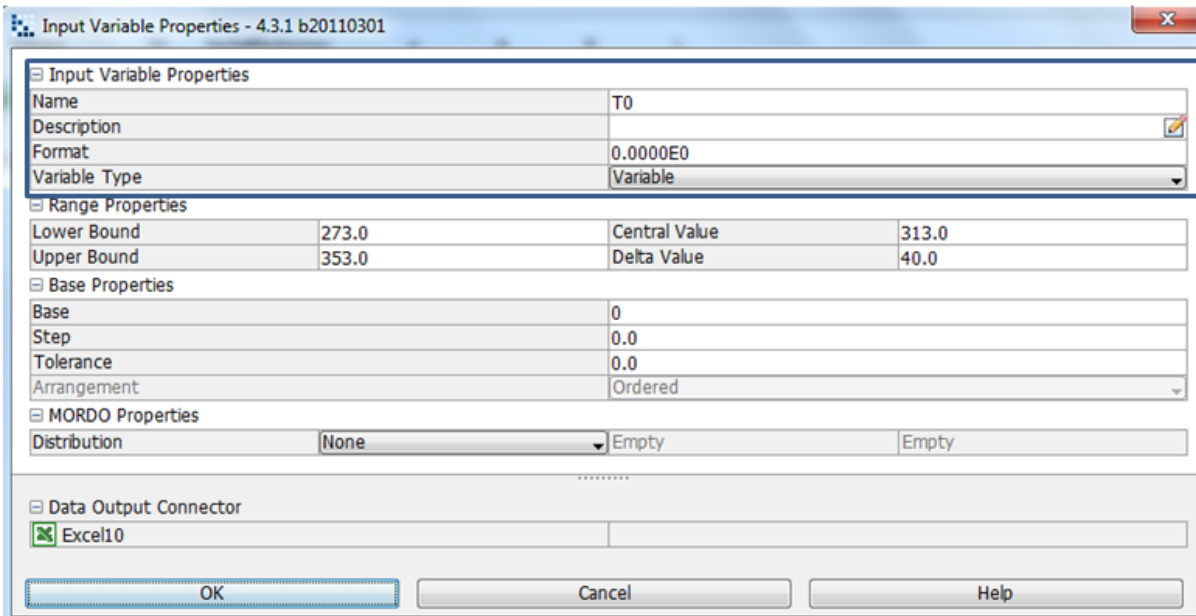


Image 8.43: Reference temperature 300 K is determined by lower and upper bound range properties, as shown in the input variable node properties dialog

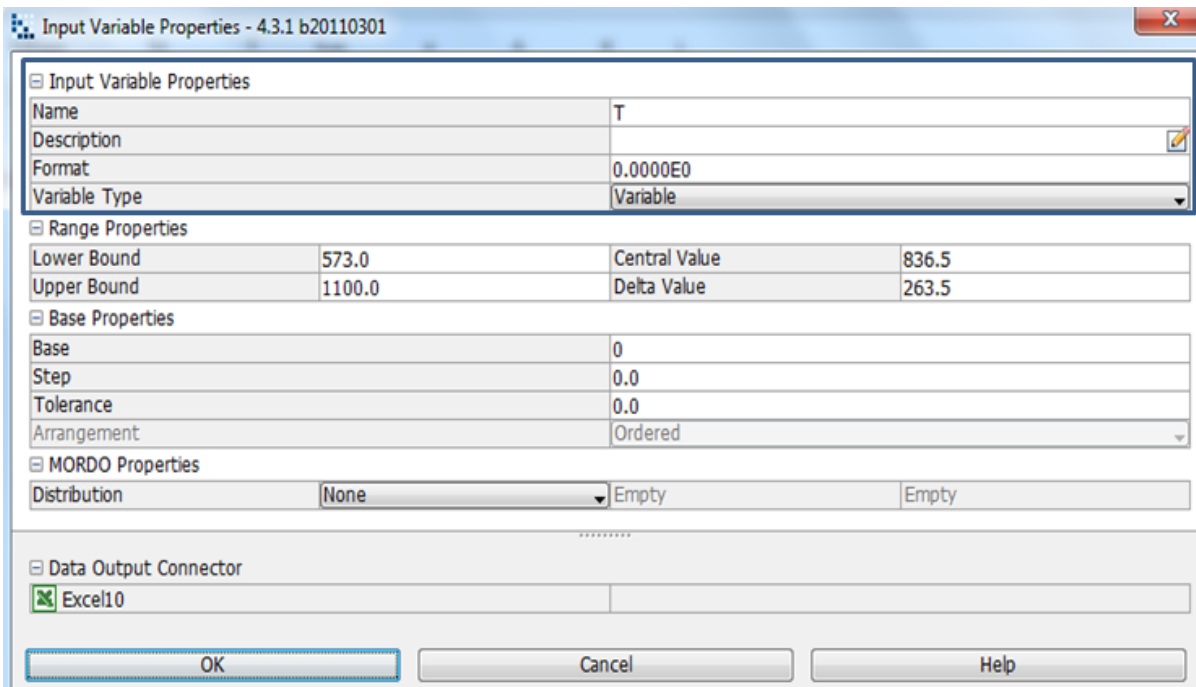


Image 8.44: Workpiece melting temperature 935 K is determined by lower and upper bound range properties, as shown in the input variable node properties dialog

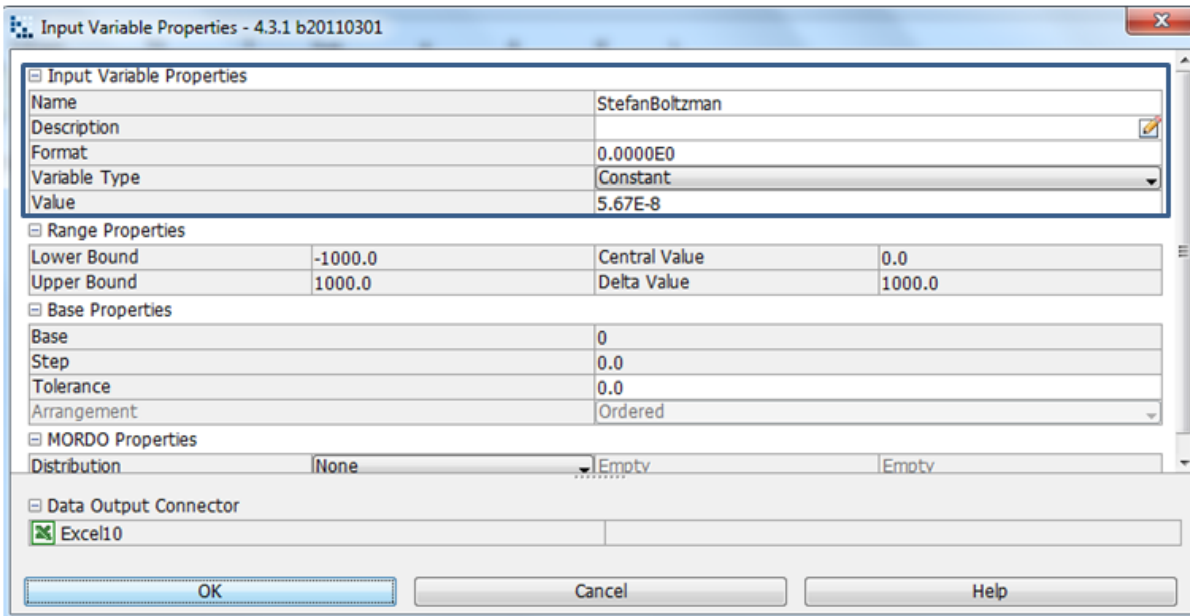


Image 8.45: σ is the Stefan-Boltzmann constant is $5.67 \times 10^{-8} \text{ Wm}^{-2}\text{K}^{-4}$ chosen, where the variable type is constant hence the lower and upper bound is fixed

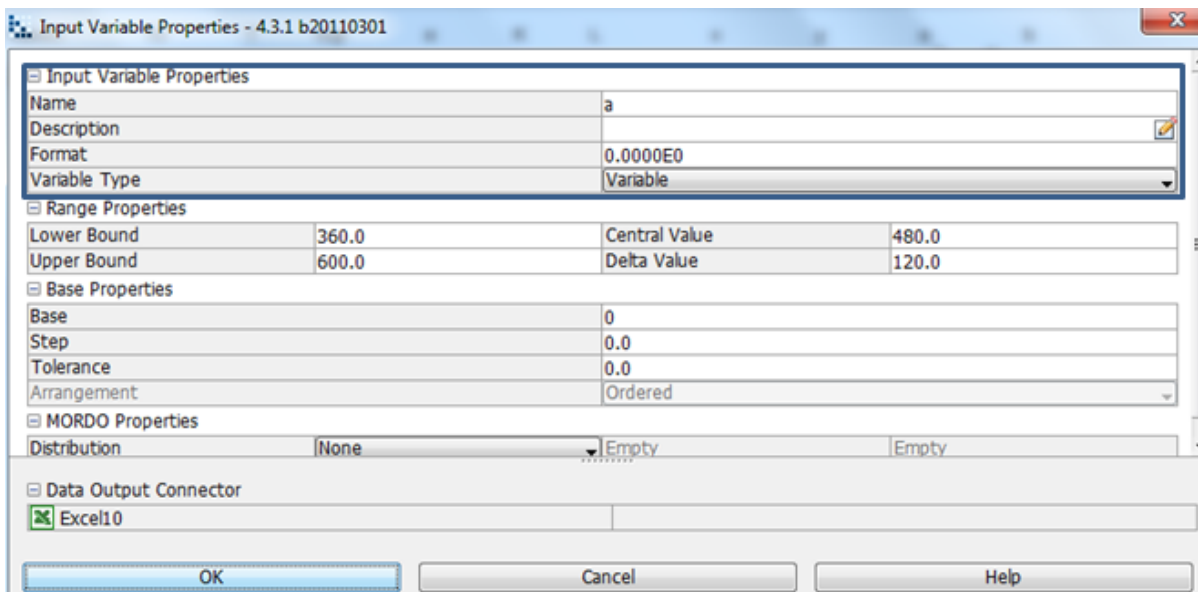


Image 8.46: a is cross-sectional area 500 mm is chosen, where the variable type is variable hence the lower and upper bound varies.

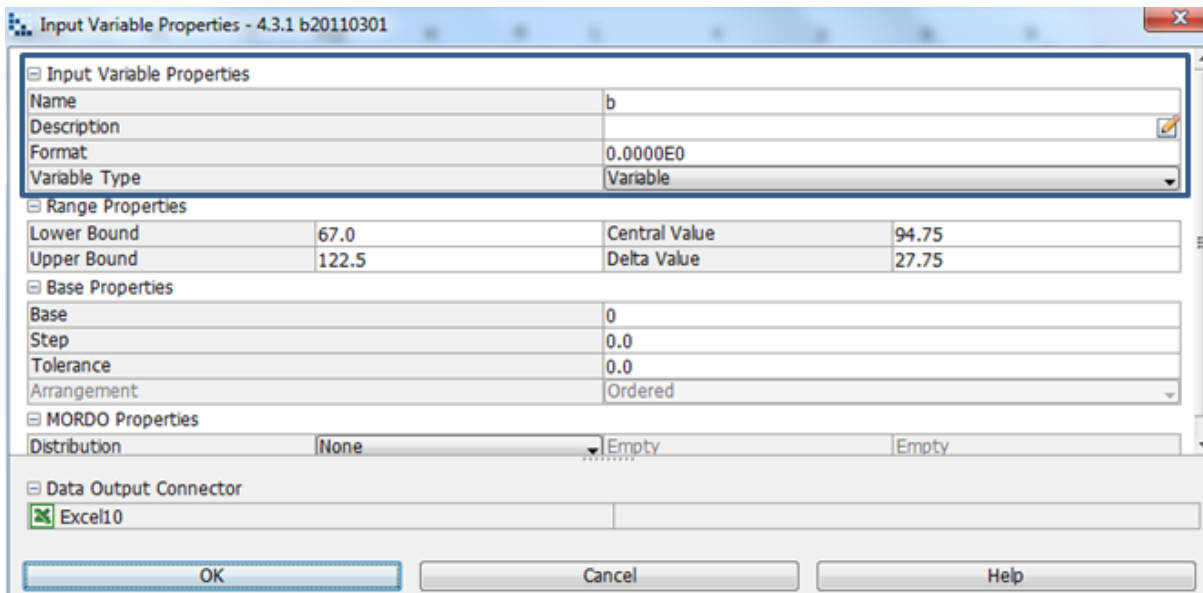


Image 8.47: b is cross-sectional area 115 mm is chosen, where the variable type is variable hence the lower and upper bound varies.

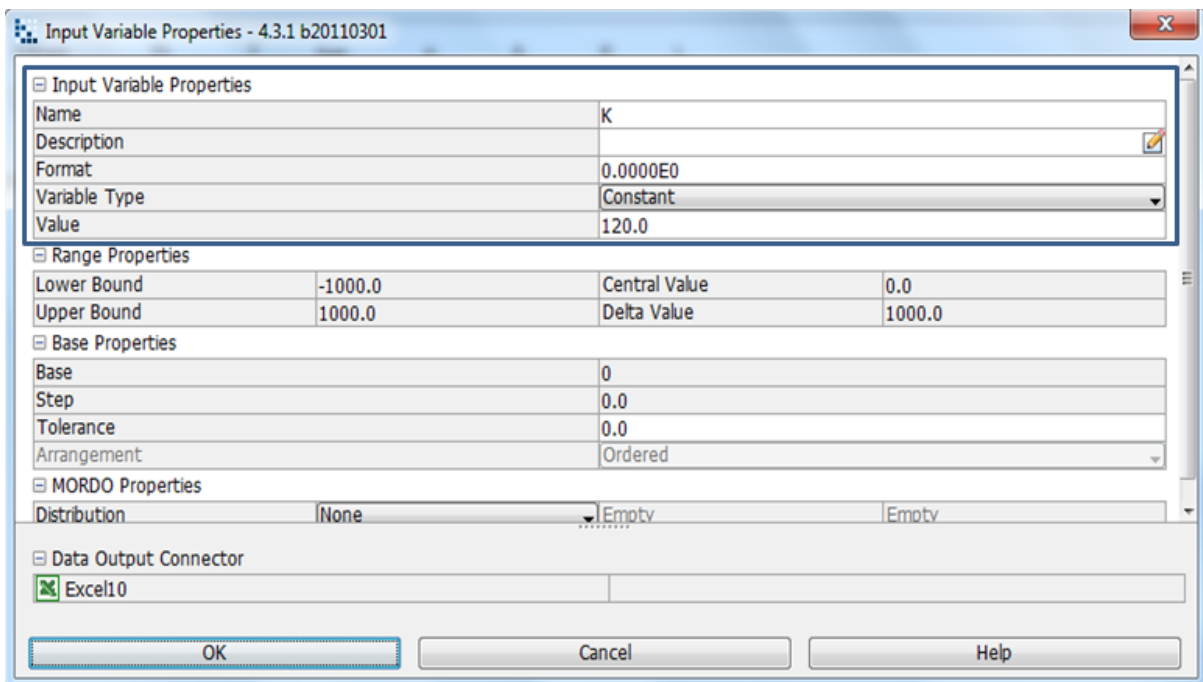


Image 8.48: Thermal conductivity 120 W/mK is chosen, where the variable type is constant hence the lower and upper bound is fixed

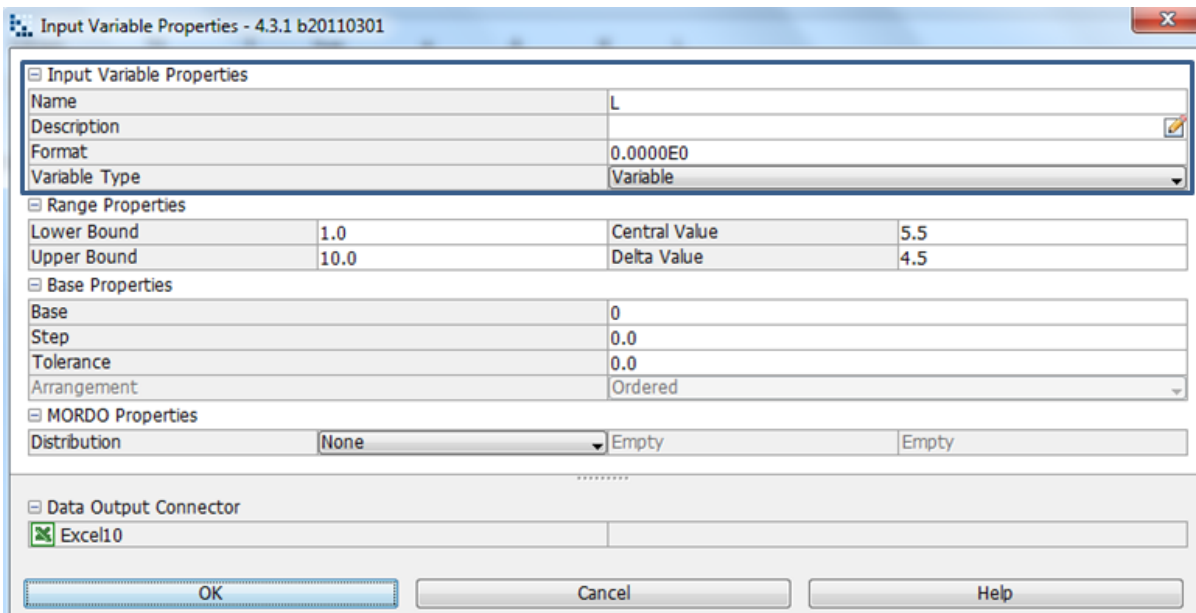


Image 8.49: The length is 4 mm chosen, where the variable type is constant hence the lower and upper bound is fixed

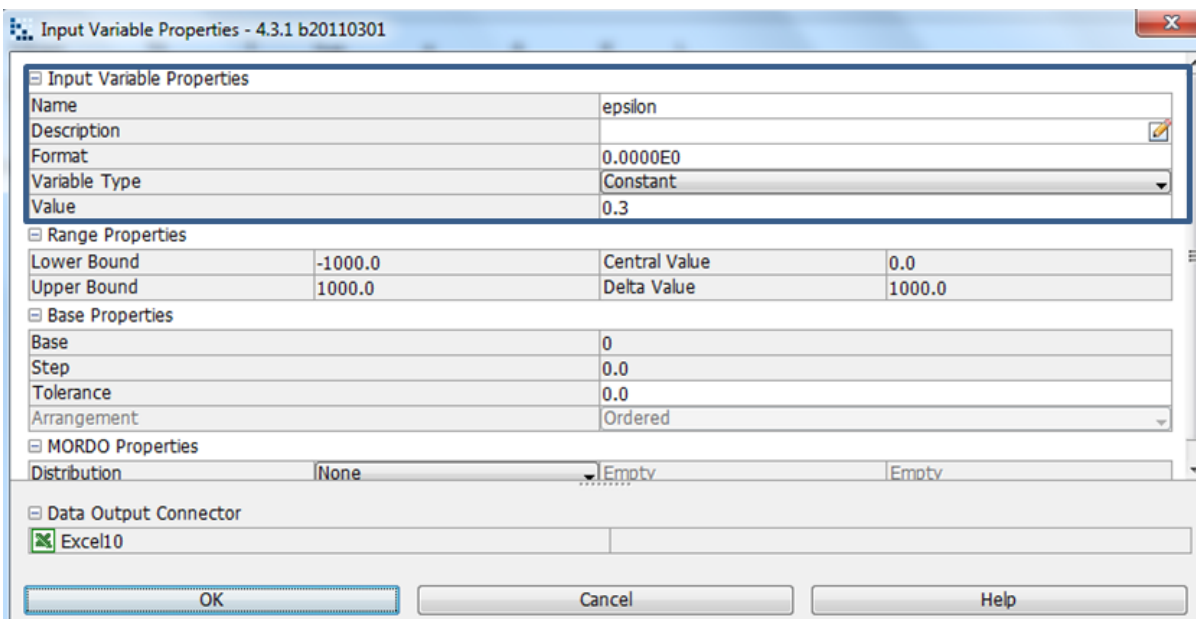


Image 8.50: Surface emissivity is 0.3 chosen, where the variable type is constant hence the lower and upper bound is fixed

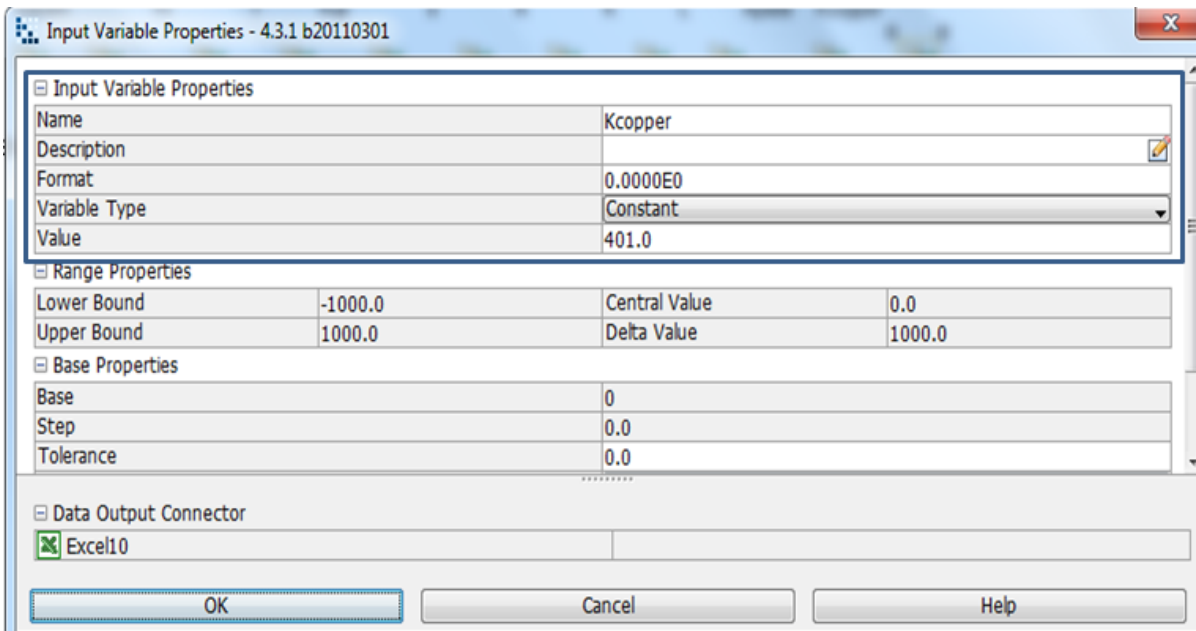


Image 8.51: The input variable property of Kcopper where the variable type is constant and the value is 401.0 with range properties that are fixed.

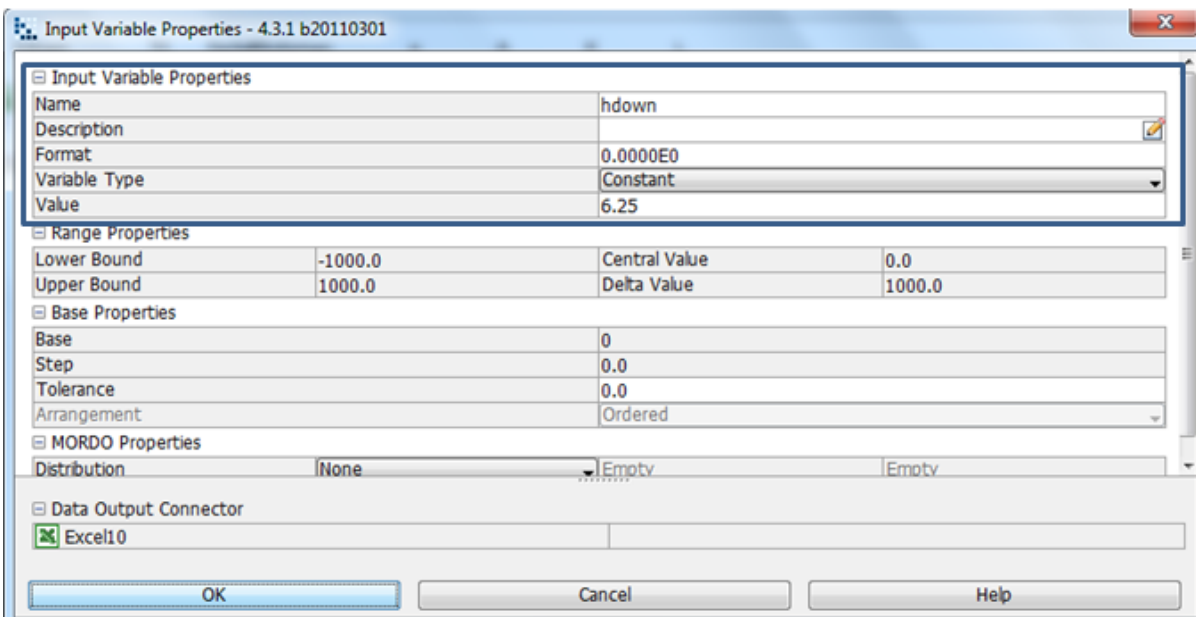


Image 8.52: hdown has a variable type that is constant with a value of 6.25 and range properties that is fixed

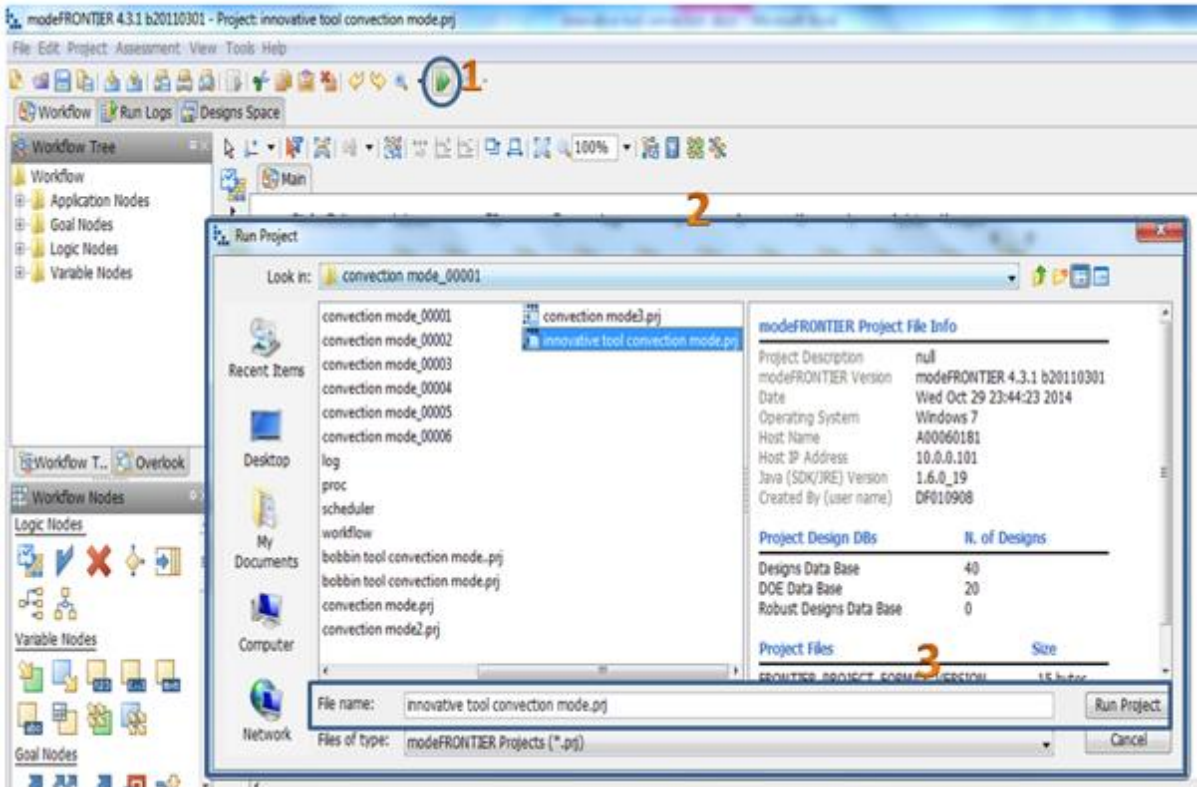


Image 8.53: Click on run/stop icon (1). Run project box will pop up (2). Click on run project (3) to start design project

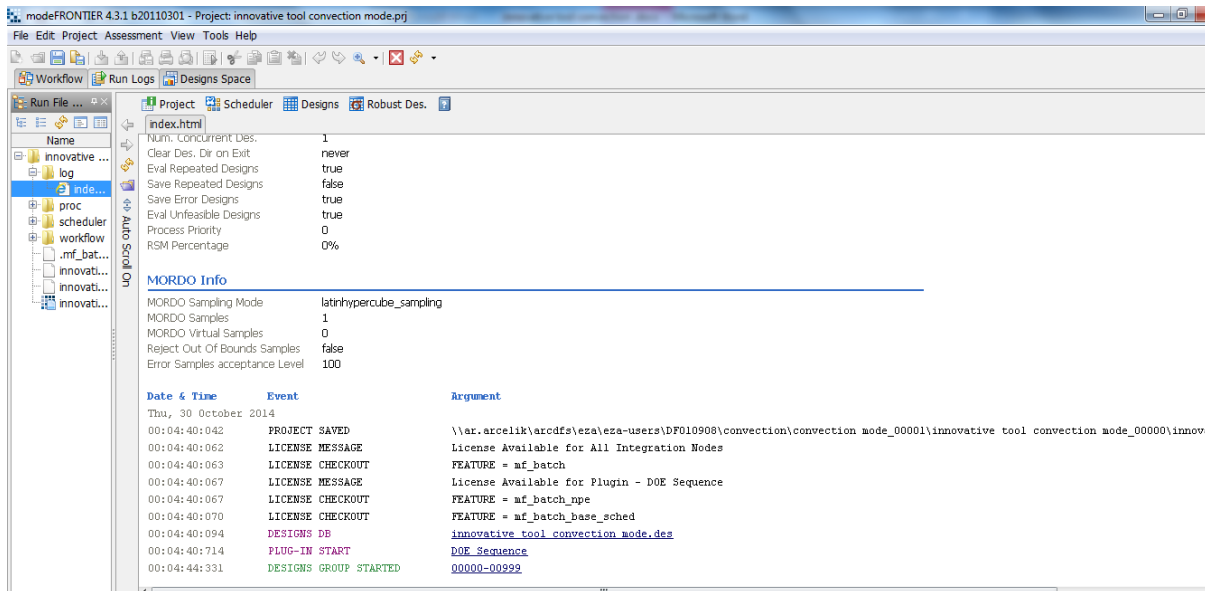


Image 8.54: Before project runs, a project info index will be shown. As seen in the above image

8.5.3. Multi History Charts : Innovative Tool Heat Loss Conditions

The Aplate multi history chart shows that the Aplate (Aluminium Plate), the heat loss by conduction on the upper surface to the qpobjective has a feasible design on a real scale (Chart 8.15), the representation of the temperature and heat conduction to the heat conduction objective is clearly indicated on the multi history chart showing the designs feasibility in reality (Chart 8.16), the multi history chart that represents the temperature and the heat loss by conduction on the upper surface to the qpobjective(heat loss on the upper surface objective) shows feasibility on a real scale (Chart 8.17), The multi history chart that represents the reference temperature and heat conduction to the heat conduction objective shows the design is feasible in reality (Chart 8.18), the multi history chart for the reference temperature and heat loss by conduction on the upper surface shows and represents that the design is feasible on a real scale (Chart 8.19), a normal quantile plot shows the length, x and qcopper against the Qcopperobjective (Chart 8.20), the multi history chart is created from the temperature and qcopper to the qcopperObj showing its feasibility for the design on a real scale(Chart 8.21), The multi history Chart on a designs space as created from the temperature and qcopper to the qcopperObj showing feasibility in reality(Chart 8.22), the Aplate and qcopper to qcopperObj is represented on a multi history chart to show the design feasibility on a real scale(Chart 8.23). The length, heat conduction from the upper surface against the Qcopperobjective is represented on the normal quantile plot (Chart 8.24).

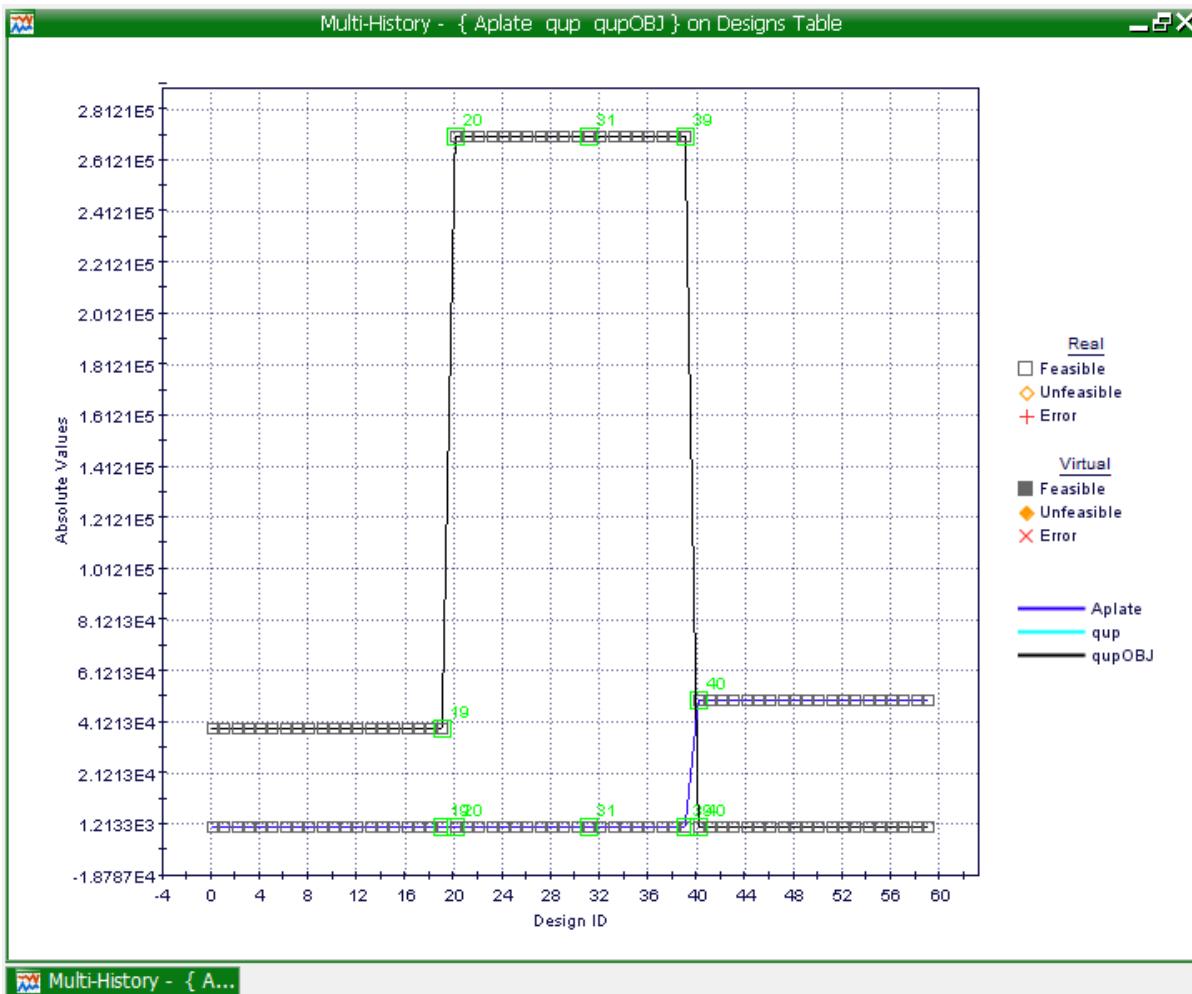


Chart 8.15: Multi-History Chart on Designs Space as created from the Aplate (Aluminium Plate), the heat loss by conduction on the upper surface to the qpobjective

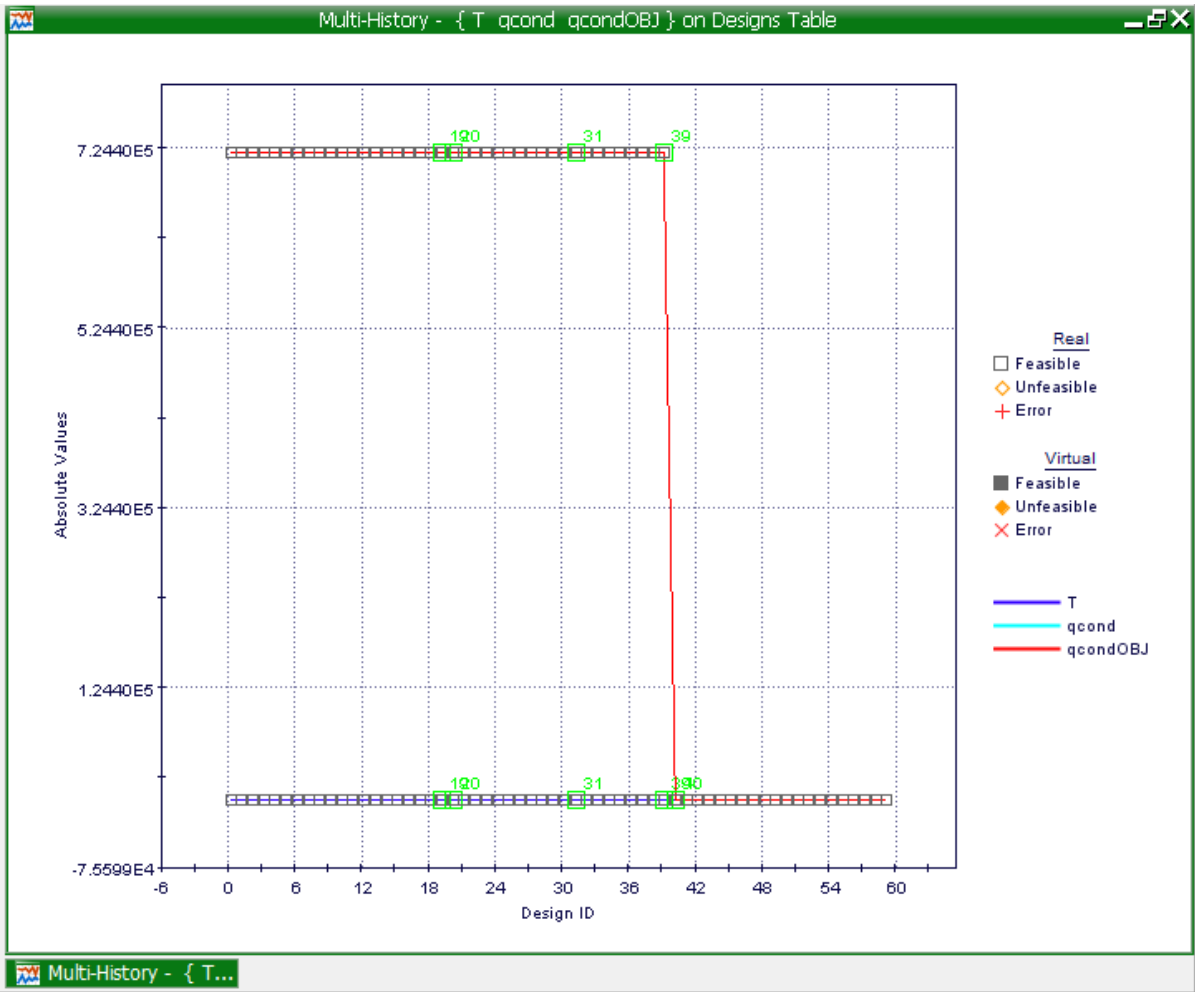


Chart 8.16: Multi-History Chart on Designs Space as created from the representation of the temperature and heat conduction to the heat conduction objective.

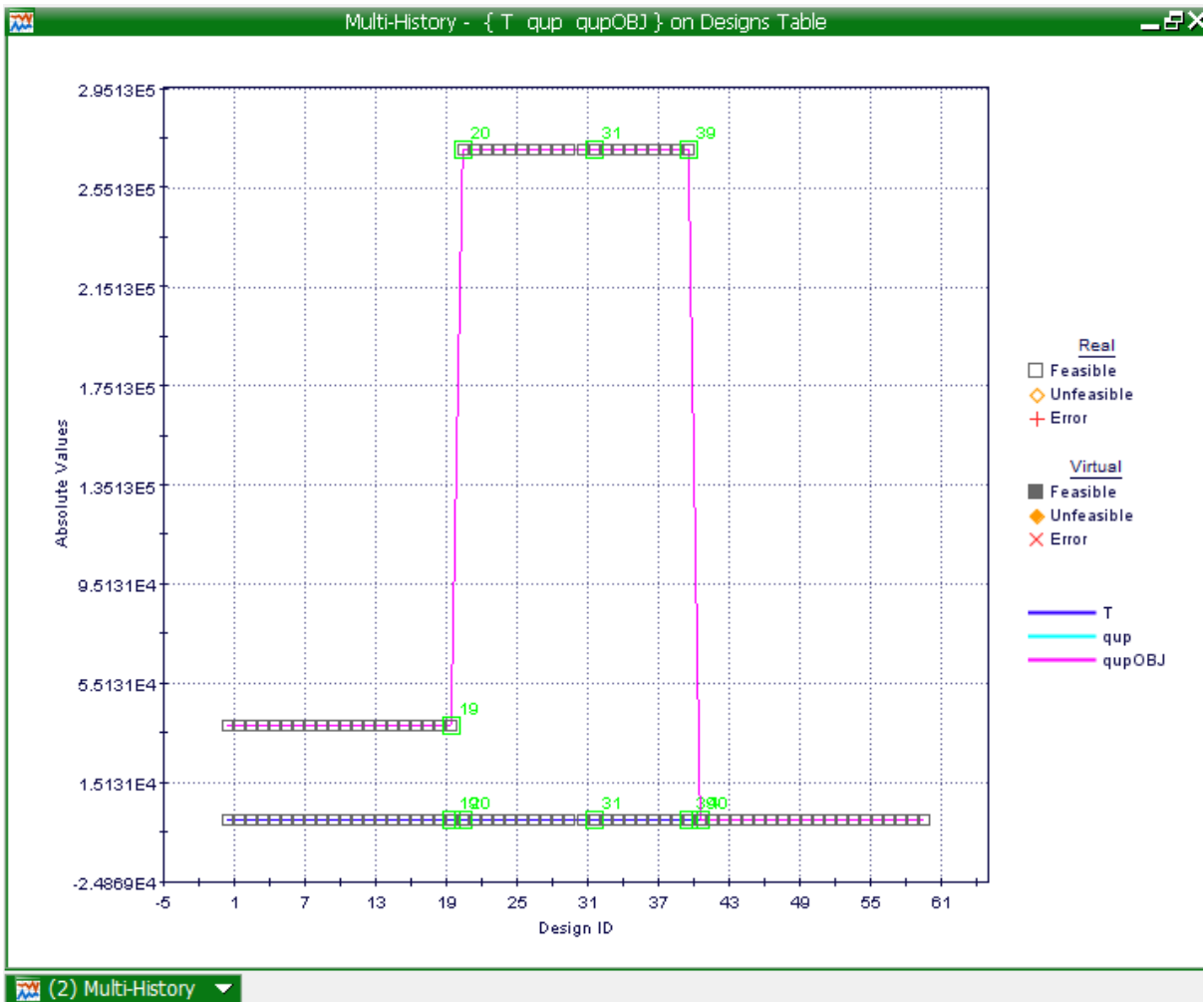


Chart 8.17: Multi-History Chart on Designs Space as created from temperature and the heat loss by conduction on the upper surface to the qcpobjective (heat loss on the upper surface objective).

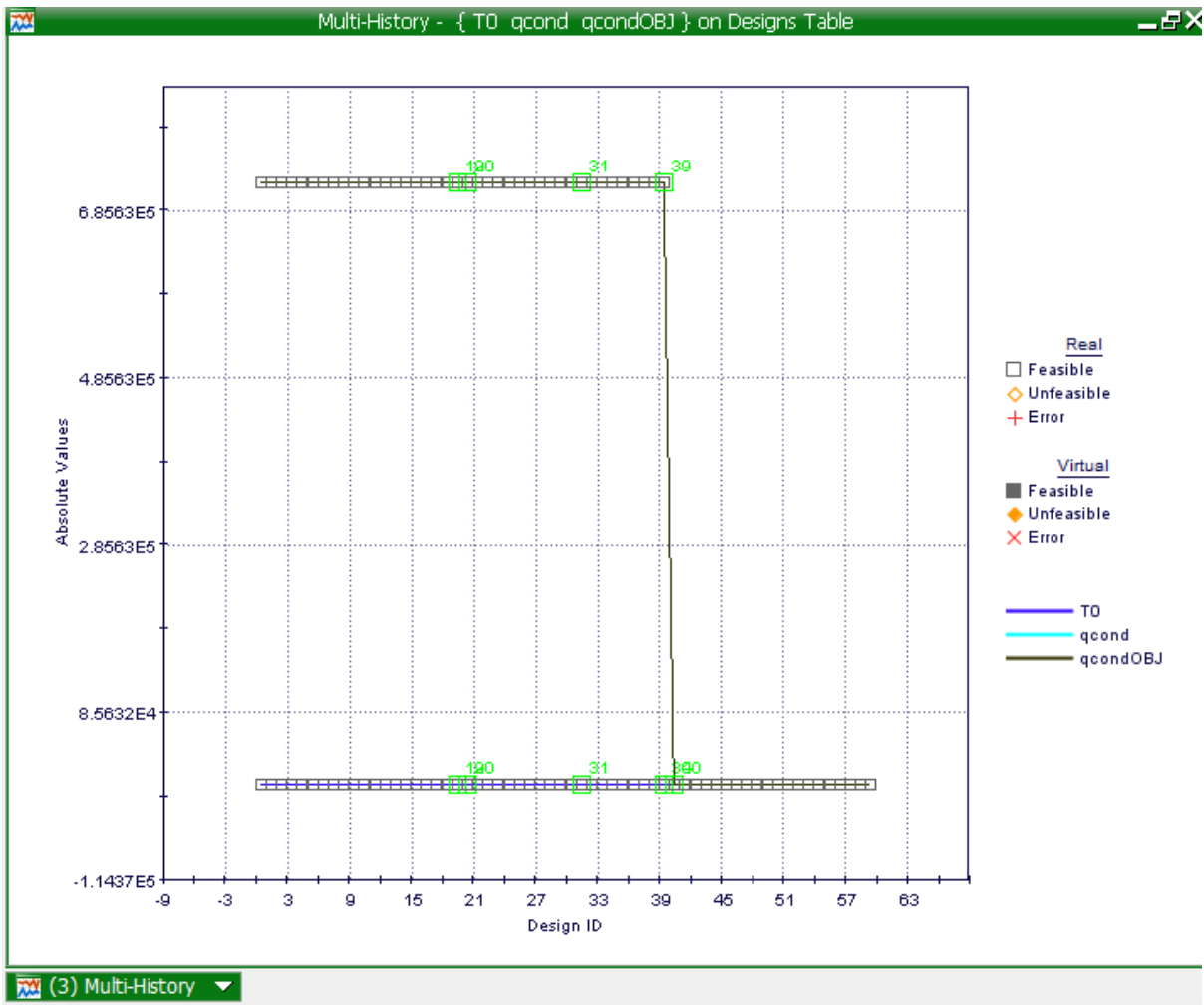


Chart 8.18: Multi-History Chart on Designs Space as created from reference temperature and heat conduction to the heat conduction objective

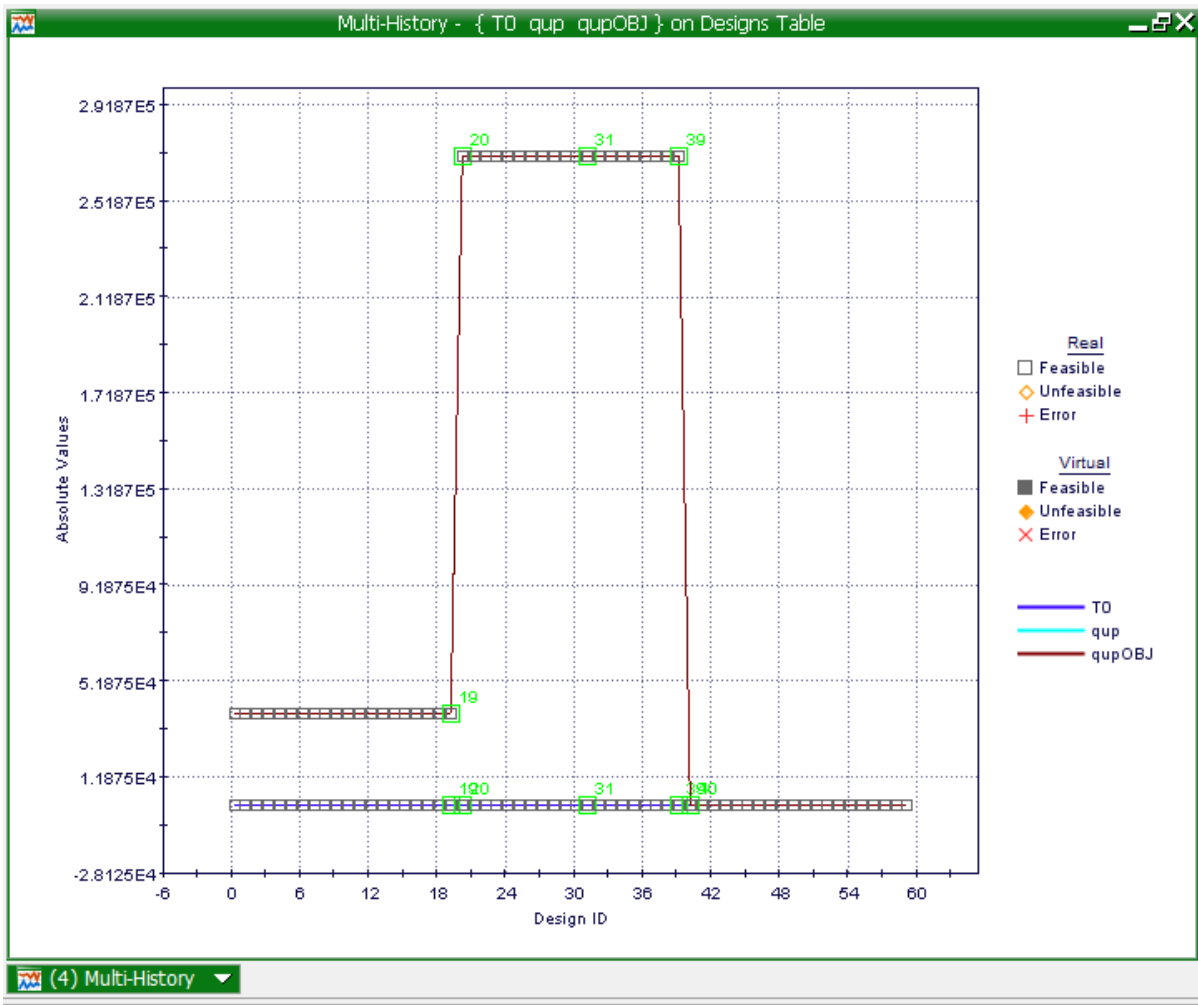


Chart 8.19: Multi-History Chart on Designs Space as created from reference temperature and heat loss by conduction on the upper surface.

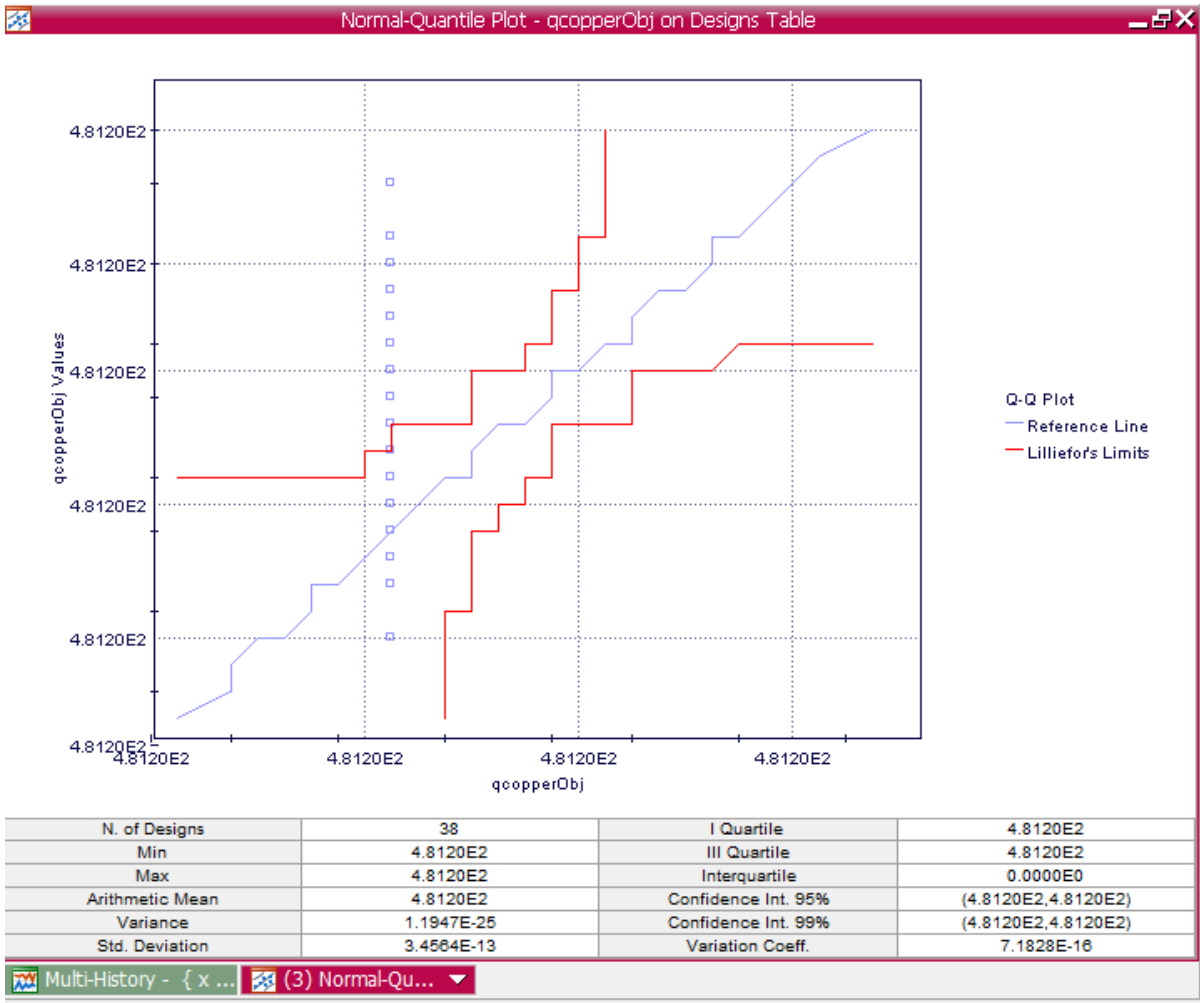


Chart 8.20: Normal Quantile Plot on Designs Space as created from x, length and qcopper to qcopperObj showing feasibility on a real scale.

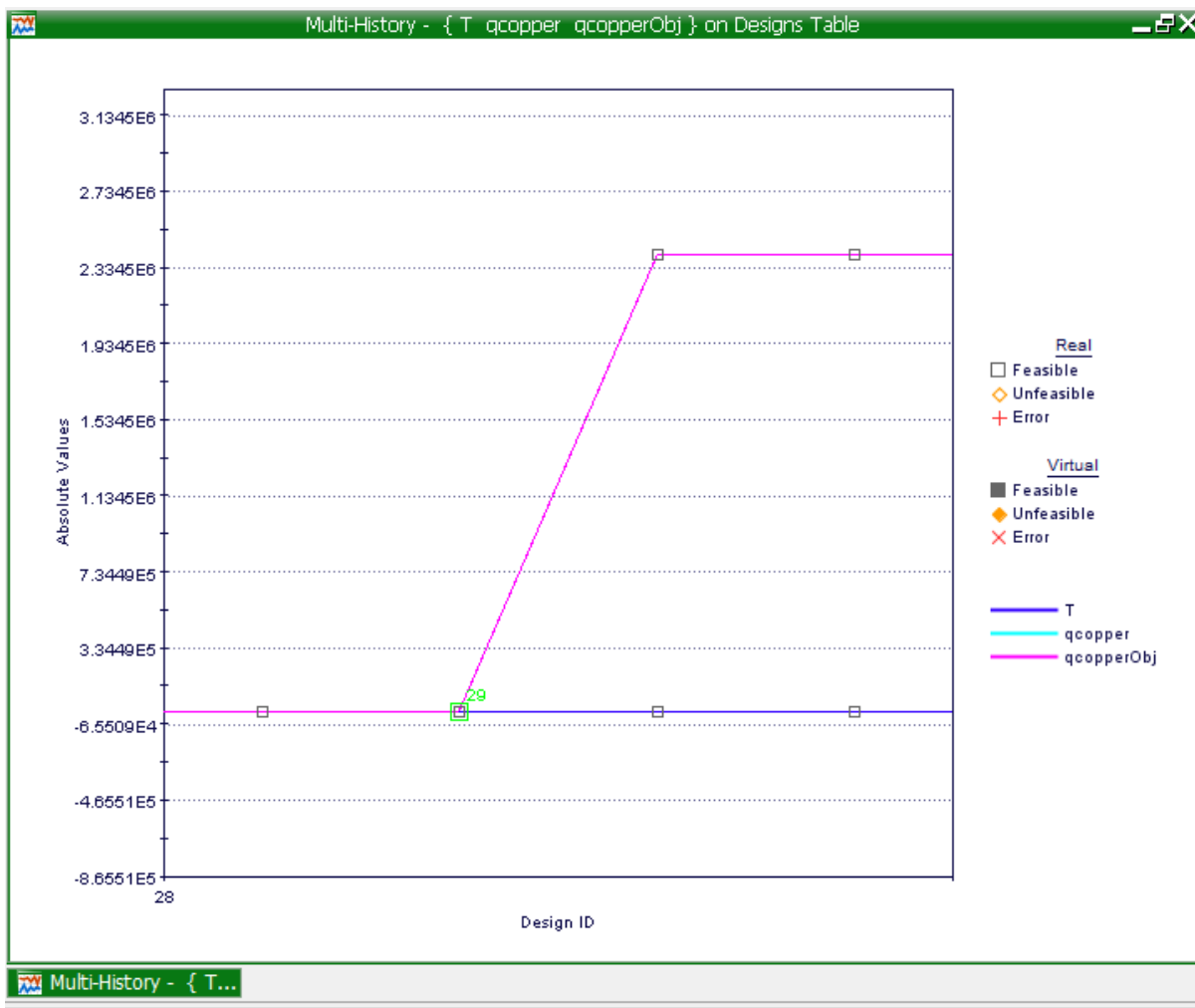


Chart 8.21: Multi-History Chart on Designs Space as created from the temperature and qcopper to the qcopperObj.

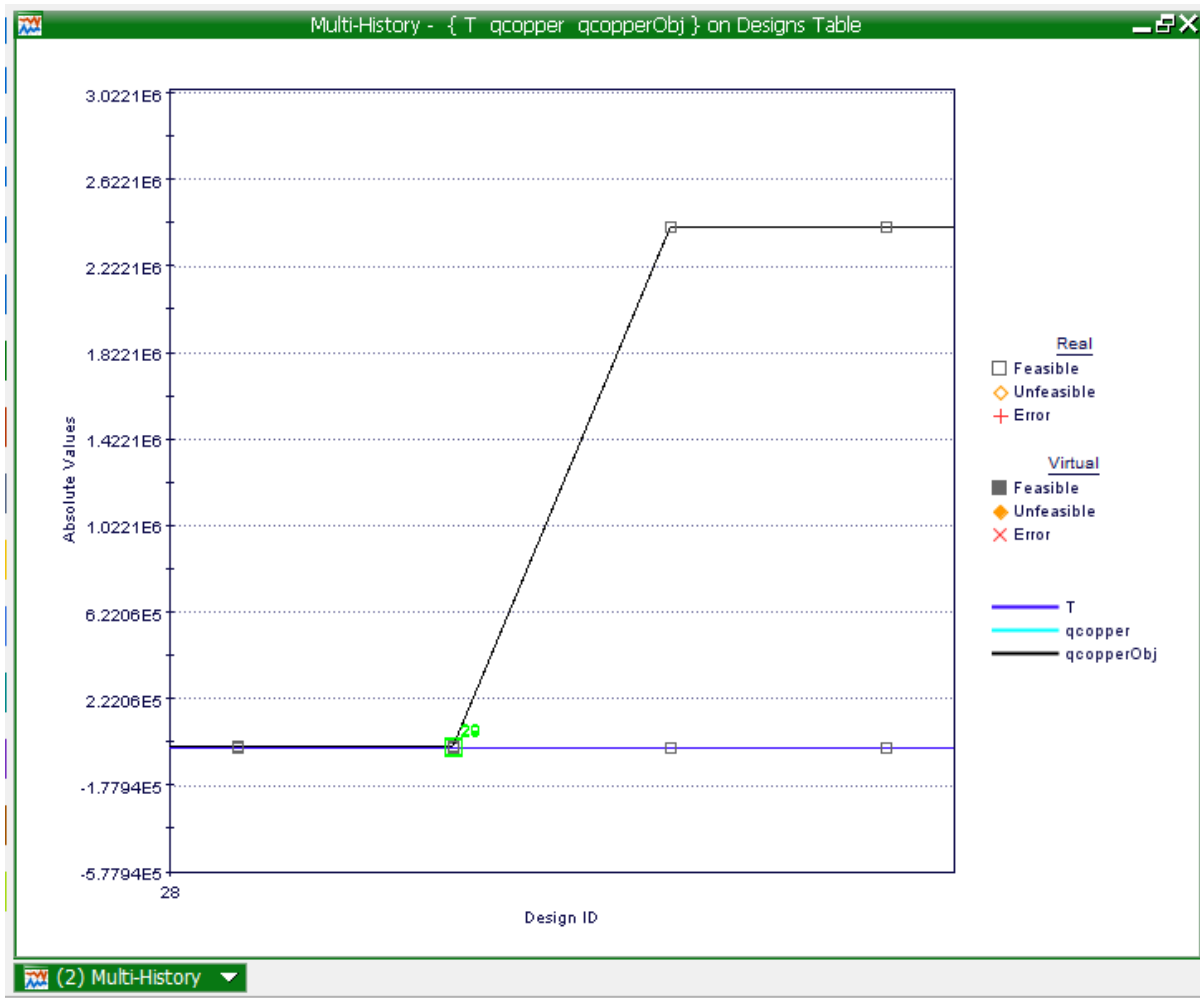


Chart 8.22: Multi-History Chart on Designs Space as created from the temperature and qcopper to the qcopperObj.

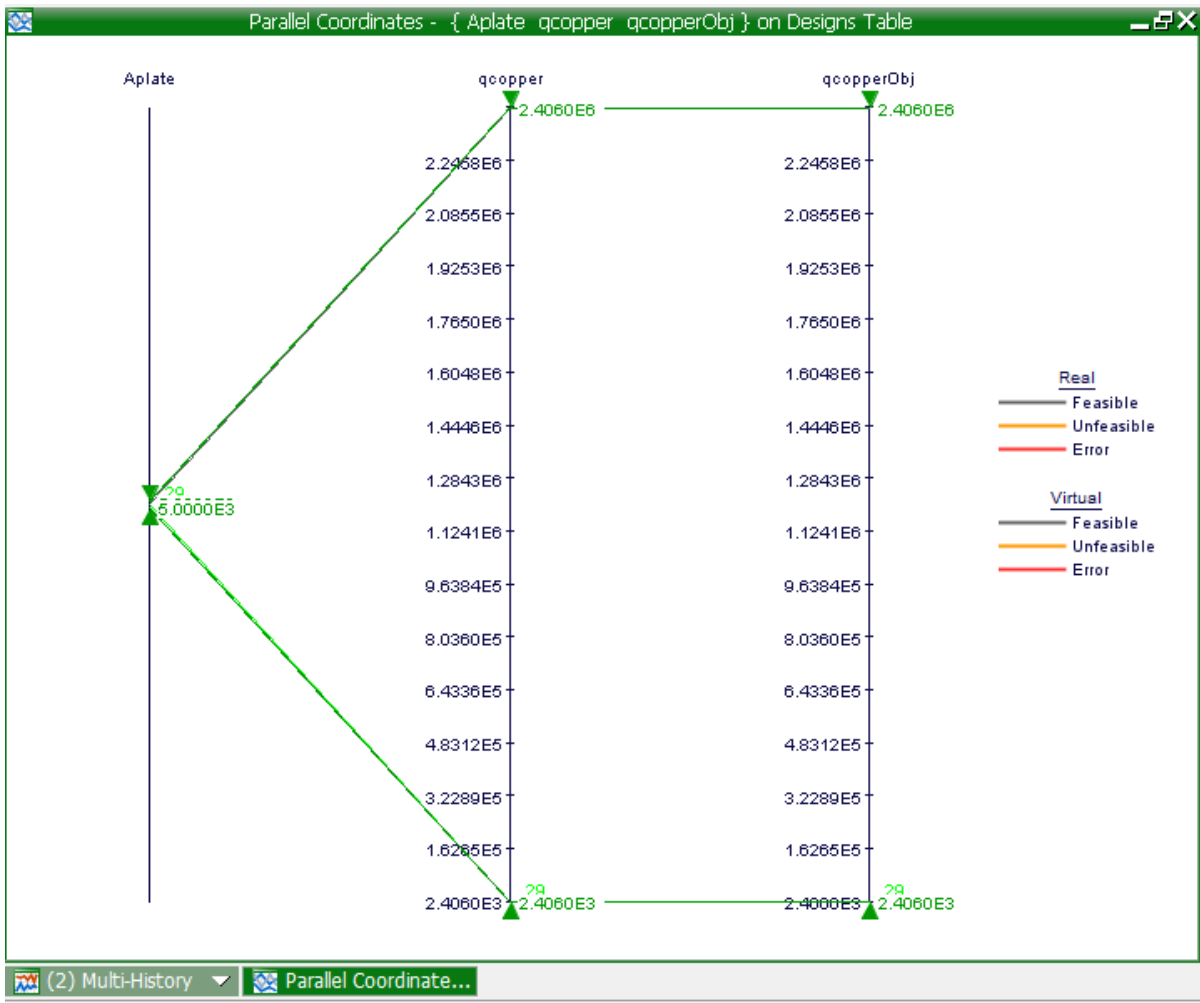


Chart 8.23: Multi-History Chart on Designs Space as created from the Aplate and qcopper to qcopperObj to show the design feasibility on a real scale.

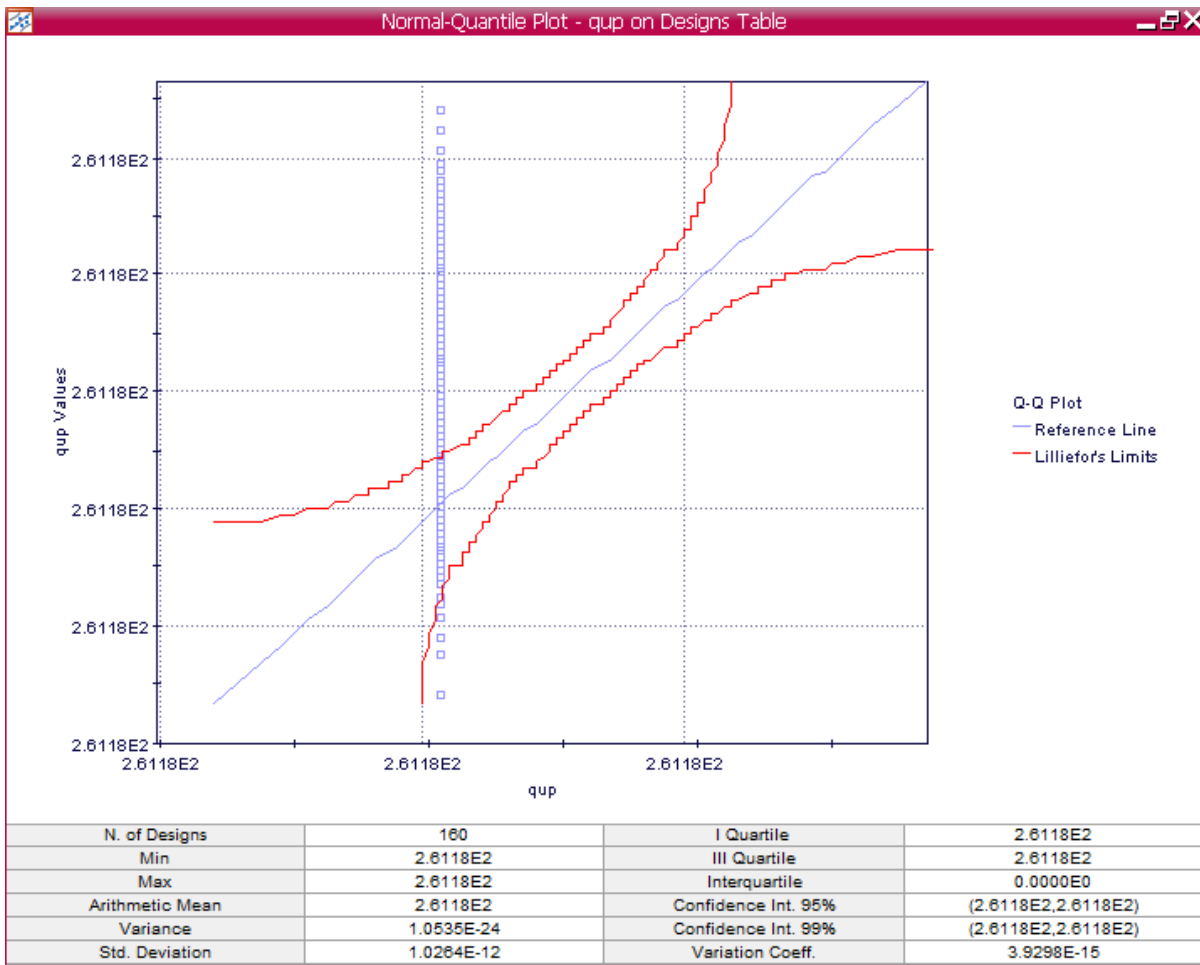


Chart 8.24: Normal Quantile Plot on Designs Space as created from a, length and qcp to qcopperObj showing feasibility on a real scale.

9. The Modification of Tools

The modification of a friction stir weld tool occurs when features are modified on a standard tool. The first modification is a bobbin tool. The friction stir welding bobbin tool is a variant of the process, the tool animated rotation consist of two shoulders and a pin geometries that are capable of complexity. The conditions needed to compose the rotation with linear movement forward during which the tool will go through the line defined by joining the material Al2024-T3 plates. Unlike the bobbin tool, the innovative tool has one shoulder; however present during a weld is a copper bush/modified copper bush. The purpose of this copper bush is to conduct any heat could possibly be a caution during a weld causing the melting of materials.

9.1. Comparison of Heat Loss and Heat Generation

The comparison of heat loss and heat generation is to determine the difference of each friction stir weld tool.

9.2. Mode Frontier for the Comparison of Heat Generation and Heat Loss

Excel sheets [comparison.xlsm](#) for both heat loss and heat generation is chosen (Images: 9.1 & 9.2), a workflow plan is then created by mode frontier as shown in image [comparison.prj](#) (Image 9.3), Input and Output data is connected as per the excel workbook (Image 9.4), an interactive selection between [comparison.xlsm](#) and [comparison.prj](#) is done to determine the excel workbook properties for the design (Image 9.5). The project starts once a run project has started. An index before the initial project design commences (Image 9.6& 9.7)

9.2.1. Multi History Charts for the Comparison of Heat Generation and Heat Loss

A history chart is created to show the difference of probe side heat generation and rotational speeds. (Image 9.8). A multi history chart representation of total heat generation from a standard tool vs the heat generation of a bobbin tool shows the feasibility in reality where the heat generation of the bobbin tool is higher than that of the standard tool (Chart 9.1). The bobbin tools heat generation vs the innovative tools heat generation is created on a multi history chart showing once again the bobbin tool has a high heat generation(Chart 9.2). The multi history chart that displays the heat generation between the standard tool and the innovative tool and the standard tool shows clearly that the heat generation of the standard tool is higher than that of the innovative too(Chart 9.3). The conduction of the bobbin tool vs the standard tool represented on a multi history chart showing that the conduction of a bobbin tool is higher compared to the standard tool (Chart 9.4). The bobbin tool vs the innovative tool conduction displayed on the multi history chart shows a feasibility of a real scale where the heat conduction differs (Chart 9.5).

HEAT LOSS					
INPUT DATA		OUTPUT DATA			
hup	12.25	qupBTC	4750.711771	QTBTC	5513.912
hdown	6.25	qcondBTC	763.2		
To	299	qupSTC	2375.355885	QTSTC	4693.472
T	935	qdownSTC	1936.515885		
σ	5.67E-08	qcondSTC	381.6		
ϵ	0.3	qupITC	2375.355885	QTITC	5968.652
A	20	qdownITC	1936.515885		
K(AI)	120	qcondITC	381.6		
L	4	qcopperITC	1275.18		
Aplate	115000				
x	4				
y	5				
a	500				
b	115				
Kcopper	401				

Image 9.1: Input Data, Output Data and boundary variables definitions as shown on this Microsoft Excel Sheet file name: comparison .xlsm is used in Mode Frontier for this Design Project

	A	B	C	D	E	F	G	H	I	J
1										
2	INPUT DATA			OUTPUT DATA	800 rpm					
3	Geometrical parameters			Q1shoulder (KW) STD	46.48					
4	Rotational Speed	800		Q2probe side (KW) STD	9.54					
5	Rshoulder	10		Q3 probe tip (KW) STD	3.18					
6	Rprobe	4.00		QT STANDARD (KW) STD	59.19					
7	α	0.00		Q1shoulder (KW) IT	11.09					
8	Hprobe	4.00		Q2probe side (KW) IT	2.28					
9	Hprobe(bobbin)	2.00		Q3 copper side (KW) IT	0.34					
10	Contact shear stress	340		QT (KW) IT	13.71					
11	Yield Strength	283		Q1shoulder (KW) BT	46.48					
12	Yield Strength COPPER	68		Q2 probeside(KW) BT	4.77					
13	Rotational Speed for copper bush	80		Q3shoulder (KW) BT	46.48					
14	Hprobe(copper)	6		QT BOBBIN (KW)	97.72					
15										
16										
17										
18										
19										
20										
21										
22										
23										
24										
25										

Image 9.2: Input Data, Output Data and boundary variables definitions as shown on this Microsoft Excel Sheet file name: comparison .xlsm is used in Mode Frontier for this Design Project

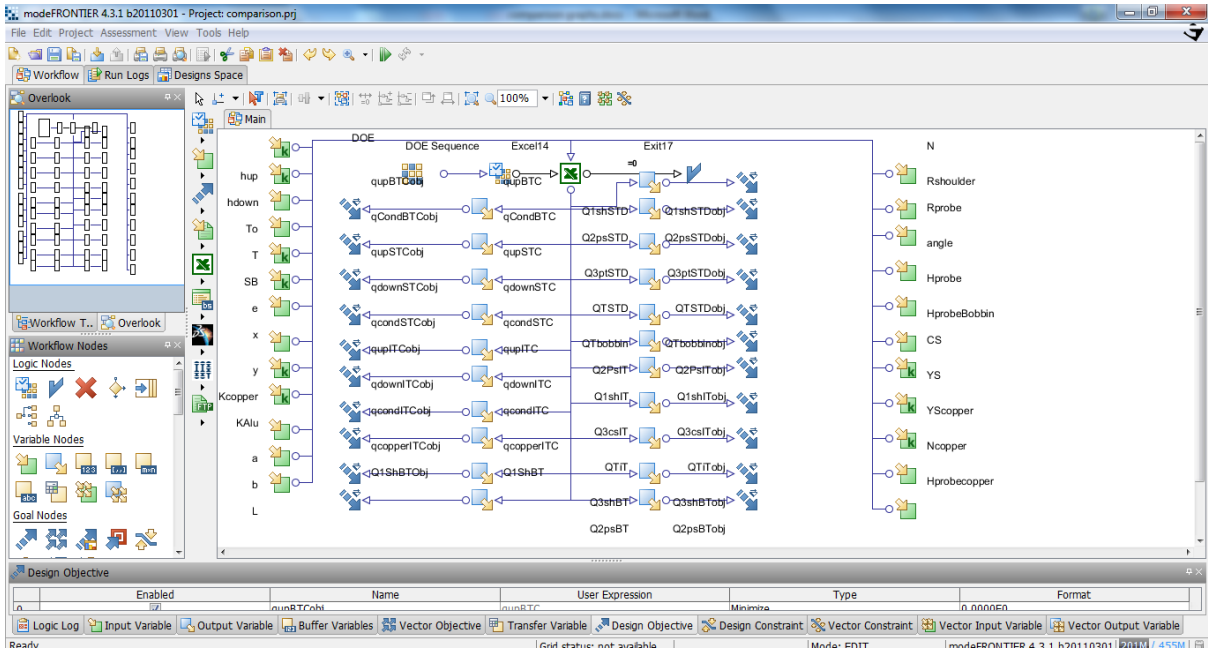


Image 9.3: Workflow Plan created by Mode Frontier Project as shown in *comparison.prj*, also includes DOE (Design of Experiments) and DOE Sequence, as well as indicating Input Variables, Output Variables, Design Objectives + Gradients, Microsoft Excel Workbook and Logic End

The screenshot shows the 'Excel Workbook Properties' dialog box for an Excel node named 'Excel14'. The dialog is divided into several sections: 'Excel Workbook Properties', 'Excel Workbook Advanced Properties', 'Excel Default Cells Properties', 'Process Input Connector', and 'Process Output Connector'. The 'Process Input Connector' section is expanded to show a list of input variables and their corresponding Excel cell references. The 'Process Output Connector' section is also expanded to show a list of output variables and their corresponding Excel cell references.

Process Input Connector	Excel Cell Reference
Scheduler	
Data Input Connector	
CS	HEAT GENERATION!\$B\$10
Hprobe	HEAT GENERATION!\$B\$8
HprobeBobbin	HEAT GENERATION!\$B\$9
Hprobecopper	HEAT GENERATION!\$B\$14
KAlu	HEAT LOSS!\$B\$11
Kcopper	HEAT LOSS!\$B\$18
L	HEAT LOSS!\$B\$12
N	HEAT GENERATION!\$B\$4
Ncopper	HEAT GENERATION!\$B\$13
Rprobe	HEAT GENERATION!\$B\$6
Rshoulder	HEAT GENERATION!\$B\$5
SB	HEAT LOSS!\$B\$8
T	HEAT LOSS!\$B\$7
To	HEAT LOSS!\$B\$6
YS	HEAT GENERATION!\$B\$11
YScopper	HEAT GENERATION!\$B\$12
a	HEAT LOSS!\$B\$16
angle	HEAT GENERATION!\$B\$7
b	HEAT LOSS!\$B\$17
e	HEAT LOSS!\$B\$9
hdown	HEAT LOSS!\$B\$5
hup	HEAT LOSS!\$B\$4
x	HEAT LOSS!\$B\$14

Process Output Connector	Excel Cell Reference
Exit17	=0
Data Output Connector	
Q1ShBT	HEAT GENERATION!\$E\$11
Q1shIT	HEAT GENERATION!\$E\$7
Q1shSTD	HEAT GENERATION!\$E\$3
Q2PsIT	HEAT GENERATION!\$E\$8
Q2psBT	HEAT GENERATION!\$E\$12
Q2psSTD	HEAT GENERATION!\$E\$4
Q3csIT	HEAT GENERATION!\$E\$9
Q3ptSTD	HEAT GENERATION!\$E\$5
Q3shBT	HEAT GENERATION!\$E\$13
Q3shIT	HEAT GENERATION!\$E\$6
QTSTD	HEAT GENERATION!\$E\$14
QTbobbIn	HEAT GENERATION!\$E\$10
QTIT	HEAT LOSS!\$D\$5
qCondBTC	HEAT LOSS!\$D\$5
qcondITC	HEAT LOSS!\$D\$11
qcondSTC	HEAT LOSS!\$D\$8
qcopperITC	HEAT LOSS!\$D\$12
qdownITC	HEAT LOSS!\$D\$10
qdownSTC	HEAT LOSS!\$D\$7
qupBTC	HEAT LOSS!\$D\$4
qupITC	HEAT LOSS!\$D\$9
qupSTC	HEAT LOSS!\$D\$6

Image 9.4: Mode Frontier Input and Output Data connected to Microsoft Excel Workbook as shown above

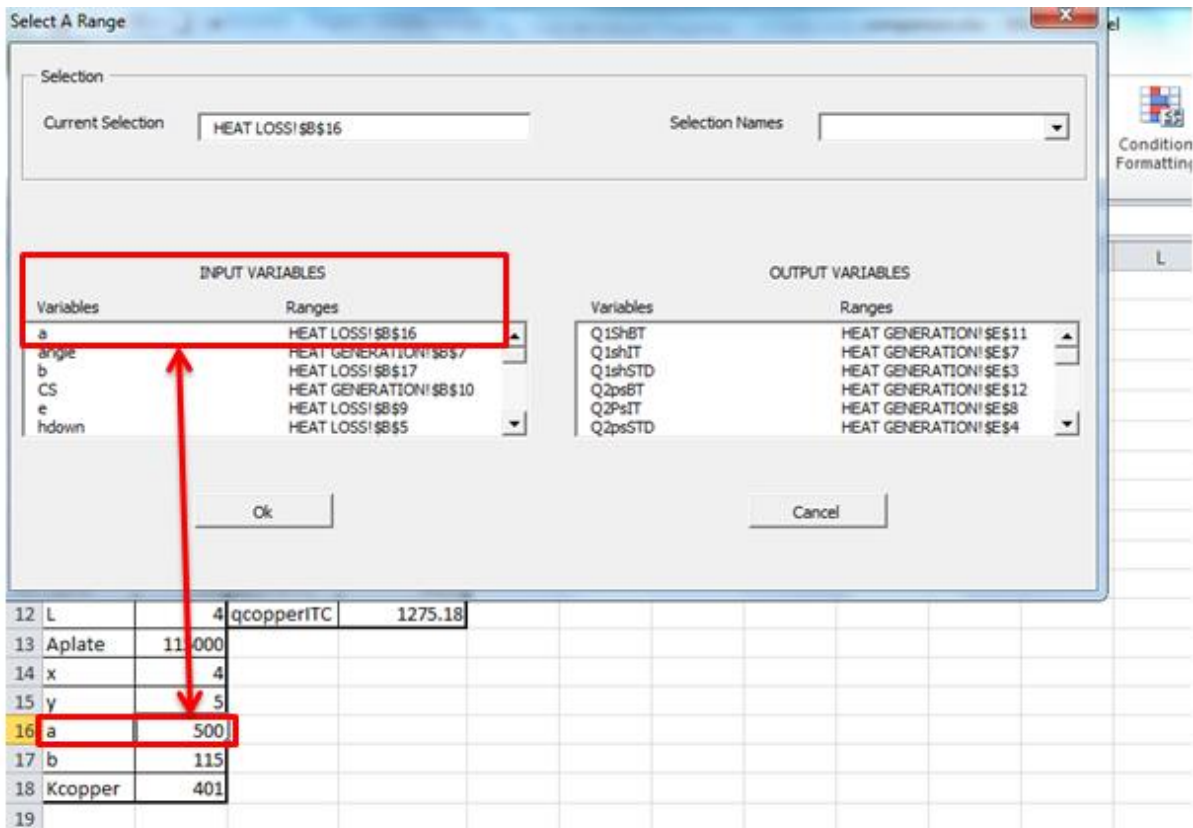


Image 9.5: Interactive Selection used between Mode Frontier *comparison.prj* and Microsoft Excel Workbook: *comparison.xlsm* to determine Excel Workbook Properties for Mode Frontier

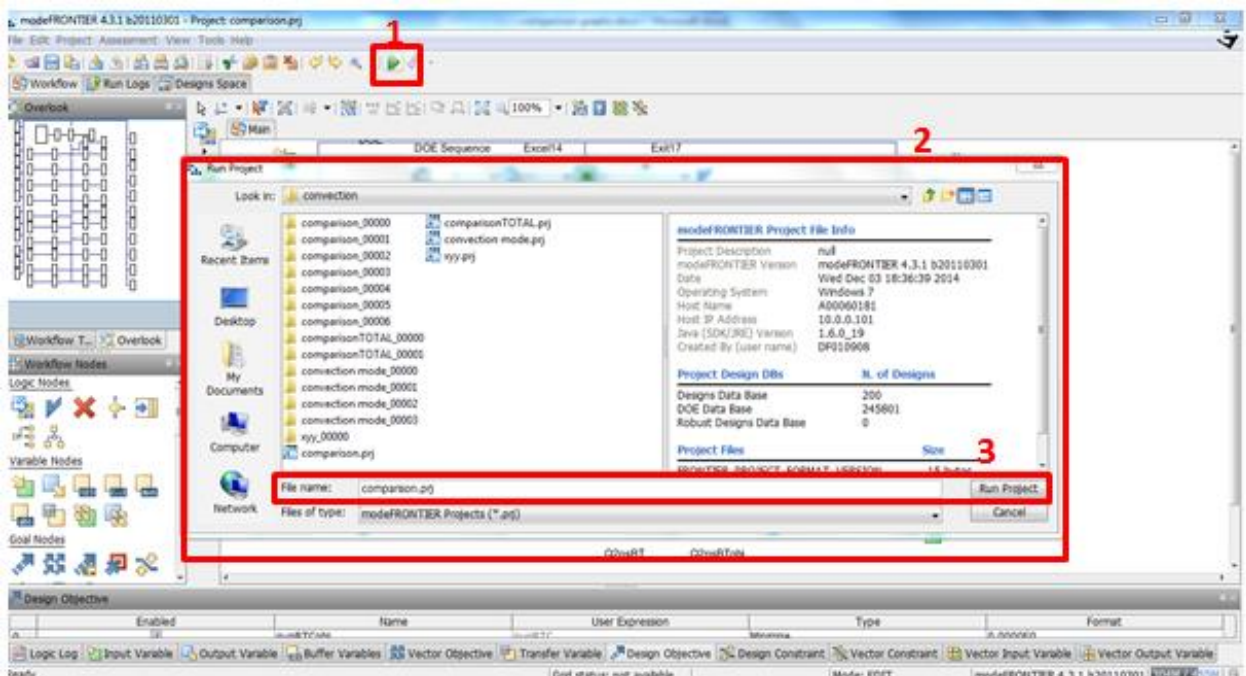


Image 9.6: Click on run/stop icon(1). Run project box will pop up(2). Click on run project(3) to start design project.

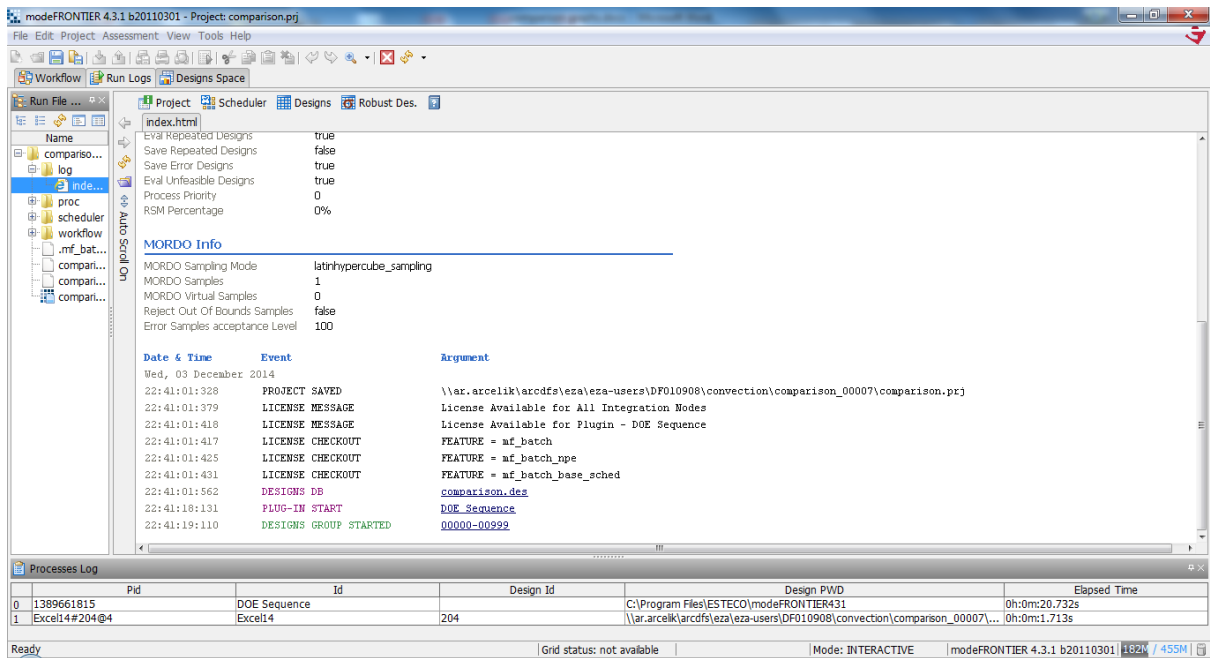


Image 9.7: Before project runs, a project info index will be shown. As seen in the above image.

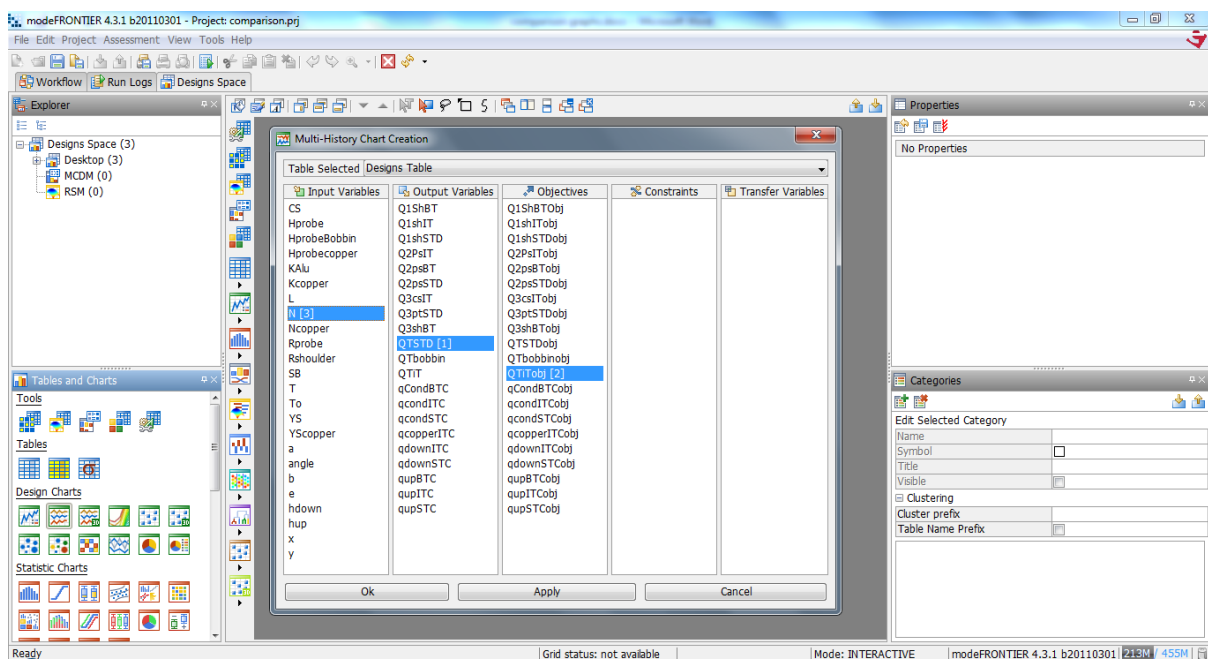


Image 9.8 : History Chart created on Mode Frontier Designs Space as shown above for Probe Side Heat Generation and Rotational Speed

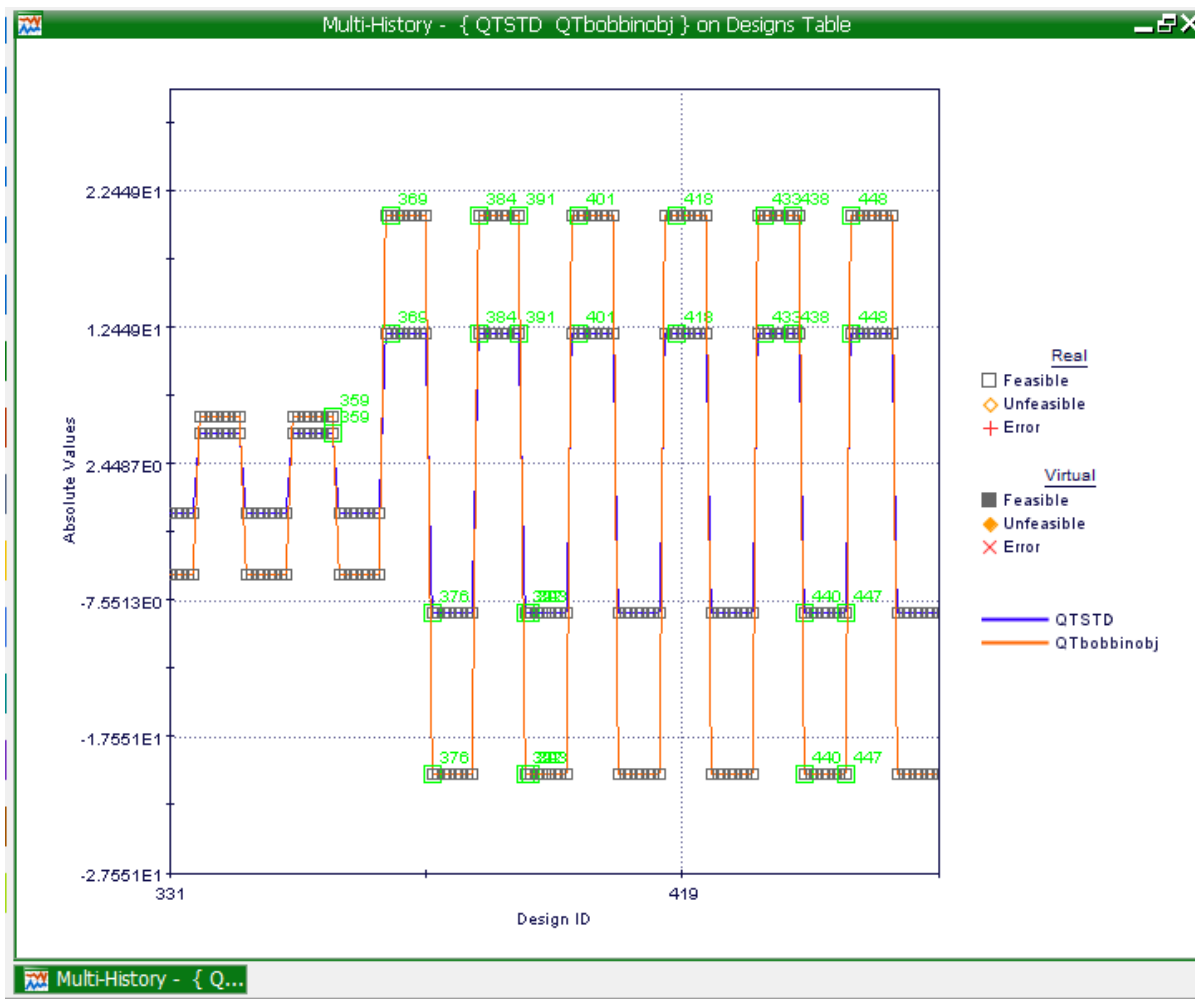


Chart 9.1: Standard tool Total Heat generation Vs Bobbin Tool Total Heat Generation

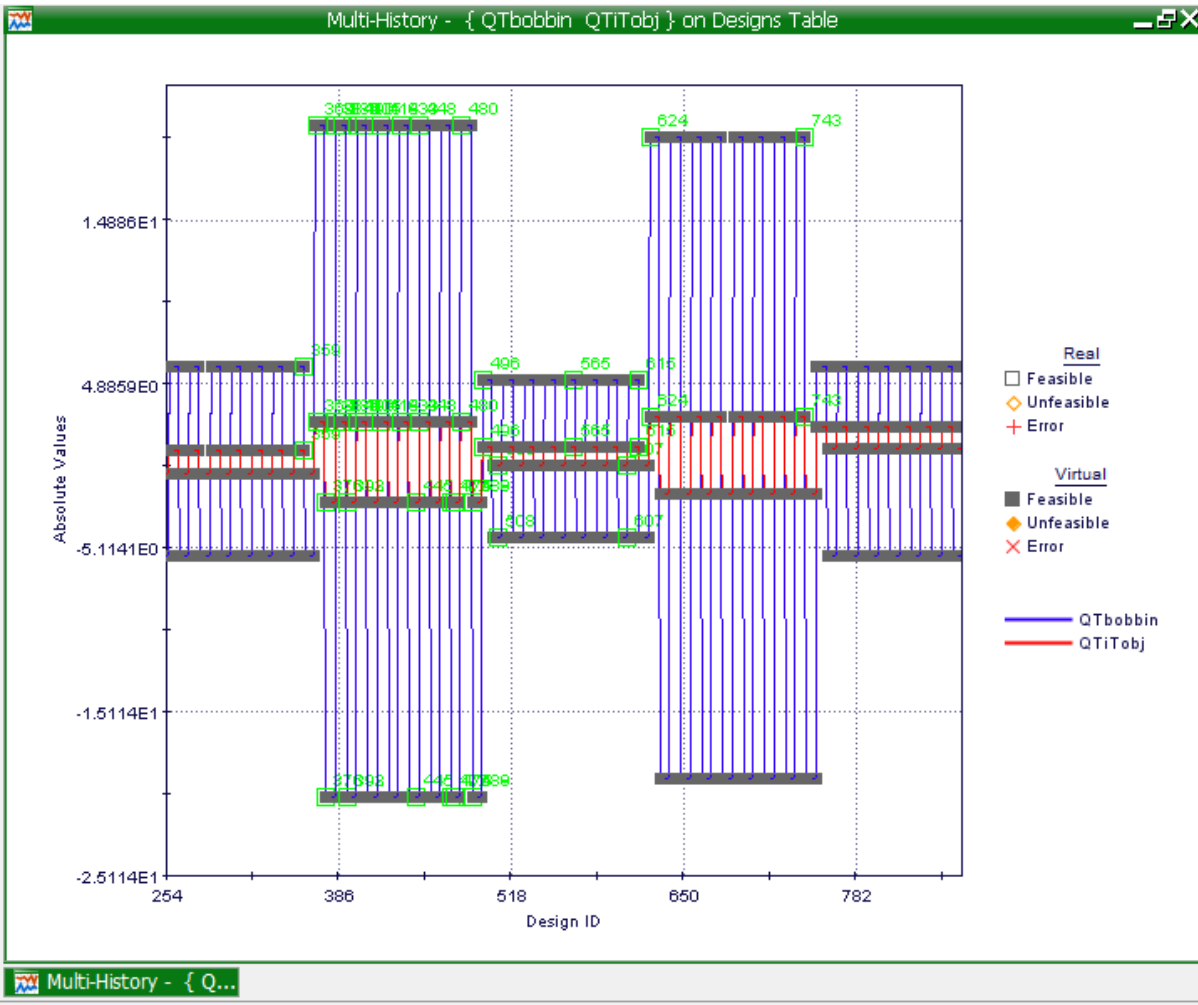


Chart 9.2: Bobbin tool total heat generation Vs Innovative Tool total heat generation

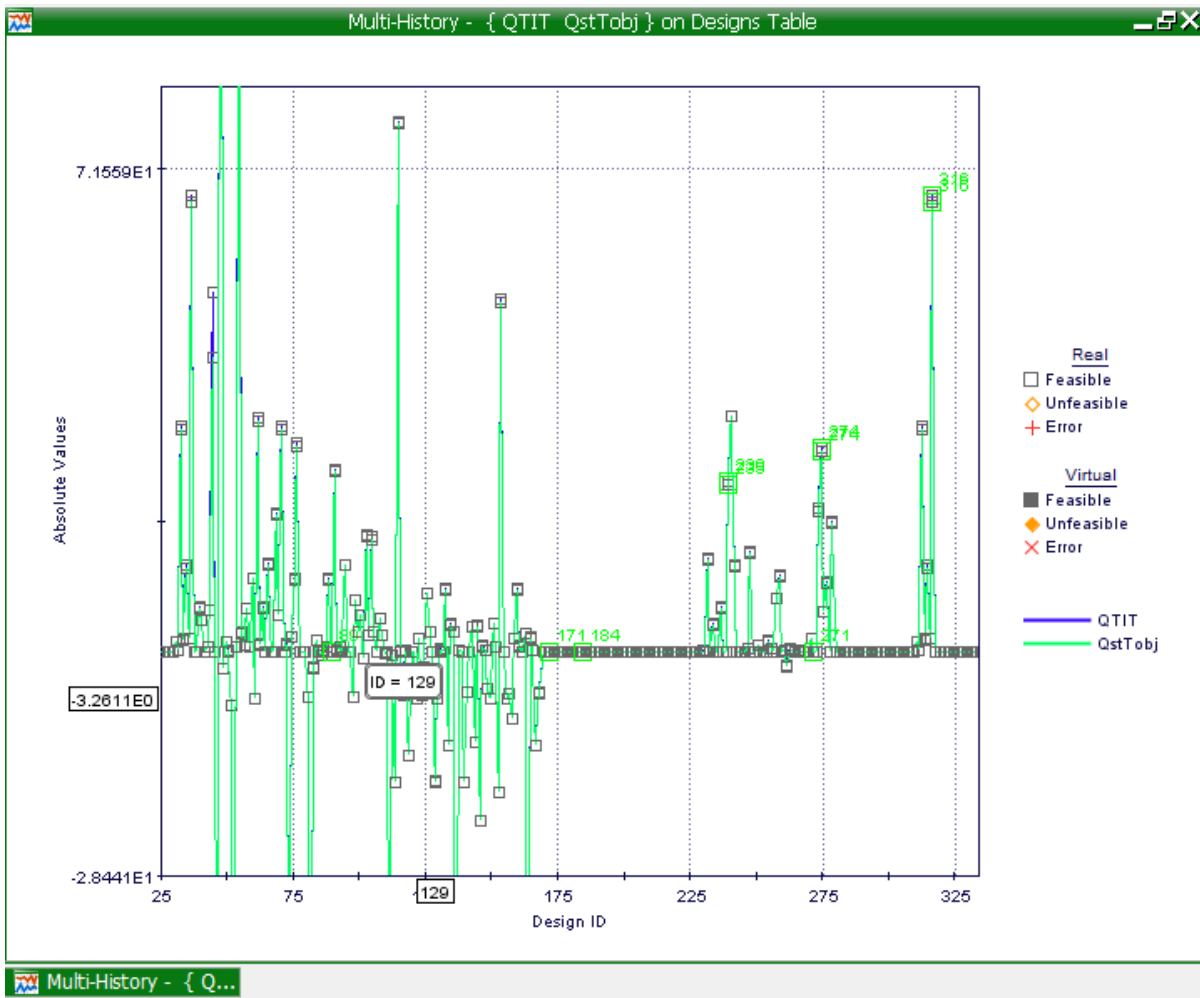


Chart 9.3: Standard tool total heat generation Vs Innovative Tool total heat generation

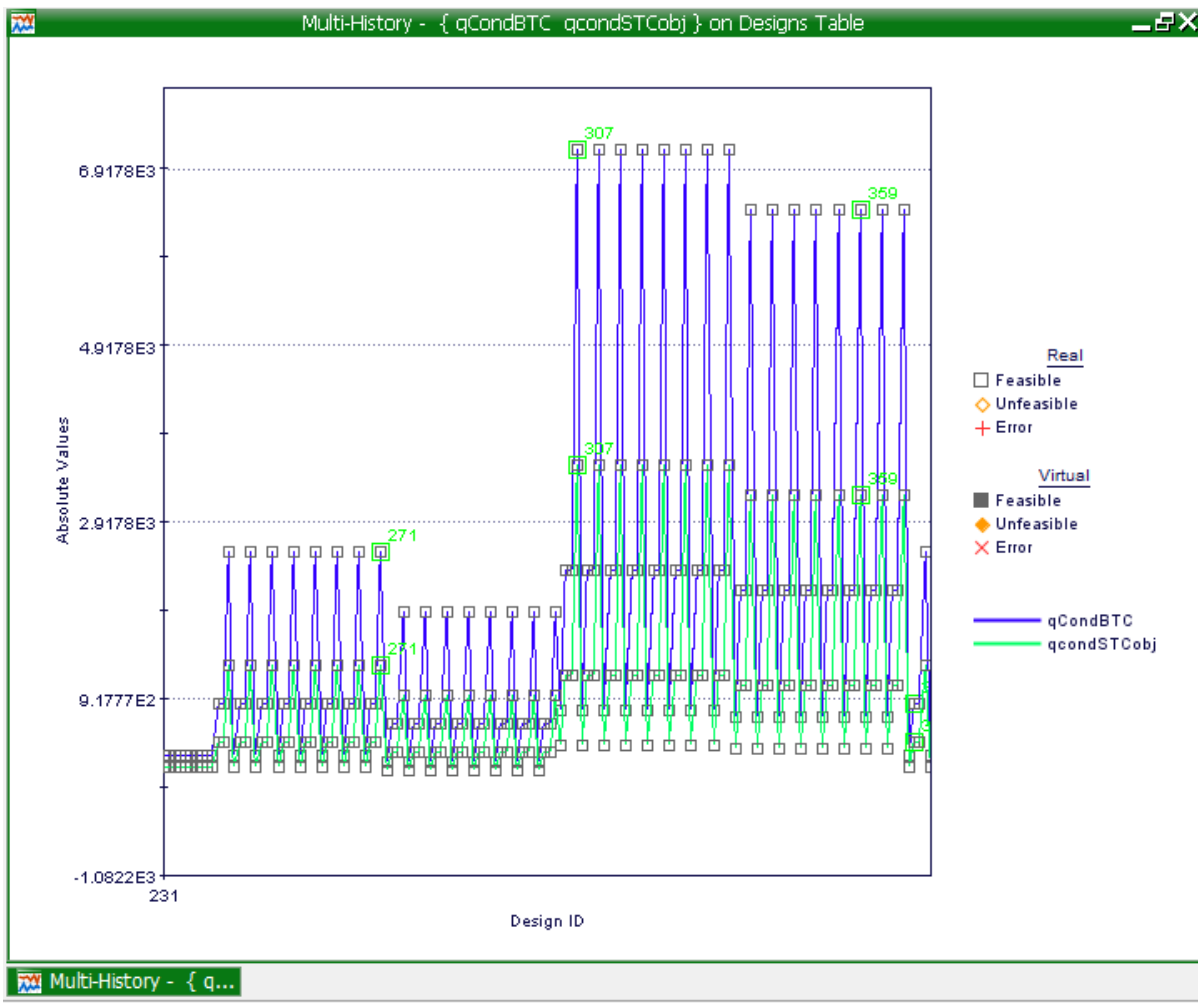


Chart 9.4: Bobbin tool conduction Vs Standard Tool Conduction

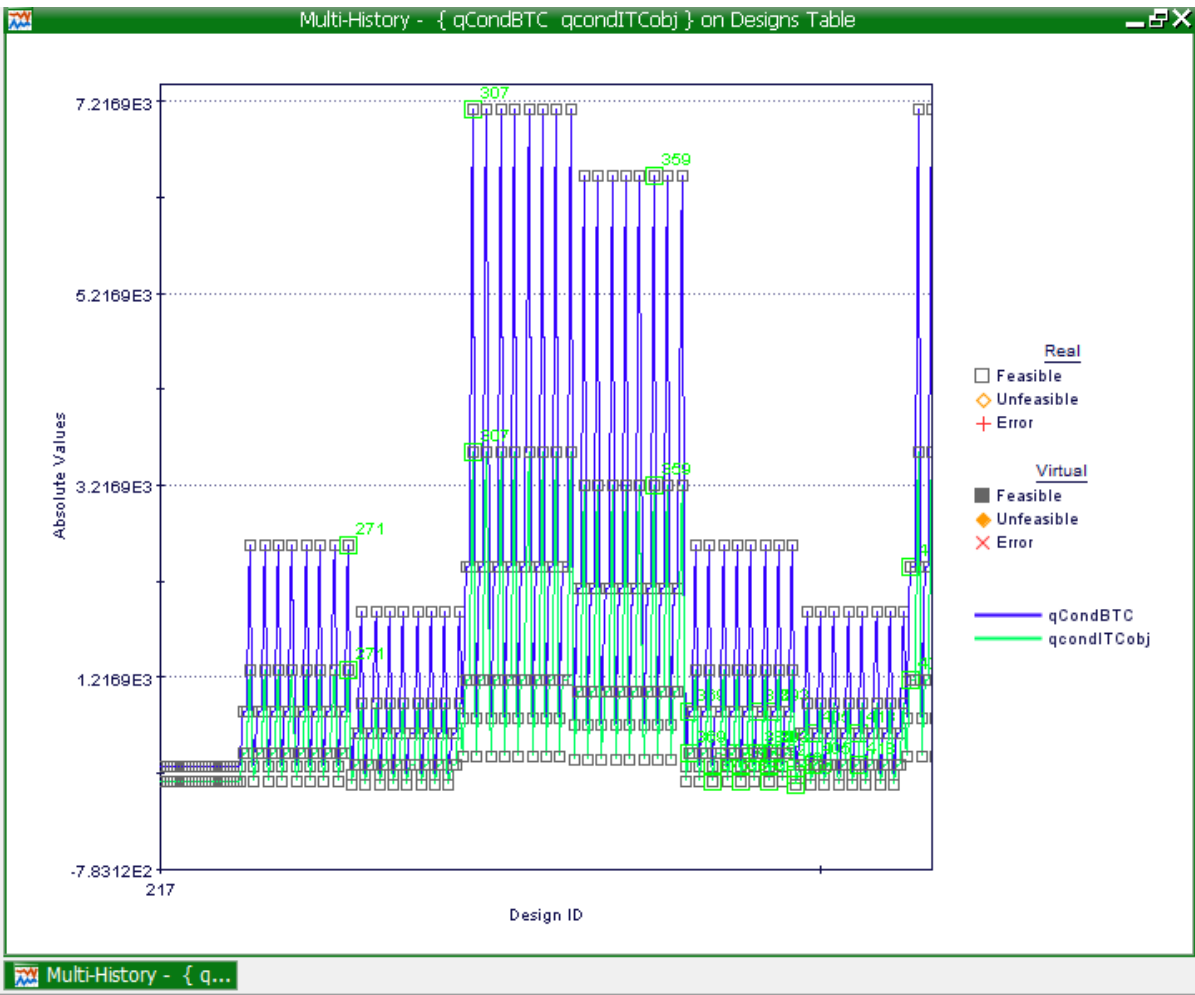
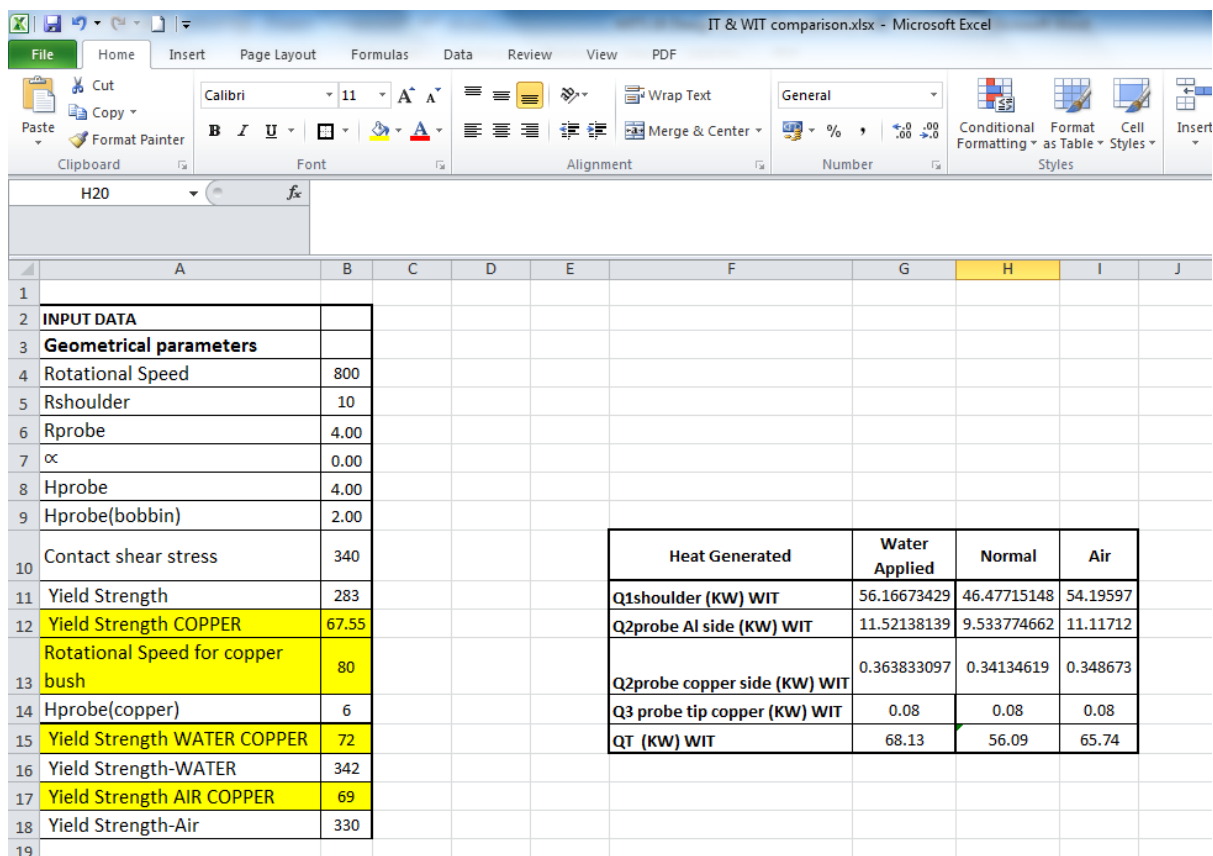


Chart 9.5: Bobbin tool conduction Vs Innovative Tool Conduction

9.2.2. Multi History Chart: Innovative tool vs The Application of Water and the Application of Air

The comparison of the Innovative tool Vs both Applied Air and Water Input and output data represented on an Excel Workbook: IT&WIT comparison.xlsx (Image 9.9) the yield strength reference was taken from (Table 9.1) for the input data variables, these References are used during the formulating of multi history charts. The Multi history chart of Applied air Vs Normal Conditions of an innovative tool (Chart 9.6) shows the representation that the temperature drops when air is applied to the innovative tool rather than in normal conditions, Applied air Vs Applied Water on an innovative tool (Chart 9.7) is represented showing the comparison between the two applied conditions making both feasible on a Real scale, the multi history chart of Applied water Vs The Normal Conditions of an innovative tool (Chart 9.8) is an indication of the temperature of the work piece drops when water is applied to the innovative tool rather than of when the tool remains in normal conditions.



INPUT DATA		Heat Generated			
Geometrical parameters		Water Applied	Normal	Air	
Rotational Speed	800				
Rshoulder	10				
Rprobe	4.00				
α	0.00				
Hprobe	4.00				
Hprobe(bobbin)	2.00				
Contact shear stress	340				
Yield Strength	283	Q1shoulder (KW) WIT	56.16673429	46.47715148	54.19597
Yield Strength COPPER	67.55	Q2probe AI side (KW) WIT	11.52138139	9.533774662	11.11712
Rotational Speed for copper bush	80	Q2probe copper side (KW) WIT	0.363833097	0.34134619	0.348673
Hprobe(copper)	6	Q3 probe tip copper (KW) WIT	0.08	0.08	0.08
Yield Strength WATER COPPER	72	QT (KW) WIT	68.13	56.09	65.74
Yield Strength-WATER	342				
Yield Strength AIR COPPER	69				
Yield Strength-Air	330				

Image 9.6: Microsoft Excel workbook showing the input and output data of the comparison of conditions.

Temper	Temperature		Tensile Strength		Yield Strength		Elongation
	°C	°F	MPa	ksi	MPa	ksi	%
T3 (Sheet)	-196	-320	586	85	427	62	18
	-80	-122	503	73	359	52	17
	-28	-18	496	72	352	51	17
	24	75	483	70	345	50	17
	100	212	455	66	331	48	16
	149	300	379	55	310	45	11
	204	400	186	27	138	20	23
	260	500	76	11	62	9	55
	316	600	52	7,5	41	6	75
	371	700	34	5	28	4	100

Table 9.1: References the tensile properties of alloy 2024-T3.

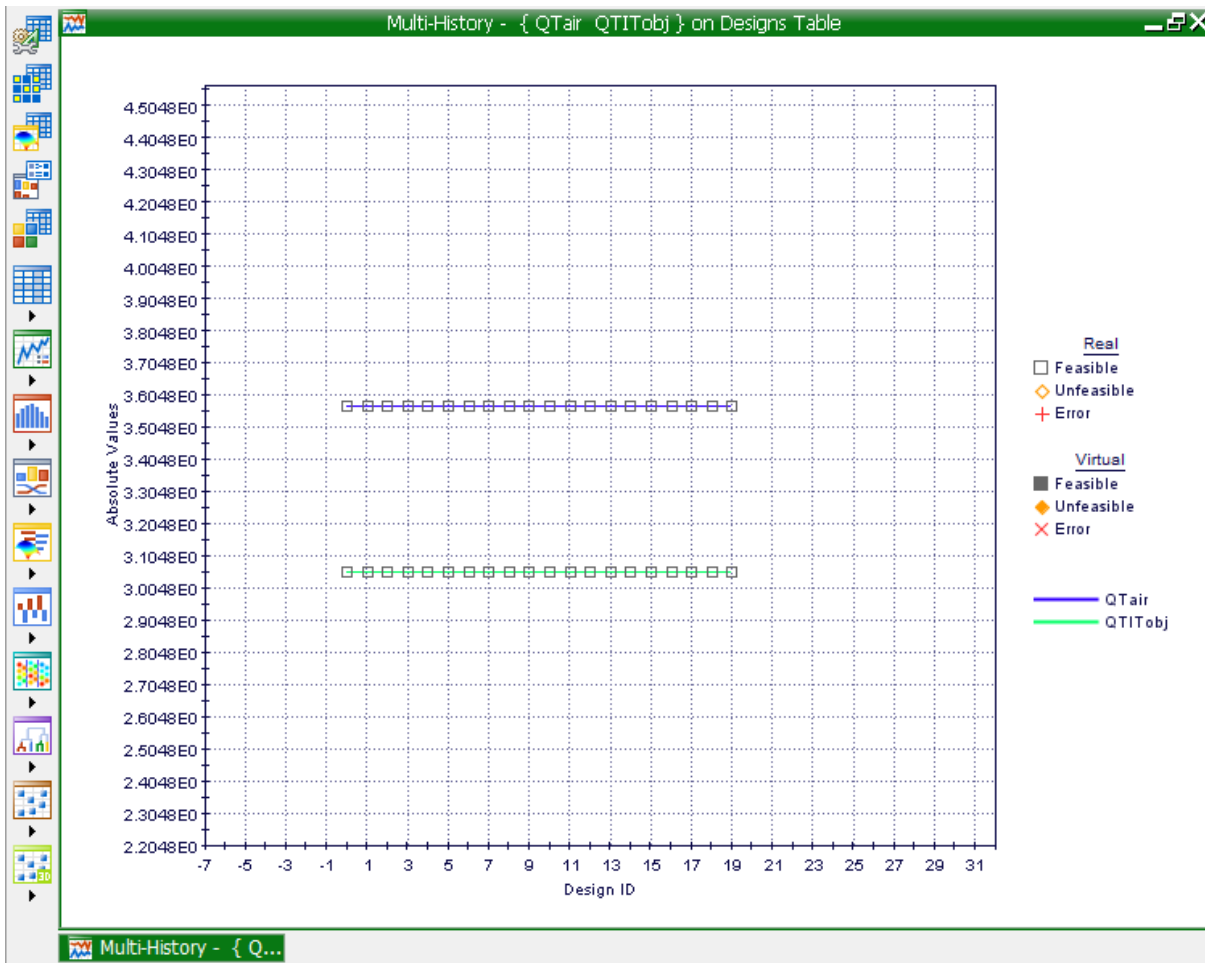


Chart 9.6: Applied air Vs Normal Conditions of an innovative tool

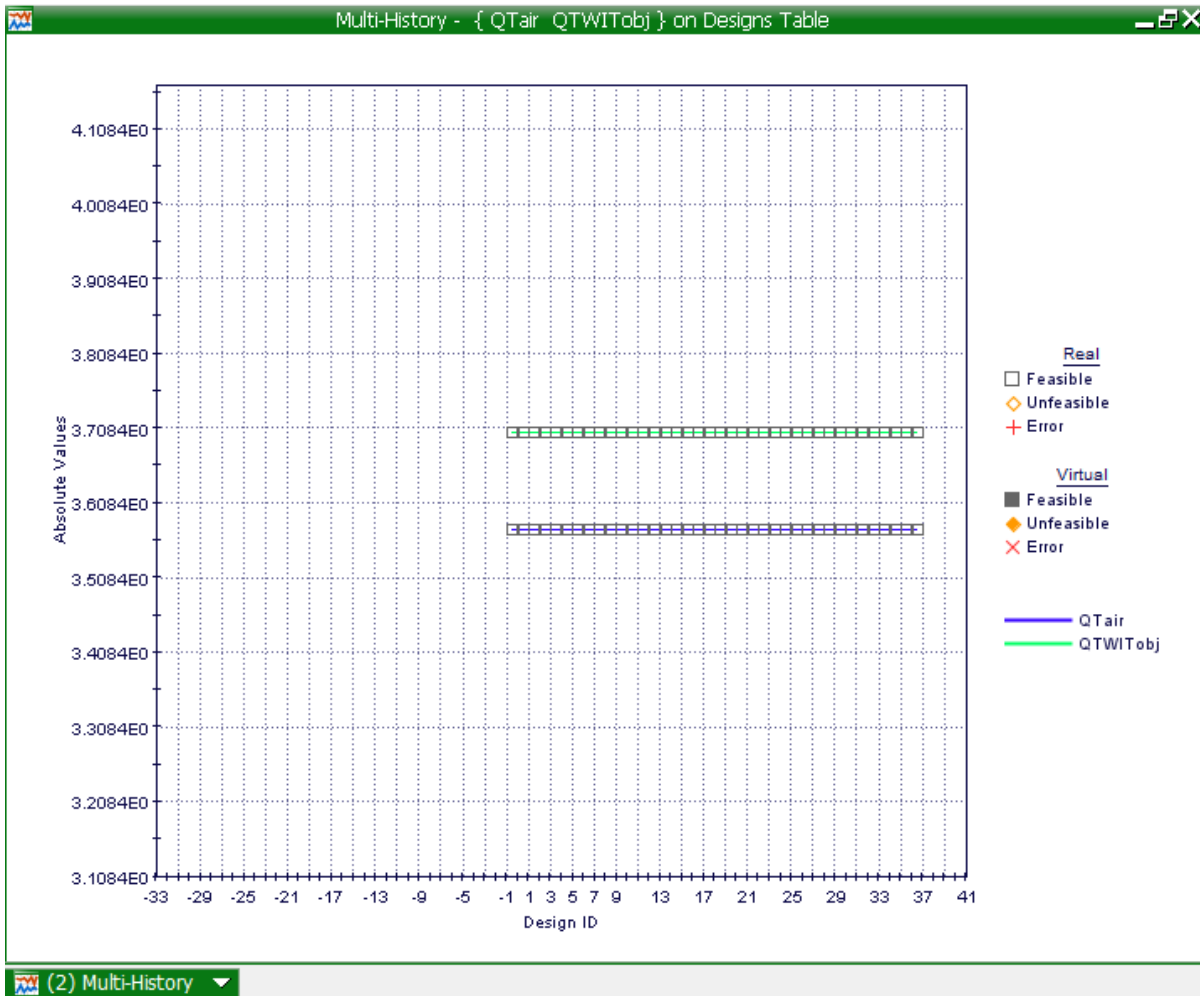


Chart 9.7: Applied air Vs Applied Water on an innovative tool

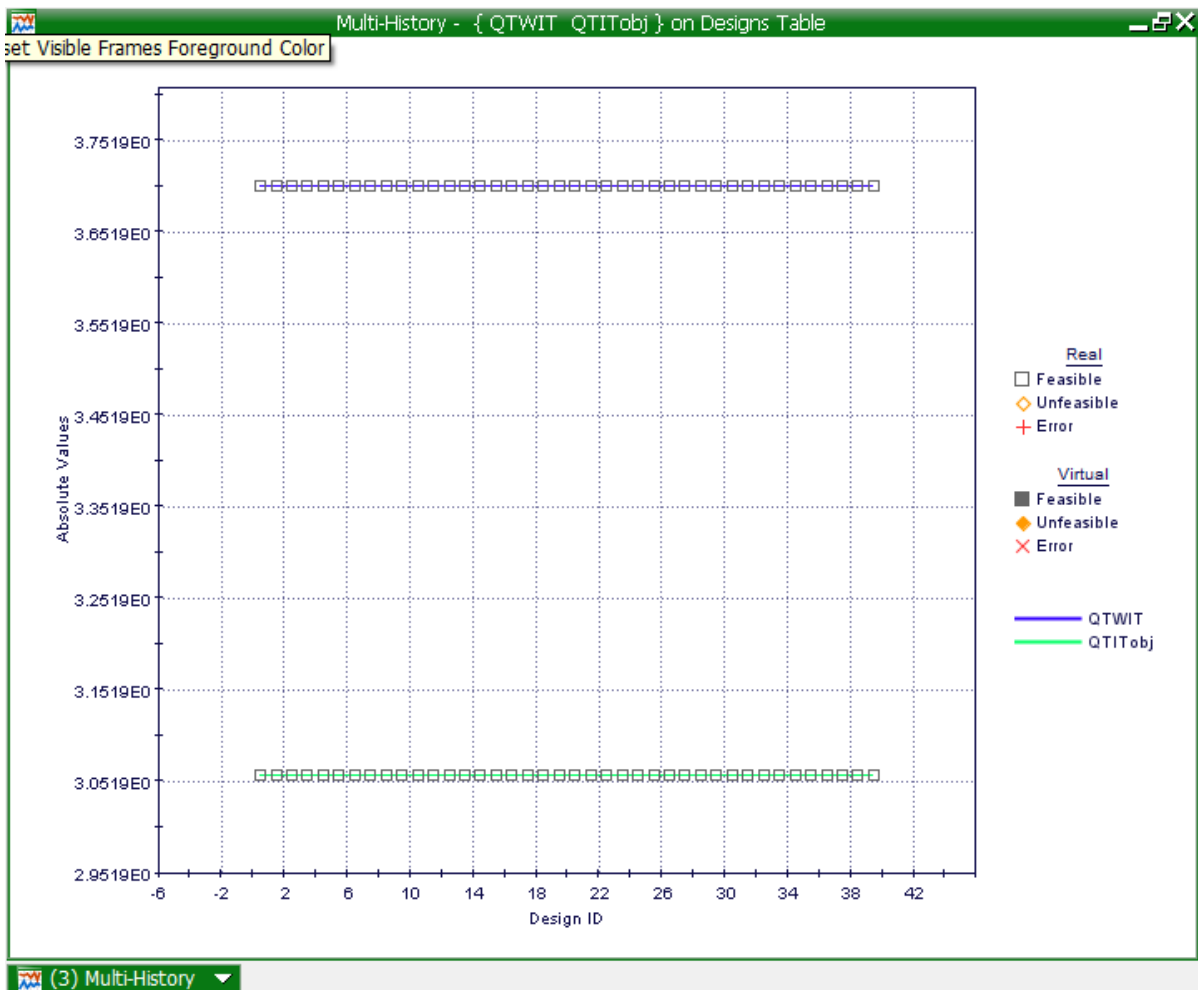


Chart 9.8: Applied water Vs the Normal Conditions of an innovative tool.

9.3. The Application of Boiling Water to the Innovative Tool

The use of boiling water on the innovative tool is to reach a higher heat generation to make it similar to that of a standard tool. As shown on a multi-history chart generated Mode Frontier, the heat generation of the innovative tool is higher than the standard tool and is feasible in a real scale. Adding the boiling water to the innovative tool affects the weld differently, A model analytically estimating the amount of heat generation during a weld shows that heat generation along with the thermo mechanical properties of 2024-T3 affects the yield strength, the contact shear stress and the contact pressures This also shows an analytical model for estimating the amount of heat generation during a friction stir weld' it recognises the geometrical, kinematic, physical and energetic possibilities during a weld, recognising a dominant parameters affects the heat generation process and use it to estimate how much mechanical power is transformed into heat, these parameters initiate other parameters that affect the heat generation process, friction co-efficient, pressure, shear stress and temperature, Where T is the temperature which is dependent on the contact shear stress $\tau_{contact}$ which is supported by the, σ_{yield} constant yield strength, μ been the co-efficient along with other supporting aspects. These are the reasons why this analysis considers only the most important dependencies, it involves more dominant parameters than previously explained, by using the more dominant parameters and neglects the fewer parameters, it decreases the calculation time. (FIG 9.1: Analytical Model for Estimating the Amount of Heat Generated During Friction Stir Welding: Application on Plates Made of Aluminium Alloy 2024 T351 Miroslav Mijajlović and Dragan Milčić). Boiling

water at the temperature of 100 °C is applied to the process in between the backing plate and the work piece with high pressure causing the temperature of the material Al2024-T3 to increase which in turn decrease the contact shear strength to 331.0 MPa and the Cooper contact shear strength to 50 MPa (Table 9.2: The Effects of Temperature On The Strength Properties Of Aluminium Alloy 2024-T3 – Adam Lipski And Stanistaw Mrozinski).

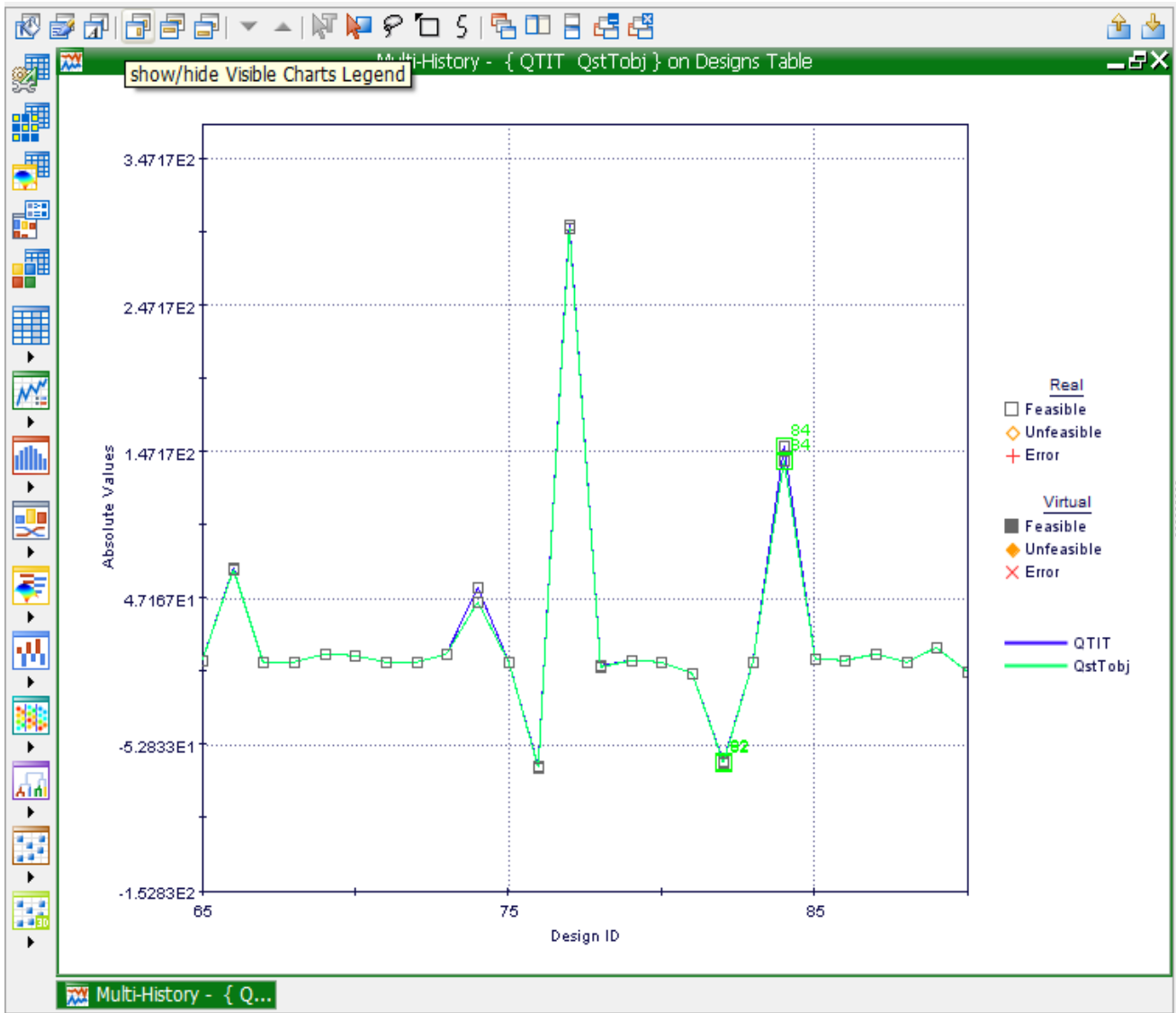


Chart 9.9: A mode frontier multi history chart showing the comparison of the innovative tool and standard tools heat generation.

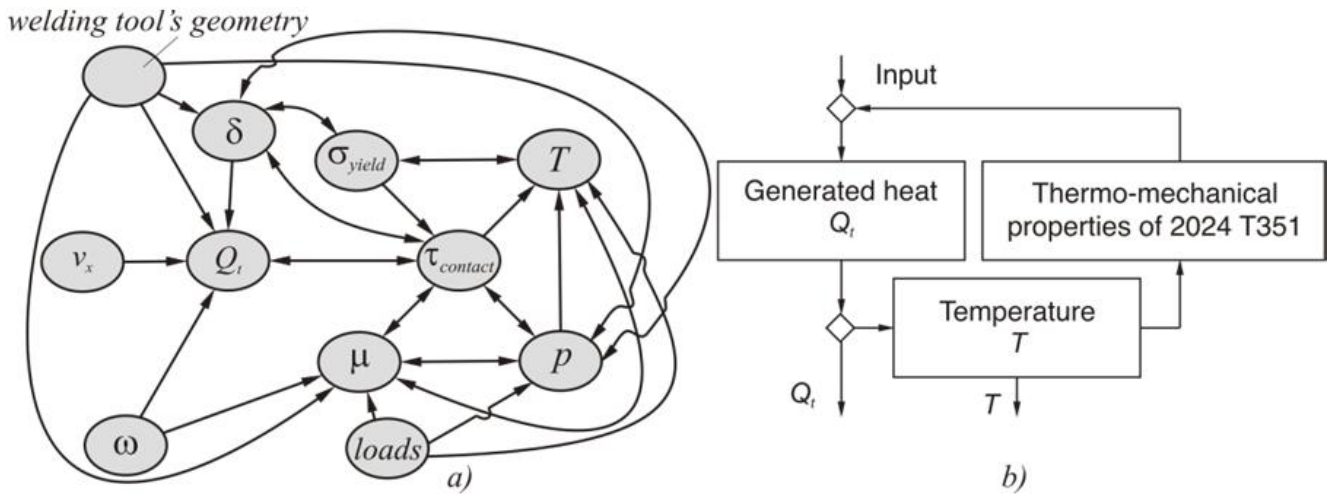


FIG 9.1: shows: (a) Schematic of mutual dependencies between generated heat and dominant influencing parameters and (b) representing Partial algorithm for generated heat estimation.

Direction	Temperature	E	R_{eL}	$R_{p0.2}$	R_m	A_t
	°C					
Parallel to the plate rolling direction	25	68 563	367.5	-	488.8	23.9
	50	66 879	367.5	-	483.0	23.2
	75	70 403	361.8	-	471.1	23.4
	100	65 564	360.3	-	466.2	18.4
	125	62 863	354.0	-	440.7	16.5
	150	62 082	348.3	-	422.5	17.7
	175	66 814	318.2	-	394.2	19.1
	200	46 624	312.9	-	383.2	22.2
Perpendicular to the plate rolling direction	25	64 456	-	323.6	478.0	21.7
	50	65 674	-	320.4	470.9	24.1
	75	72 926	-	314.4	453.3	20.0
	100	65 965	-	307.4	449.3	21.8
	125	64 721	-	279.8	433.6	21.1
	150	60 858	-	305.7	414.9	19.4
	175	66 886	-	306.7	420.2	18.8
	200	53 675	-	270.0	367.7	23.4

Table 9.2: Strength properties determined based on monotonous tensile tests of 0, 16" thick samples made of non-clad plates of aluminium alloy 2024-T3

The following formula is for the heat generation exerted from the innovative tool has been previously explained:

For tool angular rotational speed $\omega_1 = 83.80 \text{ rad/s} = 800 \text{ rpm}$

$$QT_{innovative} = Q_{ps1} + Q_{pcopper1} + Q_{st1} + Q_{coppertip1} + Q_{pt1}$$

$$QT_{innovative} = 11.62 + 3.63 + 56.65 + 0.81 + 3.87$$

$$QT_{innovative} = 76.60 \text{ kW}$$

$$QT_{standard} = Q_{pt} + Q_{ps} + Q_{st}$$

$$QT_{standard} = 3.87 + 11.62 + 56.65$$

$$QT_{standard} = 72.16 \text{ kW}$$

The calculation of the innovative tool after the boiling water of 100°C is applied:

$$QT_{innovative}(100^\circ\text{C})$$

$$= \frac{2}{3} \omega \pi \tau_{cont} \left(\left(\frac{R_{shoulder}}{2} \right)^3 + 3 \left(\frac{d}{2} \right)^2 h \right) + 2 \omega \pi \tau_{cont} \left(\frac{d}{2} \right)^2 h \left(1 + \tan \frac{\beta}{2} \right) + \frac{2}{3} \omega \pi \tau_{cont} \left(\frac{d}{2} \right)^3$$

$$QT_{innovative} = \frac{2}{3} \times \pi \times 83.80 \times 331 \times \left(\left(\frac{10}{2} \right)^3 + 3 \left(\frac{4}{2} \right)^2 \times 4 \right) + 2 \times 83.80 \times \pi \times 50 \times \left(\frac{4}{2} \right)^2 \times 6 \left(1 + \tan \frac{0}{2} \right)$$

$$+ \frac{2}{3} \times 83.80 \times \pi \times 50 \times \left(\frac{4}{2} \right)^3$$

$$QT_{innovative} = 73.67 \text{ kW}$$

9.3.1. Mode Frontier Simulation :The Application of Boiling Water to the Innovative Tool

A Mode frontier simulation shows the outcome of when boiling water is applied to the innovative tool, the boiling water of 100 °C as it is dependent on the contact shear stress for thermo-mechanical properties making the values usable in a practical experiment. A work flow plan (Image 9.10) is created to start the simulation there after the Input and Output data is connected as per the Microsoft Excel workbook. Each of the nodes has been carefully selected to insure that an innovative tool can serve the same purpose as that of a standard tool. Once the variable nodes have been selected an inter active selection between the chosen Microsoft Excel worksheet and Mode frontier (Image 9.11) takes place to ensure the results are that of target. The yield strength boundary has a range property : lower bound 28.0 and upper bound 427.0 (Image 9.12), Contact shear stress lower bound 34.0 and upper bound 586.0 (Image 9.13), the yield strength when the boiling water is applied for both the innovative tool and its copper bush has the following range properties, lower bound 28.0 and the upper bound 427.0 (Image 9.14 & 9.15) (both yield strength and contact shear stress variables were taken from Aluminium and Aluminium Alloys edited by Joseph R. Davis Pg.654), rotational speed of the tool also has variable properties where the upper bound is 3000.0 and the lower bound is 0.0 (as shown in Telco, a lab study done at the University of Witwatersrand)(Image 9.16), the shoulder radius has range properties lower bound 10.0 and upper bound 15.0 (Image 9.17), the probe radius follows with its lower bound been 4.0 and its upper bound been 6.0 (Image 9.18), the angular rotational has an lower bound of 0.0 and the upper bound of 90 degrees due to the scrolled shaped shoulder allowing for a precise weld, [97] (Image 9.19)., the height of the probe has range properties of the following lower bound of 1.0 and a upper bound of 20.0 (Image 9.20) and lastly the input variable property for the height of copper bush probe side has the following range properties lower bound 2.0 and the upper bound 10.0 (Image 9.21), in the case of the Input Variable Properties/ Boundaries a Microsoft Excel workbook case is drawn up to support each Range Property (Image 9.22), once this is completed history charts (Chart 9.10) are drawn up indicating the heat generation for the innovative tool both with boiling water with a temperature of a 100 °C (Aluminium and Aluminium Alloys edited by Joseph R. Davis Pg.654) is applied (QTWITobj) and a normal weld of an innovative tool (QTITobj). The bubble plot (Plot 9.1) shows the heat generation: QTIT vs QTWIT against the contact shear stress where it show the optimisations of the heat generation for both tools because of the heat generation and the dependencies of the contact shear stress, following this is the history chart (Chart 9.11) representing the heat generation of both the standard tool and the innovative tool showing the similarity in the feasibility of both tools and the bubble plot showing the contact shear stress optimisation (Plot 9.2), A bubble plot indicating the difference between the heat generation and the innovative tool and the innovative tool when hot liquid is applied (Plot 9.3). A multi history chart shows the difference between the standard tool and the innovative tool when boiling water is applied, this allows for better judgement on both the tools (Chart 9.12).

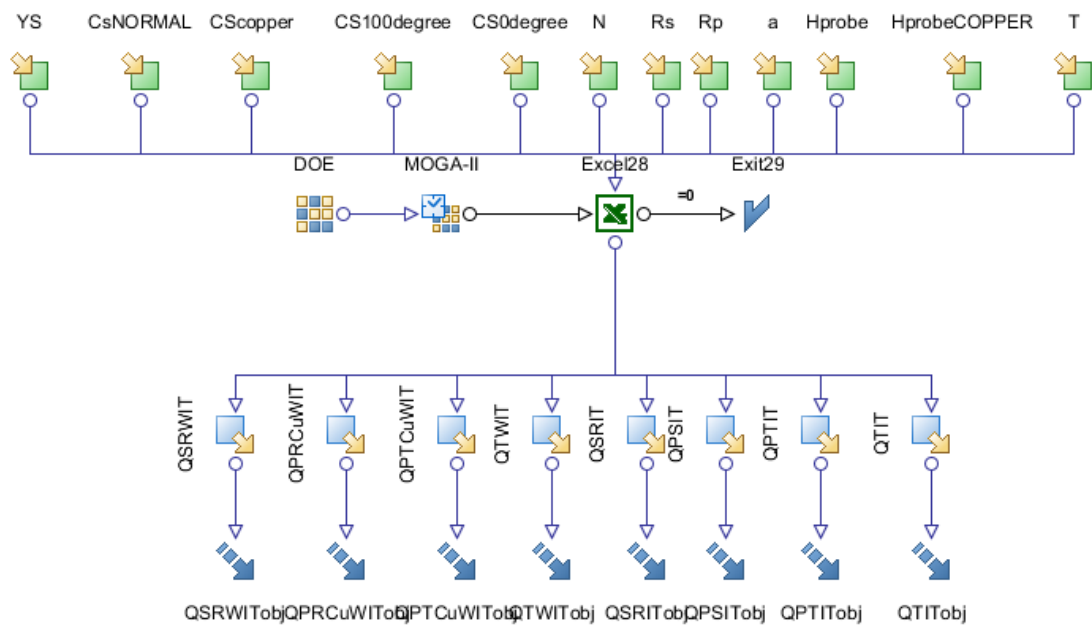


Image 9.10: Workflow Plan created by Mode Frontier Project as shown the following image, which shows the DOE (Design of Experiments) and DOE Sequence, as well as indicating Input Variables, Output Variables , Design Objectives + Gradients, Microsoft Excel Workbook and Logic End.

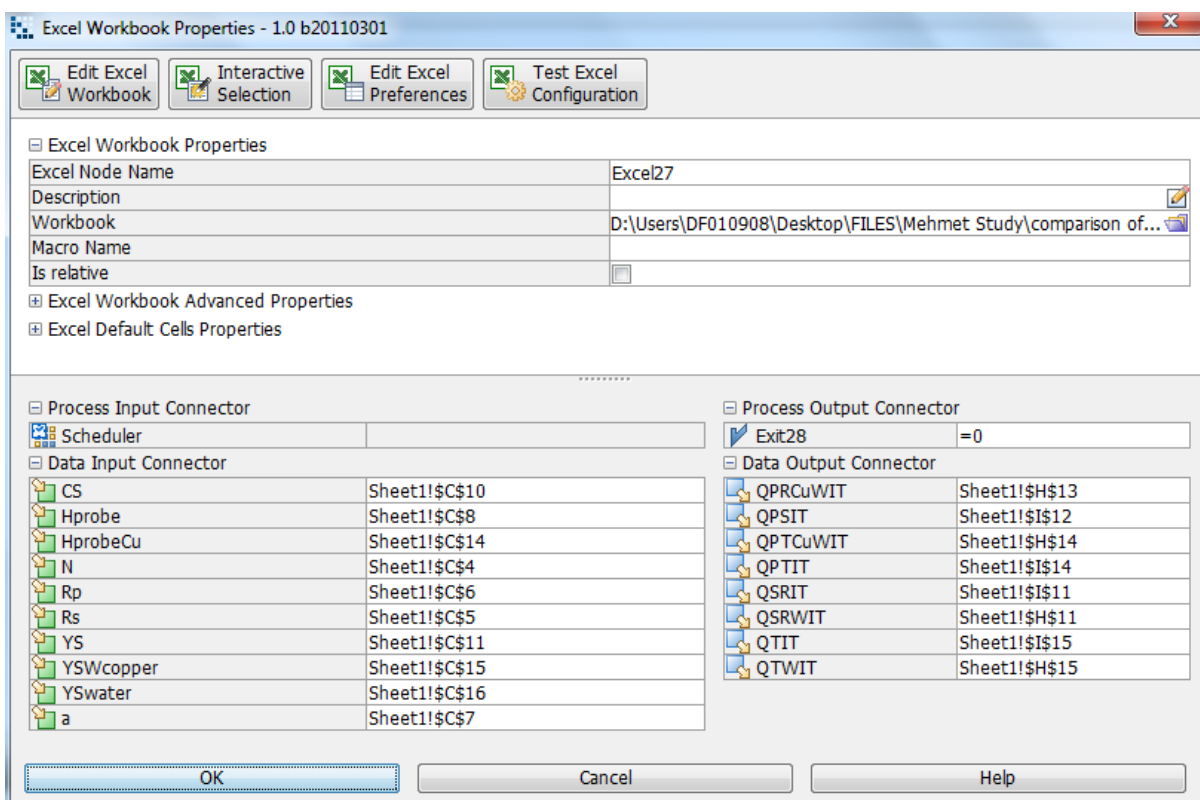


Image 9.11: Mode Frontier Input and Output Datas connected to Microsoft Excel Workbook linking it to various cells.

9.3.2. Boundaries: The Application of Boiling Water to the Innovative Tool

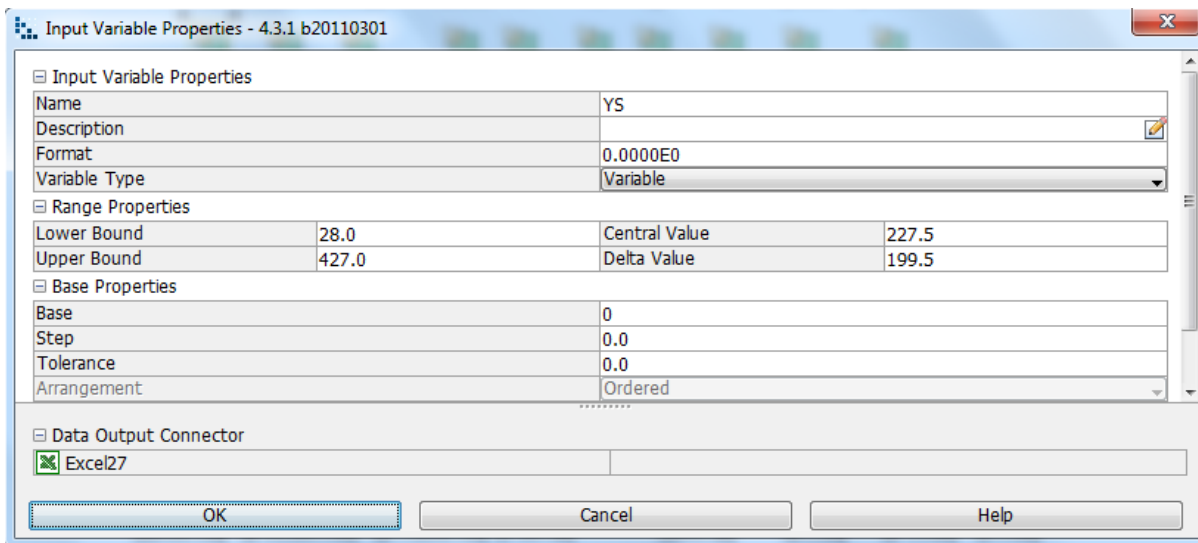


Image 9.12: The Yield Strength (YS) has a variable type that varies along with its Range Properties.

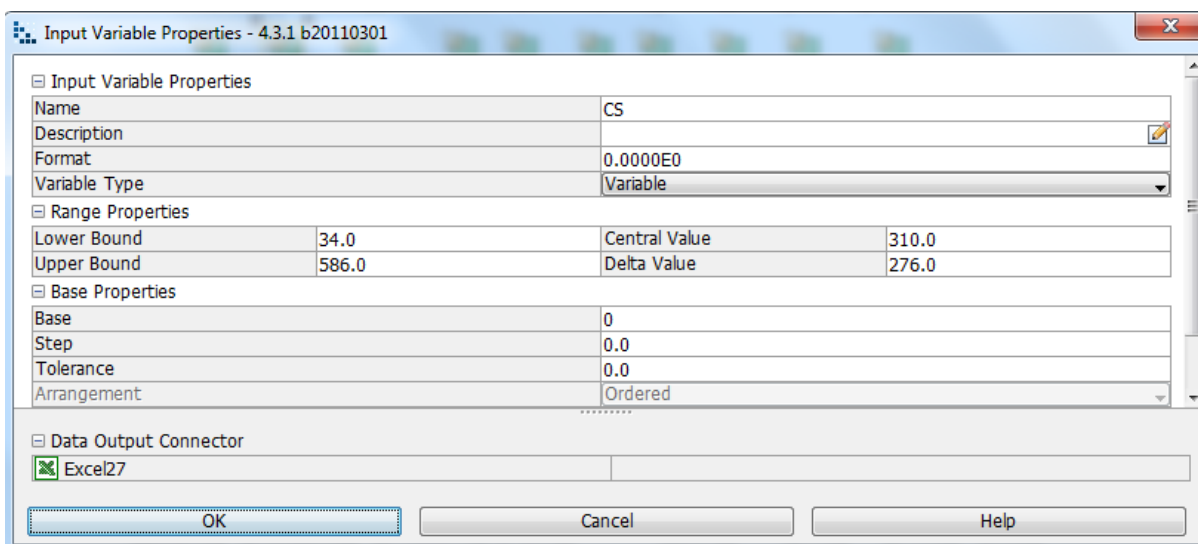


Image 9.13: The input variable property of the tools contact shear stress has a variable type that varies which allows the range properties to do so to.

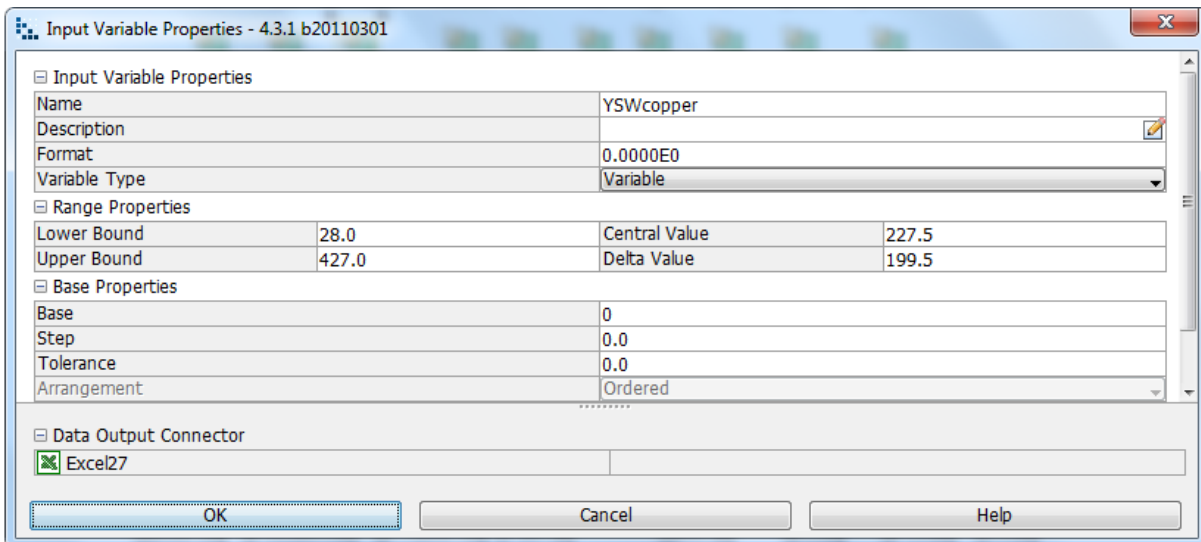


Image 9.14: The yield strength of boiling water on the copper bush is a variables that varies hence the upper bound and lower bound range properties do so as well.

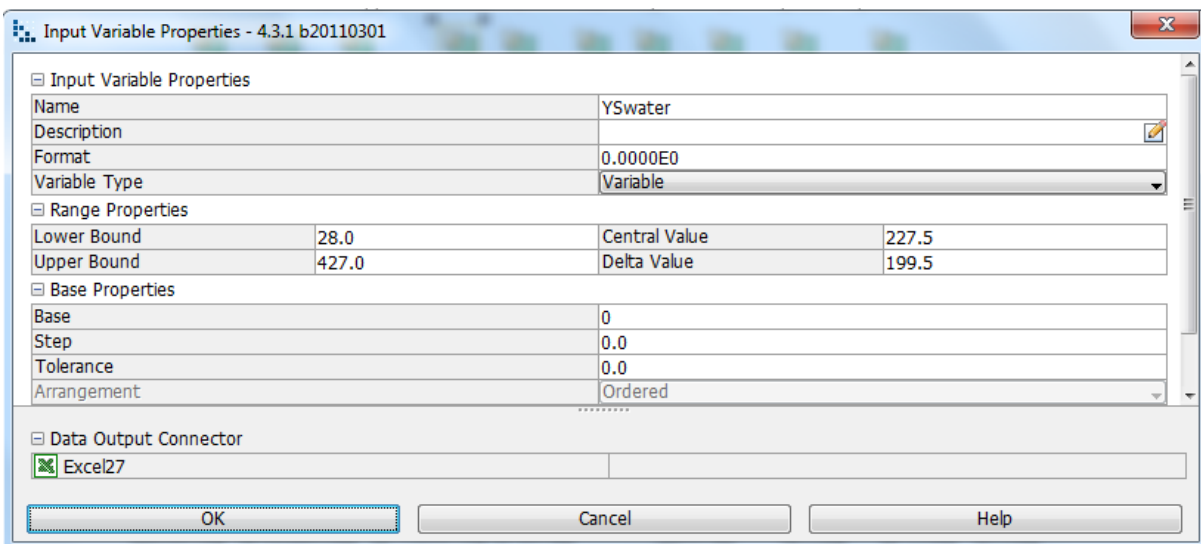


Image 9.15: The input variable property for the yield strength applied by the boiling water is one of a variable type with range properties of the same nature.

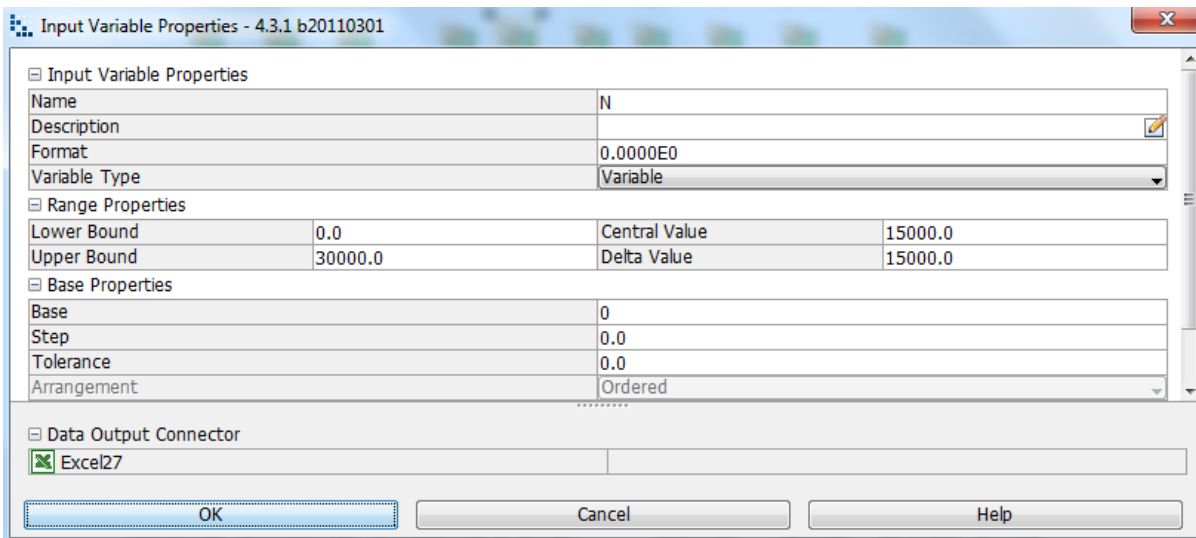


Image 9.16: The rotational speed of the tool has a variable type that varies which allows the Range Properties to do the same.

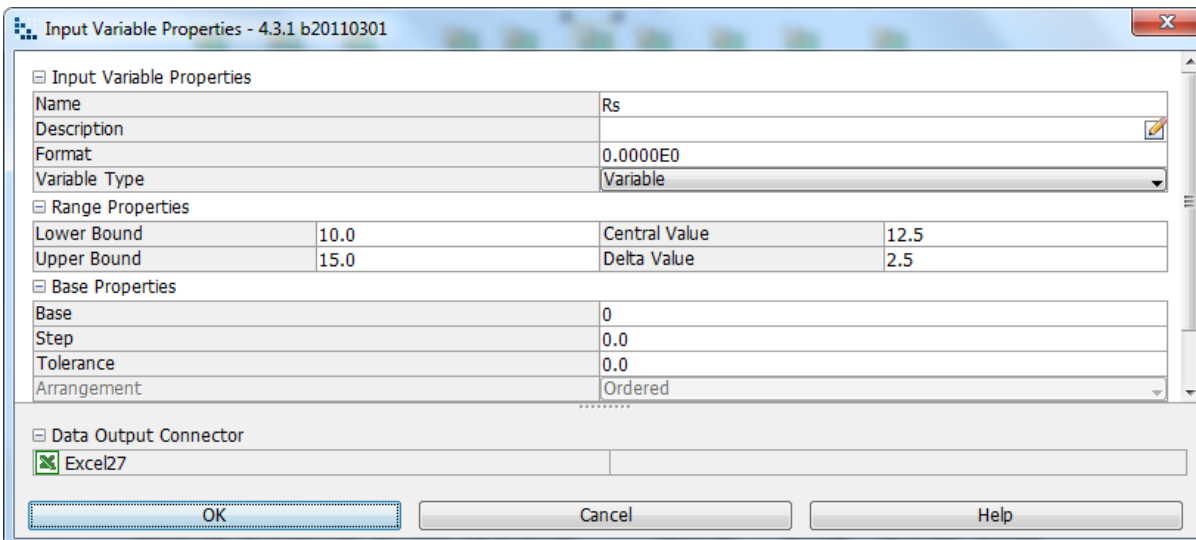


Image 9.17: The Shoulder radius has the input variable property that varies which also allows the lower and upper bound range properties vary as well

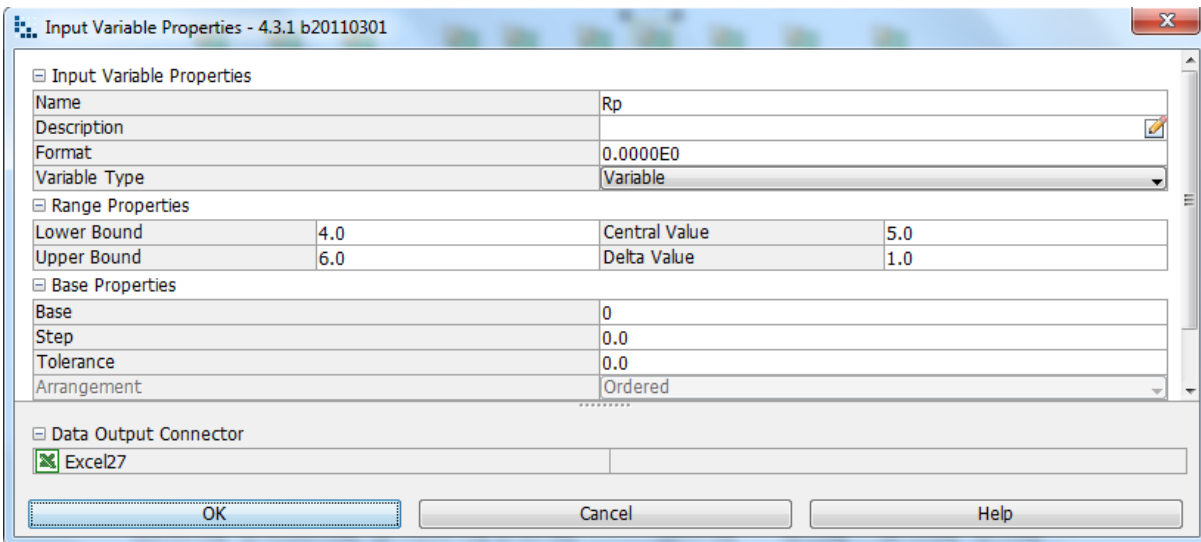


Image 9.18: The probe radius has a Variable type that varies allowing the range properties to vary as well.

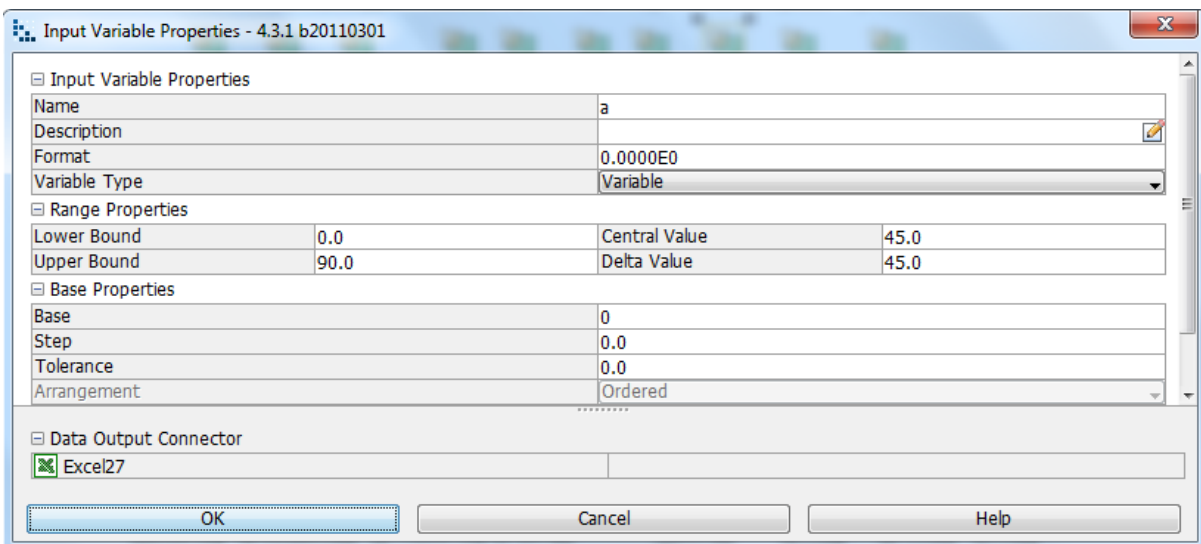


Image 9.19: Tool shoulder angle is determined by lower and upper bound range properties, as shown in the input variable node properties dialog

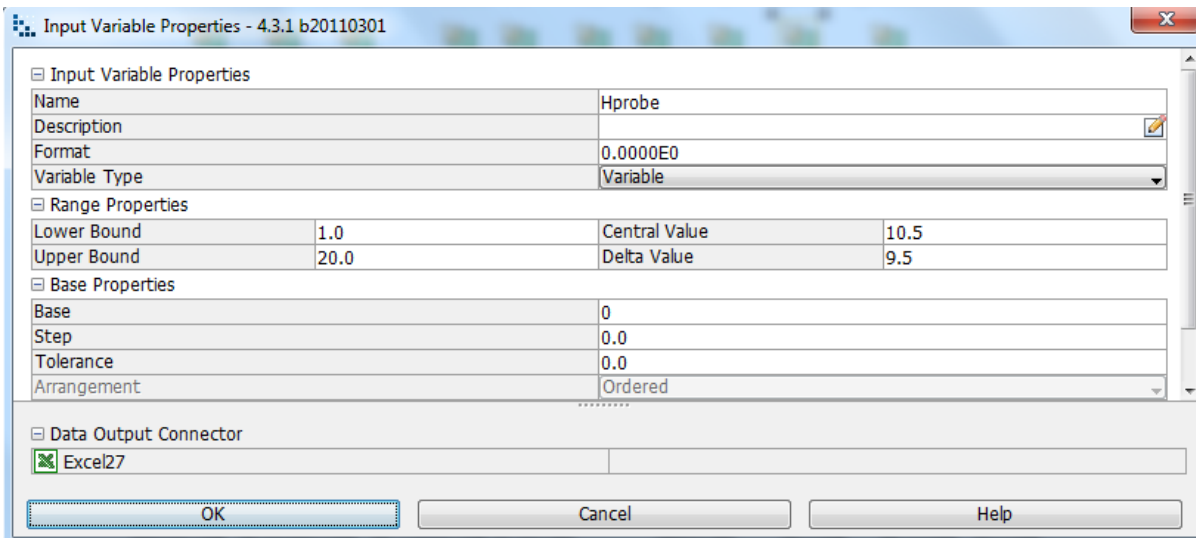


Image 9.20: Probe height is determined by lower and upper bound range properties, as shown in the input variable node properties dialog

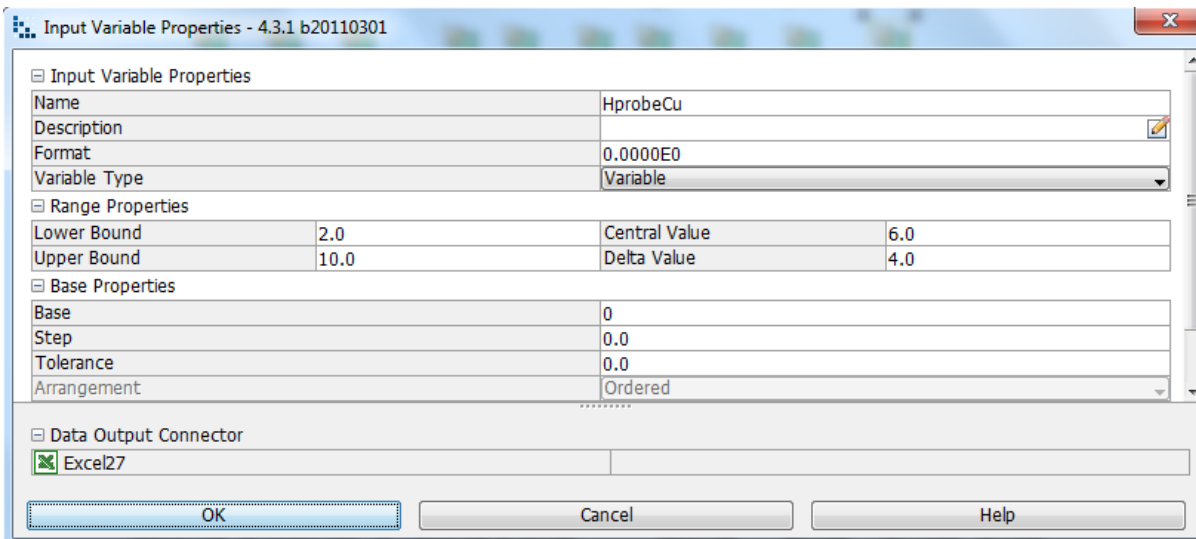


Image 9.21: The input variable properties for the probe height of the copper bush has a variable type that varies along with its range properties.

Excel Workbook Case:

Input Variables														
Rotational Speed	Rshoulder	Rprobe	α	Hprobe	Hprobe(bin)	Contact shear stress	Yield Strength	Yield Strength COPPER	Rotational Speed for copper bush	Hprobe(copper)	Yield Strength WATER COPPER	Yield Strength-WATER	Yield Strength AIR COPPER	Yield Strength-Air
800	10	4.00	0.00	4.00	2.00	340	283	67.55	80	6	72	342	69	330

$$=2/3*PI()*2*PI()/60*C4)*C16*((C5*C5*C5)-(C6*C6*C6))*(1+TAN(C7))/1000000$$

$$f_x = 2*PI()*2*PI()/60*C4)*C16*(C6*C6)*C8/1000000$$

$$f_x = 2/3*PI()*C15*(C4*2*PI()/60)*(C6*C6*C6)/1000000$$

$$Q_1 = \frac{2}{3}\pi r_{contact} \omega (R_{shoulder}^3 - R_{probe}^3)(1 + \tan \alpha)$$

$$Q_2 = 2\pi r_{contact} \omega R_{probe}^2 H_{probe}$$

$$Q_{pt} = \frac{2}{3}\omega \pi r_{cont} \left(\frac{d}{2}\right)^3$$

$$QT = Q_1 + Q_2 + Q_3$$

Output Variables														
Q1shoulder (KW)			Q2probe Al side (KW)			Q2probe copper side (KW)			Q3 probe tip copper (KW)			QT (KW)		
Water Applied	Normal	Air	Water Applied	Normal	Air	Water Applied	Normal	Air	Water Applied	Normal	Air	Water Applied	Normal	Air
56.16673	46.47715	54.19597	11.52138	9.533775	11.11712	3.64	3.41	3.49	0.808518	0.758547	0.758547	72.13	56.77	69.56

Image 9.22: Input Data, Output Data and boundary variables definitions as shown on this Microsoft Excel Sheet is used in Mode Frontier for this Design Project

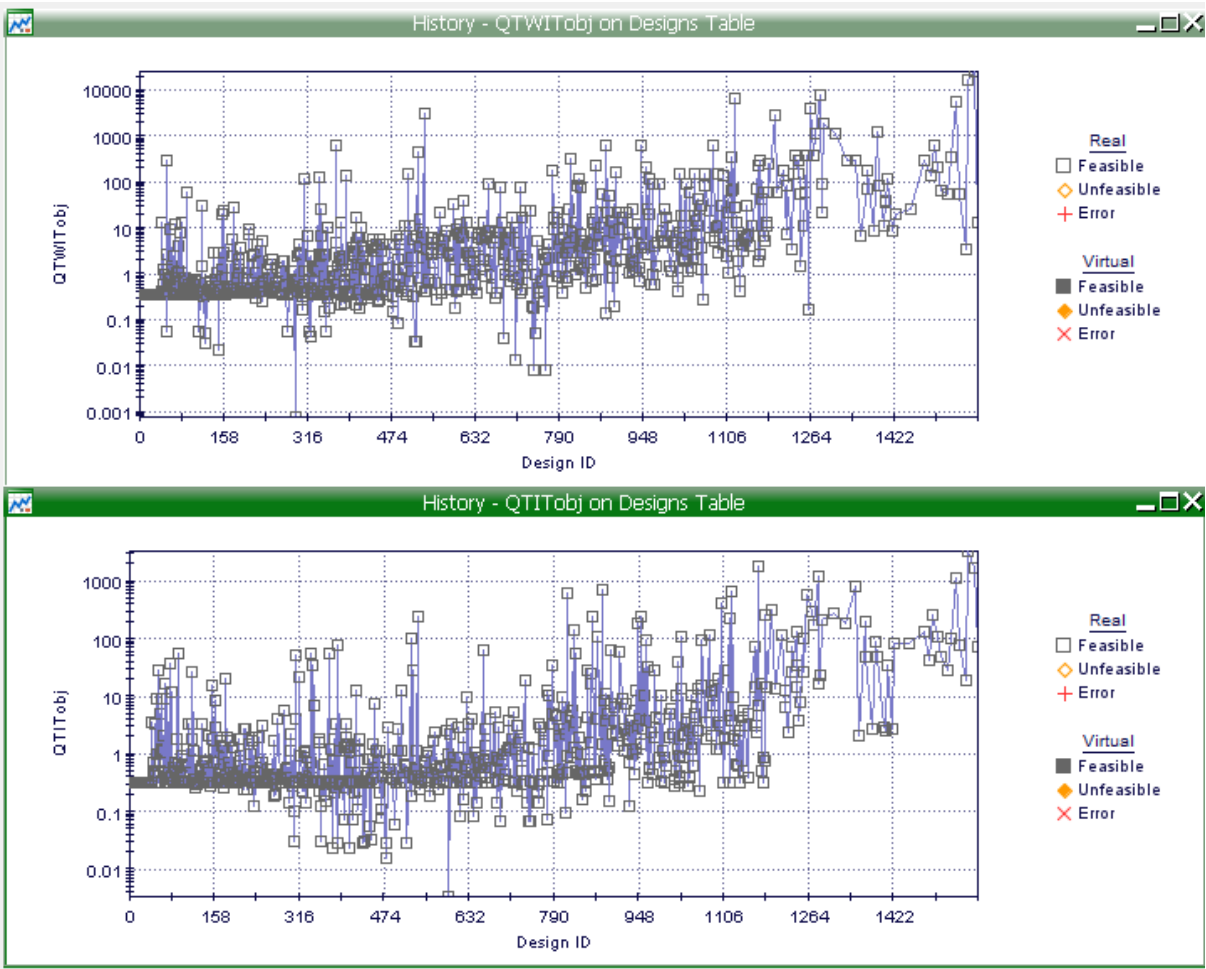
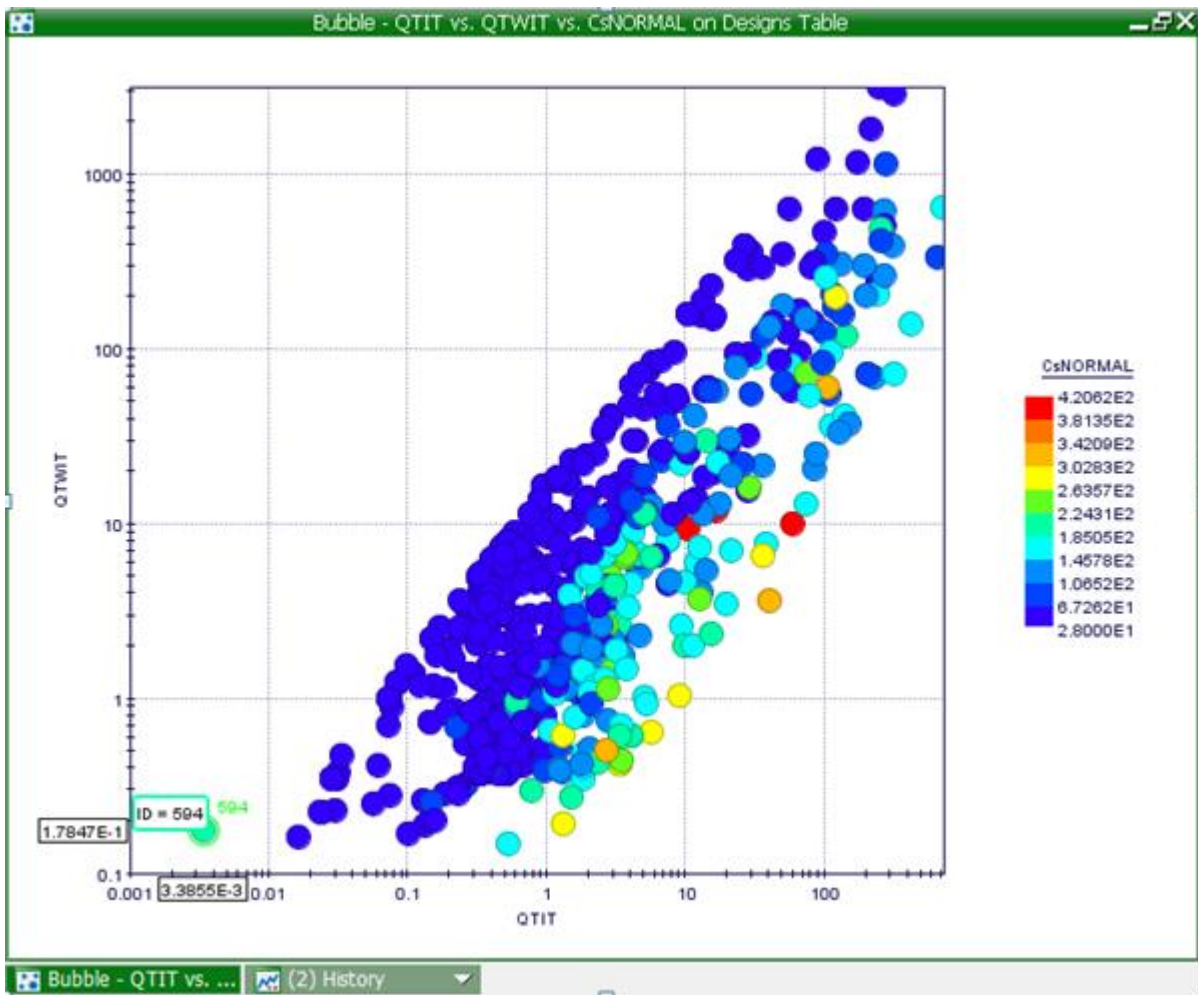


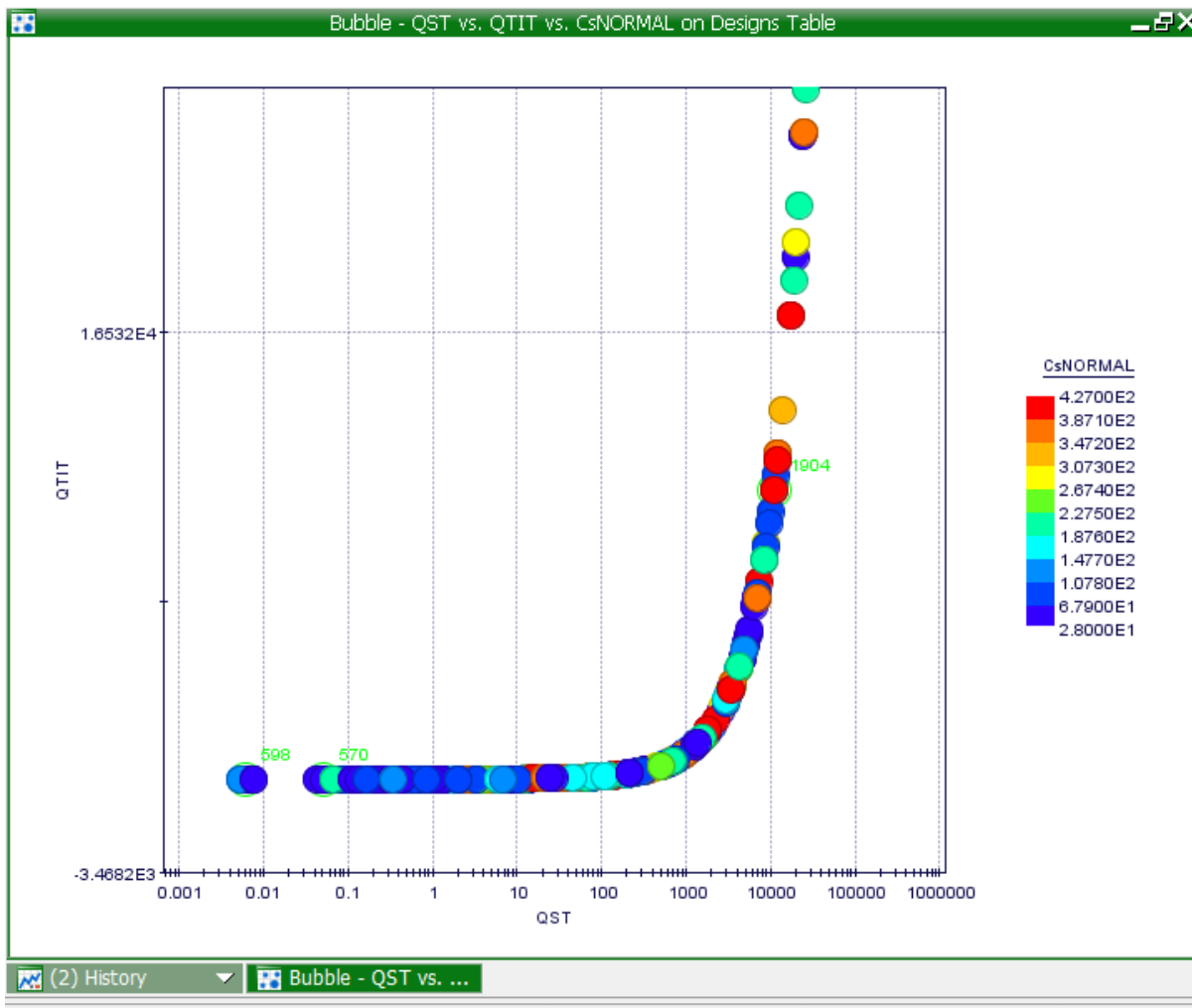
Chart 9.10: History charts indicating the heat generation for the innovative tool both with boiling water applied (QWITobj) and the innovative tools normal weld (QTITobj).



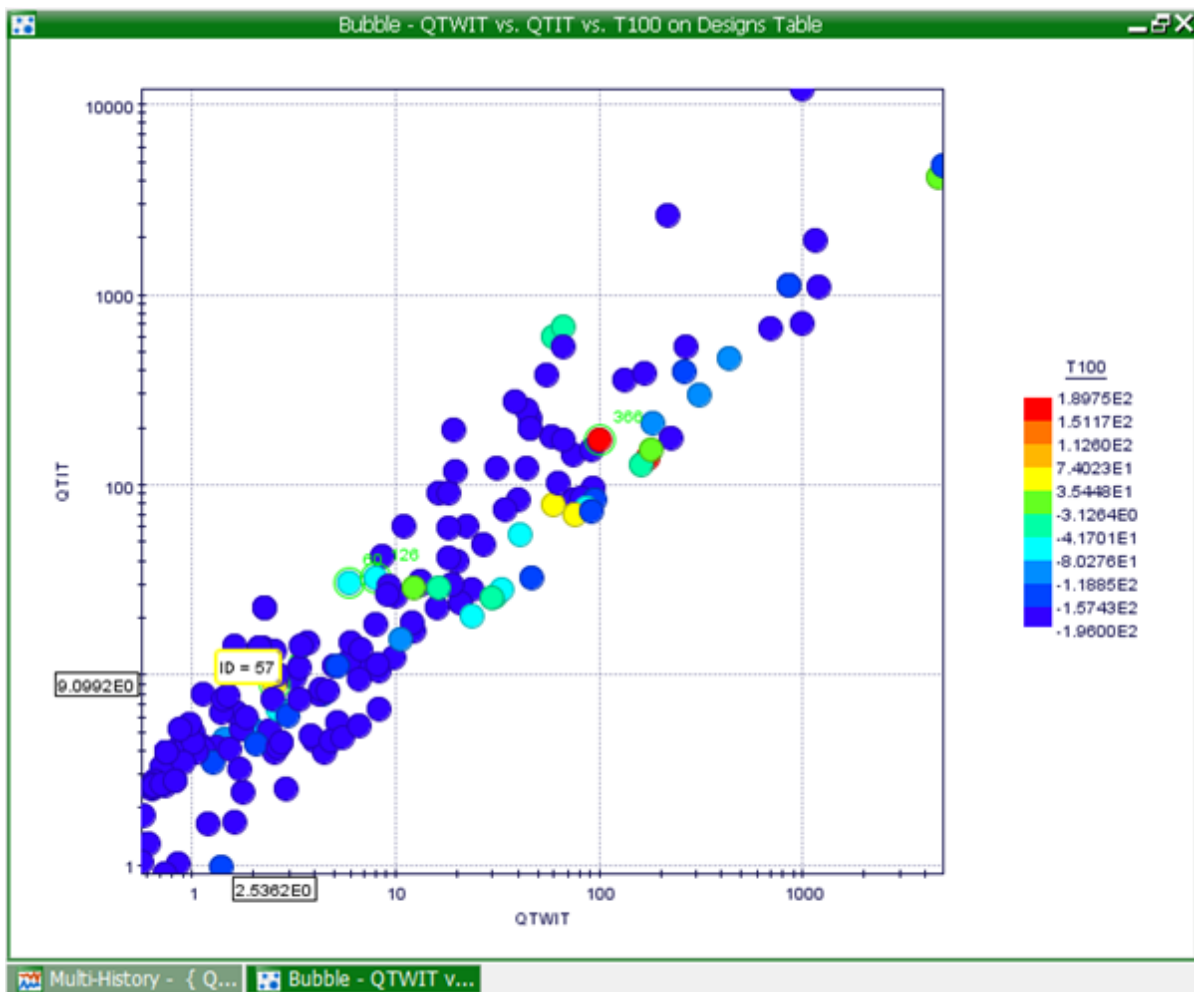
Plot 9.1: The following is a bubble plot showing the heat generation: QTIT vs QTWIT vs CsNORMAL



Chart 9.11: History chart representing the heat generation of both the standard tool and the innovative tool.



Plot 9.2: A bubble plot representing the heat generation: QTIT vs QTWIT vs CsNORMAL.



Plot 9.3: A bubble plot indicating the heat generation between the innovative tool and the innovative tool with added hot liquid.

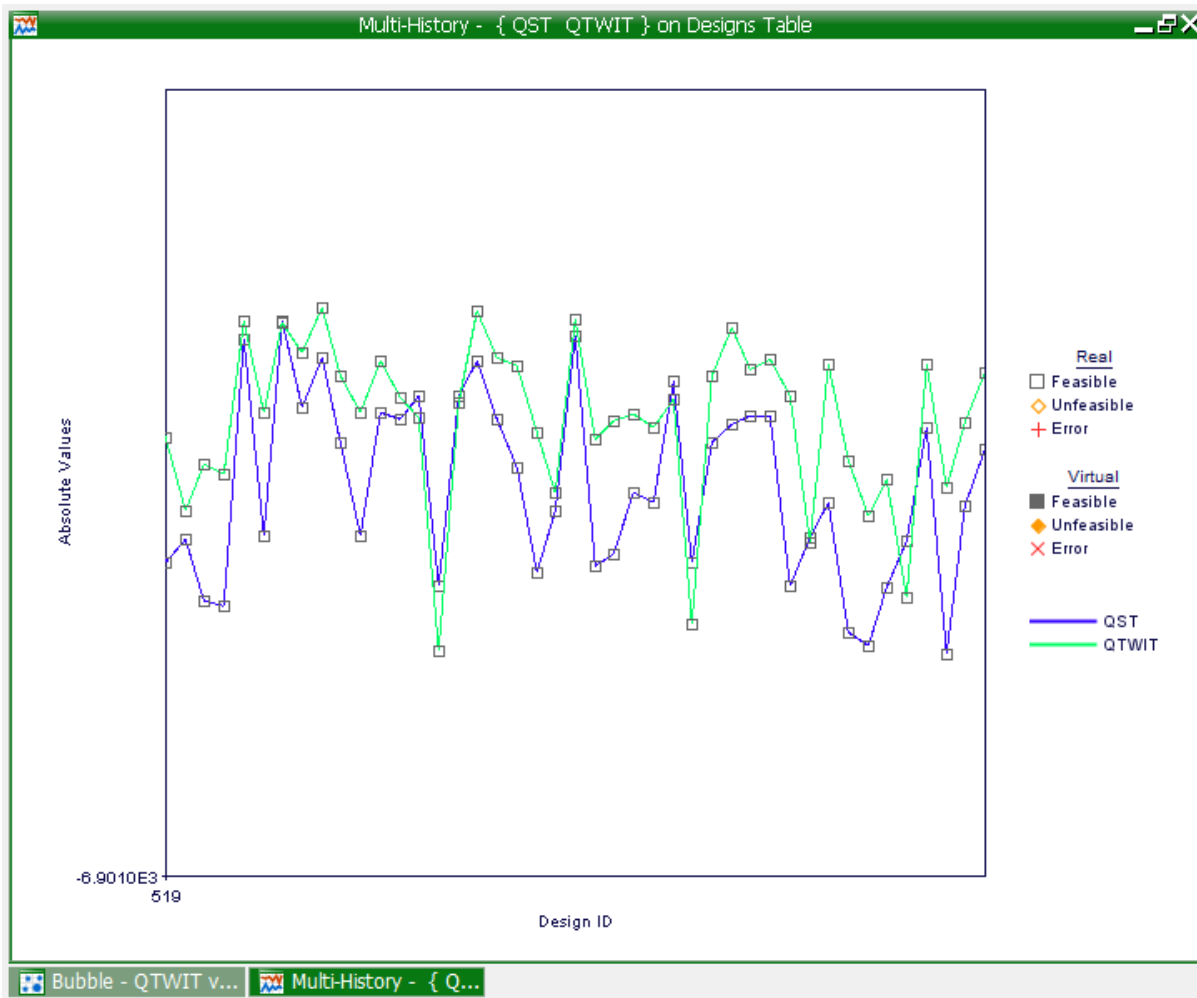
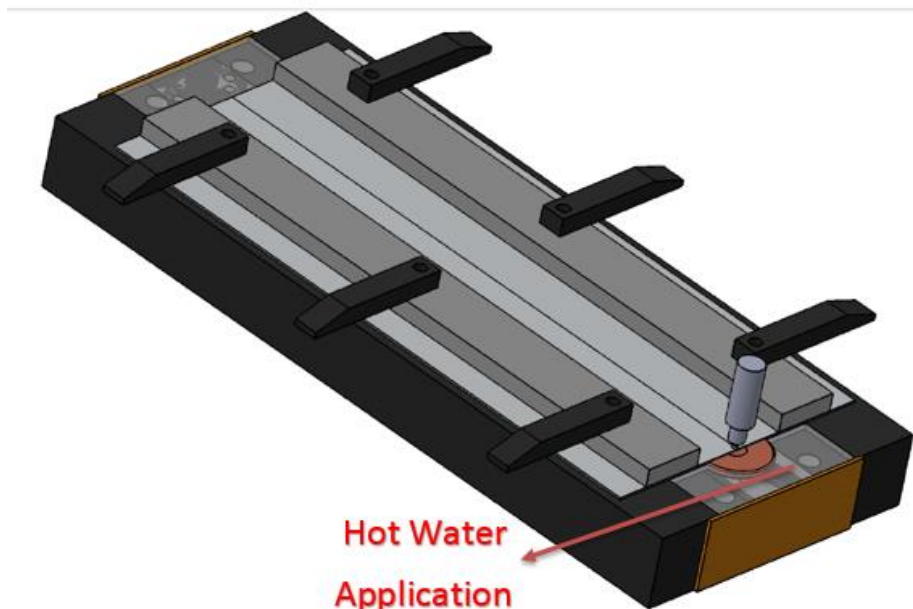


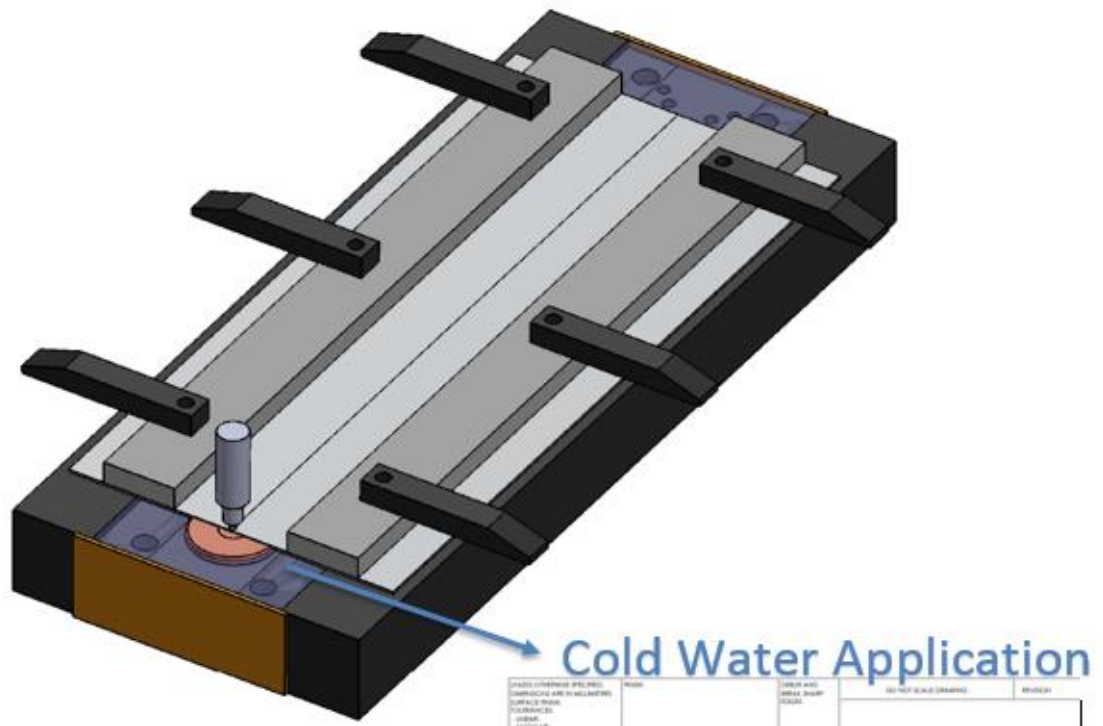
Chart 9.12: A multi history chart showing the difference between the standard tool and the innovative tool with boiling water applied.

9.4. Application of a Hot Liquid and/or Liquid Nitrogen to an Innovative Tool

The following are designs based on the study of lowering heat generation on a friction stir welding work bench, in order to lower the heat generation between 134 °C and 189 °C, the use of boiling water at 100 °C is required where the heat generation is decreased (Plot 9.4) a way to aid in the decreasing heat generation is to use a heat gun, however, another method of increasing the heat generation is liquid nitrogen at – 196 °C. The boiling water is significantly lower than that of the heat emitted from the tool rather than when decrease the temperature hot water is applied to the workbench (Drw 9.1) as the tool welds. However Friction-stir welding under liquid nitrogen (Drw 9.2) significantly suppresses the formation of intermetallic compounds because of the lower peak temperature. Furthermore, the temperature profiles plotted during this investigation indicate that the heat generated by the weld under liquid nitrogen, which is performed at the lowest temperature will increase. [98] Liquid nitrogen is nitrogen in a liquid state at an extremely low temperature. It is produced industrially by fractional distillation of liquid air. At atmospheric pressure, liquid nitrogen boils at –195.79 °C and is a cryogenic fluid that can cause rapid freezing on contact. Liquid nitrogen freezes at –210 °C despite its reputation, liquid nitrogen's efficiency as a coolant is limited by the fact that it boils immediately on contact with a warmer object, enveloping the object in insulating nitrogen gas. This effect, known as the Leidenfrost effect, applies to any liquid in contact with an object significantly hotter than its boiling point, which in turns up the heat generation between 134 °C and 198 °C. (Plot 9.5),When the tool is at the contact shear stress of 1.7 kW the use of liquid at the temperature of -85 °C is used to increase the contact shear stress to 9.9 kW on the weld in general where the temperature is meant decreases (Plot 9.6). To get the correct temperature, it is calculated with (Graph 9.1) where the contact shear stress used to find the temperature that is needed.

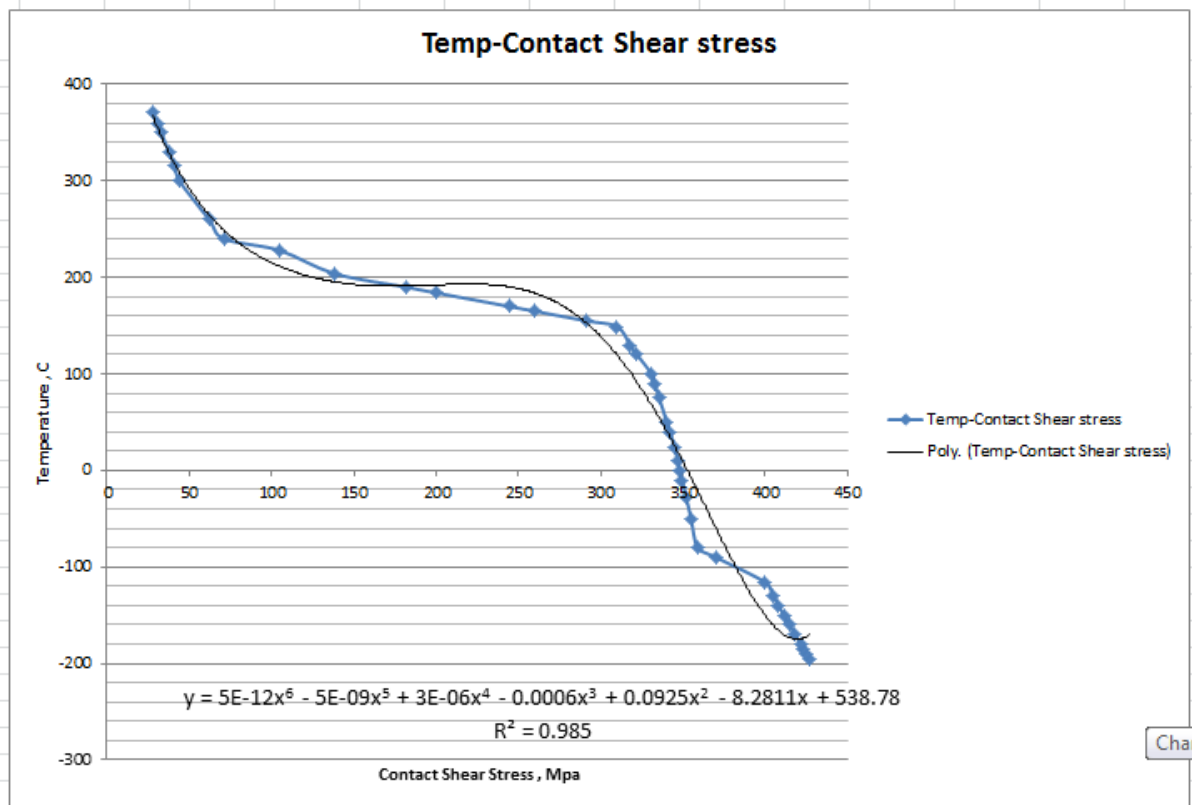
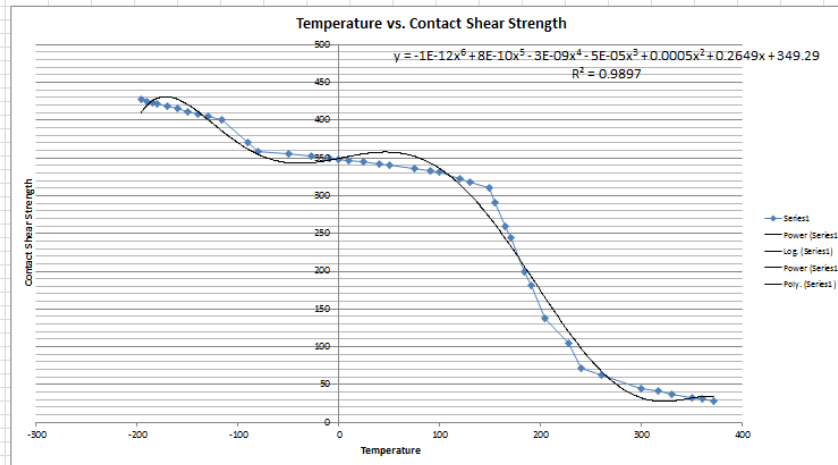


Drw.9.1: 100 °C boiling water is applied to the friction stir weld work bench to reduce heat generated from the weld tool. [Uslu, M.Y, 2017, Application of hot water to workbench, University of the Witwatersrand]



Drw.9.2: Ice Cold water is applied to the friction stir weld work bench to reduce heat generated from the weld tool. [Uslu, M.Y, 2017, Application of cold water to the workbench,University of the Witwatersrand]

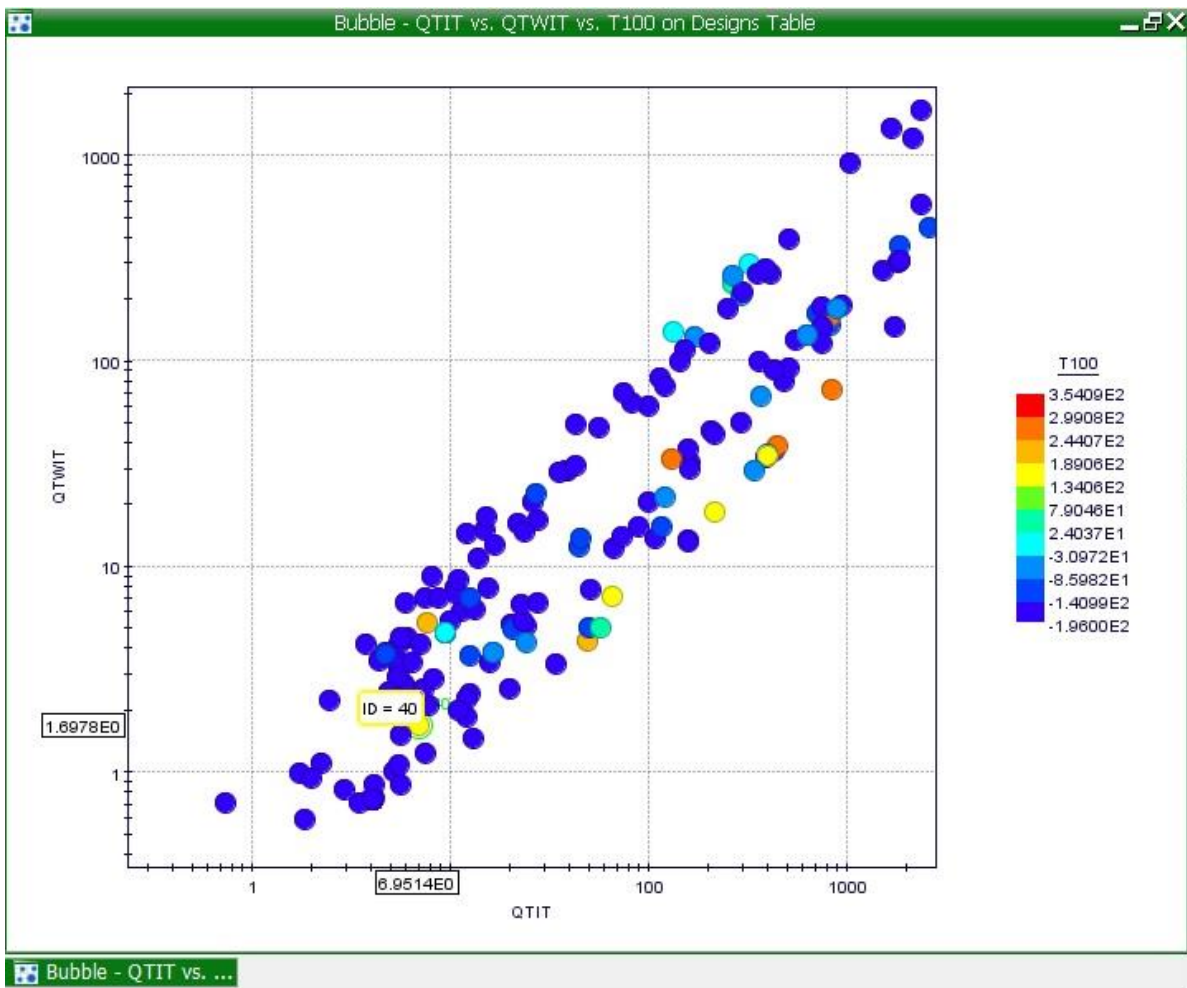
Temperature	Contact Shear strength
C	Mpa
-198	427
-190	424.625
-185	423.0625
-180	421.6
-170	418.225
-160	414.7
-150	411.475
-140	408.1
-130	404.725
-115	400
-90	370
-80	359
-50	354.96
-29	352
-10	349.43
0	348
10	346.75
24	345
40	342.052
50	340.21
75	335.605
90	332.842
100	331
120	322
130	317.86
149	310
155	291.25
165	280
170	244.21
184	200
190	181.4
204	138
225	105
240	71
260	62
300	44
316	41
330	37.7
350	33
360	30.6
371	28



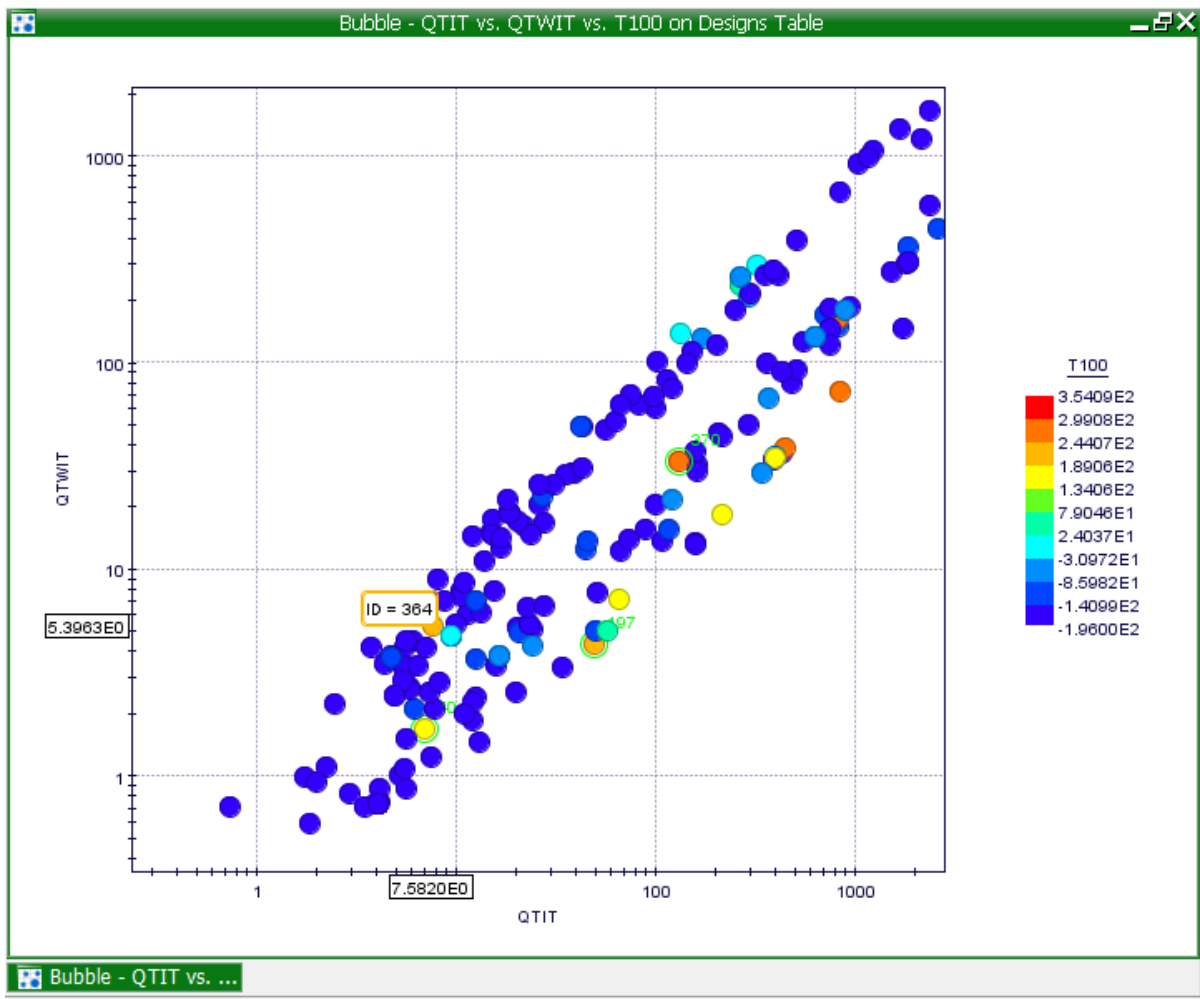
Graph 9.1: The Contact Shear stress Vs the temperature of the weld.

$$y = 5E - 12x^6 - 5E - 09x^5 + 3E - 06x^4 - 0.0006x^3 + 0.0925x^2 - 8.2811x + 538.78$$

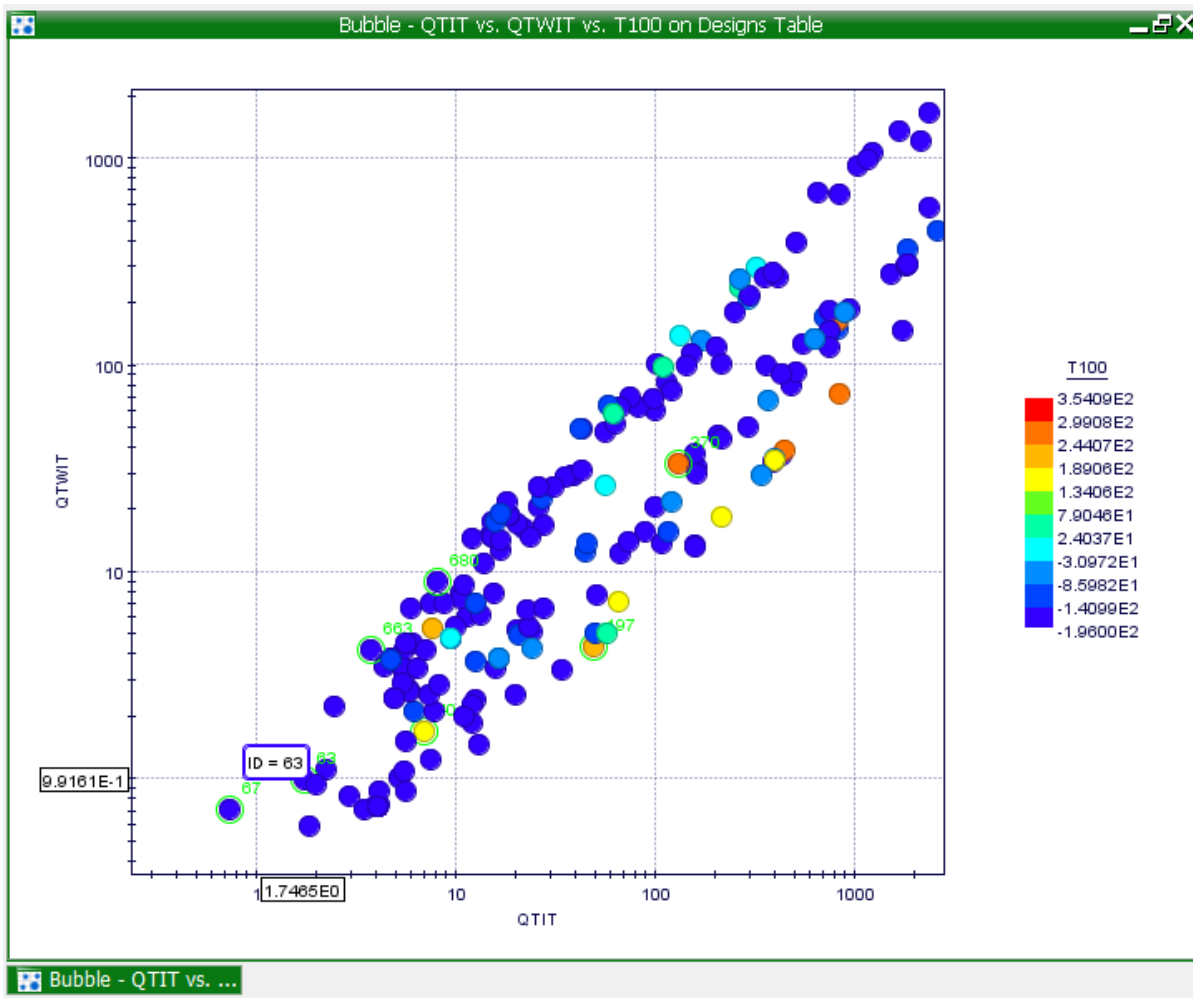
$$R^2 = 0.985$$



Plot 9.4: A bubble Graph showing the heat generation of the innovative tool Vs the heat generation of the innovative tool with boiling water at 100 °C.



Plot 9.5: A bubble Graph showing the innovative tool Vs the innovative tool when a Hot Liquid or Liquid Nitrogen at -196 °C.



Plot 9.6: The heat generation comparison between the innovative tool vs the innovative tool with cold liquid.

10. Chemical Reactions in Welding

During this experiment there is a need to determine chemical reaction on the weld most importantly to see, in the case of this study on how Nitrogen affects the weld as well as the aluminium. Basic chemical reaction during a friction stir welding process is described with effects, including gas–metal reactions and slag–metal reactions. The effect of these chemical reactions on the weld metal composition and mechanical properties is shown in Table 10.1.

10.1. Effect of Nitrogen, Oxygen, and Hydrogen

Nitrogen, oxygen, and hydrogen gases can dissolve in the weld metal during welding. These elements usually come from air, the consumables such as the shielding gas and flux, or the work piece such as the moist or dirt on its surface. Nitrogen, oxygen, and hydrogen can affect the soundness of the resultant weld significantly. Some examples of the effect of these gases are summarized in Table 10.1 [99]. As shown on the table nitrogen has no effect on aluminium.

	Nitrogen	Oxygen	Hydrogen
Steels	Increases strength but reduces toughness	Reduces toughness but improves it if acicular ferrite is promoted	Induces hydrogen cracking
Austenitic or duplex stainless steels	Reduces ferrite and promotes solidification cracking		
Aluminum		Forms oxide films that can be trapped as inclusions	Forms gas porosity and reduces both strength and ductility
Titanium	Increases strength but reduces ductility	Increases strength but reduces ductility	

Table 10.1: Effect of Nitrogen, Oxygen, and Hydrogen on Weld Soundness

10.2. The Increased Size of the Copper Bar

When the outer radius (r_1) of the copper sliding backing bar is increased to the size between 29 mm and 32 mm the heat loss increases due to the enlargement of the back bar by means of the formula: $\dot{Q}_{loss} = kA \frac{\Delta T}{L}$, where \dot{Q}_{loss} the heat loss, heat transfer is included the processes of thermal radiation, convection, and sometimes mass transfer. Usually more than one of these processes occurs in a given situation. The conventional symbol for the material property, thermal conductivity, is k , A the area of the sliding backing bar, ΔT been the delta temperature to observe the temperature change that is exerted from the probe tip and lastly L the thickness of the copper sliding backing bar. The heat loss for the copper sliding backing bar r_1 of 1771.564 W is produced by the radius size of 0.006 mm, 39690.9 W produced at a size of 0.02 mm, 90145.04 W is produced by the size of 0.029 mm, 111498.3 W is created with a radius size of 0.032 mm, and lastly 204092 W is produced at a radius size of 0.0425

mm (Table 10.2) and is plotted on (Graph 10.1). The same methodology is applied to r_2 . However when the size of r_2 increases the heat loss decreases. (Table 10.3) and is plotted on (Graph 10.2). The heat loss of the sliding backing bar decreases when the thickness of the bar (L) increases and the heat loss increases as the thickness of the sliding backing bar decreases. (Table 10.4) and is plotted on Graph 10.3).

$$\dot{Q}_{loss} = kA \frac{\Delta T}{L}$$

$$Q_{loss} = 401 \times \pi ((0.029)^2 - (0.00225)^2) \times (900 - 300) / 0.006$$

$$Q_{loss} = 90145.04 \text{ W}$$

r_1 (m)	r_2 (m)	T_1 (K)	T_2 (K)	L	Q_{loss} (W)
0.006	0.00225	900	300	0.006	1771.564
0.02	0.00225	900	300	0.006	39690.9
0.029	0.00225	900	300	0.006	90145.04
0.032	0.00225	900	300	0.006	111498.3
0.0425	0.00225	900	300	0.006	204092

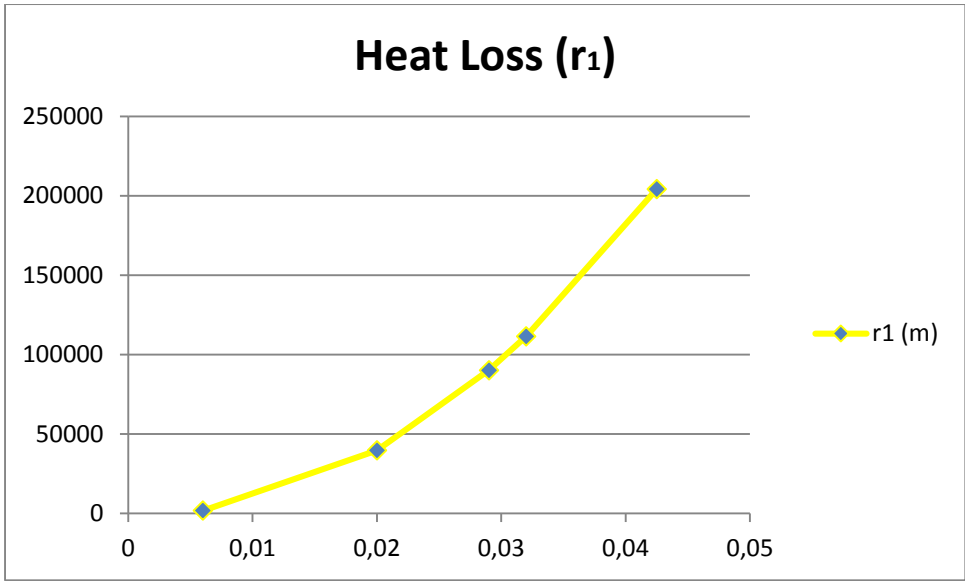
Table 10.2: The heat loss by increasing the outer area of the sliding copper bar

r_1 (m)	r_2 (m)	T_1 (K)	T_2 (K)	L	Q_{loss} (W)
0.029	0.001	900	300	0.006	98766.65
0.029	0.002	900	300	0.006	91837.86
0.029	0.00225	900	300	0.006	90145.04
0.029	0.004	900	300	0.006	78736.17
0.029	0.006	900	300	0.006	66642.29

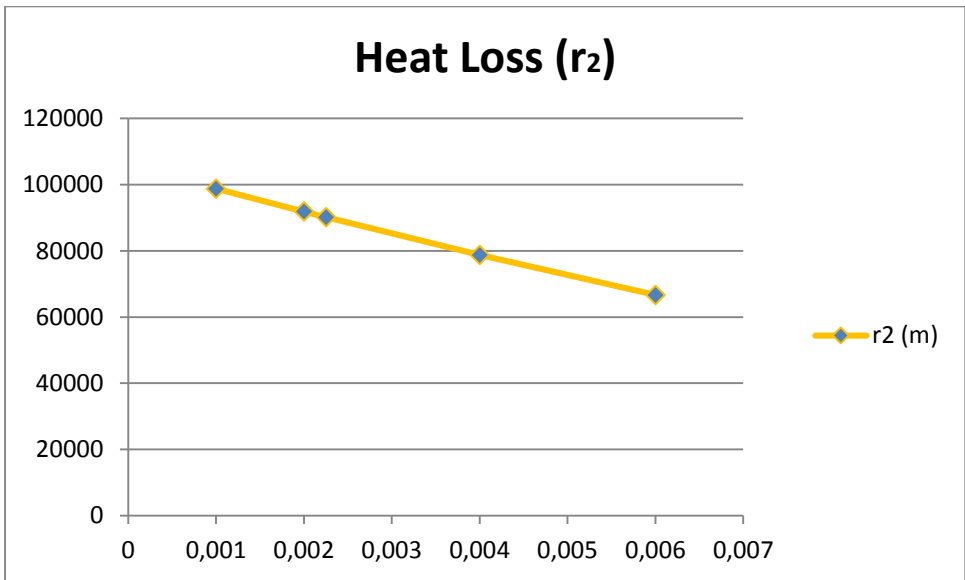
Table 10.3: The heat loss by increasing the radius of the inner area of the sliding backing bar

r_1 (m)	r_2 (m)	T_1 (K)	T_2 (K)	L	Q_{loss} (W)
0.029	0.001	900	300	0.001	592599.9
0.029	0.002	900	300	0.003	183675.7
0.029	0.00225	900	300	0.006	90145.04
0.029	0.004	900	300	0.008	59052.12
0.029	0.006	900	300	0.01	39985.37

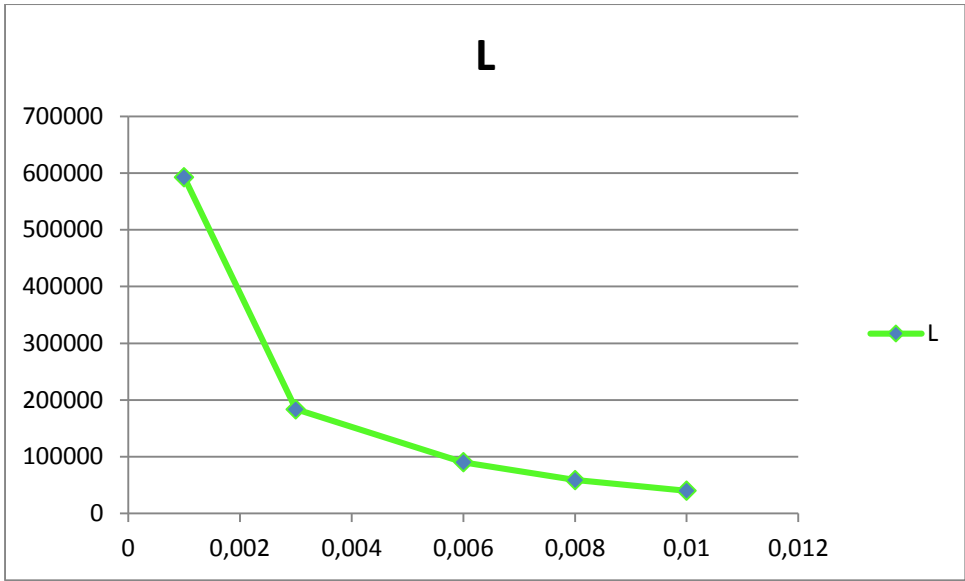
Table 10.4: The heat loss by increasing the thickness of the sliding backing bar



Graph 10.1: The heat loss by increasing the outer area of the sliding copper bar



Graph 10.2: The heat loss by increasing the radius of the inner area of the sliding backing bar



Graph 10.3: The heat loss by increasing the thickness of the sliding backing bar

10.3. Boundaries : The Increased Size of the Copper Bush

The following are Boundaries created on Mode Frontier for the sliding copper bar; these boundaries are chosen due to the geometry of the Friction Stir Welding workbench and the tool and supporting equipment. The input variable property for r_1 has a variable type that varies with range properties been lower bound that is 3.0 and an upper bound that is 32.0 (Image 10.1), The variable property of r_2 has a variable property that varies and range properties that is lower bound 0.0 and upper bound 2.25 (Image 10.2) and lastly is the variable properties of the thickness of the sliding backing bar which has input variable properties that vary hence the range properties vary where the lower bound is 0.0 and the upper bound been 6.0 (Image 10.3). The plots of both the multi history chart (Chart 10.1) and the bubble plot (Plot 10.1) shows that when the area of r_1 is increased the heat loss is more than that of when the area of r_2 is larger [100].

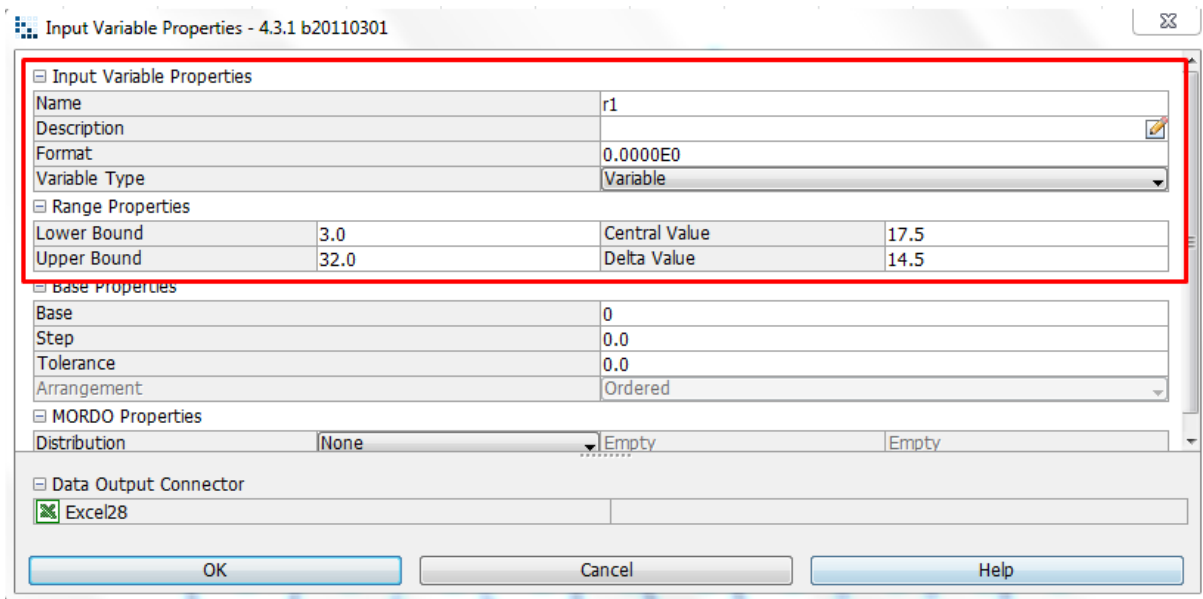


Image 10.1: Input Variable Property of the Outer radius of the sliding backing bar

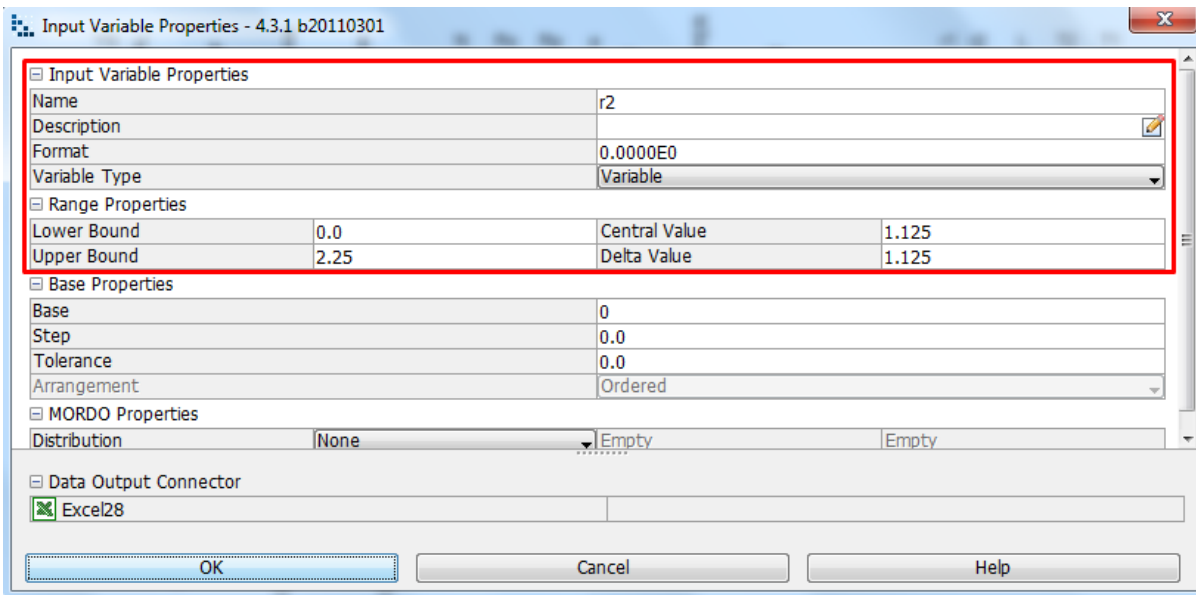


Image 10.2: Input Variable Property of the Inner radius of the sliding backing bar

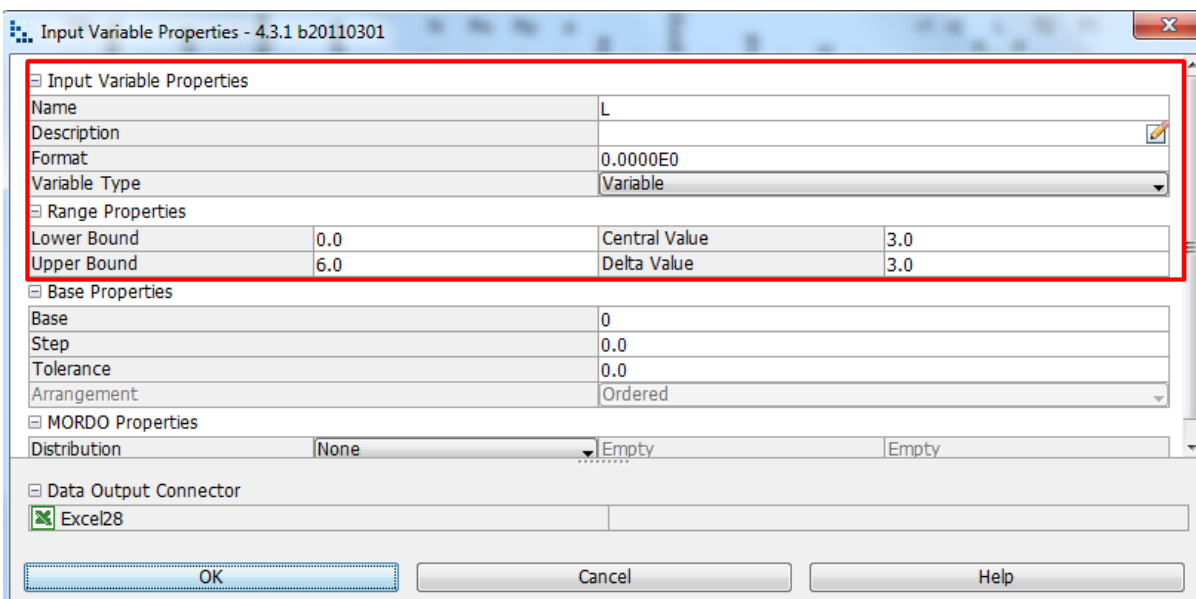


Image 10.3: Input Variable Property of the Thickness of the sliding backing bar

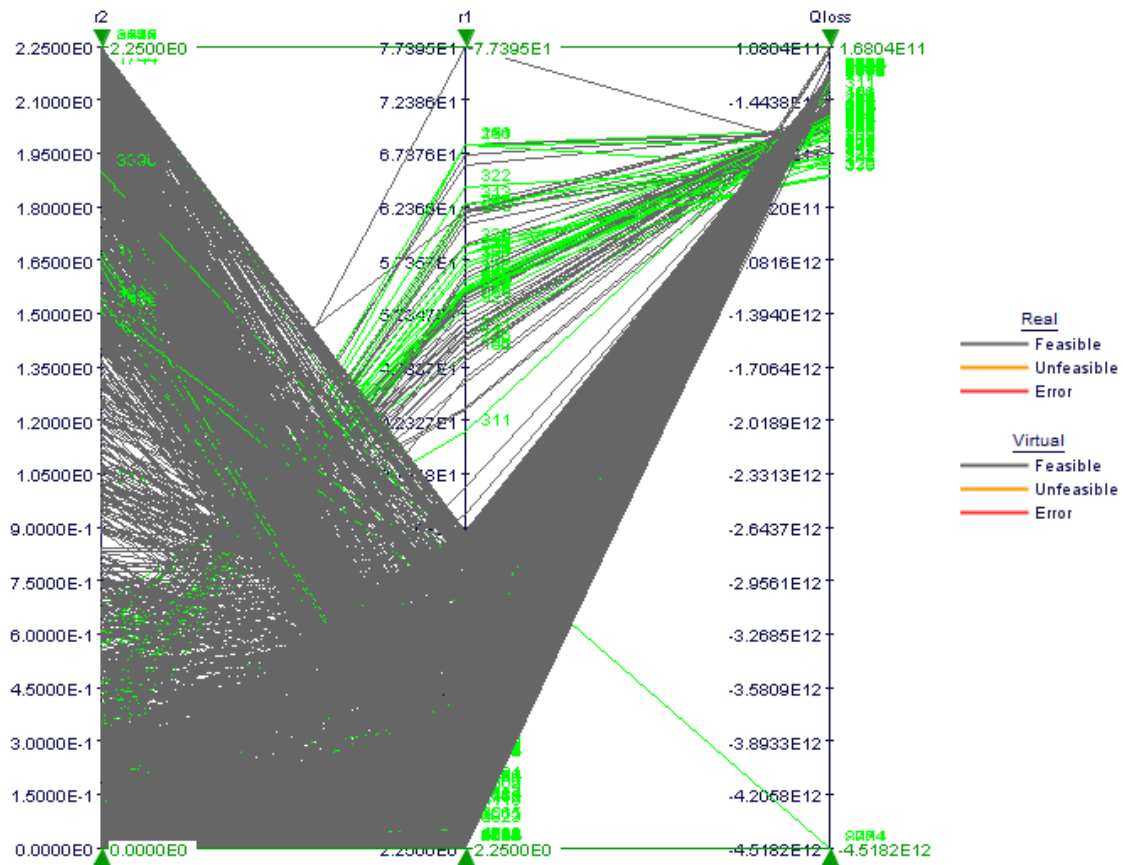
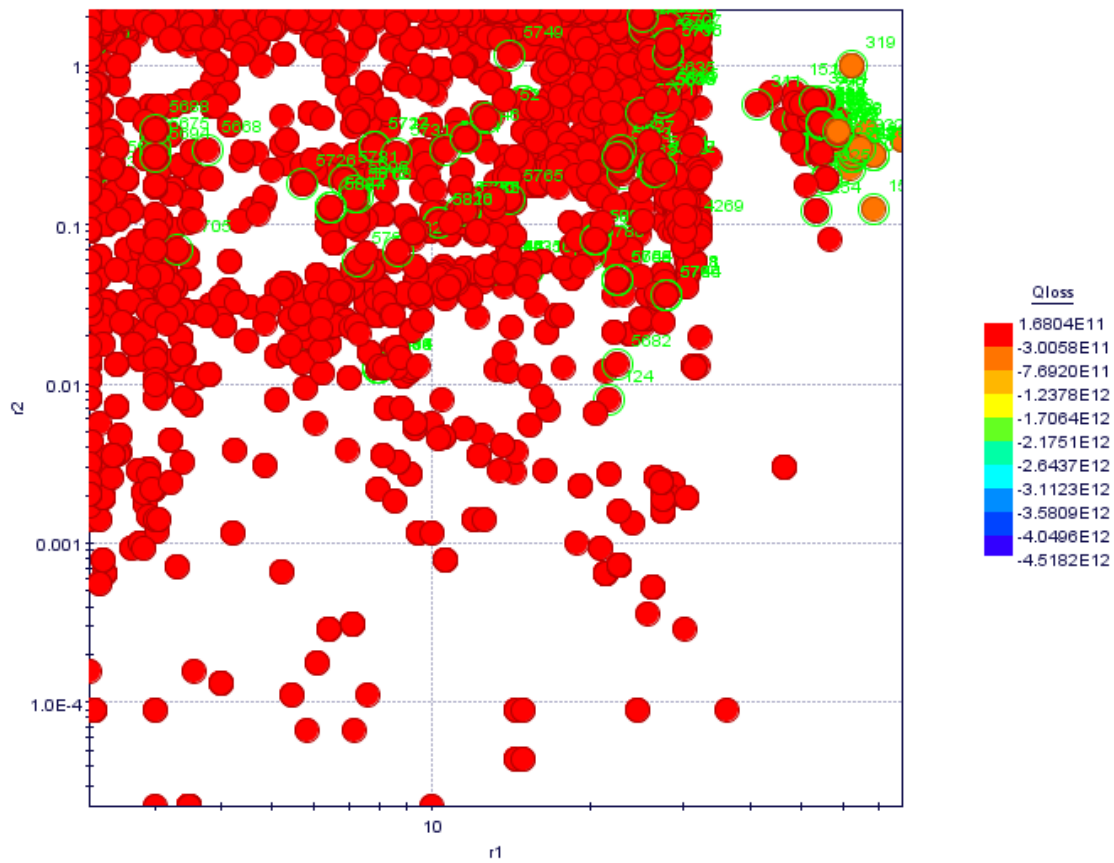


Chart 10.1: A Multi history chart showing r_1 vs r_2 vs Q_{loss}



Plot 10.1: A Bubble plot showing the difference between the heat loss of both r^1 and r^2

11. Preparation and Plans for Experimentation

In preparation for the experiment, as discussed, various parameters and variables have been considered, and the use of the innovative tool proved to be most efficient, after modifying the tool with liquid nitrogen simulation showed that it had a much lower heat generation than both the standard tool and bobbin tool. The choice of the use on liquid nitrogen is based on calculations done versus other external coolants, namely, previously iced/extremely cold water, boiling water and air that had been applied to the tool, with air giving the poorest results. In the physical test, all off the mentioned external coolant will be used for the purposed of verification

For the first run of the experiment the material AA6082-T6 (however final experiment for this thesis will involve Al2024-T3) with a Material thickness of 2 mm. Rotational speeds will be as calculated in the analytical estimation, 800 rpm, 1250 rpm, 1600 rpm and 2000 rpm. Feed rates will be measured accordingly in 300, 400 and 500 mm/min with a dwell time of 15 seconds (Table 11.1) Equipment that is need to perform the experiment are as follows, **Kistler piezoelectric sensors:** Piezoelectric sensors are versatile tools for the measurement of various processes. They are used for quality assurance, process control, and for research and development in many industries, the sensors measure changes in pressure, acceleration, temperature, strain, or force by converting them to an electrical charge. **Thermometer:** To measure temperature, **Thermal cameras:** The use of thermal cameras will indicate any possible fluxes in heat generation or heat loss as the images shot will indicate where the increase or decrease is affected.

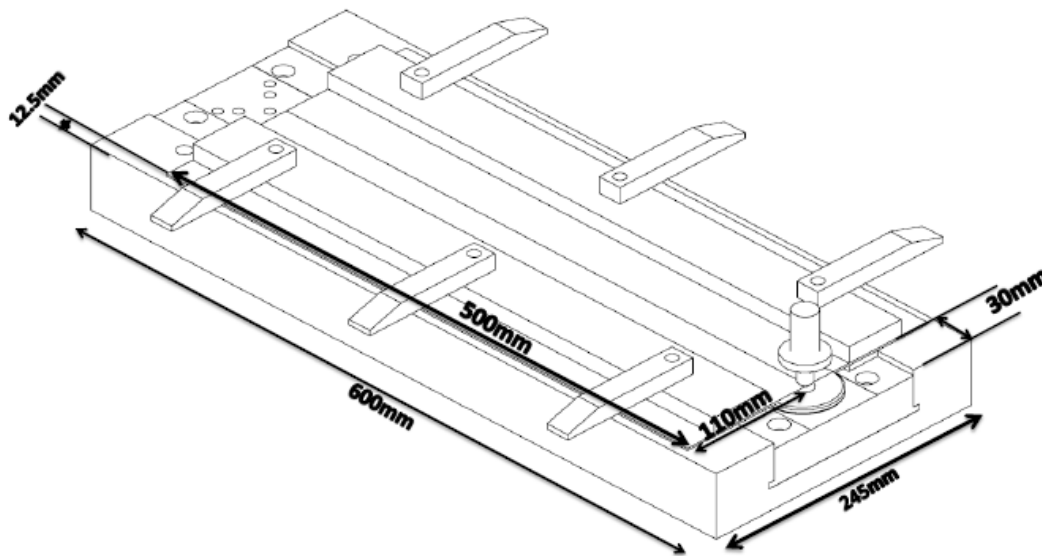
As a safety precaution, Gloves, safety glasses, and coveralls will be used at all times during the experimentation.

TABLE of EXPERIMENTS		
<u>MATERIAL</u>	<u>PLATES (mm)</u>	<u>PLUNGE DEPTH (mm)</u>
Al2024-T3	150 ×500 ×1.6	0,1
		0,2
		0,3
<u>ROTATIONAL SPEED (rpm)</u>	<u>FEED RATE (mm/min)</u>	<u>DWELL TIME (seconds)</u>
800	300	10
1250	400	15
1600	500	
2000		
<u>TEST TYPES</u>		
Standard test		
Hot water applied test		
Iced cold water applied test		
Liquid nitrogen applied test		
<u>TEST EQUIPMENT</u>		
Kistler Piezoelectric Sensors		
Thermometer		
Thermal Camera		
Gloves		
Safety Glasses		

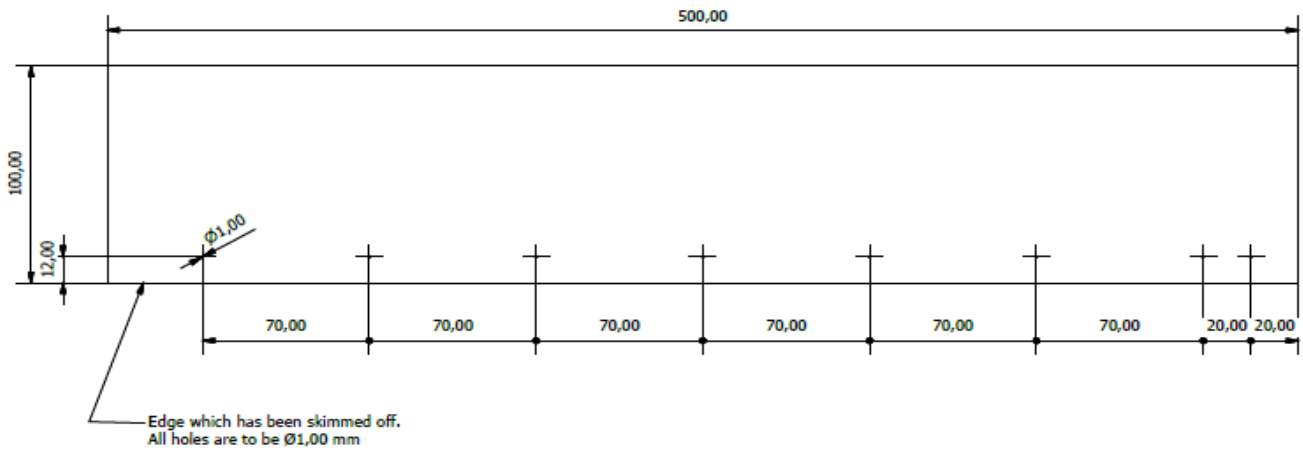
Table 11.1: Table of experiments

11.1 Design

Design of workbenches (Image 11.1), backing plates, copper bushes, welding and gage plates, designs show what the actual model will resemble along with the required measurements (Image 11.2) and copper sliding backing plates where designed and drawn on SolidWorks. The use of this 3D design programme as enabled accurate features of the workpieces that need to be used during experimentation. Drawing have exact measurement to a scale model.



Drw 11.1: workbench design on SolidWorks [Uslu, M.Y, 2016, *Workbench Design*, University of the Witwatersrand]



Drw 11.2: Friction Stir Welding Plates with thermal couple holes [Leering, M, 2016, *FSW plates with couple holes*, University of the Witwatersrand]

Models were also designed indicating heat loss for the 3 mentioned types of friction stir welds as well as on the modification of tool

11.2 Conclusion

11.2.1. Analytical Conclusion

The analytical estimation of this study starts with the standard tool and the parameters are calculated to determine the heat generation from the tool shoulder the tool pin and the tool probe side surface. Heat generation is calculated with the parameters for tool shoulder radius, tool probe radius, tool probe height, tool shoulder cone angle, friction coefficient, static conditioning, friction coefficient for sliding condition and tool angular rotational speed. Friction shear stress, contact shear stress and yield stress is determined by the material that is in use, in this study the material Al2024-T3 is used. Once calculations were complete it was noticed that the standard tool had high heat generation from the tool shoulder.

Attention was brought to the bobbin tool, which is not as simple as the standard tool, as the standard tool formulation was applied analytically by calculating the parameters for Tool shoulder radius, tool probe radius, tool probe height, tool shoulder cone angle, friction coefficient, for static condition and friction coefficient for sliding condition. Unlike the standard tool were the calculation is for one shoulder and pin, the parameters had to apply for two shoulders, a probe side surface and two pins for the bobbin tool. The heat generation was proven too high as the bobbin tool had two shoulders emitting heat generation and could potential prove problematic for the study, hence the analytical estimation of the innovative tool.

The innovative tool has the tool design of the standard tool but has other modifications to assist with the weld, in this instance a modified copper bush has been used to reduce heat generation, the copper bush is to be placed under the work piece whilst the weld is in process, copper is a cheap affordable material with all of the analytical and mechanical properties for a weld. In order to ensure that there is no problem with the innovative tool calculations of the tool shoulder radius, tool probe height, tool shoulder cone angle, friction coefficient for static condition, friction coefficient for sliding condition. Yield stress, contact shear stress as mentioned is determined by the material Al2024-T3, this also applies for the coper yield stress and contact shear stress.

The parameter calculation showed that the innovative tool had heat generation that was in between that of the standard tool and the bobbin tool.

11.2.2. Analytical Heat Loss

Heat loss on the standard tool appears during a weld when there is no backing plate, the lower surface of the work piece is assumed to be adiabatic, perfect contact is made between work piece and backing plate, perfect contact is made under the tool region only. This option is suggested by experimental observations: the high pressures under the tool lead to a visible indentation of the upper surface of the blanking plate along a width approximately equal to the diameter of the tool shoulder and lastly an introduction of a value for the convection coefficient between the work piece and the backing plate. Calculations of certain parameters were used to verify this understanding by calculating the heat transfer coefficient on the upper side (*h_{up}*), heat transfer coefficient on the down side (*h_{down}*), the reference temperature (*T₀*), melting temperature (*T*), the Stefan-Boltzmann constant (σ), the cross-sectional area (*x*), cross sectional area of 4 mm (*y*), thermal conductivity (*K*), length (*L*), surface emissivity (epsilon) and cross sectional areas of 115 mm and 500 mm (*a* and *b*), showing significant heat loss

Heat loss conditions around the bobbin tool is immensely high due to the second shoulder, there is much air flow not only from the work bench but around the tool as well. The parameters that are used to calculate the heat loss for the standard tool is the same for the bobbin tool. As with heat generation the heat loss from the innovative tool is not exceedingly high or low, however the tool loses heat on the tool, the work bench and

the copper bush, along with mentioned parameters an addition is made with parameters for the heat loss in the copper bush, thermal conductivity in a copper bush (K_{copper})

11.2.3. Simulation Conclusion

The simulation programme that was used for this study is ModeFrontier. The programme allowed the weld to run and to see if it would be feasible or not, as well as enabling the comparison of the three mentioned tools both individually and against each other. ModeFrontier simulation runs the weld by attaching a Microsoft Excel workbook that contains your input and output data along with boundary variables definitions once this is complete parameters are inserted into nodes and this becomes the input data. Parameters that input data are contact shear stress (CS), yield stress (YS), height of probe (H_{probe}), tool shoulder cone angle (α), shoulder radius (R_s), probe radius (R_p) and rotational speed (N). These variable nodes represent both the standard tool and bobbin tool; the innovative tool however has two extra copper yield stress ($Y_{Scopper}$) and copper contact shear stress (CS_{copper}). Output data nodes consist of the heat generation heat generation that is emitted out during a weld that is planned on the design of experiments (DOE). Once this complete and all node and workbooks are in place the simulation is ready to run. On the standard tool simulation, it was shown on the multi-history chart that the tool shoulder heat generation is higher than other parameters. This also applies to the bobbin tool because of its significant second shoulder. The innovative tool performed at an average, where it was not as low as the standard tool but also not high on heat generation as the bobbin tool.

11.2.4. Simulated Heat Loss

The simulation process of heat loss from the standard tool applies the same way as the heat generation but attaching an Excel workbook and interesting nodes of the require input and output variables. Variables for the standard tool need heat transfer coefficient on the upper side (h_{up}), heat transfer coefficient on the down side (h_{down}), the reference temperature (T_0), melting temperature (T), the Stefan-Boltzmann constant (σ), the cross-sectional area (x), cross sectional area of 4 mm (y), thermal conductivity (K), length (L), surface emissivity (epsilon) and cross sectional areas of 115 mm and 500 mm (a and b). the same variables apply for the bobbin tool

With mentioned variables nodes for other heat loss simulations, the node K_{copper} (thermal conductivity for the copper bush) is added to the input nodes for the simulation on the heat loss for the innovative tool.

12. Experimentation Aspect of Friction Stir Welding

12.1 Machinery

The CNC Milling Machine:

The CNC machine that is used for the friction stir weld (Image12.1) was a modified MAHO MH-C 700 CNC milling machine. The MAHO milling machine is a displacement controlled, three axes, electric-drive CNC milling machine. Each axis of the machine is controlled by its own electric servo motor which allows for the accurate displacement control of the positioning of its milling head to an accuracy of 0.01 mm. In order to perform FSW on the milling machine, the design of a FSW tool and corresponding backing plate system is required. Before the used of the machine, the tool required for the weld is required to be tightened and ensure that every aspect of the tool is to be cleaned. An unclean tool can foresee problems during a weld. Once this is done, the correct alignment of the tool is needed.



Image 12.1: MAHO CNC Milling Machine used to Perform FSW

The start of the alignment, a finger gauge (12.3) is used to find the setting for the tools plunge, as the parameters are inputted into the CNC machine via its control panel (Image 12.2). Positioning is used to regulate the plunge depth of the tool, the tool plunge is the most important part of the process as it is in this stage the tool is most susceptible to damage from unheated, pre-welded material. The depth of this tool movement is critical in maintaining a quality weld. Insufficient depth can result in poor bonding in the weld root; too much depth may break the tool [101]. An off set (Image:12.4) is used to set the axis where the tool meets the material before welding; once this set the tool (Image:12.5) is placed and a feeler gauge has the measurement of 0.1 mm between the tool and the material (Image:12.6). Positioning is strictly linked to both the configuration of the desired weld and the application for the finished material. The material must be held together with a very small tolerance for gaps and constrained so there is no possible movement in the x, y or z axis. Once this set up is complete, welding can commence.



Image 12.2: MAHO CNC Milling Machine Control Panel



Image 12.3: Finger Gauge Used to set Alignment and Direction of the Tool (Innovative Tool)

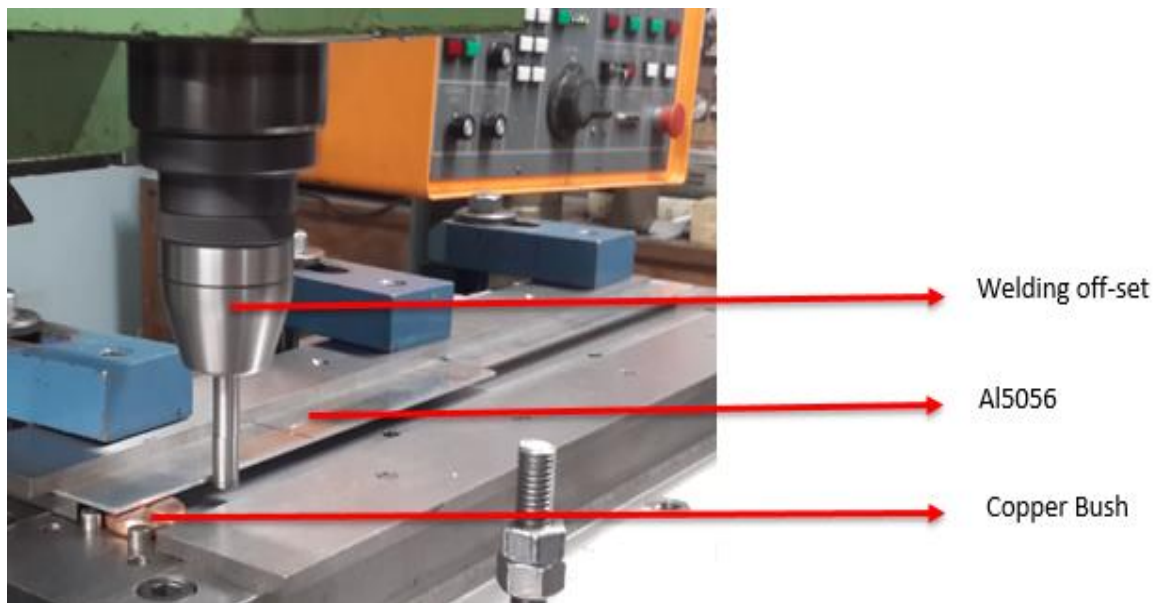


Image 12.4: Tool Off-Set used to Set the Straightness of the Tool.



Image 12.5: The Friction Stir Welding Innovative Tool with Pin

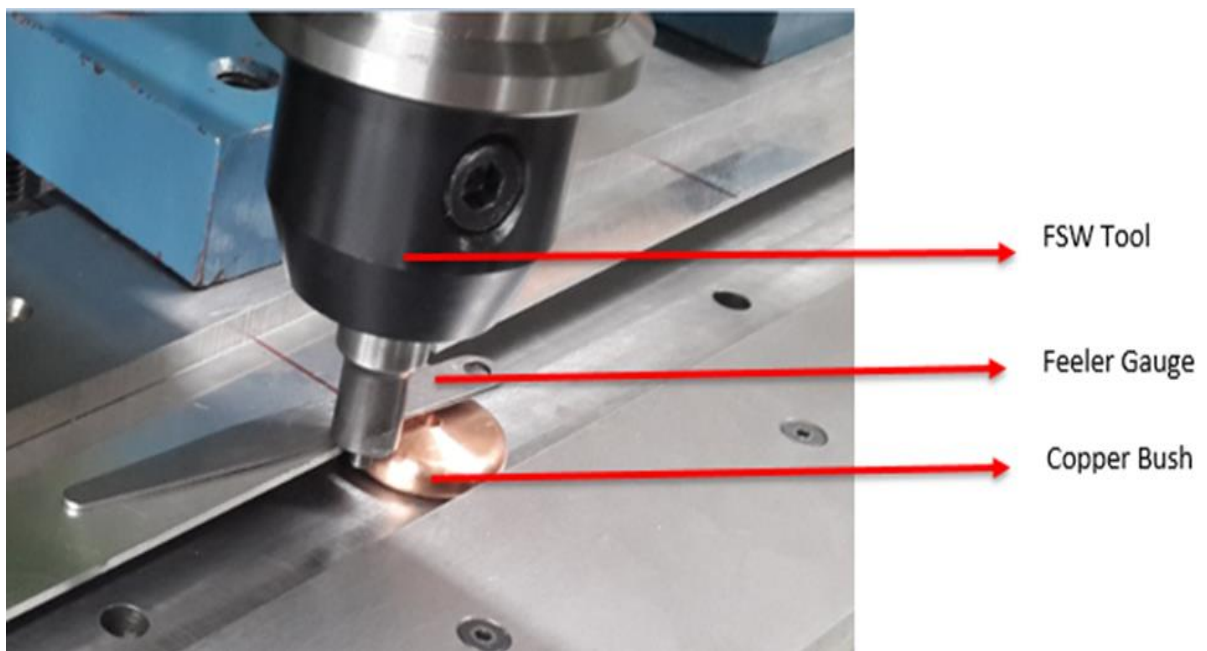


Image 12.6: Feeler gauge used to set space between the Tool and the Work Piece Material

The Kistler Piezoelectric Sensors

A piezoelectric sensor (Image 12.7) is a device that uses the piezoelectric effect, to measure changes in pressure, acceleration, temperature, strain, or force by converting them to an electrical charge in the case of the friction stir weld, it is used to measure force. Process forces are measured during the friction stir weld experiment using the Kistler Multicomponent Force Link Set type 9366CC0,5. The sensor comprised of four quartz crystal piezoelectric sensors connected to a summing box, which is connected to an amplifier (Image 12.8) which passes the signal to a DAQ to allow the data to be acquired using a computer.

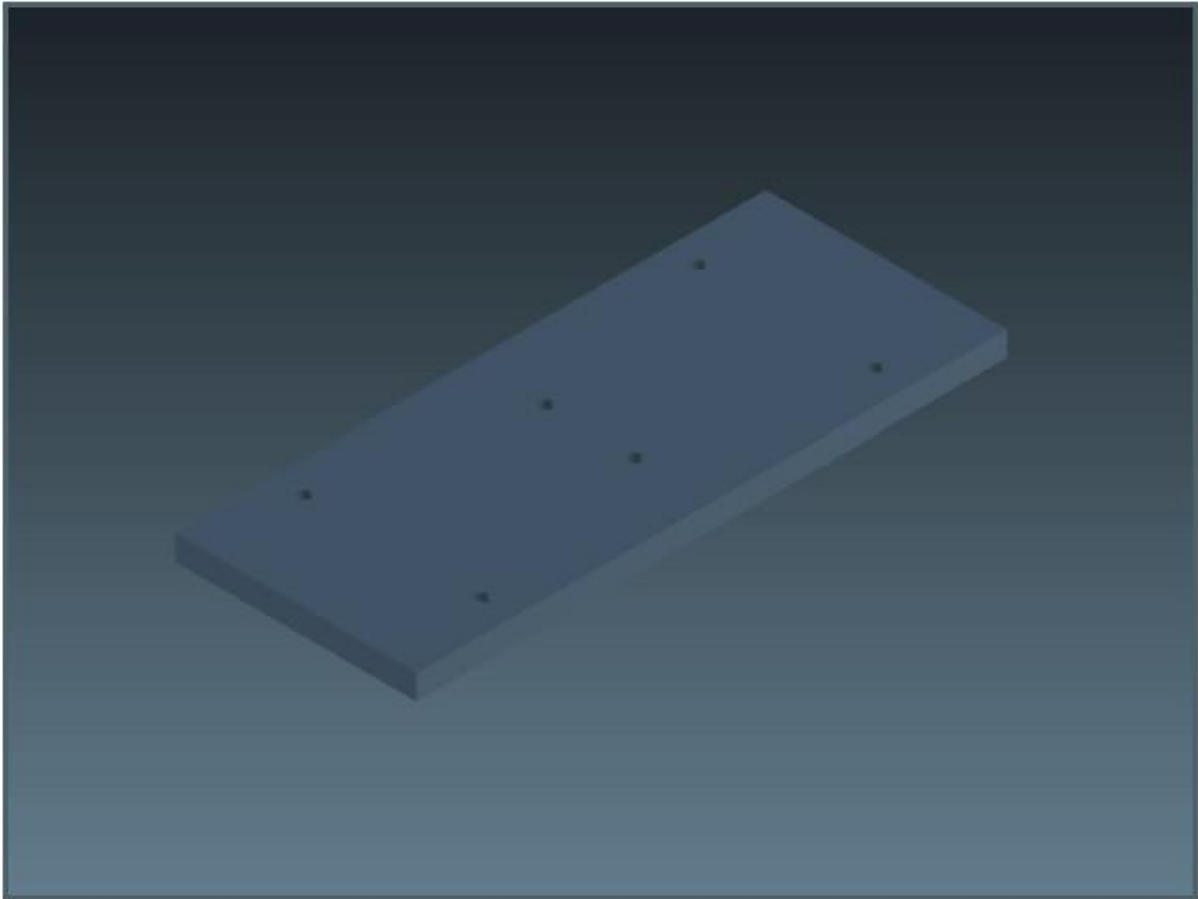
The sensors are placed beneath the backing plate (Drw 12.1) of the friction stir welding work bench (Image 12.9), which during each weld the respective sensors measure the force exerted onto the material plates from the weld that is taking place. The measuring range of the sensors is from -25kN to +25kN for F_x and F_y and -25kN to +60kN for F_z , with a sensitivity or percentage error around 2%.



Image 12.7: Kistler Multicomponent Force Link Set used to measure forces



Image 12.8: The Kistler multichannel charge amplifier



Drw 12.1 Render of Standard Backing Plate to Operate with the FSW Tool [Correia, D,(2015), *Render of Standard Backing Plate, University of the Witwatersrand*]



Image 12.9: Placement of the sensors beneath the backing plate

The FLIR T640 Thermal Camera

The FLIR T640 Thermal camera (Image: 12.10) requires line of site vision of the target area for temperature measurement and has a thermal sensitivity of $< 35 \text{ mK}$ at 30°C . The T640 is able to operate in three independent temperature ranges: 40°C to $+150^\circ\text{C}$, $+100^\circ\text{C}$ to $+650^\circ\text{C}$ and $+300^\circ\text{C}$ to $+2000^\circ\text{C}$. The camera has emissivity correction from 0.01 to 1 to allow for the accurate thermal imaging of different materials. The thermal camera is used to record all thermal activity that takes place during the weld. The camera is positioned in angle in which it will record the thermal activity (Image 12.11), in this case the purpose is to find the thermal reading of the Aluminium plates 6056 and 6082. The thermal data recordings (Image 12.12) are done on the camera are collected on a computer using the software "FLIR Tools". Using this software not only can the procurement of the thermal data for the welded plates can be found but also the thermal data for associated areas such as the tool and the tool pin can be obtained.



Image 12.10: FLIR T640 infrared thermal imaging camera used to measure temperature



Image 12.11: FLIR thermal camera setup for the during the experiment

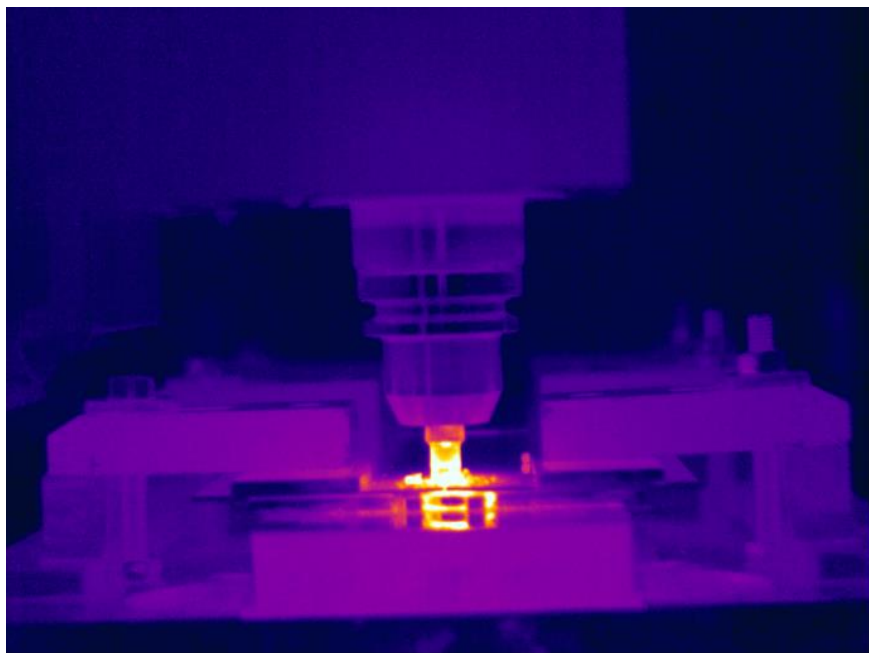


Image 12.12: Infrared thermal capture of weld process using the FLIR T640 thermal camera software “FLIR Tools”

Coolant Applied Test- The Fluke 51 II Thermometer

The use of water was used during the experiment as a coolant in two forms, boiling hot water at a temperature of 97 °C which was boiled in an electric kettle and ice cold water at 0.8 °C where ice cubes was added to regular tap water. A digital thermometer- The Fluke 51 II, was used to ensure the correct temperature reading (Image 12.13). A refrainment from using liquid nitrogen as a coolant was put in place due to safety precautions to both equipment and personnel during the experiment. The ice cold water is used to reduce the heat generation due to its extremely cold temperature when applied and poured onto the workbench. Similarly, with the same application the hot water is meant to reduce the yield strength of the material 6056 and 6082 thereby reducing the heat generation of the weld.



Image 12.13: Water being cooled down to the temperature 0.8 degrees

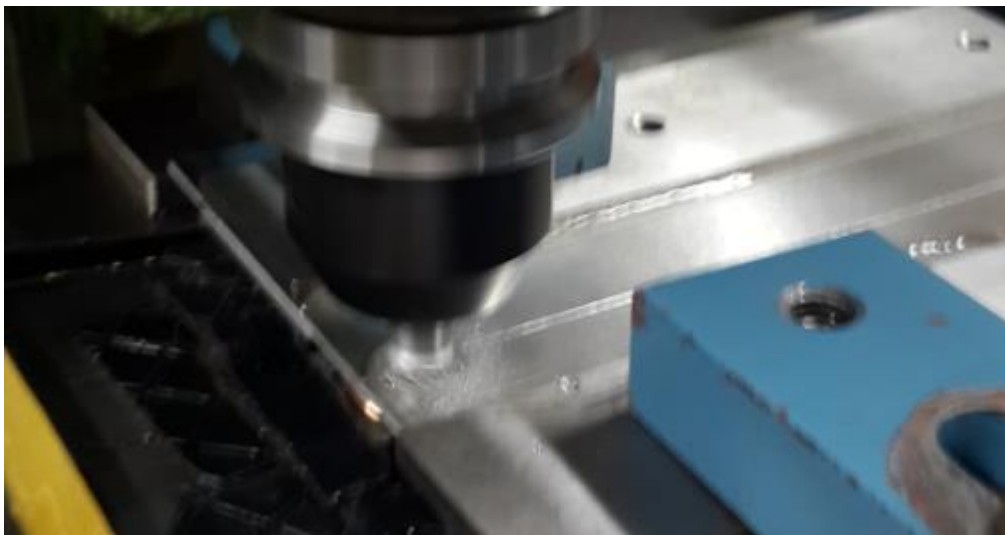


Image 12.14: A coolant applied weld – Ice cold water at 0.8 °C

12.2. Friction Stir Welding: Experiment

12.2.1. Performed Weld Results: Standard Tool Experimentation

The standard weld was the most positive weld during the process of the experiment, with the welds being successful with no to very minor degeneration of the material, the following parameters (Table 12.1) were used and were consistent for all 3 welds: The rotational speed at 800 rpm, Feed rate of 300 mm/min, a dwell time of 10 seconds and lastly a plunge depth of 0.3 mm. Welds for the standard tool were performed three times for each of the following conditions: Normal, ice cold water applied and boiling hot water applied. The ice-cold water applied test showed the lowest heat generation, temperature of water applied and poured to the weld was at 0.8 °C. This process was done by applying ice cubes to water, a thermometer was inserted into the jug to ensure the correct temperature was received. It was noticeable that the heat generation lowered as the water was poured onto the work piece during the weld (Graph 12.1) and would increase slightly during and interval before the next application of iced water was poured.

Standard Tool Parameters

Trial Number	Rotational Speed (rpm)	Feed Rate (mm/min)	Dwell Time (seconds)	Plunge Depth (mm)	Material	Coolant
1	800	300	10	0,2	Al6082	None
2	800	300	10	0,2	Al6082	Ice Water
3	800	300	10	0,2	Al6082	Hot Water

Table 12.1: Parameters for the Standard Tool Weld

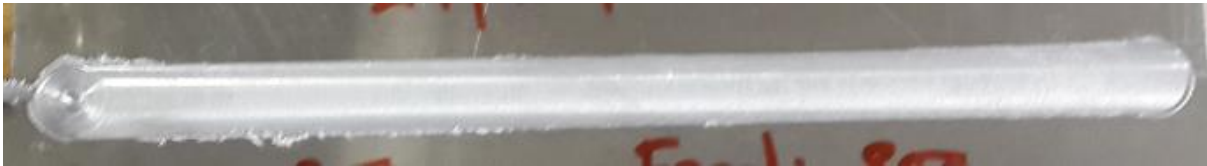
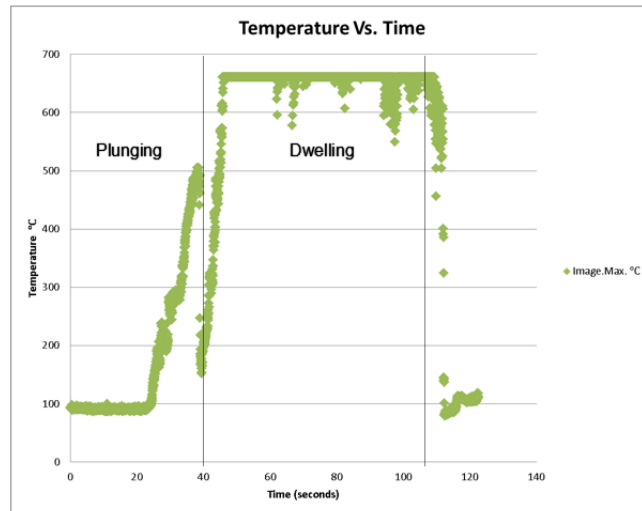


Image 12.15: The Weld for the Standard Tool Ice Water Applied Test

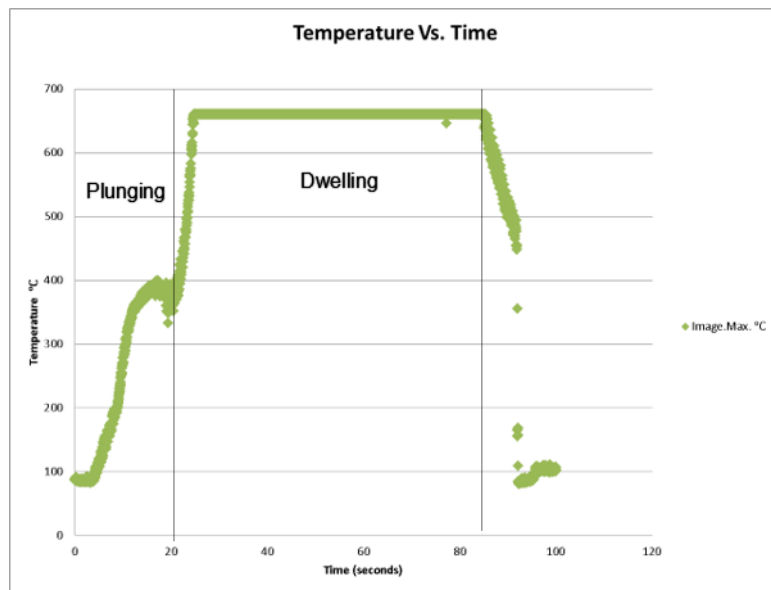


Graph 12.1: Temperature Vs Time for the Standard Tool Ice Water Applied Test

The weld that took place in normal conditions was as successful as the cold water applied test but had a higher heat generation (Graph 12.2), however as mentioned the weld was successful and neat weld with minor skirting of the material (Image2.16).

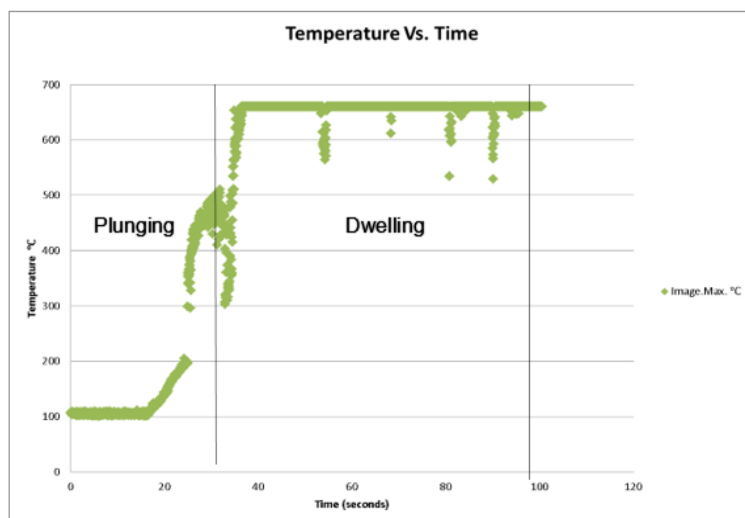


Image12.16: The Weld for the Standard Tool in Normal Conditions



Graph 12.2: Temperature vs Time for Standard Tool Normal Conditions.

Though successful, the weld with the highest heat generation (Graph 12.3) is the hot water applied test, (Image12.17) this could be for the very same reason that the innovative tool was not successful, the plates over heated and the yield stress did not reduce as expected.



Graph 12.3: Temperature vs Time for the Standard Tool Hot Water Applied



(a)



(b)

Image 12.17: Hot water applied test showing very minor degeneration on the work piece (a) otherwise a successful weld (b).

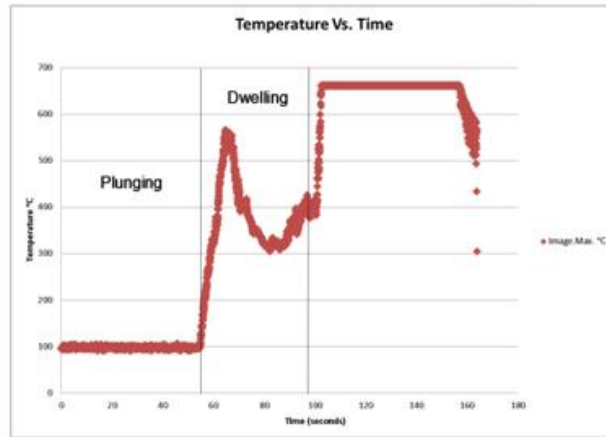
12.2.2. Performed Weld Results: Innovative Tool

During the start of the experiment the welds seemed to fail drastically. At the start of Run 1, the material that was used Al6056, with a plate size of 250 mm x 100mm seemed to break through and started severe flashing of the material and major surface defects (Image 12.18 – (a) and (b)) and it seemed significant with welds Run 5 (Image 12.19) till Run 8. This could be possible due to overheating (Image 12.18- (c)) of plates of both material Al6056 and Al6082. In all five of these welds the copper bush stuck to the work piece material. Parameters used for the respective welds changed in an attempt to find parameters suitable for each weld (Table 12.2), with Run 1 having a rotational speed of 1600 rpm, feed rate of 400mm/min a dwell time of 15 seconds and a Plunge depth of 0.2 mm, these parameters were chosen in a previous chapter as seen in the table of experiments (Table 11.1), during Run 5 the material still continued to flash, where the material spiralled outwards during the weld, deeming it unsuccessful with a rotational speed of 800 rpm, feed rate of 250 mm/min, a dwell time of 15 seconds and a plunge depth of 0.1 mm respectively. Run 2 (Image 12.20) showed promising results, however was unsuccessful due to the plates separating at the start of the weld and was not a neat weld. The rotational speed of the weld was brought down from 1600 rpm to 800 rpm, the feed rate from 400 mm to 300 mm and the dwell time from 15 seconds to 10 seconds (Table: 12.2) from Run 1. The copper bush however still remained attached after the weld. A significant drop in temperature 80 seconds into the weld could possibly show where the weld joined with little surface inconsistencies but a near good weld.



(a)

(b)



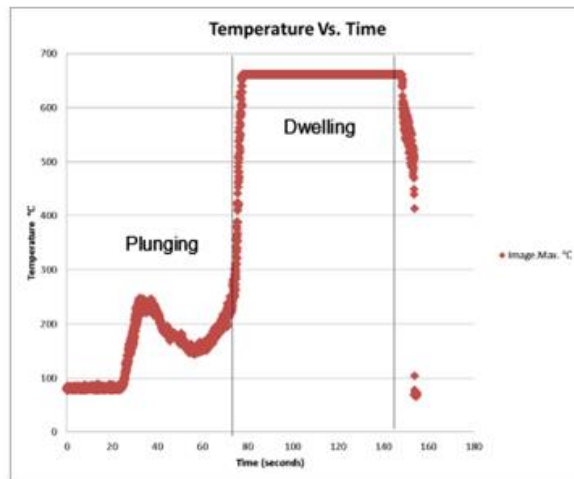
(c)

Image 12.18: Subfigures depicting Run 1 performed at a rotational speed of 1600 rpm with a feed rate of 400 mm/min. Pictures (a) is the top side surface of the weld plate Al6056 (b) is the bottom surface of the weld plate and (c) a graph representing the temperature vs time for Run 1.



(a)

(b)



(c)

Image 12.19: Subfigures showing Run 5 where the material 6082 had been used for the weld at the rotational speed of 800 rpm and a plunge depth of 1mm/min. pictures (a) is the top surface of the weld, (b) showing the bottom side surface where the copper bush remained attached and (c) the temperature vs time graph.

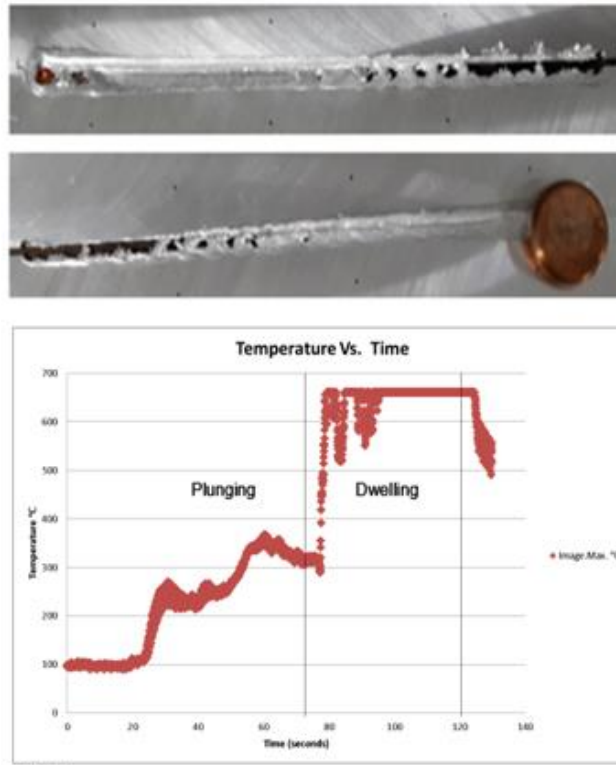


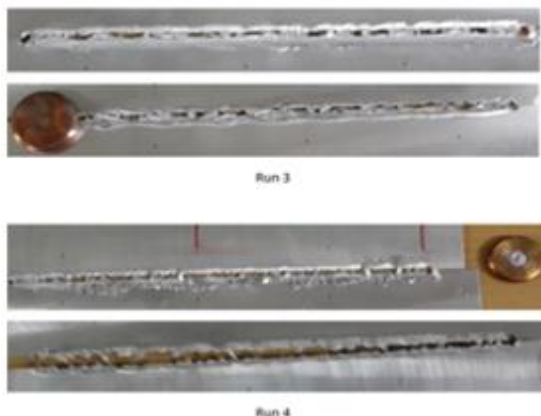
Image 12.20: Run 2 showing promising results with a rotational speed of 800 rpm and a feed rate of 400 mm/min

Trial Number	Rotational Speed (rpm)	Feed Rate (mm/min)	Dwell Time (seconds)	Plunge Depth (mm)	Material	Coolant
1	1600	400	15	0,2	Al6056	None
2	800	300	10	0,2	Al6056	None
3	800	250	10	0,2	Al6056	None
4	800	250	10	0,3	Al6056	None
5	800	250	10	1	Al6082	None
6	800	250	10	0,5	Al6082	None
7	800	250	10	0,3	Al6082	None
8	800	50	10	0,3	Al6082	None
9	800	100	10	0,3	Al6082	None
10	630	50	10	0,3	Al6082	None
11	630	50	10	0,2	Al6082	None
12	630	50	10	0,5	Al6082	None
13	630	300	10	0,3	Al6082	None
14	630	300	10	0,1	Al6082	None
15	630	100	10	0,2	Al6082	None
16	800	300	10	0,2	Al6082	Ice Water
17	800	300	10	0,2	Al6082	Ice Water
18	800	50	10	0,2	Al6082	Ice Water
19	630	50	10	0,2	Al6082	Ice Water
20	500	50	10	0,2	Al6082	Ice Water
21	800	50	10	0,2	Al6082	Hot Water

Table 12.2: Parameters used during the Innovative Tool runs.

Run 3 and Run 4 showed negative results (Image 12.21 (a)), where Run 3 showed gaps in between the weld zone and the plates separated seemed to be pushed up by the copper bush, the plates constantly separating could be due to poor clamping or heat generation

Run 4's material was poorly joined as thinning of the material took place but the copper bush did not remain attached (Image 12.21 (b)) as in previous welds, once the weld was complete and the material was removed, it showed that the material was poorly joined, this could of happened due to the copper bush sticking on to the material causing an inconsistent weld. This could be due to setting the inconsistent parameters, where the rotational speed was 800 rpm which remained the same from Run 3 the plunge depth was increased from the third weld 0.2 mm to 0.3 mm, whilst the dwell time and feed rate remained the same of 10 seconds and 250 mm/min.



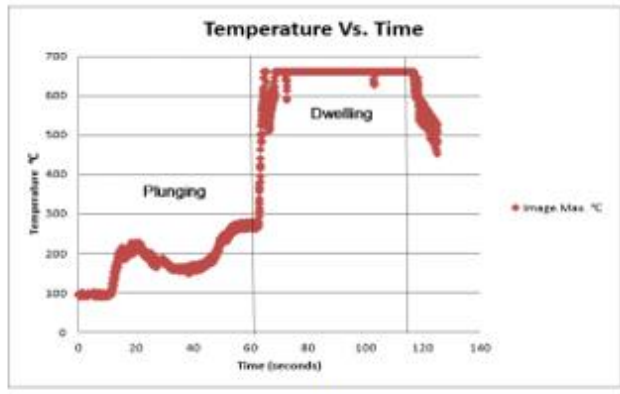
Run 3

Run 4

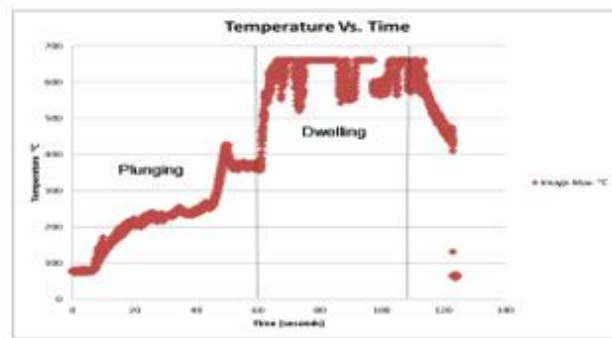
(a)



(b)



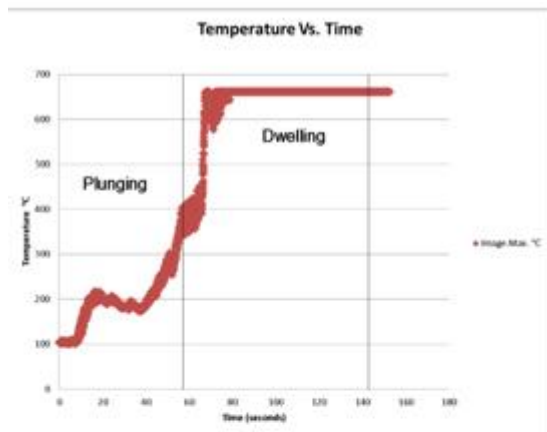
(c)



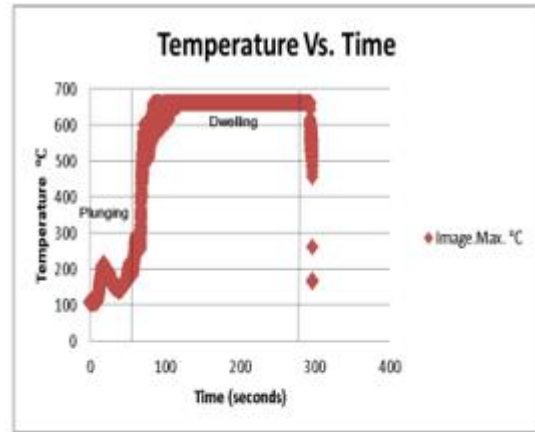
(d)

Image 12.21: Subfigures of Run 3 and Run 4 (a) showing negative results, the detached copper bush of Run 4 (b) and the temperature vs time graphs for Run 3 (c) and Run 4 (d)

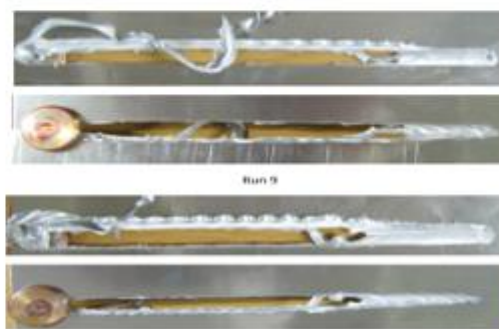
Run 9 with parameters of a rotational speed 800 rpm, feed rate of 100 mm/min, a dwell of 10 second and a plunge depth of 0,3 mm and Run 10 (Image 12.22- (c)) was the most promising of all this could be just before the temperature increases just before the weld reaches 60 seconds (Image 12.22 (a) and (b)). Both of the welds started with positive results however after 60 mm the work piece began flashing out and the copper bush remained attached, possibly due to high heat generation. A change in parameters after the Run 9, Rotation speed 630 rpm, feed rate 50 mm/min, a dwell time of 10 seconds and a plunge depth 0,3 mm showed a minor improvement in Run 10.



(a)



(b)



(c)

Image 12.22: Subfigures Run 9 with a rotational speed of 800 rpm with a feed rate of 100 mm/min and Run 10 a rotational speed of 800 rpm and a plunge of 50 mm/min showing the most promising results. High temperatures could suggest failure as seen in the temperature vs time graphs for Run 9 (a) and Run 10 (b)

On a subsequent welding run, the experiment was conducted once more. Given previous failure to the Innovative Tool on the previous experiment as well as a pin failure, certain parameters were changed during each weld in reference to Table 12.1. The use of material 6082 was used for all the welds regarding the experiment. Run 11 and Run 12 (Image 12.23 (a) and (b)) produced similar results. Run 12 had a change in parameter for the plunge depth of 0.5 mm the material melted into the copper bush and flashed out at 116 °C shows how there was a complete lack of consolidation as well as significant overheating. The material was also hot to touch. Run 13 (Image 12.23- (c)) had a disintegrated copper bush showing extreme signs of melting on the bush which stuck onto the work piece, this was the same with the Run 14 (Image: 12.23- (d)), where the copper bush melted onto the work piece and the pin seemed to engrave itself (Image 12.24 (a) and (b)) into the bush before continuing with a weld without the copper bush, it is possible that rotation was prevented momentarily hence the change in behaviour of the material. The feed rate on the weld was changed to 300 mm/min and a plunge of 0.3 mm was used. Run 12 had less than 20 mm of a good weld whilst Run 13 had 20 mm neat good weld 40mm of skirted weld and 180 mm welding without the copper bush. Similar results were shown in Run 15.



(a)



(b)



(c)



(d)



(e)

Image 12.23: Run 11(a), Run 12 (b), Run 13 (c), Run 14 (d) and Run 15 (e) done on a subsequent day due to pin failure



(a)



(b)

Image 12.24: Copper bushes showing extreme signs of melting during weld Run 13 (a) and Run 14 (b)

12.2.3. Innovative Tool Experimentation: Coolant Applied Tests

As mentioned in earlier in this chapter, the use of coolant is to be used during the experimentation. Whilst conducting the experiment on the innovative tool the use of water as used as a coolant in both ice cold and boiling hot states.

The parameters that were used was of the previous run of experiments, specifically Run 2 (Image 12.20), with parameters of the following: Rotational speed: 800 rpm, Dwell Time: 10 seconds Feed Rate of 300 mm/min and a plunge depth of 0.2 mm.

Run 16 and below before the weld commenced with a temperature of 0.8 °C, the work piece had separated at the start of the weld however gave a 40 mm neat weld and the remainder 160 mm was unsuccessful due to the copper bush melting at the start of the weld. Similar results were shown in Run 17 (Image 12.25 – (b)) however ice cold water was poured directly onto the work piece as the weld was taking place and produced 30 mm of a neat weld. This continued with Run 18 (Image 12.25- (c)) (Iced cold water applied and poured), Run 19 and Run 20 (Image 12.25- (d) and (e)) (Ice cold water applied and poured).

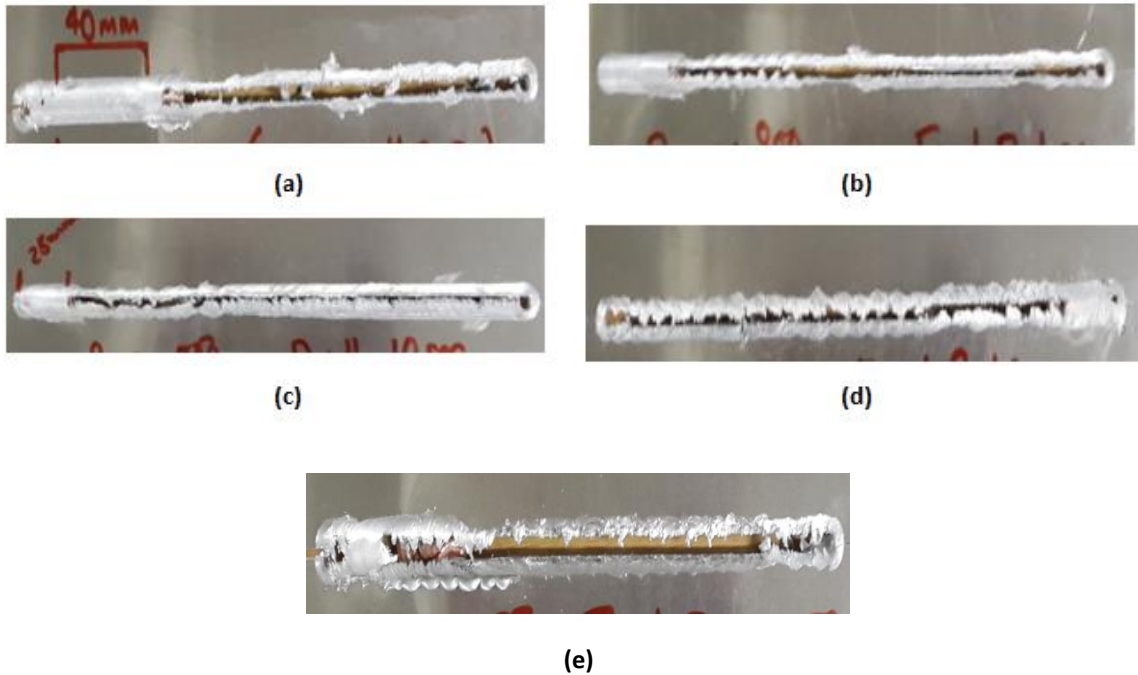
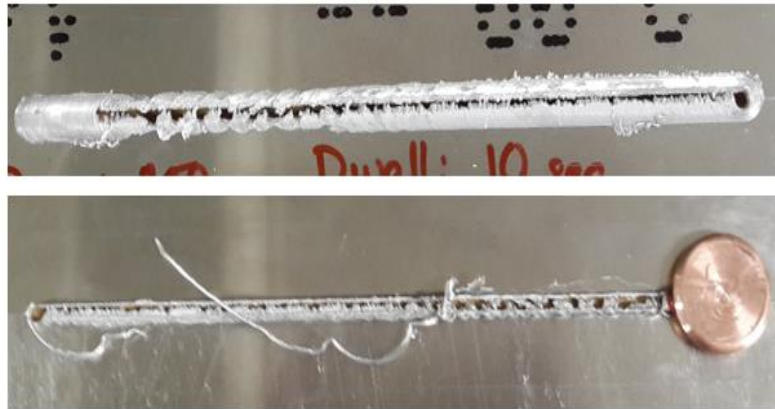


Image 12.25: The coolant applied test using ice cold water which showed significant lowering of heat generation during welds

Run 21, A boiling hot water applied test (Image 12.26), showed a significant failure similar to that of the ice-cold water applied test, however the weld on the material is not neat as the weld performed with the cold water applied test. As mentioned in this chapter, the boiling water should have been significantly lower than that of the heat emitted from the tool rather than when decrease the temperature hot water is applied to the workbench as the tool welds shown in Drw 9.1, the boiling water should have also lowered the yield stress of the material, this was not the case for Run 21 as the copper bush did not conduct the heat generation but over heated and melted into the work piece which stuck at the start of the run in turn causing the rest of the weld to continue without the copper bush.



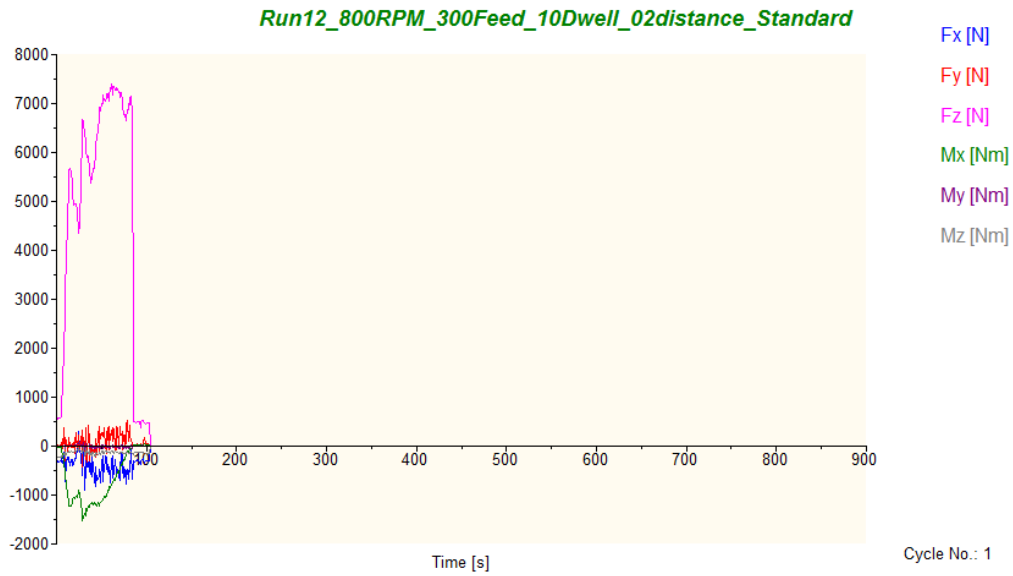
Run 11

Image 12.26: Hot water applied weld front and back showing where the copper bush stuck to the plate

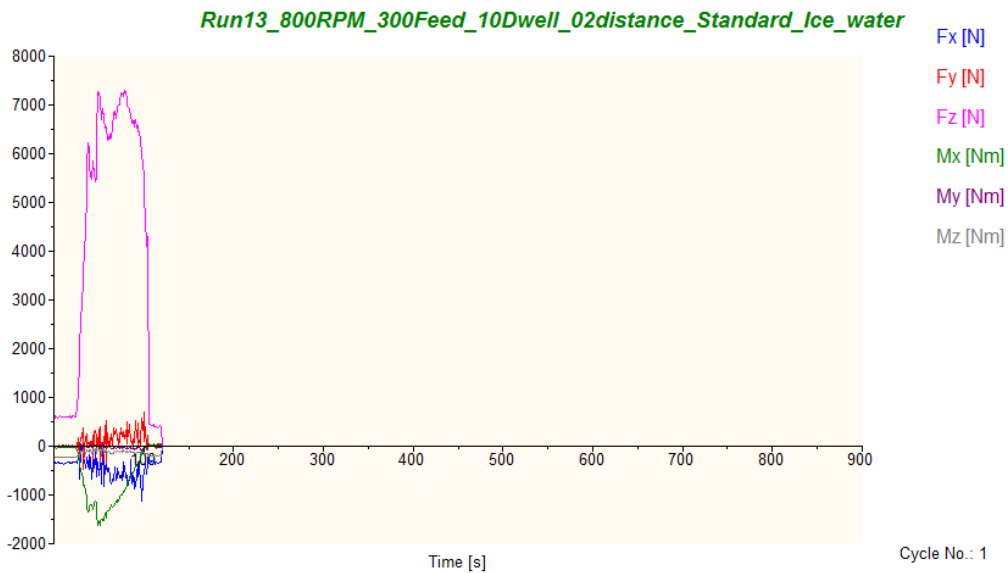
12.3 Force Data Acquisition

12.3.1. Standard Tool: Force Data

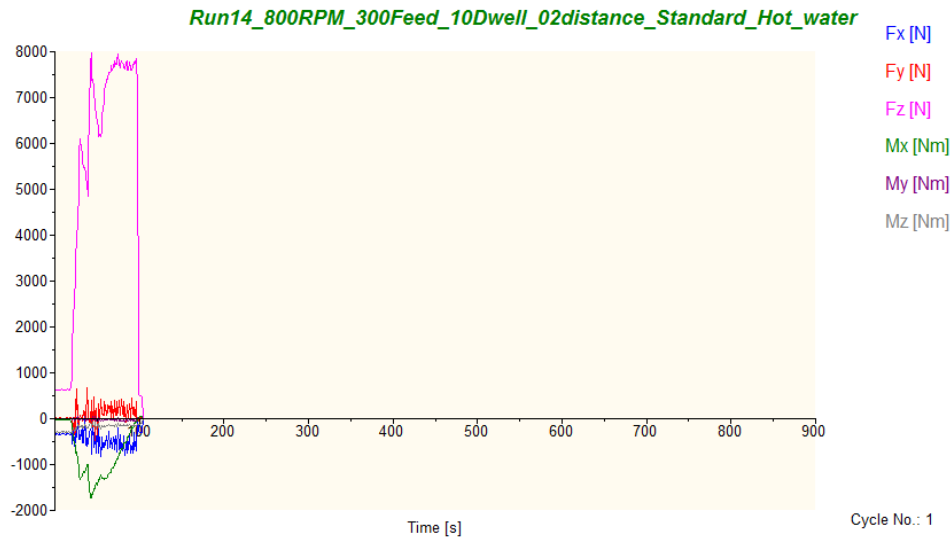
The downward force of the Standard Tool (F_z) is relatively the same with each of the variants. The highest, unlike the Innovative Tool, is the hot water applied test (Graph 12.12) with approximately 7900 N and then the cold water applied test with force that is approximately 7500 N and lastly the Standard weld in normal conditions with a downward force of approximately 7000 N. Table shows the maximum and average force data for each of the trials performed and Table indicates the parameters used for the weld that were performed as with the innovative tool runs.



Graph 12.4: Force Graph for the Standard tool weld in normal conditions



Graph 12.5: Force graph for the Standard Tool weld ice cold water applied weld



Graph 12.6: Force graph for the Standard Tool hot water applied test

	Fx (N)		Fy (N)		Fz (N)	
	Maximum	Average	Maximum	Average	Maximum	Average
Run1	306,40	-379,35	524,29	88,34	7408,45	4722,68
Run2	108,03	-438,54	701,90	100,92	7293,70	4090,26
Run3	57,98	-438,80	662,23	97,89	7980,96	5160,52

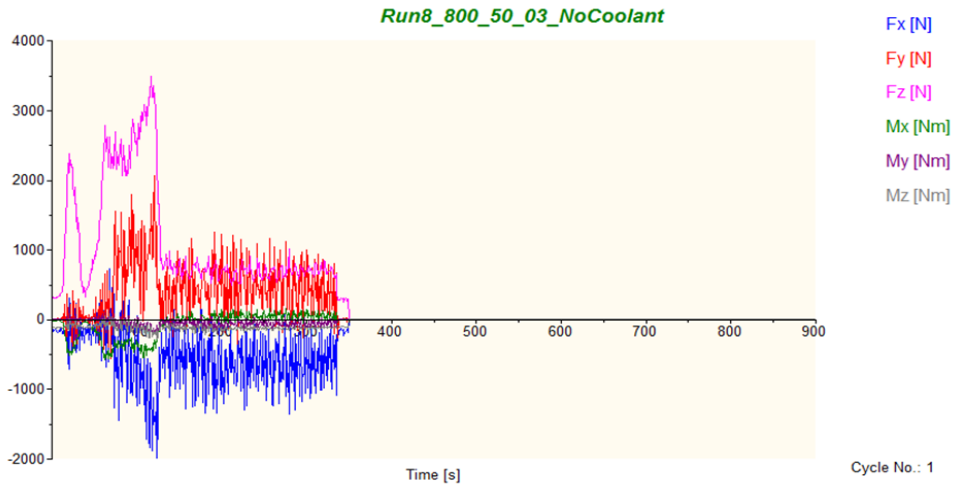
Table 12.3: Table of maximum and average force values for the Standard Tool

12.3.2 Innovative Tool: Force Data

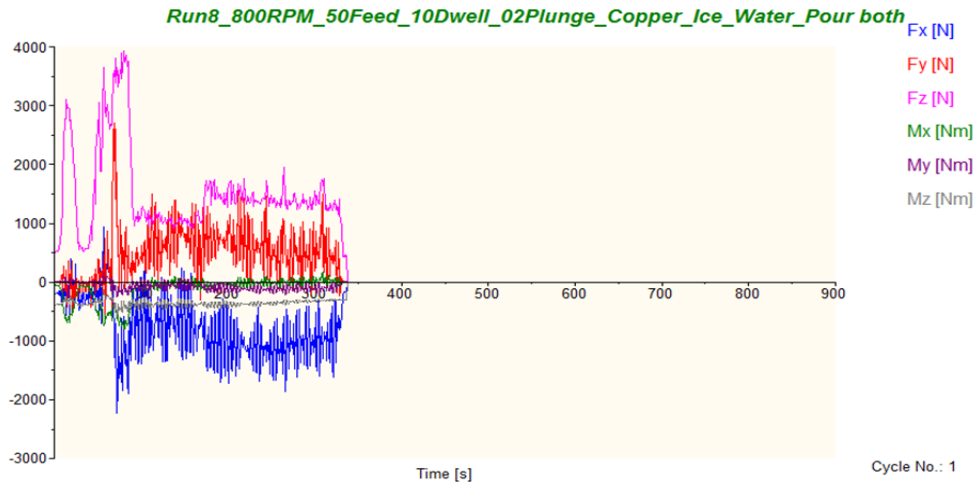
Force data was recorded using the Kistler Piezo-electric force measurement system. Throughout all the welds, values were measured for Fx, Fy and Fz which are the force in the transverse direction to the tool, the force in the welding direction of the tool and the force in the vertical or axial direction.

Force data was acquired when performing the trials outlined in chapter 12, all of the trials show similar trends with the exception of Run 21 where the pin broke. As a result, a decision was taken to display the data comparing Run 8 (Normal Conditions), Run 18 (Iced Cold Water Applied) and Run 21 (Hot Water Applied) as they have the same parameters.

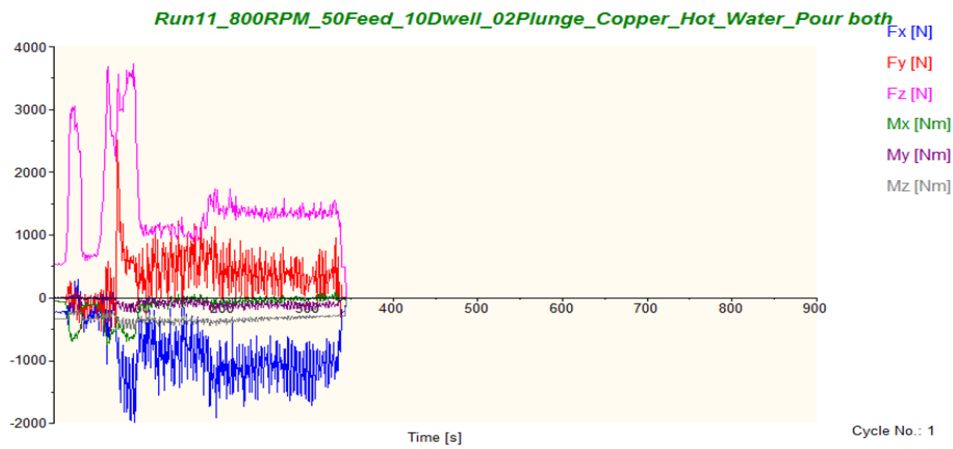
Graphs 12.13, 12.14 and 12.15 are for Fx, Fy and Fz versus time respectively. It can be seen in Graph 12.14 that Run 18- iced water applied weld experienced a maximum welding force of approximately 4000 N whereas Run 21- Hot water applied weld experienced a lesser welding force of approximately 3600 N and the Normal condition weld with the lowest force of approximately 3500 N



Graph 12.7: Innovative Tool Normal conditions force graph



Graph 12.8: Innovative Tool Iced Water applied weld force graph for Run 18



Graph 12.9: Innovative Tool Hot Water applied weld force graph for Run 21

Table 12.4 shows the maximum and average force data for each of the trials performed using the revised geometry and Table indicates the parameters used for the weld that were performed. It can be seen that the maximum Fx and Fz experienced throughout the trials was in Run 18 when the cold water was applied and poured onto the work piece. It is suspected that the forces were also increased due to the fact that the plunge depth during the dwell was inadequate, this could also be the reason for the copper bush not welding in accordance as planned. It can be seen that the maximum Fy was for Run 21 which was at exact parameters to Run 18 with an even worse plunge characteristic and a worse of weld.

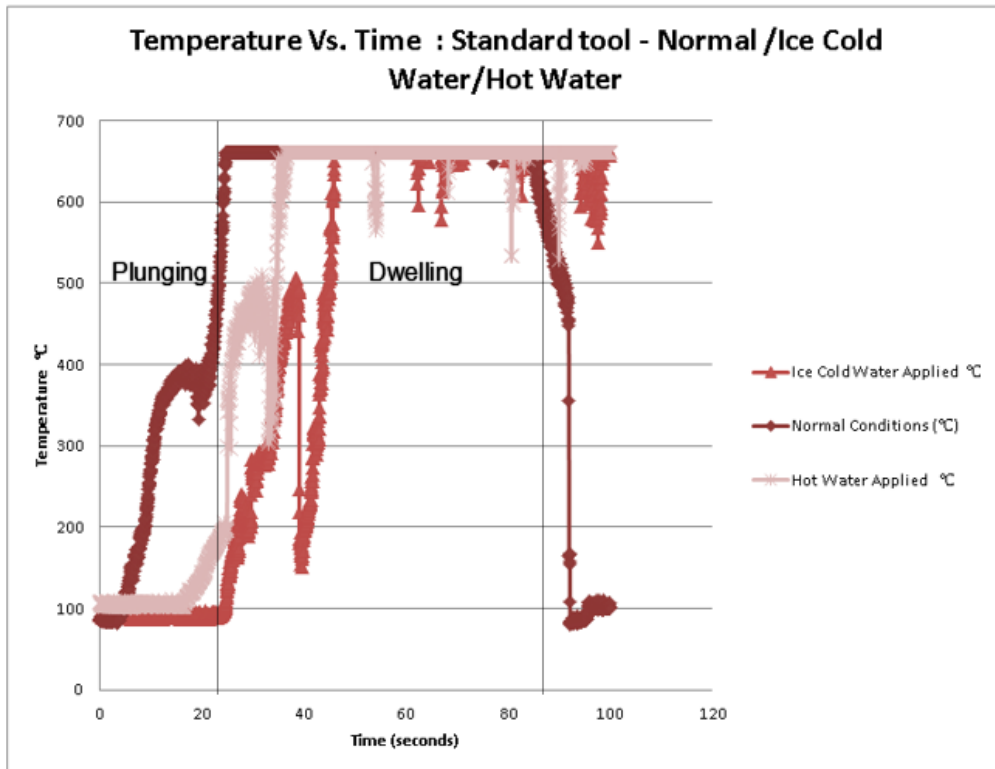
Trial Number	Fx (N)		Fy (N)		Fz (N)	
	Maximum	Average	Maximum	Average	Maximum	Average
Run1	425,42	-87,14	2484,74	263,48	3371,58	727,87
Run2	687,26	-469,68	2574,46	493,85	3839,11	1243,17
Run3	474,854	-514,67	2347,41	517,55	2958,98	1306,87
Run4	575,562	-482,98	3359,99	484,06	3232,42	1397,85
Run5	1280,52	526,27	1610,72	307,00	6817,63	1359,58
Run6	482,788	-700,88	2426,76	546,15	3895,26	1546,70
Run7	480,347	-623,23	3768,92	781,31	3671,88	1707,81
Run8	731,201	-530,10	2060,55	425,81	3492,43	1095,35
Run9	537,109	-852,85	2592,77	559,87	3948,97	1314,24
Run10	516,357	-989,95	3050,54	617,00	3508,30	1698,80
Run11	763,55	-995,47	2983,40	650,20	4149,17	1770,50
Run12	898,44	-957,77	1870,12	410,67	5465,09	1552,35
Run13	857,54	-617,54	2971,19	457,61	6300,05	1931,01
Run14	731,81	-685,70	4237,67	820,22	6220,70	2250,68
Run15	712,28	-929,28	2083,74	544,47	3945,31	1775,32
Run16	645,14	-491,15	4944,46	497,93	5390,63	1641,31
Run17	537,11	-630,91	3389,89	494,64	5666,50	1827,32
Run18	935,67	-760,93	2699,58	479,59	3928,22	1505,74
Run19	332,03	1019,72	3449,71	737,09	5217,29	1643,71
Run20	493,16	1179,16	4796,14	1255,27	6273,19	2273,61
Run21	289,31	-842,28	2513,43	340,63	3729,25	1461,32

Table: 12.4: Table of maximum and average force values for the innovative tool

12.4. Temperature Data

12.4.1. Standard Tool Temperature Data

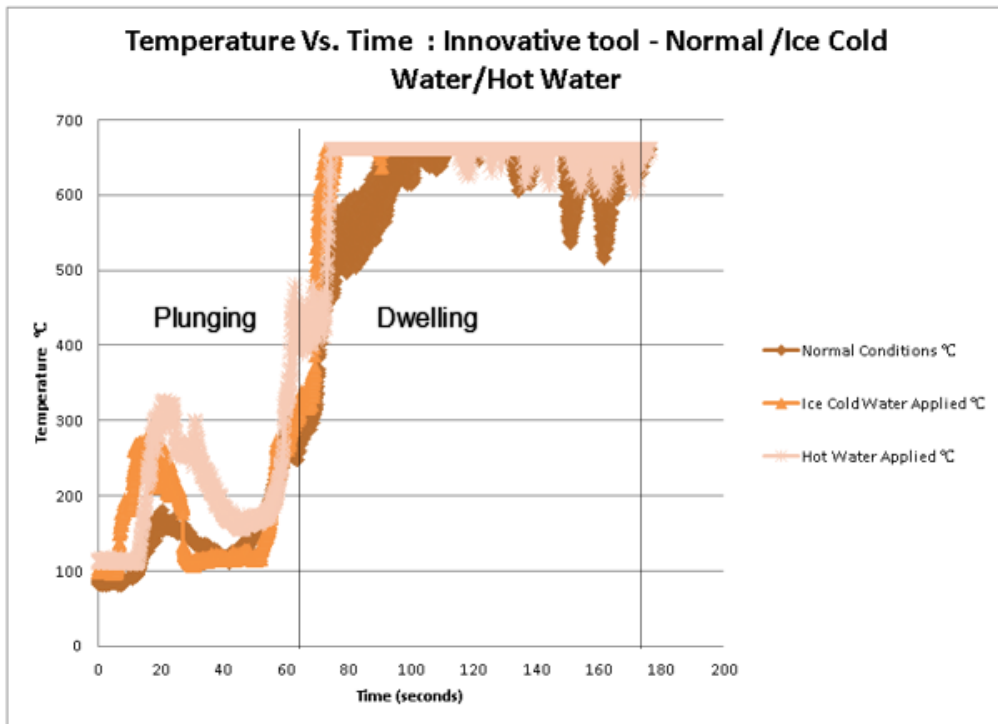
It can be seen that during the weld of the Standard Tool the heat generation is at its most when hot water is applied to the work piece, and remains stable in a normal condition and drops when ice cold water is applied to and gradually poured onto the work piece. This justifies (Graph 12.15) that the coolant that is ice water lowers heat generation as mentioned in chapter 12.



Graph 12.10: Temperature Vs Time: Standard Tool Comparison of Normal Conditions and Coolants

12.4.2. Innovative Tool Temperature Data

As with Standard Tool the iced cold lowered the heat generation substantially, whilst the hot water increased the heat generation. This could be in relation that the hot water increased the heat generation of the weld piece and the copper bush as well as other aspects of the weld that would contribute to any form of heat generation (Graph 12.16).

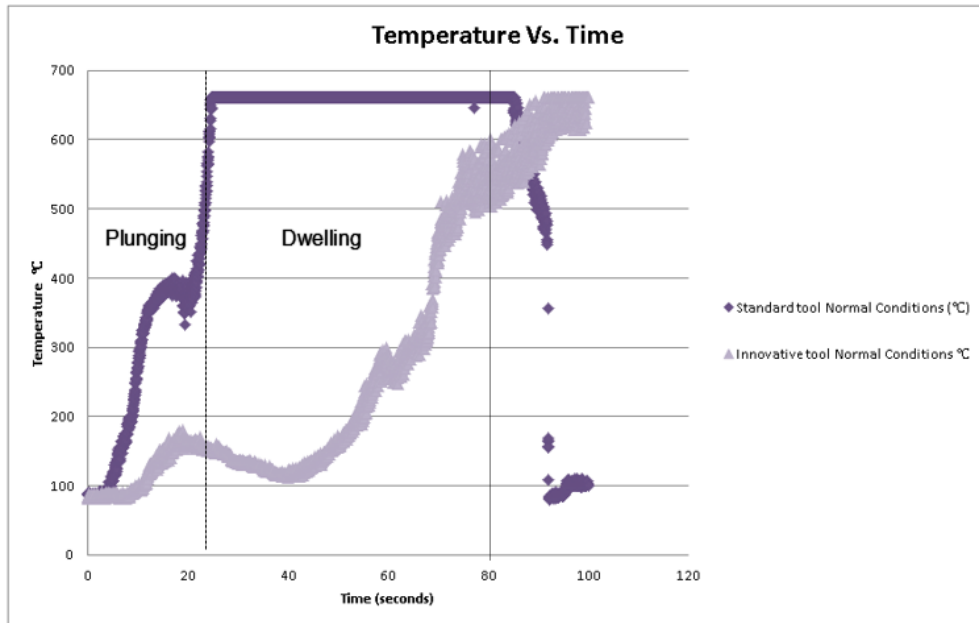


Graph 12.11: Temperature Vs time: Innovative tool comparison of Normal conditions and Coolants

12.5. Comparison Of Temperature: Standard Tool Vs Innovative Tool

The comparison of weld where chosen based on similar parameters performed on each weld.

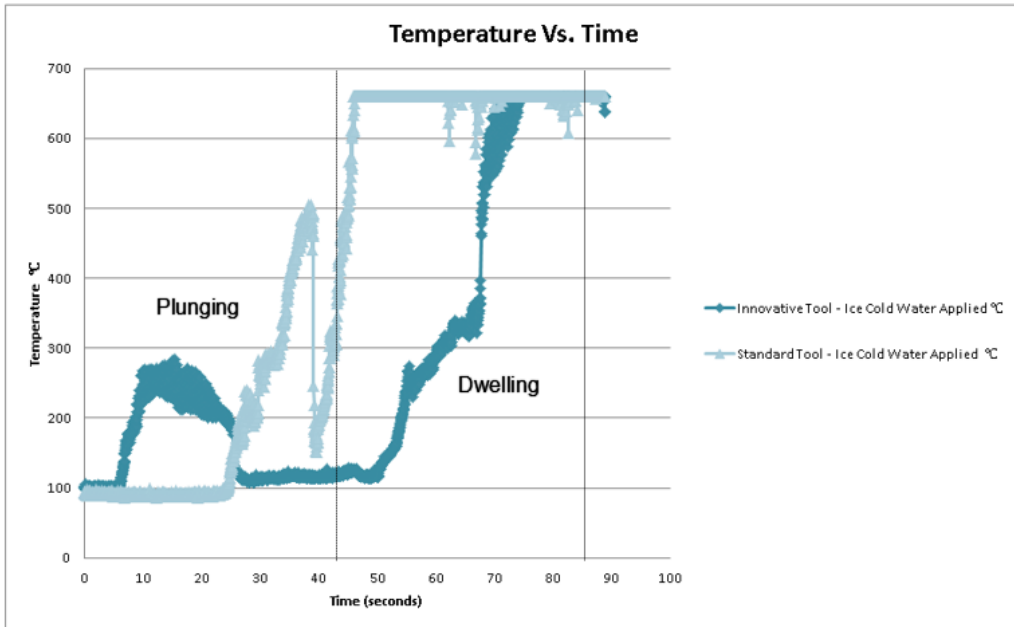
In normal conditions of both the Innovative Tool and the Standard Tool it can be seen (Graph 12.16) that the innovative tool has the least heat generation as the heat generation for the innovative tool remains low consistently threw out the weld. This is possible threw the addition of the copper bush, which conducts any excess heat generation that is emitted.



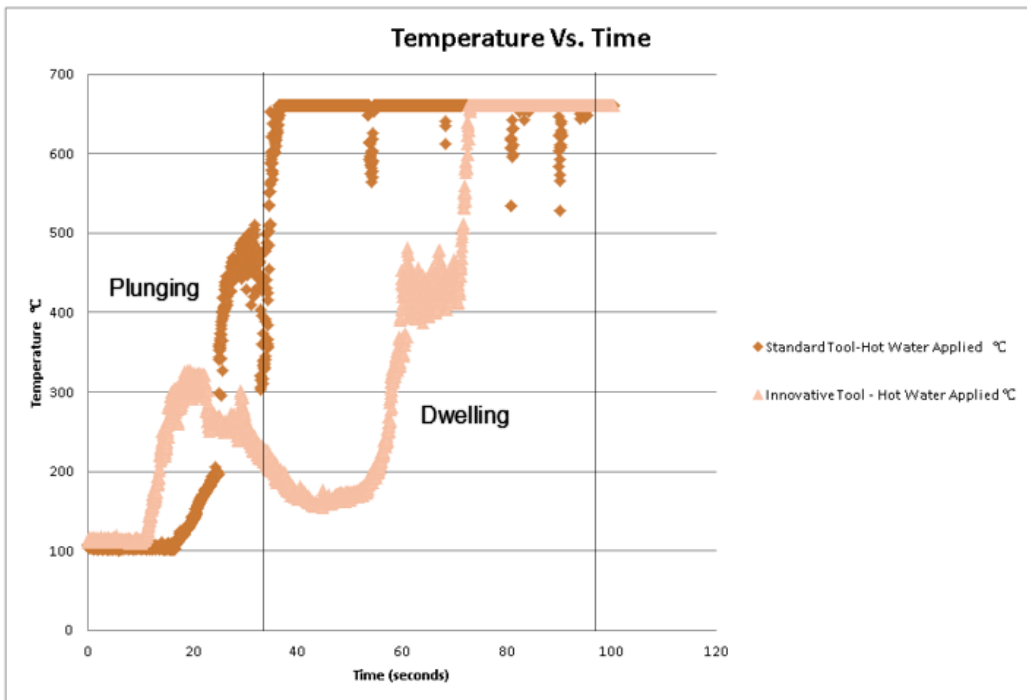
Graph 12.12: Comparison of temperature: Standard tool Vs Innovative tool

12.6. Coolant Applied Comparisons

In the cold water applied test it can be seen (Graph 12.17) that the Innovative Tool has the least amount of heat generation this could be a result of the copper bush cooling down along with the work piece causing additional cooling that assist with heat generation from the tool. The same can be said for the hot water applied test (Graph 12.18) where the copper bush assists with conducting the heat generation from the work piece allowing the Innovative Tool to have the lesser heat generation



Graph 12.13: Ice Cold Water Applied Test Comparison Standard Tool Vs Innovative Tool

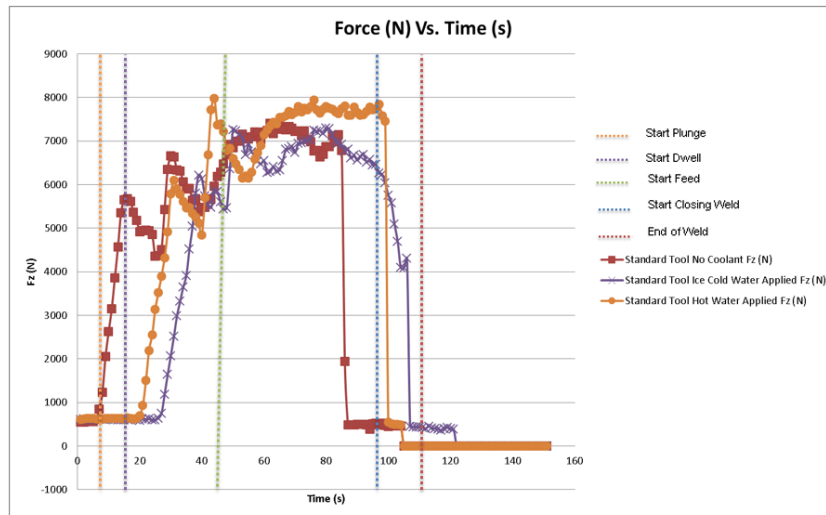


Graph:12.14: Hot Water Applied Test Comparison Standard Tool Vs Innovative Tool

12.7. Force Data

12.7.1. Standard Tool Force Data

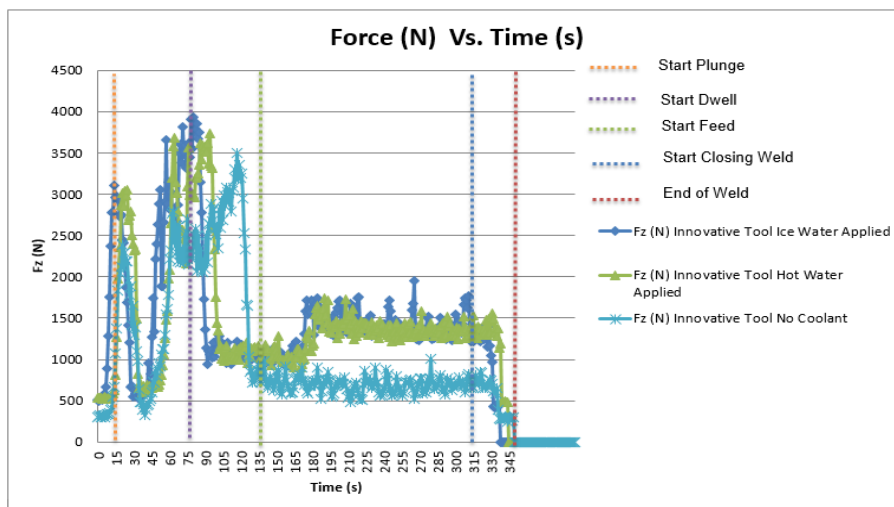
Force on the Standard Tool was show significantly higher when hot water was applied to the this could be due to the high heat generation caused by the hot water and the weld in normal condition remained in between have possibly a Standard Force. Lower force was noticed with the iced water applied test also this could be because of the temperature of the water lowering the heat generation (Graph 12.18).



Graph 12.15: Force data for the Standard tool comparison of a normal weld and coolant applied test

12.7.2. Innovative tool Force Data

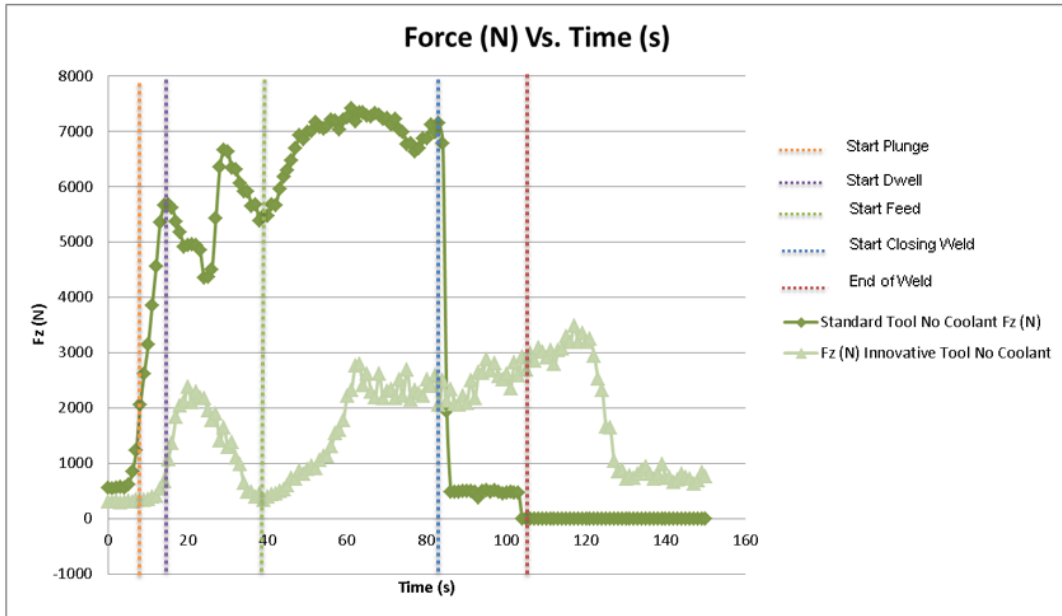
The Innovative Tool, was as similar to the standard where the force on the hot water applied weld was the highest, the weld in normal conditions had a moderate force and the weld that was iced cold water applied was the lowest (Graph 12.19)



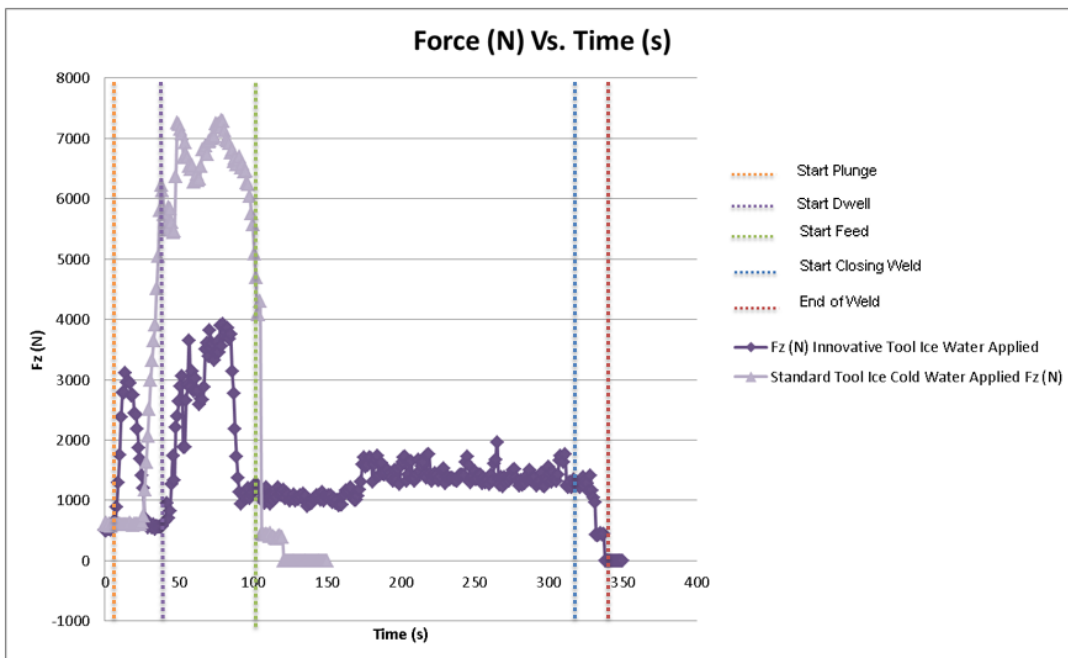
Graph 12.16: Force data for the Innovative tool comparison of a normal weld and coolant applied test

12.7.3. Comparison of Force Data: Standard tool Vs Innovative Tool

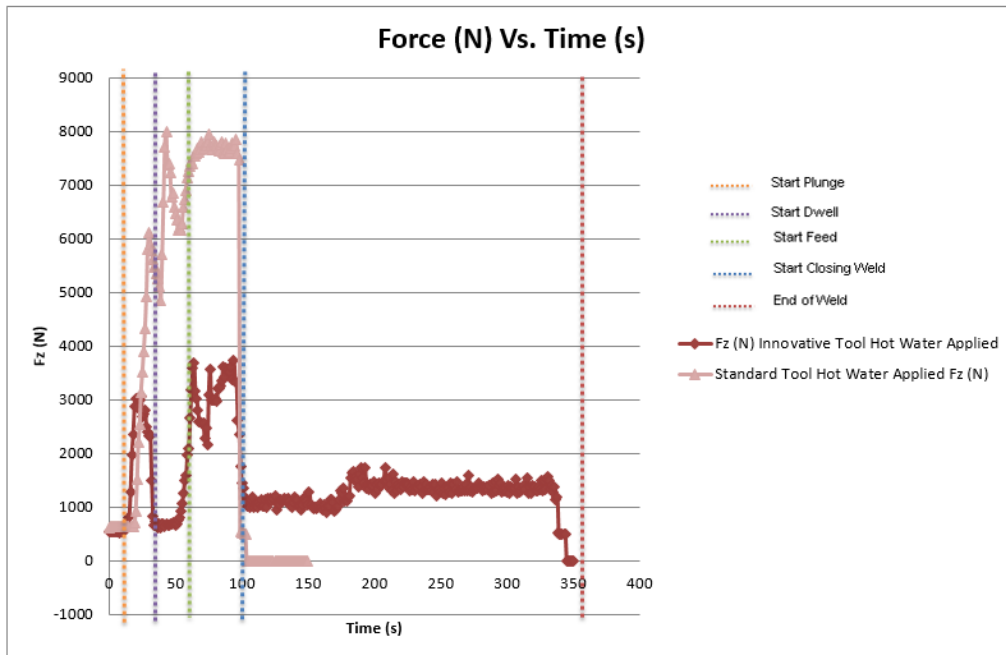
The Innovative Tool shows less force applied to its weld in all three conditions Normal (Graph 12.20), Ice Water Applied (Graph 12.21) and Hot Water Applied (Graph 12.22), this could be in regard with the copper bush once more, because the heat loss is much more in the innovative tool the force on the weld is much less unlike the standard tool. It is therefore concluded that the copper bush does not only assist with the conduction of heat generation but also assist with the impact of force on the welds.



Graph 12.17: Force Comparison for Standard Tool and Innovative Tool in Normal Conditions



Graph 12.18: Force Comparison for Standard Tool and Innovative Tool Ice Water Applied



Graph 12.19: Force comparison for Standard tool and Innovative tool hot water applied

12.8. Discussion of Experimental Benchmark

12.8.1. The Standard Tool Friction Stir Welding

The Standard weld was performed on the material 6082-T6 with a thickness of 1.6 mm, this was done to develop knowledge on the friction stir weld process and to validate as a reference to which the innovative tool welds can be compared with.

The standard tool showed positive welds as all three of the work pieces joined near perfectly and based on the success of the standard process, in terms of its quantitative heat transfer as well as the changes in the thermo-mechanical conditions formulated by the equations developed in previous chapters.

It is well known previous studies that Friction Stir Welding and the success of a weld is largely dependent on the amount of heat transfer to and from the work piece. The fundamental working mechanism of the FSW process is the thermally softened plasticisation of the third body region of the weld. In addition, the lengthened pin was expected to increase process forces due to the increased torque about the base of the tool. As a result, these were the decisive factors in designing the innovative system.

Analytical calculation for the hot water applied on a Standard Tool experimentation show a reduction in heat generation as the heat of the water is meant to reduce yield strength of the Aluminium alloy material which is 2024-T3, during experimentation when the hot water was applied caused an increase in heat generation. The cold water applied on a Standard Tool to reduce the heat generation in both the analytical calculation and the during the experimentation.

12.8.2. The Innovative Tool Friction Stir Welding

The innovative tool weld was performed with the material 6056-T4 and material 6082-T6. This was due to the lab not having the material 2024-T3. The welding of the material was accompanied by a copper bush (CuCrZr) which has a combination of thermal conductivity and shear strength. Some of the problems that was experienced with the innovative weld was, as soon as the first promising weld was given a repeat attempt. The two trials were performed one after the other with the only difference between the two trials being the work piece and a new bush was used as well as the occasional minor change in parameters. While it is entirely possible that the specifications of the bush could lead to weld failure and caused the bush to melt as well as high heat generation. This is when it was decided to use coolants during the welds.

It can be seen that the heat generation drops when iced cold water is applied and poured onto the work piece, even though the weld being unsuccessful. When boiling water is used as a coolant the heat generation rises as a result of the hot water adding to the heat generation of the work piece and the copper bush. During certain welds excess of flashing occurred and during each of the runs the copper bush remained attached and in some cases melted into the work piece. Some welds showed server surface defects these were the cases in which the copper bush melted at the start of weld or a disturbance of sort took place and cause the bush not to rotate entirely. Unfortunately, throughout the innovative experimentation, it was not possible to see beneath the work piece to observe the sliding backing bar and particularly the bush. Features that are unique to the process were observed on the underside of the weld, a cycling rough pattern with ripples embedded in the material. It was expected that possible causes for these features were:

- The 0.1 mm gap between the tool pin and the bushing material was allowing too much material to escape from the weld.
- The sliding backing bar was experiencing too much friction and as a result was being dragged below the work piece.
- The sliding backing bar or bush was rotating below the work piece and completely overheating the weld.

The analytical aspect for the Ice cold water coolant applied test show different results where the heat generation for the Innovative Tool in normal condition was less than when a coolant is applied. However, during experimentation this was reflected oppositely where the heat generation was lowered when coolant was applied to the weld.

When Boiling Hot water is applied to the Innovative weld, the heat generation is lowered, during experimentation the heat generation increases when the water is applied, this is because the Yield Strength is effected by temperature of the water, this could be why in the analytical aspect the heat generation was shown to be lower as it did not take into consideration how the temperature of the water would affect the material.

12.8.3. Standard Tool Vs Innovative Tool: Analytical Results Vs Experimentation

From an analytical aspect it can be seen that the Standard Tool had the lower heat generation than that of the innovative tool in normal conditions, during experimentation the same results were seen, hence the calculation and experimentation is trending.

12.9. Experimental Conclusion

In summary, a logical progression of experimentation principles was followed throughout the welding trials that were preceded by an unsuccessful Friction Stir Weld and thermal model that predicted the process parameters. The result of the design is that it is limited due to the fact that the sliding backing bar and bush cannot be stopped from sticking to the material and welds that had heat generation that was high. It is difficult to state the most advantageous process parameters as it would very much depend on weighted importance of the particular mechanical properties required for the weld's application, however the results of which showed promising signs that the innovative design principle is in fact possible.

A difference in heat generation, however, was taken into account when the coolant was added to the weld plates, as a result the heat generation lowered significantly. The standard tool welds in normal conditions and in conditions where the coolant was applied proved much successful, with the parameters giving weld that had no to very minor defects, grasping from this the used of the coolant Ice cold water can reduce the heat generation of a weld successfully and will surely be able to assist in the future.

13. Final Conclusion

This dissertation is based on the Parametric Thermal Study of Friction Stir Welds. The study has theoretical, analytical, simulation, experimental and design aspects. This specific study has been extensive and well researched to perform a friction stir weld with an innovative tool successfully on the material Al2024-T3. The study on Friction Stir Weld is a knowledgeable one. This study has research on relevant methodology that has been proven by various reference from well-known universities. Topics that have been discussed in this thesis are based on the types of tools, pins and shoulders as well as the use of coolants to reduce temperature.

From the knowledge gathered, the feasibility of this study is that the process of Friction Stir Welding can benefit world to a great deal. Friction Stir Welding can use purpose-designed equipment or modified existing machine tool technology and with the environment dying to pollution the use of friction stir welding becomes not only an affordable option but an eco-friendly one too.

The objective was to ensure a perfect Friction Stir Weld by using coolants to reduce heat generation, it was seen during the analytical aspect of this thesis that this could be achieved successfully, after this simulations were run and the result was constant with the analytical calculations. This allowed to move forward with experimentation, where it was seen that the use of coolants in a standard tool weld that heat generation is reduced when cold water is applied to the the weld but increases when hot water is applied.

The Innovative Tool shows the same results where heat generation is increased when hot water is applied, not only does the heat generation increase on the material but also on the copper bush that is used to assist with reducing the heat generation of the weld, however when cold water is applied to the weld, heat generation is reduced.

14. Recommendation and Future Work

From the knowledge gathered the feasibility of this study, it is learnt that, the process of friction stir welding can benefit world to a great deal. Friction stir welding can use purpose-designed equipment or modified existing machine tool technology and with the environment dying to pollution the use of friction stir welding becomes not only an affordable option but an eco-friendly one too.

The Friction Stir Welding experiments on the Innovative Tool can be tried with different coolants to improve welding process in the future. Future research could use the mean of other thermal aspects for this study, or test on other materials.

References

- [1] TWI, http://www.twi.co.uk/j32k/unprotected/band_1/fswintro.html [Last day of access : (25/07/2012)]
- [2] Chao, Y. J. and Qi, W., 2003, "Heat Transfer in Friction Stir Welding-Experimental and Numerical Studies," ASME Journal of Manufacturing Science and Engineering, 125, pp.138-145.
- [3] Khandkar, Mir Zahedul H and Khan, Jamil A., 2001, "Thermal Modelling of Overlap Friction Stir Welding for Al-Alloys", Journal of Materials Processing & Manufacturing Science.
- [4] Awang, Muccino, Feng, and David, 2005, "Thermo-Mechanical Modeling of Friction Stir Spot Welding (FSSW) Process: Use of an Explicit Adaptive Meshing Scheme", SAE International.
- [5] Heurtier, P.; Desrayaud, C.; Montheillet, F., 2002, "A Thermomechanical Analysis of the Friction Stir Welding Process", Materials Science Forum, p 1537-1542
- [6] Tang, W.; Guo, X.; McClure, J.C.; Murr, L.E.; Nunes, A., 1998, "Heat Input and Temperature Distribution in Friction Stir Welding", Journal of Materials Processing & Manufacturing Science, p 163-172.
- [7] Chao, Yuh J.; Qi, Xinhai, 1998, "Thermal and Thermo-mechanical Modeling of Friction Stir Welding of Aluminum Alloy 6061-T6", Journal of Materials Processing & Manufacturing Science, p 215-233.
- [8] Frigaard Ø, Grong Ø, Bjørneklett B and Midling O T 1999 1st Int. Symp. On Friction Stir Welding (Thousand Oaks, CA)
- [9] Xu S, Deng X and Reynolds A P 2001 Sci. Technol. Weld. Joining 6 191–93
- [10] Frigaard Ø, Grong Ø and Midling O T 2001 Metall. Mater. Trans. A 32 1189–200
- [11] Reynolds A P, Deng X, Seidel T and Xu S 2000 Proc. Joining of Advanced and Specialty Materials (St Louis, MO, ASM International) pp 172–7
- [12] Shercliff H R and Colgrove P A 2002 Math. Modelling Weld. Phenom. 6 927–74
- [13] Thomas W M et al 1991 Friction stir butt welding International Patent Application No PCT/GB92/02203
Thomas W M et al 1995 Friction stir butt welding GB Patent Application No 9125978.8
- [14] The American Society for Metals 1979 Metals Handbook 9th edn, vol 2 pp 75
- [15] Reynolds A P, Deng X, Seidel T and Xu S 2000 Proc. Joining of Advanced and Specialty Materials (St Louis, MO, ASM International) pp 172–7
- [16] Xu S, Deng X and Reynolds A P 2001 Sci. Technol. Weld. Joining 6 191–93
- [17] Frigaard Ø, Grong Ø, Bjørneklett B and Midling O T 1999 1st Int. Symp. On Friction Stir Welding (Thousand Oaks, CA)
- [18] Colegrove P 2000 2nd Int. Symp. On Friction Stir Welding (Gothenburg, Sweden)
- [19] Reynolds A P, Deng X, Seidel T and Xu S 2000 Proc. Joining of Advanced and Specialty Materials (St Louis, MO, ASM International) pp 172–7.
- [20] Chao Y J and Qi X 1999 1st Int. Symp. On Friction Stir Welding (Thousand Oaks, CA, USA)
- [21] Reynolds A P, Lockwood W D and Seidel T U 2000 Mater. Sci. Forum 331–337 1719–24 (Thousand Oaks, CA, USA)

- [22] Shercliff H R and Colgrove P A 2002 *Math. Modelling Weld. Phenom.* 6 927–74
- [23] The American Society for Metals 1979 *Metals Handbook* 9th edn, vol 2 pp 75.
- [24] Khandkar MZH, Khan JA, Reynolds AP (2003) Prediction of Temperature Distribution and Thermal History During Friction Stir Welding: Input Torque Based Model. *Sci Tech Weld Join* 8(3):165–174. Doi: 10.1179/136217103225010943
- [25] Shi Q, Dickerson T and Shercliff H R 2003 4th Int. Symp. On Friction Stir Welding (Park City, UT, USA)
- [26] Dickerson T L, Schmidt H and Shercliff H R submitted
- [27] Comsol Multiphysics, Comsol (2006)
- [28] Dickerson T L, Shercliff H R and Schmidt H 2003 4th Int. Symp. Friction Stir Welding (Park City, UT, USA)
- [29] Tang W, Guo X, McClure J C, Murr L E and Nunes A 1999–2000 *J. Mater. Process. Manuf. Sci.*
- [30] M. Collier, R. Steel, T. Nelson, C. Sorensen, and S. Packer, Grade Development of Polycrystalline Cubic Boron Nitride for Friction Stir Processing of Ferrous Alloys, *Proceedings of the Fourth International Conference on Friction Stir Welding*, May 14–16, 2003 (Park City, UT), TWI, paper on CD.
- [31] R.A. Prado, L.E. Murr, D.J. Shindo, and J.C. McClure, Friction Stir Welding: A Study of Tool Wear Variation in Aluminium Alloy 6061-20%Al₂O₃, *Friction Stir Welding and Processing*, K.V. Jata, M.W. Mahoney, R.S. Mishra, S.L. Semiatin, and D.P. Field, Ed., TMS, 2001, p 105–116.
- [32] P.R. Subramanian, N.V. Nirmalan, L.M. Young, P. Sudkamp, M. Larsen, P.L. Dupree, and A.K. Shukla, Effect of Microstructural Evolution in Mechanical and Corrosion Behaviour of Friction Stir-Processed Aluminium Alloys, *Friction Stir Welding and Processing II*, K.V. Jata, M.W. Mahoney, R.S. Mishra, S.L. Semiatin, and T. Lienert, Ed., TMS, 2003, p 235–242.
- [33] Z.W. Chen and R. Maginness, Formation of Weld Zones During Friction Stir Welding of Aluminium Alloys, *Proceedings of the Fifth International Conference on Friction Stir Welding*, Sept 14–16, 2004 (Metz, France), TWI, paper on CD.
- [34] H. Fujii, Y. Takada, N. Tsuji, and K. Nogi, Friction Stir Welding of Ultrafine Grained Materials, *Proceedings of the Fifth International Conference on Friction Stir Welding*, Sept 14–16, 2004 (Metz, France), TWI, paper on CD.
- [35] M.A. Sutton, A.P. Reynolds, J. Yan, B. Yang, and N. Yuan, Microstructure and Mixed Mode I/II Fracture of AA2524-T351 Base Material and Friction Stir Welds, *Eng. Fract. Mech.*, Vol 73 (No. 4), 2006, p 391–407.
- [36] C.G. Andersson and R.E. Andrews, Fabrication of Containment Canisters for Nuclear Waste by Friction Stir Welding, *Proceedings of the First International Conference on Friction Stir Welding*, June 14–16, 1999 (Thousand Oaks, CA), TWI, paper on CD.
- [37] L. Cederqvist, A Weld That Lasts for 100,000 Years: FSW of Copper Canisters, *Proceedings of the Fourth International Conference on Friction Stir Welding*, May 14–16, 2003 (Park City, UT), TWI, paper on CD.
- [38] L. Cederqvist, FSW to Seal 50 mm Thick Copper Canisters—A Weld That Lasts for 100,000 Years, *Proceedings of the Fifth International Conference on Friction Stir Welding*, Sept 14–16, 2004 (Metz, France), TWI, paper on CD.
- [39] A.P. Reynolds, W. Tang, T. Gnaupel-Herold, and H. Prask, Structure, Properties, and Residual Stress of 304L Stainless Steel Friction Stir Welds, *Scr. Metall*, Vol 48, 2003, p 1289–1294.

- [40] M.W. Mahoney, C.B. Fuller, W.H. Bingel, and M. Calabrese, "Friction Stir Processing of Cast NiAl Bronze," THERMEC 2006, July 4–8, 2006 (Vancouver, Canada), TMS.
- [41] H.J. Liu, H. Fujii, and K. Nogi, Wear Behaviour of Hard Alloy Tools in the Friction Stir Welding of AC4A + 30 vol.% SiCp Aluminium Matrix Composite, Proceedings of the Fifth International Conference on Friction Stir Welding, Sept 14–16, 2004 (Metz, France), TWI, paper on CD.
- [42] M.W. Mahoney, R.S. Mishra, and T.J. Lienert, Ed., TMS, 2005, p 97–104 Y.S. Sato, T.W. Nelson, and C.J. Sterling, Recrystallization in Type 304L Stainless Steel During Friction Stirring, Acta Mater., Vol 53, 2005, p 637–645.
- [43] M.A. Sutton, A.P. Reynolds, B. Yang, and R. Taylor, Mode I Fracture and Microstructure for 2024-T3 Friction Stir Welds, Mater. Sci. Eng. A, Vol 354, 2003, p 6–16
- [44] J. Yan, M.A. Sutton, and A.P. Reynolds, Process-Structure-Property Relationships for Nugget and Heat Affected Zone Regions of AA2524-T351 Friction Stir Welds, Sci. Technol. Weld. Join, Vol 10 (No. 6), 2005, p 725–736.
- [45] W.M. Thomas et al., Friction Stir Welding, U.K. Patent Application 2,306,366, Oct 17, 1996.
- [46] C.J. Dawes and W.M. Thomas, Development of Improved Tool Designs for Friction Stir Welding of Aluminium, Proceedings of the First International Conference on Friction Stir Welding, June 14–16, 1999 (Thousand Oaks, CA), TWI, paper on CD.
- [47] S. Brinckmann, A. von Strombeck, C. Schilling, J.F. dos Santos, D. Lohwasser, and M. Koçak, Mechanical and Toughness Properties of Robotic-FSW Repair Welds in 6061-T6 Aluminium Alloys, Proceedings of the Second International Conference on Friction Stir Welding, June 26–28, 2000 (Gothenburg, Sweden), TWI, paper on CD
- [48] K.J. Colligan, J. Xu, and J.R. Pickens, Welding Tool and Process Parameter Effects in Friction Stir Welding of Aluminium Alloys, Friction Stir Welding and Processing II, K.V. Jata, M.W. Mahoney, R.S. Mishra, S.L. Semiatin, and T. Lienert, Ed., TMS, 2003, p 181–190.
- [49] J. Lumsden, G. Pollock, and M. Mahoney, Effect of Tool Design on Stress Corrosion Resistance of FSW AA7050-T7451, Friction Stir Welding and Processing III, K.V. Jata, M.W. Mahoney, R.S. Mishra, and T.J. Lienert, Ed., TMS, 2005, p 19–25.
- [50] R. Zettler, S. Lomolino, J.F. dos Santos, T. Donath, F. Beckmann, T. Lipman, and D. Lohwasser, A Study of Material Flow in FSW of AA2024-T351 and AA 6056-T4 Alloys, Proceedings of the Fifth International Conference on Friction Stir Welding, Sept 14–16, 2004 (Metz, France), TWI, paper on CD.
- [51] R.W. Fonda, J.F. Bingert, and K.J. Colligan, Texture and Grain Evolutions in a 2195 Friction Stir Weld, Proceedings of the Fifth International Conference on Friction Stir Welding, Sept 14–16, 2004 (Metz, France), TWI, paper on CD.
- [51] T. Hishihara and Y. Nagasaka, Development of Micro-FSW, Proceedings of the Fifth International Conference on Friction Stir Welding, Sept 14–16, 2004 (Metz, France), TWI, paper on CD.
- [52] K. Colligan, Tapered Friction Stir Welding Tool, U.S Patent 6,669,075, Dec 30 2003.
- [53] T.J. Lienert, W.L. Stellwag, Jr., B.B. Grimmett, and R.W. Warke, Friction Stir Welding Studies on Mild Steel, Weld. J., Jan 2003, p 1-s to 9-s.
- [54] S. Packer and R. Steel, "Mega stir Technologies," unpublished research, 2006.

- [55] K.J. Colligan and J.R. Pickens, Friction Stir Welding of Aluminium Using a Tapered Shoulder Tool, Friction Stir Welding and Processing III, K.V. Jata, M.W. Mahoney, R.S. Mishra, and T.J. Lienert, Ed., TMS, 2005, p 161–170.
- [56] C.J. Dawes, P.L. Threadgill, E.J.R. Spurgin, and D.G. Staines, “Development of the New Friction Stir Technique for Welding Aluminium—Phase II,” TWI member report 5651/35/95, Nov 1995.
- [57] T.W. Nelson, H. Zhang, and T. Haynes, Friction Stir Welding of Aluminium MMC 6061-Boron Carbide, Proceedings of the Second International Conference on Friction Stir Welding, June 26–28, 2000 (Gothenburg, Sweden), TWI, paper on CD.
- [58] K. Colligan, Dynamic Material Deformation during Friction Stir Welding of Aluminium, Proceedings of the Second International Conference on Friction Stir Welding, June 26–28, 2000 (Gothenburg, Sweden), TWI, paper on CD.
- [59] B. London, M. Mahoney, M. Bingel, M. Calabrese, R.H. Bossi, and D. Waldron, Material Flow in Friction Stir Welding Monitored with Al-SiC and Al-W Composite Markers, Friction Stir Welding and Processing II, K.V. Jata, M.W. Mahoney, R.S. Mishra, S.L. Semiatin, and T. Lienert, Ed., TMS, 2003, p 3–12.
- [60] R.A. Prado, L.E. Murr, A.R. Rivera, D.J. Shindo, K.F. Soto, G.J. Fernandez, and J.C. McClure, Tool Wear and Shape Optimization in the Friction-Stir Welding of Aluminium Metal-Matrix Composite, Friction Stir Welding and Processing II, K.V. Jata, M.W. Mahoney, R.S. Mishra, S.L. Semiatin, and T. Lienert, Ed., TMS, 2003, p 23–32
- [61] M.A. Sutton, A.P. Reynolds, B. Yang, and R. Taylor, Mixed Mode I/II Fracture of 2024-T3 Friction Stir Welds, Eng. Fract. Mech., Vol 70, 2003, p. 2215–2234.
- [62] P. Volovitch, J.E. Masse, T. Baudin, B. Da Costa, J.C. Goussain, W. Saikaly, and L. Barrallier, Microstructure and Mechanical Properties of Friction Stir Welded Mg Alloy AZ91, Proceedings of the Fifth International Conference on Friction Stir Welding, Sept 14–16, 2004 (Metz, France), TWI, paper on CD.
- [63] M. Attallah and H.G. Salem, Effect of Friction Stir Welding Process Parameters on the Mechanical Properties of the As Welded and Post-Weld Heat Treated AA2095, Proceedings of the Fifth International Conference on Friction Stir Welding, Sept 14–16, 2004 (Metz, France), TWI, paper on CD.
- [64] I. Charit and R.S. Mishra, Low Temperature Super plasticity in a Friction Stir Processed Ultrafine Grained Al-Zn-Mg-Sc Alloy, Acta Mater., Vol 53, 2005, p 4211–4223.
- [65] J. Yan, M.A. Sutton, and A.P. Reynolds, Process-Structure-Property Relationships for Nugget and Heat Affected Zone Regions of AA2524-T351 Friction Stir Welds, Sci. Technol. Weld. Join, Vol 10 (No. 6), 2005, p 725–736.
- [66] F.R. Morral, Ed., Wrought Super alloys, Properties and Selection: Stainless Steels, Tool Materials, and Special Purpose Metals, Vol 3, Metals Handbook, 9th Ed., American Society for Metals, 1980, p 207–237.
- [67] M.W. Mahoney, W.H. Bingel, S.R. Sharma, and R.S. Mishra, Microstructural Modification and Resultant Properties of Friction Stir Processed Cast NiAl Bronze, Mater. Sci. Forum, Vol 426–432, 2003, p2843–2848.
- [68] L. Christodoulou, W. Palko, and C. Fuller, Equipment and Processing Variables Affecting Friction Stir Processing of NiAl Bronze, Friction Stir Welding and Processing III, K.V. Jata, M.W. Mahoney, R.S. Mishra, and T.J. Lienert, Ed., TMS, 2005, p 57–66

- [69] B.M. Tweedy, W. Arbegast, and C. Allen, Friction Stir Welding of Ferrous Alloys Using Induction Preheating, Friction Stir Welding and Processing III, K.V. Jata, M.W. Mahoney, R.S. Mishra, and T.J. Lienert, Ed., TMS, 2005, p 97–104.
- [70] U. Ramasubramanian, W.J. Arbegast, G.A. Stone, and G. Grant, Friction Stir Processing of Class 40 Grey Cast Iron, Friction Stir Welding and Processing III, K.V. Jata, M.W. Mahoney, R.S. Mishra, and T.J. Lienert, Ed., TMS, 2005, p 115–122.
- [71] C.B. Fuller, M.W. Mahoney, W.H. Bingel, M. Calabrese, and B. London, “Tensile and Fatigue Properties of Friction Stir Processed NiAl Bronze,” THERMEC 2006, July 4–8, 2006 (Vancouver, Canada), TMS.
- [72] S.H.C. Park, Y.S. Sato, H. Kokawa, K. Okamoto, S. Hirano, and M. Inagaki, Effect of Microstructure on Corrosion of Friction Stir Welded 304 Stainless Steel, Proceedings of the Fifth International Conference on Friction Stir Welding, Sept 14–16, 2004 (Metz, France), TWI, paper on CD.
- [73] R. Zettler, S. Lomolino, J.F. dos Santos, T. Donath, F. Beckmann, T. Lipman, and D. Lohwasser, A Study of Material Flow in FSW of AA2024-T351 and AA 6056-T4 Alloys, Proceedings of the Fifth International Conference on Friction Stir Welding, Sept 14–16, 2004 (Metz, France), TWI, paper on CD.
- [74] W.M. Thomas, E.D. Nicholas, and S.D. Smith, Friction Stir Welding-Tool Developments, Aluminium 2001, Proceedings of the TMS 2001 Aluminium Automotive and Joining Sessions, S.K. Das, J.G. Kaufman, and T.J. Lienert, Ed., TMS, 2001, p 213.
- [75] W.M. Thomas, D.G. Staines, I.M. Norris, and R. de Frias, “Friction Stir Welding Tools and Developments,” FSW Seminar, Dec 3 2002 (Porto, Portugal), Instituto de Soldadura e Qualidade.
- [76] M. Strangwood, C. Davis, and M. Attallah, Microstructural Development and Thermal Fields Modelling in Friction Stir Welds of Strain-Hardenable Al-Alloys, Proceedings of the Fifth International Conference on Friction Stir Welding, Sept 14–16, 2004 (Metz, France), TWI, paper on CD.
- [77] L. Cederqvist, A Weld That Lasts for 100,000 Years: FSW of Copper Canisters, Proceedings of the Fourth International Conference on Friction Stir Welding, May 14–16, 2003 (Park City, UT), TWI.
- [78] Z.Y. Ma, S.R. Sharma, R.S. Mishra, and M.W. Mahoney, Microstructural Modification of Cast Aluminium Alloys via Friction Stir Processing, Mater. Sci. Forum, Vol 426–432, 2003, p 2891–2896
- [79] P.A. Colegrove, H.R. Shercliff, and P.L. Threadgill, Modelling and Development of the Trivex Friction Stir Welding Tool, Proceedings of the Fourth International Conference on Friction Stir Welding, May 14–16, 2003 (Park City, UT), TWI, paper on CD
- [80] P.A. Colegrove and H.R. Shercliff, Development of Trivex Friction Stir Welding Tool, Part 1: Two-Dimensional Flow Modelling, Sci. Technol. Weld. Join. Vol 9 (No. 4), 2004, p 345–351
- [81] R.J. Ding and P.A. Oelgoetz, Auto adjustable Pin Tool for Friction Stir Welding, U.S. Patent 5893507, April 13, 1999
- [82] R.J. Ding, Force Characterization on the Welding Pin of a Friction Stir Welding Retractable Pin-Tool Using Aluminium-Lithium 2195, Proceedings of the Second International Conference on Friction Stir Welding, June 26–28, 2000 (Gothenburg, Sweden), TWI.
- [83] H Schmidt, J Hattel and J Wert: An analytical model of the heat generation in friction stir welding. Pg. 147-148

- [84] H Schmidt, J Hattel and J Wert: An analytical model of the heat generation in friction stir welding. Pg. 149
- [85] M. Skinner and R.L. Edwards, Improvements to the FSW Process Using the Self- Reacting Technology, Mater. Sci. Forum, Vol 426–432, 2003, p 2849–2854.
- [86] G. Sylva, R. Edwards, and T. Sassa, A Feasibility Study for Self-Reacting Pin Tool Welding of Thin Section Aluminium, Proceedings of the Fifth International Conference on Friction Stir Welding, Sept 14–16, 2004 (Metz, France), TWI.
- [87] F. Marie, D. Allehaux, and B. Esmiller, Development of the Bobbin Tool Technique on Various Aluminium Alloys, Proceedings of the Fifth International Conference on Friction Stir Welding, Sept14–16, 2004 (Metz, France), TWI.
- [88] Lammlein DH (2007) Computational Modelling of Friction Stir Welding.
- [89] Nandan R, Roy GG, Debroy T (2006) Numerical Simulation of Three-Dimensional Heat Transfer and Plastic Flow during Friction Stir Welding. Metall Mater Trans 37(4):1247–1259. Doi: 10.1007/s11661-006-1076-9
- [90] Simar A, Pardoën T, de Meester B (2007) Effect of rotational material flow on temperature distribution in friction stir welds. Sci Tech Weld Join 12(4):324–333. Doi: 10.1179/174329307X197584
- [91] Schmidt H, Hattel J (2005b) Modelling heat flow around tool probe in friction stir welding. Sci-Tech Weld Join 10(2):176–186. Doi: 10.1179/174329305X36070.
- [92] Simar A, Lecomte-Beckers J, Pardoën T, Meester B (2006) Effect of boundary conditions and heat source distribution on temperature distribution in friction stir welding. Sci Tech Weld Join 11(2):170–177. Doi: 10.1179/174329306X84409
- [93] Ulysse P (2002) Three-dimensional modelling of the friction stir-welding process. Int J Mach Tools & Manuf 42(14):1549–1557. Doi: 10.1016/S0890-6955(02)00114-1.
- [94] Hamilton C, Dymek S, Sommers A (2008) A thermal model of friction stir welding in aluminium alloys. Int J Mach Tools & Manuf 48(10):1120–1130. Doi: 10.1016/j.ijmachtools.2008.02.001
- [95] A. Bejan, Heat Transfer 1993.
- [96] Colegrove et Al, 2007
- [97] Friction Stir Welding and Processing, Rajiv. S. Mishra, University of Missouri, Pg.14
- [98] Mofid, Mohammad; Abdollah-Zadeh, Amir; Ghaini, Farshid; Gür and Cemil on published article: Submerged Friction-Stir Welding (SFSW) Underwater and Under Liquid Nitrogen: An Improved Method to Join Al Alloys to Mg Alloys Book Ref: Metallurgical & Materials Transactions. Part A; Dec2012, Vol. 43 Issue 13, p5106
- [99] Welding Metallurgy 2nd Edition, Sindo Kou Professor and Chair: Department Of Materials Science and Engineering University of Wisconsin
- [100] EGE University, Dr Hüseyin Günerhan
- [101]Timorthy. J. Minton- Friction Stir Welding of Commercially Available Superplastics- Department of Engineering and Design, Burnrel University.